

ADVANCES in ENGINEERING MECHANICS and MATERIALS

**Proceedings of the 2014 International Conference on Civil Engineering
(CIVILENG 2014)**

**Proceedings of the 2014 International Conference on Industrial
Engineering (INDE 2014)**

**Proceedings of the 2014 International Conference on Continuum
Mechanics (COME 2014)**

**Proceedings of the 2014 International Conference on Materials
(MATERIALS 2014)**

**Santorini Island, Greece
July 17-21, 2014**

ADVANCES in ENGINEERING MECHANICS and MATERIALS

**Proceedings of the 2014 International Conference on Civil Engineering
(CIVILENG 2014)**

**Proceedings of the 2014 International Conference on Industrial
Engineering (INDE 2014)**

**Proceedings of the 2014 International Conference on Continuum
Mechanics (COME 2014)**

**Proceedings of the 2014 International Conference on Materials
(MATERIALS 2014)**

**Santorini Island, Greece
July 17-21, 2014**

Copyright © 2014, by the editors

All the copyright of the present book belongs to the editors. All rights reserved. No part of this publication may be reproduced, stored in a retrieval system, or transmitted in any form or by any means, electronic, mechanical, photocopying, recording, or otherwise, without the prior written permission of the editors.

All papers of the present volume were peer reviewed by no less than two independent reviewers. Acceptance was granted when both reviewers' recommendations were positive.

ISBN: 978-1-61804-241-5

ADVANCES in ENGINEERING MECHANICS and MATERIALS

**Proceedings of the 2014 International Conference on Civil Engineering
(CIVILENG 2014)**

**Proceedings of the 2014 International Conference on Industrial
Engineering (INDE 2014)**

**Proceedings of the 2014 International Conference on Continuum
Mechanics (COME 2014)**

**Proceedings of the 2014 International Conference on Materials
(MATERIALS 2014)**

**Santorini Island, Greece
July 17-21, 2014**

Organizing Committee

General Chairs (EDITORS)

- Prof. Nikos Mastorakis, Technical University of Sofia, Bulgaria
- Prof. J. D. Yau, Tamkang University, Taiwan
- Prof. Vladimir Sokolov, University of Karlsruhe, Germany
- Prof. Ottavia Corbi, University of Naples Federico II, Italy
- Prof. Rui Pedro Juliao, Universidade Nova De Lisboa, Portugal
- Prof. Reinhard Neck, Klagenfurt University, Austria
- Prof. Bogdan Epureanu, University of Michigan, USA
- Prof. Cho W. Solomon To, University of Nebraska, USA
- Prof. Hyung Hee Cho, Yonsei University and The National Academy of Engineering of Korea, Korea
- Prof. Manijeh Razeghi, Northwestern University, USA
- Prof. Jun Zhang, Inner Mongolia University, P. R. China
- Prof. Samuel Lofland, Rowan University, USA

Associate Editors:

- Viacheslav Pshikhopov
- Dora Foti

Senior Program Chair

- Prof. Shoji Arai, Kanazawa University,
Kanazawa, Ishikawa Prefecture,
Japan

Program Chairs

- Prof. Panos Pardalos,
Department of University of Florida,
USA
- Prof. Filippo Neri
Dipartimento di Informatica e Sistemistica
University of Naples "Federico II"
Naples, Italy
- Prof. A. Stamou,
National Technical University
of Athens, Greece

Tutorials Chair

- Prof. M.Mimikou
National Technical University
of Athens, Greece

Special Session Chair

- Prof. E.Baltas
National Technical University
of Athens, Greece

Workshops Chair

- Prof. Hyung Hee Cho, ASME Fellow,
Yonsei University (and National
Academy of Engineering of Korea),
Korea

Local Organizing Chair

- Dr. Claudio Guarnaccia, University of Salerno, Italy

Publication Chair

- Prof. Marcin Kaminski,
Department of Structural Mechanics,
Al. Politechniki 6, 90-924 Lodz, Poland

Publicity Committee

- Prof. Kumar Tamma,
University of Minnesota,
Minneapolis, MN, USA
- Prof. Gang Yao,
University of Illinois at Urbana -
Champaign, USA

International Liaisons

- Prof. Quan Wen,
Department of Economics University of Washington,
Seattle, WA, USA
- Prof. Fotios Rigas,
School of Chemical Engineering,
National Technical University of Athens,
Greece.
- Prof. Vincenzo Niola
Departement of Mechanical Engineering for Energetics
University of Naples "Federico II"
Naples, Italy
- Prof. Christopher G. Provatidis,
National Technical University of Athens,
Zografou, Athens, Greece

Steering Committee

- Prof. Aida Bulucea, University of Craiova, Romania
- Prof. Zoran Bojkovic, Univ. of Belgrade, Serbia
- Prof. Reinhard Neck, Klagenfurt University, Klagenfurt, Austria
- Prof. Imre Rudas, Obuda University, Budapest, Hungary
- Prof. Metin Demiralp, Istanbul Technical University, Turkey
- Prof. Ottavia Corbi, University of Naples Federico II, Italy

Program Committee

Prof. Gang-Yu Liu, University of California, Davis Campus, CA, USA
Prof. Zhibing Zhang, University of Birmingham, Birmingham, UK
Prof. Jean-Francois Gohy, Université catholique de Louvain, Belgium
Prof. Waler Caseri, ETH, Zurich, Switzerland
Prof. Jacques Desbrieres, Universite De Pau Et Des Pays De L'Adour, France
Prof. Adrian Schumpe, Technical University of Braunschweig, Germany
Prof. Chris Bowen, University of Bath, Bath, UK
Prof. Jerzy Baldyga, Technical Univeristy Warszawska, Poland
Prof. Alirio Rodrigues, University of Porto, Portugal
Prof. Mostafa Barigou, University of Birmingham, Birmingham, UK
Prof. Jaime Wisniak, Ben-Gurion University of the Negev, Beer-Sheva, Israel
Prof. Sohail Murad, University of Illinois at Chicago, USA
Prof. Konstantinos E. Kakosimos, Texas A&M University at Qatar, Doha, Qatar
Prof. Raghunath V. Chaudhari, University of Kansas, USA
Prof. Xijun Hu, The Hong Kong University of Science and Technology, Kowloon, Hong Kong
Prof. Deepak Kunzru, Indian Institute of Technology, Kanpur, India
Prof. Amit Bandyopadhyay, AAAS Fellow , ASM International Fellow , AIMBE Fellow and ACerS Fellow, Washington State University, Pullman, State of Washington, USA
Prof. Yong Ding, Georgia Institute of Technology, Atlanta, GA, USA
Prof. Yulin Deng, Georgia Institute of Technology, Atlanta, GA, USA
Prof. Paul H. Holloway, Distinguished Prof., University of Florida, Gainesville FL, USA
Prof. Saad Khan, North Carolina State University, Raleigh, North Carolina, USA
Prof. Manijeh Razeghi, Northwestern University, Evanston, IL, USA
Prof. Igor Sevostianov, New Mexico State University, Las Cruces, New Mexico, USA
Prof. Mohindar S. Seehra, West Virginia University, Morgantown, West Virginia, USA
Prof. Tao Liu, Florida State University, Tallahassee, Florida, USA
Prof. Daniel Guay, Institut National de la Recherche Scientifique, Universite du Quebec, Quebec, Canada
Prof. Tian Tang, University of Alberta, Edmonton, Alberta, Canada
Prof. Roland Frankenberger, University of Marburg, Marburg, Germany
Prof. Mohamedally Kurmoo, Universite de Strasbourg, Strasbourg, France
Prof. C. C. Sorrell, University of New South Wales, Sydney, NSW, Australia
Prof. Concepcion Lopez, Universitat de Barcelona, Barcelona, Spain
Prof. Alan Dalton, University of Surrey, Guildford, Surrey, UK
Prof. Kourosh Kalantar-Zadeh, RMIT University, Melbourne, Australia
Prof. Constantinos Tsitsilianis, University of Patras, Patras, Greece
Prof. Tetsu Yonezawa, Hokkaido University, Kita Ward, Sapporo, Hokkaido Prefecture, Japan
Prof. Daolun Chen, Ryerson University, Toronto, Ontario, Canada
Prof. Mohamed M. Chehimi, Universite Paris Diderot, Paris, France
Prof. Vincenzo Fiorentini, Universita degli studi di Cagliari, Cagliari, Italy
Prof. Tamas Ungar, Eotvos Lorand University (ELTE), Budapest, Hungary
Prof. Anthony W. Coleman, Universite Claude Bernard Lyon 1, Lyon, France
Prof. Albert Chin, IEEE Fellow, OSA Fellow, National Chiao Tung University, Hsinchu, Taiwan
Prof. Artur Cavaco-Paulo, Universidade do Minho, Braga, Portugal
Prof. Yoshihiro Tomita, Kobe University, Kobe, Japan
Prof. Jian Wang, Los Alamos National Laboratory, Los Alamos, NM, USA
Prof. Byung K. Kim, Pusan National University, Busan, South Korea
Prof. John T. Sheridan, University College Dublin, Belfield, Dublin, Ireland
Prof. Chi-Wai Chow, National Chiao Tung University, Hsinchu, Taiwan
Prof. Christian M. Julien, Universite Paris-6, Paris, France
Prof. Chun-Hway Hsueh, National Taiwan University, Taipei, Taiwan
Prof. Hyung-Ho Park, Yonsei University, Seodaemun-gu, Seoul, Korea
Prof. Victor M. Castano, Universidad Nacional Autonoma de Mexico, Mexioco City, Mexico
Prof. Peter Chang, University of Saskatchewan, Saskatoon, Saskatchewan, Canada

Prof. Dean-Mo Liu, National Chiao Tung University, HsinChu, Taiwan
Prof. Rui Vilar, Instituto Superior Tecnico, Lisboa, Portugal
Prof. Hugh J. Byrne, Dublin Institute of Technology, Dublin, Ireland
Prof. Won-Chun Oh, Hanseo University, Seosan-si, Chungcheongnam-do, South Korea
Prof. Yuanhua Lin, Tsinghua University, Haidian, Beijing, China
Prof. S.C. Tjong, City University of Hong Kong, Sham Shui Po District, New Kowloon, Hong Kong
Prof. Huan-Tsung Chang, National Taiwan University, Taipei City, Taiwan
Prof. Yoshitake Masuda, National Institute of Advanced Industrial Science and Technology, Tokyo, Japan
Prof. Jing Zhang, Donghua University, Shanghai, China
Prof. Veronica Cortes de Zea Bermudez, Universidade de Tras-os-Montes e Alto Douro, Vila Real, Portugal
Prof. Jun Zhang, Inner Mongolia University, Hohhot, Inner Mongolia, China
Prof. Israel Felner, Hebrew University of Jerusalem, Jerusalem, Israel
Prof. Sukhvinder Badwal, CSIRO Energy Technology, Australia
Prof. Te-Hua Fang, National Kaohsiung University of Applied Sciences (KUAS), Kaohsiung, Taiwan
Prof. Belkheir Hammouti, Mohammed Premier University, Oujda, Morocco
Prof. Mohd Sapuan Salit, Universiti Putra Malaysia, Selangor, Malaysia
Prof. Kwansoo Chung, Seoul National University, Seoul, South Korea
Prof. Zhongfang Chen, University of Puerto Rico, San Juan, Puerto Rico
Prof. Soon-Ku Hong, Chungnam National University, Daejeon, South Korea
Prof. Hannes Jonsson, University of Iceland, Reykjavik, Iceland
Prof. Culea Eugen, Technical University of Cluj-Napoca, Cluj-Napoca, Romania
Prof. Vesselin Dimitrov, University of Chemical Technology and Metallurgy, Sofia, Bulgaria
Prof. Shadpour Mallakpour, Isfahan University of Technology, Isfahan, Iran
Dr. Stergios Pispas, National Hellenic Research Foundation (NHRF), Athens, Greece
Dr. Anna Lukowiak, Polish Academy of Science, Wroclaw, Poland
Dr. Dimitris Tsiourvas, NCSR "Demokritos", IAMPPNM, Dept. of Physical Chemistry, 15310 Aghia Paraskevi, Attiki, Greece.

Additional Reviewers

Santoso Wibowo	CQ University, Australia
Lesley Farmer	California State University Long Beach, CA, USA
Xiang Bai	Huazhong University of Science and Technology, China
Jon Burley	Michigan State University, MI, USA
Genqi Xu	Tianjin University, China
Zhong-Jie Han	Tianjin University, China
Kazuhiko Natori	Toho University, Japan
João Bastos	Instituto Superior de Engenharia do Porto, Portugal
José Carlos Metrôlho	Instituto Politecnico de Castelo Branco, Portugal
Hessam Ghasemnejad	Kingston University London, UK
Matthias Buyle	Artesis Hogeschool Antwerpen, Belgium
Minhui Yan	Shanghai Maritime University, China
Takuya Yamano	Kanagawa University, Japan
Yamagishi Hiromitsu	Ehime University, Japan
Francesco Zirilli	Sapienza Università di Roma, Italy
Sorinel Oprisan	College of Charleston, CA, USA
Ole Christian Boe	Norwegian Military Academy, Norway
Deolinda Rasteiro	Coimbra Institute of Engineering, Portugal
James Vance	The University of Virginia's College at Wise, VA, USA
Valeri Mladenov	Technical University of Sofia, Bulgaria
Angel F. Tenorio	Universidad Pablo de Olavide, Spain
Bazil Taha Ahmed	Universidad Autonoma de Madrid, Spain
Francesco Rotondo	Polytechnic of Bari University, Italy
Jose Flores	The University of South Dakota, SD, USA
Masaji Tanaka	Okayama University of Science, Japan
M. Javed Khan	Tuskegee University, AL, USA
Frederic Kuznik	National Institute of Applied Sciences, Lyon, France
Shinji Osada	Gifu University School of Medicine, Japan
Dmitrijs Serdjuks	Riga Technical University, Latvia
Philippe Dondon	Institut polytechnique de Bordeaux, France
Abelha Antonio	Universidade do Minho, Portugal
Konstantin Volkov	Kingston University London, UK
Manoj K. Jha	Morgan State University in Baltimore, USA
Eleazar Jimenez Serrano	Kyushu University, Japan
Imre Rudas	Obuda University, Budapest, Hungary
Andrey Dmitriev	Russian Academy of Sciences, Russia
Tetsuya Yoshida	Hokkaido University, Japan
Alejandro Fuentes-Penna	Universidad Autónoma del Estado de Hidalgo, Mexico
Stavros Ponis	National Technical University of Athens, Greece
Moran Wang	Tsinghua University, China
Kei Eguchi	Fukuoka Institute of Technology, Japan
Miguel Carriegos	Universidad de Leon, Spain
George Barreto	Pontificia Universidad Javeriana, Colombia
Tetsuya Shimamura	Saitama University, Japan

Table of Contents

Plenary Lecture 1: Investigate of Air Core Phenomenon in Cylindrical Tank during Draining <i>Chang Hyun Sohn</i>	15
Research of the Controlled Flight Dynamics based on the Full and Simplified Quadrotor Models <i>I. Shapovalov, V. Soloviev, V. Finaev, D. Beloglazov, J. Zargaryan, E. Kosenko</i>	17
Nonlinear Optical Response of a Coupled Quantum Dot - Metal Nanoparticle System <i>Spyridon G. Kosionis, Andreas F. Terzis, John Boviatsis, Emmanuel Paspalakis</i>	23
Design of the Intelligent Adaptive Hybrid Control System for Autonomous Mobile Robot on the Basis of Neuro-Fuzzy Networks <i>V. Finaev, I. Kobersy, D. Beloglazov, I. Shapovalov, E. Kosenko, V. Soloviev</i>	28
BBIPED: BCAM-Baltogar Industrial Platform for Engineering Design <i>C. Alonso-Montes, I. Garcia, A. Ramezani, L. Remaki</i>	34
Performance Analysis of a Self Driven Phase Shifted Full Bridge Converter for Data Center Applications <i>Sevilay Cetin</i>	41
Mobile Objects Control in Unknown Environments <i>Viacheslav Pshikhopov</i>	48
Dimensional Accuracy Optimization of Prototypes produced by PolyJet Direct 3D Printing Technology <i>J. Kechagias, P. Stavropoulos, A. Koutsomichalis, I. Ntintakis, N. Vaxevanidis</i>	61
Shape Optimization of Composite Structure under Uncertainty <i>J. Auzins, A. Janushevskis, A. Melnikovs, J. Janushevskis</i>	66
The Application of Variational Principles in Hydrodynamic Theory of Lubrication <i>L. Savin, A. Kornaev, E. Kornaeva</i>	72
Natural Frequency Automatic Variation in Earthquake Isolation System <i>Federico Bartolozzi</i>	77
Mechanical Properties of Composite Hydrogel Materials based on Poly(Acrylamide) and Clay Minerals and their Potential Application for Cleaning of the Internal Surface of Pipes <i>Zhanar Ibrayeva, Evgeniy Blagikh, Sarkyt Kudaibergenov</i>	80
Mathematical Modelling of Orbits for Geodetic Satellites <i>Jaroslav Klokočník, Aleš Bezděk, Jan Kostelecký</i>	85

Design of a 22kW Charging Station for LV Distribution Grid Control	89
<i>Dario De Santis, Gaetano Abbatantuono, Sergio Bruno, Massimo La Scala</i>	
Retrofitting of Precast Reinforced Concrete Wall Panel using Carbon Fiber Strips	93
<i>M. Fofiu, I. A. Bindean, E. Partene, V. Stoian</i>	
Influence of Substrate Properties on Evaporation of the Sessile Drop	98
<i>O. V. Nagornov, N. V. Starostin</i>	
(Bio) Polymer Packaging Films and their Properties	101
<i>A. Tesarikova, A. Kalendova, D. Merinska</i>	
Optimal Model of a Masonry Building Structure with Wooden Floors	105
<i>Mariella Diaferio, Dora Foti, Nicola Ivan Giannoccaro, Salvador Ivorra</i>	
TRM Strengthening of Precast Reinforced Concrete Wall Panel with Cut-Out Opening - Experimental Investigation	110
<i>C. Todut, D. Dan, V. Stoian</i>	
Evaluation of Concrete Deterioration through Artificial Neural Networks based Systems	117
<i>Guida Gomes, Henrique Vicente, José Neves</i>	
Non-Destructive Detection of Metal Fibres in Cementitious Composites	125
<i>Jiri Vala, Leonard Hobst, Vladislav Kozak</i>	
Planning the Coastal Management. The Apulia Region Plan	129
<i>C. Piscitelli, F. Rotondo, F. Selicato, S. Selicato</i>	
About the Place of Installation of a Gas Cooker in the Kitchen	137
<i>Iu. H. Polandov, M. A. Barg, V. A. Babankov</i>	
Effect of Carburizing on Fatigue Life of Highstrength Steel Specimen under Push-Pull Loading	143
<i>Štěpán Major, Vladimír Jakl, Štěpán Hubálovský</i>	
PERPETUATE Project: Guidelines for the Seismic Performance-based Assessment of Cultural Heritage Assets	147
<i>Sergio Lagomarsino</i>	
Anchoring Influence in RC Beams Flexural Strengthening Using CFRP Fabric	155
<i>D. Diaconu, V. Stoian, T. Nagy-Gyorgy, S. C. Florut</i>	
Rotor Blade Stress and Vibration Amplitudes Monitoring During Operation Condition in One-Pass Jet Engine	160
<i>Ryszard Szczepanik</i>	

Profile of Heat Transfer between Two Different Materials	165
<i>K. Gherfi, S. Boulkroune, H. Bendjama, D. Idiou</i>	
Axial Compression Resistance of Cold-Formed Steel Lipped Channel at Elevated Temperature	169
<i>A. A. S. C. Neto, P. D. A. Neto, A. A. R. Costa, R. B. Caldas, F. C. Rodrigues</i>	
Forging by Rocket Driven Hammer: Dynamics and Experiments	174
<i>Dimitar N. Karastoyanov, Vladimir K. Kotev, Todor N. Penchev</i>	
Turbulence Models Comparison for the Numerical Study of the Air Flow, an Internal Combustion Engine	178
<i>Ioannis Pantokratoras, Charalampos Arapatsakos</i>	
Implementing Knowledge based PCB Design Support System	185
<i>A. Pataki, G. Horváth</i>	
Stability Analysis of Nonparallel Unsteady Flows by a Symmetry-Based Method	191
<i>Georgy I. Burde, Ildar Sh. Nasibullayev, Alexander Zhalij</i>	
Feasibility of Power Flow Control on LV Distribution Systems	197
<i>Dario De Santis, Gaetano Abbatantuono, Sergio Bruno, Massimo La Scala, Roberto Sbrizzai</i>	
Efficient Management Methods of Project Transfers	203
<i>Florina-Cristina Filip, Vladimir Mărăscu-Klein</i>	
Research on the Intelligent Adaptive Hybrid Control System for an Autonomous Mobile Robot	211
<i>I. Kobersy, V. Finaev, D. Beloglazov, I. Shapovalov, J. Zargaryan, V. Soloviev</i>	
Fuzzy MCDM Approach to Evaluate Wastewater Treatment Alternatives	217
<i>Mehtap Dursun</i>	
Magnetic Hysteresis under an Applied Continuous External Magnetic Field	221
<i>Hamza Houassine, Djelloul Moussaoui, Samir Moulahoum</i>	
A Branching Variables Rule for the B & B Algorithm based on the Flatness of the Polyhedron	226
<i>Iván Sergio Derpich Contreras, Claudio Javier Macuada Silva</i>	
Modern Company Maintenance Management based on the Principle Computerized Maintenance Management System (CMMS) Implementation	233
<i>Peter Poór, Michal Šimon</i>	
Physical Modeling of Flow Characteristic in Dissolved Air Flotation Tank with Chitosan and Bentonite as Coagulant	241
<i>M. A. Z. Mohd Remy Rozainy, M. Hasif, S. Syafalny, P. Puganeshwary</i>	

Cyclic In-Plane Testing for Evaluation of Shear Capacity for Ceramic Block Walls <i>Eva Partene, Andrei Bindean, Mihai Fofiu, Valeriu Stoian, Luminita Fekete-Nagy</i>	247
AUV Localization Using a Single Transponder Acoustic Positioning System <i>Igor N. Burdinsky, Semen A. Otcheskiy</i>	252
Novel Aortic Cannula with Spiral Flow Inducing Design <i>Nadia S. Shafii, N. Darlis, Jeswant Dillon, Kahar Osman, Ahmad Zahran Md Khudzari, E. Supriyanto</i>	258
Diagnostics of Existing Steel Roof Structure of Winter Sports Stadium <i>Marcela Karmazínová, Jindrich Melcher, Lubomír Vítek, Petr Cikrle, Jaromír Láník</i>	264
Shafts Renovation using Coatings with Nano Elements <i>Dimitar N. Karastoyanov, Mara K. Kandeve, Kostadin G. Kostadinov</i>	270
Analyzing Emission Sounds: A Way for Early Detection of Bearing Faults in Rotating Machines <i>Mohamed Fezari, Zahra Taif</i>	275
PE and PP Clay Nanocomposite Films – The Comparison of the Influence of a Clay Type and a Compatibilizer Concentration <i>D. Merinska, A. Tesarikova, M. Pospisil</i>	281
Using the CONVAL® Software for the Petrochemical Plant Control Valves Checking. Case Study <i>C. Patrascioiu, G. Stamatescu, C. Lazar</i>	285
Activation Energies for Initial and Intermediate Stage Sintering of Li_2TiO_3 Determined by a Two-Stage Master Sintering Curve Approach <i>Ahmad Reza Abbasian, Mohammad Reza Rahimipour, Zohreh Hamnabard</i>	291
Numerical Prediction of the Fracture Performance of Wires for Civil Engineering Applications with Longitudinal Crack-Like Laminations at Varying Locations <i>Kazeem K. Adewole, Nikos E. Mastorakis</i>	297
A Novel Meta Heuristic Inspired of the Biologic Nephron Performance <i>Reza Behmanesh, Fatemeh Rokni</i>	303
Estimation of Failure Probability of B737 Pneumatics System by Fault Tree Analysis <i>H. Mahfoud, A. Elbarkany, A. Elbiyaali</i>	309
Factors affecting Productivity of Infrastructure Development Project attributable to Insecurity due to Terrorism <i>Muhammad Sohail Anwar Malik, Shazia Nauman</i>	313
Authors Index	320

Plenary Lecture 1

Investigate of Air Core Phenomenon in Cylindrical Tank during Draining



Prof. Chang Hyun Sohn

School of Mechanical Engineering
Kyungpook National University
1370, Sangyeok-Dong Buk-gu
Daegu 702-701, KOREA
E-mail: chsohn@knu.ac.kr

Abstract: An air core phenomenon observed from lavatory bowl draining in our daily lives has a very important scientific meaning because it is also observed from many industrial applications and related with a natural phenomenon such as tornado. Moreover since the air core affects the drain flow rate, it is deeply connected with a disaster such as flood from local heavy rain. In order to prevent air core generation, various ideas have been suggested and demonstrated experimentally: for example, inclining the tank's bottom wall, positioning the drain port eccentrically, and other types of vortex suppressing device. Very recently, we found that the generation of air core highly depends on the temperature of water. To investigate the mechanism of air core suppressing while draining, the numerical simulation on air core phenomenon is introduced and a lot of simulating results will be presented. In addition, 3-D flow structures such as toroidal Taylor vortex rings and spiral waves on free surface which could not be obtained in axisymmetric simulations will also be demonstrated.

Brief Biography of the Speaker:

Professional Experience and Honours:

1991 to 1994 : ADD Team Manager of Small Jet Engine development

1994 to 1996 : Assistant Professor, Kyungpook National University

1996 to 1997 : Visiting Professor. University of Cambridge

1996 to 2000 : Associate Professor, Kyungpook National University

From 2000 : Professor, Kyungpook National University

1999 to 2003 : Vice Head of School of Mechanical Eng.

2003 to 2005 : Head of School of Mechanical Eng.

2005 to 2006 : Visiting Professor in University of Tennessee, Knoxville

2007 to 2008: Vice Dean of College of Engineering

Director, Industrial-University Consortium Center

Director, Industrial Technology Support Hotline Center

2012 to 2013 :President of Daegu-Kyungpook Branch of the Korean Society of Mechanical Engineers(KSME),

2011 to 2013 President of Daegu-Kyungpook Branch of the Korean Society of Automotive

Engineers(KASE),

2011 to 2012 Vice-Chairman, Faculty Assembly of Kyungpook National University

2012 to 2013 : Chairman, Faculty Assembly of Kyungpook National University

Major Research Field

a) CFD Analysis and Study for Thermal-Fluid Flow Phenomena

b) PIV Measurement for Thermal-Fluid Flow Phenomena

c) Flow Induced Vibration

Publications in Journals : 87

Research of the controlled flight dynamics based on the full and simplified quadrotor models

I. Shapovalov, V. Soloviev, V. Finaev, D. Beloglazov, J. Zargaryan, and E. Kosenko

Abstract — For the control of quadrotor flight, it is necessary to take into account gyroscopic effect and inertial forces affecting the quadrotor. Here we consider influence of gyroscopic effect, Coriolis force, friction force and centripetal acceleration on the motion of quadrotor. These impacts are taken into account in the model of quadrotor dynamics. We estimated influence of gyroscopic effect and inertial forces to validate the quadrotor model simplification. To confirm the results of theoretical analysis, we designed the cascade PDD² controller of quadrotor flight and simulated complex flight mode on the basis of simplified model, full model, and full model without aerodynamic friction.

Keywords — Centripetal acceleration, Coriolis force, gyroscopic effect, dynamics, quadrotor.

I. INTRODUCTION

Unmanned autonomous rotary-wing aircrafts have become very popular in the last few years. Many research works are dedicated to such aircrafts control [1] – [4]. Rotary-wing aircrafts with four rotors are referred as quadrotors. Rotating propellers create vertical lift force and so provide the motion of quadrotor. Propellers placed on different diagonals of the quadrotor frame rotate in different directions. Such approach provides compensation of counter torques.

Quadrotors have significant advantages: increased load-carrying capacity, simplicity of propeller system control, vertical take-off and landing, etc. Quadrotors also have disadvantages: significant power consumption, instability, incomplete controllability, etc. Overcoming of above listed disadvantages is possible thanks to modern electronics,

This work was supported by the Russian Scientific Foundation Grant 14-19-01533 and made at the Southern Federal University, Russia.

I. Shapovalov is with the Southern Federal University, Rostov-on-Don, Russia (+7(8634)37-16-89; e-mail: shapovalovio@gmail.com).

V. Soloviev is with the Southern Federal University, Rostov-on-Don, Russia (+7(8634)37-16-89; e-mail: soloviev-tti@mail.ru).

V. Finaev, is with the Southern Federal University, Rostov-on-Don, Russia (+7(8634)37-17-73; e-mail: finaev_val_iv@tgn.sfedu.ru).

D. Beloglazov is with the Southern Federal University, Rostov-on-Don, Russia (e-mail: d.beloglazov@gmail.com).

J. Zargaryan is with the Southern Federal University, Rostov-on-Don, Russia (+7(8634)37-16-89; e-mail: jury.zargaryan@gmail.com).

E. Kosenko is with the Southern Federal University, Rostov-on-Don, Russia (+7(8634)37-16-89; fax: +7(8634) 37-16-89; e-mail: kosenko@tti.sfedu.ru).

microprocessor technologies, mechatronics, control theory, and communication systems.

To control operation modes of the quadrotor or any other autonomous vehicles, we should design convenient automatic control system [5] - [7]. Development of the control system requires a qualitative mathematical model and the description of controlled vehicle. Analysis of the model allows understanding quadrotor dynamics and creating a qualitative motion controller. It can be, for example, robust controller [8], [9].

We need assessment of external disturbances, gyroscopic effect and inertial forces affecting the quadrotor for analysis of operation modes. The character of disturbances depends on the environment and changes uninterruptedly. But the influence of inertial forces and gyroscopic effect is determined by the parameters of quadrotor and by the flight mode.

In papers [10] – [15] authors pay little attention or don't pay attention at all ([1], [4], [16]) to analysis of different components of the vehicle model. So the research of gyroscopic effect and centripetal acceleration influence is a topical task. Paper [17] contains analysis of gyroscopic effect, centripetal acceleration and Coriolis force influence on the flight of helicopter. The results of papers [17] – [20] are basic for the analysis of quadrotor behavior.

II. MATHEMATICAL MODEL

We described the quadrotor flight through conceptions of inertial and body-fixed coordinate frames. The inertial frame $O_oX_gY_gZ_g$ is connected with the earth. The body fixed frame $OXYZ$ is rigidly connected with the quadrotor. Fig. 1 shows the quadrotor with the relevant coordinate frames.

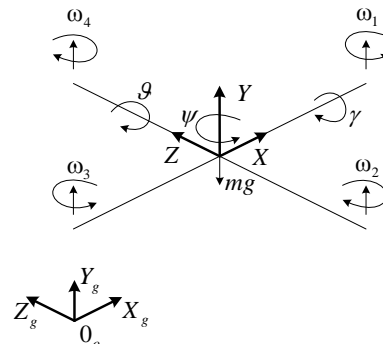


Fig. 1 Simplified representation of quadrotor

We developed equations of motion with respect to OXYZ frame for the following reasons: the matrix of inertia moments is invariant; equations of motion are simple due to the quadrotor model symmetry; on-board measures can be easily used; lift force doesn't change its orientation.

Lift forces of the rotors change orientation and position of OXYZ frame with respect to $0_oX_gY_gZ_g$ frame. The rotation rate of propellers determines the value of lift forces. The quadrotor moves strictly vertically when the lift forces of propellers are equal. The quadrotor orientation changes when the torques are not compensated. Torques appear because of unbalanced rotation rates of the propellers. If the angles of roll and pitch are nonzero, the lift forces have nonzero components on the plane $0_oX_gZ_g$. These components provoke horizontal motion of the quadrotor.

The position of OXYZ frame with respect to $0_oX_gY_gZ_g$ frame is described by the coordinate vector $\xi=[x, y, z]$, and orientation is described by the vector $\eta=[\gamma, \psi, \vartheta]$ of roll, pitch and yaw angles. The vector $V=[V_x, V_y, V_z]$ describes the linear velocity of quadrotor in body-fixed frame. The vector $\Omega=[\Omega_x, \Omega_y, \Omega_z]$ describes the angular velocity of quadrotor in body-fixed frame. Because of two coordinate frames, we use operators for transformation of linear and angular variables. We describe the relation between linear and angular velocities in body-fixed and inertial frames by formulas [21]:

$$\dot{\xi} = R_l V, \quad \Omega = R_r \dot{\eta}, \quad (1)$$

where R_l, R_r are the matrixes of linear and angular variables transformation.

Transformation matrix for linear variables from OXYZ frame to $0_oX_gY_gZ_g$ frame is

$$R_l = \begin{bmatrix} c\psi c\vartheta & s\psi s\gamma - c\psi s\vartheta c\gamma & s\psi c\gamma + c\psi s\vartheta s\gamma \\ s\vartheta & c\vartheta c\gamma & -c\vartheta s\gamma \\ -s\psi c\vartheta & c\psi s\gamma + s\psi s\vartheta c\gamma & c\psi c\gamma - s\psi s\vartheta s\gamma \end{bmatrix}, \quad (2)$$

where we denote $c \leftrightarrow \cos, s \leftrightarrow \sin$.

Transformation matrix for angular variables from OXYZ frame to $0_oX_gY_gZ_g$ frame is

$$R_r = \begin{bmatrix} 1 & \cos \gamma \tan \vartheta & \sin \gamma \tan \vartheta \\ 0 & \cos \gamma / \cos \vartheta & -\sin \gamma / \cos \vartheta \\ 0 & \sin \gamma & \cos \gamma \end{bmatrix}. \quad (3)$$

Derivation of equations describing dynamics of quadrotors is carried out with the use of Euler-Langrage formalism [4], [12], [22], or on the basis of Newton laws [10], [16], [23]. Let's consider equations on the basis of Newton laws of mechanics, because this approach is more intuitive. The matrix equitation of quadrotor dynamics in body-fixed frame is

$$\begin{bmatrix} mE & 0_{3 \times 3} \\ 0_{3 \times 3} & I \end{bmatrix} \cdot \begin{bmatrix} \dot{V} \\ \dot{\Omega} \end{bmatrix} + \begin{bmatrix} \Omega \times (mV) \\ \Omega \times (I\Omega) \end{bmatrix} = \begin{bmatrix} F \\ M \end{bmatrix}, \quad (4)$$

where m is the mass of quadrotor; E is the identity matrix of size 3×3 ; I is the diagonal matrix of quadrotor inertia moments; V is the linear velocity of quadrotor; Ω is the

angular velocity of quadrotor; F is the force vector affecting quadrotor; M is the vector of torques.

The second term in the left part of equation (4) determines the influence of inertial forces and has form

$$\begin{bmatrix} \Omega \times (mV) \\ \Omega \times (I\Omega) \end{bmatrix} = \begin{bmatrix} \Omega_x & \Omega_y & \Omega_z \end{bmatrix} \begin{bmatrix} 0 & -mV_z & mV_y \\ mV_z & 0 & -mV_x \\ -mV_y & mV_x & 0 \\ 0 & -I_{zz}\Omega_z & I_{yy}\Omega_y \\ I_{zz}\Omega_z & 0 & -I_{xx}\Omega_x \\ -I_{yy}\Omega_y & I_{xx}\Omega_x & 0 \end{bmatrix}, \quad (5)$$

$$\text{where } I = \begin{bmatrix} I_{xx} & 0 & 0 \\ 0 & I_{yy} & 0 \\ 0 & 0 & I_{zz} \end{bmatrix}.$$

There are four components characterizing forces and torques effecting on the quadrotor in the right part of equation (4). The first component is the vector of gravity force:

$$F_G = R_l^{-1} F_{G_o} = R_l^{-1} \begin{bmatrix} 0 \\ -mg \\ 0 \end{bmatrix} = \begin{bmatrix} -mgs\vartheta \\ -mgc\vartheta c\gamma \\ mgc\vartheta s\gamma \end{bmatrix}, \quad (6)$$

where F_{G_o} is the gravity vector in inertial frame; F_G is the gravity vector in body-fixed frame; g is the free fall acceleration.

The second component is gyroscopic effect. Gyroscopic effect arises when the shafts of motors change their orientation. The second component influences only the change of angular components of dynamics and is described by expression

$$\begin{aligned} M'_{gyr} &= -\sum_{k=1}^4 J_r \left(\Omega \times \begin{bmatrix} 0 \\ 1 \\ 0 \end{bmatrix} \right) (-1)^k \omega_k = \\ &= J_r \begin{bmatrix} -\Omega_z \\ 0 \\ \Omega_x \end{bmatrix} \varpi = J_r \begin{bmatrix} \Omega_z & -\Omega_z & \Omega_z & -\Omega_z \\ 0 & 0 & 0 & 0 \\ -\Omega_x & \Omega_x & -\Omega_x & \Omega_x \end{bmatrix} \varpi, \quad (7) \end{aligned}$$

where J_r is the inertia moment of motor with propeller; $\varpi = [\omega_1 \ \omega_2 \ \omega_3 \ \omega_4]^T$ is the vector of rates of propellers.

The third component is lift force and torques of rotors. These force and torques are proportional to the squared rotation rates of propellers and can be described by expression

$$U = \begin{bmatrix} U_1 \\ U_2 \\ U_3 \\ U_4 \end{bmatrix} = \begin{bmatrix} b(\omega_1^2 + \omega_2^2 + \omega_3^2 + \omega_4^2) \\ bl(\omega_4^2 - \omega_2^2) \\ bl(\omega_3^2 - \omega_1^2) \\ d(\omega_2^2 + \omega_4^2 - \omega_1^2 - \omega_3^2) \end{bmatrix}, \quad (8)$$

where l is the distance between the center of quadrotor symmetry and motor shafts; b, d are the proportional coefficients. Equitation (8) doesn't take into account the component of angular acceleration of motor shafts.

The fourth component is aerodynamic forces and moments. Air drag force is determined by expression

$$F_{AG} = -A \cdot \begin{bmatrix} |V_x| \cdot V_x \\ |V_y| \cdot V_y \\ |V_z| \cdot V_z \end{bmatrix} = \begin{bmatrix} -A_x \cdot |V_x| \cdot V_x \\ -A_y \cdot |V_y| \cdot V_y \\ -A_z \cdot |V_z| \cdot V_z \end{bmatrix}, \quad (9)$$

where A is the diagonal matrix of drag force coefficients.

Authors of [24], [25] take into account the fifth component, that is the influence of atmospheric disturbances. For the purpose of dynamics equations simplification we assume that the quadrotor flights in the air without atmospheric disturbances.

Full equations of the quadrotor dynamics in body-fixed frame have form

$$\begin{cases} \dot{V}_x = (V_y \Omega_z - V_z \Omega_y) + g s \vartheta - A_x \cdot |V_x| \cdot V_x, \\ \dot{V}_y = (V_z \Omega_x - V_x \Omega_z) - g c \vartheta c \gamma + \frac{U_1}{m} - A_y \cdot |V_y| \cdot V_y, \\ \dot{V}_z = (V_x \Omega_y - V_y \Omega_x) - g c \vartheta s \gamma - A_z \cdot |V_z| \cdot V_z, \\ \dot{\Omega}_x = \frac{I_{yy} - I_{zz}}{I_{xx}} \Omega_y \Omega_z - \frac{J_{\dot{N}D}}{I_{xx}} \Omega_z \varpi + \frac{U_2}{I_{xx}}, \\ \dot{\Omega}_y = \frac{I_{zz} - I_{xx}}{I_{yy}} \Omega_x \Omega_z + \frac{U_3}{I_{yy}}, \\ \dot{\Omega}_z = \frac{I_{xx} - I_{yy}}{I_{zz}} \Omega_x \Omega_y + \frac{J_{\dot{N}D}}{I_{yy}} \Omega_x \varpi + \frac{U_4}{I_{zz}}. \end{cases} \quad (10)$$

The first terms on the right side of equations (10) describe the effect of Coriolis and centripetal forces on the motion of quadrotor [16, 26]. The influence of gyroscopic effect on the quadrotor dynamics becomes apparent when the orientation of motor shafts changes [27]. One can observe the influence of centripetal force when the angular velocity of quadrotor has more than one non-zero component relative to the axes of body-fixed frame. It can be called either a centripetal acceleration effect [16, 28] or gyroscopic effect of the rigid body rotation [4].

The dynamics of brushless DC motors most commonly used in quadrotors is described by equations

$$U_i = R i_i + L \frac{d i_i}{dt} + k_e \omega_i, \quad (11)$$

$$\dot{\omega}_i = k_M i_i - d \omega_i^2, \quad (12)$$

where U_i , i_i , ω_i are the voltage, the current and the shaft rotation rate of the i -th motor; R and L are the resistance and inductance of the stator winding; k_e and k_M are the constructive elements of motor; d is the air drag coefficient.

III. GYROSCOPIC EFFECT INFLUENCE

Gyroscopic effect is observed in systems with a noncollinear rotation axis and the resultant vector of applied torques [27].

Fig. 2 shows the disk representing the quadrotor structure, inertial frame $0_o X_g Y_g Z_g$, and body-fixed frame $0XYZ$. The frame $0XYZ$ is rigidly connected with the disk in such a way that frame origin matches with the disk center, and the disk plane lies on the plane $0XZ$. The disk rotates around $0Y$ axis with a velocity ω_z . Also this disk rotates around $0X$ axis with a velocity ω_x . The torque determined by the cross product $[\omega_x,$

$\omega_y]$ arises as a result of two orthogonal rotation vectors interaction.

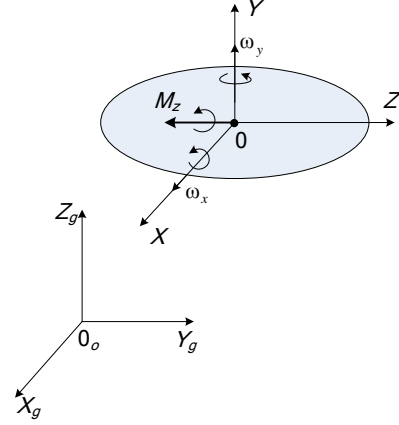


Fig. 2 Gyroscopic effect influence

We suppose that in initial state the quadrotor is hovering above the earth. Let's consider the influence of gyroscopic effect on the turn of quadrotor around every axis of body-fixed frame. We introduce four additional coordinate frames $0X_i Y_i Z_i$, axes of which are directed as the corresponding axes of $0XYZ$ frame and origins are located in the points of intersection of axes $0X$ and $0Z$ with the shafts of motors.

To rotate the quadrotor clockwise around $0Y$ without changing of position, it's necessary to increase ω_2 and ω_4 , and decrease ω_1 and ω_3 (see fig. 1). The motor shafts and axis $0Y$ are collinear, and their cross product is equal to zero, so gyroscopic effect doesn't occur.

For the quadrotor clockwise rotation around $0X$, it's necessary to increase ω_4 in comparison with ω_2 . The quadrotor rotation around $0X$ has a velocity ω_x . The angular velocity ω_x is equal for all four rotors, although the second and the fourth rotors perform larger linear movement in inertial frame comparing with the first and the third rotors.

The torque vector $M_{y1(3)}$ shown in fig. 3a tends to turn the first (third) rotor counter-clockwise around axis $0Y_{1(3)}$. The value of torque is $M_{z1(3)} = |\omega_{1(3)}| |\omega_x|$.

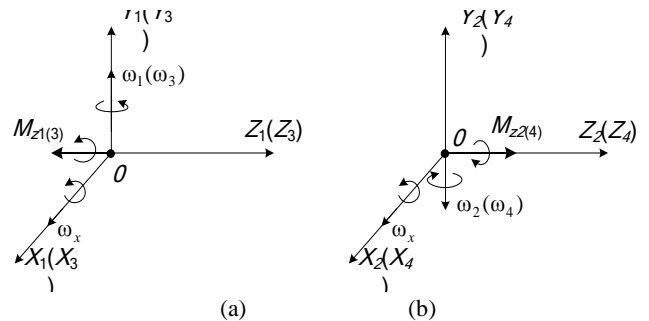


Fig. 3 Gyroscopic effect caused by turn of motor shafts around $0X$

When the second (fourth) rotor rotates clockwise around $0X_{1(3)}$ axis, the torque $M_{z2(4)} = [\omega_x, \omega_{2(4)}]$ appears as it is shown in fig. 3b. This torque tends to turn the second (fourth) rotor clockwise around $0Z_{2(4)}$ axis.

Thus, when the quadrotor rotates around OX axis, four torques appear. These torques tend to turn the motors with propellers around axes OY_i , $i = \overline{1,4}$. The value of resulting torque caused by gyroscopic effect is determined by expression

$$M_z = -M_{z1} + M_{z2} - M_{z3} + M_{z4} = \omega_x \cdot (-\omega_1 + \omega_2 - \omega_3 + \omega_4). \quad (13)$$

This expression allows making conclusion that gyroscopic effects of motors will be compensated and will not influence the quadrotor dynamics when the condition $|\omega_1 + \omega_3| = |\omega_2 + \omega_4|$ is satisfied. If $|\omega_1 + \omega_3| > |\omega_2 + \omega_4|$, the torque rotating the quadrotor clockwise around OZ will appear. If $|\omega_1 + \omega_3| < |\omega_2 + \omega_4|$, the torque will rotate the quadrotor counter-clockwise.

Analysis of the gyroscopic effect influence in the case of quadrotor rotation around OZ axis with a velocity ω_z can be provided in a similar way.

IV. CENTRIPETAL ACCELERATION INFLUENCE

In this section we suppose the quadrotor hovering above the earth and rotating clockwise around OY axis in the initial state ($|\omega_2 + \omega_4| > |\omega_1 + \omega_3| > 0$). We considered the influence of gyroscopic effect when the quadrotor rotates around axes OX and OY of body-fixed frame.

Let's imagine the quadrotor rotates clockwise around OY axis and simultaneously rotates clockwise around OX axis as we showed in fig. 4a. As a result the torque M_{zk} determined by the cross production $[\omega_x, \omega_y]$ appears. This torque turns the quadrotor counter-clockwise around the axis OZ .

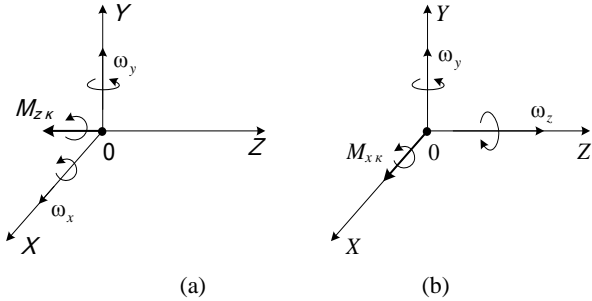


Fig. 4 Influence of centripetal acceleration on quadrotor

The torque M_{zk} appears when the quadrotor rotates clockwise around OY and simultaneously clockwise around OZ . This torque determined by the cross product $[\omega_z, \omega_y]$ tends to rotate the quadrotor around OX axis, as one can see in fig. 4b.

In cross product the order of multiplying vectors determines the direction of resultant vector. Vectors $c_1 = [a, b]$ and $c_2 = [b, a]$ have opposite directions. So it is important to carefully product rotation velocity vectors.

V. CONTROL SYSTEM

Since some components of equations (10) effect the flight dynamics, make model nonlinear, and complicate the analysis of quadrotor behavior, the control system design is rather complex. Therefore, we made the tuning of control system on the simplified model described by equations

$$\begin{cases} \dot{V}_x = g s \vartheta, \\ \dot{V}_y = g c \vartheta c \gamma + \frac{U_1}{m}, \\ \dot{V}_z = g c \vartheta s \gamma, \\ \dot{\Omega}_x = \frac{U_2}{I_{xx}}, \\ \dot{\Omega}_y = \frac{U_3}{I_{yy}}, \\ \dot{\Omega}_z = \frac{U_4}{I_{zz}}. \end{cases} \quad (14)$$

When the quadrotor takes-off from earth to a desired altitude, the orientation angles do not change, so the system is linear. Simple PID controllers are appropriate for such systems control. We decided, it is best to apply the PD controller to increase the quadrotor stability, because the transfer function between the forces acting in vertical plane and y coordinate is integrator of the second order.

When quadrotor flights in complex dynamic modes, nonlinearities of the system begin to play an increasingly important role. Furthermore, when we try to control multiple channels with double integration, the problem of stability ensuring becomes very difficult. So we decided to control not the coordinates, but the velocity with PDD² controller. The structure of controller tuned through equations (14) is shown in fig. 5.

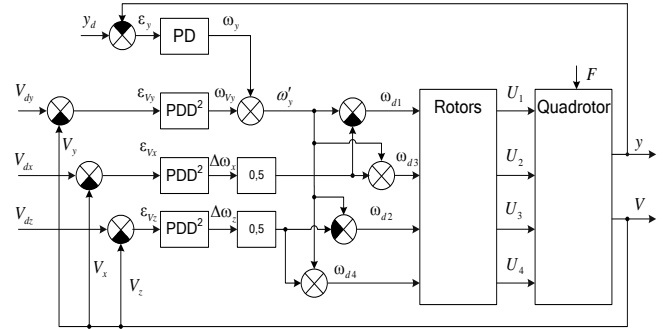


Fig. 5 Block-diagram of cascade PDD² control system

We used the following notations in fig. 5: y_d is the desired altitude (sustained in the hovering mode); y is the altitude of quadrotor; $\varepsilon = [\varepsilon_{vy} \ \varepsilon_{vx} \ \varepsilon_{vz}]$ is the vector of velocity deviation from desired value; ω_y is the output of altitude controller; ω_{vy} , $\Delta\omega_x$, $\Delta\omega_z$ are outputs of velocity controllers; ω_{di} is the desired value of the i -th motor rotational speed; $U_{1..4}$ are the force and torques from equation (8); F is the vector of external disturbances. The block Rotors includes the embedded PD-controllers of rotational speed.

VI. SIMULATION

For quantitative assessment of the gyroscopic effect, centripetal acceleration, and friction force influence on the quadrotor flight modes characterized by angular coordinates

changing, we developed simulation model in Simulink on the basis of equations (10). In the research we used the following values of model parameters: $J_r = 73,9 \cdot 10^{-6} \text{ kg}\cdot\text{m}^2$; $m = 1 \text{ kg}$; $I_{xx} = I_{yy} = 0,081 \text{ kg}\cdot\text{m}^2$; $I_{zz} = 0,142 \text{ kg}\cdot\text{m}^2$; $l = 0,24 \text{ m}$; $b = 53,81 \cdot 10^{-6} \text{ N}\cdot\text{s}^2/\text{rad}^2$; $d = 1,1 \cdot 10^{-6} \text{ N}\cdot\text{m}\cdot\text{s}^2/\text{rad}^2$; $A_{x'} = A_{y'} = A_{z'} = 0,1 \text{ kg/m}$. Initially the quadrotor was in a motionless state on the earth and had coordinates $\xi = [0, 0, 0]$, rotational speeds of propellers were $\omega_i = 0 \text{ rad/s}$, $i = 1, 4$. The parameters of motors were taken from [16].

The simulation was performed in the following scenario: the quadrotor took-off to hovering at the altitude $y = 1 \text{ m}$, then in $t = 5 \text{ s}$ the quadrotor moved in accordance with the desired velocity vector $\dot{\xi}_d = [\sin(t), 0.5, \sin(t + \pi/2)]$. Fig. 6 - 8 show the simulation results for the three models of quadrotor dynamics: model (14), model (10) without friction force and full model (10).

As we can see on fig 6, rotational speeds of rotors significantly change only in the take-off mode. The curves in fig. 7 representing behavior of the full model without friction have some noise caused by the discrete PDD² control. Such noise is one of main disadvantages of the PDD² control. Also fig. 7 shows that aerodynamic friction force makes the noise of PDD² control damping.

Character of difference between the curves in fig. 7 and fig. 8 proves very important role of aerodynamic effects (friction force in our case) in flight control.

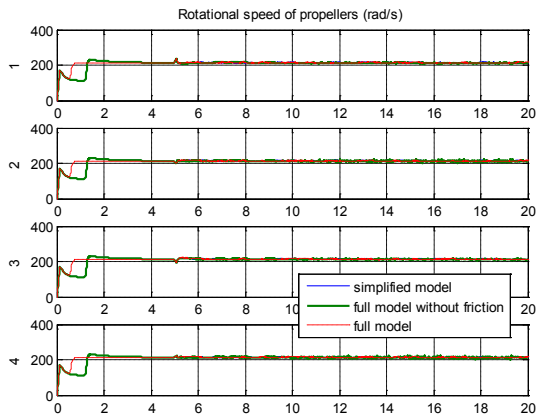


Fig. 6 Rotational speeds of quadrotor propellers

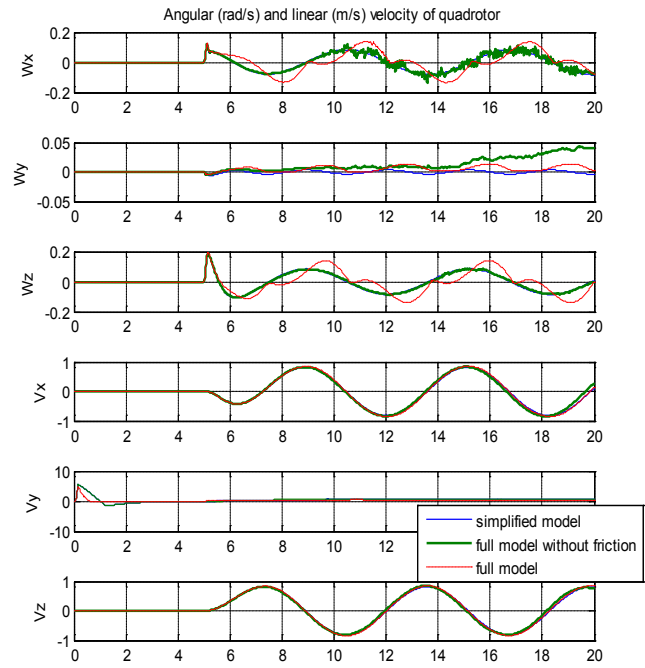


Fig. 7 Components of quadrotor linear and angular velocity in inertial frame

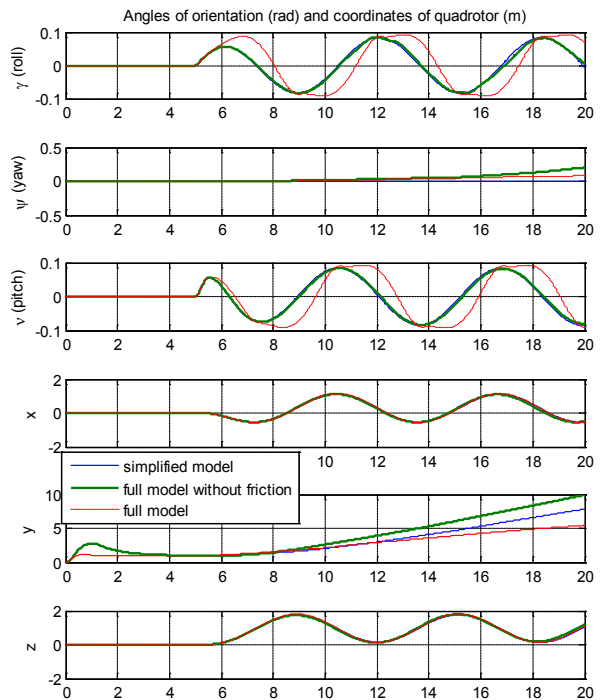


Fig. 8 Quadrotor linear and angular coordinates in inertial frame

VII. CONCLUSIONS

To analyze the behavior of quadrotor in space, we need to consider all set of factors affecting it. For this purpose we derived the model of quadrotor dynamics in the form of differential equations. The model takes into account various types of external and internal forces and torques including gravity force, gyroscopic effect, forces and moments of rotors, centripetal acceleration, Coriolis force, and aerodynamic friction force.

We have analyzed the influence of gyroscopic effect and centripetal acceleration on the quadrotor motion in details. Research was carried out in the conditions of rotor shaft orientation changing and when the rotation speed of quadrotor has more than one nonzero component in body-fixed frame.

We designed the cascade control system based on PD (PDD²) control law to estimate the influence of researched effects on the controlled flight dynamics of quadrotor. Tuning of the controllers was made on the simplified model.

The simulation results showed that centripetal acceleration, gyroscopic effect and Coriolis force have a significant influence on the change of angular variables. Friction force has even more noticeable impact on the angular variables. What concerns linear variables, only altitude and rate of rise appreciably depend on the completeness of model.

We think that results of performed research can be used in the tasks of quadrotor flight control. Our research allows understanding the peculiarities and character of disturbances in the control model. Taking into account these disturbances gives the opportunity to effectively solve flight control tasks.

REFERENCES

- [1] McKerrow P. Modelling the Draganflyer four-rotor helicopter // Proceedings of the IEEE International Conference on Robotics and Automation, Vol. 4, 2004. P. 3596-3601.
- [2] Pshikhopov, V.Kh., Krukhmalev V.A., Medvedev M.Yu., Fedorenko R.V., Kopylov S.A., Budko A.Yu., Chufistov V.M. Adaptive control system design for robotic aircrafts // 2013, IEEE Latin American Robotics Symposium, pp. 67-70.
- [3] Mellinger D., Michael N., Kumar V. Trajectory Generation and Control for Precise Aggressive Maneuvers with Quadrotors // International Journal of Robotics Research, Vol. 31(5), 2012. P. 664-674.
- [4] Bouabdallah S. Design and control of quadrotors with application to autonomous flying // Ph.D. dissertation, EPFL, 2006. – 127 p.
- [5] Pshikhopov V.Kh., Ali A.S. Hybrid control of a mobile robot in dynamic environments // Proceedings of 2011 IEEE International Conference on Mechatronics, 2011. P. 540-545.
- [6] Pshikhopov V. Kh., Krukhmalev V.A., Medvedev M. Yu., Budko A. Yu., Chufistov V.M. Adaptive control system design for robotic aircrafts // Proceedings of 2013 IEEE Latin American Robotics Symposium, 2013. P. 67-70.
- [7] Pshikhopov V.Kh., Medvedev M.Yu. Robust control of nonlinear dynamic systems // 2010, IEEE ANDESCON Conference Proceedings, ANDESCON.
- [8] Pshikhopov V.Kh., Ali A.S. Hybrid motion control of a mobile robot in dynamic environments // 2011, International Conference on Mechatronics, ICM 2011, pp. 540-545
- [9] Pshikhopov V.Kh., Medvedev M.Yu. Block design of robust control systems by direct Lyapunov method // 2011, IFAC Proceedings Volumes (IFAC-PapersOnline), pp. 10875-10880.
- [10] Bolandi H., Rezaei M., Mohsenipour R., Nemati H., Smailzadeh S.M. Attitude Control of a Quadrotor with Optimized PID Controller // Intelligent Control and Automation, 4, 2013. P. 335-342.
- [11] Pshikhopov V.Kh., Medvedev M.Yu., Gaiduk A.R., Gurenko B.V. Control system design for autonomous underwater vehicle // 2013, Latin American Robotics Symposium, pp. 77-82
- [12] Castillo P., Dzul A., Lozano R. Real-time stabilization and tracking of a four-rotor mini rotorcraft // IEEE Transactions on Control Systems Technology, 12(4), 2004. P. 510–516.
- [13] Pounds P., Mahony R., Corke P. Modelling and Control of a Quad-Rotor Robot // In Proc. Australasian Conference on Robotics and Automation, New Zealand, 2006.
- [14] Pshikhopov V.K., Medvedev M.Yu., Gurenko B.V. Homing and Docking Autopilot Design for Autonomous Underwater Vehicle // 2014, Applied Mechanics and Materials, pp. 490-491.
- [15] Pshikhopov V., Krukhmalev V., Medvedev M., Neydorf R. Estimation of energy potential for control of feeder of novel cruise/feeder MAAT // 2012, SAE Technical Papers.
- [16] Bresciani T. Modelling, Identification and Control of a Quadrotor Helicopter // Master's Thesis, Lund University, 2008.
- [17] Padfield G.D. Helicopter flight dynamics: the theory and application of flying qualities and simulation modelling, 2nd ed., Blackwell Publishing, Washington DC, 2007.
- [18] Pshikhopov V., Medvedev M., Kostjukov V., Fedorenko R. et al. Airship Autopilot Design // 2011, SAE Technical Paper.
- [19] Pshikhopov V., Medvedev M., Neydorf R., Krukhmalev V. et al. Impact of the feeder aerodynamics characteristics on the power of control actions in steady and transient regimes // 2012, SAE Technical Papers
- [20] Pshikhopov V., Sergeev N., Medvedev M., Kulchenko A. The design of helicopter autopilot // 2012, SAE Technical Papers.
- [21] Madani T., Benallegue A. Backstepping control for a quadrotor helicopter // Proceedings of the IEEE/RSJ International Conference on Intelligent Robots and Systems, 2006. P. 3255–3260.
- [22] Raffo G.V., Ortega M.G., Rubio F.R. Nonlinear H_∞ Controller for the Quad-Rotor Helicopter with Input Coupling // Proceedings of the 18th IFAC World Congress, 2011. P. 13834-13839.
- [23] Mian A.A., Ahmad M.I., Wang D. Backstepping based PID Control Strategy for an Underactuated Aerial Robot // Proceedings of the 17th IFAC World Congress, 2008. P. 15636-15641.
- [24] Cook M.V. Flight Dynamics Principles, 2nd ed., Elsevier, 2007.
- [25] Neydorf R., Krukhmalev V., Kudinov N., Pshikhopov V. Methods of statistical processing of meteorological data for the tasks of trajectory planning of MAAT feeders // SAE Technical Papers, 2013.
- [26] Etkin B. Dynamics of Atmospheric Flight. Jihn Wiley & Sons, Toronto, 1972.
- [27] Young H.D., Freedman R.A., Ford A.L. Sears and Zemansky's university physics: with modern physics. – 13th ed. Addison-Wesley, 2012.
- [28] Bramwell A.R.S., Done G., Balmford D. Bramwell's Helicopter Dynamics, 2nd ed., Butterworth-Heinemann, 2001.

Nonlinear Optical Response of a Coupled Quantum Dot - Metal Nanoparticle System

Spyridon G. Kosionis, Andreas F. Terzis, John Boviatis, and Emmanuel Paspalakis

Abstract—We theoretically study nonlinear optical effects in a semiconductor quantum dot coupled via Coulomb interaction to a spherical metal nanoparticle. We consider the case of interaction of the system with a weak probe electromagnetic field and a strong pump electromagnetic field and present results from the solution of the relevant density matrix equations for the behavior of the effective third-order (Kerr-type) susceptibility. We find that the spectrum of the nonlinear susceptibility depends strongly on the interparticle distance and present an explanation of the observed behavior in terms of an effective Rabi frequency.

Keywords—Semiconductor quantum dot, metal nanoparticle, nonlinear optics, third-order nonlinearity, Kerr-type susceptibility, Rabi frequency.

I. INTRODUCTION

In recent years the optical properties of a hybrid nanocrystal complex composed of a semiconductor quantum dot coupled to a spherical metal nanoparticle via Coulomb interaction have attracted significant attention [1], [2], [3], [4], [5], [6], [7], [8]. The nonlinear optical response arising from the interaction of this structure with a weak probe electromagnetic field of varying frequency and a strong pump electromagnetic field of fixed frequency has already been considered [9], [10], [11], [12], [13], [14], [15].

Some of these studies have analyzed the behavior of the effective Kerr-type nonlinearity. Initially, Lu and Zhu [9] calculated the real and imaginary part of the relevant effective $\chi^{(3)}$ susceptibility and showed that significantly enhanced Kerr-type nonlinearity can occur due to exciton-plasmon interaction. Also recently, Li *et al.* [12] predicted induced bistable behavior of the real and imaginary part of the effective $\chi^{(3)}$ susceptibility. They also showed that the bistability region can be tuned by adjusting the size of metal nanoparticle, the interparticle distance and the intensity of the pump field.

In this work we also address the behavior of the effective Kerr-type susceptibility in a coupled semiconductor quantum dot - spherical metal nanoparticle structure that interacts with a weak probe electromagnetic field of varying frequency and a strong pump electromagnetic field of fixed frequency and give emphasis to the behavior of the effective $\chi^{(3)}$ nonlinearity

This research has been co-financed by the European Union (European Social Fund - ESF) and Greek national funds through the Operational Program "Education and Lifelong Learning" of the National Strategic Reference Framework (NSRF) - Research Funding Program: Archimedes III.

Spyridon G. Kosionis and Andreas F. Terzis are with the Department of Physics, University of Patras, Patras 265 04, Greece.

John Boviatis is with the Technological and Educational Institute of Western Greece, Megalou Alexandrou 1, Patras 263 34, Greece.

Emmanuel Paspalakis is with the Materials Science Department, University of Patras, Patras 265 04, Greece (corresponding author, phone: 0030-2610-969346; fax: 0030-2610-996358; e-mail: paspalak@upatras.gr).

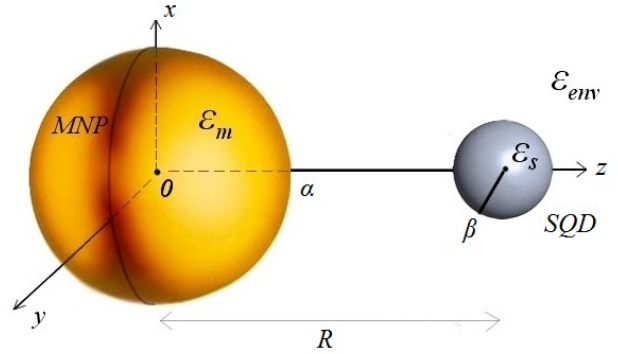


Fig. 1. The coupled quantum dot - metal nanoparticle system consists of a semiconductor quantum dot of radius β and a spherical metallic nanoparticle of radius α . The centers of the two particles are separated by distance R .

spectrum with the interparticle distance. We find that there is a critical interparticle distance that strongly modifies this spectrum. Above this critical distance an ordinary behavior is found while below this critical distance the $\chi^{(3)}$ spectrum is strongly suppressed.

II. THEORETICAL MODEL

The coupled structure that we analyze is composed of a spherical metal nanoparticle of radius α and a small spherical semiconductor quantum dot of radius β , in an environment with real dielectric constant ϵ_{env} , see Fig. 1. The center-to-center distance between the two particles is denoted by R . We also assume that $\beta \ll \alpha$ and consider that $R > \alpha$. The quantum dot is characterized by a two-level system, with $|1\rangle$ being the ground state and $|2\rangle$ being the single exciton state. The energy difference between the two states is $\hbar\omega_0$. This system interacts with two linearly polarized oscillating electromagnetic fields, a pump and a probe field, with total electric field

$$\vec{E}(t) = \hat{z} [E_a \cos(\omega_a t) + E_b \cos(\omega_b t)], \quad (1)$$

that excite the interband transition between the two energy levels of the semiconductor quantum dot. Here, \hat{z} is the polarization unit vector (along the z direction), E_a (E_b) is the electric field amplitude of the pump (probe) field, and ω_a (ω_b) is the angular frequency of the pump (probe) applied field. The dielectric constant of the semiconductor quantum dot is represented by ϵ_s , while we treat the metal nanoparticle as a classical dielectric particle with dielectric function $\epsilon_m(\omega)$.

The electromagnetic fields also excite plasmons, on the surface of the metal nanoparticle. These plasmonic excitations provide a strong continuous spectral response. Such surface plasmons influence the excitons and induce electromagnetic interactions between excitons and plasmons [1], [3].

We take that the pump field is a strong field and its interaction with the system will be treated to all orders while the probe field is a weak field and its interaction with the system will be treated to first order. Following the methodology presented in detail in [14] we obtain the following differential equations for the density matrix elements:

$$\begin{aligned} \dot{w}^{(0)}(t) &= i \left[\Omega_a \sigma_{12}^{(-\omega_a)}(t) - \Omega_a^* \sigma_{21}^{(\omega_a)}(t) \right] \\ &- 4G_I \sigma_{12}^{(-\omega_a)}(t) \sigma_{21}^{(\omega_a)}(t) \\ &- \frac{w^{(0)}(t) + 1}{T_1}, \end{aligned} \quad (2)$$

$$\begin{aligned} \dot{w}^{(-\delta)}(t) &= - \left(i\delta + \frac{1}{T_1} \right) w^{(-\delta)}(t) \\ &+ i\Omega_a \sigma_{12}^{(-\omega_b)}(t) - i\Omega_a^* \sigma_{21}^{(2\omega_a - \omega_b)}(t) \\ &- i\Omega_b^* \sigma_{21}^{(\omega_a)}(t) \\ &- 4G_I \left[\sigma_{12}^{(-\omega_b)}(t) \sigma_{21}^{(\omega_a)}(t) \right. \\ &\left. + \sigma_{12}^{(-\omega_a)}(t) \sigma_{21}^{(2\omega_a - \omega_b)}(t) \right], \end{aligned} \quad (3)$$

$$\begin{aligned} \dot{\sigma}_{21}^{(\omega_a)}(t) &= - \left(i\Delta_a + \frac{1}{T_2} \right) \sigma_{21}^{(\omega_a)}(t) \\ &- i\frac{\Omega_a}{2} w^{(0)}(t) - iG\sigma_{21}^{(\omega_a)}(t) w^{(0)}(t), \end{aligned} \quad (4)$$

$$\begin{aligned} \dot{\sigma}_{21}^{(\omega_b)}(t) &= - \left(i\Delta_a - i\delta + \frac{1}{T_2} \right) \sigma_{21}^{(\omega_b)}(t) \\ &- i\frac{\Omega_a}{2} w^{(\delta)}(t) - iG\sigma_{21}^{(\omega_a)}(t) w^{(\delta)}(t) \\ &- iG\sigma_{21}^{(\omega_b)}(t) w^{(0)}(t) - i\frac{\Omega_b}{2} w^{(0)}(t), \end{aligned} \quad (5)$$

$$\begin{aligned} \dot{\sigma}_{21}^{(2\omega_a - \omega_b)}(t) &= - \left(i\Delta_a + i\delta + \frac{1}{T_2} \right) \sigma_{21}^{(2\omega_a - \omega_b)}(t) \\ &- i\frac{\Omega_a}{2} w^{(-\delta)}(t) - iG\sigma_{21}^{(\omega_a)}(t) w^{(-\delta)}(t) \\ &- iG\sigma_{21}^{(2\omega_a - \omega_b)}(t) w^{(0)}(t). \end{aligned} \quad (6)$$

Here, $w^{(0)}(t)$ is the population inversion and $\sigma_{21}^{(\omega_a)}(t)$ is the off-diagonal term of the matrix element in the case that $E_b = 0$. Also, $w^{(\delta)}(t) = w^{(-\delta)*}(t)$ as the population difference should be real. The last two terms describe the effect of population pulsation in the system. The terms $\sigma_{21}^{(\omega_b)}(t)$, $\sigma_{21}^{(2\omega_a - \omega_b)}(t)$, $w^{(-\delta)}(t)$, $w^{(\delta)}(t)$ are considered to be small, in the sense that $|\sigma_{21}^{(\omega_b)}(t)|$, $|\sigma_{21}^{(2\omega_a - \omega_b)}(t)| \ll |\sigma_{21}^{(\omega_a)}(t)|$ and $|w^{(-\delta)}(t)|$, $|w^{(\delta)}(t)| \ll |w^{(0)}(t)|$. We also define $\sigma_{12}^{(-\omega_a)}(t) = \sigma_{21}^{(\omega_a)*}(t)$, $\sigma_{12}^{(-\omega_b)}(t) = \sigma_{21}^{(\omega_b)*}(t)$ and $\sigma_{12}^{(\omega_b - 2\omega_a)}(t) = \sigma_{21}^{(2\omega_a - \omega_b)*}(t)$.

Here, we have defined the plasmonically-modified Rabi frequencies [1], [3] of the pump (Ω_a) and probe (Ω_b) fields as

$$\Omega_n = \frac{\mu E_n}{\hbar \varepsilon_{eff} S} \left(1 + \frac{s_n \gamma_n \alpha^3}{R^3} \right), \quad (7)$$

and the self-interaction parameter G_n [1], [3] as

$$G_n = \frac{1}{4\pi \varepsilon_{env}} \frac{s_n^2 \gamma_n \alpha^3 \mu^2}{\hbar \varepsilon_{eff}^2 R^6}. \quad (8)$$

Above, μ represents the dipole moment of the semiconductor quantum dot corresponding to the single exciton transition, $\varepsilon_{eff} S = \frac{2\varepsilon_{env} + \varepsilon_S}{3\varepsilon_{env}}$, $\gamma_n = \frac{\varepsilon_m(\omega_n) - \varepsilon_{env}}{\varepsilon_m(\omega_n) + 2\varepsilon_{env}}$ with $n = a, b$, and $s_n = 2$ as the applied field is taken parallel to the interparticle axis of the system (the interparticle axis is the z -axis). Also, $\Delta_a = \omega_0 - \omega_a$ is the detuning of the pump field from resonance, $\delta = \omega_b - \omega_a$ is the detuning between the two fields, and G_I represents the imaginary part of the parameter $G = G_a + G_b$. Finally, T_1 is the population relaxation time due to spontaneous emission and T_2 is the relaxation due to dephasing processes of the semiconductor quantum dot.

We will solve Eqs. (2)-(6) numerically using a Runge-Kutta method for the study of the effective $\chi^{(3)}$ susceptibility. The effective Kerr-type susceptibility is given by [16]

$$\chi^{(3)} = \frac{8\Gamma \sigma_{21}^{(2\omega_a - \omega_b)}(T)}{3V \varepsilon_0 E_a^2 E_b}, \quad (9)$$

where Γ is the optical confinement factor, V is the volume of the quantum dot, ε_0 is the dielectric constant of the vacuum, and T is the time duration of the applied electromagnetic fields that is taken long enough so as the system has reached steady state behavior.

III. RESULTS AND ANALYSIS

In all the calculations we take the quantum dot initially in the ground state, leading to $w^{(0)}(0) = -1$ and the rest density matrix elements being zero. The parameters that we use are $T_1 = 0.8$ ns, $T_2 = 0.3$ ns, $\varepsilon_{env} = \varepsilon_0$, $\alpha = 7.5$ nm, $\mu = 0.65 e$ nm, $\hbar\omega_0 = 2.5$ eV, and $\varepsilon_S = 6\varepsilon_0$. These values correspond to colloidal quantum dots (typically CdSe-based quantum dots) and have been used in various studies [2], [3], [4], [5], [7], [14]. For $\varepsilon_m(\omega)$ we use experimental values of gold [17]. We solve numerically Eqs. (2)-(6) for $T = 100$ ns to obtain the steady state behavior of the effective Kerr-type susceptibility. Below, in all calculations the intensity of the probe field is taken four orders of magnitude smaller than the intensity of the pump field.

In Fig. 2 we present the real and imaginary part of $\chi^{(3)}$ [actually each case we plot the real and imaginary part of $\sigma_{21}^{(2\omega_a - \omega_b)}(T)$] for different interparticle distances when the pump field is at exact resonance with the quantum dot, $\Delta_a = 0$. For long interparticle distances typical $\chi^{(3)}$ spectra are shown. The strong peaks/dips of the spectra are called Rabi sidebands. The decrease of the interparticle distance increases the magnitude of the effective $\chi^{(3)}$ susceptibility. In addition, the positions of the Rabi sidebands change to larger detunings as the interparticle distance decreases. These results are in agreement with that of refs. [9], [12].

However, for even smaller interparticle distances the results are markedly different, as can be seen in Figs. 3(a) and 3(b). There, the effective $\chi^{(3)}$ nonlinearity spectrum changes form and is strongly suppressed. Also, as the interparticle distance decreases further the spectrum is further suppressed. The same

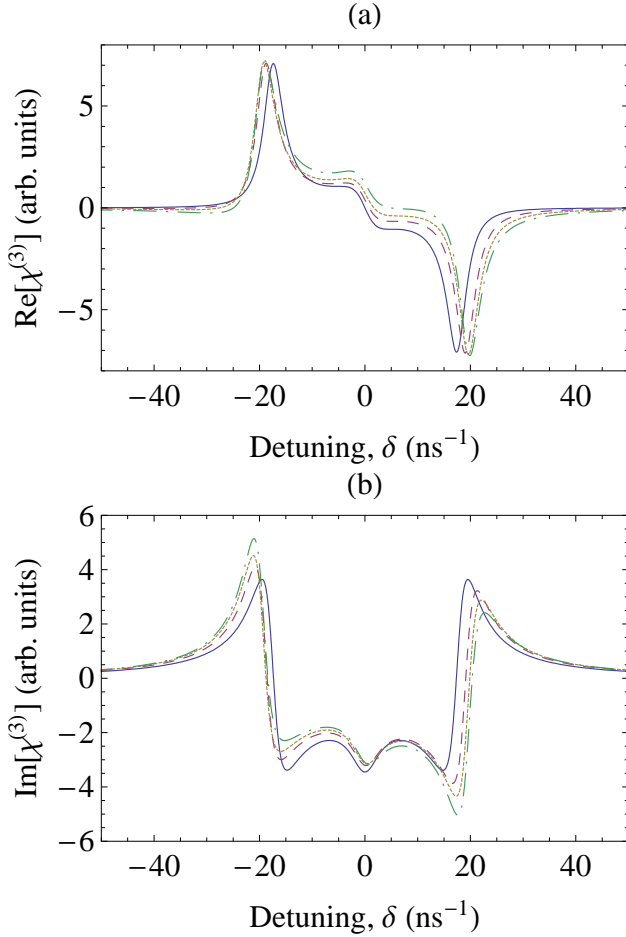


Fig. 2. The real (a) and imaginary (b) parts of the effective $\chi^{(3)}$ susceptibility (in arbitrary units) in the coupled system as a function of the detuning δ . The intensity of the pump field is $I_a = 3 \times 10^2$ W/cm². The pump field excitation is at exact resonance, $\Delta_a = 0$. Solid curve $R = 100$ nm, dashed curve $R = 20$ nm, dotted curve $R = 17$ nm and dot-dashed curve $R = 15$ nm.

general behavior is found in Figs. 4 and 5 that the pump field is (positively) detuned from resonance. We note that the form of the spectrum and the actual distance for which the form of the spectrum strongly changes depends on the pump field frequency and also pump field intensity (the latter is not shown here).

The explanation of the form of the effective $\chi^{(3)}$ susceptibility shown in Figs. 2 to 5 lies in the behavior of the effective Rabi frequency

$$\Omega_{\text{eff}} = \Omega_a + 2G\sigma_{21}^{(\omega_a)^{ss}}, \quad (10)$$

where $\sigma_{21}^{(\omega_a)^{ss}}$ denotes the value of $\sigma_{21}^{(\omega_a)}(t)$ in steady state [2], [11]. The effective Rabi frequency Ω_{eff} is defined in order to make the nonlinear density matrix equations (2)-(6) in steady state to be written in the same form as the (linear) density matrix equations of a regular two-level system [16], where the pump field Rabi frequency has been replaced by the effective Rabi frequency.

From Fig. 6 we note that the value of the effective Rabi frequency changes strongly with interparticle distance. This change denotes two regions, the region of large value of Ω_{eff}

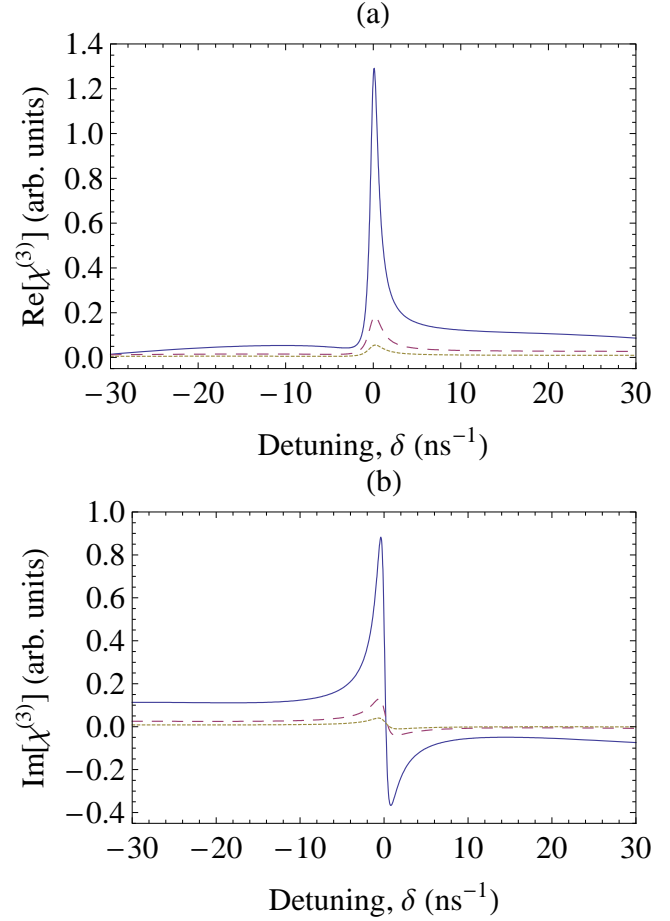


Fig. 3. The real (a) and imaginary (b) parts of the effective $\chi^{(3)}$ susceptibility (in arbitrary units) in the coupled system as a function of the detuning δ . The intensity of the pump field is $I_a = 3 \times 10^2$ W/cm². The pump field excitation is at exact resonance, $\Delta_a = 0$. Solid curve $R = 14$ nm, dashed curve $R = 13.5$ nm and dotted curve $R = 13$ nm.

where the regular spectrum appears and the region of low value of Ω_{eff} where the suppressed spectrum appears. This is an indication of plasmonic metaresonances in the system, a concept proposed and explored by Sadeghi [2], [11], [13]. These metaresonances are molecular-like resonances resulting by the conjugation of the quantum dot excitonic and the metal nanoparticle plasmonic excitations. It has been revealed by Sadeghi that these metaresonances can be associated with two distinct metastates of the quantum dot - metal nanoparticle system. The B(right) state where after an initial delay the effective electric field of the quantum dot can be quite significant resulting in an emitting quantum dot and the D(ark) state where the field experienced by the quantum dot is screened significantly at all times [13]. Actually, the same author defines the normalized Rabi frequency, which coincides with our effective Rabi frequency defined in Eq. (10). These two characteristic states are practically distinguished by means of the two well-separated regions found in the plots of the real and imaginary part of the normalized Rabi frequency. We also find that the positions of the Rabi sidebands in $\chi^{(3)}$ spectra are approximated by $\delta = \pm \sqrt{\Delta_a^2 + |\Omega_{\text{eff}}|^2}$.

The behavior of $|\Omega_{\text{eff}}|$ can be used for determining the

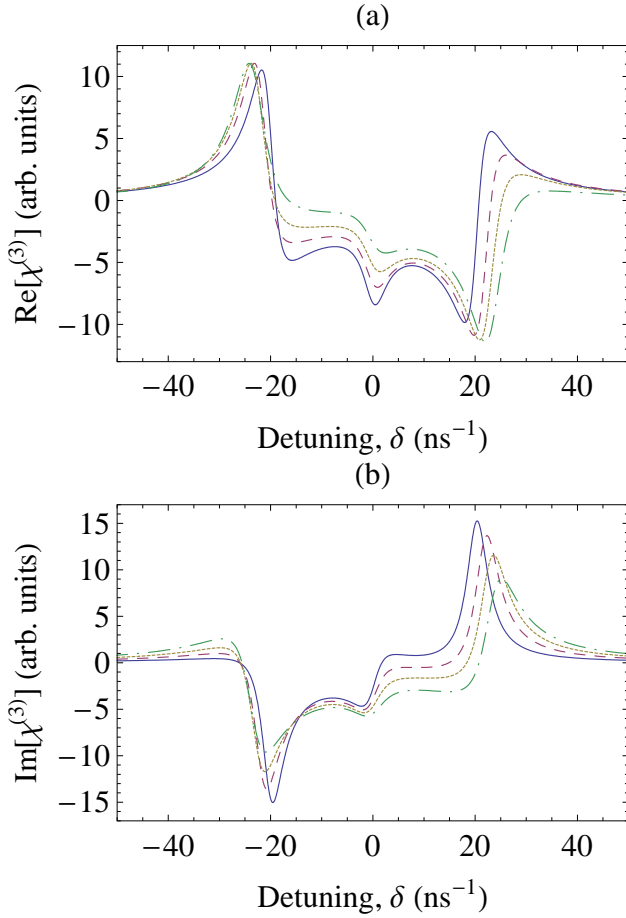


Fig. 4. The real (a) and imaginary (b) parts of the effective $\chi^{(3)}$ susceptibility (in arbitrary units) in the coupled system as a function of the detuning δ . The intensity of the pump field is $I_a = 3 \times 10^2 \text{ W/cm}^2$. The pump field excitation is detuned by $\Delta_a = 10 \text{ ns}^{-1}$. Solid curve $R = 100 \text{ nm}$, dashed curve $R = 20 \text{ nm}$, dotted curve $R = 17 \text{ nm}$ and dot-dashed curve $R = 15 \text{ nm}$.

critical distance that strongly changes the form of the spectrum as the distance decreases. The critical distance is the distance that the abrupt change in the value of $|\Omega_{\text{eff}}|$ occurs. For the explanation of the behavior of $|\Omega_{\text{eff}}|$ the relation between $|\Omega_{\text{eff}}|$ and $w_{ss}^{(0)}$ will be used, where $w_{ss}^{(0)}$ denotes the value of $w^{(0)}(t)$ in steady state. From Eqs. (2) and (4), with the use of Eq. (10), we obtain:

$$|\Omega_{\text{eff}}|^2 = -\frac{1 + T_2^2 \Delta_a^2}{T_1 T_2} \left(1 + \frac{1}{w_{ss}^{(0)}} \right). \quad (11)$$

Combining the steady state solutions of Eqs. (2) and (4), we find that the steady state population inversion can be calculated as one of the roots of a third-order equation [5], [14]:

$$w_{ss}^{(0)3} + c_2 w_{ss}^{(0)2} + c_1 w_{ss}^{(0)} + c_0 = 0, \quad (12)$$

where

$$c_2 = 1 + \frac{2T_2^2 \Delta_a G_R - 2T_2 G_I}{T_2^2 |G|^2}, \quad (13)$$

$$c_1 = \frac{T_1 T_2 |\Omega_a|^2 + T_2^2 \Delta_a^2 + 2T_2^2 \Delta_a G_R - 2T_2 G_I + 1}{T_2^2 |G|^2} \quad (14)$$

$$c_0 = \frac{1 + T_2^2 \Delta_a^2}{T_2^2 |G|^2}, \quad (15)$$

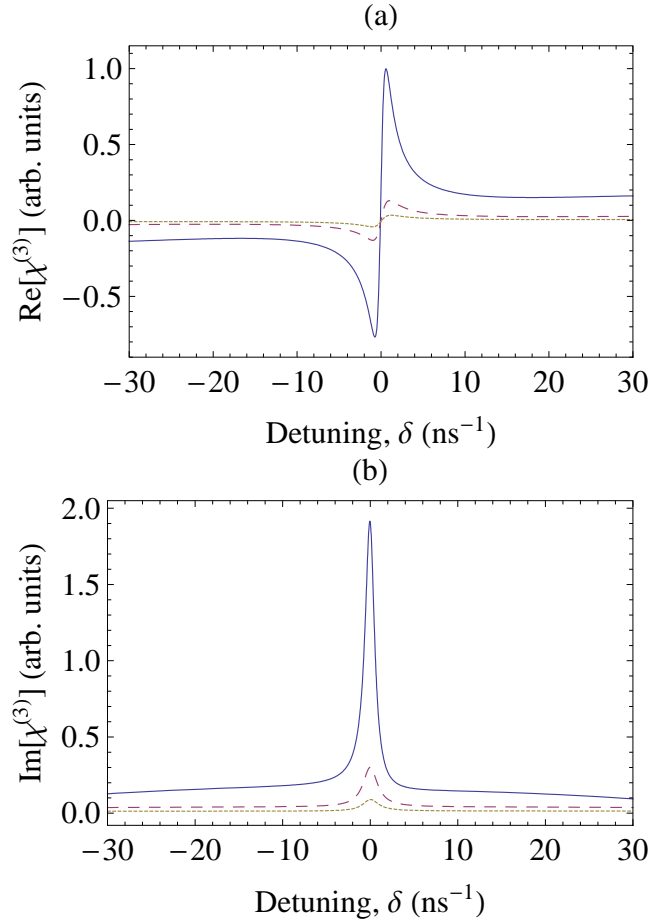


Fig. 5. The real (a) and imaginary (b) parts of the effective $\chi^{(3)}$ susceptibility (in arbitrary units) in the coupled system as a function of the detuning δ . The intensity of the pump field is $I_a = 3 \times 10^2 \text{ W/cm}^2$. The pump field excitation is detuned by $\Delta_a = 10 \text{ ns}^{-1}$. Solid curve $R = 13.5 \text{ nm}$, dashed curve $R = 13 \text{ nm}$ and dotted curve $R = 12.5 \text{ nm}$.

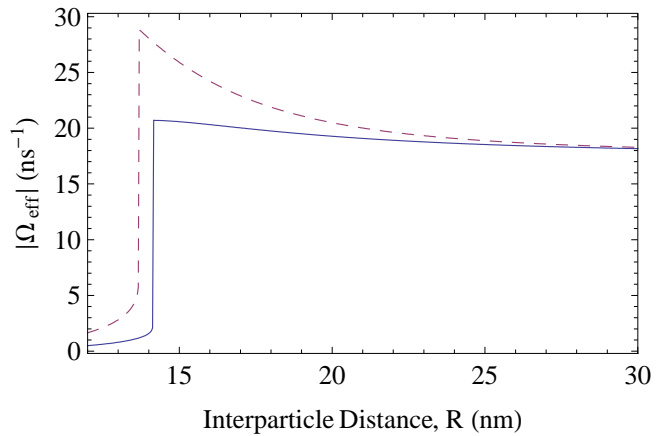


Fig. 6. The absolute value of the effective Rabi frequency Ω_{eff} as a function of the interparticle distance R . The intensity of the pump field is $I_a = 3 \times 10^2 \text{ W/cm}^2$ and the pump field detuning is $\Delta_a = 0$ (solid curve) and $\Delta_a = 10 \text{ ns}^{-1}$ (dashed curve).

with G_R being the real part of the parameter G .

The solutions for $w_{ss}^{(0)}$ are

$$(w_{ss}^{(0)})_1 = p_+ + p_- - \frac{c_2}{3}, \quad (16)$$

$$(w_{ss}^{(0)})_2 = -\frac{p_+ + p_-}{2} - \frac{c_2}{3} + i\frac{\sqrt{3}}{2}(p_+ - p_-), \quad (17)$$

$$(w_{ss}^{(0)})_3 = -\frac{p_+ + p_-}{2} - \frac{c_2}{3} - i\frac{\sqrt{3}}{2}(p_+ - p_-), \quad (18)$$

where

$$p_{\pm} = \left(r \pm \sqrt{S}\right)^{1/3}, \quad (19)$$

$$q = \frac{3c_1 - c_2^2}{9}, \quad (20)$$

$$r = \frac{9c_1c_2 - 27c_0 - 2c_2^3}{54}, \quad (21)$$

$$S = q^3 + r^2. \quad (22)$$

As $w_{ss}^{(0)}$ represents the population inversion, we only account for the real roots that satisfy the condition $-1 \leq w_{ss}^{(0)} \leq 1$.

These solutions can be used for the explanation of the behavior of the effective $\chi^{(3)}$ susceptibility. The solutions of the third-order equation describing $w_{ss}^{(0)}$, Eqs. (16)-(18) strongly depend on the values of the parameters of the system, as can be seen by the expressions for the coefficients of the third-order algebraic equation, Eqs. (13)-(15). The nature of the roots is purely determined by the parameter S . We have one real root and two complex roots, with $(w_{ss}^{(0)})_2 = (w_{ss}^{(0)})_3^*$, when $S \geq 0$ and three real roots (bistability case [8], [12]) when $S < 0$.

From detailed analysis we conclude that the most important parameter in the explanation of the abrupt change in the magnitude of Ω_{eff} is the S -parameter and especially the largest distance at which it becomes zero. Applying this condition, we find that the distance which the behavior of the effective $\chi^{(3)}$ susceptibility strongly changes is $R = 14.15$ nm for $\Delta_a = 0$ and $R = 13.65$ nm for $\Delta_a = 10$ ns⁻¹. These values are in excellent agreement with the values obtained in Fig. 6(c).

IV. SUMMARY

In summary, we have studied the effective $\chi^{(3)}$ susceptibility in a coupled semiconductor quantum dot - spherical metal nanoparticle structure giving emphasis to the influence of the interparticle distance. We find that there is a critical distance that changes the form of the effective $\chi^{(3)}$ nonlinearity spectrum. Above this distance the $\chi^{(3)}$ spectrum has a regular form and relatively small changes of the magnitude and shape of the spectrum by changing the interparticle distance can be obtained. Below this critical distance the effective $\chi^{(3)}$ nonlinearity spectrum is strongly suppressed. The behavior of the system is explained by the effective Rabi frequency that creates plasmonic metaresonances in the coupled structure and the behavior of the effective Rabi frequency is explained via an analytical solution of the density matrix equations.

ACKNOWLEDGEMENTS

We thank Dr. Sofia Evangelou for useful discussions and help.

REFERENCES

- [1] W. Zhang, A. O. Govorov, and G. W. Bryant, "Semiconductor-metal nanoparticle molecules: Hybrid excitons and the nonlinear Fano effect," *Phys. Rev. Lett.*, vol. 97, art. no. 146804, 2006.
- [2] S. M. Sadeghi, "The inhibition of optical excitations and enhancement of Rabi flopping in hybrid quantum dot-metallic nanoparticle systems," *Nanotechnology*, vol. 20, art. no. 225401, 2009.
- [3] R. D. Artuso and G. W. Bryant, "Strongly coupled quantum dot-metal nanoparticle systems: Exciton-induced transparency, discontinuous response, and suppression as driven quantum oscillator effects," *Phys. Rev. B*, vol. 82, art. no. 195419, 2010.
- [4] S. M. Sadeghi and R. G. West, "Coherent control of Forster energy transfer in nanoparticle molecules: energy nanogates and plasmonic heat pulses," *J. Phys.: Condens. Matter*, vol. 23, art. no. 425302, 2011.
- [5] S. G. Kosionis, A. F. Terzis, V. Yannopapas, and E. Paspalakis, "Nonlocal effects in energy absorption of coupled quantum dot-metal nanoparticle systems," *J. Phys. Chem. C*, vol. 116, pp. 23663-23670, 2012.
- [6] M. A. Antón, F. Carreño, S. Melle, O. G. Calderón, E. Cabrera-Granado, J. Cox, and M. R. Singh, "Plasmonic effects in excitonic population transfer in a driven semiconductor-metal nanoparticle hybrid system," *Phys. Rev. B*, vol. 86, art. no. 155305, 2012.
- [7] E. Paspalakis, S. Evangelou, and A. F. Terzis, "Control of excitonic population inversion in a coupled semiconductor quantum dot-metal nanoparticle system," *Phys. Rev. B*, vol. 87, art. no. 235302, 2013.
- [8] B. S. Nugroho, A. A. Iskandar, V. A. Malyshev, and J. Knoester, "Bistable optical response of a nanoparticle heterodimer: Mechanism, phase diagram, and switching time," *J. Chem. Phys.*, vol. 139, art. no. 014303, 2013.
- [9] Z. Lu and K.-D. Zhu, "Enhancing Kerr nonlinearity of a strong coupled exciton-plasmon in hybrid nanocrystal molecules," *J. Phys. B*, vol. 41, art. no. 185503, 2008.
- [10] Z. Lu and K.-D. Zhu, "Slow light in an artificial hybrid nanocrystal complex," *J. Phys. B*, vol. 42, art. no. 015502, 2009.
- [11] S. M. Sadeghi, "Gain without inversion in hybrid quantum dot-metallic nanoparticle systems," *Nanotechnology*, vol. 21, art. no. 455401, 2010.
- [12] J.-B. Li, N.-C. Kim, M.-T. Cheng, L. Zhou, Z.-H. Hao, and Q.-Q. Wang, "Optical bistability and nonlinearity of coherently coupled exciton-plasmon systems," *Opt. Express*, vol. 20, pp. 1856-1861, 2012.
- [13] S. M. Sadeghi, "Ultrafast plasmonic field oscillations and optics of molecular resonances caused by coherent exciton-plasmon coupling," *Phys. Rev. A*, vol. 88, art. no. 013831, 2013.
- [14] E. Paspalakis, S. Evangelou, S. G. Kosionis, and A. F. Terzis, "Strongly modified four-wave mixing in a coupled semiconductor quantum dot-metal nanoparticle system," *J. Appl. Phys.*, vol. 115, art. no. 083106, 2014.
- [15] J.-J. Li and K.-D. Zhu, "Recent advances of light propagation in surface plasmon enhanced quantum dot devices," *Crit. Rev. Sol. State Mater. Sci.*, vol. 39, pp. 25-45, 2014.
- [16] R. W. Boyd, *Nonlinear Optics*, 3rd edition, San Diego: Academic Press, 2008, chapt. 6.6.
- [17] P. B. Johnson and R. W. Christy, "Optical constants of the noble metals," *Phys. Rev. B*, vol. 6, pp. 4370-4379, 1972.

Design of the intelligent adaptive hybrid control system for autonomous mobile robot on the basis of neuro-fuzzy networks

V. Finaev, I. Kobersy, D. Beloglazov, I. Shapovalov, E. Kosenko, and V. Soloviev

Abstract— The paper is devoted to design of the adaptive hybrid system for motion control of an autonomous mobile robot. We designed the control system on the basis of artificial neuro-fuzzy networks. The aim of control consists in safe obstacle avoidance during movement and regulation of velocity without operator participation. The structure of adaptive hybrid control system consisting of three modules is given. The stages of each module design are defined and the structures of neuro-fuzzy networks for the modules implementation are chosen. Here we present the operation algorithms of movement direction control module, velocity control module, and obstacle identification module.

Keywords— Adaptation, hybrid system, neuro-fuzzy networks, uncertainty, vehicles.

I. INTRODUCTION

The problem of the autonomous mobile robot (vehicle) motion along a desired path with the obstacle avoidance is one of the most important tasks in robotics [1]-[5]. It can be solved by different methods, for example, by methods of the classical control theory, position-trajectory control [1], [6], etc. There is a strong interest in alternative solutions, the use of artificial intelligence methodology despite the positive results of above mentioned approaches.

We propose to use the artificial neuro-fuzzy networks (NFNs) of modified architecture [7], [9] to solve the problem of vehicle control.

Fuzzy control is one of the most promising development lines of advanced control theory. The use of fuzzy logic allows providing the opportunity of adaptive hybrid control system (AHCS) operation with incomplete, inaccurate data about the

state of vehicle and environment [10] – [15].

The task of autonomous vehicle control system development can be represented in the form of a specific sequence of subtasks [13], [15]: the creation of idea about the environment state by transmitting and receiving sensor signals; the classification of situations based on the sensor data about the environment state; making decisions to change velocity, direction of the vehicle movement.

II. THE ALGORITHM OF MOVEMENT DIRECTION CONTROL MODULE OPERATION

The structure of the AHCS is given in Fig.1. The module of motion direction control was implemented on the basis of neuro-fuzzy network 1 (NFS₁). NFS₂ is used to control the vehicle velocity. The NFS3 carries out classification of obstacles on the way of vehicle based on the distance between obstacles and vehicle.

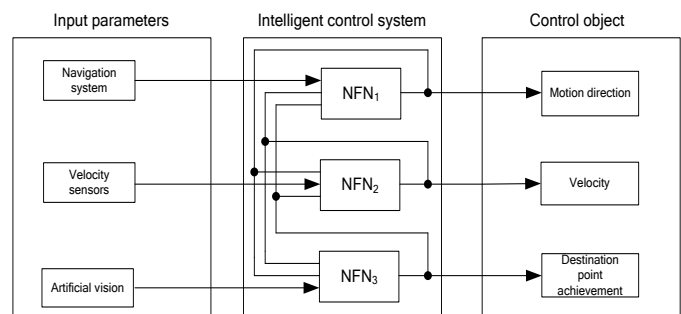


Fig. 1 Structure of hybrid vehicle control system

Distinctive feature of these neuro-fuzzy networks (NFN₁, NFN₂, NFN₃) is the use of artificial neural networks as a defuzzification subsystem in their structure.

The overall structure of adaptive neuro-fuzzy control system is similar in structure to a simple feed-forward neural network (FFNN) [7] (individual neurons are the neuro-fuzzy networks).

The design of AHCS modules using fuzzy logic consists of the following stages: selection of module architecture; development of module structure; development of module training algorithm; development of AHCS training algorithms. The process of parameters adaptation in individual modules and in the control system as a whole depends on the algorithms used, as they determine the quality of training.

Data from the navigation system, the modules of velocity

This work was supported by the Russian Scientific Foundation Grant 14-19-01533 and made at the Southern Federal University, Russia.

V. Finaev is with the Southern Federal University, Rostov-on-Don, Russia (+7(8634)37-17-73; e-mail: finaev_val_iv@tgn.sfedu.ru).

I. Kobersy is with the Southern Federal University, Rostov-on-Don, Russia (+7(8634)37-16-89; fax: +7(8634) 37-16-89; e-mail: iskobersi@gmail.com).

D. Beloglazov is with the Southern Federal University, Rostov-on-Don, Russia (e-mail: d.beloglazov@gmail.com).

I. Shapovalov is with the Southern Federal University, Rostov-on-Don, Russia (+7(8634)37-16-89; e-mail: shapovalovio@gmail.com).

E. Kosenko is with the Southern Federal University, Rostov-on-Don, Russia (+7(8634)37-16-89; e-mail: kosenko@tti.sfedu.ru).

V. Soloviev is with the Southern Federal University, Rostov-on-Don, Russia (+7(8634)37-16-89; e-mail: soloviev-tti@mail.ru).

control, and obstacle identification is received at the input of direction control module (NFN₁). The NFN₁ with three inputs and one output allows control only “motion direction” parameter. The algorithm of NFN₁ architecture design consists of the following steps.

Step 1. In order to solve the vehicle motion direction control task it is necessary to define input and output parameters of the module, the term sets of these parameters. We used the triangular form of membership functions as a basic form of fuzzy variable term sets, because this versatile form is the most commonly used by developers [16] – [18].

Let’s define the term sets of input and output linguistic variables.

The first linguistic variable T_{11} defines the obstacle position in space relative to the vehicle and has the term set $T_{11} = \{t_1^1, t_2^1, t_3^1, \dots, t_{26}^1\} = \{\text{front area: in a center, far from center - near to right area, very far from center - very close to right area, far from center - near to left area, very far from center - very close to left sight, close to center, very close to center; left area: in a center, far from center - close to front area, very far from center - very close to front area, far from center - close to back area, very far from center - very close to back area, close to center, very close to center; right area: in a center, far from center - close to front area, very far from center - very close to front area, far from center - close to back area, very far from center - very close to back area, close to center, very close to center; back area: in a center, far from center - closer to right area, very far from center - very close to right area, far from center - closer to left area, very far from center - very close to left area, close to center, very close to center}\}$. The term set $T_{11} = \{t_1^1, t_2^1, t_3^1, \dots, t_{26}^1\}$ includes twenty six fuzzy variables defining the linguistic variable “obstacle position”.

The structure of fuzzy variables composing the linguistic variable T_{11} is shown in Fig. 2.

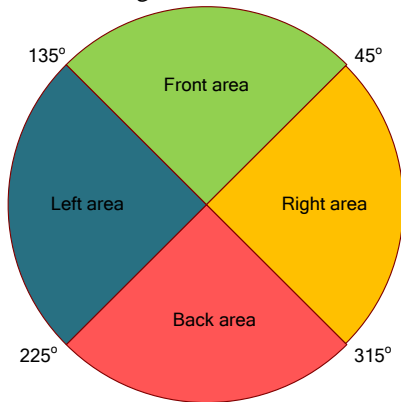


Fig. 2. The separation of external space

Measured vehicle velocity value T_{12} comes to the second input of NFN₁ and fuzzy variables from the term set $T_{12} = \{t_1^2, t_2^2, t_3^2, \dots, t_5^2\} = \{\text{high velocity; very high velocity; low velocity; very low velocity; stop}\}$ define this value.

The third linguistic variable T_{13} describes the distance from the vehicle to the destination point. This linguistic variable has the term set $T_{13} = \{t_1^3, t_2^3, t_3^3, \dots, t_7^3\} = \{\text{very far from destination; far from destination; middle of route; not very far from destination; not very close to destination; very close to destination; destination}\}$. The term set T_{13} includes seven fuzzy variables.

The process of setting membership functions parameters begins after defining the linguistic variables and their term sets.

Step 2. At this step the number of fuzzy neurons in the first layer of NFN₁ is calculated. The number L_1 of fuzzy neurons in the first layer of NFN₁ is equal to sum of cardinal numbers of input linguistic variables term set: $L_1 = T_{11} + T_{12} + T_{13} = 38$.

The membership function of fuzzy neurons is described by expression:

$$\mu_{A_i^k} = \begin{cases} 0, & x \in]-\infty, a_i^k] \\ \frac{x_i - a_i^k}{b_i^k - a_i^k}, & x \in [a_i^k, b_i^k] \\ \frac{x_i - c_i^k}{b_i^k - c_i^k}, & x \in [b_i^k, c_i^k] \\ 0, & x \in [c_i^k, +\infty[\end{cases} \quad (1)$$

The following parameters define the shape of such membership function: a_i^k , b_i^k , and c_i^k , where b_i^k is the center; a_i^k and c_i^k are the borders of membership function.

Step 3. The number of fuzzy neurons in the second layer of NFN₁ is calculated. The output block defining the degree of fulfillment of the fuzzy rules conditions is implemented in the second layer of NFN₁

$$\tau_k = \min_{i=1, \dots, n} \{\mu_{A_i^k}(\bar{x}_i)\} \quad (2)$$

The number of elements in the second layer is equal to the number of fuzzy rules: $L_2 = N_1 \times N_2 \times N_3$. In our case: $L_2 = 5 \times 9 \times 24 = 1080$.

Step 4. The quantity of fuzzy sets defines the number of elements in the third layer by formula:

$$L_3 = \frac{L_2}{M} \quad (3)$$

As the number of rules in the second layer is L_2 , the number of fuzzy neurons is $L_3 = 360$.

All the layers have weights of connections. These weights are usually equal to 0 (no connection) or 1. Such approach is convenient for connection of the third and the second layer according to a principle “each with each”. If the third layer contains r elements, we can write

$$y_r = \max_{i=1, \dots, n} \{\tau_k, w_{kr}\}, \quad (4)$$

where $r=1, \dots, m$ is the number of element in the third layer, $1, \dots, N$ is the rule number, w_{kr} are the weights of connections between element k in the second layer and element r in the

third layer.

Fig. 3 shows the structure of the process of fuzzy rules conclusions goodness calculation based on the given conditions.

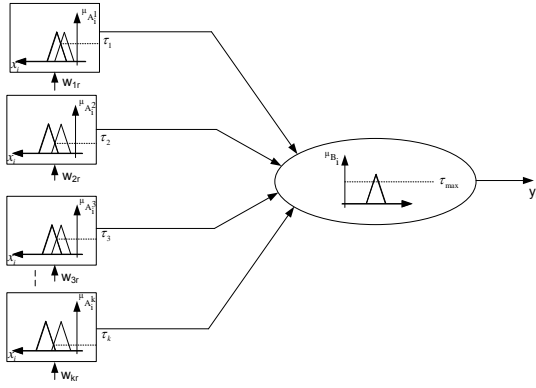


Fig. 3. The structure of goodness calculation

In the NFN_1 each element of the second layer is connected to only one element of the third layer. The same condition cannot have several conclusions in the base of fuzzy rules, but the same conclusion can be drawn based on different conditions. The second, the third, and the fourth steps are the solution of fuzzification and fuzzy rule base development tasks.

Step 5. The fuzzification task is complex. We face the problem of robot rotational displacement relative to a current motion trajectory in the task of vehicle motion direction control.

We use the rotational displacement with the range of value $(-a, a)$ as an output variable. If we have the membership functions $\langle -a, 0, 0, 0, 0, a \rangle$ as a result of output block operation, we would expect the numerical value of control signal close to a or to $-a^0$. The majority of fuzzification methods cannot handle this condition and give the angle value equal to 0^0 .

To solve this problem, we will use neural networks, which are capable to implement different mathematical dependencies.

The input layer of neural network from the fuzzification block is connected to the last, the third layer of previously mentioned module. Let's denote weight vectors of these i -th neurons connection as $w_i^{(1)}$. The number of elements in this layer is defined by the number of previous layer fuzzy rules. Values from the first layer of defuzzification neural network enter to inputs of the second hidden layer of defuzzification neural network.

The calculation of the neurons number in the hidden layer is a very important part of a whole neural network architecture design. For this calculation the next rules can be used [20]: the number of hidden neurons should be in a range of the input and output layer size; the number of hidden neurons should be 2/3 of the input and output layer size; the number of hidden neurons should be twice less than the output layer size. We chose the number of hidden neurons equal to 180.

We denote the connection between input and hidden layers

as $w_i^{(2)}$. The neurons number of output (last) layer is equal to 1. This layer produces control signal that is defuzzificated fuzzy conclusions.

The NFN_1 module training consists in tuning of parameters of the neural network responsible for control signal defuzzification. The complete structure of NFN_1 is shown in Fig. 4.

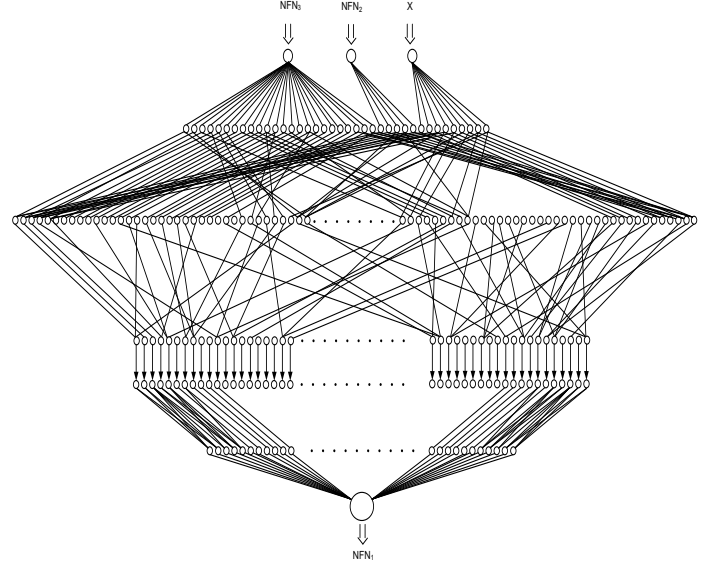


Fig. 4. Complete structure of NFN_1

The NFN (from the first to the third layer) purpose consists in definition the degree of input data compliance with each inference rule. Different learning algorithms are used in order to adapt this network to given task. These algorithms define the difference between the given (reference) value and the real value of output signal.

III. THE ALGORITHMS OF VELOCITY CONTROL MODULE OPERATION.

The second stage of the vehicle control system design is a development of the velocity control module. The fuzzy control system as a standard neural network is described by the membership function of fuzzy set B_k

$$\mu_{B_k}(\bar{y}_k) = \prod_{i=1}^n \exp \left[- \left(\frac{\bar{x}_i - \bar{x}_i^k}{\sigma_j^k} \right)^2 \right]. \quad (5)$$

The membership function describing defuzzification operation has a form

$$\bar{y} = \frac{\sum_{k=1}^N \bar{y}^k \exp \left(h^k \left(\sum_{i=1}^n \bar{x}_i \bar{x}_i^k - 1 \right) \right)}{\sum_{k=1}^N \exp \left(h^k \left(\sum_{i=1}^n \bar{x}_i \bar{x}_i^k - 1 \right) \right)}. \quad (6)$$

The structure shown on Fig. 5 is a modification of neuro-fuzzy control system with an artificial neural network as a defuzzification block.

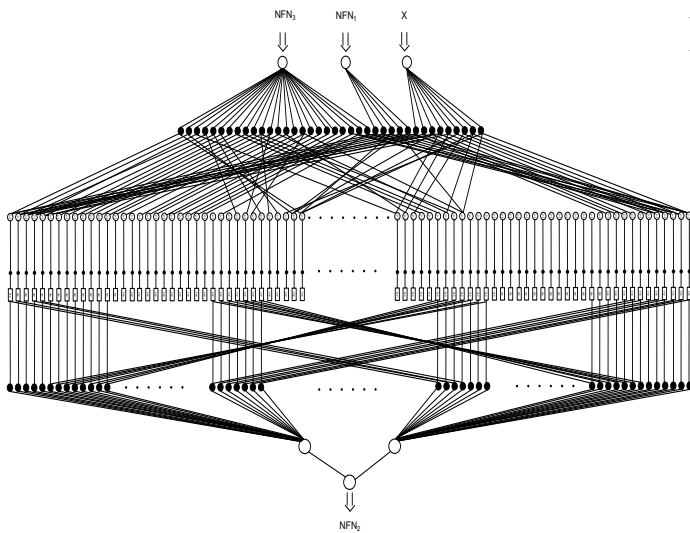


Fig. 5. Complete structure of NFN₂

The inputs of NFN₂ are the following: X_2 is the signal from sensors of distance to obstacle; Y_1 is the output of NFN₁ controlling the motion direction; Y_3 is the output of NFN₃ classifying obstacles based on their distance to the vehicle. The output of NFN₂ module is the velocity control signal Y_2 .

The first layer is formed by classical neurons with a weighted sum of inputs and an exponential activation function. Each neuron of the first layer corresponds to one fuzzy rule. The distance from obstacle to vehicle, the motion direction, and obstacle classifier are the linguistic variables T_{2i} ($i=1, 2, 3$) of module.

The first input linguistic variable “distance from vehicle to obstacle” T_{21} has the term set $T_{21} = \{t_1^2, t_2^2, t_3^2, \dots, t_7^2\} = \{\text{very large distance; large distance; medium distance; not very large distance; not very small distance; very small distance; almost collision}\}$.

The second linguistic variable «motion direction» T_{22} has the term set $T_{22} = \{t_1^2, t_2^2, t_3^2, \dots, t_7^2\} = \{\text{to the left; sharply to the left; smoothly to the left; keep direct course; to the right; sharply to the right; smoothly to the right}\}$.

The third linguistic variable «class of obstacle» T_{23} has the term set $T_{23} = \{t_1^3, t_2^3, t_3^3, \dots, t_5^3\} = \{\text{high degree of need to change the direction of motion; very high degree of need to change the direction of motion; low degree of need to change the direction of motion; change the direction of motion; stop}\}$.

The size of fuzzy rule base of the velocity control module is defined by expression $L_1 = T_{21} \times T_{22} \times T_{23} = 245$ on the basis of cardinality number of the linguistic variable term set.

The second and the third layers of neural network perform the defuzzification operation. These layers consist of neurons with a linear activation function.

Weights of the first neuron from the second layer are interpreted as centers of fuzzy set membership functions, and they are modified by the training process. Weights of the second neuron are the constants equal to 1. The last layer of

the NFN₂ module contains one neuron that outputs the final value of vehicle velocity correction.

IV. THE ALGORITHMS OF OPERATION OF OBSTACLE CLASSIFICATION MODULE

The third stage of the vehicle control system design consists in the obstacle classification module development on the basis of NFN. We suppose the NFN₃ having the almost same structure as the NFN₂. The differences are the sets of input and output signals and a solved task.

The inputs of NFN₃ are the following parameters: X_3 is the signal from navigation systems determining distance between obstacles and the vehicle; Y_1 is the output of NFN₁ controlling the motion direction; Y_2 is the output of NFN₂ controlling the vehicle velocity.

The output Y_3 of NFN₃ is the obstacle class defined on the basis of distance to the vehicle, etc.

Let’s verbally define the term set of NFN₃ input variables. The first linguistic variable T_{31} «distance from vehicle to obstacle» has the term set $T_{31} = \{t_1^1, t_2^1, t_3^1, \dots, t_7^1\} = \{\text{in central area; far from center - near to vehicle; very far from center - very close to vehicle; close to center - far from vehicle; very close to center - very far from vehicle; close to area borders; very close to area borders}\}$.

The second linguistic variable T_{32} «motion direction» has the term set $T_{32} = \{t_1^2, t_2^2, t_3^2, \dots, t_7^2\} = \{\text{to the left; sharply to the left; smoothly to the left; keep straight course; to the right; sharply to the right; smoothly to the right}\}$.

The third linguistic variable T_{33} «vehicle velocity» has the term set $T_{33} = \{t_1^3, t_2^3, t_3^3, \dots, t_5^3\} = \{\text{very high velocity; high velocity; middle velocity; low velocity; very low velocity}\}$.

The first layer of fuzzy module NFN₃ consists of $L_1 = T_{31} \times T_{32} \times T_{33} = 245$ fuzzy rules. The second module consists of $L_2 = 2$ neurons. Parameters of the NFN₃ are calculated as in NFN₂ module. The training algorithm of vehicle state control modules consists in a reduction of previous weight by the value of error derivative. This process continues while the output error of the system is greater than a priori given minimal value.

V. STRUCTURE OF THE INTELLIGENT AHCS

The developed modules NFN₁, NFN₂, NFN₃ are the basis of the control system block-diagram shown in Fig 6.

Let’s consider the common algorithms of system operation. The data formed by sensors about the environment is transmitted to the common control system input. Further the data goes to inputs of corresponding control modules (NFN₁, NFN₂, NFN₃).

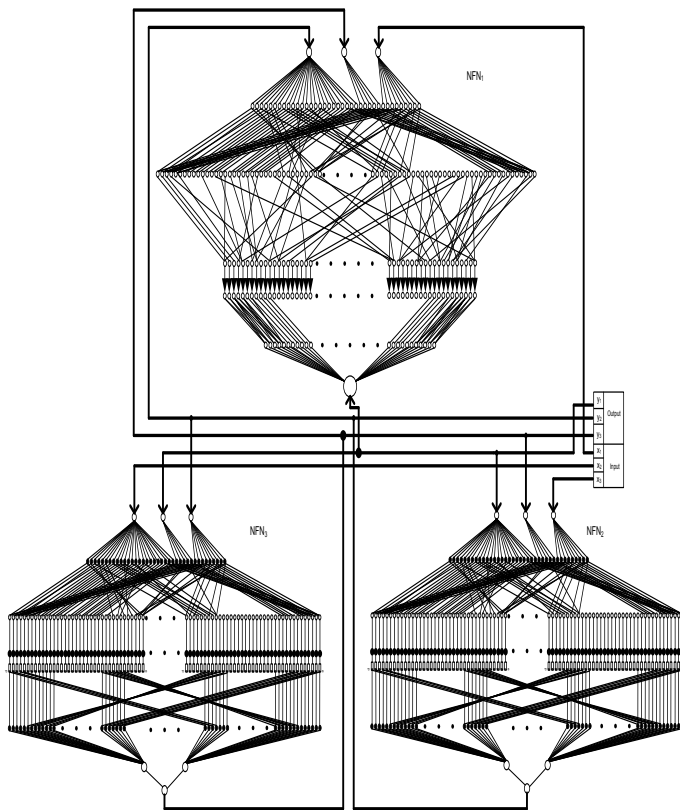


Fig. 6. Structure of the intelligent vehicle AHCS.

Operation of the first module NFN_1 begins from the fuzzification of vehicle velocity values and parameters of obstacles. The forming of output signal on the basis of fuzzy rules and fuzzy inference takes place on the next step. Then defuzzification is performed using the neural network consisting of three layers. Control signals correcting the motion direction are formed at the output of neural network. Obtained value comes to input of the second control module. Information about obstacles and the vehicle position also comes to the second input of NFN_2 .

Received data is fuzzificated and processed on the base of fuzzy rules. The fuzzy output of module is defuzzificated, and the velocity control signals are formed at the output of NFN_3 module.

The data received from the NFN_1 and the NFN_2 is transmitted to inputs of the third module. Information about the obstacle location comes to the third input of NFN_3 . The module output and defuzzification are calculated after the fuzzification procedure on the base of fuzzy rules. The information received on the output of NFN_3 is transmitted to inputs of the NFN_1 and the NFN_2 .

The developed system operates in the closed cycle. Operation would continue while sensor information about the parameters of environment, vehicle, and obstacles is received or until the desired location is achieved.

VI. CONCLUSIONS

To solve the autonomous mobile robot control problem in the data incompleteness conditions, we propose the structure

of AHCS. This structure is similar to FFNNs by the operation principles. We implemented operational modules of the AHCS on the basis of neuro-fuzzy networks. We developed the algorithms of modules operation for the control of motion direction, velocity, and the obstacle classification. Also we designed the structures of modules in the form of NFNs. The input parameters as linguistic and fuzzy variables were defined.

REFERENCES

- [1] Pshikhopov V.K., Medvedev M.Yu., Gurenko B.V. Homing and Docking Autopilot Design for Autonomous Underwater Vehicle // 2014, Applied Mechanics and Materials, pp. 490-491.
- [2] Neydorf R., Krukhmalev V., Kudinov N., Pshikhopov V. Methods of statistical processing of meteorological data for the tasks of trajectory planning of MAAT feeders // 2013, SAE Technical Papers.
- [3] Pshikhopov, V.Kh., Krukhmalev V.A., Medvedev M.Yu., Fedorenko R.V., Kopylov S.A., Budko A.Yu., Chufistov V.M. Adaptive control system design for robotic aircrafts // 2013, IEEE Latin American Robotics Symposium, pp. 67-70.
- [4] Pshikhopov V.Kh., Medvedev M.Yu., Gaiduk A.R., Gurenko B.V Control system design for autonomous underwater vehicle // 2013, Latin American Robotics Symposium, pp. 77-82
- [5] Pshikhopov V., Medvedev M., Neydorf R., Krukhmalev V. et al. Impact of the feeder aerodynamics characteristics on the power of control actions in steady and transient regimes // 2012, SAE Technical Papers.
- [6] Pshikhopov V.Kh., Ali A.S. Hybrid control of a mobile robot in dynamic environments // Proceedings of 2011 IEEE International Conference on Mechatronics, 2011. P. 540-545.
- [7] Коберси И.С. Разработка интеллектуального адаптивного обучаемого гибридного модуля управления безопасностью автомобиля. Неделя науки – 2009: Материалы научных работ. – Таганрог: Изд-во ТТИ ЮФУ, 2009. – С. 56 – 58.
- [8] Белоглазов Д.А., Коберси И.С. Интеллектуальная адаптивная гибридная обучаемая система управления транспортными средствами // Методы и средства адаптивного управления в электроэнергетике: тематический выпуск // Известия ЮФУ. Технические науки. – Таганрог: Изд-во ТТИ ЮФУ, 2010, №1 (102). – 260 с., С. 110-117. – Библиогр.: с. 117.
- [9] Рутковская Д., Пилинский М., Рутковский Л. Нейронные сети, генетические алгоритмы и нечеткие системы: Пер. с польск. И.Д. Рудинского. – М.: Горячая линия – Телеком. 2004. – С. 452.
- [10] Pshikhopov V., Krukhmalev V., Medvedev M., Neydorf R. Estimation of energy potential for control of feeder of novel cruise/feeder MAAT // 2012, SAE Technical Papers.
- [11] Pshikhopov V., Sergeev N., Medvedev M., Kulchenko A. The design of helicopter autopilot // 2012, SAE Technical Papers
- [12] Pshikhopov V.Kh., Medvedev M.Yu. Document Block design of robust control systems by direct Lyapunov method // 2011, IFAC Proceedings Volumes (IFAC-PapersOnline), pp. 10875-10880.
- [13] Pshikhopov V., Medvedev M., Kostjukov V., Fedorenko R. et al. Airship Autopilot Design // 2011, SAE Technical Paper.
- [14] Pshikhopov V.Kh., Ali A.S. Hybrid motion control of a mobile robot in dynamic environments // 2011, International Conference on Mechatronics, ICM 2011, pp. 540-545
- [15] Pshikhopov V.Kh., Medvedev M.Yu. Robust control of nonlinear dynamic systems // 2010, IEEE ANDESCON Conference Proceedings, ANDESCON
- [16] Lic C., Lee G. Neural-network-based fuzzy logic control and decision system. IEEE Transaction on computers, December 1991. - PP. 1320-1336.
- [17] Papageorgiou E.I., Stylios C.D., Groumpos P.P. Active Hebbian learning algorithm to train fuzzy cognitive maps // 2004, International Journal of Approximate Reasoning 37. – pp. 219–249.
- [18] Stylios C.D. Urinary bladder tumor grading using nonlinear Hebbian learning for fuzzy cognitive maps // 2004, Department of automatic control and systems engineering university of Patras.
- [19] Абрахин С.И., Беликова О.С. Аппроксимация функций с применением интеллектуальных технологий идентификации //

Труды XVI Всероссийской научно-методической конференции «Телематика'2009». - Санкт-Петербург, т.2., 2009. - С. 387-389.

- [20] Gang L., Thomas M. Design for self-organizing fuzzy neural networks based on genetic algorithms // 2006, IEEE Transactions on fuzzy systems, Vol. 14, N. 6, December. - pp. 755-776.

BBIPED: BCAM-Baltogar Industrial Platform for Engineering Design

C. Alonso-Montes, I. Garcia, A. Ramezani, L. Remaki

Abstract—Currently, commercial software for computational fluid dynamics offers a good set of features to deal with traditional designs. Within a competitive market industrial innovation is a key factor that must be faced by companies. However, the design of solutions to deal with industrial challenges cannot be done within commercial software due to the lack of flexibility. Open source initiatives are a good option but the learning curve is high, specially for industrial engineers profiles. In this paper, we present the BBIPED platform which has been designed to deal with turbomachinery applications in a simple and friendly way. The main goal is to keep the platform as simpler as possible providing the enough flexibility to include out-of-the-box solutions to cope with industrial challenges. BBIPED platform provides links with currently existing remarkable open source initiatives altogether with our own developments. Particularly, it is remarkable a first approach for automatic mesh generation based on geometry parametrization solution, and the provision of novel techniques to deal with multiple rotating frame (MRF): Multizone MRF an Virtual MRF. Case tests were designed to test the solutions and to assess and validate the results against commercial suites with promising results.

Keywords—CFD, Virtual Rotating Frame, Multizone Rotating Frame, Automatic mesh parametrization

I. INTRODUCTION

COMPUTATIONAL FLUID DYNAMICS (CFD) is a key area extensively used in a wide range of industrial processes in domains like aeronautics, automotive, ventilation, chemical manufacturing, oil industry, power generation, etc. Commercial software tools are currently available in the market that cope with the whole **CFD workflow** (meshing, solver simulation, data post-processing) to deal with traditional industrial problems, providing a good set of powerful and robust solutions. However, these tools lacks the flexibility to design out-of-the-box CFD solutions to deal with new scientific industrial challenges. In this sense, open-source alternatives provides enough flexibility for engineers to define their own and customised solutions. Some of them have gained a strong reputation due to its robustness, accuracy and flexibility within the scientific community, such as: Salome Platform [1] for CAD and mesh generator, SU² [2], [3] or FeNICS [4] for solver engines, or Paraview [5] for data postprocessing. One of the biggest open source tool players is OpenFoam [6], which covers the full CFD workflow providing flexible solutions for a wide range of industrial domains. Although the great performance and flexibility of OpenFoam, its learning curve

for engineers is huge, specially in terms of the tailoring it for novel solutions within the platform.

In this context, and particularly focusing on turbomachinery applications, there is a need of an open-source solution capable of reducing the learning step for industrial engineers, and maintaining the flexibility to add new CFD solutions. Following this approach and with the collaboration of Baltogar S.A, the **BCAM-Baltogar Industrial Platform for Engineering Design (BBIPED)** platform was designed to cope with the full CFD workflow for turbomachinery applications; from CAD and mesh design and generation, solver simulation and data post-processing. BBIPED design aims to take advantage of the integration of existing open-source cutting edge technologies together with new module developments, fulfilling industrial needs in terms of accuracy and performance. BBIPED platform uses the following open-source initiatives: Salome Platform for (CAD/mesh generation), SU² for CFD solver simulation, and Paraview for data post-processing and visualization. All of them are integrated through a common interface that will help the engineers to easily set up the working environment. BBIPED platform offers also novel features and functionalities tailored to turbomachinery applications, e.g. automatic geometric adjustments and generation for specific fan design, specific developments to tackle with the Multiple rotating frame method (multi zone and virtual multiple rotating frames). The main aim of the platform is to ease the usage of these applications within turbomachinery applications, with special emphasis on the final end users.

In this paper, the BBIPED platform will be explained in detail, specially focusing on the novel modules. In Section II the BBIPED platform is presented from a technical perspective, with special emphasize on the virtual rotating and multi-zone approaches, as well as the automatic geometry generation; in Section III some experiments are shown in order to demonstrate the usability of the platform; and in Section IV some conclusions and the future work are presented.

II. BBIPED IN A NUTSHELL

BCAM and Baltogar joined efforts to overcome the gap among industrial engineer needs and the usage of open-source initiatives tailored to turbomachinery applications. BBIPED is a fluid dynamic simulator aimed to handle efficiently challenging industrial fluid based applications. The main goal is to take advantage of existing technologies, and to provide new solutions for challenging industrial problems. In this section, the BBIPED platform will be presented, and the main innovative modules will be explained in detail.

The authors are members of the Computational Fluid Dynamics Group, Basque Center for Applied Mathematics - BCAM. SPAIN
{calonso, igarcia, aramezani, lremaki}@bcamath.org

This work was partly funded by the Department of Economic Promotion of the Biscay Foral Council (BFA/DFB - 6/12/TK/2012/00020), through the funding plan for Research Projects in Excellence Centres 2012

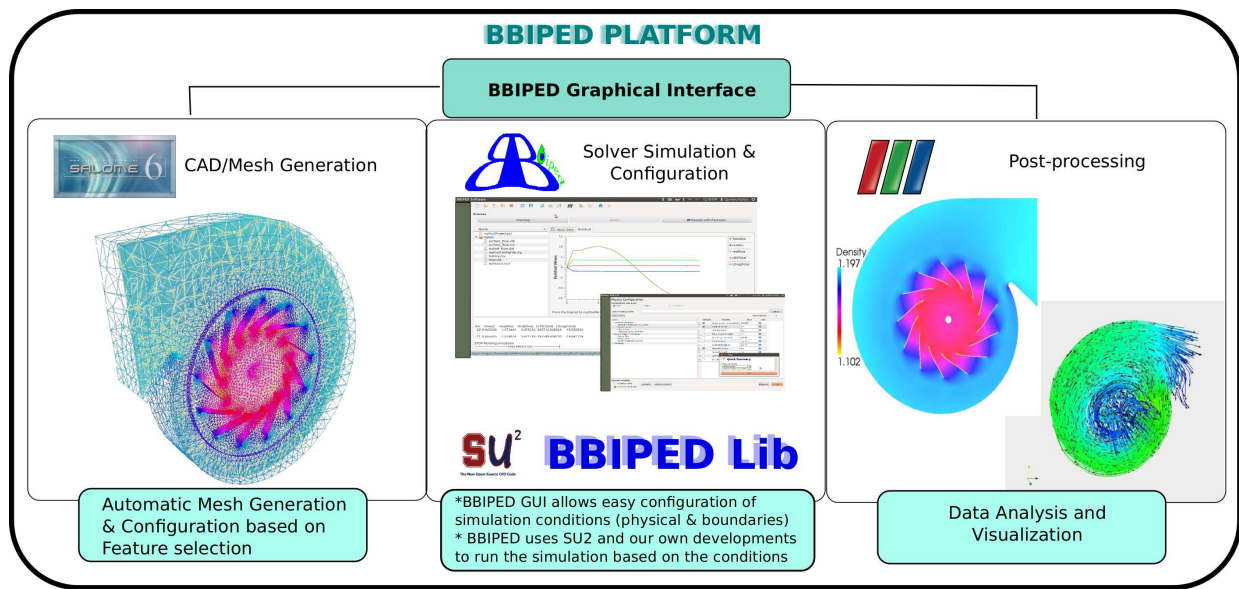


Fig. 1. BBIPED Platform Schema. The BBIPED Platform is composed by 3 main blocks (from left to right): CAD/Mesh generation, Solver configuration and simulation, and Post-processing. Each of the blocks are integrated through a common interface, the so-called BBIPED Graphical Interface (BBIPED GUI).

A. The BBIPED platform

BBIPED platform is conceptually split into three main blocks integrated through a common and user-friendly graphical interface (BBIPED GUI) (see Fig. 1):

- CAD and mesh generation
- Solver Simulation
- Data Postprocessing and Visualization

There are well-known and reputable open source initiatives that could cope with the requirements of the different blocks. So, BBIPED platform has been designed to integrate those valuable initiatives and giving room for easily adding ad-hoc initiatives. A first selection of open source initiatives have been integrated within the first version of BBIPED.

- The CAD and mesh generation will be managed through Salome platform, since there is the possibility to provide the flexibility to add customised functionality for automatic geometric parametrization. In BBIPED, some automation for specific geometry parametrization is provided (see subsection II-C for further details).
- Solver simulation is based on SU² tool suite. Customized developments regarding multizone rotating approaches are also provided by BBIPED site (see subsection II-D for further details)
- For the data post-processing and visualization, the Paraview tool was the best option for our needs.

In any case, the user has the possibility to change the CAD/Mesh tool as well as the data post-processors. Notice that OpenFoam was not selected, due to its size, complexity and generic nature. Indeed, tailoring OpenFoam to our requirements would be expensive in terms of cost and time. Furthermore, the learning curve for industrial engineers will be quite big.

A graphical user interface (GUI) is essential to ease industrial adoption of any software tool suit. In this sense, the BBIPED platform offers their own GUI (BBIPED GUI, see

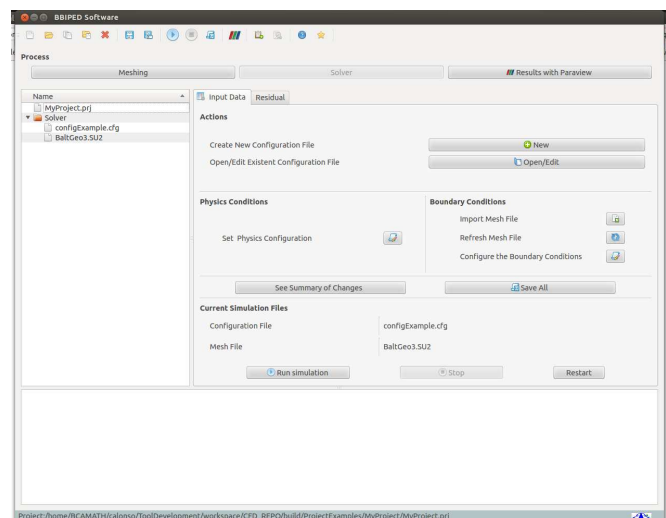


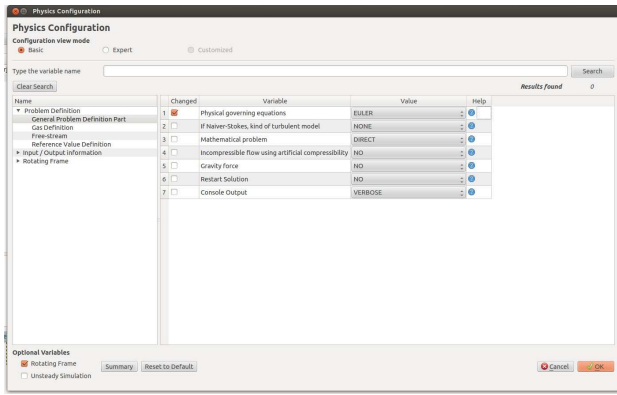
Fig. 2. BBIPED Graphical User Interface (GUI) example. The solver configuration is made and controlled through this window.

Fig. 2). This GUI has been designed to ease the usage by the engineers by means of the promotion of a standardisation and unification of the configuration process for the solver simulation. This GUI is offered to supply the lack of a SU² GUI, and to integrate our own conditions to run BBIPED Lib modules. In this sense, any change in the Solver engine will be transparent for the user

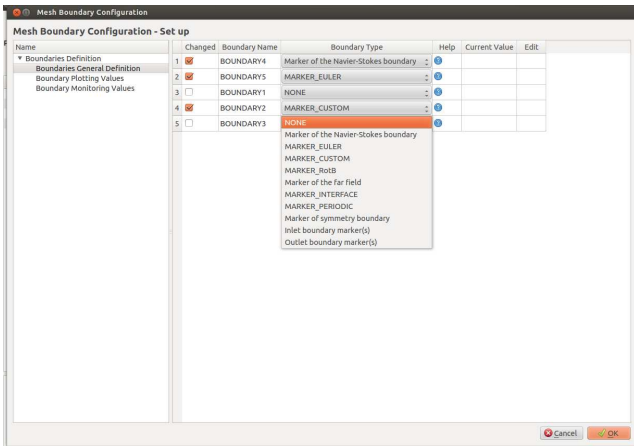
B. BBIPED Graphical User Interface

The main aim of the BBIPED GUI is to offer an automated and standardized CFD workflow to better manage the whole process from CAD generation, meshing, solving, and post-processing. Its main features are:

- Mesh Creation based on Salome Open Source platform, launched through BBIPED GUI



(a)



(b)

Fig. 3. Configuration of the simulation conditions: 3(a) helps in the definition of physical conditions and 3(b) helps in the boundary conditions associated to the mesh

- Case Tailored templates for automatic CAD and mesh generation for specific turbomachinery cases
- Innovative virtual multiple rotating frame and multi-domain approaches implemented to cope with industrial needs (included in BBIPED lib)
- Post-processing for data visualization launching Paraview tool

For mesh generation, Salome Platform has been considered from the very beginning. Some facilities to automate the mesh generation are also provided with the GUI, see II-C for further details.

For solver simulation, the main solver engine tested was SU². One of the drawbacks of using SU² as a solver engine is the lack of graphical interface. To overcome this issue, the BBIPED GUI has been designed to offer solver configuration capabilities compatible with SU². Moreover, the new functionalities provided by the BBIPED Lib, are smoothly integrated within the BBIPED GUI. This GUI has been developed using Qt technology [7] in order to easily integrate C++ developments, c++ based libraries and the possibility of OS-cross platform development. Currently, the first release has been fully tested in Ubuntu 12.04 and 13.0. In order to run any simulation, the main physical and boundary conditions must be established. BBIPED GUI offers the possibility to

independently configure from one side the physical conditions and from other side, the boundary conditions. The **physical conditions menu** (see Fig. 3(a)) are those conditions related with the solver and physical equations needed for the CFD simulation. In this case, BBIPED GUI offers different operating modes depending on the expertise of the engineer: *basic, advanced or personalized configuration view mode*. The basic one shows only those values to be configured for engineers with no expert knowledge in solver equations, setting some values by default. The advanced view shows all the variables but it is recommended only for real experts. The personalized view shows only a subset of variables to be configured. This is specially oriented for those projects where only a small set of variables need to be configured. The **boundary conditions menu** (see Fig. 3(b)) allows to the engineer to configure the boundaries of the correspondent mesh. The boundary mesh names are automatically extracted from the mesh file, avoiding naming errors and focusing the engineering work in the boundary set up. From the configuration done in both physical and boundary menus, an unique configuration file is obtained, which is also a SU² compliant. Notice that customized solver engines could be also used to run the same project, but they must be SU² format compliant. The evolution of the simulation and the residuals could be checked in two ways, numerically from the BBIPED GUI Console or graphically.

C. Geometry Parametrization and Automatic Mesh Generation

Usually, industrial applications uses variants of similar geometries or meshes of their products. However, it is a real challenge to provide a general automatic geometry generator. In BBIPED, we provided some specific automatic mesh generation based on geometry parametrization. We defined a formal procedure based on parametrization points and rules (see Fig. 4).

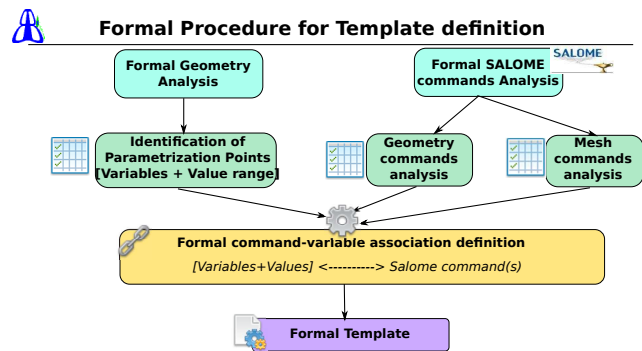


Fig. 4. Formal procedure to manually build up the templates for automatic geometry generation

Firstly, a formal and deep analysis of the geometry must be performed in order to define and identify the appropriate parametrization rules that are governing the different variants. However, this process is completely manual. In our case, and after analysing industrial fans used at Baltogar, suitable parameters were extracted to completely define a set of similar industrial fans in terms of bald curvature, bald number, casing

shape, etc. These terms are considered as the parametrization points, formed by a variable name and a range or set of feasible values. Notice that these parametrization points will be used later on by the engineer to define the different variants of the mesh.

One of the best features of Salome platform is the possibility to define customized programs for mesh generation (in Python language). So, once the parametrization points and the formal analysis of the mesh has been performed, the identification of the Salome commands must be done. This step needs an expert knowledge on Salome platform. Once the set of parametrization points are identified and the Salome commands are defined, the engineer must define the appropriate template command file to build up the geometry associating the commands with the correspondent variables. This will conform a formal template. The formal template will serve as the basis for building up the geometry according to the correspondent variables and values. This formal template is generic for the specific set of variables. Currently, a set of already predefined templates is provided for the generation of industrial fans.

Once the formal template is defined, BBIPED GUI allows an easy and user friendly way to use them by the engineers. BBIPED GUI can load the templates and the set of predefined parametrization points. The final user can configure the desired values for each of the variables (parametrization points). Then, the BBIPED geometry engine will build a specific Salome compliant geometry file based on the user input and the associated formal template to build the final mesh in an automatic way. The full process is shown in Fig. 5.

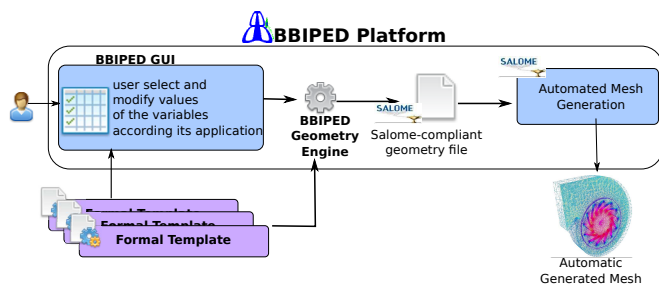


Fig. 5. BBIPED Geometry Automated Schema: showing how the template system works

The presented functionality is worthy for those situations where variants of the same geometry need to be produced, speeding up the initial mesh generation. Furthermore, new variants of the same geometry could be easily adopted by the company based on the analysis already made. This approach forces an standardised mesh generation reducing human errors and speeding up the mesh creation.

D. Multiple Rotating Frame

Realistic flow simulation is a key success factor as the basis of optimal design in turbomachinery. Indeed, the accurate and cost effective simulation of vortex flow caused by fixed and rotating frames interactions is one of the biggest challenges in turbomachinery [8], [9]. One of the most popular methods

used to simulate the rotating effect is the so called **Multiple Rotating Frame (MRF)** introduced by [3], [10]. This technique consists in the creation of an interface among rotating and static parts of the geometry, splitting the geometry into several zones independently meshed that communicate through **interfaces** by variables or fluxes exchange.

One of the most interesting features of MRF is that the unsteady flow could be solved as an steady state problem. Notice that due to the presence of fixed (volute) and rotating parts (rotor) simultaneously in the domain, this domain is unsteady (the flow in the domain is time dependent). But, in the MRF schema, the physics are viewed by the observer who is attached to the rotating frame [11] and on that view the flow is steady. So, the interface vertices belong to two different zones: rotating and stationary. The control volume for duplicated vertices (ones on the interface) should be the same, resulting in an automatic matching of the solution of both zones. Notice that in this approach it is not guaranteed that in both zones the flow properties on these common nodes to be identical. The Navier-Stokes equations, solved in a relative frame (associated to the rotating part), have just some extra terms to consider constant angular velocity of the domain. In each iteration, the information is transferred through the interfaces; so, the scheme which is applied for is important. Besides, since physically on the interface the velocity should has minimum radial velocity, the interface definition, which is the outer boundary of the rotating part, is crucial since any misplacing may cause divergence or non physical phenomena [12]. Another advantage of the MRF technique is the preservation of the autonomy in every zone. Furthermore, it is also suitable for zones that have common faces but not necessarily common nodes, like in sliding meshes or mixing planes or in some over-set grids approaches.

One of its main drawbacks is its inherent technical complexity in terms of geometry and from numerical simulation perspective. For the geometrical point of view, the interface must be created at CAD-level, which complexity grows specially in those with strongly connected rotating and static parts. Furthermore, the interface definition at CAD-level must be supported by a suitable mesh tool capable to build a grid with more than one closed domain and this could not be achieved by a mesher using a simple Delaunay strategy for instance. Even if nowadays modern meshers could achieve such a task, it is still not the case for many simple mesh generators. Finally, appropriate boundary conditions should be defined in the solver level to ensure adequate transfer of the information between the rotating and stationary domains. In terms of numerical simulation, two different set of equations (in stationary and rotating frame) are solved at both sides of the interface, so its position will affect the results and convergence [13]. In this sense, both the optimal position and the boundary condition at the interface must be defined a priori. Indeed, the optimal position cannot be accurately defined prior the simulation. So, its adjustment must be done at CAD level, re-meshed and simulated again.

SU² implements rotating frames and some basic multi-zone facility. In BBIPED platform, a new implementation has been included following the classical MRF technique which

special consideration on the data transfer techniques at the interface, the so-called **Multi-zone-MRF approach (MMRF)**. The whole description and motivation is described in [14]. In the MMRF approach, a user can set an arbitrary number of rotating and static parts and the correspondent number of meshes in a single simulation. So, the user can have in a single simulation a complete view of the residuals.

To overcome some of the drawbacks of MRF, in [15] a simplified approach of MRF was proposed, the **Virtual Multiple Rotating Frame (VMRF)**. In this technique, a virtual interface among rotating and stationary parts is built at the solver level, defining a virtual axisymmetric zone containing the rotating domain. The virtual zone can be made by a revolving curve which makes it easy to identify rotating nodes. Complex interfaces could be obtained by assembling simple geometries like cylinders, cones, spheres and so on. In this approach, the virtual interface is easily identified by the edges that have one vertex in the rotating zone (cylinder) and the other outside, which are the ones that actually need a specific treatment.

Both techniques were numerically tested against commercial software with promising results, as it is shown in [15]. Both methods are integrated into the BBIPED platform (within the BBIPED Lib), providing a formal procedure with both methods which eases the learning step for engineers. In one hand, VMRF projects are treated as traditional BBIPED projects, this is, the engineer will define the correspondent boundary and physical conditions, and then the specific rotating features. The BBIPED GUI automatically set up the environment to proceed with rotating features. On the other hand, BBIPED GUI offers the possibility to create specific multi-zone projects to handle MMRF approach. This Multi-zone facility prepares the working environment for the multi-zone execution, keeping the same configuration step workflow. In this case, the engineer will need to individually define a mesh for each zone with their corresponding physical and boundaries conditions following the traditional project structure. This philosophy unifies the treatment of the multi-zone mesh avoiding to add new complexity to this step.

III. EXPERIMENTS

As it has been previously commented, BBIPED Platform has been tailored to turbomachinery applications. BBIPED GUI has been designed using Qt Technology developed under Linux environment (tested on Ubuntu 12.04 LTS and Ubuntu 13.0). Initially, only the linux version has been delivered, although it is expected to release for other OS, on demand. The BBIPED Lib including the developments for MMRF and VMRF have been developed using C++ and SU² version 2.3 as a library. Currently, we are migrating the developments towards the new version of SU² version 3.0. The developments for the automatic mesh generation approach has been developed using Python and the correspondent API of Salome Platform. In this section some practical examples will be shown for the main modules presented before: *automatic mesh generation, MMRF and VMRF*.

A. Automatic mesh generation approach: An example

Automatic mesh generation based on geometry parametrization is a current challenge in industry. We analysed several fan geometries from Baltogar to extract the parametrization rules and points. As a matter of example, some of the parametrization points identified are the following: number of blades, blade stagger angle, blade leading edge radius, etc. All of them characterise the full set of different variants of Baltogar fan geometries. Once the set of parametrization points are identified, the correspondent Salome commands must be identified. An example of the Salome command for the blade number selection is shown:

```
Multi_Rotation_1 =
geompy.MultiRotatate1DNbTimes
(Blade_Base_Surface,OZ,"Blade_Number")
```

The engineer will select through the BBIPED GUI the number of desired blades for the fan, and the BBIPED platform (through Salome) will automatically generate the mesh with the correspondent number of blades (see Fig. 6).

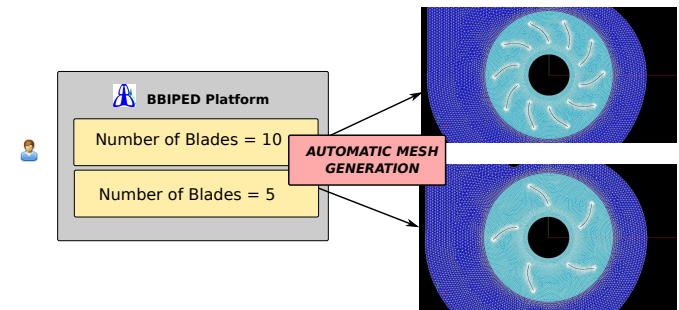


Fig. 6. Example of automatic generation of a fan with different number of blades. In one case, 5 are selected and the final mesh will contain 5 blades, whereas 10 is selected, it implies the generation of the correspondent 10 blades. Notice, that only the number of blades are needed and the mesh is automatically generated in accordance

B. MMRF and VMRF: examples

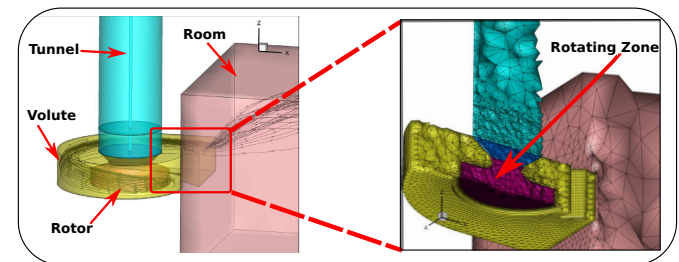


Fig. 7. Multi-zone Rotating Frame example. On the left, the original domain is shown: a fan to extract the air from a tunnel to another room. On the right side, a section of the mesh is shown. Notice that the fan has a rotating part (rotor) inside a static one (volute)

MMRF and VMRF approaches have been shown as powerful alternatives to deal with rotating and static elements within the same domain. Both of them are available within the BBIPED platform. In this section, we are going to show the usage of both within the platform through the example

proposed in Fig. 7. In this example, the fan extracts the air from the tunnel into the volute (yellow part) through the rotating rotor (orange part) towards the room. Each of the domain elements is discretized and every zone must be clearly defined through the different meshes. Notice that physically each element of the domain (tunnel, room, volute and rotor) has their own physical mesh.

In this particular example, for the MMRF approach needs so many meshes as areas explicitly indicating the interface between them. However, the VMRF approach allows the engineers to identify which are the interface areas within a global mesh without explicitly providing the physical mesh. BBIPED platform can handle both approaches. In Fig. 8, it is shown the different procedure in both cases within the platform. The MMRF needs as much meshes as parts are considered, in the example for the rotor and for the volute. This must be handled at the Mesh generation step (this is in Salome platform). Then, the BBIPED GUI provides a mechanism to configure each mesh independently. The simulation is performed simultaneously over all the meshes and the configuration files. In the case of the VMRF, only one mesh is actually needed. This implies that the engineer needs a single configuration for the whole domain, just indicating the rotating parts.

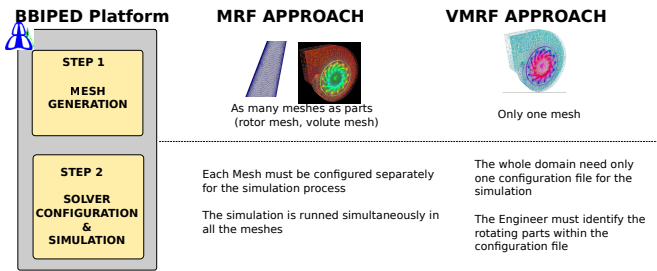


Fig. 8. Handling MMRF and VMRF approaches within BBIPED platform

Both methods, MMRF and VMRF from the BBIPED platform were assessed and validated against commercial tools to assure meeting industrial accuracy requirements. The assessment has been performed through the specific design of a 2D case, including all basic aspects of turbomachinery cases including rotating fan, fix volute and mixing zone with high speed free stream (see Fig. 9). This case has been solved using BBIPED platform and the commercial platform.

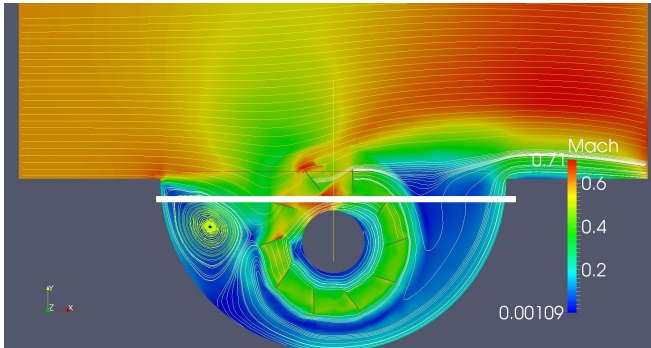


Fig. 9. Mach contours and streamlines

A 0.6 Mach flow through a fan with an angular speed of 150 rad/s is simulated. The flow is assumed to be inviscid and compressible. The domain is discretized by a full unstructured quads. This case has been solved respectively by VMRF, MMRF and Ansys-Fluent v. 14.5 (using MRF) [16]. Due to the interaction of the free stream and the rotating fan, a complex flow is observed which is depicted using streamlines and Mach contours in Fig. 9.

The pressure contours of VMRF and Fluent can be compared visually in Fig. 10. For a quantitative comparison, the pressure distribution is extracted from a horizontal line (horizontal white line in Fig. 9), then it is plotted in Fig. 11. These figures show a good agreement of both VMRF and MMRF with the highly reliable commercial software.

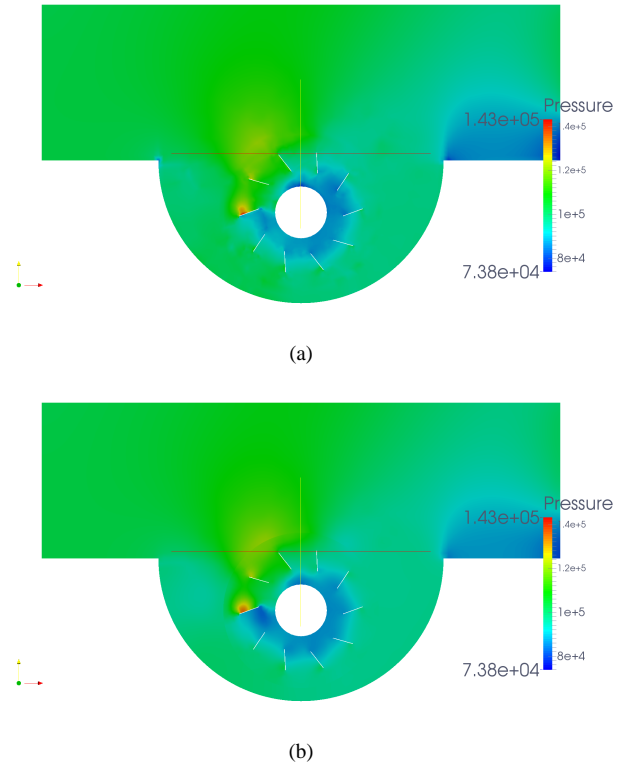


Fig. 10. Pressure Contours Comparison: 10(a) using BBIPED platform with VMRF, 10(b) using FLUENT

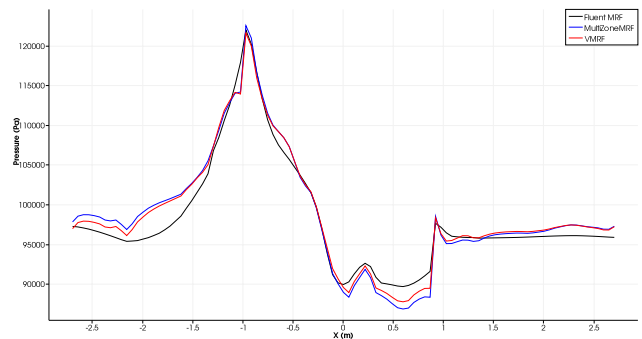


Fig. 11. Pressure values comparison along an arbitrary line among the MRF version of Fluent (black line), and the BBIPED approaches (MMRF -blue line- and VMRF-red line-)

IV. CONCLUSIONS AND FUTURE WORK

BBIPED platform has been designed and tested by industrial engineers with real fan cases to analyse weakness and new features to tailor this solution to turbomachinery applications. The set of new features is a potential innovation worthy for real industrial cases. The automatic mesh generation helps in speed up the mesh generation process, as well as reduces the human errors. Moreover, the manual step of analysing geometries could be seen as a good exercise to standardise the geometry design within the company. The usage of SU² as a solver allows BBIPED to be used as a valid GUI for a wide range of applications on top of the solver engine. The integration of our own solutions (MMRF and VMRF) was easily integrated through the interface and with the SU² tool. This process is transparent for the end user. So, if the user can use different SU² compliant solver engines, through BBIPED GUI. Moreover, we have tested the results obtained using the MMRF and VMRF approach against commercial software to validate the accuracy levels, with very promising results. The main aim of the whole platform is to offer the complete workflow for CFD processes keeping as much simple as possible, to ease the early adoption by industry.

The BBIPED platform is currently under test at Baltogar company. A public version will be released to the general public by the end of the project, in June 2014. Future developments are envisaged to extend the capabilities of the platform to new domains and facilities: turbulence models, vortex filaments, medicine simulations, etc.

ACKNOWLEDGMENT

The authors gratefully acknowledge the financial support of Diputación Foral de Bizkaia (DFB) for this research and the whole BCAM-BALTOGAR project on turbomachinery (grant BFA/DFB-6/12/TK/2012/00020).

REFERENCES

- [1] "Salome Platform." <http://www.salome-platform.org/>, 2014.
- [2] F. Palacios, T. D. Economon, A. C. Aranake, S. R. Copeland, A. K. Lonkar, T. W. Lukaczyk, D. E. Manosalvas, K. R. Naik, A. S. Padron, B. Tracey, A. Variyar, and J. J. Alonso, "Stanford University Unstructured (SU2): Open-source analysis and design technology for turbulent flows," in *AIAA Paper*, 2014.
- [3] F. Palacios, M. R. Colonna, A. C. Aranake, A. Campos, S. R. Copeland, T. D. Economon, A. K. Lonkar, T. W. Lukaczyk, T. W. R. Taylor, and J. J. Alonso, "Stanford University Unstructured (SU2): An open-source integrated computational environment for multi-physics simulation and design," in *AIAA Paper*, AIAA, 2013.
- [4] "FeNICS tool." <http://fenicsproject.org/>.
- [5] "Paraview Tool." <http://paraview.org/>, 2014.
- [6] "OpenFoam Tool." <http://www.openfoam.com/>, 2014.
- [7] "Qt technology." <http://qt.digia.com/>, 2014.
- [8] C. R. Meng Wanli, "Study of helicopter autorotation landing following engine failure based on a six-degree-of-freedom rigid-body dynamic model," *Chinese Journal of Aeronautics*, vol. 26, no. 6, p. 1380, 2013.
- [9] A. Califano and S. Steen, "Analysis of different propeller ventilation mechanisms by means of rans simulations," in *First International Symposium on Marine Propulsorsmp*, vol. 9, 2009.
- [10] J. Y. Luido, A. D. Gosman, and I. R. Issa, "Prediction of impeller-induced flows in mixing vessels using multiple frames of reference," *Inst. Chem. Eng. Sympo Ser.*, vol. 136, pp. 549–556, 1994.
- [11] J. D. Denton, "Some limitations of turbomachinery cfd," in *ASME Turbo Expo 2010: Power for Land, Sea, and Air*, vol. 7, 2010.

- [12] Z. Liu and D. L. Hill, "Issues surrounding multiple frames of reference models for turbo compressor applications," in *Int. Compressor Eng. Conf.*, vol. 1369, 2000.
- [13] M. Zdravec, S. Basic, and M. Hribersek, "The influence of rotating domain size in a rotating frame of reference approach for simulation of rotating impeller in a mixing vessel," *Journal of Engineering Science and Technology*, vol. 2, no. 2, pp. 126–138, 2007.
- [14] A. Ramezani, L. Remaki, and J. A. Suarez, "Bbiped an su2-based open-source: New multiple rotating frame developments," in *Open Source CFD Int. Conf.*, 2013.
- [15] L. Remaki, A. Ramezani, J. M. Blanco, and J. Antolin, "Efficient rotating frame simulation in turbomachinery," in *Proc. ASME Turbo Expo 2014: Turbine Technical Conference and Exposition (To Appear)*, 2014.
- [16] "Ansys fluent: Computational fluid dynamics simulator." <http://www.ansys.com/Products/Simulation+Technology/Fluid+Dynamics/Fluid+Dynamics+Products/ANSYS+Fluent>, 2014.

Carmen Alonso-Montes Carmen Alonso-Montes obtained her PhD. in Computer Science and Artificial Intelligence at the Univ. A Corua (Spain) in 2008. She worked in Tecnalia Research and Innovation in more than 20 National and European projects related with embedded systems, decision-making systems, and robotics. Then, she was project leader of machine vision projects in Ik4-Ideko for machine tool image-based applications. Currently, she is a post-doctoral fellow at BCAM, in the Computational Fluid Dynamics group.

Imanol Garcia Imanol Garcia obtained the BSc. Chemical Engineer (Univ. of Basque Country, Spain) and the MSc. Process System Engineering degree (Cranfield Univ, UK), both in 2011. He hold a MSc in Research in Mathematics (Univ. Basque Country, Spain) since 2012. Currently, he is doing his PhD on CFD at BCAM, supervised by Professor Lakhdar Remaki. His main research interests are: aero-acoustics and mesh generation techniques for turbomachinery problems.

Ali Ramezani Ali Ramezani obtained his PhD in Aerospace Engineering. He is a CFD specialist. His interests and experiences are focused on numerical methods including: Computational Fluid Dynamics, grid generation, moving boundary problems, parallel processing and dynamic load balancing, Multi-grid, turbulence modelling, overset grids, heat transfer, Finite Volume, Finite Element, Discontinuous Galerkin and Finite Difference, etc. He is a post-doctoral fellow at BCAM, in the Computational Fluid Dynamics group.

Lakhdar Remaki Lakhdar Remaki is a BCAM-BALTOGAR research professor and CFD group leader at Basque Centre of Applied Mathematics (BCAM). He received his PhD degree in Applied Mathematics from Claude Bernard University of Lyon, France. He has been a post-doctoral, research associate and research officer at Ecole Polytechnique of Montreal (Canada), McGill University (Canada), Swansea University (UK) and Sherbrooke University (Canada) respectively. His research expertise include computational fluid dynamic, PDEs, finite element and finite volume methods, shock detection, aerodynamic, gas-particle interaction, acoustics, mesh generation and adaptivity, signal and image analysis. He made several scientific contributions to the different fields published in over 60 journals and proceedings.

Performance Analysis of A Self Driven Phase Shifted Full Bridge Converter For Data Center Applications

Sevilay Cetin
Pamukkale University
Technology Faculty
Denizli, Turkey
scetin@pau.edu.tr

Abstract—For medium power applications, phase shifted full bridge (PSFB) converter is widely used because of its inherent zero voltage switching (ZVS) turn on feature for primary switches, operation at constant switching frequency and simple control procedure. Using of the synchronous rectifier (SR) for secondary side to cope with the high conduction loss is very common especially in the low output voltage applications. Two methods are possible to drive SRs; one is self driven method using directly secondary side voltage to generate driving signal and the other is active method. Obviously generating driving signal directly from secondary side of power transformer is easier and has advantage when isolation is requirement and where weight/power density is important. In this work, a self driven and synchronous rectified PSFB converter for a server adapter is proposed. A detailed performance analysis of self driver to generate reliable control signals for parallel connected SRs is evaluated. Finally, a simulation study operating at 80kHz and rated 1kW (12V-83A) has been carried out to verify the proposed theoretical analysis and evaluations.

Keywords-Phase shifted converter, synchronous rectifier, self driven, parallel connected synchronous rectifier.

I. INTRODUCTION

Recently, research in power converters area has focused on high power density due to the advantage of cost reduction, limited space and weight requirements in some application area like telecom/data center, electric vehicle/aircraft [1]. Besides, in data center application, increasing energy consumption due to more energy demand and rising energy price require high efficiency power conversion. Therefore high efficiency power conversion is getting more important key parameter in converter design in order to save energy and reduce cooling size.

Phase shifted full bridge (PSFB) converter is used widely for data center or telecom applications due to its high conversion efficiency, high power density, simple control structure and low electromagnetic interface (EMI) [2]-[10]. PSFB converter is usually used as second stage dc-dc conversion with low output voltage and high output current of a two stage systems such as server adapter. In these systems, total conversion losses are dominated by rectifier conduction losses at the secondary side. Therefore, optimum design taking into consideration of secondary side conduction losses will achieve high conversion efficiency.

Using synchronous rectifier (SR) is very common way to cope with high conduction losses especially in the low output voltage applications. In [4], a design evaluation which uses

parallel connected SRs in order to obtain best efficiency has been proposed and 99% efficiency has been achieved at 25 kHz operation frequency. However, active gate driver design for parallel connected SRs increases complexity and makes systems heavy due to the requirement of large PCB surface to place SRs drivers and their isolated power supply.

Obviously, self driving method using directly power transformer to generate driving signals seems more attractive compared to active gate drive method due to its simplicity and easy implementation especially when SRs are connected in parallel. In [11], a self driving method for low output voltage and high output current applications is proposed. In the method, output current is sensed with a current transformer and added power conversion circuit delivers sensing current to a DC voltage source. Here, added extra circuit increases complexity and cost of driver circuit. Optimum design consideration and analysis of synchronous rectified PSFB converter are given in [2] and [7]. In this design, using complex self driver circuit [12] to drive SRs makes circuit design more complicated compared to active method. Another method using auxiliary winding to generate driving signals is given in [13], this method is very simple and also provides conduction of both SRs when primary voltage is zero during dead time compared to conventional self driver method using directly secondary voltage of the power transformer. The performance of proposed self driver was evaluated with different transformer designs and validated by a prototype rated 25W. However, a detailed performance analysis taken into consideration of parallel connected SRs, parasitic inductance on the gate line, body diode conduction interval was not evaluated.

In this paper, a synchronous rectified PSFB converter design approach in order to obtain high efficiency for a server adapter is presented. Parallel connected SRs are used for center taped rectifier at the secondary side to reduce high conduction losses. A self-driven circuit is considered to avoid the need for an additional active control circuitry on the secondary. The self-driver method proposed in [13] is applied to generate control signals for the parallel connected SRs. Here, a resonance between large gate capacitance and parasitic inductance on the gate line due to long interconnects to the gate terminals of the SRs can influence the quality of driving signals. Therefore, a detailed performance analysis taken into account of the ringing on the gate voltage and the body diode

conduction is presented. Finally, a simulation study has been carried out for a server adapter application operating at 80kHz and rated 1kW output power to validate proposed theoretical performance analysis.

The rest of paper is organized as follows: Section II gives operation of power stages of PSFB converter, Section III evaluates the detailed SR self driver analysis, Section IV gives simulation results. Section V provides conclusions and future work.

II. OPERATION PRINCIPLE OF POWER STAGE

The schematic diagram of PSFB Converter with a center tapped rectifier is shown in Figure 1. Here, S_1 - S_4 are the primary side switches and they include antiparallel diodes and parasitic capacitors. SR_1 and SR_2 represent the parallel connected synchronous rectifier in order to reduce conduction losses. L_M is the mutual inductance, L_s is the equivalent inductance which is the sum of total leakage inductance and additional inductance connected series to primary side. TR is the high frequency power transformer with n turns ratio, L_o and C_o are output filter components, V_{in} is the input voltage source and V_o is the output voltage.

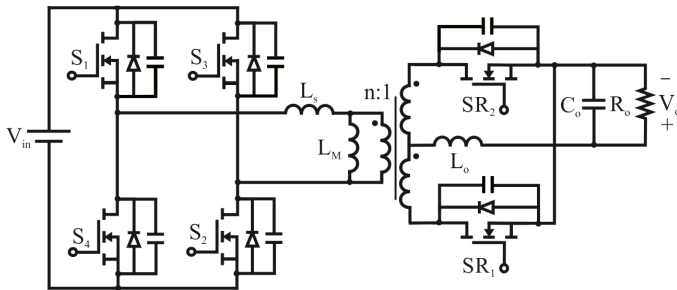


Figure 1 The schematic diagram of PSFB converter with center tapped rectifier.

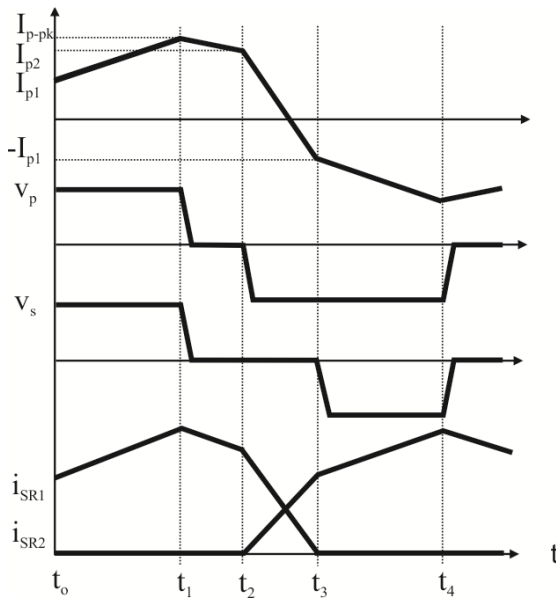


Figure 2 Operational key waveforms of PSFB converter.

Stage 1: (t_0 - t_1)

In this stage, V_{in} input voltage is applied to across the primary of the transformer and primary current increases linearly from I_{p1} to I_{p-pk} . Power is transferred from the input to the output. Primary current changes as follows,

$$\frac{di_p}{dt} = \frac{V_{in} - V_o'}{L_o' + L_s} \quad (1)$$

Here, V_o' , and L_o' are reflected output voltage and reflected output inductance to the primary side, respectively. The change of primary current is determined by the output filter inductance and the equivalent inductance. Reflected output filter inductance and output voltage definition can be written as

$$L_o' = n^2 L_o \quad (2)$$

$$V_o' = n V_o \quad (3)$$

Stage 2: (t_1 - t_2)

At the beginning of this mode, S_1 is turned-off so the output capacitor of the S_1 and S_4 is charged and discharged, respectively. Then converter starts to work in freewheeling mode; primary side of transformer is short circuited by conduction S_4 MOSFET and antiparallel diode of opposite side S_2 MOSFET. Therefore, there is no power transfer from the input to the output in this interval. The output current continues to flow through the SR_1 and L_o at the secondary side. Thus primary current slope in freewheeling mode is determined by output side and it can be written as

$$\frac{di_p}{dt} = \frac{V_o'}{L_o' + L_s} \quad (4)$$

At the end of this stage primary current reaches i_{p2} value and the operation of converter changes for the active stage.

Stage 3: (t_2 - t_3)

At $t=t_2$, S_2 is turned-off and S_4 is turned on so output capacitor of S_2 and S_3 is charged and discharged, respectively. The antiparallel diode of S_3 conducts after the output capacitor of S_3 discharges completely. Then negative input voltage, $-V_{in}$, is applied to the primary by the change of freewheeling mode to the active mode. During this stage both SR_1 and SR_2 are turned on for output current commutation. Therefore, secondary side of transformer is short circuited and there is no power transfer from the input to the output in this interval. At the beginning, charge/discharge interval is very short so it can be neglected. Thus, primary current can be written as equal to the reflected output current for this mode and its change can be determined as follows

$$\frac{di_p}{dt} = -\frac{V_{in}}{L_s} \quad (5)$$

At the end of this stage primary current is changed from I_{p2} to $-I_{p1}$ and the half of one switching period is completed. Remain half cycle operates with same principle proposed above but with a changed direction of primary current and voltage.

III. ANALYSIS OF SELF DRIVER

The self-driven method uses directly power transformer to generate the control signals so its implementation is very simple, cheap and it has an advantage where power density/weight is important like electric vehicle and data centers applications. In this study, a self-driver proposed in [13] is used for parallel connected SRs. The circuit schematic of the self-driven circuit and its operational waveforms are given in Figure. 3. Here, L_c represents the sum of the leakage inductance of auxiliary winding and stray inductance on the gate line. R_g is the series resistor, R_p is the parallel resistor to the gate terminal of SR, C_{GS} is the equivalent gate-source capacitance of each SR. D_1 and D_2 diodes provide for low conduction loss during turn-off. G_1 and G_2 are the gate terminal of the parallel connected SRs and S point is the source terminal.

The auxiliary winding is implemented directly on the power transformer and reflected primary voltage to the auxiliary winding is used for the driving voltage. Here, it is supposed that auxiliary winding voltage is constant and equal to the V_g or $-V_g$ to keep analysis simple. When auxiliary voltage is positive, upper side capacitor is charged and lower side one is discharged. When lower side capacitor voltage is about zero, v_{G2S} is clamped to $-V_{D2}$ and SR1 is turned on. When there is a voltage transition of the transformer, same current charges the lower side capacitor and discharges the upper side capacitor. Thus SR2 is turned on and gate of SR1 is clamped to $-V_{D1}$.

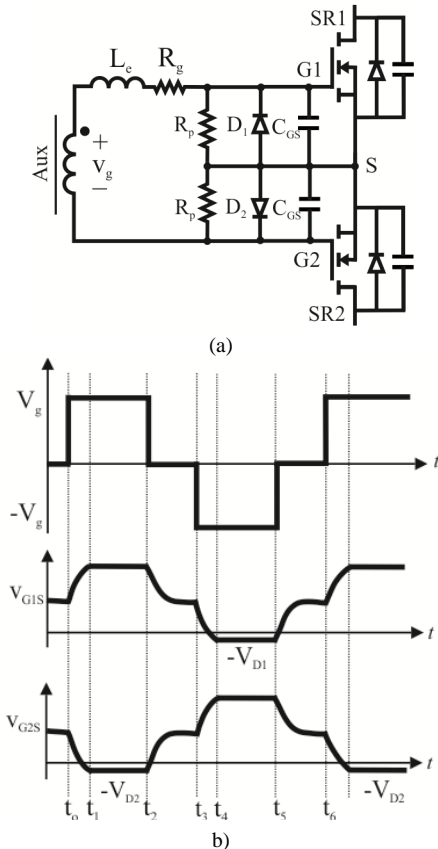


Figure. 3 The self driven circuit proposed in [13] and its operational waveforms.

During dead time, discharge of one capacitor charges the other capacitor and both capacitor voltage level can be kept at the same voltage level by using equal parallel balance resistors. Thus gate voltage of both SRs can be kept above the threshold voltage with a proper design while transformer voltage is zero.

PSFB converter design approach proposed in this study requires multiple parallel connected SRs to cope with high conduction loss. In this approach, the parasitic inductance due to long interconnections to the gate of parallel connected SRs can create low frequency resonance which can destroy the gate terminals. This low frequency resonance can be damped by series resistance taking into consideration turn-on and turn-off delay times to prevent body diode conduction loss. The body diode conduction time is an important parameter to reduce conduction loss as well as revers recovery loss. Therefore, a detailed performance analysis evaluating the ringing on the gate voltage, body diode conduction time should be presented to determine the optimum and reliable driver design parameters.

A. Gate Voltage Ringing Analysis

The auxiliary winding leakage inductance and trace inductance due to long interconnections to the gate terminal of the SRs can cause a resonance with large gate capacitance because of the multiple parallel connected SRs. Figure 4 defines the simulated resonance situation and shows the ringing occurred at the different stages of the driver operation. Here, the peak value of the gate voltage should be kept at the reliable value when auxiliary winding has voltage. During dead time, the gate voltage shouldn't turn back to the zero where it should be above threshold voltage at the turn-on and turn-off transitions. The ringing analysis can be evaluated separately while the auxiliary winding has a voltage and for the dead time interval.

Auxiliary winding has a voltage: The equivalent circuit when auxiliary winding has a voltage is given in Figure 5. The operational waveforms for this mode are given in Figure 3 for the interval of t_0-t_1 .

The gate voltage expressions for each SR can be written as follows according to the equivalent circuit analysis. In the analysis, it is supposed that $v_{G1S}(t_0)=v_{G2S}(t_0)=0$, $v_g(t_0)=V_g$. The maximum value of the gate voltage can be kept at the reliable level by the using of the following expressions.

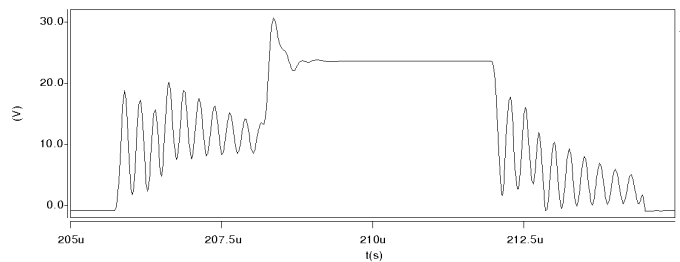


Figure 4 SR gate voltage ringing without damping.

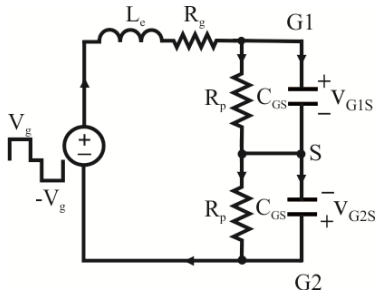


Figure 5. The equivalent circuit diagram of self driver when the auxiliary winding has a voltage.

$$v_{G1S}(t) = v_{G1S}(t_0) + \frac{V_g R_p}{2R_p + R_g} \times \left[1 + e^{-\frac{1}{2}\alpha(t-t_0)} \left(-\cosh\left(\frac{1}{2}(t-t_0)\sqrt{\alpha^2 - 4\beta}\right) - \frac{\alpha}{\sqrt{\alpha^2 - 4\beta}} \sinh\left(\frac{1}{2}(t-t_0)\sqrt{\alpha^2 - 4\beta}\right) \right) \right] \quad (6)$$

$$v_{G2S}(t) = v_{G2S}(t_0) - \frac{V_g R_p}{2R_p + R_g} \times \left[1 + e^{-\frac{1}{2}\alpha(t-t_0)} \left(-\cosh\left(\frac{1}{2}(t-t_0)\sqrt{\alpha^2 - 4\beta}\right) - \frac{\alpha}{\sqrt{\alpha^2 - 4\beta}} \sinh\left(\frac{1}{2}(t-t_0)\sqrt{\alpha^2 - 4\beta}\right) \right) \right] \quad (7)$$

$$\alpha = \frac{R_g R_p C_{GS} + L_e}{L_e C_{GS} R_p} \quad (8)$$

$$\beta = \frac{2R_p + R_g}{L_e C_{GS} R_p} \quad (9)$$

In the design of the driver, peak value of the gate voltage of each SR should be lower than maximum gate voltage rate given in datasheet. During the turn-off, the minimum value of the gate voltage should be equal to the voltage drop of the diode which is anti-parallel to the gate terminals.

The peak value of the gate voltage can be calculated and plotted as function of R_g and R_p for different L_e as shown in Figure 6. Figure 6(a) shows that low leakage inductance or high series gate resistance limits the gate voltage ringing and gate voltage level stays at the same level for different L_e above 1.8Ω of R_g due to well damping with bigger gate resistors. Decreasing the parallel resistors connected to the gate terminal improves the gate voltage behavior while ringing is not well damped by using 0.1Ω of R_g as shown in Figure 6(b). However, R_p value cannot change ringing situation very much so R_g and L_e are the most important key parameters for ringing damping.

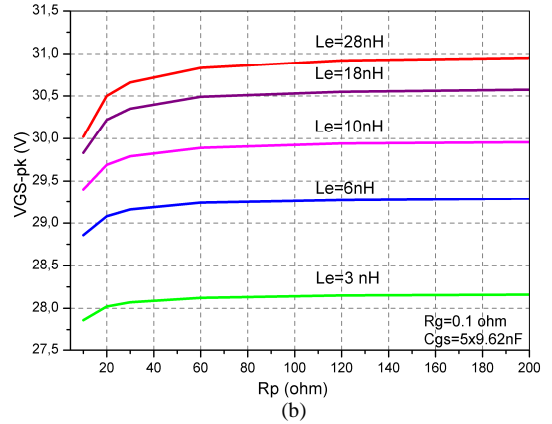
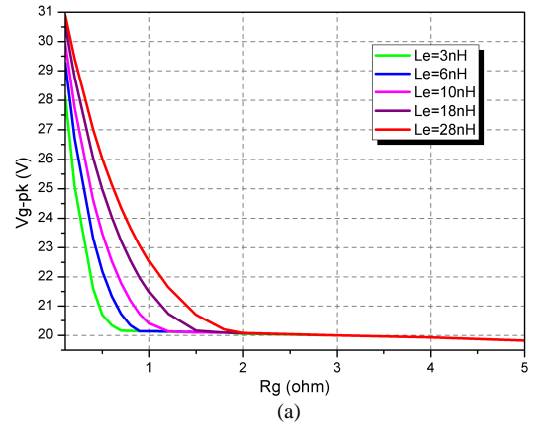


Fig. 6. The gate voltage peak value as function of (a) R_g and (b) R_p for different L_e values.

During the dead time: The equivalent circuit of the gate driver during the dead time is given in Figure 7 and its operational waveforms between t_2 and t_3 are shown in Figure 3. In this time interval, upper side capacitor starts to discharge and its discharge current charges the lower side capacitor. The voltage expressions for this time interval can be written according to the equivalent circuit analysis. The previous interval (t_1 - t_2) represents the steady state operation of the gate voltage and it is supposed that $v_{G1S}(t_2) = V_g - V_{Rg} - V_{D1}$, $v_{G2S}(t_2) = -V_{D1}$ at the beginning of the dead time. Here, V_{Rg} and V_{D1} represent the voltage drop of R_g and D_1 , respectively.

The gate voltages expressions for each SR can be written as follows,

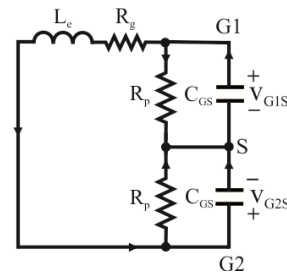


Figure 7. The equivalent circuit diagram of the self driver during dead time.

$$v_{G1S}(t) = v_{G1S}(t_2) - \frac{(V_g - V_{Rg} - V_{D1})R_p}{2R_p + R_g} \times \left[1 + e^{-\frac{1}{2}\alpha(t-t_2)} \left(-\cosh\left(\frac{1}{2}(t-t_2)\sqrt{\alpha^2 - 4\beta}\right) - \frac{\alpha}{\sqrt{\alpha^2 - 4\beta}} \sinh\left(\frac{1}{2}(t-t_2)\sqrt{\alpha^2 - 4\beta}\right) \right) \right] \quad (10)$$

$$v_{G2S}(t) = v_{G2S}(t_2) + \frac{(V_g - V_{Rg} - V_{D1})R_p}{2R_p + R_g} \times \left[1 + e^{-\frac{1}{2}\alpha(t-t_2)} \left(-\cosh\left(\frac{1}{2}(t-t_2)\sqrt{\alpha^2 - 4\beta}\right) - \frac{\alpha}{\sqrt{\alpha^2 - 4\beta}} \sinh\left(\frac{1}{2}(t-t_2)\sqrt{\alpha^2 - 4\beta}\right) \right) \right] \quad (11)$$

$$v_{G1S}(t_2) = v_{G2S}(t_2) \geq V_{th} \quad (12)$$

In this mode, effects of the driver parameters on the ringing analysis are similar to analysis proposed when auxiliary winding has voltage. The voltage level of the each SR should be above the threshold voltage, V_{th} , after determined turn on delay time, t_{don} and before determined turn off delay time, t_{doff} . Here, turn on delay and turn off delay time should be chosen as short as possible in order to reduce body diode conduction loss.

B. Body Diode Conduction Analysis

Body diode of the SR conducts when the gate voltage is below the threshold voltage due to delay caused by the resistance and the inductance on the gate line. Thus, conduction of the body diode increases the conduction losses and also creates the extra reverse recovery losses. The obtained equations during the dead time give the gate voltage waveforms to determine turn-on and turn-off delay time. Calculated and plotted rising and falling edge delay times as function of R_g for different L_e are shown in Figure 8. In the calculations, threshold voltage, V_{th} , for IRFP4110Pbf MOSFET is 2V and five MOSFETs in parallel are used for each SR to extract delay times as function of R_g and R_p .

Figure 8(a) shows that increasing L_e and R_g on the gate line increases rising edge delay time as expected. At the turn-off transition, larger L_e shortens the falling edge delay time for same R_g as shown in Figure 8(b). However, resonance between C_{gs} and L_e cannot be damped completely for low R_g values so falling edge delay time looks short for lower L_e values and looks long for larger L_e values due to increasing resonance frequency. Here, rising of R_g resistor also slows down the discharge of the gate-source capacitance and leads to long delay time for falling edges.

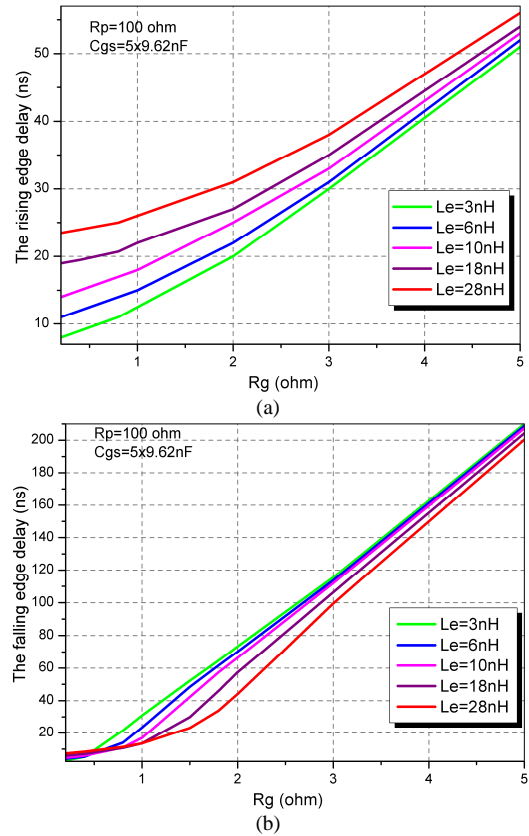
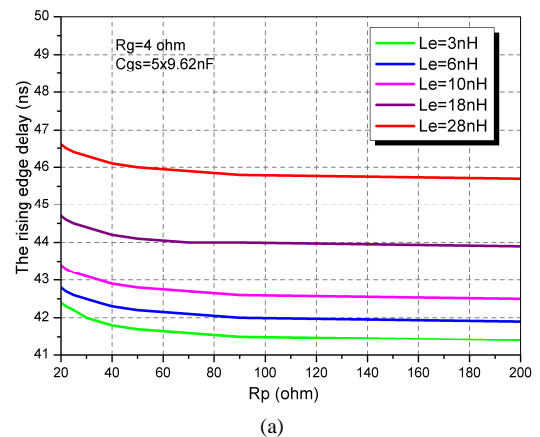


Figure 8. (a) Turn-on and (b) turn-off delay times as function of R_g for different L_e .

The impact of the parallel resistors on delay time is calculated and plotted in Figure 9. The rising edge is long for low R_p values due to limited capacitor charge current and short while R_p increases as shown in Figure 9(a). Due to the short circuit behavior of the gate-source capacitance during the turn-on transition, rising edge delay time is not affected very much by the R_p variation. However, falling edge is affected seriously as shown in the Figure 9(b). The falling edge delay time is very long for low R_p values and gate voltage cannot drop to the zero under 25Ω. However, increasing R_p value shortens the falling edge delay time and body diode conduction period as well due to extension of capacitor discharge time. Therefore R_p value should be selected as high as possible.



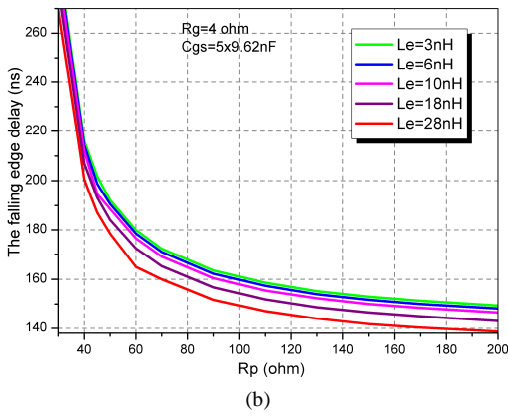


Figure 9. (a) Turn-on and (b) turn-off delay times as function of R_p for different L_e .

IV. SIMULATION RESULTS

The Saber simulation tool is used to validate theoretical analysis proposed above. A synchronous rectified PSFB converter for server adapter application with 12V output voltage and rated 1kW was simulated. The simulated circuit schematic is shown in Figure 10. 300V DC input voltage is used as input source. Real switching and magnetic components are modeled and simulated at 80kHz operation frequency. Here 20nH of L_e on the SR gate line was extracted from transformer implementation and PCB design of converter.

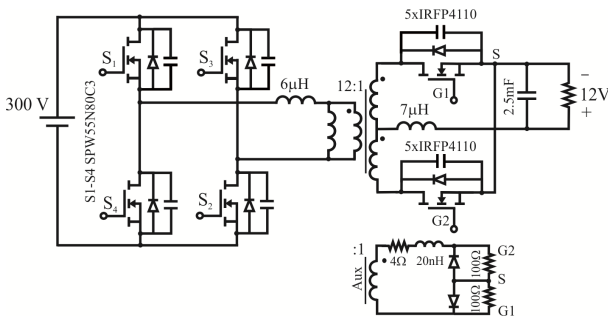


Figure 10. The simulated circuit schematic of synchronous rectified PSFB converter.

Simulated gate-source voltage waveform for each SR can be shown in Figure 11. The peak value of the gate voltages is acceptable; there is no overvoltage which can destroy the switches. The voltage level during dead time is also above the threshold voltage. The flowing SR current and its body diode conduction are shown in Figure 12.

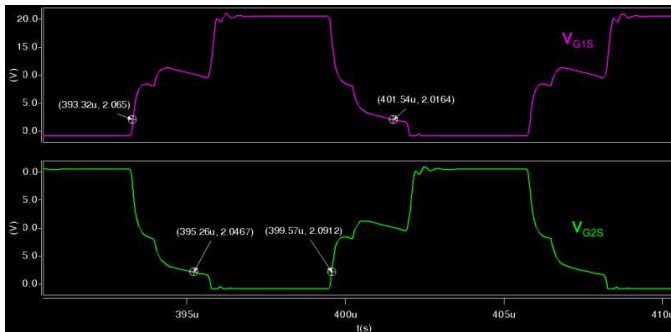


Figure 11. The gate control voltage of each SR.

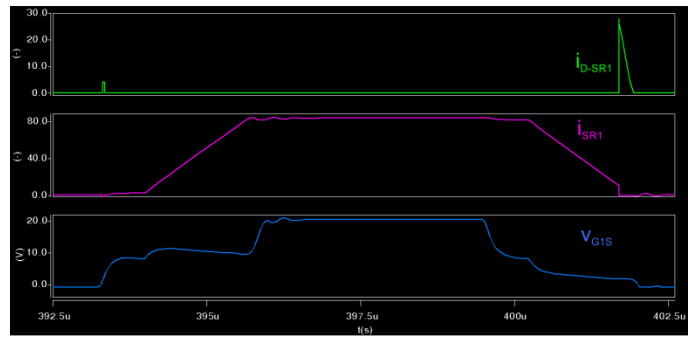


Figure 12. The gate control voltage of SR1, currents flowing through SR1 and its body diode.

Body diode conducts until gate voltage reaches threshold voltage during the turn-on transition and also when the gate voltage falls threshold voltage during the turn-off transition. Here, total body diode conduction period including turn-on and turn-off transition is around 210ns and it is around 4% of SR conduction period.

The efficiency comparison for the diode rectified and the synchronous rectified PSFB converter is shown in Figure 13. The simulated efficiency of synchronous rectified PSFB converter is 10% higher than diode rectified PSFB converter at full load condition.

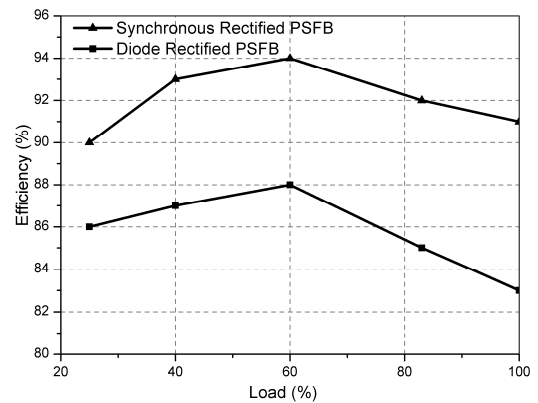


Figure 13. The efficiency comparison of diode rectified and synchronous rectified PSFB converter.

V. CONCLUSION

A self driven synchronous rectified PSFB converter design approach for server adapter is proposed. To reduce conduction loss, parallel connected SRs for the center tapped rectifier on the secondary side is discussed. A detailed performance analysis of a self driver for parallel connected SRs is proposed in order to obtain the quality and the reliable driving signals. In the analysis, ringing of the gate drive voltage caused by the inductance on the gate line and also body diode conduction are discussed. Finally, analysis is verified by Saber simulation for five parallel connected SRs. Obtained driving signals provide SR conduction in the most of total conduction period.

REFERENCES

[1] J. W. Kolar, U. Drogenik, J. Biela, M. Heldwein, H. Ertl, T. Friedli, S. Round, "PWM Converter Power Density Barriers", IEEJ Trans. Industrial Application, vol.128, no.4, pp. 1-14, 2008.

- [2] C. Zhao, X. Wu, P. Meng, and Z. Qian, "Optimum Design Consideration and Implementation of a Novel Synchronous ectified Soft-Switched Phase-Shift Full-Bridge Converter for Low-Output-Voltage High-Output-Current Applications", *IEEE Trans. On Power Electronics*, vol.24, no.2, pp.388-397, February 2009.
- [3] U. Badstuebner, J. Biela, D. Christen, J. W. Kolar, "Optimization of a 5-kW Telecom Phase-Shift DC-DC Converter With Magnetically Integrated Current Doubler", *IEEE Trans. On Power Electronics*, vol. 58, no.10, pp.4736-4745, October 2011.
- [4] U. Badstuebner, J. Biela, and J.W. Kolar, "An Optimized, 99 % Efficient, 5kW, Phase-Shift PWM DC-DC Converter for Data Centers and Telecom Applications", *Applied Power Electronics Conference and Exposition (APEC), 2010 Twenty-Fifth Annual IEEE*, pp.773-780, 21-25 February 2010, Palm Springs, California.
- [5] J.W. Kim, D.Y. Kim, C.E. Kim, and G.W. Moon, "A Simple Switching Control Technique for Improving Light Load Efficiency in a Phase-Shifted Full-Bridge Converter with a Server Power System", *IEEE Trans. On Power Electronics*, vol. 29, nNo.4, pp. 1562-1566, April 2014.
- [6] B. Gu, C.Y. Lin, B. Chen, J. Dominic, and J.S. Lai, "Zero-Voltage-Switching PWM Resonant Full-Bridge Converter With Minimized Circulating Losses and Minimal Voltage Stresses of Bridge Rectifiers for Electric Vehicle Battery Chargers", *IEEE Trans. On Power Electronics*, vol. 28, no. 10, pp. 4657-4667, October 2013.
- [7] C. Zhao, X. Wu, W. Yao, and Z. Qian, "Synchronous Rectified Soft-Switched Phase-Shift Full-Bridge Converter with Primary Energy Storage Inductor", *Applied Power Electronics Conference and Exposition*, pp. 581-586, 24-28 February 2008, Austin, TX.
- [8] J. Biela, U. Badstuebner, and J.W. Kolar, "Design of a 5-kW, 1-U, 10-kW/dm³ Resonant DC-DC Converter for Telecom Applications", *IEEE Trans. On Power Electronics*, vol. 24, no.7, pp. 1701-1710, July 2009.
- [9] J. Biela, U. Badstuebner, and J.W. Kolar, "Impact of Power Density Maximization on Efficiency of DC-DC Converter Systems", *IEEE Trans. On Power Electronics*, vol. 24, no.1, pp. 288-300, January 2009.
- [10] M. Xu, Yu. Ren, J. Zhou, and F. C. Lee, "1-MHz Self-Driven ZVS Full-Bridge Converter for 48-V Power Pod and DC/DC Brick", *IEEE Trans. On Power Electronics*, vol. 20, no.5, pp. 997-1006, September 2005.
- [11] X. Xie, J. C. P. Liu, F. N. K. Poon, and M. H. Pong, "A Novel High Frequency Current-Driven Synchronous Rectifier Applicable to Most Switching Topologies", *IEEE Trans. On Power Electronics*, vol. 16, no.5, pp. 635-648, September 2001.
- [12] J. M. Zhang, X.G. Xie, D.Z. Jiao, and Zhaoming Qian, "A High Efficiency Adapter with Novel Current Driven Synchronous Rectifier", *Telecommunications Energy Conference*, pp. 205-210, 23-23 Oct. 2003, Yokohoma.
- [13] P. Alou, J. A. Cobos, O. García, R. Prieto, J. Uceda, "A New Driving Scheme for Synchronous Rectifiers: Single Winding Self-Driven Synchronous Rectification", *IEEE Trans. On Power Electronics*, vol. 16, no.6, pp. 803-811, November 2001.

Mobile Objects Control in Unknown Environments

Viacheslav Pshikhopov

Abstract – In this paper an approach to mobile objects motion organization in unknown environments is presented. Novelty of proposed solutions is in using of bifurcational parameter for forming an unstable motion mode while switching from one stable mode to another. Proposed approach neither requires intelligent planning or control technologies nor preliminary mapping and complex navigation system. Modeling and experiment results of wheeled mobile robot motions in environments with stationary and mobile target points and obstacles of various forms are presented.

I. INTRODUCTION

A number of papers devoted to mobile objects (MO) motion control in unknown environments [1]-[6]. Proposed solutions are realized both in the class of intelligent motion planning and control systems (strategic level) and using tactical motion control methods. For example, work [5] proposes control algorithms requiring a preliminary MO motion trajectory planning, which is not always possible in the unpredictable and unknown environment. Also those algorithms requiring computation of two components of control law: stabilizing MO motion trajectory and deforming trajectory in the vicinity of obstacle. Control algorithms, proposed in [8] also suppose both preliminary mapping of MO functioning area and determining of obstacle size and motion parameters.

From our point of view the main problems connected with a use of mentioned approaches and methods of tactical level control are the following: requirement of preliminary trajectory planning and MO functioning area mapping, which is making significant limitations on objects motions in an unknown environments; imperfectness of coordination procedures of strategic planning levels and tactical control levels; necessity of additional information about geometry, phase coordinates of control object etc.

In this paper on the base of the results, obtained by the author in [9]-[11], proposed an approach to implementation of tactical level control of MO, functioning in an unknown environment. This approach involves third Lyapunov theorem (instability theorem) [12], [13], which allows to form controls in a real-time with a significantly lower requirements to strategic level and with minimal requirements to sensors.

This work was supported by Russian Scientific Foundation (project 14-19-01533) in Southern Federal University, Rostov-on-Don, Russian Federation.

Viacheslav Pshikhopov is with Southern Federal University, Rostov-on-Don, Russian Federation (e-mail: pshichop@rambler.ru).

II. MATHEMATICAL MODEL OF MO AND PROBLEM DEFINITION

Let the model of dynamics of MO and its kinematic properties are defined by the following set of equations [18]-[22]:

$$\dot{X} = M^{-1}(F_u - F_d - F_v), \quad (1)$$

$$\dot{\delta} = KU, \quad (2)$$

$$\dot{Y} = \Sigma(\Theta, X) = \begin{pmatrix} \Sigma_P(\Theta, X) \\ \Sigma_\Theta(\Theta, X) \end{pmatrix}, \quad (3)$$

where X is the m -vector of internal coordinates; M ($m \times m$) is the matrix of mass and inertia parameters, consisting of mass, moments of inertia and associated masses of MO; $F_u(X, Y, \delta, l)$ is the m -vector of control forces and torques, where l is the vector of constructive parameters; $F_d(X, Y, l)$ is the m -vector of non-linear elements of MO dynamics; F_v is the m -vector of measurable and unmeasurable external disturbances; δ is the m -vector of controllable coordinates; K – ($m \times m$) is the matrix of control coefficients; U is the m -vector of controls; $Y = (P, \Theta)^T$ is the n -vector of position P and orientation Θ of object coordinate system relative to base coordinate system, $n \leq 6$; $\Sigma(\Theta, X)$ is the n -vector of kinematic constrains; $\Sigma_P(\Theta, X)$ is the ν -vector of linear velocities of object coordinate system relative to base coordinate system; $\Sigma_\Theta(\Theta, X)$ is the $(n-\nu)$ -vector of angular of object coordinate system relative to base coordinate system.

It should be noted that the equations (1)-(3) describes a wide class of mobile objects: aerial vehicles, wheeled ground vehicles, airship based objects, etc.

Let us consider that the mobile object motion area contains mobile and stationary obstacles C_j , the coordinates (x, y, z) of characteristic point in a base coordinate system are known, also a target point coordinates $A_f(x_A, y_A, z_A)$ are set at the same coordinate system. In a general case point A_f could be non-stationary. Let also consider that sensor system of an object allows to measure a distance R_c , $c = \overline{1, k}$ from characteristic point of MO (for example an origin of object coordinate system) to closest points belonging to one or several obstacles C_j , placed at the sensor working area.

Problem statement is as follows: for a MO, defined by the equations (1), (3) it is needed to synthesize such a control law $F_u(P, X)$ and functioning algorithm of control system tactical level, which would provide the motion of

object from an arbitrary point (x_0, y_0, z_0) to target point A_f (x_A, y_A, z_A) (also requirements to orientation of MO in the point A_f could be stated) meeting the following conditions:

$$R_c \geq R, c = \overline{1, k}, \quad (4)$$

where k is a number of closest points, belonging to one or several obstacles; R is a constant, defining an acceptable shortest distance from characteristic point of MO to any of obstacles C_j .

In this case, different to the tasks stated in [10], [11], knowledge about velocity and acceleration of obstacles C_j is not required, number of obstacles and its motion behavior are not limited and no need to estimate the coordinates of any characteristic points. Thus we extend the representation of obstacles to geometrically complex figures without knowledge of its geometrical characteristics, but knowing only a distance R_c .

III. CONTROLS SYNTHESIS

As it was shown in the papers [23]-[27], all the set of requirement to MO steady state motion in the space $R^{n \times n}$ of base coordinates Y and velocities \dot{Y} in a general case could be represented as a vector-function Ψ of base coordinates and orientation angles, and also its derivatives:

$$\Psi = \Psi_{tr} + \tilde{A} \Psi_{ck} = 0, \quad (5)$$

$$\Psi_{tr} = \begin{vmatrix} N(P, t) \\ W(P, \Theta, t) \end{vmatrix} = \begin{vmatrix} P^T A_{i1}(t)P + A_{i2}(t)P + A_{i3}(t) \\ W_j(P, \Theta, t) \end{vmatrix} = 0,$$

$$i = \overline{1, v}, j = \overline{1, \mu},$$

$$N(v) = \bar{\xi} \left(P^T A_{v1}(t)P + A_{v2}(t)P + A_{v3}(t) \right),$$

$$\tilde{V} = \left(0_{v-1}, \xi \left(V^2 - V^{*2} \right), 0_{\mu} \right)^T,$$

$$\Psi_{ck} = J_s \dot{Y} + J_t + \tilde{V} = 0, \dim \Psi_{tr} = \dim \Psi_{cr} = v + \mu = m,$$

$$J_s = \begin{vmatrix} \frac{\partial N}{\partial P^T} & \frac{\partial N}{\partial \Theta^T} \\ \frac{\partial W}{\partial P^T} & \frac{\partial W}{\partial \Theta^T} \end{vmatrix} = \begin{vmatrix} J_{NP} & J_{N\Theta} \\ J_{FP} & J_{F\Theta} \end{vmatrix} = \begin{vmatrix} 2P^T A_{i1}(t) + A_{i2}(t) & 0 \\ \frac{\partial W_j}{\partial P^T} & \frac{\partial W_j}{\partial \Theta^T} \end{vmatrix},$$

$$\dim J_s = (m \times n),$$

$$J_t = \begin{vmatrix} P^T \dot{A}_{i1}(t) + \dot{A}_{i2}(t)P + \dot{A}_{i3} \\ \frac{\partial W_j(P, \Theta, t)}{\partial t} \end{vmatrix},$$

$$\tilde{A} = \begin{vmatrix} A & 0 \\ 0 & A_W \end{vmatrix},$$

where \tilde{A} is the block-diagonal matrix of coefficients, $\dim \tilde{A} = (m \times m)$; A_W ($\mu \times \mu$) is the matrix of coefficients, defining the character of transient process using orientation angles of MO, here μ is the a dimension of vector W_{μ} , defining requirements to orientation angles of MO; A is the diagonal ($v \times v$)-matrix, defining the character of MO motion relatively to trajectory manifold Ψ_{tr} , here v is a dimension of MO functioning space; A_{ij} are matrices of coefficients of

corresponding dimensions, produced by the motion planners using sensorial data and defining the form of non-stationary trajectory; \dot{A}_{ij} is the matrix of time derivatives of A_{ij} or estimates of its changing speed; W_{μ} – twice differentiable function of its arguments reflecting the requirements to MO orientation angles; ξ is the parameter, taking value of 0 (for the positioning task) or 1 (for the case of motion with a given speed); V, V^* are the MO velocity and its desired value; $0_{v-1}, 0_{\mu}$ are vectors of zero-elements of $v-1$ and μ dimensions correspondingly.

In the case of 2D MO motion control, $Y = (x \ y \ a)^T$, $v = 2$, $\mu = 1$, here x, y, a are MO position coordinates and orientation angle. Depending on certain task, manifolds (5) are defined as follows:

– motion along straight line $y = kx + b$ through two stationary points (x_0, y_0) and (x_f, y_f) with a constant speed V^* :

$$A_{12} = (-k \ 1), A_{13} = b, A_{11} = A_{21} \equiv 0, A_{22} \equiv 0, A_{23} = 0,$$

$$\tilde{V} = \left(0, (V^2 - V^{*2}) \right)^T, J_s = \begin{vmatrix} -k & 1 & 0 \\ 0 & 0 & 0 \end{vmatrix}, J_t \equiv 0, \quad (6)$$

$$\text{here } k = \frac{y_f - y_0}{x_f - x_0}, b = y_0 - x_0 k;$$

– turn to some desired angle a^* while moving with some desired speed V^* :

$$F_1 = \alpha - \alpha^*, \quad \tilde{V} = \left((V^2 - V^{*2}), 0 \right)^T, \quad J_s = \begin{vmatrix} 0 & 0 & 0 \\ 0 & 0 & 1 \end{vmatrix},$$

$$J_t = \begin{vmatrix} 0 \\ \dot{\alpha} \end{vmatrix}; \quad (7)$$

– positioning into stationary point (x_f, y_f) with zero speed:

$$A_{11} = A_{21} \equiv 0, A_{12} = (1 \ 0), A_{22} = (0 \ 1),$$

$$A_{13} = -x_f, A_{23} = -y_f, \tilde{V} \equiv 0, J_s = \begin{vmatrix} 1 & 0 & 0 \\ 0 & 1 & 0 \end{vmatrix}, J_t \equiv 0; \quad (8)$$

– motion along trajectory, passing through two non-stationary points $(x_0(t), y_0(t))$ and $(x_f(t), y_f(t))$, with constant speed V^* :

$$A_{12} = (-k(t) \ 1), A_{13} = b(t),$$

$$A_{11} = A_{21} \equiv 0, A_{22} \equiv 0, A_{23} = 0,$$

$$\tilde{V} = \left(0, (V^2 - V^{*2}) \right)^T,$$

$$J_s = \begin{vmatrix} -k(t) & 1 & 0 \\ 0 & 0 & 0 \end{vmatrix}, J_t = \begin{vmatrix} -\dot{k}(t)x + y - \dot{b}(t) \\ 0 \end{vmatrix}. \quad (9)$$

Control laws (autopilots), stabilizing manifolds (5), was synthesized in works [9, 10, 11]:

$$F_u = -M(\tilde{T}\tilde{A}K_0)^{-1}(\tilde{T}\tilde{A}K_1\Sigma_{\Theta} + K_2\Sigma + K_3 + K_4(t)) + F_d + \hat{F}_v, \quad (10)$$

$$K_0 = (JJ_{\Sigma P_x} + J_{\Theta}J_{\Sigma\Theta_x}), K_1 = (JJ_{\Sigma P_{\Theta}} + J_{\Theta}J_{\Sigma\Theta\Theta}),$$

$$K_2 = (\tilde{T} + \tilde{A})J_s + \tilde{T}\tilde{A}G_s,$$

$$K_3 = \tilde{A}\tilde{V} + \Psi_{tr}, K_4 = (\tilde{T} + \tilde{A})J_t + \tilde{T}\tilde{A}J_t^*, J = (J_P + J_V),$$

$$J_V = \begin{pmatrix} 0_{(v-1) \times v} & 2\Sigma_P^T & 0_{\mu \times v} \end{pmatrix}^T,$$

$$J_{\Sigma_{ij}} = \frac{\partial \Sigma_i}{\partial j}, \quad \text{здесь } i = \{P, \Theta\}, \quad j = \{x, \Theta\},$$

$$J_P = \begin{pmatrix} J_{NP} \\ J_{WP} \end{pmatrix}, \quad J_\Theta = \begin{pmatrix} J_{N\Theta} \\ J_{W\Theta} \end{pmatrix},$$

$$J_t^* = \left(j_t^*(1, 1), j_t^*(1, 2), j_t^*(1, 3), \frac{\partial^2 W_1}{\partial t^2}, \frac{\partial^2 W_2}{\partial t^2}, \frac{\partial^2 W_3}{\partial t^2} \right)^T,$$

$$j_t^*(1, k) = \left((P^T \ddot{A}_{k1} + \ddot{A}_{k2})P + 2(2P^T \dot{A}_{k1} + \dot{A}_{k2})\dot{P} + \ddot{A}_{k3} \right),$$

where G_s is the first time derivative of matrix J_s ; \ddot{A} is the second time derivative of matrix A or its estimate; \hat{F}_v is the estimate of the unknown forces and torques vector, \tilde{T} is the diagonal, sign-defined matrix of coefficients, defining the character of transient processes, $\dim \tilde{T} = (m \times m)$.

Matrix \tilde{T} have the following structure:

$$\tilde{T} = \begin{pmatrix} T & 0 \\ 0 & T_W \end{pmatrix},$$

where $T_W - (\mu \times \mu)$ is the matrix of coefficients, defining the character of MO orientation angles transient processes; T is the diagonal $(v \times v)$ -matrix, defining the character of MO motion relatively to trajectory manifold Ψ_{tr} . By $\xi = 1$, element $T(v, v)$ will define the character of trajectory velocity V_k change in transient mode.

In the case, when initial mathematical model of MO given only by the kinematic equations (3), it turns to a kinematic control algorithm synthesis [2]. Including additional dynamic chains in the form of integrators $\dot{X} = U$, on m controller outputs one can obtain the following kinematic control algorithm:

$$F_u = -M(\tilde{T}\tilde{A}K_0)^{-1}(\tilde{T}\tilde{A}K_1\Sigma_\Theta + K_2\Sigma + K_3 + K_4(t)), \quad (11)$$

where functional matrices K_0, K_1, K_2, K_3, K_4 have the same meaning as in equation (10).

It should be noted that implementation of algorithm (11) not allows an estimation of external disturbances vector \hat{F}_v and nonlinear dynamics vector F_d . This is substantially affecting the quality of MO tasks performing in the conditions of high speeds and significant external disturbances.

Algorithm (10) providing stabilization of manifolds (6)-(9) with the following values of functional coefficients in (10):

$$J_P = \begin{pmatrix} -k & 1 \\ 0 & 0 \end{pmatrix}, \quad J_\Theta \equiv 0, \quad J_t^* \equiv 0, \quad G_s \equiv 0. \quad (12)$$

$$G_s \equiv 0, \quad J_P = \begin{pmatrix} 0 & 0 \\ 0 & 0 \end{pmatrix}, \quad J_\Theta = \begin{pmatrix} 0 \\ 1 \end{pmatrix}, \quad J_t^* = \begin{pmatrix} 0 \\ \ddot{\alpha} \end{pmatrix}. \quad (13)$$

$$G_s \equiv 0, \quad J_P = \begin{pmatrix} 1 & 0 \\ 0 & 1 \end{pmatrix}, \quad J_\Theta = \begin{pmatrix} 0 \\ 0 \end{pmatrix}, \quad J_t^* = J_t \equiv 0. \quad (14)$$

$$J_P = \begin{pmatrix} -k(t) & 1 \\ 0 & 0 \end{pmatrix}, \quad J_\Theta \equiv 0,$$

$$G_s = \begin{pmatrix} -\dot{k}(t) & 0 & 0 \\ 0 & 0 & 0 \end{pmatrix}, \quad J_t^* = \begin{pmatrix} -\dot{k}(t)\dot{x} - \ddot{k}(t)x + \dot{y} - \ddot{b}(t) \\ 0 \end{pmatrix}. \quad (15)$$

Matrices $J_{\Sigma_{ij}}$ and J_V are explicitly defined by the dynamic equations (3) of a certain MO according to the expressions shown in (10).

IV. STRUCTURAL AND ALGORITHMIC REALIZATION OF MO CONTROL SYSTEM

The key idea of proposed approach for algorithmic implementation of MO control system consists of use of controls (6)-(9), stabilizing trajectories (5) in the areas free of obstacles, and application of third Lyapunov theorem (instability theorem) through inequalities (4) violation for the MO in the area of stationary or non-stationary objects at the distances R_c , less than acceptable value R .

In other words, according to the current position of MO in obstacles-free area, when inequalities (4) are met, or area, where those conditions are not met, it is proposed to organize such a modes of MO motion, at which planned trajectories given by the manifolds (5) become stable in a first case and instable in a second.

Papers [14, 15] have shown that inequalities (4) could be represented by one equation, which is proposed to form in this paper as follows:

$$\beta = \sum_j |R_c - R| + \sum_j (R_c - R), \quad (16)$$

where j – is a number of closest points in MO sensorial system coverage area and belonging to one or several obstacles.

Obviously, that compliance with all equations (4) value of parameter β (16) is equal to zero and not equal to zero if at least one of the equations (4) is violated. In the second case the value of β always positive.

Paper [10] has shown that stable character of MO motion along the trajectory Ψ_{tr} is provided by the positive definition of matrices T and A . Thus violation of conditions (4) causes one or both matrices T and A according to the third Lyapunov theorem, should be negative defined. Without loss of generality let us suppose that $T = A = \text{diag } s_i$, $i = \overline{1, v}$, where s_i – some functional parameter, defining the sign of matrices T and A .

With a glance of mentioned, elements of matrices T and A proposed to define as a following function:

$$s_i = \begin{cases} s_0 = \text{const} > 0, & \text{при } \beta = 0, \\ -\frac{1}{\beta}, & \text{при } \beta \neq 0, \end{cases} \quad (17)$$

here s_0 defines the character of motion in an obstacle-free area.

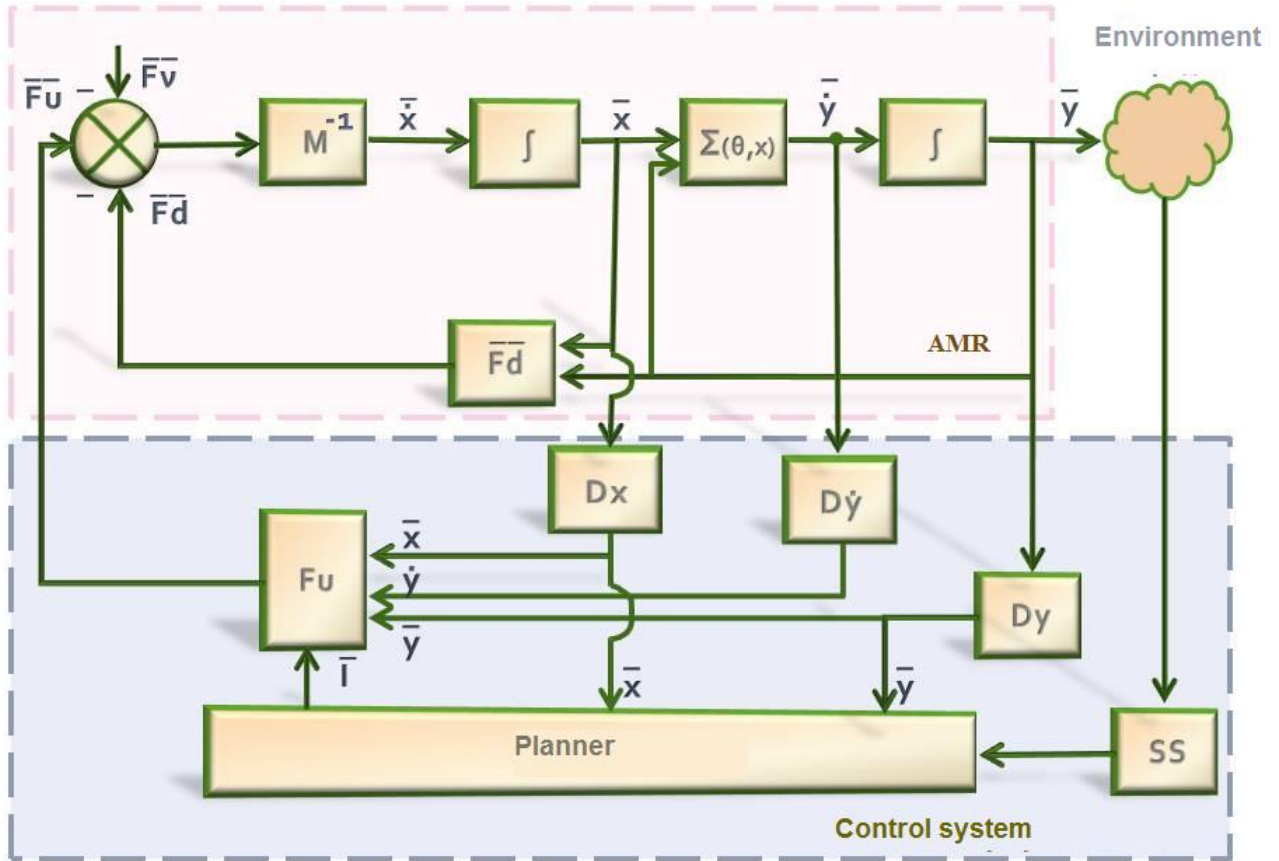


Fig. 1. Structural scheme of closed-loop system

Thus, forming the elements of matrices T and A according to expression (17), we provide a stable character of MO motion along manifold Ψ_r , excluding areas, where inequalities (4) are violated.

Since the proposed MO motion control supposes transfer from one stable state through the unstable motion to another stable state, β is proposed to be called bifurcational.

Structure scheme of closed-loop system, implementing the proposed algorithm is shown on Fig. 1. It includes following components: blocks M , F_d , $\Sigma(\theta, x)$, summator, integrators and connections, reflecting the structure of control object (1), (3); MO motion planner (operator, on-board computer, neural network etc), intended for forming manifolds (5), (6)-(9) coefficients and matrices \tilde{T} and \tilde{A} elements; internal D_x and external D_y coordinates sensors; control calculation block F_u according to expressions (10), (12)-(15); sensor R for measuring distance to the closest points belonging to one or several obstacles.

Closed-loop system is functioning as follows. After control system initialization block R measures distances R_c and calculates according to expression (16) the value of bifurcational parameter β , which is transmitted to planner for forming the elements of matrices T and A .

Planner forms the vector I of the motion parameters: coordinates of target point A_f , which is non-stationary in a general case; elements of matrices A_{ij} , defining the requirements to steady motions of MO (in the initial time, in case of absence of obstacles elements of matrices A_{ij} defines a straight line, connecting initial position of MO with the point A_f); desired speed of object V^* ; parameters s_i , defined by the expression (17) and specifying the character of MO motion in transient states; parameter ζ , characterizing the type of control task; and, in case of need construction parameters and external disturbances estimation vectors \hat{l} and \hat{F}_v [16].

Block F_u forms controls F_u on a base of parameters I , received from planner, according to expression (10), (12). These controls are sent to MO's actuators and supports its motion along line, connecting initial position of MO with point A_f .

In the case of conditions (4) violation, planner, according to expression (17), changes values of parameters s_i and MO switching to unstable motion mode until the bifurcation parameter β is set to zero, i.e. object is get to the free of obstacles area.

After entering the area free of obstacles planner forms the elements of matrices A_{ij} in expression (7) and object according to controls, calculated using equations (10), (13), makes a turn until it meets condition $a_A - a < \pi/2$, where a_A , a – correspondingly target point A_f direction angle and current value of object orientation angle. In the case of zero bifurcational parameter β planner forms and elements of matrices A_{ij} , defining straight line, connecting the current position of MO with point A_f , and block F_u performs the motion of MO along the newly planned line. Otherwise when $\beta \neq 0$, object switching to unstable motion mode until the bifurcational parameter β is set to zero.

It should be noted that object turning is used for the additional definition of its motion along newly planned line. In case of using another procedures for forming the requirements to trajectory speed V [4], turning step could be excluded from the proposed algorithm.

After object enters to A_f area free of obstacles planner forms elements of matrices A_{ij} according to expressions (8) or (9), which is corresponds to controls (10), (14) or (10), (15) respectively.

The declared MO motion control system functioning algorithm states some limitations on its usage. Thus, for example, if some obstacles or other MO are blocking object's motion, it could not get out from the unstable mode. In case when obstacles have a complex form, like maze, a stated task could be not solved within the proposed algorithm and without some intelligent planner, for example with use of neural network [17]. Control target could be not reached, if there's not enough energy for MO to deal with high dynamic mobile obstacles and target.

Main advantages of the proposed approach are easy of its implementation and no need to compute trajectories in the obstacle area, which is not always possible in real time, while performing obstacle avoidance task.

Described algorithm could use expressions for generating controls to stabilize planned trajectories in an area free of obstacles other than (10), (12)-(15).

V. MO MOTION MODELING

Motion modeling of MO based on wheeled platform with front steering wheel and two driving wheels, which is controlled by one drive in an unknown environments is performed using described algorithm and Matlab. Mathematical model of MO is presented in [10].

Functional coefficients from (10) are defined according to

following statements:

$$\Sigma_P = \begin{pmatrix} r^* \omega \left(c\beta c\alpha - h \frac{s\beta c\alpha}{d} \right) \\ r^* \omega \left(c\beta s\alpha + h \frac{s\beta c\alpha}{d} \right) \end{pmatrix}, \quad \Sigma_\Theta = \left| \frac{r^* \omega s\beta}{d} \right|, \quad (18)$$

$s(\cdot) = \sin(\cdot)$, $c(\cdot) = \cos(\cdot)$, $P = (x \ y)$, $\Theta = \alpha$, $X = (\omega \ \beta)^T$, where ω – angular speed of rear wheels; β – turn angle of steering wheel; α – orientation angle of longitudinal axis of platform relatively to base coordinate system; r^* , h , d , a , b – constructive parameters.

Thereafter,

$$J_{\Sigma P \Theta} = \begin{pmatrix} r^* \omega \left(-c\beta s\alpha - \frac{hs\beta c\alpha}{d} \right) \\ r^* \omega \left(c\beta c\alpha - \frac{hs\beta s\alpha}{d} \right) \end{pmatrix},$$

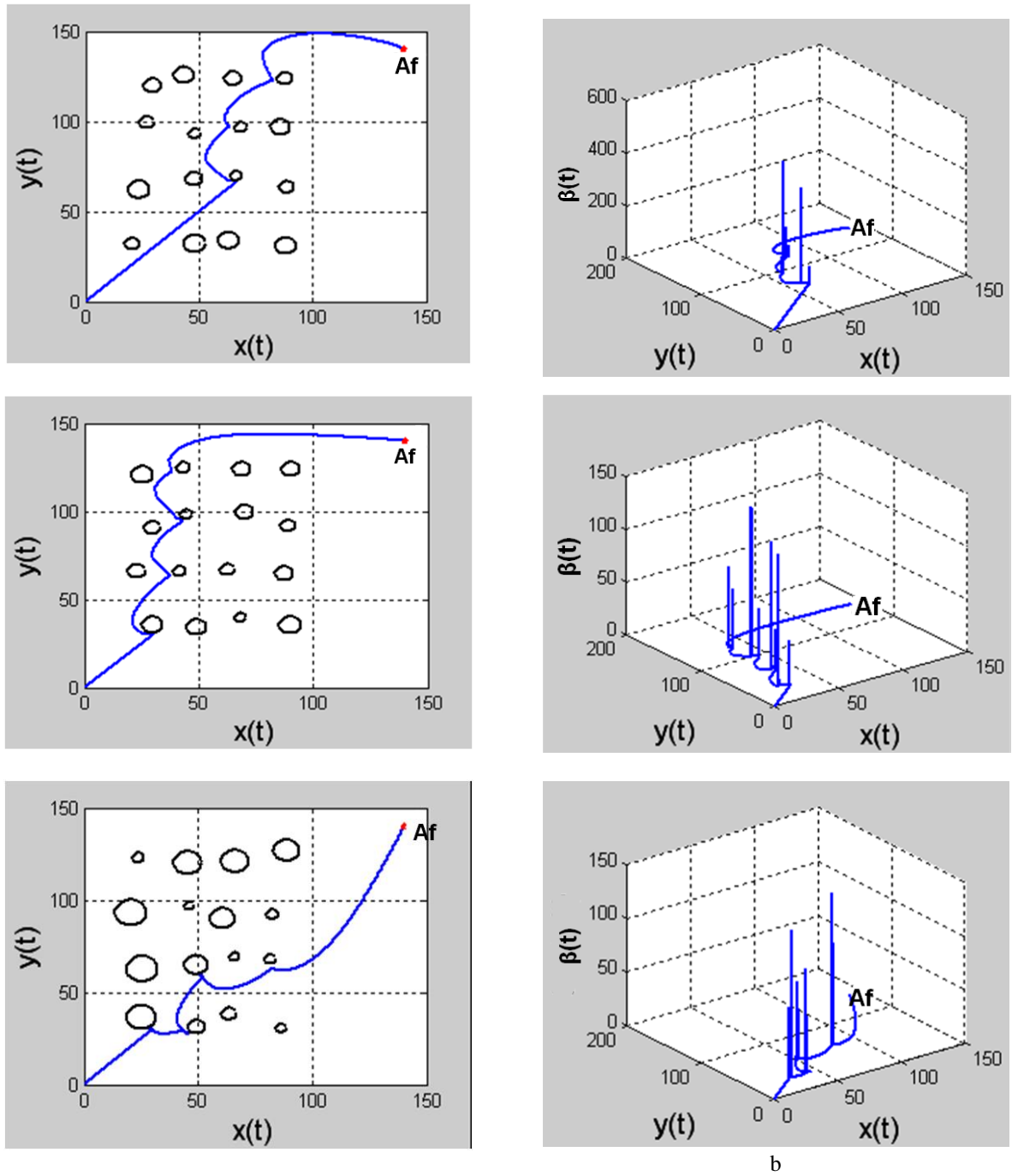
$$J_{\Sigma \Theta \Theta} = 0, \quad J_{\Sigma \Theta \alpha} = \left| \frac{r^* s\beta}{d} \quad \frac{r^* \omega c\beta}{d} \right|,$$

$$J_{\Sigma P x} = \begin{pmatrix} r^* \left(c\beta c\alpha - \frac{hs\beta s\alpha}{d} \right) & r^* \omega \left(-s\beta c\alpha - \frac{hc\beta s\alpha}{d} \right) \\ r^* \left(c\beta s\alpha + \frac{hs\beta c\alpha}{d} \right) & r^* \omega \left(-s\beta s\alpha + \frac{hc\beta c\alpha}{d} \right) \end{pmatrix}.$$

Fig. 2 presents results of modeling of MO motion from initial point (0;0) to stationary point A_f (140; 140) in the environment with convex obstacles: a) MO motion trajectories with various positions and geometry of stationary obstacles and b) plots of bifurcational parameter β change merged with motion trajectory.

Fig. 3 shows results of modeling MO motion from initial point (30;30) to stationary points A_f in an environment with linear obstacles with speeds $V=3$ m/s and $V=2$ m/s a) motion trajectories and b) values of trajectory speed of MO. Lower figure 3,a demonstrating limitations on application of proposed approach. Control task could be successfully solved by giving the planner intelligent properties [28].

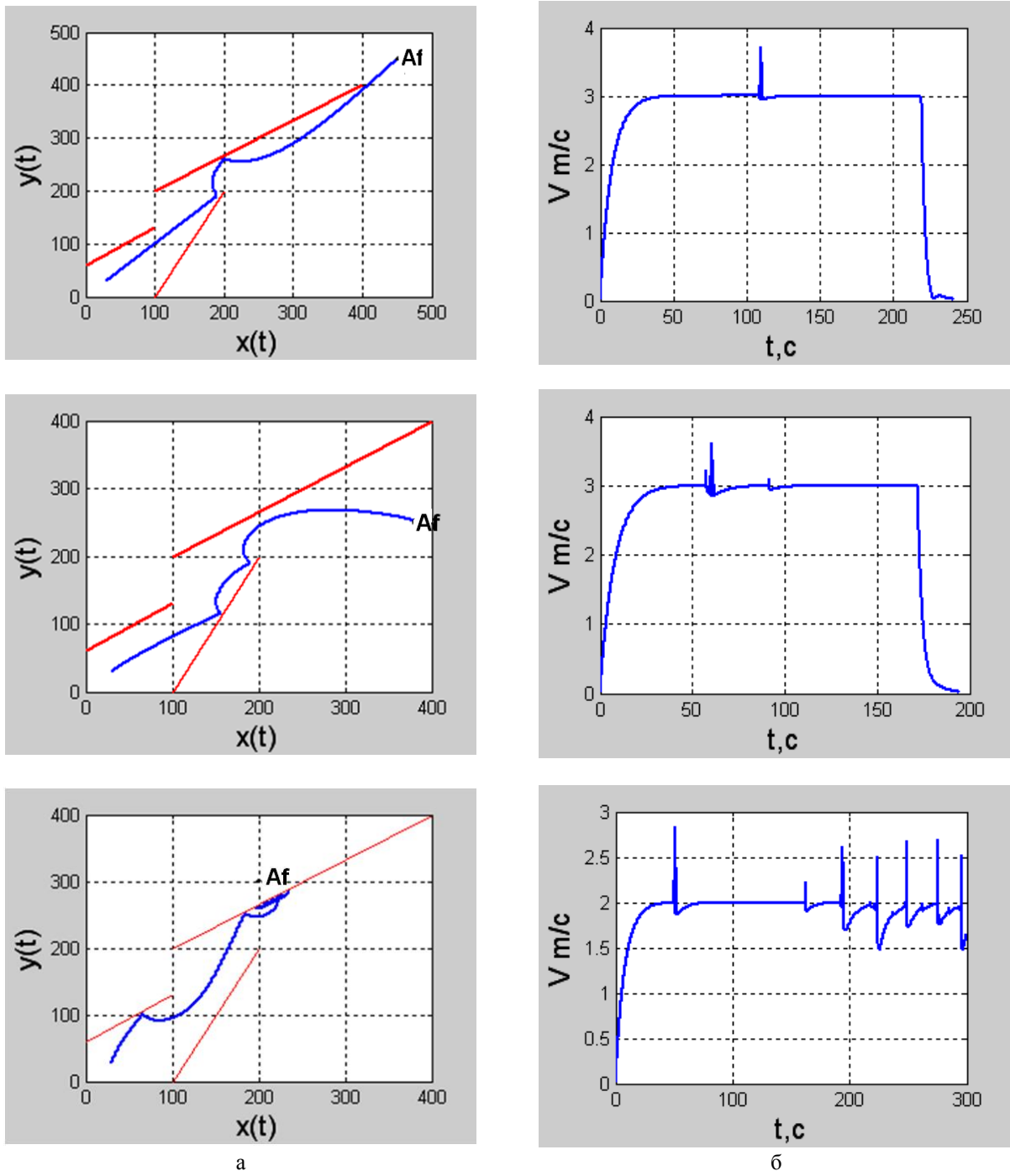
Fig. 4 shows MO motion trajectories to target non-stationary point in the environment with various placements of convex obstacles. Target point moving along straight line from point A_0 to point A_f .



a – MO motion trajectory

b – plots of bifurcational parameter β change merged with motion trajectory

Fig. 2. Results of modeling MO motion to stationary point A_f in the environment with convex obstacles



a – MO motion trajectory

b – trajectory speed change V change plots

Fig. 3. Results of modeling MO motion to stationary point A_f in the environment with linear obstacles

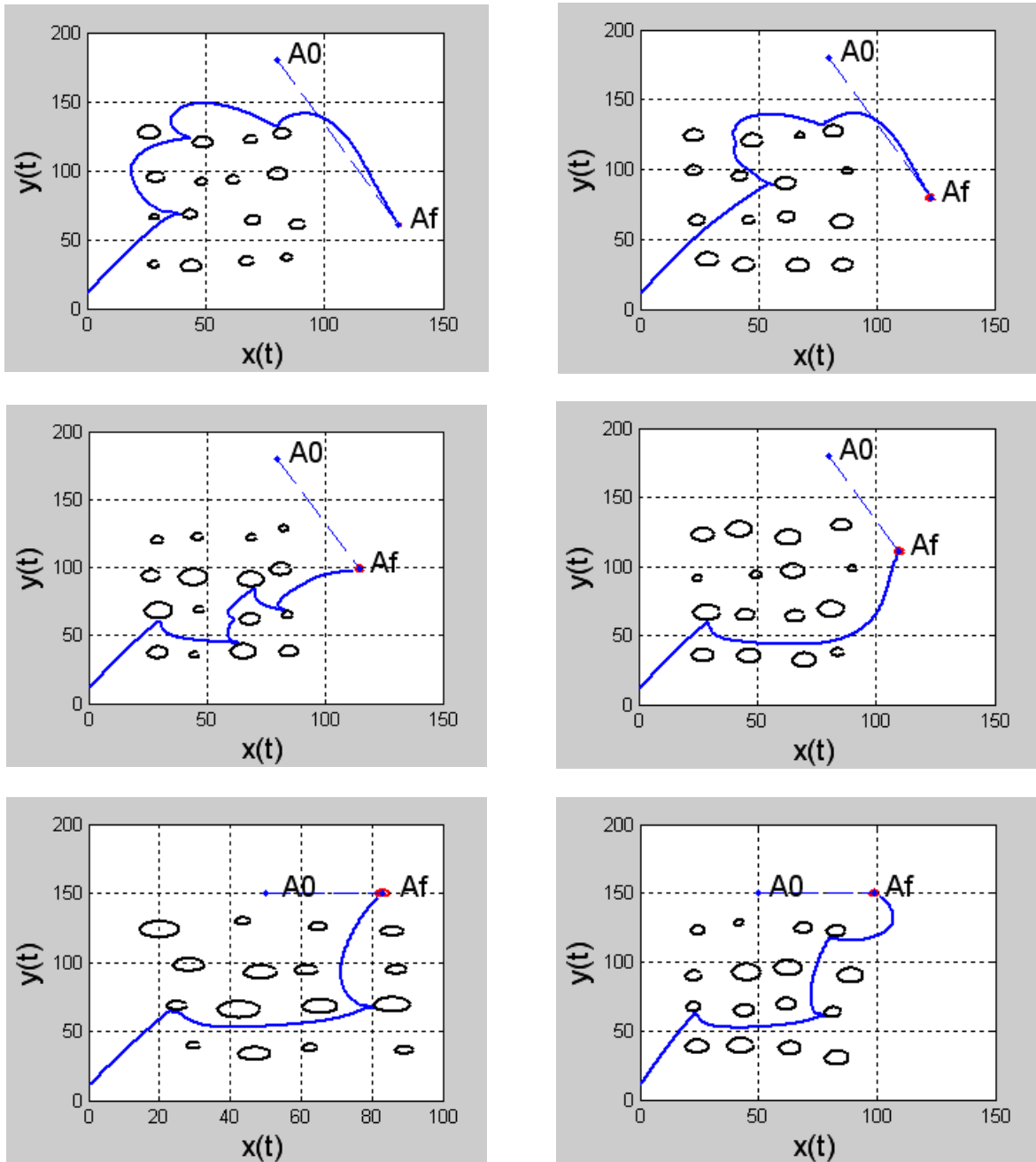


Fig. 4. MO motion trajectories to non-stationary point A_f in the environment with convex obstacles

Fig. 5 shows the results of MO motion to target stationary point A_f (150, 150) in the environment with non stationary obstacles, moving uniformly along straight lines. Motion trajectories are depicted with dashed line.

It should be noted that proposed approach puts no limitations except energetic on either the target point motion character or initial MO position.

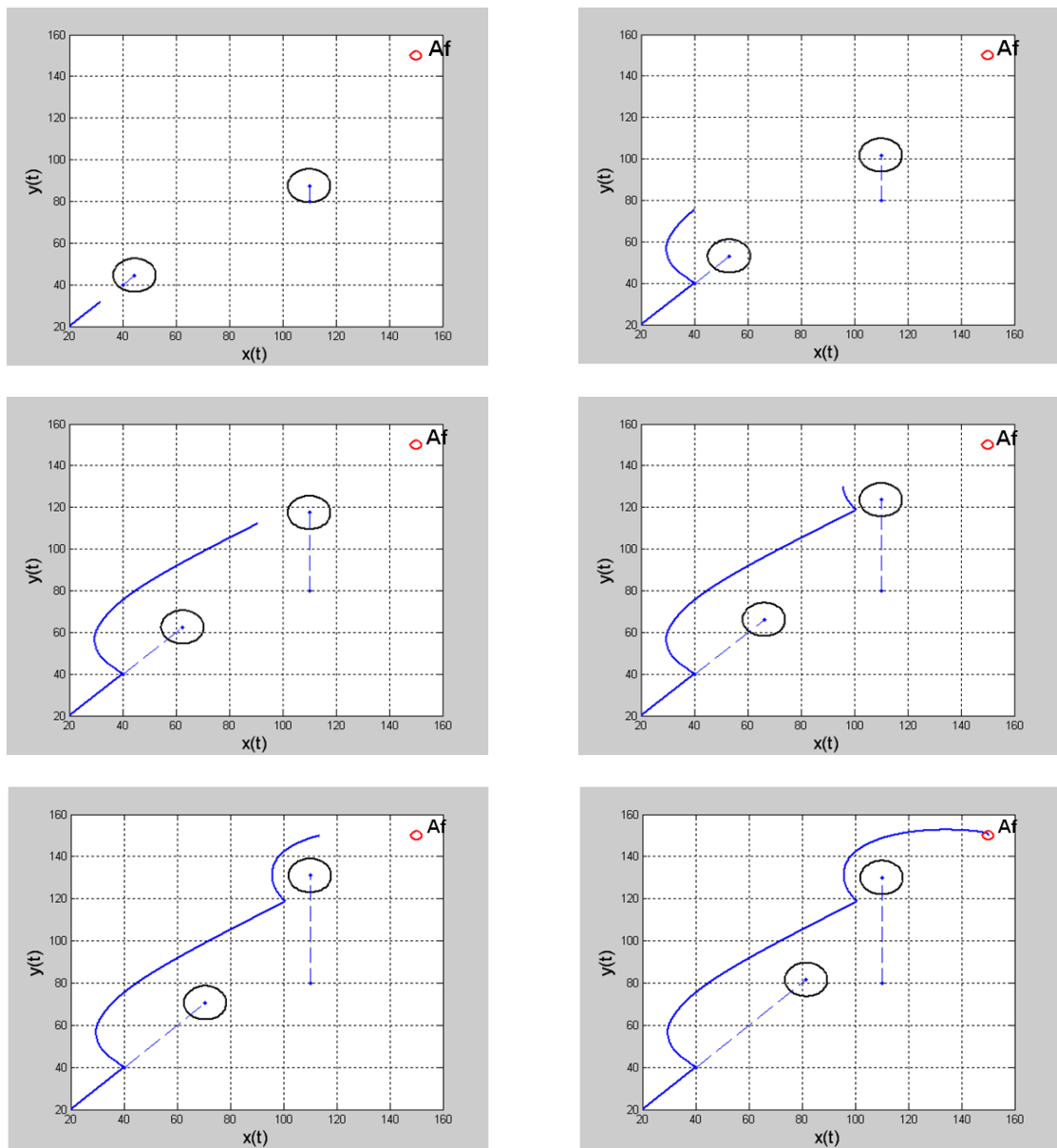


Fig. 5. MO motion trajectories to stationary point A_f in the environment with non stationary obstacles

VI. EXPERIMENT

The experiment was held using autonomous wheeled robot “Skif-3”, developed on Department of Electrical Engineering and Mechatronics of Taganrog Institute of Technology of Southern Federal University. Robot shown on fig. 6.

Algorithm (10) was implemented using Advantech onboard computer. Distance to obstacles measured by stereo vision using two cameras. Current coordinates of robot determined by integrating kinematic equations (18).

It should be noted that in real control systems more simple sensors could be used for distance to obstacles measurement.

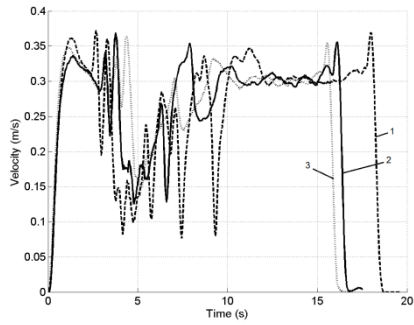
Experiments results for various types of obstacles are shown on fig. 7 and 8.



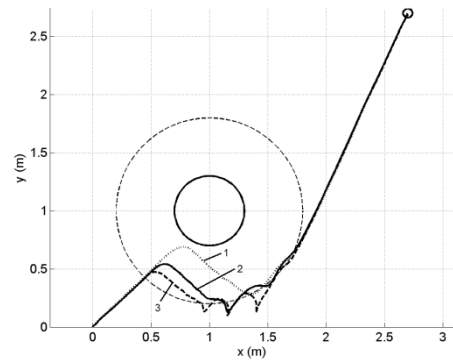
Fig. 6. Autonomous mobile robot “Skif 3”



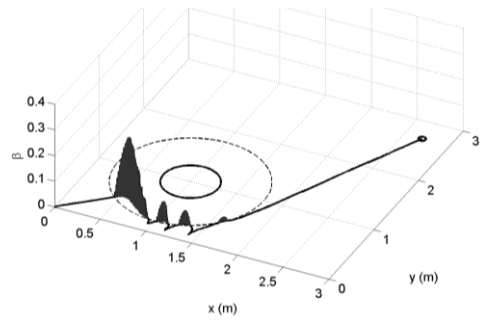
General view of scene with one convex obstacle



Speed change plot: $1 - s = -0,005/\beta$;
 $2 - s = -0,1/\beta$; $3 - s = -0,4/\beta$



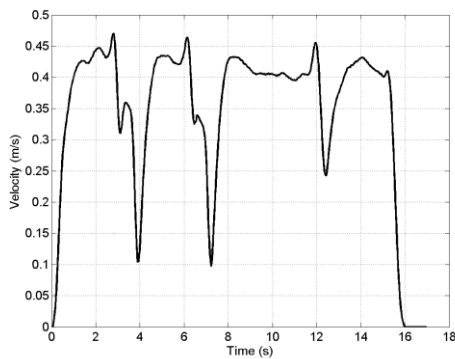
Motion trajectory: $1 - s = -0,005/\beta$;
 $2 - s = -0,1/\beta$; $3 - s = -0,4/\beta$



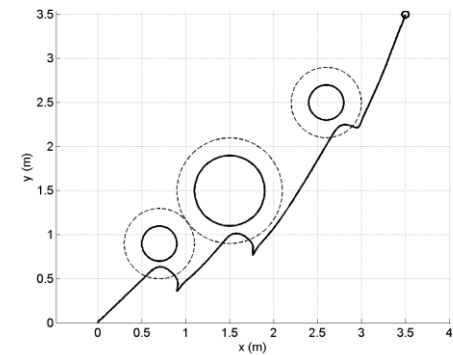
Bifurcational parameter change plot with
 $s = -0,1/\beta$



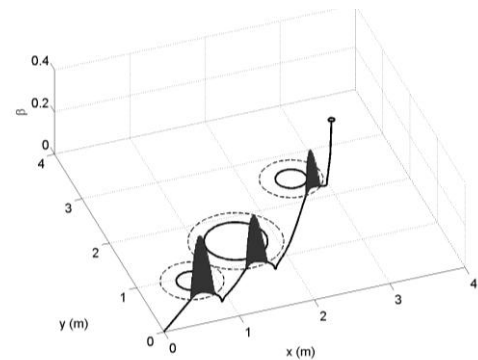
General view of scene with a group of convex obstacles



Speed change plot

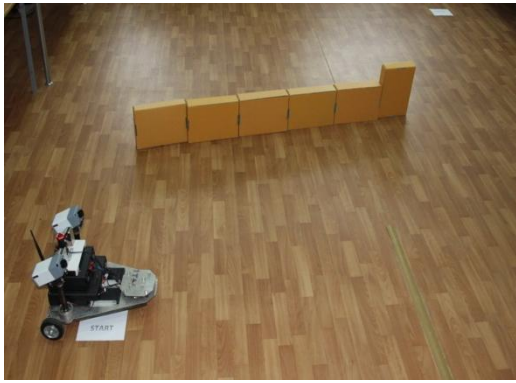


Motion trajectory

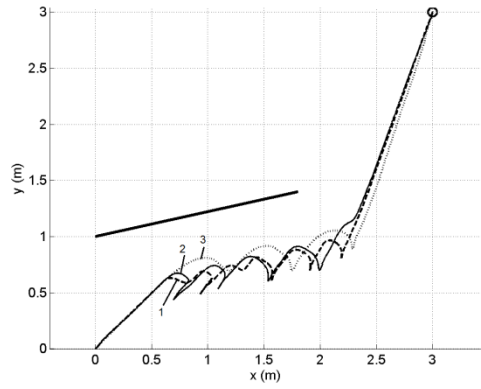


Bifurcational parameter change plot

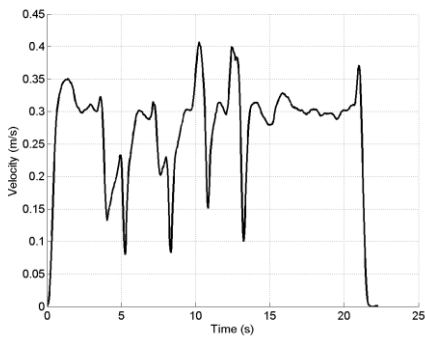
Fig. 7. Experimental results for the case of convex obstacles



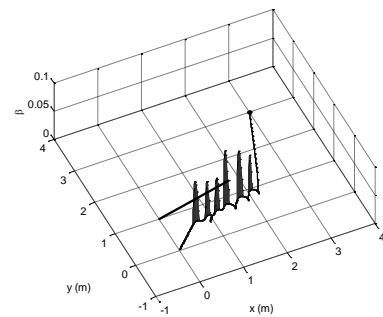
General view of scene with one linear obstacle



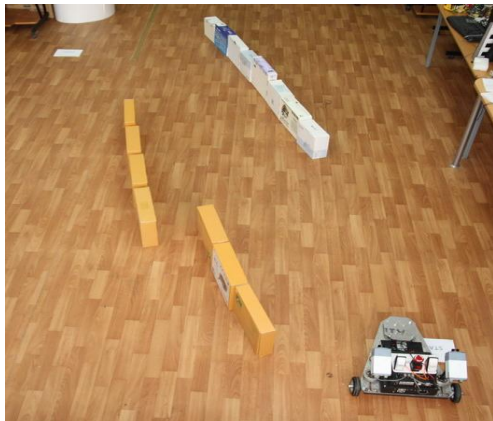
Motion trajectory: 1 - $s = 0,005/\beta$;
2 - $s = 0,05/\beta$; 3 - $s = 0,4/\beta$



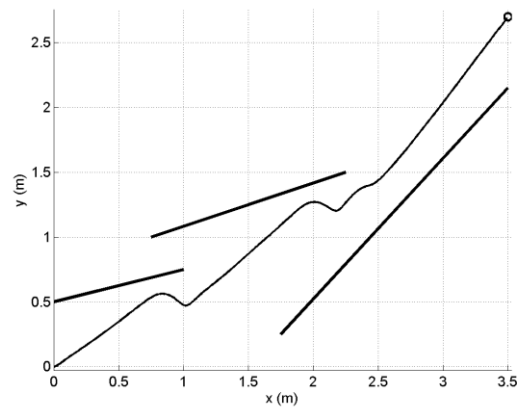
Trajectory speed change plot with $s = 0,005/\beta$



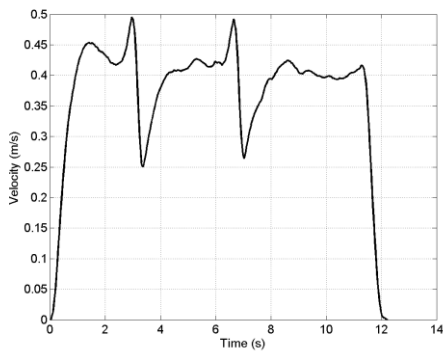
Bifurcational parameter values with $s = 0,005/\beta$



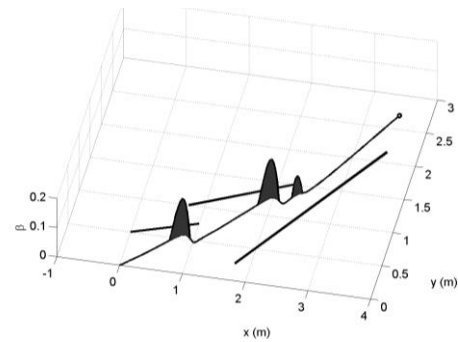
General scene view with a group of linear obstacles



Motion trajectory



Trajectory speed change plot



Bifurcational parameter values

Fig. 8. Experimental results for the case of linear obstacles

MO motion results shown in various unknown environments demonstrating efficiency of approach proposed in this paper.

VII. ACKNOWLEDGEMENTS

Author thanks his colleagues Sirotenko M.Y., Fedorenko R.V., Gurenko B.V. for help in experiments execution.

VIII. CONCLUSION

The approach to control motion of mobile objects in unknown environments proposed in this paper is based on a bifurcational parameter depending on distance to obstacle. This parameter makes system unstable in a transient mode from one stable state to another. It also allows to lower requirements to planning and control technologies, needs neither preliminary mapping nor complex navigation system. Proposed procedures of controls computation and tactical level control system functioning algorithm allows to organize motion of MO in environments with stationary and mobile target points and obstacles of various forms.

Proposed solutions could be used while constructing autopilots for wheeled platforms, aerial, underwater or aerostatic vehicles.

REFERENCES

- [1] *Intelligent automatic control systems* / Eds.: I.M. Makarov, V.M. Lokhin. – M.: Fizmatlit, 2001, p. 576.
- [2] P.D. Krutko, P.A. Osipov, “Kinematic motion control algorithms for mobile robots transport systems”, *RAN bulletin. Control systems and theory*, №3, pp.153-160, 1999.
- [3] B. Siciliano, O. Khatib. *Springer Handbook of Robotics*. 1611 p. 1375 illus., 422 in color. With DVD., Hardcover. 2008. ISBN: 978-3-540-23957-4.
- [4] S.F. Burdakov, I.V. Miroshnik, R.E. Stelmanov, *Wheeled robots motion control systems*. Spb.: Science, 2001.
- [5] O. Khatib, “Real-Time Obstacle Avoidance for Manipulators and Mobile Robots”, *The Int. Journal of Robotics Researches*, vol. 5, no. 1, pp. 90-98, 1986.
- [6] J. Borenstein, Y. Koren, “Real-time Obstacle Avoidance for Fast Mobile Robots”, *IEEE Transactions on Systems, Man, and Cybernetics*, vol. 19, no. 5, pp. 1179-1187, Sept./Oct. 1989.
- [7] Canudas de Wit, C.H. Khennouf, C. Samson and O.J. Sordalen, “Nonlinear control design for mobile robots”, Y. Zheng (ed.) *Recent trends in mobile robots*, World Scientific, pp. 121-156, 1993.
- [8] B.V. Topchiev, “Synergetic control of mobile robots”, *Nonlinear world*, vol. 2, no. 4, pp. 239-249, 2004.
- [9] Yu.V. Chernukhin, V.Kh. Pshikhopov, S.N. Pisarenko, O.N. Trubachev, “Software environment for adaptive mobile robots with two-level control system modeling”, *Mechatronics*, no. 6, pp. 26-30, 2000.
- [10] V.Kh. Pshikhopov, “Organization of repellers in mobile robots motion in the environment with obstacles”, *Mechatronics, automation, control*, no. 2, pp. 34-41, 2008.
- [11] V.H. Pshikhopov, “Attractors and repellers in mobile objects control systems construction”, *TSURE bulletin. Theme issue. Perspective control systems and tasks*, Taganrog: TSURE publishing, no. 3 (58). pp. 117–123, 2006.
- [12] B.P. Demidovich, *Mathematical stability theory lecture notes*, M.: Science, 1967, p. 472.
- [13] A.M. Lyapunov, *General problem of motion stability*. Cherepovets: Mercury-press, 2000, p. 386.
- [14] M.F. Zimin, “Equations determining areas, volumes and its boundaries”, *Mathematical education*, 1980, no. 1.
- [15] L.M. Boychuk, *Non-linear automatic control systems structural synthesis method*. M: Energy, 1971, p. 112.
- [16] V.Kh. Pshikhopov, M.Y. Medvedev, “Structural synthesis of mobile objects autopilots with disturbances estimation”, *Information measurement and control systems*, 2006, no. 1, pp.103-109.
- [17] V.Kh. Pshikhopov, M.Yu. Sirotenko, “Structure-Algorithmic Realization Of Autonomous Mobile Robot With Neural Network Motion Planner”, *TSURE Transactions*, no. 3, 2004, pp. 185-191.
- [18] Pshikhopov, V., Medvedev, M., Neydorf, R., Krukhmalev, V. et al., "Impact of the Feeder Aerodynamics Characteristics on the Power of Control Actions in Steady and Transient Regimes," SAE Technical Paper 2012-01-2112, 2012, doi:10.4271/2012-01-2112.
- [19] Pshikhopov, V., Krukhmalev, V., Medvedev, M., and Neydorf, R., "Estimation of Energy Potential for Control of Feeder of Novel Cruiser/Feeder MAAT System," SAE Technical Paper 2012-01-2099, 2012, doi:10.4271/2012-01-2099.
- [20] Pshikhopov, V.K., Medvedev, M.Y., Gurenko, “Homing and docking autopilot design for autonomous underwater vehicle”, 2014, Applied Mechanics and Materials
- [21] Pshikhopov, V.Kh., Medvedev, M.Yu., Gaiduk, A.R., Gurenko, B.V., Control system design for autonomous underwater vehicle, 2013, Proceedings - 2013 IEEE Latin American Robotics Symposium, LARS 2013, doi:10.1109/LARS.2013.61
- [22] Pshikhopov, V., Sergeev, N., Medvedev, M., and Kulchenko, A., "The Design of Helicopter Autopilot," SAE Technical Paper 2012-01-2098, 2012, doi:10.4271/2012-01-2098.
- [23] Pshikhopov, V., Medvedev, M., Kostjukov, V., Fedorenko, R., Gurenko, B., Krukhmalev, V. "Airship Autopilot Design," SAE Technical Paper 2011-01-2736, 2011, doi:10.4271/2011-01-2736
- [24] Pshikhopov, V.Kh., Krukhmalev, V.A., Medvedev, M.Yu., Budko, A.Yu., Chufistov, V.M., Adaptive control system design for robotic aircrafts, 2013 IEEE Latin American Robotics Symposium, LARS 2013, doi:10.1109/LARS.2013.59
- [25] Pshikhopov, V.Kh., Medvedev, M.Yu., Block design of robust control systems by direct Lyapunov method, 2011, IFAC Proceedings Volumes (IFAC-

PapersOnline), doi: 10.3182/20110828-6-IT-1002.00006

- [26] Pshikhopov, V.Kh., Ali, A.S., Hybrid motion control of a mobile robot in dynamic environments, 2011, IEEE International Conference on Mechatronics, ICM 2011 - Proceedings
- [27] Pshikhopov, V.Kh., Medvedev, M.Yu, Robust control of nonlinear dynamic systems, 2010, IEEE ANDESCON Conference Proceedings, ANDESCON 2010
- [28] Neydorf, R., Krukhmalev, V., Kudinov, N., and Pshikhopov, V., "Methods of Statistical Processing of Meteorological Data for the Tasks of Trajectory Planning of MAAT Feeders," SAE Technical Paper 2013-01-2266, 2013, doi:10.4271/2013-01-2266

Dimensional Accuracy Optimization of Prototypes produced by PolyJet Direct 3D Printing Technology

J. Kechagias^{*1}, P. Stavropoulos², A. Koutsomichalis³, I. Ntintakis⁴ and N. Vaxevanidis⁵

Abstract— In the current study an investigation of the process parameters effects, concerning the dimensional accuracy of parts produced by the Polyjet Direct 3D Printing Process, is presented. Following the initial identification and preparation of in STL format four experiments have been conducted utilizing the Taguchi L₄ (2³) array. Process parameters investigated include the Layer Thickness, Build Style and Model Scale. Linear (external) and Diametric (internal) dimensions have been measured using a digital caliper with an accuracy of 0.01 mm. The effect of each parameter has been examined in terms of ANOM (Analysis of Means) diagrams. Optimum levels for each parameter have been proposed according to performance measures. ANOVA (Analysis of Variances) has been performed aiming in the importance identification of each parameter variance onto the performance measure as a percentage value. The results indicate that the dimensional accuracy of external dimensions are affected in principle by the blade movement and the Layer Thickness, while the internal, primary by the Layer Thickness and the Scale factor.

Keywords—3D Printing, Prototypes, Dimensional Accuracy, Optimum Levels, ANOM, ANOVA.

I. INTRODUCTION

The transition from the Rapid Prototyping (RP) and Rapid Tooling (RT) to the 3D Printing era has been taking place over the last years. The potentials brought about from such technology aim to affect the way products are produced in a similar way that RP and RT transformed the traditional approaches for the design and development of a product. RP is

an advanced manufacturing technology commercialized in the mid '80s. Currently, RP technology is widely utilized in manufacturing for conceptual and functional models. The application of RP has been shown to greatly shorten the design-manufacturing cycle, hence reducing the cost of product and increasing competitiveness. Further development of this technology is focusing on short and long term tooling which again has been shown in some cases to reduce costs and cycle times. Evolution of RP is the so called 3D printing processes. Recently developed technologies, such as Selective Laser Sintering (SLS), three-dimensional printing (3DP) and PolyJet enable to produce customized and complex parts in a short amount of time [1], compared to traditional RP technologies such as Stereolithography (SL). The Polyjet Direct 3D Printing (PJD-3DP) system builds detailed models with smooth surfaces by a process of addition photopolymer resin layers. This is enabled by a technology utilizing simultaneous jetting of modeling materials to create physical free form prototypes [2]. It is capable of creating parts of complex geometry with materials such as photo-curable resins that can be used at the areas of automotive, electronics, consumer goods, medical development, etc. In the 3D printing, layers of a photopolymer resin are selectively jetted onto a build-tray via inkjet printing [3]. The printing head, composed by a number of micro jetting heads, injects a 16 μm thick layer of resin onto the built tray, corresponding to the built cross-sectional profile. The jetted photopolymer droplets are immediately cured with ultraviolet lamps that are mounted onto the print carriage. The repeated addition and solidification of resin layers produces an acrylic 3D model with a dimensional resolution of 0.016 mm. The PJD-3DP process has the ability to simultaneously jet multiple materials with different mechanical and optical properties. 3D printing could be considered a fully controllable process, since the majority of the process parameters can be altered on user's demand. Consequently the quality of the part does depend on a number of factors. As basic quality indicators for the specific processes two can be considered as major i.e. the model's surface roughness and model's dimensional accuracy. Both depend on the machine and the process variables [4]. Several attempts have been made to make a systematic analysis of errors and the quality of the prototypes.

^{*1}J. Kechagias is with the Department of Mechanical Engineering, Technological Educational Institute of Thessaly, Larissa 41110, Greece (corresponding author: phone: 0030 2410684322, fax: 0030 2410684305, email: jkechag@teilar.gr)

²P. Stavropoulos is with the Department of Aeronautical Studies, Hellenic Air Force Academy, Dekelia Air-Force Base, 1010 Athens, Greece (email: pstavropoulos.hafa@haf.gr, pgstavr@gmail.com)

³A. Koutsomichalis is with the Department of Aeronautical Studies, Hellenic Air Force Academy, Dekelia Air-Force Base, 1010 Athens, Greece (email: akoutsomichalis.hafa@haf.gr, a.koutsomichalis@gmail.com)

⁴I. Ntintakis is with the Department of Wood and Furniture Design, Technological Educational Institute of Thessaly, Karditsa 43100, Greece (email: ntintakis@teilar.gr)

⁵N. Vaxevanidis is with the Department of Mechanical Engineering Educators, School of Pedagogical and Technological Education (ASPETE), Athens, 14121, Greece. (email: vaxe@aspete.gr)

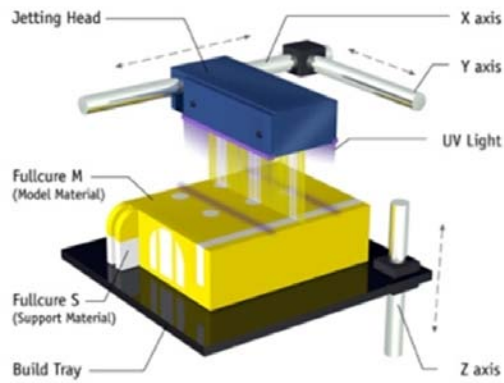


Fig. 1: The PolyJet Direct 3DP Process [2]

Experimental analysis of dimensions, surface roughness, and mechanical properties between PJD-3DP and ZCORP-3DP processes have been investigated in study [5]. Determination of surface texture parameters R_a and R_z for horizontal surfaces of parts produced by PJD-3DP have been performed in [6]. The results indicate that for mate surfaces R_a equals approximately $1.04\mu\text{m}$ while R_z about $5.6\mu\text{m}$. For glossy surfaces R_a is approximately $0.84\mu\text{m}$ and R_z $3.8\mu\text{m}$. Mechanical properties of parts produced by PJD-3DP, has been investigated in [7]. The study concluded that the part orientation has an effect on mechanical properties due to the heterogeneity of light energy by the photopolymer material during jetting process. The variability in the mechanical properties of parts manufactured via PJD-3DP has also been examined in [3]. It has been concluded that part orientation affects tensile strength and tensile modulus with highest tensile modulus occurred in the XZ orientation. Concerning the effect of the process parameters in Polyjet Direct 3D Printing an investigation is presented in [8].

The dimensional accuracy of a 3D model depends also on a number of factors. The current issue has been studied mainly experimentally [9-13]. Semi-empirical models have been developed, based on the Statistical Design of Experiments method [14, 15] and Analytic Hierarchy Process [16] that indicate the influence of certain process parameters to the quality characteristics of the 3D model. As an overall outcome of the afore mentioned studies the process parameters that mainly affect dimensional accuracy are: Layer Thickness, Hatch Spacing, Blade Gap, Part position on the platform and Hatch Overcure. Despite the experimental studies few theoretical works have been published capable of predicting the dimensional accuracy have been presented. The current study investigates the effects of the process parameters of PJD-3DP on the dimensional accuracy of parts fabricated.

II. EXPERIMENTAL SETUP

A part has been designed, based on the research of [6] accommodating modifications (indicated in Fig. 2) so that to absorb the particularities of the PJD-3DP process. An investigation of the effects of the layer thickness, build style and model scale on to the dimensional accuracy of parts

produced by Polyjet 3D printing process is presented. The selected part geometry has been prepared in STL format. Following step included execution of four experiments utilizing the $L_4(2^3)$ Taguchi orthogonal array [17]. The parameters tested have been Layer Thickness, Build Style and Model Scale. Dimensional accuracy measurements have been performed using a digital caliper with an accuracy of 0.01 mm. Linear and diametric dimensions have been measured for each experiment and the effect of each parameter has been analyzed using Analysis of Means (ANOM) and Analysis of Variances (ANOVA). Finally, the best levels have been exported and the optimized combination has been built and evaluated. The optimum parameter levels is planned to be used in future work in order to characterize surface quality of sloped surfaces of part produced via the current technology.

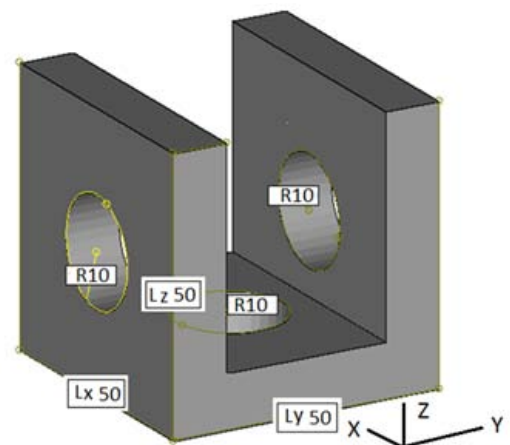


Fig. 2: CAD file of the test part

The test part has the dimensions as indicated in Fig. 2. Four test parts have been built according to the $L_4(2^3)$ Taguchi orthogonal array. Dimensional accuracy is a widely used index characterizing a product's quality, and is measured off-line - when the component is already produced. The four prototypes have been built on an Objet Eden 250 using the Objet Fullcure 720 RGD material (Fig.5), while the experimental procedure steps are illustrated in Fig.4.



Fig. 3. Eden250™ 3D Printing System

Taguchi design method is a simple and robust technique for process parameters optimisation, involving the damping

(reduction) of variation in a manufacturing process through robust design of experiments.



Fig. 4. Experimental Process Flow Chart



Fig. 5. Objet Fullcure 720 RGD Prototypes

The main parameters, that are assumed to have an influence on the process outcome, are located in different rows in a designed orthogonal array – so called orthogonal matrix experiment. Dimensional accuracy parameters i.e. linear (external) and diametric (internal) dimensions have been measured using a digital caliper with an accuracy of 0.01 mm.

The process parameters used were the Layer Thickness (Lt), the Build Style (BS), and the Scale (SC) of the model. The Layer Thickness is measured in μm and has two levels which are defined by the control parameters ‘high quality=16 μm ’ and ‘high speed=30 μm ’. The Build Style defined by the control factor ‘Mate-M’ or ‘Glossy-G’, where glossy means that the sides of the part are built without support material. Finally, for the Scale parameter two levels equal to 50%, and 90% of the actual dimensions of the part shown on Fig. 5 have been selected. Table 1 indicates the process parameters and their respective levels. Table 2 indicates the experimental results.

No	Process Parameters	Levels	
		1	2
1	Layer Thickness (Lt, μm)	16	30
2	Build Style (BS, M,G)	Mate	Glossy
3	Scale (SC, %)	50	90

Table 1: Parameter design

Measure	Dimension	Experiment			
		1	2	3	4
Linear	Lx	0,1	0,06	0,33	0,11
	Ly	-0,05	-0,05	0,18	0,13
	Lz	-0,05	-0,02	0,06	-0,06
Diametric	Dx	-0,173	-0,226	-0,41	-0,25
	Dy	-0,05	-0,2	-0,39	-0,2
	Dz	-0,145	-0,095	-0,15	-0,175

Table 2: Matrix experiment

III. DISCUSSION OF THE RESULTS – ANOM/ANOVA

For each experiment, the x, y, z Linear and x, y, z, Diametric dimensional parameters have been measured (Table 2). Based on these values, the Analysis of Means (ANOM) and Analysis of Variance (ANOVA) has been conducted, indicating the impact of each factor level on the dimensional accuracy of the measured values. Based on the ANOM, the optimum combination of the process values could also be derived, with respect to the dimensional accuracy. The optimum level for a factor is the level that gives the lower deviation value compared to the theoretical/expected values as per the CAD file.

Linear (External)

	Lx		Ly		Lz	
	Level 1	Level 2	Level 1	Level 2	Level 1	Level 2
mLTi	0,080	0,220	-0,050	0,155	-0,035	0,000
mBSi	0,215	0,085	0,065	0,040	0,005	-0,040
mSci	0,105	0,195	0,040	0,065	-0,055	0,020

Table 3: Analysis of means for Linear (External) Dimensions

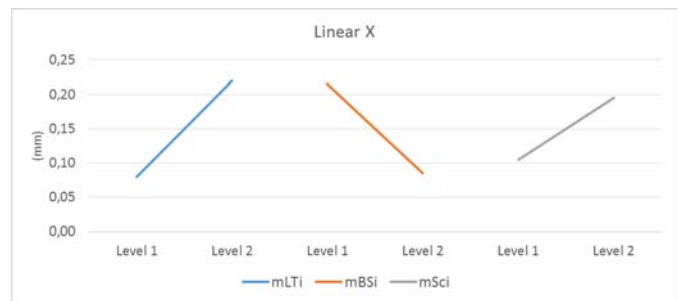


Fig. 6. ANOM diagram for External – Linear X

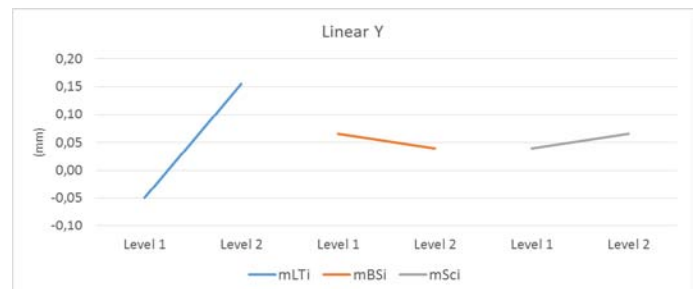


Fig. 7. ANOM diagram for External – Linear Y

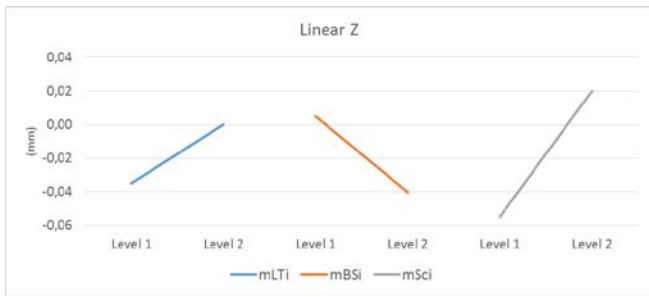


Fig. 8. ANOM diagram for External – Linear Z

	DoF	SoS	MS	%
LT	1	0,0196	0,0196	44%
BS	1	0,0169	0,0169	38%
Sc	1	0,0081	0,0081	18%
Error	-	-	-	-
Total	3	0,0446	-	-

Table 4: Analysis of variances for Linear - Direction X

	DoF	SoS	MS	%
LT	1	0,0420	0,0420	97%
BS	1	0,0006	0,0006	1%
Sc	1	0,0006	0,0006	1%
Error	-	-	-	-
Total	3	0,0433	-	-

Table 5: Analysis of variances for Linear - Direction Y

	DoF	SoS	MS	%
LT	1	0,0012	0,0012	14%
BS	1	0,0020	0,0020	23%
Sc	1	0,0056	0,0056	63%
Error	-	-	-	-
Total	3	0,0089	-	-

Table 6: Analysis of variances for Linear - Direction Y

Diametric (Internal)

	Dx		Dy		Dz	
	Level 1	Level 2	Level 1	Level 2	Level 1	Level 2
mLTi	-0,200	-0,330	-0,125	-0,295	-0,120	-0,163
mBSi	-0,292	-0,238	-0,220	-0,200	-0,148	-0,135
mSci	-0,212	-0,318	-0,125	-0,295	-0,160	-0,123

Table 7: Analysis of means for Diametric (Internal) Dimensions

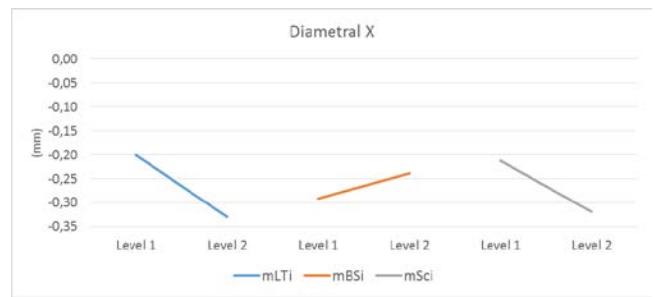


Fig. 9. ANOM diagram for Internal – Linear X

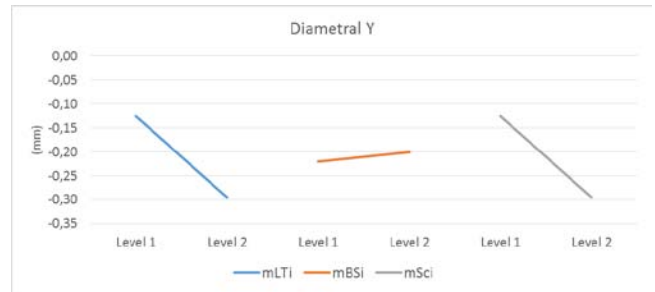


Fig. 10. ANOM diagram for Internal – Linear Y

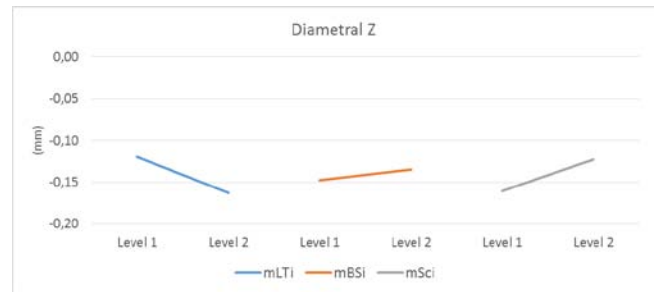


Fig. 11. ANOM diagram for Internal – Linear Z

	DoF	SoS	MS	%
LT	1	0,0169	0,0169	54%
BS	1	0,0028	0,0028	9%
Sc	1	0,0114	0,0114	37%
Error	-	-	-	-
Total	3	0,0311	-	-

Table 8: Analysis of variances for Diametric - Direction X

	DoF	SoS	MS	%
LT	1	0,0289	0,0289	50%
BS	1	0,0004	0,0004	1%
Sc	1	0,0289	0,0289	50%
Error	-	-	-	-
Total	3	0,0582	-	-

Table 9: Analysis of variances for Diametric - Direction Y

	DoF	SoS	MS	%
LT	1	0,0018	0,0018	54%
BS	1	0,0002	0,0002	5%
Sc	1	0,0014	0,0014	42%
Error	-	-	-	-
Total	3	0,0034	-	-

Table 10: Analysis of variances for Diametric - Direction Z

IV. CONCLUSIONS

The Linear external dimensions and the Diametric internal have been selected as quality indicators for the PJD-3DP process parameter investigation using design of experiments and statistical analysis. The experimental results indicate that:

The Linear External Dimensions

1. The X direction as indicated in fig. 2 coincides with the direction of the blade movement. All factors are of importance. The factorial weight of Layer Thickness (Lt) is found to be equal to 44% followed by the Build Style (BS) with a weight of 38%, and finally by the Scale (SC) with a weight of 18%.
2. In the Y direction analysis indicate that the dominant factor is the Layer Thickness (Lt) found equal to 97%. The blade movement does not affect the current dimension. The afore-mentioned conclusion is with agreement with previous studies [18].
3. For the vertical, as indicated in fig. 2, Z direction all parameters are important with dominant the Scale (SC) with a weight of 37%, followed by Build Style (BS) 23% and Layer Thickness (Lt) 14%.

The Diametric Internal Dimensions

4. The Layer Thickness (Lt) and the Scale factor (SC) are to be considered as the most important factors for all the directions, with a weighting of 50% respectively.

Following the analysis for all dimensions investigated, it could be concluded that the dimensional accuracy of external dimensions is affected in principle by the blade movement and the Layer Thickness. As it regards the internal diametric dimensions they are affected on the same direction and primary by the Layer Thickness and the Scale factors.

REFERENCES

- [1] M.F. Zaeh, 2006, "Wirtschaftliche Fertigung mit Rapid-Technologien. Anwender-Leitfaden zur Auswahl geeigneter Verfahren, iwB Application Centre Augsburg", Technische Universitaet Muenchen. Munich, Germany, Hanser, ISBN:9783446228542.
- [2] "Objet Polyjet Process." Objet Geometries Ltd. www.Objet.com, n.d. Web. <http://www.objet.com/products/polyjet_technology/>.
- [3] M.W. Barclift, C.B. Williams, 2012, "Examining variability in the mechanical properties of parts manufactured via polyjet direct 3D printing", International Solid Freeform Fabrication Symposium, August 6-8, Austin, TX.
- [4] W. Konig, I. Celi, St. Noken, 1992, "Stereolithography process technology", Proceedings of the 3rd European Conference on RP&M
- [5] A. Pilipovic, P. Raos, M. Sercer, 2009, "Experimental analysis of properties of materials for rapid prototyping", Int J Adv Manuf Technol., 40, 105-115.
- [6] R. Udroui, L.A. Mihail, 2009, "Experimental determination of surface roughness of parts obtained by rapid prototyping, CSECS'09 Proceedings of the 8th WSEAS International Conference on Circuits, systems, electronics, control & signal processing, 283-286.
- [7] A. Keszy, J. Kotlinski, 2010, "Mechanical properties of parts produced by using polymer jetting technology", Archives of civil and mechanical engineering, Vol. X, No.3, pp. 37-50.
- [8] J. Kechagias, V. Iakovakis, E. Giorgo, P. Stavropoulos, A. Koutsomichalis and N. Vaxevanidis, 2014, "Surface roughness optimization of prototypes produced by Polyjet Direct 3D printing Technology", Proceedings of the OPT-i, International Conference on Engineering and Applied Sciences Optimization, Kos Island, Greece, 4-6 June.
- [9] D.A. Schaub, K. Chu, D.C. Montgomery, 1997, "Optimizing stereolithography throughput", Journal of Manufacturing Systems, Vol. 16, No. 4, pp. 290 - 303.
- [10] P.T. Lan, S.Y. Chou, L.L. Chen, D. Gemmill, 1997, "Determining fabrication orientations for rapid prototyping with Stereolithography apparatus", Journal of Computer-Aided Design, Vo. 29, No. 1, pp. 53 - 62.
- [11] S. Throup, 1996, "A comparison of build accuracy for a Stereolithography Build Using two different resins", European Stereolithography User Association.
- [12] M. N. Islam, Brian Boswell and A. Pramanik, 2013, "An Investigation of Dimensional Accuracy of Parts Produced by Three-Dimensional Printing", Proceedings of the World Congress on Engineering Vol I, WCE 2013, July 3 - 5, London, U.K.,
- [13] G. Hirpa, K. Lemu and K. Safet, 2012, "3D Printing for Rapid Manufacturing: Study of Dimensional and Geometrical Accuracy, J. Frick and B. Laugen (Eds.), APMS 2011, IFIP AICT 384, pp. 470-479.
- [14] J.G. Zhou, D. Herscovici, C.C. Chen, 2000, "Parametric process optimization to improve the accuracy of rapid prototyped stereolithography parts", Journal of Machine Tools and Manufacture, Vol. 40, 363-379.
- [15] S.O. Onuh, K.K.B. Hon, 1998, "Optimizing build parameters for improved surface finish in stereolithography", Journal of Machine Tools and Manufacture, Vol. 38, No. 4, pp. 329-392.
- [16] A. Carosi, D. Pocci, L. Luluiano, L. Settineri, 1996, "Investigation on Stereolithography accuracy on both solid and QuickCast parts", Proceedings of the 5th European Conference on Rapid Prototyping and Manufacturing,
- [17] M.S., Phadke, 1989, "Quality Engineering Using Robust Design, Prentice-Hall, Englewood Cliffs, NJ.
- [18] J. Kechagias J, 2007, "Investigation of LOM process quality using design of experiments approach", Rapid Prototyping Journal, Vol. 13, No. 5, pp. 316-323.

Shape Optimization of Composite Structure under Uncertainty

J. Auzins, A. Janushevskis, A. Melnikovs, J. Janushevskis

Abstract—The developed methods and software tool for robust optimization have been tested on the two bar truss problem and applied to the shape optimization of the new composite pallet structure. Sensitivity analyses for probabilistic performances are given. Deterministic structural shape optimization problem of pallet is solved in the first stage. Next the same problem is considered as non-deterministic taking into account possible uncertainties of supporting conditions. The obtained results from deterministic and non-deterministic optimization are compared and appropriate solution for design of pallet is proposed.

Keywords—composite structures, metamodeling, robust optimization, shape optimization.

I. INTRODUCTION

POWERFUL methods for shape and topology optimization of mechanical engineering objects such as ground structure [1], homogenization [2] and solid isotropic material with penalization [3] are broadly used for industry problem solving. Popular new approaches for shape optimization are morphing, implicit parameterization and CAD-based direct parameterization [4], [5], [6]. Nevertheless real life problems are almost always non-deterministic. Uncertainties appear for example due to material, load and geometry fluctuations: manufacturing tolerances, model errors, changing environments and noisy measurements. Robust optimization approaches [7], [8], [9], and [10] seek to limit the effects in quality of the solutions due to uncertainties.

In recent years the CAD-based direct parameterization approaches [11] have become highly effective and popular due to rapid development of the integrated CAD/CAE software systems and advanced metamodeling techniques [12], [13], [14], and [15]. NURBS utilization for the freeform curves representation of CAD models can give even more benefits for

This work has been supported by the European Social Fund within the Project No. 2013/0025/1DP/1.1.1.2.0/13/APIA/VIAA/019 “New “Smart” Nanocomposite Materials for Roads, Bridges, Buildings and Transport Vehicle”.

J. Auzins is Corresponding Member of the Latvian Academy of Science and with the Institute of Mechanics, Riga Technical University, Riga, Latvia (phone: +371 67089396; e-mail: auzinsj@latnet.lv).

A. Janushevskis is Head of Machine and Mechanism Dynamics Research Laboratory with the Institute of Mechanics, Riga Technical University, Riga, Latvia (e-mail: janush@latnet.lv).

A. Melnikovs is with the Institute of Mechanics, Riga Technical University, Riga, Latvia (e-mail: anatolijs.melnikovs@inbox.lv).

J. Janusevskis is with the Institute of Mechanics, Riga Technical University, Riga, Latvia (e-mail: janisj@latnet.lv).

those techniques. Also references to the kriging based optimization methods [16] and [17] are commonly given to solve deterministic optimization problems. For non-deterministic optimization problems, such as composite structures that account for uncertainties, the optimization is usually based on double loop approaches where the uncertainty propagation is recursively performed inside the optimization iterations. Often the uncertainty estimation for the given point is based on a meta-model, thus allowing reduction of computational time but introducing additional bias in the estimates. In the previous work [18] a single loop kriging based method for minimizing the mean of an objective function is proposed: simulation points are calculated in order to simultaneously propagate uncertainties, i.e., estimate the mean objective function, and optimize this mean.

II. KEDRO SOFTWARE

KEDRO (previous name EDAOpt) was originally developed as a collection of non-gradient-based optimization software. KEDRO now includes methods and tools for statistical data sampling, approximation and metamodeling methods, and metamodel-based multiobjective optimization.

KEDRO and CAE simulation code (mainly FE, CFD and multibody dynamics software) remain entirely independent, with data being transferred between KEDRO and the simulation code through writing and reading text files. KEDRO does not require access to the source code of the user's simulation software.

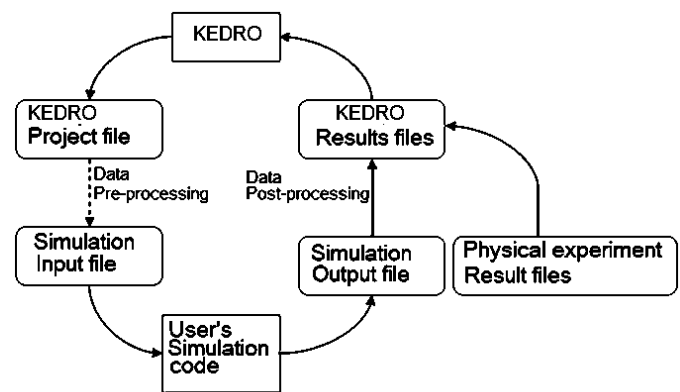


Fig. 1 Information exchange between KEDRO, user-supplied simulation code and experimental equipment

Fig. 1 shows the information exchange between KEDRO,

simulation software and physical experiment equipment.

Fig. 2 shows a typical flowchart of metamodeling-based optimization. Different optimization software packages may use different components for each stage, but the principle remains the same.

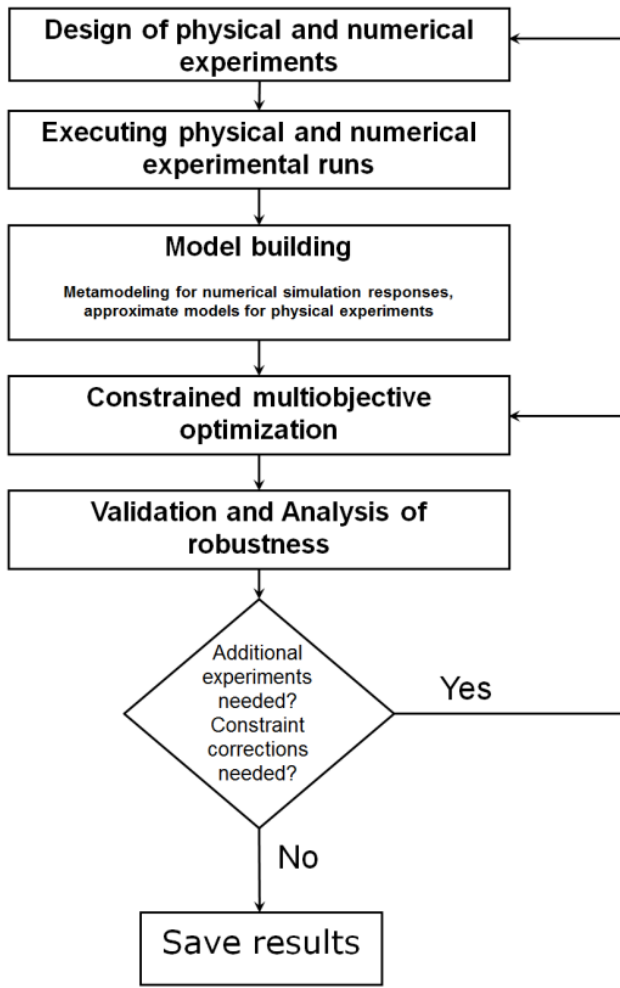


Fig. 2 The flowchart of metamodel-based optimization

Fig. 3 shows the main capabilities of KEDRO software for experimental design, analysis and multiobjective robust optimization using physical and numerical experiments.

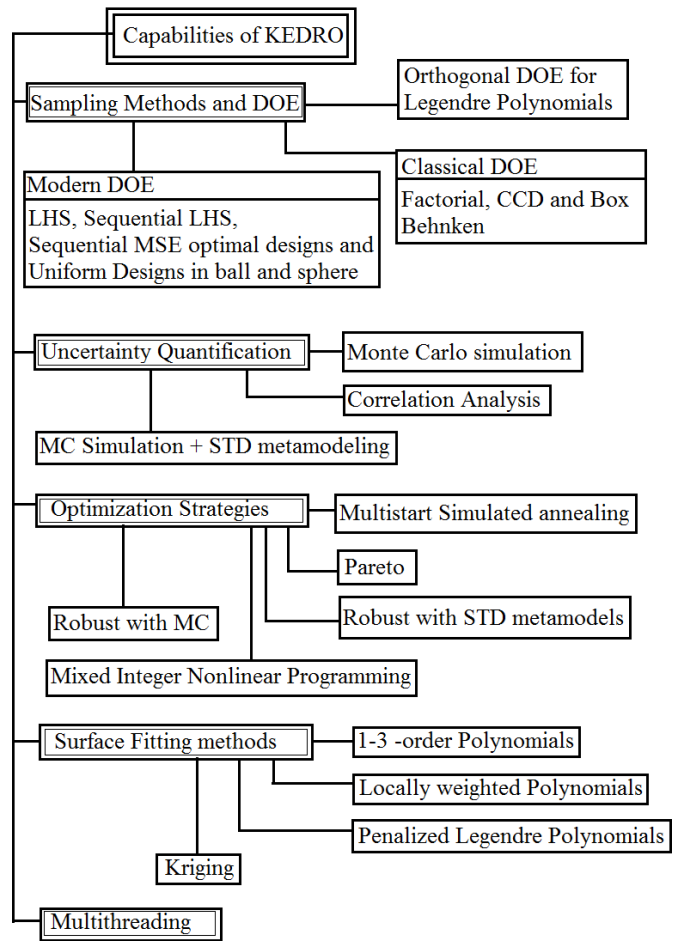


Fig. 3 Capabilities of the KEDRO software

III. CASE STUDY 1: TWO BAR TRUSS

Here we demonstrate the use of KEDRO for the two-bar truss optimization, which is a popular testing example for metamodeling, constrained optimization and robust optimization [19].

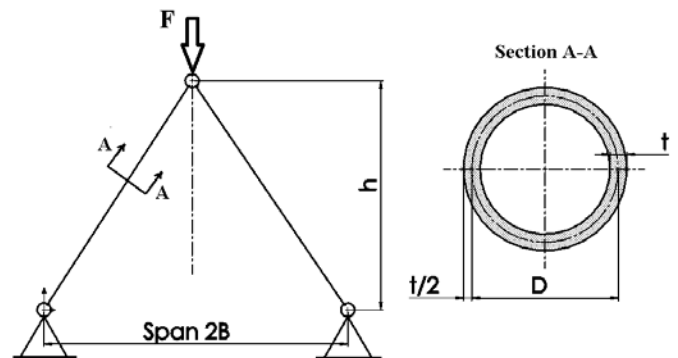


Fig. 4 Two-bar truss

The two-bar test case aims at designing a structure made of two cylindrical bars joined together at the top as shown in Fig. 4. A downwards force F is applied to the top of the structure.

The design variables are the bar diameter D and structure height h . The objective is to minimize the total volume V . Buckling and strength failures give the formulation constraints:

$$\min_{D, h} V \text{ such that } \sigma \leq \sigma_{\max} \text{ and } \sigma \leq \sigma_{\text{crit}} \quad (1)$$

where σ is the stress on the bar, σ_{\max} is the yield strength, and σ_{crit} is the maximum buckling load. The two-bar problem is simple enough to have analytical expressions for the objective function and constraints:

$$2\pi D t \sqrt{B^2 + h^2}, \quad \sigma = \frac{F \sqrt{B^2 + h^2}}{2\pi D h}, \quad \sigma_{\text{crit}} = \frac{\pi^2 E (D^2 + t^2)}{8(B^2 + h^2)} \quad (2)$$

For the robust optimization we have two design variables D and h , and additional four parameters – constants with fluctuations (unmapped analysis variables, see [20]). All parameter nominal values and their standard deviations are given in Table I.

Table I. Two-bar truss parameters. The fluctuations around the nominal values are Gaussian and all parameters are independent of each other

Parameter	Nominal value	Std. Dev.
D bar diameter (mm)	20-80	1
t bar wall thickness (mm)	2.5	0.1
h structure height (mm)	278-936	3
B half structure width (mm)	750	5
E Young's modulus (N/mm ²)	210000	21000
F applied force (N)	150000	15000
s_{\max} Yield strength (N/mm ²)	400	-----

The solution of the deterministic problem is $D = 37.876$ mm, $h = 608.89$ mm, in which case $V = 0.5747631$ dm³, $\sigma = 399.99995$ N/mm², $\sigma_{\text{crit}} = 400.00019$ N/mm².

To show the possibilities of metamodeling, we will use numerical experiments by calculating the response functions V , σ , σ_{crit} according to the design of experiments. We will use 6 input factors for metamodels. Table II shows the notation and limits of variation for all input factors

Table II Two-bar truss parameters. The fluctuations around the nominal values are Gaussian and all parameters are independent of each other

Factor = Parameter	Limits
$x_1 = D$	20-80
$x_2 = t$	2.4-2.6
$x_3 = h$	278-936
$x_4 = B$	745-755
$x_5 = E$	190000-230000
$x_6 = F$	120000-150000

111-point 6-factor MSE optimized design of experiments was used. The limits for “noisy constants” x_2, x_4, x_5, x_6 were set \pm one standard deviation from nominal value.

The responses are y_1 – stress σ , y_2 – buckling stress σ_{crit} and y_3 – volume V . The accuracy of approximation for tests with known response functions f_{test} was measured with the relative average prediction error σ_{test} in additional confirmation points not used in model building

$$\sigma_{\text{test}} = 100\% \frac{\sqrt{\frac{1}{N} \sum_{i=1}^N (f_{\text{test}}(z_i) - \hat{f}_{\text{test}}(z_i))^2}}{\sqrt{\frac{1}{N} \sum_{i=1}^N (f_{\text{test}}(z_i) - \bar{f}_{\text{test}})^2}} = 100\% \sqrt{\frac{\text{MeanSquareError}}{\text{Variance}}} \quad (3)$$

where z_i – confirmation points ($i=1, \dots, N$), $\hat{f}_{\text{test}}(w_i)$ – approximated value of test function, \bar{f}_{test} – average value of test function in confirmation points. 100000 uniformly randomly selected confirmation points (Latin hypercube sample) were used in the region of interest.

The kriging approximation was used for all three responses. The greatest approximation relative error was f or y_1 – 1.53%. Fig. 5 shows the relative cross-validation 1.95%, in most cases the cross-validation error is pessimistic – the actual error is less than the cross-validation prediction. 1.53% is a good result; if the error would be measured relative to the full range of the change of the stress response (1087N/mm²), the relative error would be 0.28%.

TestSigma=1.52915901975475%

Functions Yt	Strength	CrStrength	Volume
Method	Kriging		Kriging
Sigma Cross	3.933738	1.758704	287.692699
Sigma Cross%	1.952612%	0.314628%	0.101197%
Sigma	0.000179	0.000002	0.022784
Sigma%	0.000089	0.000000	0.000008
Sigma0	0.000185	0.000003	0.023538
Sigma0%	0.000092	0.000000	0.000008
MeanExpValue	384.541103	801.853137	766800.103027
StDev of Exp	201.460314	558.979362	284291.025622
Exp. Range	1087.954072	2492.878252	1224913.739257
MaxError	-0.000694	-0.000009	0.065113
Bad Point No.	82	59	84
Max Rel Error	0.00%	0.00%	0.00%
BadRelPointNo.	82	61	84
No. of Actual Exp	111	111	111

Fig. 5 Kriging approximation results

The solution of the deterministic problem is $D = 37.876$ mm, $h = 608.89$ mm, in which case $V = 0.5747631$ dm³, $\sigma = 399.99995$ N/mm², $\sigma_{\text{crit}} = 400.00019$ N/mm².

Table III shows the deterministic and robust optimization results for exact mathematical models and kriging metamodels. The optimization results obtained by the 111-run 6-factor experimental design are relatively close to the result obtained

by using the exact mathematical model. It must be noted that the difference between the metamodel and the exact model is less than the standard deviation system parameters. The optimization method used was the reliability type optimization [19] and [20] and requires 95% probability of satisfaction both constraints (1).

Table III The results of two-bar truss optimization. Robust optimization with 95% confidence probability

	Deterministic exact	Robust exact 95%	Deterministic metamodels	Robust metamodels 95%
D	37.88	46.61	37.95	45.53
h	608.89	711.65	611.23	747
V	0.574763	0.75713	0.576746	0.757050
Worst case V	0.631675	0.82869	0.622671	0.815109
$\bar{\sigma}$	399.9999	297.65	399.99	481.14
5th and 95th percentile σ	235-567	194-400	-----	198-400
$\bar{\sigma}_{crit}$	400.00128	528	400	481
5th and 95th percentile σ_{crit}	307-493	409-645	-----	398-568

IV. CASE STUDY 2: PALLET SHAPE OPTIMIZATION

Nowadays wood pallets are often replaced by composite pallets due to obvious benefits - superior strength and weight ratio, nestable design concept, increased service life, better corrosion and impact resistance, and many others depending on area of application. The proposed new design of composite pallet (with dimensions 1200x800x160mm) (Fig. 6) could be a solution for modern automated distribution systems if its design is able to carry loads up to 19620 N during operation conditions with the factor of safety (FOS) of at least 2. For this reason fiber-reinforced polymer (FRP) [21] compression molding process [22] must be used for pallet manufacturing and also appropriate shapes of strengthening ribs 1-3 (Fig. 6) must be found for maximal performance of the structure.

At the beginning of the previously developed optimization loop [23] and [18], we need to minimize the number of required parameters to accurately specify shapes of strengthening ribs of the pallet. We want to consider only smooth shapes for stiffness ribs that at same time are effective from the aspect of structural integrity. Therefore, due to the symmetry of the pallet the shape effective parameterization with 4 parameters (X1, X2, X3 and X4) is proposed, as shown in Fig. 7. The shape of each stiffness rib is controlled by control points of a non-uniform rational basis spline (NURBS) polygon. The shape is controlled using a small number of parameters that is important for successful optimization, especially for the non-deterministic case.

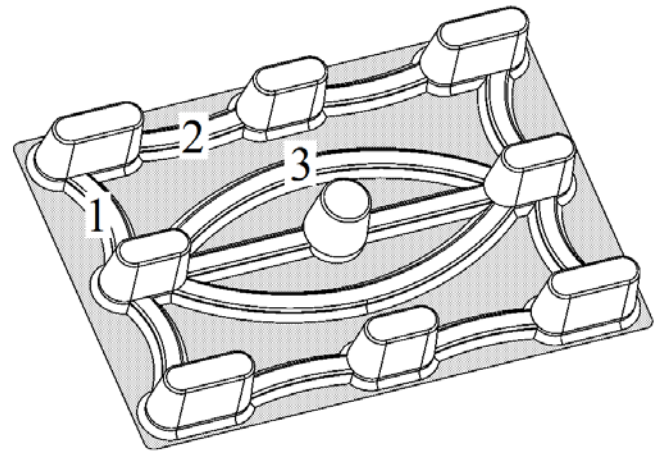


Fig. 6 3D model of loaded pallet and its stiffness ribs 1-3

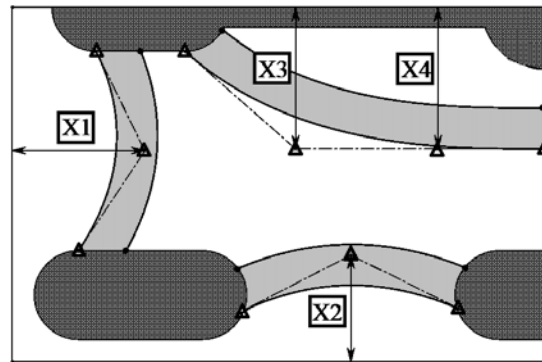


Fig. 7 NURBS parameterization of pallets stiffness ribs in 1/4 pallet layout

The composite material of the pallet consists of two plies of FRP (Table IV), each has 3 mm thickness. The fibers of the second ply are orientated perpendicular to the fibers of the first ply (Fig. 8) in XY plane that provides high strength in both X and Y directions. The strength of the pallet is defined with FOS using the Tsai-Wu criterion [24] which is best applied to orthotropic FRP that has unequal strength in tension and compression. The shell finite elements model of the composite pallet is considered and solved as a multi-ply structure (Fig. 9), taking into account the symmetry of the pallet structure.

Table IV Mechanical properties of FRP

Elastic Modulus	EX = 40000 MPa; EY = 10000 MPa; EZ = 10000 MPa
Poisson's Ratio	NUXY = 0.26; NUYZ = 0.25; NUXZ = 0.26
Shear Modulus	XY = 4500 MPa; YZ = 4000 MPa; XZ = 4500 MPa
Mass Density	$\rho = 1900 \text{ kg/m}^3$
Tensile Strength	SIGXT = 1060 MPa
Compressive Strength	SIGXC = 600 MPa
Shear strength	SIGXY = 70 MPa

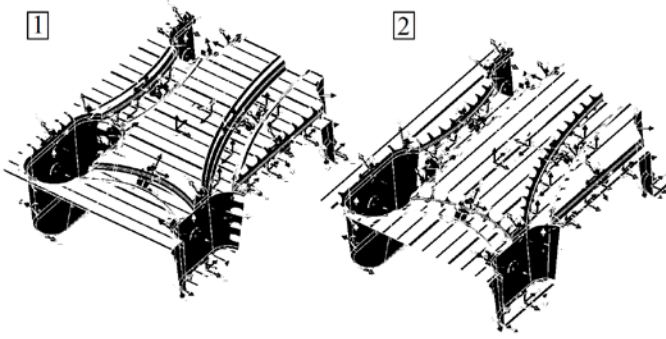


Fig. 8 Definition of fibers directions in 2 plies for 1/4 of 3D model

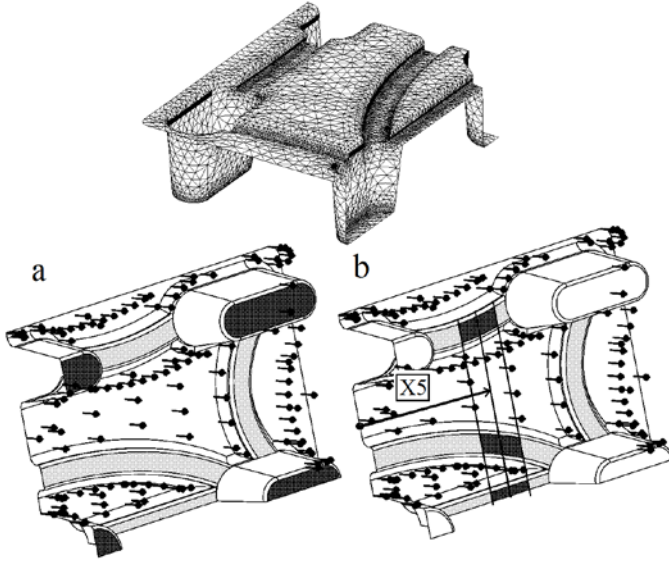


Fig. 9 The shell FE model of 1/4 pallet, and operation cases (a) & (b): arrows – load direction, areas colored black - supporting areas

Two main operation cases of the loaded pallet are simulated: (a) the pallet stays on the rigid basis and (b) the pallet is transported on forks (Fig. 9). In both operation cases the load is assumed to be deterministic and uniformly distributed and applied normally downward to the top surface of the pallet. The case (b) cannot be solved solely as deterministic problem due to uncertainties of supporting conditions (the distance between forks of the lifting equipment is variable). Therefore in the case (b) the problem of the rib shape optimization must take into consideration the random uncertainty in the pallet supports. It is assumed to be symmetric but non-deterministic: supporting areas have constant width but different support placements – X5 on the stiffness ribs as shown in Figs. 9b & 10(I-II).

The results of finite elements analysis show obvious importance of the rib shapes for pallet structure stiffness and strength properties. Also a known fact is confirmed: pallet case (b) causes higher deflection and lower FOS. Therefore, only case (b) is considered during optimization.

Next the deterministic shape optimization problem is defined:

$$\min_{X_n} \delta \quad \text{such that } FOS \geq 2 \text{ and } m \leq 4.688 \quad (4)$$

where X_n = factors X1-X5; δ = pallet maximal deflection; and m = pallet mass. In the first step X5 is assumed taking 2 extreme values: the results are shown in Fig. 10(I-II) and in Table V for each case. By moving supporting conditions to the side of the pallet (increasing X5), the maximal deflection of the pallets tends to relocate from the side of pallet to the center part (Fig. 11) and at same time the level of deflections decreases.

Table V The results of pallet shape optimization

	Range, mm	Optimization cases (see Fig. 10)		
		I	II	III
X1	95-220	182.6448	192.5575	219.827
X2	25-220	79.7038	62.8432	114.209
X3	135-195	135		
X4	160-195	160		
X5	200-270	200 (fixed)	270 (fixed)	160-270
FOS	metamodels	2	2.5	4.72*
	actual	2.2	2.53	
δ , mm	metamodels	3.6869	1.7313	4.719*
	actual	3.6806	1.7213	
m, kg		4.688		4.695*

* 96th percentile

In the next step robust optimization is performed. The uncertainty in X5 is assumed uniform and is propagated using MC simulations on kriging metamodels. The constant number of MC simulations 10E4 is used which is further increased to 10E6 when higher MC accuracy is needed. The 96th percentile is used for criterion and constraint satisfaction. Obtained stiffness ribs shapes and indices are shown on Fig. 10(III) and in Table 5.

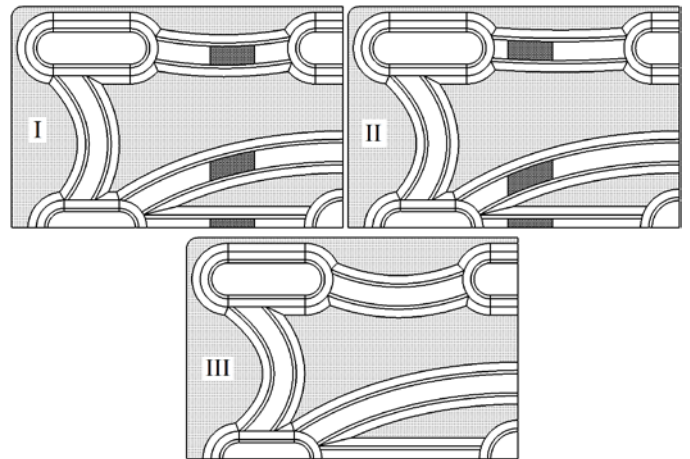


Fig. 10 The results of stiffness ribs shape optimization in 1/4 3D model of pallet for case (b): deterministic optimization for I) X5=200 and II) X5=270; III) robust optimization (the fluctuations around the nominal values are uniform)

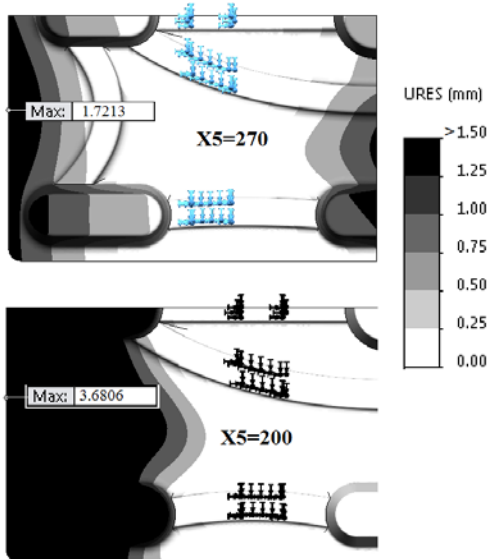


Fig. 11 The maximal deflection of the pallet for case (b): deterministic optimization I) $X5=200$, and II) $X5=270$

V. CONCLUSION

The software KEDRO developed for design of numerical and physical experiments, creating metamodels on basis of parametric and nonparametric approximations and multiobjective robust optimization can be used for practical optimization tasks with a small number (<12) of optimization variables. The test problem of two bar truss confirmed that it is possible to obtain a different solution considering structure optimization problem as non-deterministic. The uncertainties in pallet supports considerably affect the pallet rib shapes. The pallet manufacturing technology could be the main cause of uncertainties in design, e.g., improper dimensions and material properties due to characteristics of compression molding. In this case additional uncertainties must be considered during robust optimization.

REFERENCES

- [1] T. Sokół, and G. I. N. Rozvany. On the adaptive ground structure approach for multi-load truss topology optimization. Proc.10th World Congress on Structural and Multidisciplinary Optimization. May 19 -24, 2013, Orlando, Florida, USA, 10 p. (CD-ROM). Available: <http://www2.mae.ufl.edu/mdo/Papers/5428.pdf>
- [2] M. P. Bendsøe and N. Kikuchi, Generating optimal topologies in structural design using a homogenization method, *Comput. Methods Appl. Mech. Engrg.* 71 (2) (1988) 197-224.
- [3] M. P. Bendsøe and O. Sigmund, Material interpolation schemes in topology optimization, *Applied Mechanics*, vol. 69, pp. 635-654, 1999.
- [4] J. Haslinger, and R. A. E. Makinen, *Introduction to Shape Optimization: Theory, Approximation, and Computation*, SIAM, 2003, 273 p.
- [5] J. S. Arora, *Optimization of Structural and Mechanical Systems*, World Scientific, 2007, 595 p.
- [6] G. N. Vanderplaats, *Multidiscipline Design Optimization*, VR&D, 2007, 477 p.
- [7] R. T. Haftka, and Z. Gurdal, *Elements of Structural Optimization*, 3rd ed, Springer, 1992, 481 p.
- [8] A. Ben-Tal, L. E. Ghaoui, A. Nemirovski, *Robust Optimization*, Princeton University Press, 2009, 544 p.
- [9] A. E. Hami, and R. Bouchaib, *Uncertainty and Optimization in Structural Mechanics*, John Wiley & Sons, 2013, 144 p.

- [10] X. Du, and W. Chen, Towards a better understanding of modeling feasibility robustness in engineering design, *ASME J. Mech. Des.* 122, pp. 385-394.
- [11] A. Saxena, and B. Sahay, *Computer Aided Engineering Design*, Springer, 2005, 394 p.
- [12] T.H. Lee, and J.J. Jung, Metamodel-based Shape Optimization of Connecting Rod Considering Fatigue Life, *Key Engineering Materials*, VOL 306/308; 2006, pp. 211-216. Available: <http://citeseerx.ist.psu.edu/viewdoc/download?doi=10.1.1.111.4200&rep=rep1&type=pdf>
- [13] T. W. Simpson., A. J. Booker, D. Ghosh, A. A. Giunta, N. P. Koch, and R. Yang, *Approximation Methods in Multidisciplinary Analysis and Optimization: A Panel Discussion. Structural and Multidisciplinary Optimization*, vol. 27, 2004, pp. 320- 313.
- [14] D. C. Montgomery, *Design and Analysis of Experiments*, 8th ed, Wiley, 2012, 752 p.
- [15] S. Koziel, D. E. Ciaurri, and L. Leifsson, *Surrogate-Based Methods*, Chaper 3 in "Computational Optimization, Methods and Algorithms", Springer, 2011, pp. 33 -59.
- [16] C. E. Rasmussen, and Christopher K. I. Williams, *Gaussian Processes for Machine Learning (Adaptive Computation and Machine Learning)*, The MIT Press, 2005, 248 p.
- [17] J. Sacks, J.W. Welch, J. T. Mitchell, and H. P. Wynn, Design and analysis of computer experiments, *Statistical Science*, 4(4), Nov. 1989, pp. 409 -423.
- [18] J. Janusevskis, and R. Le Riche, Simultaneous kriging-based estimation and optimization of mean response, *Journal of Global Optimization*, vol. 55, issue 2, Springer, 2013, pp. 313-336. Available: <http://link.springer.com/article/10.1007%2Fs10898-011-9836-5>
- [19] D.S . Aponte, R. Le Riche, G. Pujol, and X. Bay, An Empirical Study of the Use of Confidence Levels in RBDO with Monte-Carlo Simulations, Chapter 9. in the book *Multidisciplinary Design Optimization in Computational Mechanics*, Edited by P. Breitkopf , R.F. Coelho, Wiley-ISTE, 2010.
- [20] A.R. Parkinson, R. Balling, and J.D. Hedengren, *Optimization Methods for Engineering Design*, Brigham Young University, 2013.
- [21] D. V. Rosato, D. V. Rosato, and J. Murphy, *Reinforced plastics handbook*, Elsevier, 2004, 586 p.
- [22] B. Davis, and P. Gramann, T. Osswald, and A. Rios, *Compression Molding*, Hanser Publication, 2003, 196 p.
- [23] A. Janusevskis, J. Auzins, A. Melnikovs, A. Gerina-Ancane, *Shape Optimization of Mechanical Components of Measurement Systems*, OAB Advanced Topics in Measurements, InTech, 2012, pp. 243-262. Available: <http://www.intechopen.com/books/advanced-topics-in-measurements/shape-optimization-of-mechanical-components-for-measurement-systems>
- [24] S. W. Tsai, and E. M. Wu, "A general theory of strength for anisotropic materials". *Journal of Composite Materials*. vol. 5, 1971, pp. 58-80.

The application of variational principles in hydrodynamic theory of lubrication

L. Savin, A. Kornaev, E. Kornaeva

Abstract—The paper examines the modeling of the viscous fluid flux in circle orifices of fluid-film bearings with application of continuum mechanics principles. A modification of the target functional is proposed and the equivalence of the classical approach is shown by solving a closed set of equations and finding the extremum of the objective functional with some integral constraint. A problem of a flux in an infinitely long bearing is concerned and the results of solving it are compared to the results of other authors.

Keywords—Continuum mechanics, hydrodynamic theory of lubrication, isoperimetric variational problem.

I. INTRODUCTION

THE development of the numerical methods and the software aimed at solving the boundary value problems of hydrodynamic lubrication theory, along with its obvious advantages [1-3], has several drawbacks. First of all, due to the small width of the film, the proportions of the flux area have different orders of magnitude, thus the discretisation of the area requires a huge number of partitions. In most of the cases this problem is solved by applying the simplified O. Reynold's [4] approach, according to which the numerical integration of the thickness of the film can be replaced by analytic, however in case of complex rheology fluid this method becomes difficult to apply. Secondly, results obtained in discrete form are harder to analyze and check. The following approach to solving the problems of continuum mechanics is free from the drawbacks mentioned above [5]. It would be fair to say that the field of application is very specific and has a considerable number of constraints, e.g. the flux geometry simplicity, flux process stationarity (quasistationarity), dependence of the accuracy on the choice of the array, where the solution is searched.

This work was supported in part by the Ministry of Education and Science of the Russian Federation under the projects No 9.101.2014/K and No 363 of a part of the state task for the "State University - ESPC" in 2014, and under grant of the President of the Russian Federation No 14.Z56.14.6000-MK.

L. A. Savin is with the Faculty of New Technologies and Production Automation, State University – Education-Science-Production Complex, Oryol, 302020, Russia (e-mail: savin@ostu.ru).

A. V. Kornaev is with the Faculty of New Technologies and Production Automation, State University – Education-Science-Production Complex, Oryol, 302020, Russia (corresponding author to provide phone: +7953-478-1591; e-mail: rusakor@inbox.ru).

E. P. Kornaeva is with the Education-Science-research institute of information technologies, State University – Education-Science-Production Complex, Oryol, 302020, Russia (e-mail: lenoks_box@mail.ru).

II. JUSTIFICATION OF THE ISOPERIMETRIC VARIATIONAL PROBLEM FORMULATION

The classic approach to solution of the boundary values problems of viscous incompressible fluid flux by means of integrating of the differential equations array [5] can be replaced by equivalent approach to finding the extremum of some target functional [5]. The fact that the first approach is equivalent to the second can be demonstrated in the case when the set of generalized Euler–Lagrange differential equations [6], which were obtained for the target functional, matches the differential equations of equilibrium.

In [5] a principal possibility of applying the power of internal forces as such functional is shown:

$$Int = \int_{\Omega} T_{\sigma} \cdot (\nabla \otimes \vec{V}) d\Omega, \quad (1)$$

where T_{σ} is stress tensor with components σ_{ij} , \vec{V} is velocity vector.

The same paper shows that the set of generalized Euler–Lagrange differential equations gives two families of equations. The first family $\frac{\partial F}{\partial \sigma_{ij}} = 0$ results in trivial solution

corresponding to the translational motion of the media, the second family matches exactly the equations of equilibrium [5].

However one must notice that with incompressible media moving the power of internal forces is determined by the deviator of the stress tensor [5]:

$$Int = \int_{\Omega} D_{\sigma} \cdot (\nabla \otimes \vec{V}) d\Omega, \quad (2)$$

where D_{σ} is a stress deviator with components s_{ij} .

Then it can be seen that the second family of the generalized Euler–Lagrange differential equations, mentioned above, does not match the equation of equilibrium due to it lacking the middle stress p_0 (hydrostatic pressure).

In this paper a modified target functional is proposed which includes the power of internal forces (2) and the power of the flux across the closed area S which is characterized by a unit

external normal vector \vec{n} , bounds the volume of Ω and developing due to the hydrostatic pressure p_0 :

$$I = \int_{\Omega} D_{\sigma} \cdot (\nabla \otimes \vec{V}) d\Omega + \int_S (p_0 \vec{V}) \cdot \vec{n} dS. \quad (3)$$

In case when the contribution of the deviator of the stress tensor D_{σ} on the surface of S to the flux of full stress $\vec{\sigma}^n$ across this surface is small or absent, the second term in (3) is the power of “pumping” the medium across the volume Ω .

Applying the M.V. Ostrogradsky - C. Gauss formula allows the convert the functional (3) to the following form:

$$I = \int_{\Omega} \left[D_{\sigma} \cdot (\nabla \otimes \vec{V}) + \nabla \cdot (p_0 \vec{V}) \right] d\Omega. \quad (4)$$

In Cartesian coordinates the integral (4) in the scalar form given the incompressibility of the medium is the following¹:

$$I = \int_{\Omega} \left[s_{ij} \frac{\partial V_i}{\partial x_j} + \frac{\partial p_0}{\partial x_k} V_k \right] d\Omega. \quad (5)$$

It is possible to see that, when determining the set of generalized Euler–Lagrange differential equations, the family of equations obtained with functions s_{ij} results in trivial solution, the family of equations obtained with functions V_i results in equations of equilibrium, when the family of equations obtained with the function p_0 results in the equation of continuity.

The essence of isoperimetric variational formulation of the problem of motion of a continuous medium, proposed by B.V. Koutcheryaev [5], is limiting the target functional by the power balance. Such conditions are equivalent to static boundary conditions. Then, the variational problem can be formulated as follows:

$$\begin{cases} I \Rightarrow \min, \\ Int - Ext = 0, \end{cases} \quad (6)$$

where Ext is the power of external forces.

So, the following can be concluded: 1) the functions V_i , which deliver the extremum to the functional (3), satisfy the set of equations of equilibrium, thus the problem of determining the extremum of the function (3) in the given set of cinematically possible velocity fields (CPVF) $V_i = V_i(x_j)$ is equivalent to solving a set of differential equations of equilibrium; 2) cinematic boundary conditions and the incompressibility condition were considered when forming the CPVF, the integral constraint in the form of the balance of

power [1] can act as an equivalent to static boundary conditions.

It is necessary to note that tensor form of equations is invariant, while in the scalar form the rules of differentials operations in curvilinear coordinates have to be taken into account [7, 5].

III. MATHEMATICAL MODEL OF THE FLUID-FILM BEARING

Two-dimensional isothermal flux of the Newtonian fluid in the gap between the spinning at a constant peripheral speed pin and static bearing. Motion is taken stationary and volume and mass forces are weak. On the surfaces of the pin and the bearing the no-slip condition is applied.

The medium motion is better to study not in the set of Cartesian coordinates x_i but in the bipolar coordinates β_i [7], isolines of which coincide with the edges of the area. Isolines of the β_1 coordinate are the eccentrically located circles, to two of which, i.e. $\beta_1 = \beta_1^+$ and $\beta_1 = \beta_1^-$, can be associated with two circles with radius r as the pin and radius R as the bearing (Fig. 1). Then, e^{β_1} is the ratio of the polar radius of a point C. The coordinate β_2 in the Cartesian set of coordinates x_i is the angle between the beams from the pole A $(-a, 0)$ and B $(a, 0)$. The limits $\beta_2 = \beta_2^- = -\pi$ and $\beta_2 = \beta_2^+ = \pi$ determine the uniqueness condition of the flux area in the set of coordinates β_i . In the bipolar coordinates the flux area is the rectangle.

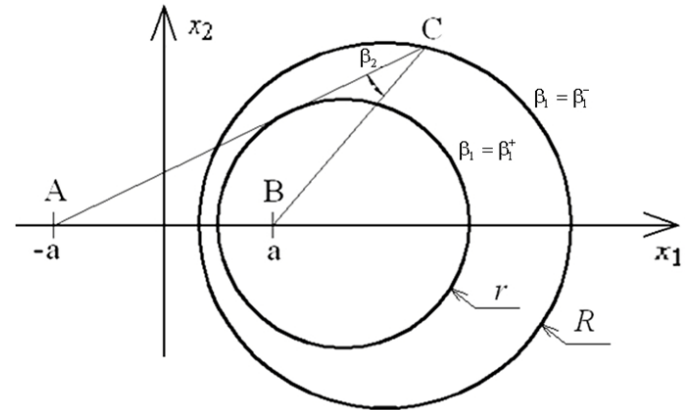


Fig. 1 Cartesian and bipolar set of coordinates correspondence

Lamés coefficients for the coordinate transformation are [7]:

$$\begin{aligned} H_1 = H_2 = H &= \frac{a}{ch(\beta_1) - \cos(\beta_2)}, \\ H_3 &= 1. \end{aligned} \quad (7)$$

Cinematically possible velocity field can be easily determined with a flux function Ψ [8] as follows:

¹ The A. Einstein's summation notation and the A.I. Lourie's exception are used.

$$\begin{aligned} V_1 &= \frac{1}{H} \frac{\partial \Psi}{\partial \beta_2}, \\ V_2 &= -\frac{1}{H} \frac{\partial \Psi}{\partial \beta_1}. \end{aligned} \quad (8)$$

The velocity field (8) draws the incompressibility condition to identity, which shortens the number of equations to solve.

The flow function Ψ can be shown as a set as follows:

$$\Psi(\tilde{\beta}_i) = c \alpha_k \beta_1^{k\tilde{h}}, \quad (9)$$

where $\tilde{\beta}_i$ are dimensionless coordinates $\tilde{\beta}_i = \frac{\beta_i - \beta_i^-}{\beta_i^+ - \beta_i^-}$, c a constant coefficient that provides the non-slip condition met, α_k are unknown coefficients of the set ($k=1,2,\dots$), \tilde{h} is Lamé's dimensionless coefficient (7) on the surface of the pin $\beta_1 = \beta_1^+$.

Then, CPVF (7) will be as follows:

$$\begin{aligned} V_1 &= \frac{1}{H} \frac{ck\alpha_k}{(\beta_2^+ - \beta_2^-)} \frac{\partial \tilde{h}}{\partial \tilde{\beta}_2} \beta_1^{k\tilde{h}} \ln(\beta_1), \\ V_2 &= -\frac{1}{H} \frac{ck\alpha_k}{h(\beta_1^+ - \beta_1^-)} \tilde{h} \beta_1^{k\tilde{h}-1}. \end{aligned} \quad (10)$$

Then, the components of the strain rate tensor can be determined with the J. Stokes's formula:

$$T_{\xi} = \frac{1}{2} (\nabla \otimes \vec{V} + \vec{V} \otimes \nabla) \quad (11)$$

The connection between the stress and strain states for viscous incompressible medium is determined by the generalized R. Hooke's law:

$$D_{\sigma} = 2\mu D_{\xi}, \quad (12)$$

where μ is the coefficient of the dynamic viscosity, D_{ξ} is the deviator of the strain rate tensor T_{ξ} (for the incompressible medium $T_{\xi} = D_{\xi}$).

The components of the pressure gradient in the functional (4) can be obtained from the equation of equilibrium:

$$\nabla \cdot S_{\sigma} = -\nabla \cdot D_{\sigma}, \quad (13)$$

where S_{σ} is a spherical part of the stress tensor with diagonal components $-p_0$.

The balance of power includes the power of internal forces (2) and the power of the external forces, which develops on the

surface of the bearing due to the fact of it spinning at the velocity V^0 and medium resistance. The power of external forces is as follows:

$$Ext = 2V^0 \left(\beta_2^+ - \beta_2^- \right) \int_0^1 (H\mu\xi_{12}) \Big|_{\beta_1=1} d\tilde{\beta}_2. \quad (14)$$

In the isoperimetric form (6) the process of obtaining the extremum of the target functional with integral constraint can be replaced by the process of finding the extremum of the auxiliary functional [5]:

$$J_L = I + \lambda(Int - Ext) \Rightarrow \min, \quad (15)$$

where λ is a Lagrange's undetermined multiplier.

Substitution of (10-14) in the functional (15) allows it to be determined by the set of CPVF (10). Representation of the CPVF (10) in the form of a set makes the W. Ritz's method easy to use [5].

IV. RESULTS OF THE IMITATIONAL MODEL OF THE FLUID-FILM BEARING TESTING

The mathematical model was developed as a program by means of a free software «GNU Octave» [9], using MATLAB compatible high-level programming language. The search for the minimum of the functional (15) was implemented with an inbuilt combined algorithm of finding the extremum of the function of several variables.

As a test the problem of the flow of Newtonian fluid with viscosity $\mu_0 = 0.032$ Pa·s, $\rho_f = 886$ kg/m³ density in the

flow area between the pin with $r = 2.5 \cdot 10^{-2}$ m radius, and bearing with $R = 2.51 \cdot 10^{-2}$ m radius was considered. Pressure on the surface of the pin in the point of minimal gap is $P_0 = 2.5 \cdot 10^6$ Pa and the peripheral speed of the pin is $V^0 = 3$ m/s.

After a series of computational experiments with different values of the eccentricity e_p of the pin in the bearing the following results were achieved.

In the Fig. 2 contour graphs of the flux function fields are shown, isolines of which represent the trajectory of the flux, and the vector velocity fields (10). Due to the small value of the average gap $h_0 = R - r$, are in the Fig. 2 was stretched in the direction of the coordinate β_1 so that the results are clear to see. As one can notice in the Fig. 2, the increase in eccentricity results in partial locking and backflow. Similar results were obtained by other authors theoretically [10, 11] and experimentally [12].

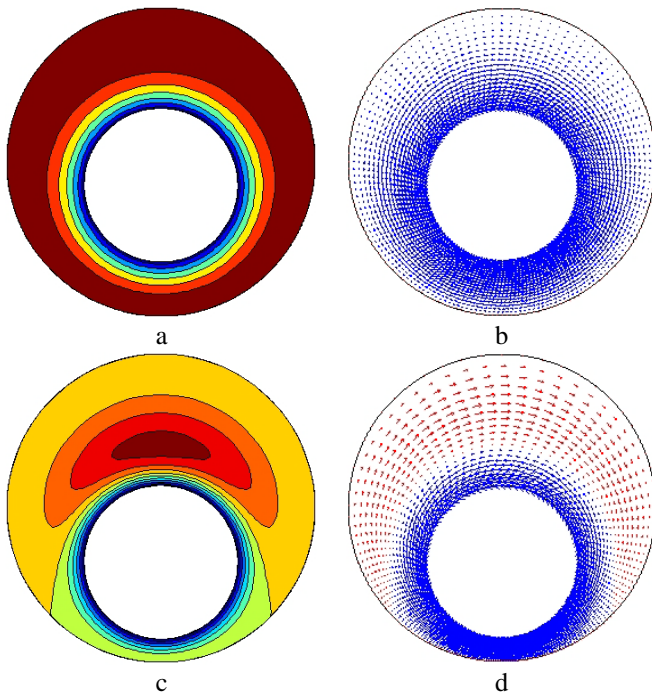


Fig. 2 flux and velocity functions fields; (a) and (b) with relative eccentricity $e_p/h_0 = 0.3$, (c) and (d) - $e_p/h_0 = 0.7$

Fig. 3 depicts the graphs of the pressure fields on the surface of the pin with different values of eccentricity. It can be seen that with increase in eccentricity the pressure field distorts in the area of the maximum gap. It can be assumed that a certain effect of capacity of the fluid growth slowdown takes place, similar to the Magnus's effect in aerodynamics [8].

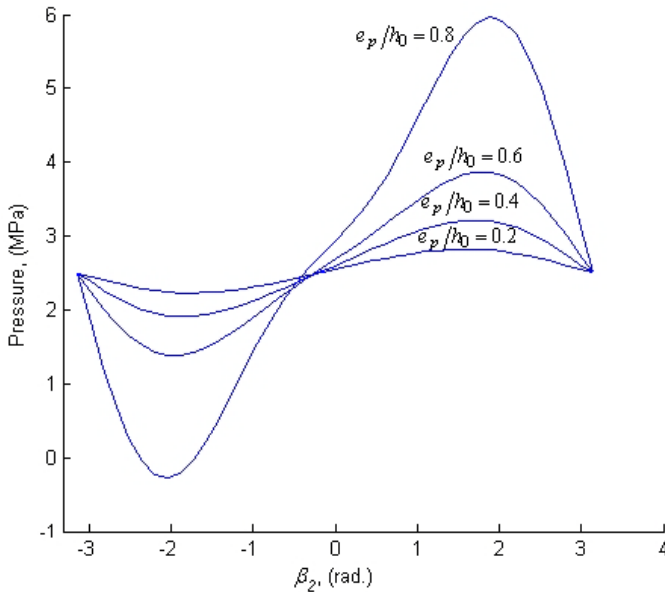


Fig. 3 the pressure field on the surface of the pin

The results of friction coefficient calculation as a relation of the resulting friction force T to the resulting lifting force P showed the presence of a minimum (Fig. 4) which could also be the expression of the Magnus's effect.

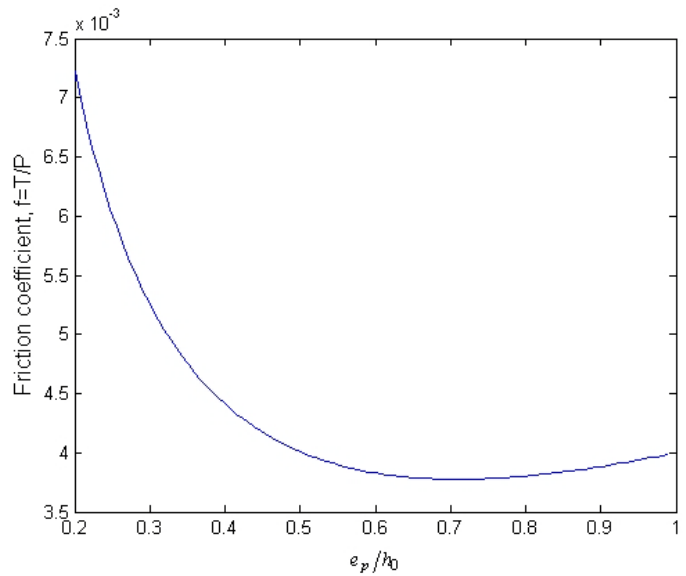


Fig. 4 dependence of the friction coefficient value on the relative eccentricity

Quantitative comparison of the results of calculation of hydrodynamic forces in the developed program with the results of the calculation using the method of N.E. Zhukovsky and S.A. Chaplygin [13] showed a divergence of not more than 2%, which most likely occurred due to the rounding error.

V. CONCLUSION

The paper examined the possibility of application of the isoperimetric form of the variational problem of the viscous incompressible fluid flux in the gap in the fluid-film bearing, the use of the modified target functional was proposed and justified. The application of variational principles allows the substitution of the differential equations integration with the search for the extremum of the function of several variables as well as to obtain the solution in analytic form. One of the most important advantages of the approach is the possibility to study the medium with complex rheology. As for the drawbacks of the method, the relative complexity of CPVF formation procedure, inability to solve the time-dependent and complex flux area form problems can be highlighted.

ACKNOWLEDGMENT

This work was supported in part by the Ministry of Education and Science of the Russian Federation under the projects No 9.101.2014/K and No 363 of a part of the state task for the "State University - ESPC" in 2014, and under grant of the President of the Russian Federation No 14.Z56.14.6000-MK.

REFERENCES

- [1] S. V. Patankar, *Numerical Heat Transfer and Fluid Flow*. McGraw-Hill, Hemisphere Publishing Corporation, 1980.
- [2] M. G. Salvatory, *Numerical Methods in Engineering*. New York, 1952.

- [3] C. Cuvelier, C. Segal, A. A. van Steenhoven, Finite Element Methods and Navier-Stokes Equations Introduction to Signal Detection and Estimation. *Series: Mathematics and its Application*, Vol. 22, New York: Springer-Verlag, 1986.
- [4] O. Reynolds, "On the Theory of Lubrication", *Ibid.*, 177 (1886), pp. 157–234.
- [5] B. V. Koutcheryaev, *Mechanics of Continua: Theoretical Basics of Processing Metals under the pressure*. Moscow, MISiS Publishing, 2006 (In Russian).
- [6] L. E. Elsgoltz, *M Differential equations and calculus of variations*. Moscow, Nauka (Science) Publishing, 1969 (In Russian).
- [7] G. A. Korn, T. M. Korn, *Mathematical Handbook for Scientists and Engineers*. Dover Publications, 2000.
- [8] L.M. Milne-Thomson. *Theoretical hidrodinamics*. Fours edition, London: Macmilan and Co LTD, 1960.
- [9] GNU Octave. Available online: <http://www.gnu.org/software/octave/> (accessed on 1 October 2013).
- [10] C. Shu, L. Wang, Y. T. Chew, N. Zhao, "Numerical study of eccentric Couette-Taylor flows and effect of eccentricity on flow patterns". *Theoretical and Computational Fluid Dynamics*, vol. 18, 2004, pp. 43–59.
- [11] A. Z. Szeri, A. Al-Sharif, "Flow Between Finite, Steady Rotating Eccentric Cylinders". *Theoretical and Computational Fluid Dynamics*, vol. 7, 1995, pp. 1–28.
- [12] J. H. Vohr, "An Experimental Study of Taylor Vortices and Turbulence in Flow Between Eccentric Rotating Cylinders" in *Proc. of ASLE – ASME Conf.*, Chicago, 1967, pp. 299–315.
- [13] N. E. Jukovskiy, S. A. Chapligyn, *About Friction between pin and journal*. Collected works, Vol. 3, Moscow, 1949.

Natural Frequency Automatic Variation in Earthquake Isolation System

Federico Bartolozzi

Civil Engineer & Independent Researcher, via dei Carracci, 4 – 21100 Varese, Italy
ciuciuzza@iol.it

Horizontal Translation

The problem concerning the dynamic equilibrium is spatial and it is statically determined by the six equations of the Rigid Systems Statics. At each instant of the motion, they express the equilibrium of all external forces (building weight, bearings reactions, friction forces and inertial force). The equations system is expressed by the following correlation:

$$\varphi_{j,1} V'_1 + \varphi_{j,2} V'_2 + \varphi_{j,3} V'_3 + \varphi_{j,4} V'_4 + \varphi_{j,5} F_{i,x} + \varphi_{j,6} F_{i,y} = \zeta_j \quad (1)$$

with: $j = 1,2,3,4,5,6$ and where: V'_1, V'_2, V'_3, V'_4 are the bearings reactions and $F_{i,x}, F_{i,y}$ are the inertial force components in the directions X and Y .

Vertical Translation

In order to safeguard the building against the danger of resonance, which takes place when, because of the sub-undulatory shock, the seismic frequency equalises the natural frequency of the building, it is necessary to fix a frequencies interval, containing the resonance one, in which the seismic frequencies are not compatible with the building safety. In this interval it is, therefore, indispensable that a system of auxiliary springs is automatically started up in each bearing. These springs, strengthening the action of the main springs, increase the vertical natural frequency of the building, noticeably decreasing the vertical displacements of the building, which must be not greater than the fixed values of project. If $\phi_r = \phi_n$ is the resonance frequency, the emergency lower limit frequency is $\phi_{i,e} = c_{s,i} \phi_r$, where $c_{s,i} < 1$ is the lower safety coefficient. The emergency higher limit frequency is $\phi_{s,e} = c_{s,s} \phi_r$, where: $c_{s,s} = \sqrt{2 - c_{s,i}^2} > 1$ is the higher safety coefficient. When the seismic frequency equalises the emergency limit frequencies, that is for $\phi = \phi_{i,e}$ and $\phi = \phi_{s,e}$, the vertical displacement of the building is expressed by all of the following formulas: $S_c = S_v / (1 - c_{s,i}^2)$ and $S_c = S_v / (1 - c_{s,s}^2)$, respectively in phase and in phase opposition with the vertical displacement S_v of the soil. With respect to the maximum vertical

displacement of the soil, we design the maximum vertical displacement of the building, which is valid both for emergency limit frequencies and, generally, for the frequencies outside the emergency interval:

$$\xi_1 = |S_{v,max} / (1 - c_{s,i}^2)| = |S_{v,max} / (1 - c_{s,s}^2)| \quad (2)$$

where: $S_{v,max}$ is the maximum vertical displacement of the soil. When the seismic frequency is inside the emergency interval, including the resonance one, that is for $\phi = \phi_e$, we impose the condition that the maximum vertical displacement of the building, with reference to the resonance, is $\xi_{max} = \xi_1 + \xi_2$, where: ξ_1 has the value of (2) and:

$$\xi_2 = S_{v,max} / [1 - (\phi_n^2 / \phi_n^{*2})] \quad (3)$$

being ϕ_n the first natural frequency of the building, due to action of the main springs and also the resonance frequency, ϕ_n^* the second natural frequency, due to the combined action of the main and auxiliary springs. Developing and solving (3), we have:

$$\phi_n^* = \phi_n \sqrt{[\xi_2 / (\xi_2 - S_{v,max})]} \quad (4)$$

with $\xi_2 > S_{v,max}$. The total elastic constant of the main and auxiliary springs is:

$$k_t^* = 4 \pi^2 \phi_n^{*2} P_c / g = 4.024 \phi_n^{*2} P_c \quad (5)$$

where: g is the gravity acceleration, expressed in m/s^2 and P_c is the building weight.

Operating Principle of the Bearing

(See Fig. 1) When the soil is in a state of quiet, the bearing is subjected to the static load transmitted from the building and the main springs 13 become shorter because of compression. The building is perfectly centred because of the level inclined surface 3 and it is motionless. In the presence of an earthquake, due to the undulatory shock, the foundation-soil complex translates in a horizontal direction with respect to the building, and the variation of vertical rigid deflection due to the

variation of thickness of the level inclined surface 3 is perfectly balanced by the corresponding elastic deformation of the main springs 13 in any instant and for any value of the displacement. The building remains motionless with respect to the horizontal translation of the foundation-soil complex. The horizontal inertial force does not change the static equilibrium of the building, because it has a minor value when using bearings with sliding friction and it is negligible when using bearings with rolling friction. Due to the sub-undulatory shock, the vertical motion of the soil does not modify notably the behaviour of the building. In fact, it preserves the verticality, and its vertical displacements, both in phase and in phase opposition with the corresponding displacements of the soil, are always compatible with project fixed values. When the earthquake frequency is outside to the emergency interval or coincides with the emergency limit frequencies, the mass 11 vertically translates without the participation of the auxiliary springs 12. Vice versa, due to the vertical motion of the mass 11, the participation of the auxiliary springs 12 takes place when the earthquake frequency is inside the emergency interval, including the resonance one. In this case, due to the combined action of the main and auxiliary springs, the increase of natural frequency of the building considerably decreases the vertical displacements of the building to values compatible with the safety conditions of the building.

Planning Aspect

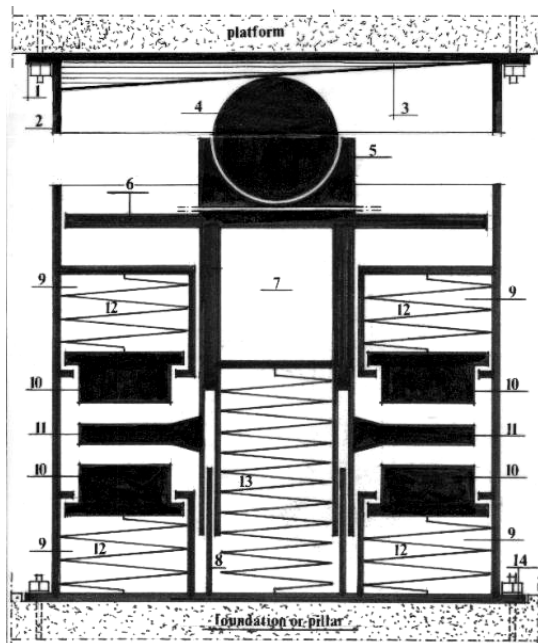


Fig. 1 Bearing with Centred Main Spring

Conclusions

The theoretical results make evident the following characteristics of the proposed system: 1. self-centring of the building at the end of the earthquake; 2. the undulatory seismic energy absorbed by the building is constant and about 1% of the building weight, using bearings with sliding friction (pure Teflon) and it is negligible using bearings with rolling friction (steel balls). It is independent from the seismic frequency and from the degree of the motion; 3. the building remains motionless with respect the horizontal translation of the foundation-soil complex for any value of the direction angle of the earthquake, of the soil displacement and of the acceleration, both with bearings with sliding friction and bearings with rolling friction; 4. the choice of the horizontal displacement for the project of the main spring elastic constant 13 is theoretically. In practice, the choice issues from the opportuneness of using a not very elastic spring, which would cause a very high static yielding of the spring; 5. in order to prevent the resonance danger, due to the sub-undulatory shock, the natural frequency variability takes place because of auxiliary springs, which automatically increase the action of the main springs during an emergency, characterised by an vertical seismic frequencies interval, including the resonance one; 6. the system has the characteristics of extreme economical competitiveness with all existing anti-seismic systems, due to the considerable decrease of the seismic energy in the building, to the almost total lack of the psycho-physical discomfort in the inhabitants and to the easy maintenance.

References

1. Bartolozzi F., System of Base Seismic Isolation with the Project of the Fixed Bearing with Alternative Function of Multidirectional Movable Bearing, *Proceedings of the International Conference on Earthquakes, Volcanoes and Tsunamis*, Vancouver, Canada, (1996), Paper in CD-rom and Abstract in Book, 23.
2. Bartolozzi F., Self-centring Aseismic System with Four Rigid Movable Bearings, *Proceedings of the Fourth National Conference on Earthquake Engineering*, Ankara, Turkey, (1997), 536-541.
3. Bartolozzi, F., Centring and Locking Aseismic Bearing, *Proceedings of the 2nd International Conference on Control of Oscillations and Chaos*, St. Petersburg, Russia, (2000), Volume 1, 124-125.
4. Bartolozzi F., Aseismic Bearing with Partially or Totally Curved Sliding Surface and with Angular Corrector, *Proceedings of TIEMS2001, International Conference on Emergency Management*, Oslo, Norway, (2001), Paper in CD-rom.

5. Bartolozzi F., Aseismic System with Magnetic Insulators, *Proceedings of 7th International Conference on Inspection, Appraisal, Repairs & Maintenance of Building & Structures*, Nottingham, United Kingdom, (2001), 219-223.
6. Bartolozzi B., Bartolozzi F., Complete Calculation of Lamé Plinth at Constant Height, *Proceedings of 2nd International Specialty Conference on the Conceptual Approach to Structural Design*, Milan, Italy, (2003), 273-282.

Mechanical properties of composite hydrogel materials based on poly(acrylamide) and clay minerals and their potential application for cleaning of the internal surface of pipes

Zhanar IBRAYEVA, Evgeniy BLAGIKH, Sarkyt KUDAIBERGENOV

I. INTRODUCTION

Abstract: Clay minerals such as bentonite, montmorillonite, and kaolin as well as silica and titanium dioxides with average size of 1 μm were embedded within the network of poly(acrylamide) hydrogel (PAAH) by in situ radical polymerization. Dynamic swelling behavior of PAAH/Clay Mineral composites reveals that the swelling process follows by non Fickian law and the swelling degree decreases with increasing of clay content. The increase of inorganic component concentration in PAAH matrix results in increase of volume fraction of polymer (ϕ_2). The enthalpy of polymer-water mixing (ΔH_m) calculated according to Gibbs-Helmholtz equation indicates that the swelling process is endothermic. The increase of clay quantity in hydrogel leads to reinforcing of mechanical properties of composite materials. It is shown that hydrogel composites can potentially be used as “pigs” for the cleaning of the internal surface of main pipes from debris, sand and asphaltene-resin-paraffin deposits.

Keywords: clay, composites, hydrogels, mechanical properties, swelling.

This work was supported by Ministry of Education and Science of the Republic of Kazakhstan (Grant no.751)

Zh. E. Ibrayeva
Department of Printing Production, K.I. Satpayev Kazakh National Technical University, 050013, Satpaev Str. 22, Almaty, Kazakhstan. Fax: +001(7272)925080; Tel: +001(7272)925080; E-mail: zhanar-ibraeva@mail.ru

E. Blagih
Laboratory of Engineering Profile, K.I. Satpayev Kazakh National Technical University, 050013, Satpaev Str. 22, Almaty, Kazakhstan. Fax: +001(7272)925080; Tel: +001(7272)925080

S. E. Kudaibergenov
Institute of Polymer Materials and Technology, 050004, Almaty, Panfilov Str.52/105, Almaty, Kazakhstan. Tel: +001(7272)925808; E-mail: ipmtkau@usa.net

Laboratory of Engineering Profile, K.I. Satpayev Kazakh National Technical University, 050013, Satpaev Str. 22, Almaty, Kazakhstan. Fax: +001(7272)925080; Tel: +001(7272)925080; E-mail: skudai@mail.ru

At present hybrid materials based on inorganic-organic compounds have attracted considerable interest in research and industrial spheres. Due to composite structure and unique properties such as improved mechanical, thermal, electrical and optical characteristics they have found a wide application in medicine, membrane technology, optical engineering and catalysis [1-4]. Some attempts have been made to modify the properties of hydrogels by embedding of inorganic materials, such as montmorillonite, bentonite, mica, and sercite within the gel matrix [5-8]. The pioneering works to strength the mechanical properties of gel specimen adding inorganic components were done by Haraguchi and co. [9, 10]. Gel sample made from montmorillonite and N-isopropylacrylamide (PNIPA) is elastically stretched to about 10 times its original length [11]. This kind of nanocomposite hydrogel exhibited high transparency, high deswelling rate and extraordinary mechanical properties with elongation at break in excess of 103%. The organic/inorganic network structure was formed by in situ free-radical polymerization, in which the PNIPA chains were attached to the surface of clay sheets which acted as effective multifunctional cross-linkers through ionic or polar interactions. Authors [12] used kaolin as an inorganic component in polymerization of acrylic acid. Presence of kaolin particles in gel matrix caused a reduction of swelling coefficient but enhanced gel strength as high as 21-35%. A series of poly(acrylic acid-co-acrylamide)/kaolin composites were prepared by aqueous solution copolymerization of partially neutralized acrylic acid and acrylamide in the presence of kaolin nanopowder, which was synthesized to act as a release carrier of urea fertilizer and superabsorbent in agricultural industry [13,14]. The layered structure of aluminum silicates and the ability to swell in water allows polymer chains to diffuse into clay layers. Therefore kaolin and another aluminosilicates can act as co-crosslinker of hydrophilic polymers in solution. The overall stability of composite materials directly depends on whether exfoliation or intercalation process takes place and on the choice of monomer or initiator that can be adsorbed to the clay surface [15-17]. The aim of this paper is to describe the influence of immobilized clay minerals on swelling, thermodynamic and mechanical properties of poly(acrylamide) hydrogel (PAAH)

and to show the potential application of composite materials in particular for cleaning of internal surface of pipes.

II. EXPERIMENTAL PART

Materials

Acrylamide (AAM), N,N'-methylenebisacrylamide (MBAA), ammonium persulfate (APS) and N,N,N',N'-tetramethylethylenediamine (TMED) were purchased from "Aldrich" and used further without additional purification. As natural minerals micronized bentonite kaolin and montmorillonite powders as well as silicon and titanium dioxide with average particles size 200 nm purchased from "Aldrich" were used.

Methods

The elemental composition of the minerals was determined on X-ray fluorescence analyzer Epsilon 3 SW LTU PANalytical (The Netherlands). The FTIR spectra of dry samples were registered in KBr pellets with the help of a Thermo 5700 model instrument. The Raman spectra of the solid samples were registered using Thermo Almega XR model at the excitation wavelength of 780 nm. The X-ray diffractions were measured using a PANalytical (The Netherlands) Model-X-ray diffractometer. Morphology of dried PAAm/Kaolin and PAAH/TiO₂ composites (coated with a thin layer of palladium and gold alloy) was evaluated with the help of FE-SEM (EDS) model H-4300 (Hitachi, Japan). Thermal characteristics of the samples were investigated by differential scanning calorimeter DSC Evo Setaram (France) in the temperature range 50-500 °C at a heating rate 5 K/min. Mechanical experiments were carried out on PSM-2 (Williams's type) and RMI-60 instruments. Typical duration of a stress-strain measurement was around 2 min. Thickness and width of each sample was measured at room temperature using a digital caliper. The crosshead speed was 10 mm·min⁻¹. All samples were tested in triplicate and the results were averaged.

Synthesis of composite hydrogels

Composite materials based on polyacrylamide hydrogel (PAAH) and clay minerals (bentonite, kaolin and montmorillonite), SiO₂ and TiO₂ were synthesized by "in situ" free-radical polymerization [18]. An appropriate amount of suspension containing 2.5; 5; 10; 15 and 20 wt.% of clay minerals and SiO₂ (or TiO₂) microparticles was dropwisely added to aqueous solution (15 mL) of AAm (1.5 g) under stirring and the mixture left for 24 hours. After the crosslinking agent - MBAA (30 mg), the initiator - APS (25 mg) and the catalytic agent - TMED (1 µL) were added into the system. The reaction mixture was placed into the plastic syringe (length – 85 mm and diameter – 20 mm) with closed outlet at the bottom, bubbled by nitrogen during 10-15 min to remove the dissolved oxygen and thermostated at 60 °C during 5 h. After polymerization the samples were removed and washed by distilled water during 5-6 days refreshing the distilled water daily. Figure 1 represents samples of composite hydrogel materials based on PAAH and natural minerals.



Fig 1. Samples of the composite materials based on PAAH and kaolin (1), SiO₂ (2), bentonite (3) and montmorillonite (4).

Swelling characteristics of composite hydrogels

The washed out hydrogel samples were cut into several pieces and weighed. The swelling coefficient *KS* of hydrogel samples was calculated by equation (1):

$$KS = \frac{m_s - m_d}{m_d} \quad (1)$$

where *m_d* is the mass of dry gel, *m_s* is the mass of equilibrium swollen gel.

The gel density ρ was determined according to ASTM [19] using the equation (2):

$$\rho = \frac{m_1 - \rho_1}{m_1 - m_2} \quad (2)$$

where *m₁* is the mass of gel in air, *m₂* is the mass of gel in water and ρ_1 is the density of water (ρ_{H_2O}). Volume fraction of polymer in hydrogel (ϕ_2) was calculated according to equation (3):

$$\phi_2 = \frac{m_d / \rho_d}{m_d / \rho_d + (m_s - m_d) / \rho_{H_2O}} \quad (3)$$

The dynamic swelling behavior of composite gels in aqueous solutions was measured by the procedure described in [19]. The swelling rate was expressed as equation (4):

$$kt^n = M_t / M_\infty \quad (4)$$

where *k* is the swelling rate constant, *n* is a characteristic exponent describing the mode of the penetrant (e.g. water) transport mechanism, *t* is the absorption time, *M_t* is the mass of water absorbed at time *t*, *M_∞* is the mass of water absorbed at infinite time *t_∞*. The constants *k* and *n* were calculated from the slopes and intercepts of the plots of $\ln(M_t / M_\infty)$ versus $\ln t$ for *M_t / M_∞* less than 0,6.

Formation of asphaltene-resin-paraffin deposition

Asphaltene-resin-paraffin deposition (ARPD) of crude oils from Kumkol and Usen oilfields was studied by modified "cold finger" method that simulates the process of precipitation of ARPD on the trunk of pipeline. Pipeline within of which oil flows at temperature 300C was put into cryostate bath with temperature 50C. Precipitation of ARPD on the wall of internal surface of the tube was performed during 5 hours. After the tube was removed and immersed into acetone for

removing of oil. Precipitated ARPD was used to study the potential application of hydrogel “pigs” for cleaning purpose.

III. RESULTS AND DISCUSSION

Swelling-deswelling, volume-phase and mechanical properties of hydrogel composite materials depend on the choice of clay minerals and their structure. Crystalline structure of silicates is based on two types of two-dimensional structural elements: tetrahedral silica oxygen network and octahedral network where oxygen and hydroxide ions are in the corners of the elemental octahedron network while the atoms of aluminum, iron or magnesium occupy the central place. The combination of such networks forms the elementary layer, which may consist of two (tetrahedral and octahedral), three (two tetrahedral and one octahedral) or more networks. The composition of used in our case minerals is mainly represented by silicon (54-60 wt.%), aluminum (13.5-39.3 wt.%) and iron (2-16.7 wt.%). The content of such elements as K, Mg, Ca, P, Cl is less than 5%. Mechanism of formation of the composite structures can be represented as diffusion of AAm monomers to the layered clay structure. After monomer intercalation to the space of minerals and polymerization with simultaneous crosslinking a composite hydrogel materials are formed where nano- and microsized clay particles play the role of additional physical crosslinking centers. It leads to a significant increasing in mechanical properties of composite material

Dynamic swelling behavior of PAAH/Clay minerals composites

Figure 4 shows the dynamic swelling behavior of PAAH containing various clay minerals at 30 °C. According to [20] the dynamic swelling behavior of hydrogels depends on the relative contribution of penetrant diffusion and relaxation of crosslinked polymer chains. A value of $n = 0.5$ corresponds to Fickian diffusion, e.g. the process is diffusion controlled, whereas transport is considered to be relaxation controlled for $n = 1$ and as anomalous when the value of n lies between 0.5 and 1.

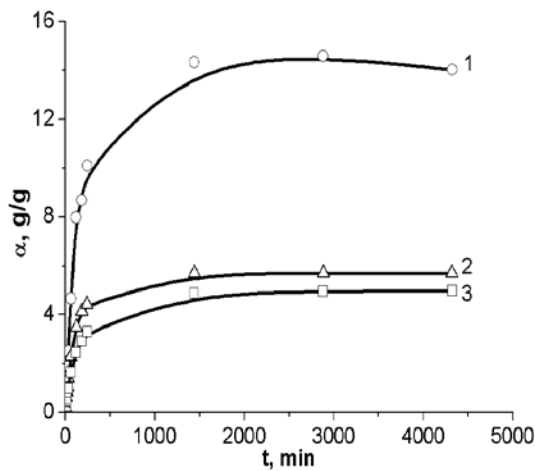


Fig. 2. Dynamic swelling behavior of PAAH/Clay minerals composites. The content of bentonite (curve 1), SiO₂ (curve 2) and kaolin (curve 3) in PAAH matrix is 10 wt.%.

The maximum degree of swelling for PAAH/Kaolin, PAAH/SiO₂, and PAAH/TiO₂, PAAH/Bentonite is around 4-14 g/g, the values of n are equal to 0.6-0.94. For the PAAH/Bentonite, PAAH/Kaolin, PAAH/TiO₂, and PAAH/SiO₂ composites the values of n are greater than 0.5 and correspond to an anomalous swelling mechanism, e.g. non Fickian diffusion. Gradually decreasing of n values from 0.94 to 0.64 with increasing of kaolin content from 2.5 wt.% to 20 wt.% in composite gel is explained by the fact that clay particles act as additional crosslinker or knots for polymer chains. For PAAH/Kaolin and PAAH/Bentonite the swelling degree decreases with increasing of the content of MBAA and bentonite respectively. In the former case it is connected with increasing of the density of chemical crosslinks in the latter case – with physical crosslinks. The influence of MBAA concentration at constant amount of kaoline (10 wt.%) and the influence of kaoline content at constant concentration of MBAA (20 mg) on the values of n is summarized in Tables 1 and 2.

Table 1. The influence of MBAA concentration at constant amount of kaoline (10 wt.%) on the values of n .

Kaoline, wt.%	MBAA, mg	n
10	15	0.42
	20	0.47
	30	0.78

Table 2. The influence of kaoline content at constant concentration of MBAA (20 mg) on the values of n .

MBAA, mg	Kaoline, wt.%	n
20	10	0.47
	15	0.52
	20	0.49

As seen from Tables 1 and 2 that the values of $n = 0.47 \pm 0.05$ in all cases excepting for PAAH/Kaolin (10 wt.%) and MBAA 30 mg coincide well with Fickian law.

Mechanical properties of PAAH/Kaolin composites

In general, the mixing of kaolin with acrylamide hydrogel matrix yields the diffusion of the polymer chains into basal space of the silicate layers of the clay and creates strong interfacial interactions. It is forecasted that the composite hydrogel materials may bear more external load than that of pure hydrogel. Mechanical stability of PAAH/Kaolin and PAAH/SiO₂ samples in comparison with pure PAAH is shown in Figures 3 and 4.

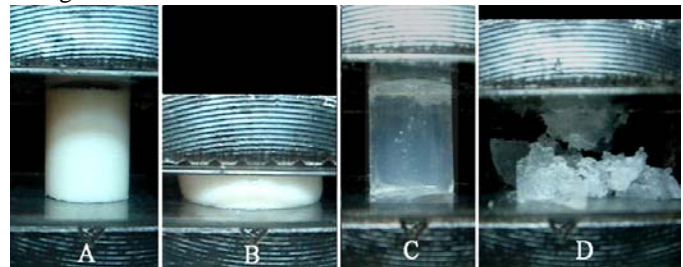


Fig. 3. Mechanical stability of PAAH/Kaolin (A, B) and pristine PAAH (C, D) composite gels.

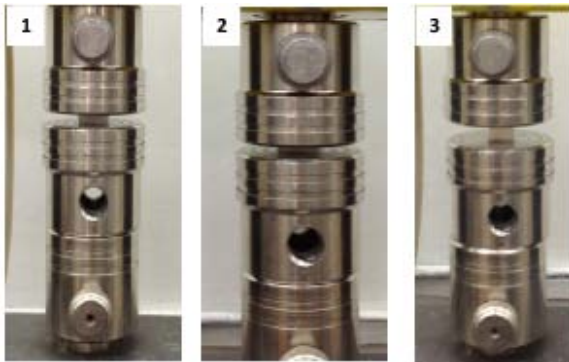


Fig. 4. Behavior of composite hydrogel PAAH/SiO₂ (10 wt.%) during the stress (1,2) and after removal of stress (3).

In contrast to ordinary hydrogels the composite materials consisting of hydrogels and clay minerals exhibit an improved physical-mechanical property. On the basis of such composite hydrogels we have developed flexible, elastic, and mechanically stable materials that are able to undergo big deformations against bending, stress and elongation.

Tensile properties of PAAH/Kaolin networks are given in Table 3. Increasing of clay content in PAAH matrix increases the values of elongation at break, tensile strength and Young's modulus (E). Improvement of mechanical properties of PAAH/Kaolin composites may be due to strengthening of polymer-polymer and weakening of polymer-water interactions. The kaolin particles which play the role of crosslinker can also contribute an additional yield.

Table 3 Tensile properties of PAAH/Kaolin samples

Sample	Volume % of Kaolin	Elongation at break, %	Tensile strength, kPa	E, MPa
PAAm/Kaolin	20	54	280	0.8815
PAAm/Kaolin	15	68	421	1.2413
PAAm/Kaolin	10	49	367	0.9453
PAAm/Kaolin	5	41	245	0.7234
PAAm/Kaolin	2.5	38	168	0.3278

Potential application of PAAH/Kaolin as “pigs” for cleaning of the internal surface of main pipes

Pigging is an operation to remove debris or unwanted deposit build-up in a pipeline. Debris, sand and ARPD in a pipeline will result in a pressure build-up and if no pigging exists their build-up could continue to rise and will create greater back pressure on the line, causing higher maintenance on pumps and the line could eventually become blocked (Fig.5). For certain tasks and in certain conditions, a viable alternative to running mechanical “pigs” is the use of gel “pigs”. In this work we have used composite hydrogel “pigs” – a unique organic-inorganic network structure with excellent mechanical properties – for cleaning of model pipeline from ARPD and water. Fig. 6 shows the cleaning of U-type model pipeline containing the crude oil and water with the help of composite

hydrogel “pigs” together with potential application of gel “pigs” for separate transportation of benzene and petrol in the same pipe.



Fig.5. Inner part of pipeline containing the debris and sand mixed with the ARPD.

As seen from Table 4 the effectiveness of cleaning of deposited paraffins from Kumkol and Usen oilfields by composite hydrogel “pigs” ranges between 94 and 96%. Another potential application of gel “pigs” might be deposition of anticorrosion solution to inner part of pipe.

Table 4. Results of cleaning of model pipeline inner part from ARPD by composite hydrogel “pigs”.

Diameter of model pipe, mm	Oilfield	Amount of ARPD, %	Cleaning effectiveness, %
13,5±1	Uzen	20	94
	Kumkol	18	96

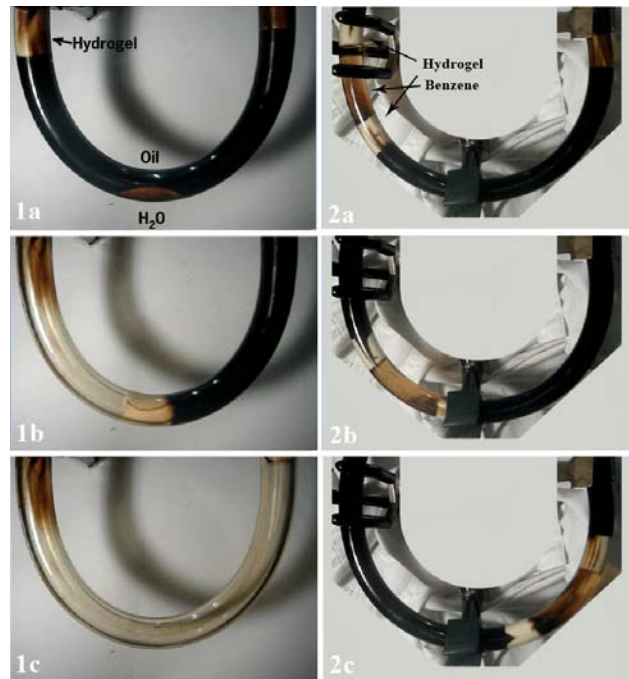


Fig.6. Cleaning of U-type model pipeline (1a-1c) and transportation of different mixtures (2a-2c) using hydrogel “pigs”.

IV. CONCLUSION

The composite hydrogel materials based on clay minerals, TiO₂, SiO₂ and polyacrylamide hydrogel were obtained by one-step "in situ" polymerization. As a result the flexible, elastic, and mechanically stable composite materials were designed. The swelling degree of samples increases in the following order: PAAH/Bentonite > PAAH/TiO₂ > PAAH/ > PAAH/Kaolin ≈ PAAH/Montmorillonite. For the PAAH/Bentonite, PAAH/Kaolin, PAAH/TiO₂, and PAAH/SiO₂ composites the values of *n* that are between 0.6 and 0.94 correspond to an anomalous swelling mechanism, e.g. non Fickian diffusion. The swelling coefficient decreased and volume fraction of polymer in hydrogel increased with clay content increasing. The increase of clay quantity in PAAH volume leads to reinforcing of mechanical properties of composite materials. It is concluded that PAAH/Clay Minerals composites can potentially be used as "pigs" for cleaning of the internal surface of main pipes from debris, sand and asphaltene-resin-paraffin deposits.

REFERENCES

- [1] Frimpong R.A., Fraser S, Hilt J.Z. Synthesis and temperature response analysis of magnetic-hydrogel nanocomposites// J. Biomed. Mater. Res: Part A. 2006. V. 80A.P.1–6.
- [2] Serksen S.R., Westcott S.L., Halas N.J., West J.L. Temperature-sensitive polymer-nanoshell composites for photothermally modulated drug delivery// J. Biomed. Mater. Res. 2000. V.51. P.293–298.
- [3] Serksen S.R., Mensing G.A., Ng M., Halas N.J., Beebe D.J., West J.L. Independent optical control of microfluidic valves formed from optomechanically responsive nanocomposite hydrogels// Adv. Mater. 2005. V.17. P.1366–1368.
- [4] Lao L.L., Ramanujan R.V. Magnetic and hydrogel composite materials for hyperthermia applications// J.Mater. Sci.:Mater.Med. 2004. V.15. P1061–1064.
- [5] Lee W.F., Yang L.G. Superabsorbent polymeric materials. XII. Effect of montmorillonite on water absorbency for poly(sodium acrylate) and montmorillonite nanocomposite superabsorbents// J. Appl. Polym. Sci. 2004. V.92. P. 3422–3429.
- [6] Kabiri K., Zohuriaan-Mehr M.J. Superabsorbent hydrogel composites// Polym. Adv. Technol. 2003. V.14. P.438–444.
- [7] Lin J., Wu J., Yang Z., Pu M. Synthesis and properties of poly(acrylic acid)/mica superabsorbent nanocomposite// Macromol. Rapid.Comm. 2001. V.22. P.422–424.
- [8] Starodoubtsev S.G., Churochkina N.A., Khokhlov A.R. Hydrogel composites of neutral and slightly charged poly(acrylamide) gels with incorporated bentonite interaction with salt and ionic surfactants// Langmuir 2000. V.16. P.1529–1534.
- [9] Haraguchi K., Farnworth R., Ohbayashi A., Takehisa T. Compositional effects on mechanical properties of nanocomposite hydrogels composed of poly(N,N-dimethylacrylamide) and clay// Macromolecules 2003. V.36. P.5732–5741.
- [10] Haraguchi K., Takehisa T., Fan S. Effects of clay content on the properties of nanocomposite hydrogels composed of poly(N-isopropylacrylamide) and clay// Macromolecules 2002. P.35. P.10162–10171.
- [11] Haraguchi K., Takehisa T. Nanocomposite hydrogels: a unique organic-inorganic network structure with extraordinary mechanical, optical, and swelling/deswelling properties// Adv. Mater. 2002. V.14. P.1120–1124.
- [12] Kabiri K., Zohuriaan-Mehr M.J. Superabsorbent hydrogel composites// Polym. Adv. Technol. 2003. V.14. P.438 – 444.
- [13] Rui Liang, Mingzhu Liu. Preparation of poly(acrylic acid-co-acrylamide)/kaolin and release kinetics of urea from it// J. Appl. Polym. Sci. 2007. V.106. P.3007 – 3015.
- [14] Rui Lianga, Mingzhu Liu, Lan Wu. Controlled release NPK compound fertilizer with the function of water retention// React. Funct. Polym. 2007. V.67. P.769-779.
- [15] Tanaka Y., Ping Gong J., Osada Y. Novel hydrogels with excellent mechanical performance// Prog. Polym. Sci. 2005. V.30. P.1–9.
- [16] Haraguchi K., Li H.J. Mechanical properties and structure of polymer-clay nanocomposite gels with high clay content// Macromolecules 2006. V.39(5). P.1898–1905.
- [17] Xia X.H., Yih J., D'Souza N.A., Hu Z.B. Swelling and mechanical behavior of poly(N-isopropylacrylamide)/namontmorillonite layered silicates composite gels// Polymer 2003. V.44. P.3389–3393.
- [18] X. Jia, Y. Lia, B. Zhanga, Q. Chenga, Sh. Zhanga, Mater. Res. Bull. 2008, 43, 611
- [19] Ravi N., Wan K.T., Swindle K., Hamilton P.D., Duan G. Development of techniques to compare mechanical properties of reversible hydrogels with spherical, square columnar and ocular lens geometry// Polymer 2006. V.47. P.4203–4209.
- [20] Kim B., Flamme K.L., Peppas N.A Dynamic swelling behavior of pH sensitive anionic hydrogels for protein delivery// J. Appl. Polym. Sci. 2003. V.89. P.1606-1613.

Mathematical modelling of orbits for geodetic satellites

Jaroslav Klokočník, Aleš Bezděk, and Jan Kostelecký

Abstract— Orbits of artificial Earth satellites are not arbitrary but have to conform with the goal for which the satellites were launched – to do specific measurements. The problem of orbit design is primarily about choosing appropriate orbit inclination, semimajor axis and eccentricity. The special category is a geodetic satellite, intended to determine parameters of the Earth's gravitational field (so called geopotential harmonic coefficients or Stokes parameters). There is very important relationship between the orbit height (or semimajor axis of satellite orbit), inclination and orbital resonance. We recall the 3rd Kepler law from which a relationship between the mean motion and selected mean semi-major axis of the satellite orbit accounting for the polar flattening of the Earth is derived. This simple tool has amazing applications in the orbit selection of artificial satellites to fulfil given tasks at the best. There is a close relation between the density of ground tracks by satellite data, on which in turn precision and resolution of products derived from such measurements are dependent, and the semi-major axis of the satellite used. We tell the story of the pair of GRACE satellites, which during their free decay in the atmosphere encountered important orbit resonances at which the density of ground tracks significantly (but temporarily) decreased. Consequently, in these periods also the quality of the monthly solutions for the variations of the gravity field decreased. What we learned from GRACE, we applied for orbit choice of GOCE, the first satellite equipped by space gradiometer. GOCE was also equipped by ultra-precise ion motor for orbit corrections so that the height of flight could be kept within a very small range of ± 5 meters. It is feasible to choose and keep the orbit at selected high order resonances and, by this way, to reach the maximum quality of products derived from gradiometry measurements. This process of orbit selection (in semimajor axis) is called „*fine orbit tuning*“. Now we are aware: orbit choice for remote sensing and other Earth satellites affects significantly the accuracy of the results derived from their measurements, thus the fine orbit tuning can be a very useful tool also for future missions.

Keywords— Geodesy, geodetic satellites, gravitational field of the Earth, orbit choice, fine orbit tuning, GRACE, GOCE

I. INTRODUCTION

KNOWLEDGE of gravity field of the Earth globally and with as high resolution as possible has many geoapplications. Satellites became a useful tool for the global gravity field

J. Klokočník, senior researcher at the Astronomical Institute, Academy of Sciences of the Czech Republic, Ondřejov, Czech Republic (corresponding author, phone: +420-323-620-158; e-mail: jklokocn@asu.cas.cz).

A. Bezděk, researcher at the Astronomical Institute, Academy of Sciences of the Czech Republic, Ondřejov, Czech Republic (bezdek@asu.cas.cz).

J. Kostelecký, senior researcher at the Research Institute of Geodesy, Topography and Cartography, Zdíby, Czech Republic (kost@fsv.cvut.cz).

studies and contributed significantly to generation of s/c gravity field models (sets of harmonic geopotential coefficients known also as Stokes parameters). From recent solutions with high resolution we have to mention EGM 2008 [1] and EIGEN 6C4 [2], both combined from satellite and terrestrial data. The EGM 2008 reached the resolution on the ground about 10 km.

Orbit of satellites cannot be arbitrary but must have specific size, orientation and shape, which is expressed namely by satellite semimajor axis (or height of flight above a reference surface), inclination (of satellite orbit with respect to the equator) and eccentricity.

In this short review we describe for non-specialists the problem of orbit choice for optimum gravity field determination and we comment on the cases of GRACE [3] and GOCE [4] gravity missions, where we present our own results. For GOCE we have completely new situation given by the existence of the gradiometer (a combination of microaccelerometers) to measure the second derivatives of the disturbing potential and ion motor on the board. It enables fine orbit tuning as never before. While before GOCE, the orbit keeping (in height) was possible within 1 km precision, now it reaches ± 5 meters ([4] and Rune Floberghagen, priv. commun.)

II. GRACE AND DISCOVERY OF RELATIONSHIP BETWEEN DENSITY OF GROUND TRACKS AND QUALITY OF GRAVITY FIELD PARAMETERS

First we will define the orbital resonance of the Earth artificial satellite in the Earth gravitational field. The satellite is in the exact β/α orbital resonance when it performs β nodal periods (from one orbital node to the same type of the node) while the Earth rotates α times with respect to the precessing orbit plane (known also as nodal revolutions); α, β are prime integers, the ratio β/α is irreducible. After this interval the path of the satellite relative to the Earth repeats exactly, which is the physical reason for the resonance effect [5].

We recall the situation of GRACE and its orbit resonance $\beta/\alpha = 61/4$ (61 nodal revolutions of GRACE during 4 nodal days). Precision of monthly solutions for gravity field variations, derived from the GRACE data by various authors, temporarily decreased in autumn 2004, as is shown in Fig. 1. At that time this dramatic drop in precision of the gravity field products without obvious reasons (the same type and quality of observations, their processing, etc.) was unexpected. It was

explained by the negative influence of vicinity and pass through the 61/4 resonance [6], [7]. GRACE, freely decaying in the atmosphere, encountered various resonances [8] and this one (a typical low order resonance) has enormous (fortunately temporal) effect on quality of the data derived from GRACE measurements near the resonance (see the plots of ground tracks below).

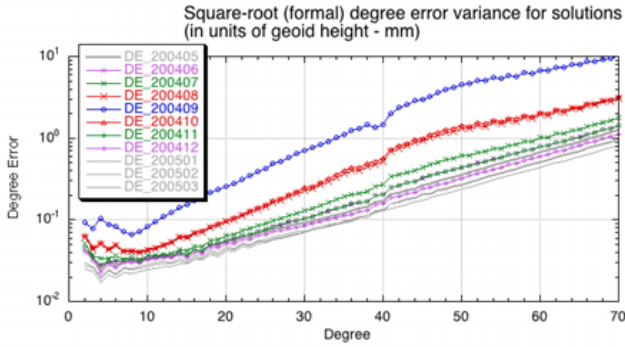


Fig. 1. Precision of monthly solutions for gravity field variations derived from the GRACE data temporarily decreased at vicinity of the 61/4 resonance (see the red curves and the blue curve). Note logarithmic scale on the y-axis. Courtesy by S. Bettadpur (2004) from archive of J. Klokočník.

The relationship between mean motion, semimajor axis, β/a , and inclination, based on the 3rd Kepler law, reads [9]:

$$n = \frac{\beta}{\alpha} |\dot{S}| \left\{ 1 - \frac{3}{2} J_2 \left(\frac{R}{a} \right)^2 \left(4 \cos^2 I - \frac{\beta}{\alpha} \cos I - 1 \right) \right\} \quad (1)$$

where \dot{S} is time derivative of the sidereal angle, i.e. rotational speed of the Earth (equals to 1.00274 rev/day), R is semimajor axis of a reference ellipsoid for the Earth or a radius of a reference sphere (we make use of 6371 km), the gravitational field is represented by only the first zonal (fully normalized) harmonic coefficient $J_2 = -\sqrt{5} \bar{C}_{20}$ and a, I are semimajor axis and orbital inclination.

We plot α versus height for various β (Fig. 2). Days of α are on the x-axis, height on the y-axis and β in the field of the figure. Time goes in the direction of decreasing height (due to the drag of the atmosphere for satellite not equipped by correction motors) and satellite freely passes in the atmosphere throughout the various β/a resonances. Those with small β has as a consequence low density of ground tracks. We show dramatic difference between ground track density at low order resonance (the case of 61/4 for GRACE, Fig. 3, upper panel) and sufficiently far from it (Fig. 3, lower panel). Obviously, sparse ground track coverage has a severe influence on the quality of gravity field solutions as well as on time variations of the gravity field parameters, in general on any data gathered from the orbits.

We also present the density of ground tracks as a function of time and latitude (Fig. 4). It reveals more than graphs in Fig. 3. The dependence of density of the individual resonances, it means of the parity $(\beta-a)$, is very important as well as the dependence on latitude. Not always the density is

the largest at the equator. This evidently depends also on orbital inclination (more in [8]).

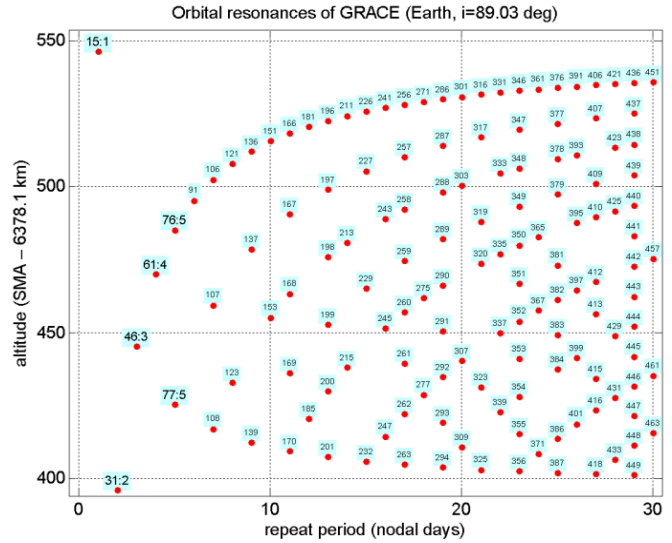


Fig. 2. Resonances encountered in the orbit of freely decaying GRACE A/B satellites.

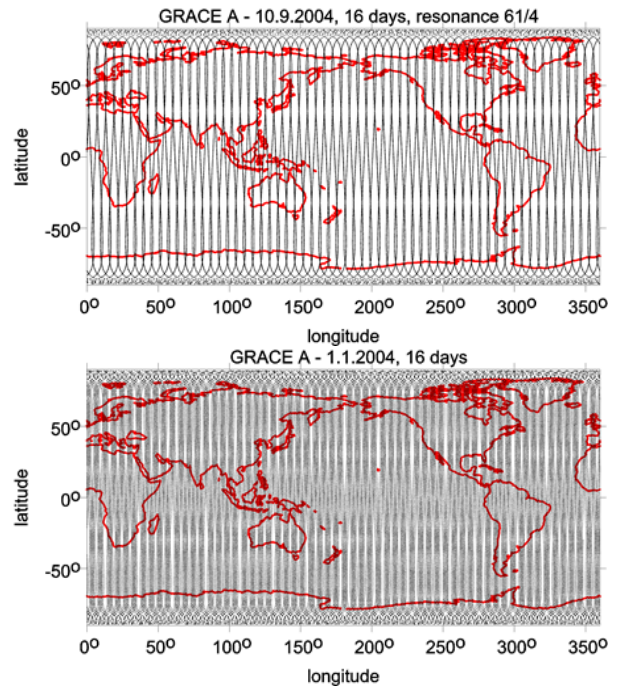


Fig. 3. Ground-tracks of GRACE A a few months before the 61/4 resonance (situation in January 2004) and at the exact 61/4 resonance (September 2004). This density difference correlates with the accuracy changes of the monthly solutions derived from data from GRACE A/B, as is shown in Fig. 1.

For GRACE, user of its data has to be aware of forthcoming resonances and has to account with them, as they are inevitable. Another possibility is to equip satellite with motors to correct the orbit height and to avoid selected low order resonances or to choose them. It was the case of altimetric satellites like ERS 1, 2, TOPEX/Poseidon, Jason 1,

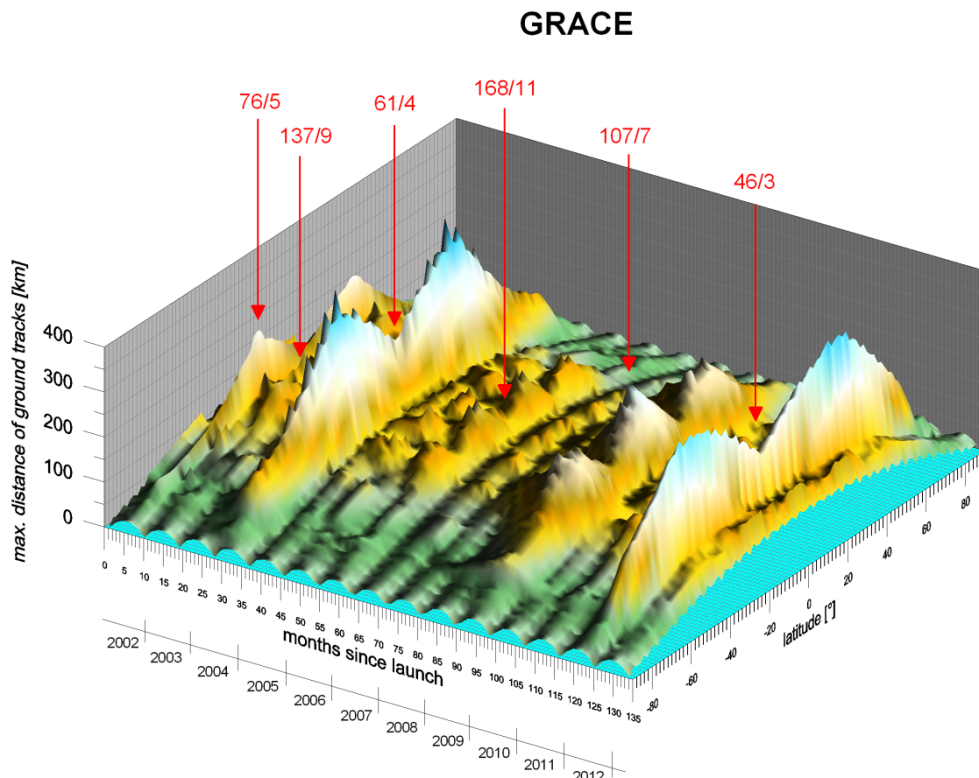


Fig. 4. The evolution of ground track density for GRACE. The maximum distance of the ground tracks is plotted as a function of time and latitude. Important resonances are marked. Computed with the actual NASA 2 line elements. From [8].

2.

ENVISAT. Orbit manoeuvres were possible and the orbit has been selected to fulfil requirements pre-defined by community of geodesists for certain time span and by oceanographers for other time intervals.

2311/143 at 223.880 km, starting from early June 2013 till the decay at the end of 2013.

There is not enough space to describe all details about the fine orbit tuning of GOCE. We refer to our analyses [8] and [10].

III. GOCE – INTENTIONAL FINE ORBIT TUNING

GOCE [4] is specific as for the resonant evolution graph (Fig. 5) as well as the densities because of intentional fine orbit tuning by which the pre-defined high order resonant orbits were selected for optimum gravity field determination. The following orbits were selected and kept (Floberghagen, priv. commun.) by means of ion motor on board of GOCE (with precision up to 5 meters in height):

- 979/61 at 254.9 km equatorial altitude,
held for about 3 years of operations,
- 997/62 at 246 km, held for 1 cycle in Sep/Oct 2012,
- 1079/67 at 240 km, held for 1 cycle in Dec 2012/Jan 2013,
- 1177/73 at 235 km, held for 1 cycle in March/April 2013, and

IV. CONCLUSION

It was evident for a long time that the proper orbit selection (mainly the choice of the orbital semimajor axis and inclination) is an important factor for various satellites to fulfil their specific goals. The orbit tuning has been recognized as a useful tool already for first altimetric satellites to accomplish various, sometimes antagonistic requirements posed by oceanographic and geodetic communities, having one satellite available in the given time. The orbit keeping by onboard correction motors has at that time precision about one kilometre.

The new gravity field missions like CHAMP, GRACE and GOCE contributed significantly to our knowledge of the Earth gravity field. As an important prerequisite to do that was the right orbit choice. For GRACE freely decaying in the atmosphere, many resonances were encountered and at vicinity of low order resonances (repeat periods only few

days), the density of ground tracks was temporarily low, and in turn, the quality of products derived from the data gathered during such periods, was significantly poorer.

For GOCE, equipped by the first onboard gradiometer and by very fine orbit correcting ion motor, the fine orbit tuning was possible with precision (height inaccuracy) to 5 meters, which never has been possible before. Thanks to this the orbit for gradiometric measurement phases has been selected with unprecedented precision which is reflected in the quality of GOCE gravity field description.

Similar orbit tuning is possible theoretically for any satellite equipped by orbit correcting motors as well as for orbiters of the Moon and the planets.

ACKNOWLEDGMENT

This work is supported by grants RVO #67985815 and GA ČR #13-36843S.

REFERENCES

[1] Pavlis N K, Holmes S A, Kenyon S C, Factor J K (2012), The development and evaluation of the Earth Gravitational Model 2008 (EGM2008), *J. Geophys. Res.* 17, B04406
 [2] Förste, Ch., Bruinsma, S., Abrikosov, O., Fletchner, F. et al. (2014), EIGEN-6C4 – The latest combined global gravity field model including GOCE data up to degree and order 1949 of GFZ Potsdam and GRGS Toulouse. EGU General Assembly (2014), EGU2014-3707.
 [3] Tapley, B.D., Bettadpur, S., Watkins, M., Reigber, C., 2004. The gravity recovery and climate experiment: mission overview and early results. *Geophys. Res. Lett.* 31, L09607.
 [4] Floberghagen R, Fehringer M, Lamarre D, Muzi D, Frommknecht B,

Steiger Ch, Pineiro J, da Costa A (2011), Mission design, operation and exploitation of the gravity Field and steady-state ocean circulation explorer mission, *Journal of Geodesy* 85, 749-758.
 [5] Allan R. R. (1973) Satellite resonance with longitude-dependent gravity—III, inclination changes for close satellites, *Planetary & Space Sci.* 21, 205–225.
 [6] Wagner C, McAdoo D (2004) Time variations in the GRACE gravity field: constraints on global hydrologic mass flux. In: Reigber Ch, Tapley B (eds) Proceedings of the joint CHAMP/GRACE science meeting, GFZ Potsdam, 6–8 July
 [7] Wagner C.A., Mc Adoo D., Kklokočník J., Kostecký J. (2006) Degradation of geopotential recovery from short repeat-cycle orbits: application to GRACE monthly fields, *Journal of Geodesy* 80, 94-103.
 [8] Klokočník J, Wagner Ca, Kostecký J, Bezděk A, Novák P, McAdoo D (2008) Variations in the accuracy of gravity recovery due to ground track variability: GRACE, CHAMP, and GOCE, *Journal of Geodesy* 82: 917–927.
 [9] Klokočník J, Gooding RH, Wagner CA, Kostecký J, Bezděk A (2013) The Use of Resonant Orbits in Satellite Geodesy: A Review, *Surv Geophys* 34: 43–72. ISSN 0169-3298
 [10] Bezděk A, Sebera J, Klokočník J, Kostecký J (2014), Gravity field models from kinematic orbits of CHAMP, GRACE and GOCE satellites. *Advances in Space Research* 53, 412–429.

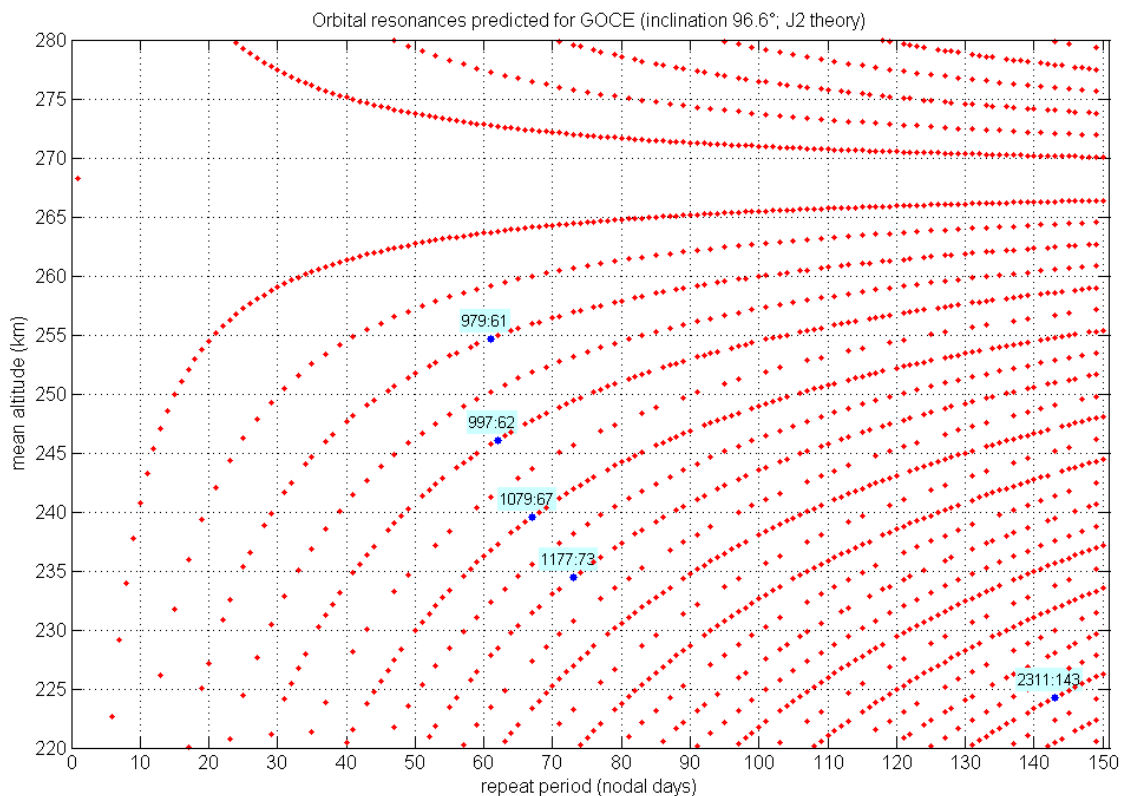


Fig. 5. Resonant evolution graph for theoretical orbit decay of GOCE. In reality, the orbit of GOCE was tuned to specific, pre-selected resonances (conditions defined by ESA). The resonances selected for the gradiometry measurement phases are emphasized.

Design of a 22kW Charging Station for LV distribution Grid control

Dario De Santis, Gaetano Abbatantuono, Sergio Bruno, Massimo La Scala

Abstract-Electric mobility is one of the main features concerning the development of a smart city. The huge quantity of electric vehicles that will be soon daily used by thousands of people will also represent a severe test for the actual low voltage urban distribution grids, that will have to face and manage new technical challenges. EV's charging operations have to be controlled with high precision and efficiency, in order to avoid grid congestion, bad power quality and many other problems. In this paper, a methodology aimed at optimizing EVs charge, taking into account technical constraints of power networks, congestions or other security constrained issues at LV level is presented.

Keywords-charging station, electric vehicles, low voltage distribution networks, storage systems.

I. INTRODUCTION

THE number of electric and hybrid vehicles circulating on our city streets is growing day by day [1-3]. EVs have an advantage compared to self-contained hybrid electric vehicles (HEV) and traditional internal combustion engines (ICE) vehicles: their connection to the electric power grid, that makes them capable to act in discharge mode as vehicle-to-grid (V2G) devices and in charge mode as grid-to-vehicle (G2V) devices [4].

V2G configuration allows benefits to be shared among grid operators and vehicle owners and is accelerating EV deployment, but controls and usage patterns must be evaluated for short-term and long-term impacts on battery life and urban LV distribution networks. EVs can behave either as electric loads or as generators. The charging behavior of EVs is affected by different factors, such as the type of connection (unidirectional or bidirectional), geographical location, number of vehicles being charged in a given vicinity, their charging voltage and current levels, battery status and capacity, charging duration, and so on.

G2V includes conventional and fast battery charging systems, but fast charging can stress the grid distribution network because power is high. Charging practices in different locations also have an effect on the amount of power taken from the electric grid by a fleet of EVs. Daily charging at work in congested urban centers, for example, can lead to undesirable peak loads and could require investments in expensive peaking generation. Injected harmonics and low power factor can be serious problems if the charger does not employ well engineered conversion devices [5].

Advanced connections to the grid, realized through smart charging stations with adequate onboard power electronics devices and BES systems, can make EVs able to serve as stored energy resources and as a reserve against unexpected outages.

Coordinated smart charging and discharging can optimize time and power demand appears and could

become the most beneficial and efficient strategy for both the grid operator and EV owners [6,7]: V2G-capable vehicles offer a possible backup for renewable energy sources (RES) such as wind and solar power, supporting efficient integration of intermittent power production. V2G can also provide additional opportunities for grid operators, such as reactive power support, active power regulation, load balancing by valley filling peak load shaving and current harmonic filtering [8-10]. In a next future, these systems will also perform ancillary services as frequency control and spinning reserves, and can improve grid efficiency, stability, reliability and generation dispatch [11-13].

In this paper, aiming at fulfilling the objectives of an urban level smart city project, the authors present a methodology aimed at optimizing EVs charge, taking into account technical constraints of power networks, congestions or other security constrained issues at LV level.

II. CHARGING STATIONS AND CONTROL DEVICES

The idea is focused on the development of smart EVs recharging stations that can be used not only for their original scope, but also to manage and improve the power quality of LV distribution systems without making any kind of economically expensive operations on existing gears.

The developed charging stations operate at 22kW with a DC recharge system and are able to supply electric power not only to EV's batteries but also to auxiliary storage systems placed under their pedestals. Charging columns are linked to the network through a front-end active rectifier; they can manage their power flows with two bidirectional DC/DC converters in order to exploit the auxiliary storage systems to shorten EVs recharge times or to improve the number of recharging operations that can be accomplished in a specific period. The auxiliary storage systems will even store the exceeding power generated from RES units connected to LV network and use it for peak shaving operations during the day. Figure 1 shows the main architecture of the charging stations, while Figure 2 represents the diagram of the interface control device. Some operational parameters are indicated in table 1.

Vn (grid)	400 V
fn (grid)	50 Hz
Icc (grid)	10 kA
cosφcc	0,5
An(charging station)	27,5 kVA
Pn (charging station)	22 kW
cosφn (charging station)	0,8
Vdc	800V
Switching frequency	10kHz
E (storage)	400V

Table 1

The charging station is also able to manage voltage levels of the system injecting reactive power through the nodes where it's been placed. Reactive power set points are automatically calculated by the charging station controller or settled by a centralized LV network control system, in order to get a constant voltage profile on a specific node of the net.

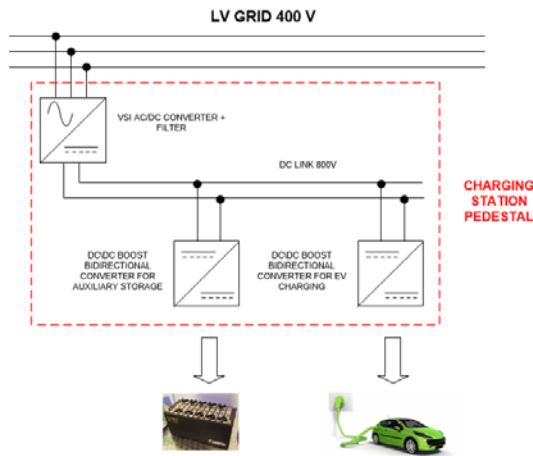


Fig.1 Architecture of the charging station

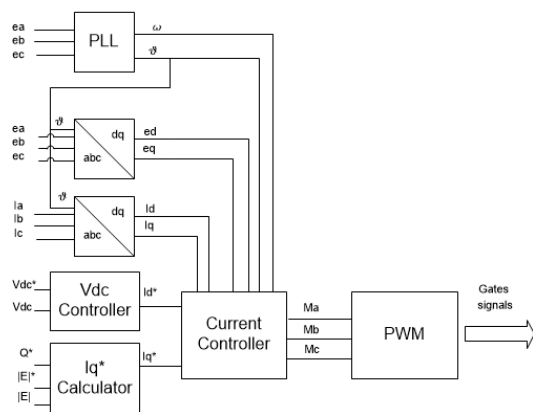


Fig.2 AC/DC converter control

III. MATHEMATICAL FORMULATION

The converter control strategy has been developed through equations based on the d,q rotating coordinate system. Plant equations used for designing the PIs current controllers are:

$$V_d = RI_d + L \frac{dI_d}{dt} - \omega LI_q + E_d \quad (1)$$

$$V_q = RI_q + L \frac{dI_q}{dt} + \omega LI_d + E_q \quad (2)$$

where V_d, V_q are the values of voltages of the converter; I_d, I_q are the values of current exchanged (injected in or absorbed from) with the grid; R and L are referred to the total resistance and inductance provided by the grid, the transformer and the philter; E_d, E_q are the voltage levels of the grid which the converter is connected to.

The d axis of the chosen coordinate system is aligned with the grid voltage vector, according voltage oriented control technique (VOC). Therefore, the relations between active and reactive power and I_d and I_q currents can be written as follows:

$$P = \frac{3}{2} E_d I_d \quad (3)$$

$$Q = -\frac{3}{2} E_d I_q \quad (4)$$

In order to determinate current set point on d axis, it's necessary to control the DC link voltage level V_{dc} . The value settled for our test is equal to 800 V. P_{dc} represents the power exchanged through DC/DC converters and the interface converter. Variations of P_{dc} value have their consequences also on V_{dc} : when P_{dc} increases, the capacitor start to charge itself and V_{dc} grows; on the contrary, when P_{dc} decreases, the capacitor is discharging and causes decurtation on V_{dc} level.

V_{dc} controller detects voltage variation and decides the right I_d^* setpoint in order to keep V_{dc} value as constant as possible and gain $P = P_{dc}$, where P is the power exchanged with the AC/DC converter and is equal to active power exchanged with the grid (excepting the losses).

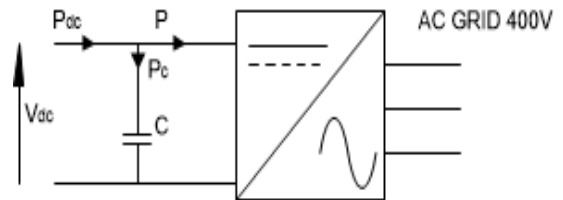


Fig.3 Power exchanges on DC link

The power exchange equations are

$$P_{dc} = P_c + P \quad (5)$$

$$V_{dc} * I_{dc} = V_{dc} * C \frac{dV_{dc}}{dt} + \frac{3}{2} E_d I_d \quad (6)$$

I_q^* setpoint can be obtained by I_q^* calculator in two different ways. The calculator can set this value using (4), where Q in this case is equal to a Q^* value settled by the main control system of the grid, but in a future upgrade of the whole system this setting could be decided by a control ring that has to keep constant the voltage level on the node of the grid in which the charging station is

connected. This level is also settled by the main control system and is represented by $|E^*|$.

Two current controlled DC/DC bidirectional boost converters are linked to the DC link. The charging/discharging setpoints of storage systems are automatically determined by a DC power controller. Even those power setpoints are decided by the main control system.

These current controls have been designed considering (7):

$$V = RI + L \frac{dI}{dt} + E \quad (7)$$

this equation refers to the plant constituted by the storage system and the inductive filter for both DC/DC converters. V is the voltage value applied from each converter on the plant, E and R are referred to the Thevenin equivalent model of the battery, L is the filter inductance, I is the current value of a single battery.

IV. TEST RESULTS

The charging station has been tested on three different cases, namely Case 1, Case 2 and Case 3.

In Case 1, a grid congestion scenario was simulated. As consequence of the congestion, a maximum amount of 11kW can be supplied by the network. This means that, in order to increase charging speed, electric power must be supplied by the auxiliary battery. In the proposed scheme, maximum discharge power is about 5 kW and, therefore, overall charging power is about 16 kW (11kW from the network plus 5 kW from the battery).

In Fig. 4, active and reactive power transients are shown. Please note that in the figures power imports are assumed always positive; power to/from the battery and the EV is positive during charge and negative during discharge. The charging station rapidly adjusts electricity import from the network and regulates the discharge of the auxiliary battery. After few cycles, steady-state conditions are reached and the EV charging power is set to 16 kW. Figure 5 shows the current transient.

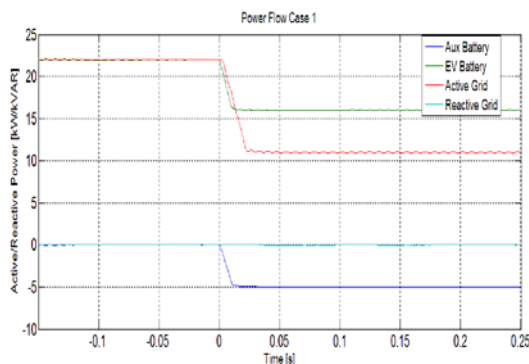


Fig.4 Power flows in case 1

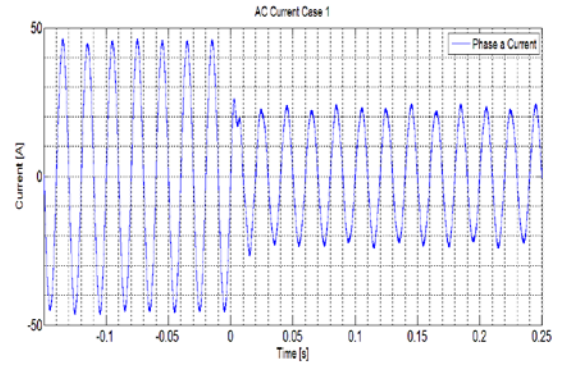


Fig.5 AC Current in case 1 (phase a)

Case 2 simulates conditions where a sudden request of active power arises, due for example to an unexpected load peak that has to be shaved. In this case, it was hypothesized that, before the controlling action takes place, no active and reactive power is exchanged with the network. In Fig. 6, it is shown how the charging station is able to inject the requested amount of power (10 kW) within very few cycles.

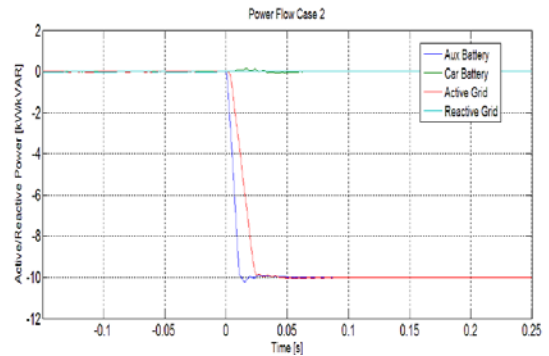


Fig.6 Power flows in case 2

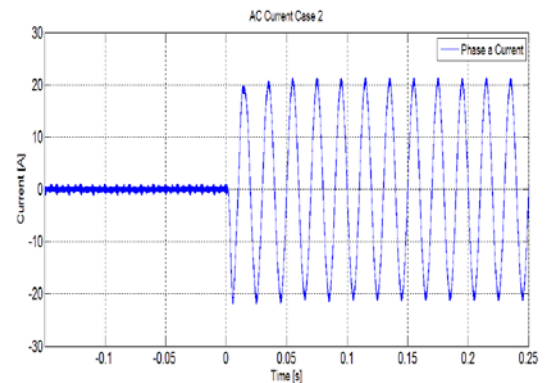


Fig.7 AC Current in case 2 (phase a)

In Case 3, it is assumed that, due to the implementation of centralized control actions, an injection of 25 kVAr is requested. Moreover, it is hypothesized that before the implementation of such control action the charging station is absorbing 22 kW from the network.

In Fig. 8 it is shown how the charging station is able to provide the requested reactive support within a very short amount of time. Moreover, the proposed control scheme is able to adjust active power flows in order to respect capability constraints on the AC/DC interface controller.

This controller is rated 27,5 kVA and, therefore, the active power import is reduced to 11 kW. The auxiliary battery is also dispatched in order to increase power charge to 16 kW.

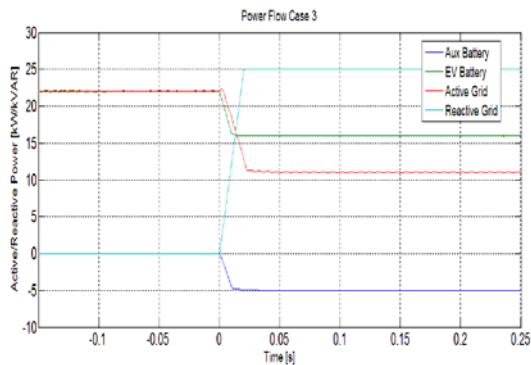


Fig.8 Power flows in case 3

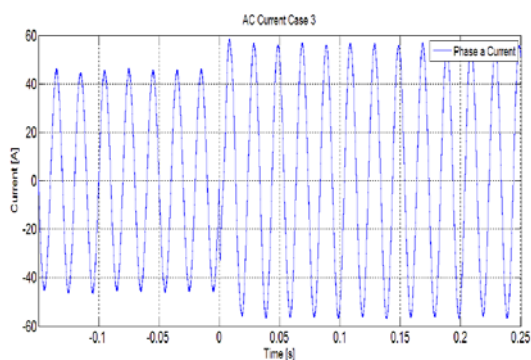


Fig.9 AC Current in case 3 (phase a)

V. CONCLUSIONS

In this paper, a methodology aimed at optimizing EVs charge, taking into account technical constraints of power networks, congestions or other security constrained issues at LV level has been presented. The developed charging stations operates at 22kW with a DC recharge system and are able to supply electric power not only to EV's batteries but also to auxiliary storage systems placed under their pedestals. Test results show how they can be used even for LV grid congestion management, for peak shaving and for reactive power balancing operations. The flexibility of the charging station can also be applied to a great number of grid control and management operations that will be investigated in future works.

REFERENCES

- [1] M. Ehsani, Y. Gao, S. E. Gay, A. Emadi, "Modern Electric, Hybrid Electric, and Fuel Cell Vehicles", Boca Raton, FL: CRC Press, 2005.
- [2] M. Yilmaz, P.T. Krein, "Review of the Impact of Vehicle-to-Grid Technologies on Distribution Systems and Utility Interfaces", *IEEE Transactions on power electronics*, vol. 28, no. 12, pp.5673-5689, Dec. 2013
- [3] S. G. Wirasingha A. Emadi, "Pihef: Plug-in hybrid electric factor," *IEEE Trans. Veh. Technol.*, vol. 60, no. 3, pp. 1279–1284, Mar. 2011.
- [4] W.Kempton, J. Tomić, "Vehicle-to-grid power implementation: From stabilizing the grid to supporting large-scale renewable energy," *Journal of PowerSources*, vol. 144, no. 1, pp. 268–279, 2005.

- [5] W. Shireen, S. Patel, "Plug-in hybrid electric vehicles in the smart grid environment," in *Proc. Rec. IEEE Power Energy Syst. Transm. Distrib. Conf. Expo.*, 2010, pp. 1–4.
- [6] K. Qian, C. Zhou, M. Allan, Y. Yuan, "Modeling of load demand due to EV battery charging in distribution systems," *IEEE Trans. PowerSystems*, vol. 26, no. 2, pp. 802–810, May 2011.
- [7] S. D. Breucker, P. Jacqmaer, D. Brabandere, J. Driesen, R. Belmans, "Grid power quality improvements using grid-coupled hybrid electric vehicles," in *Proc. Power Electron., Mach. Drives Conf.*, 2006, pp. 505–509.
- [8] M. Takagi, Y. Iwafune, K. Yamaji, H. Yamamoto, K. Okano, R. Hiwatari, T. Ikeya, "Electricity pricing for plug-in hybrid electric vehicles bottom charge in daily load curve based on variation method," in *Proc. Rec. IEEE Power Energy Syst. Innovative Smart Grid Tech. Conf.*, Jan. 2012.
- [9] M. Kintner-Meyer, K. P. Schneider, R. G. Pratt, "Impacts assessment of plug-in hybrid vehicles on electric utilities and regional US power grids Part 1: Technical analysis Pacific Northwest National Laboratory," Pacific Northwest Natl. Lab., Richland, WA, Tech. Rep. PNNL-SA-61669, 2007.
- [10] E. Sortomme and M. A. El-Sharkawi, "Optimal scheduling of vehicle-to-grid energy and ancillary services," *IEEE Trans. Smart Grid*, vol. 3, no. 1, pp. 351–359, Mar. 2012.
- [11] E. Keane and D. Flynn, "Potential for electric vehicles to provide powersystem reserve," in *Proc. Rec. IEEE Power Energy Syst. Innovative Smart Grid Tech. Conf.*, Jan. 2012.
- [12] A. K. Srivastava, B. Annabathina, and S. Kamalasan, "The challenges and policy options for integrating plug-in hybrid electric vehicle into the electric grid," *The Electr. J.*, vol. 23, no. 3, pp. 83–91, 2010.
- [13] P. Denholm and W. Short, "An evaluation of utility system impacts and benefits of optimally dispatched PHEVs," Natl. Renewable Energy Lab., Golden, CO, Tech. Rep. TP- 620-40293, Oct. 2006.

Retrofitting of Precast Reinforced Concrete Wall Panel using Carbon Fiber Strips

Drd. Ing. M. Fofiu, Drd. Ing. I.A. Bindean, Drd. Ing. E.Partene and Prof. Dr. Ing. V. Stoian

Abstract—The authors of this paper present an experimental study regarding the seismic behavior of an Precast Reinforced Concrete Wall Panel (PRCWP) with large widow opening (L3) retrofitted post damage using carbon fiber strips anchored with carbon fiber mesh. The experimental element is a typical PRCWP used in Romania to build apartment building throughout the 80’s and is considered to be at the ground floor of a 5 story high building. The test set-up was designed to reproduce the shear behavior and not the flexural one thus the element was subjected to in plane cyclic loading and two constant vertical loads were applied to counter the rocking effect. The lateral loads were applied in displacement control of 0.1% drift ratio (2.15mm). The specimen was retrofitted post damage using externally bonded carbon fiber strips anchored with Carbon Fiber Reinforced Polymers (CFRP) mesh. The measurements included the lateral forces and the drift of the specimen for every loading cycle, up until the failure criteria was met. The purpose of this experiment is to gather information about the influence of this retrofitting procedure and compare the results with the unstrengthen specimen.

Keywords—Carbon Fiber Strips, Experimental Test, Reinforced Concrete, Seismic Behavior

I. INTRODUCTION

BECAUSE in Romania in the past 50 years the vast majority of new apartment buildings were made using Precast Reinforced Concrete Wall Panels (PRCWP) as structural system [1], that most of this buildings are now over 30 years old and were subjected during this time to several seismic movements, it is imperative that we study the behavior of these structural elements under seismic loading, and try to retrofit them. In this case the authors are using Carbon Fiber Reinforced Polymers (CFRP). The purpose of this paper is to experimentally evaluate the seismic load bearing capacity of a PRCWP with large window opening (L3) retrofitted post

damage using externally bonded carbon fiber strips anchored with (CFRP), describe the retrofitting strategy and compare the results with the unstrengthen specimen.

II. EXPERIMENTAL PROGRAM

A. Description of the specimen

The experimental test specimen’s features like: dimensions, reinforcement details and material properties are all taken from an existing building which was build according to a 1982 typical plan. The wall element had to be scaled down by a factor of 1:1.2 due to limitations imposed by the crane in the testing laboratory.

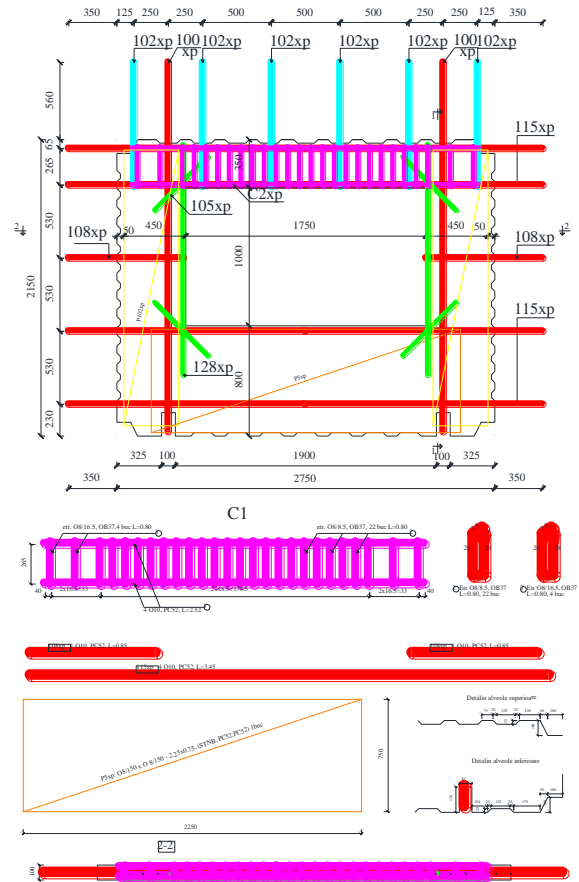


Fig. 1 Dimensions of the specimen and reinforcement distribution

This work was partially funded by:

1. MAPEI Company by representative Mr. Cristi Cartas.
2. This work was partially supported by the strategic grant POSDRU/159/1.5/S/134378 (2014) of the Ministry of National Education, Romania, co-financed by the European Social Fund – Investing in People, within the Sectoral Operational Programme Human Resources Development 2007-2013

M. Fofiu is with “Politehnica” University of Timisoara, Piata Victoriei 2, 300006, Romania phone:+40-746-022-991; e-mail: mihai.fofiu@student.upt.ro

E.Partene is with “Politehnica” University of Timisoara, Piata Victoriei 2, 300006, Romania e-mail:eva.partene@student.upt.ro

I. A. Bindean, is with “Politehnica” University of Timisoara, Piata Victoriei 2, 300006, Romania e-mail: andrei.bindean@student.upt.ro

V. Stoian. is with “Politehnica” University of Timisoara, Piata Victoriei 2, 300006, Romania e-mail: valeriu.stoian@upt.ro

B. Experimental Stand

The test set-up was conceived in such way that it simulates the seismic behavior of the tested element. In order to achieve this, we had to reproduce the shear behavior and not the flexural one [2]. For this, two composite steel-reinforced concrete beams were used as force transmitting system (upper) and foundation (lower) elements. The remaining gap between the tested PRCWP and the beams was filled with high-strength mortar. The stand consists of four reaction frames, two for the vertical (gravitational) forces and two for the in-plane (seismic) forces which were all induced with four hydraulic jacks. In Fig.2 the experimental stand can be seen with all its elements

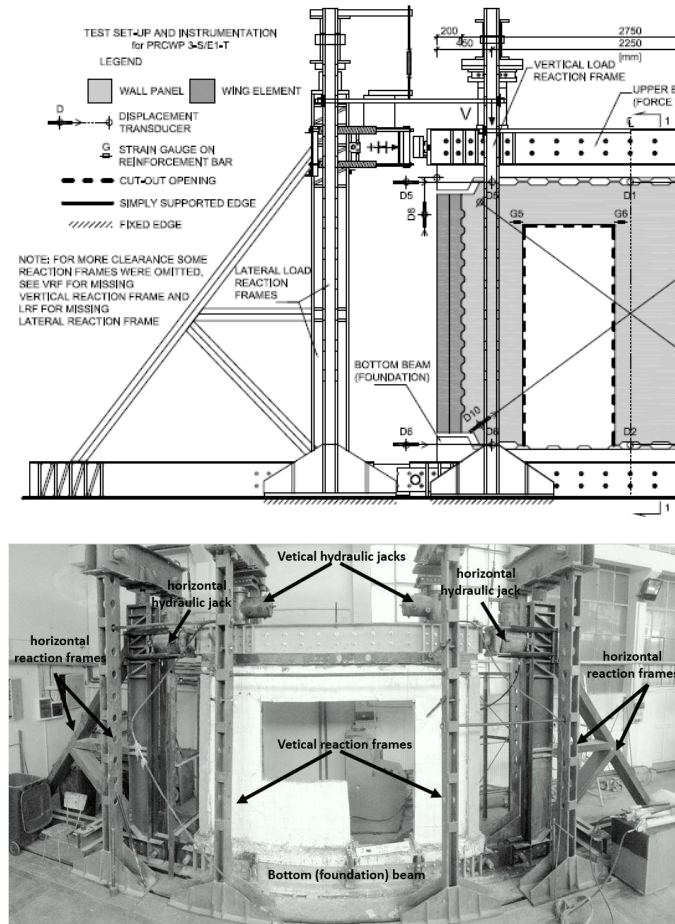


Fig. 2 Experimental stand

The two vertical forces were kept constant at 150 kN and were increased on the horizontally loaded end of the upper beam in order to counter the rocking effect of the element, for each 1 mm of vertical displacement the force was increased by 100 kN. The seismic loading history was comprised of displacement controlled range [3], this control was defined in terms of constant displacement increments of 0.1% drift ratio (2.15 mm) and two cycles on each displacement level. The subsequent displacement levels, expressed in mm and drift ratio (%), are as follows: ± 2.15 mm, ± 4.3 mm, ± 6.45 mm, ± 8.6 mm, etc. and $\pm 0.1\%$, $\pm 0.2\%$, $\pm 0.3\%$, $\pm 0.4\%$ etc., respectively.

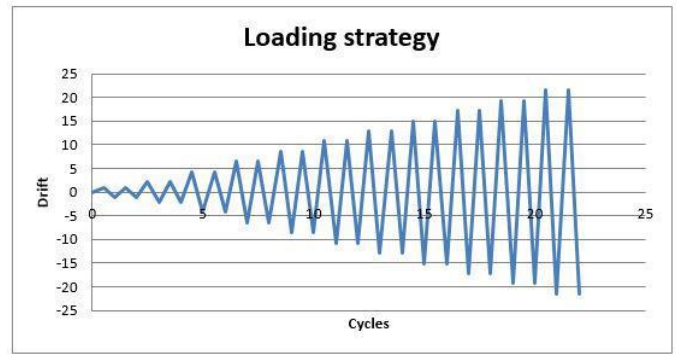


Fig. 3 Loading strategy

The failure criteria was assigned to the displacement level and was considered fulfilled when 20% decrease in the load bearing capacity from one cycle to another was obtained.

In order to measure the forces three pressure transducers were used and to measure the movement 10 displacement transducers placed on the element. In fig.4 the displacement transducers position can be seen.

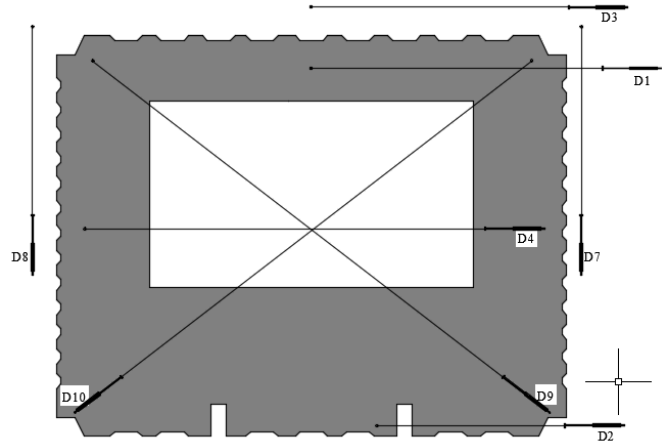


Fig. 4 Experimental stand

III. STRENGTHENING PROCEDURE

The principles of the strengthening strategy were based on the behavior and failure observed during the testing of the unstrengthen specimen. The behavior pattern noticed was as follows: shear cracking of the piers with large diagonal cracks. So the strengthening strategy was to increase the shear capacity of the wall piers and to prevent the reopening and further increasing in width of the diagonal cracks.

The retrofitting was performed by means of Carbon Fiber Reinforced Polymers (CFRP) using Externally Bonded Reinforcement (EBR) technique for both increasing the shear strength and to stitch the cracks. The properties of the materials used in this procedure are given in Table 1. The first step of the retrofitting procedure was to prepare the concrete surface on the areas where the carbon fiber strips would be placed by grinding the surface using a rotating diamond disc in order to remove all prominent imperfections, debris of mortar and irregularities of the surface. Then drilling the holes were the

anchorage CFRP mesh would be introduced and finally removing the dust particles by blowing the surface with compressed air. The main crack of the wall which caused the failure of the unstrengthen specimen was filled with epoxy resin and further stitched on both sides with 4 200 mm long strips of carbon fiber on each side. The second step was to cut the carbon fiber strips and anchorages to the specified dimensions which were as follow: 30 mm wide and 1.4 mm thick for the carbon strips and 300 mm in length and 100 mm in width for the anchorages. Fig.5 depicts the position of the carbon fiber strips and the CFRP anchorages. A total of 3 2950 mm and 6 600 mm long strips were used for each side of the wall, the sides being symmetrically reinforced. For the anchorage part a total of 21 CFRP anchorages were used.

3	Carbon mesh	0.166	1.8	4830	-
---	-------------	-------	-----	------	---



Fig. 6 CFRP Anchors

The third step was to insert the anchorages in the previously drilled holes and spread their ends so that the carbon fiber strips would be anchored. The last step was to mix the resin and place the carbon strips in their position on the wall surface.

IV. BEHAVIOR AND RESULTS

During the first cycles of the experimental test the tested specimen had a very predictable ductile behavior, the main diagonal crack which lead to the failure of the unstrengthen element started to exert tension on the stitching strips at the drift of 4.3 (0.2%) mm and by the time we reached the 6.45 mm (0.3%) drift one of the stiches started to lose its grip on the concrete surface and began to detach. The first noticeable crack width reopening was at the drift level of 0.4% (8.6 mm) when a part of the infield epoxy resin started to crack. By the time we reached 15.05 mm (0.7%) drift ratio all the stiches on the right pier for the main crack had detached from the concrete surface and were no longer effective. The element failed due to a diagonal crack which appeared in the left pier at the drift ratio of 0.8% (17.2 mm), load level of 230 kN seismic (horizontal load) and 303 kN vertical load and lost 30% of its load bearing capacity at 0.9% (19.35 mm) with a maximum seismic force of 194 kN. The behavior was characterized by the reopening of the large diagonal crack in the right pier which lead to the unstrengthen specimen failure, concrete crushing at the bottom edges of the widow opening, deboning of the carbon fiber strips and by the appearance of the large diagonal crack in the left pier which ultimately lead to the complete failure of the specimen. In Fig. 6 the force displacement diagram is presented for the seismic (horizontal) force and the drift ratio.

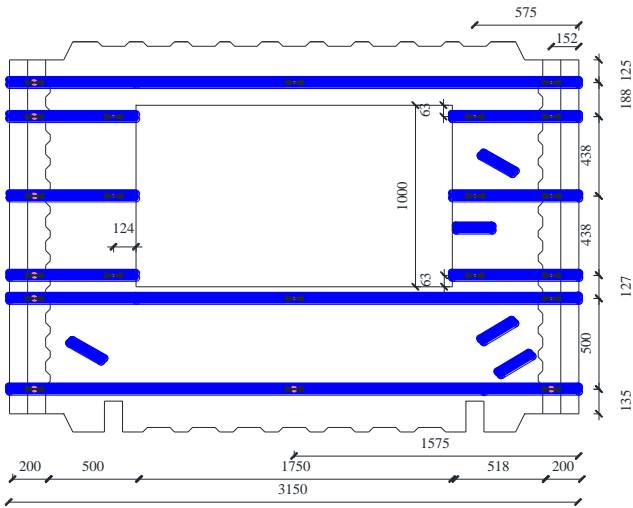


Fig. 5 Experimental stand

Table 1

Nr.	Name	Thickness mm	Density g/cm ³	Tensile strength N/mm ²	Viscosity MPas
1	Carbon strips	1.4	0.00161	3100	-
2	Epoxy resin	-	1.06	40	7000

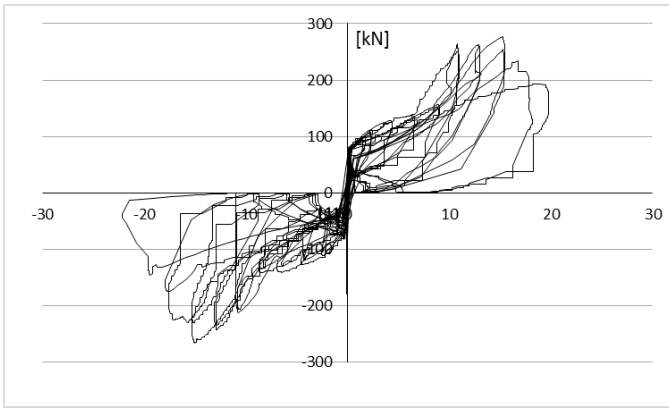


Fig. 6 Force displacement diagram (seismic)

The specimen reached a maximum seismic force of 277 kN at a drift level of 15.05 mm (0.7%) drift level while the values for the vertical (gravity) loads were as follows: $N_{1left}=401.5$ kN and $N_{2right}=159$ kN. After reaching its peak value for the seismic force the element lost 19% at its load bearing capacity in the next cycle at a drift level of 17.2 mm (0.8%) reaching a maximum force of 224 kN. Since the failure criteria was not fulfilled we continued with the testing until the drift reached 19.35 mm (0.9%) and we noticed the failure criteria was met.

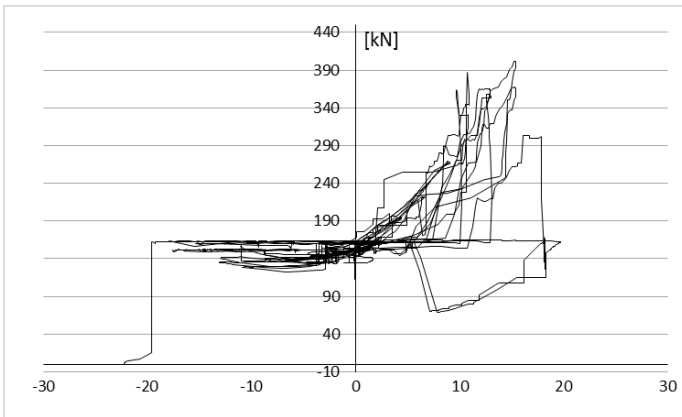


Fig. 7 Force displacement diagram (N1st)

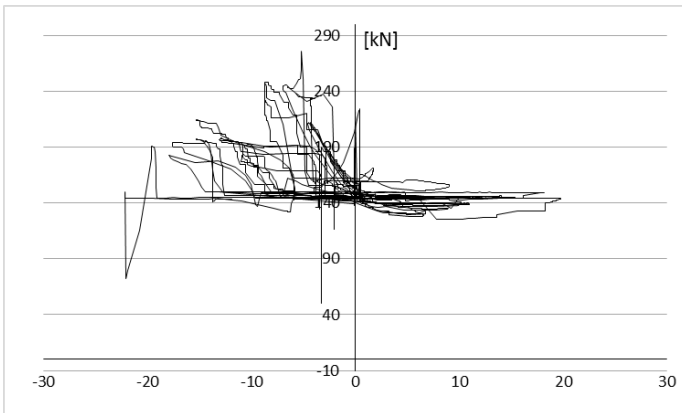


Fig. 8 Force displacement diagram (N2dr)

Fig.9 presents the specimen after the failure criteria was fulfilled and it can be observed the large diagonal crack in the left pier which lead to the failure of the specimen as well as the

reopening of the initial diagonal crack in the right pier with the missing stitches which fell due to bond issues.



Fig. 9 Failure of the specimen

In Fig.10, Fig.11 and Fig.12 the failure details are presented. The first figure shows the diagonal crack in the left pier while the second figure depicts the details regarding the bond issues on the initial crack in the right pier. The last figure presents the crushed concrete at the opening lower right corner and the bent reinforcement from the specimen.



Fig. 9 Crack in the left pier



Fig. 10 Existing crack in the right pier



Fig. 11 Lower right corner of the opening detail

V. COMPARISON AND CONCLUSIONS

The purpose of this paper was to observe the behavior of the retrofitting strategy employed and try to reestablish the initial load bearing capacity of the precast reinforced concrete wall panel. The specimen had an initial maximum load bearing capacity of 307 kN at the drift level of 12.9 mm (6%) with the vertical (gravity) force being $N_{1st}=216$ kN. From Fig.12 it can be seen that the tested specimen reached a maximum horizontal (seismic) force which was 9,8% smaller compared to the initial PRCWP, but we increased the maximum drift ratio with 50% as seen in Fig.13 so the retrofitted element had a more ductile behavior.

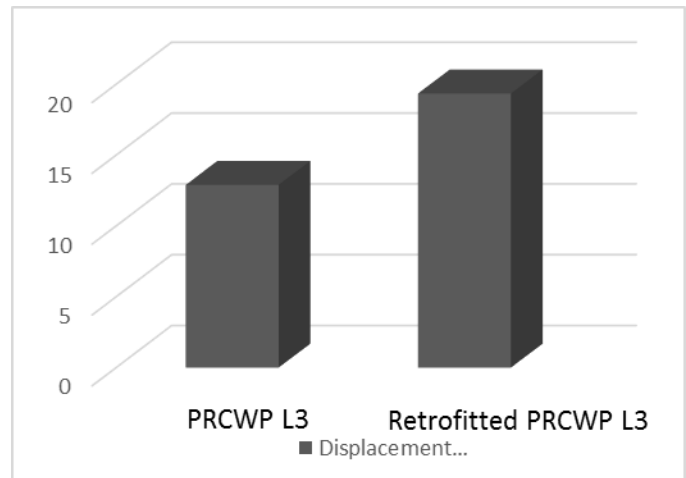


Fig. 12 Difference in drift level

The presented experimental research was performed in order to assess the efficiency of the retrofitting strategy using carbon fiber strips externally bonded. The retrofitting technique was able to reestablish 90,2% of the initial load bearing capacity of the element and increase the drift ratio, so in conclusion it can be said that the experimental test was a success and the retrofitting strategy is a viable alternative to classic procedures.

REFERENCES

- [1] I. Demeter, "Short history of large panel structures in Romania Scientific Bulletin of the "Politehnica" University of Timisoara, 51(65), 1, 2005, pp 87-94
- [2] Gulec, C.K. and Whittaker, A.S. (2009), "performance-based assessment and design of squat reinforced concrete shear walls", *Technical Report MCEER-09-0010*.
- [3] C. Todut, V. Stoian, I. Demeter, T. Nagy-György, D. Dan, V. Ungureanu, "Seismic Strengthening of a Precast Reinforced Concrete Wall Panel Using Combined NSM and CFRP-EBR Method". *11th International Symposium on Fiber Reinforced Polymers for Reinforced Concrete Structures (FRPRCS11)*, pp. 269-270, (2013)..

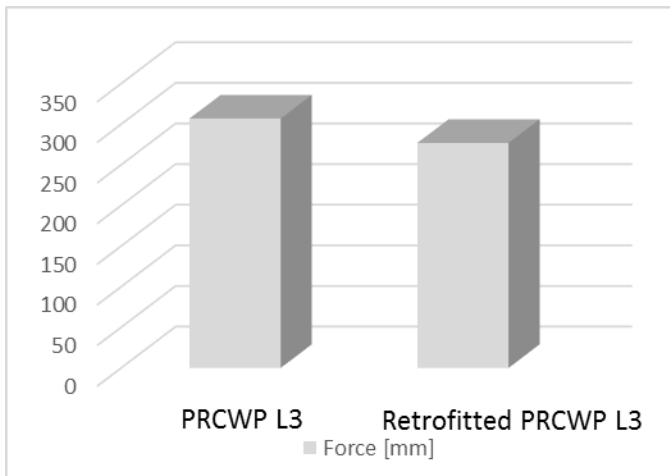


Fig. 12 Difference in load bearing capacity

Influence of substrate properties on evaporation of the sessile drop

O.V. Nagornov, N.V. Starostin

Abstract— The evaporation of sessile drop is investigated by mathematical modelling based on the finite element method (FEM). The evaporation is considered as a quasi-steady-state process. The vapor concentration above the droplet satisfies the Laplace equation with a temperature-dependent boundary condition. Nonuniform temperature distribution on the droplet surface induces Marangoni thermal flows. We investigate influence of substrate geometry on temperature minimums and maximums on the surface.

Keywords— finite elements method; heat transfer; mathematical modelling

I. INTRODUCTION

THE evaporating sessile drop is a system which gains attention of scientists for a long time. There are plenty technological processes connected with drops drying in different conditions. These technologies used for DNA mapping, lithography, material science, biology, and others.

In earlier studies the flow inside sessile drop was observed and the main reason for flow was considered the nonuniform mass loss from the surface of the droplet [1]. Besides the mass conservation law there are different reasons for inducing and controlling flow inside droplet. Various methods to describe process of drying were created to solve different practical problems such as forming solute deposits with predefined properties or drying of colloidal and biological liquids [2]-[5].

In some studies stated that under identical conditions flow can be in different directions [6]-[10]. This phenomenon occurs because evaporating depends on the thermal conductivities of liquid and substrate [11], [12]. Position of the turn point where the flow changes direction, varies for different materials and can be controlled.

Dunn *et al.* [11], [12] stated that the major factor influencing on evaporation is the size of substrate. They demonstrated differences in temperature's distribution in extreme cases of infinite substrate and drop-sized substrate under thin-drop approximation.

II. MODELING

We consider a drop of spherical shape cap resting on the flat surface. There are no any assumptions about drop and substrate thickness. Under room conditions, the evaporation is a slow process. For instance, the desiccation time of a 15 mg sessile water drop is larger than 3500 s. It allows us to assume a quasi-steady-state process. Thus, the temperature T obeys

the equation:

$$\Delta T = 0 \quad (1)$$

We consider bottom substrate boundary at the ambient temperature T_0 . On the drop surface the heat flux equals to heat loss due to phase transitioning liquid into vapor. On the open substrate surface we assume no heat flux at all. So, the boundary conditions are:

$$\begin{cases} T = T_0 \\ k_s (\mathbf{n} \nabla T) = aL(\mathbf{n} \nabla c) \\ \nabla T = 0 \end{cases} \quad (2)$$

where k_s is the substrate thermal conductivity coefficient, a is the ambient thermal diffusivity, L is the specific vaporization heat, and \mathbf{n} is the normal vector.

At the inner boundary the continuity of temperature and heat flux conditions take place:

$$\begin{cases} k_s (\mathbf{n} \nabla T) = k_l (\mathbf{n} \nabla T) \\ T_s = T_l \end{cases} \quad (3)$$

where k_s and k_l are thermal conductivity coefficients of substrate and liquid respectively, T_s and T_l are temperatures in substrate and liquid.

Using the assumptions of Deegan's "basic model", we assume the concentration satisfies Laplace's equation:

$$\Delta c = 0 \quad (4)$$

On the droplet surface we consider vapor to be saturated. The concentration of saturated vapor is a strong function of temperature. The concentration of saturated vapor and temperature are connected according to [14]. At the boundary between environment and substrate we assume no concentration flow. On remote boundaries concentration equals to the ambient value c_{amb} .

$$\begin{cases} c = c_0(T) \\ \nabla c = 0 \\ c = c_{amb} \end{cases} \quad (5)$$

The dimensionless parameters for solution are $k_r = k_l/k_s$ and $r_d/R - 1$, where r_d and R are drop and substrate radii, respectively.

The tangential stress τ is

$$\boldsymbol{\tau} = \mathbf{t} \cdot \nabla_s \boldsymbol{\sigma} = \beta (\mathbf{t} \cdot \nabla_s T) \quad (6)$$

where \mathbf{t} is tangential unit vector, $\boldsymbol{\sigma}$ is surface tension, ∇_s is

the surface gradient, and $\beta \equiv \frac{\partial \boldsymbol{\sigma}}{\partial T}$ is the material parameter

that is negative for most liquids. The direction of Marangoni flow determined by temperature gradient over the droplet surface. The reason why this problem solved numerically is that impossible to separate it into independent ones. The temperature and concentration have strong influence on each other, and there is no analytical solution for such self-conjugated problems. To solve this problem we used the finite elements method (FEM) based on commercial software package, COMSOL Multiphysics 4.3.

III. RESULTS

Heat flux from substrate results in the cooling due to evaporation. Varying substrate and droplet sizes allows us to control magnitude of total heat flux. Due to geometry of the system and assumptions made, more significant variation of heat flux magnitude occurs near the edge of the drop. Fig. 1-3 show temperature over the droplet surface for different ratios of droplet radius and substrate size r_d / R .

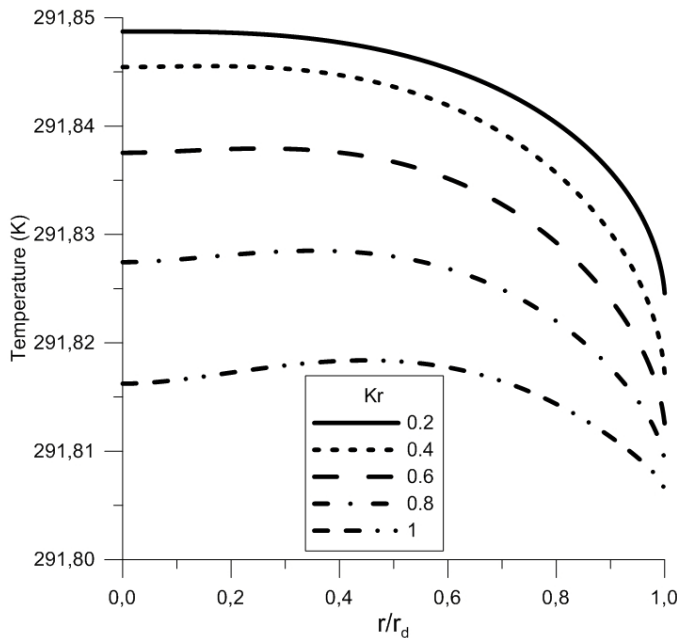


Fig. 1. The drop temperature at $r_d/R - 1 = 0$

In case of $r_d/R - 1 = 0$ the surface temperature appears to be monotone decreasing from center of the droplet to border (Fig. 1). Such behavior arises because the heat loss from boundary region is more significant than from center. Heat flux in substrate in this case has no horizontal component and provides uniform heating to base of the droplet. So the only reason for nonuniform temperature distribution is the heat flux from edge of the drop due to its geometry. These results are in a good agreement with Dunn's ones acquired experimentally [11].

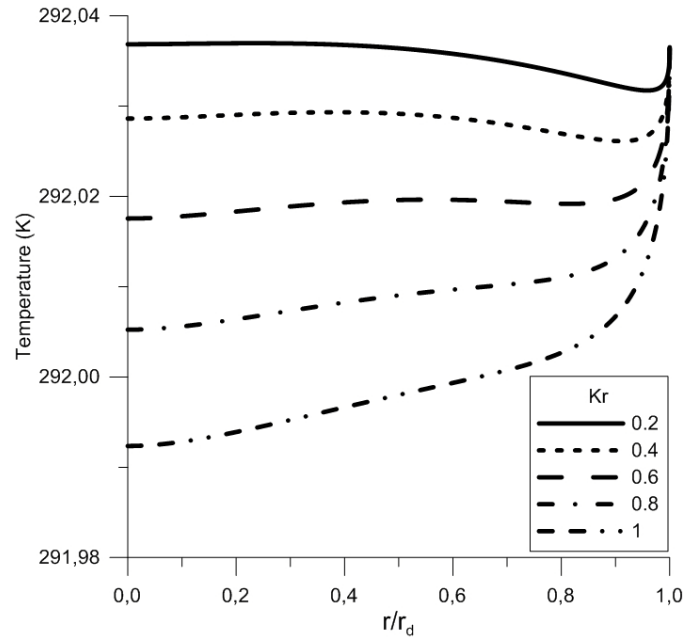


Fig. 2. The drop temperature at $r_d/R - 1 = 0.07$

For the substrate sizes larger than the drop radius the additional horizontal heat flux arises from area $r_d > R$. This flux causes greater heating of boundary area leading to non-monotone temperature distribution with extremes, in which the Marangoni flow changes direction (Fig. 2). Such phenomena were observed by Hu and Larson *et al.* in their experimental work [8].

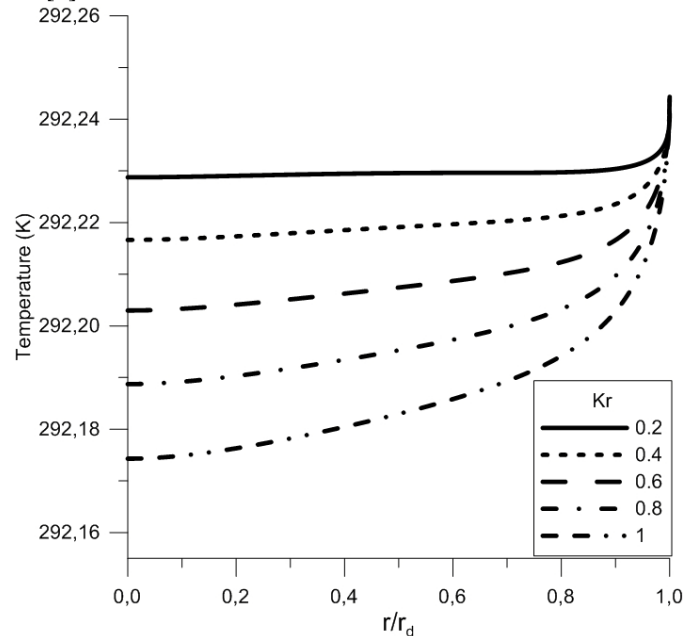


Fig. 3. The drop temperature at $r_d/R - 1 = 0.15$

With further increasing of substrate size temperature distribution depends on the heat flux from area $r_d > R$. Temperature evenly increases from center of the droplet to the border as shown on Fig.3. Flux magnitude fully compensates heat loss from droplet surface. Such behavior was observed in

experimental work [12].

IV. CONCLUSION

In this paper we formulated and solved a mathematical model for the quasi-steady diffusion-limited evaporation of an axisymmetric sessile droplet of liquid with a pinned contact line on finite-sized substrate which generalizes the theoretical model proposed by Deegan *et al.* [1] to include the effect of evaporative cooling on the saturation concentration of vapor at the free surface of the droplet, the dependence of the coefficient of diffusion of vapor in the atmosphere and geometry of the substrate. The predictions of the model were found out to be in a good agreement with the recent experimental results.

REFERENCES

- [1] R. D. Deegan, O. Bakajin, T. F. Dupont, G. Huber, S. R. Nagel, T. A. Witten, Capillary flow as the cause of ring stains from dried liquid drops. *Nature* 389, 827-829, 1997.
- [2] P. Lebedev-Stepanov, K. Vlasov, Simulation of self-assembly in an evaporating droplet of colloidal solution by dissipative particle dynamics, *Colloids and Surfaces A: Physicochemical and Engineering Aspects*, Volume 432, Pages 132–138, 5 September 2013
- [3] L.V. Andreeva, A.V. Koshkin, P.V. Lebedev-Stepanov, A.N. Petrov, M.V. Alfimov, Driving forces of the solute self-organization in an evaporating liquid microdroplet, *Colloids and Surfaces A: Physicochem. Eng. Aspects* 300, 300–306, 2007.
- [4] Yu.Yu. Tarasevich, I.V. Vodolazskaya, O.P. Bondarenko, Modeling of spatial-temporal distribution of the components in the drying sessile droplet of biological fluid, *Colloids and Surfaces A: Physicochem. Eng. Aspects* 432, 99–103, 2013
- [5] Yu.Yu. Tarasevich, D.M. Pravoslavnova, Segregation in desiccated sessile drops of biological fluids, *Eur. Phys. J. E22*, 311–314, 2007
- [6] R. D. Deegan, O. Bakajin, T. F. Dupont, G. Huber, S. R. Nagel, T. A. Witten, Contact line deposits in an evaporating drop. *Phys. Rev. E* 62, 756-765, 2000.
- [7] H. Hu, R. G. Larson, Evaporation of a sessile droplet on a substrate. *J. Phys. Chem. B* 106, 1334-1344, 2002.
- [8] H. Hu, R. G. Larson, Analysis of the micro fluid flow in an evaporating sessile droplet. *Langmuir* 21, 3963-3971, 2005.
- [9] H. Hu, R. G. Larson, Analysis of the effects of Marangoni stresses on the microflow in an evaporating sessile droplet. *Langmuir* 21, 3972-3980, 2005.
- [10] H. Hu, R. G. Larson, Marangoni effect reverses coffee-ring depositions. *J. Phys. Chem. B* 110, 7090-7094, 2006.
- [11] G. J. Dunn, S. K. Wilson, B. R. Duffy, S. David, K. Sefiane, A mathematical model for the evaporation of a thin sessile liquid droplet: comparison between experiment and theory. *Colloids and Surfaces A: Physicochem. Eng. Aspects* 323, 50-55, 2008.
- [12] G. J. Dunn, S. K. Wilson, B. R. Duffy, S. David and K. Sefiane The Strong Influence of Substrate Conductivity on Droplet Evaporation, *Journal of Fluid Mechanics*, Volume 623, pp 329-351, March 2009
- [13] N. N. Lebedev, *Special Functions & Their Applications*, Moscow, 1963 (in Russian)
- [14] N. B. Vargaftik, *Tables on the Thermophysical Properties of Liquids and Gases*, Moscow, 1972 (in Russian)

(Bio) polymer Packaging films and their Properties

A. Tesarikova, A. Kalendova, D Merinska

Abstract— The article deals with the preparation, properties and the usage of (bio)polymer barrier films. The problem of exfoliation and dispersion of the filler in the polymer and biopolymer matrix, mechanical and barrier properties of barrier films is discussed. This problem is connected with the use of nanofiller either in the synthetic polymer matrix or PLA prepared films. Together the evaluating comparison of used nanofillers is done. Polypropylene, polyethylene, Surlyn and PLA were used like polymer matrices. Organically modified montmorillonite (Cloisite 93A, 30B, 10A, Dellite 67) were used like nanofillers. Morphology (TEM, XRD) mechanical and barrier properties were observed.

Keywords— nanocomposites, nanofillers, clays, montmorillonite, polymers, mechanical properties, barrier properties, PLA

I. INTRODUCTION

A new trend in chemical engineering is the development of new technologies and new types of active nanocomposites presented as the active ingredient nanomaterials. Such materials, especially packaging films are still on the market in limited quantities. Goal is to develop new technologies and materials that help to eliminate causes problems of production and technical limits of current commercial materials. Nanofillers can significantly affect their structure. Polymers with improved properties must have some degree of polarity, the resistance against gases (polar groups that enable the polymer to absorb moisture from the surrounding environment), good interaction between chains and a high glass transition temperature. To compare the improved properties of nanocomposites used example of mechanical resistance, barrier properties and exfoliation determination or comparison of morphology and more[1, 2].

Polyethylene is one of the thermoplastics from the group of polyolefin and is produced by polymerization of ethene. It was first prepared in 1898 by Hans von Peckmann heating

diazomethane. Currently it represents classic PE packaging material. Its physico-mechanical properties depend on the molecular weight, the spatial arrangement of monomeric units in the chain of the macromolecule and the degree of crystallization [3,4].

Polypropylene is a good chemically resistant, thermally stable, transparent and durable. It is a highly crystalline polymer with a melting point of about 170 ° C, resistant to aggressive agents especially at higher temperatures. Polyolefins are polymers that are placed one double bond at first hydrocarbon. These include most processed materials due to their affordability, most of the technological possibilities of processing procedures and a wide range of applications. Among the most produced and processed polyolefins are polyethylene, polypropylene.

Poly(lactic acid) or polylactide (PLA) is a thermoplastic aliphatic polyester derived from renewable resources , such as corn starch (in the United States), tapioca roots, chips or starch (mostly in Asia), or sugarcane (in the rest of the world). In 2010, PLA had the second highest consumption volume of any bioplastic of the world.

The name "poly(lactic acid)" does not comply with IUPAC standard nomenclature, and is potentially ambiguous or confusing, because PLA is not a polyacid (polyelectrolyte), but rather a polyester. There are several industrial routes to usable (ie high molecular weight) PLA. Two main monomers are used: lactic acid , and the cyclic di-ester, lactide . The most common route to PLA is the ring-opening polymerization of lactide with various metal catalysts (typically tin octoate) in solution , in the melt , or as a suspension. The metal-catalyzed reaction tends to cause racemization of the PLA, reducing its stereoregularity compared to the starting material [3, 4].

Due to the good biocompatibility in the human body is the use of PLA in medical applications such as absorbable sutures, carrier tissues and prosthetic materials. Material may not be toxic, carcinogenic, mutagenic, allergenic and shall not contain impurities.

Nanocomposites are materials comprising a polymer matrix, a nanofiller. To obtain nanocomposite with the required properties, especially in case of nonpolar ones it is necessary to apply a modification of clay nanofiller leading to the "organofilization" of filler. This modification improves the affinity of nonpolar polymer matrix and polar clay surface.

This step can be also named “intercalation”. The lowering of bond energy accompanying this intercalation process leads to the exfoliation of nanofiller in the moment of its compounding with the polymer matrix. [5-6].

Nanocomposites differ from traditional plastic composites by providing improvements with minimal impact on density and do it without processing penalty. This article builds on our research in the area of packaging films. In this section, the mechanical and barrier properties of polyethylene, polypropylene, PLA nanocomposites are studied [7-9]. Among the most produced and processed polyolefins are polyethylene, polypropylene.

II. EXPERIMENTAL

The polymer matrix used as carrier materials were Polyethylene (Borealis RB 707 CF fy Borealis AG) and Polyethylen (Bralen RB 03-23, fy Slovnaft Petrochemicalis Bratislava), PLA 2003D Nature Works. To increase compatibility between the polymer matrix and the filler was used for maleinized PP polypropylene (PP - MA) Exxelor PO 1015 K 1,909,201 1 3 EXXON and PE maleinized polyethylene (PE - Ma) AMPLIFY GR 216

Organically modified montmorillonites with tradenames Cloisite 93A, 30B, 10A (fa Southern Clay Products, Inc.), and Dellite 67G (fa Laviosa Chimica Mineraria S. p A.) were used.

Polymers with the fillers (mass fraction 5 %) were compounded in a twin screw extruder ZE Berstorf 25, screw diameter was 2 x 28 mm and a L / D ratio of 38 The temperature of the individual heating zones and the extrusion head was set at 210 ° C for PP and PE, 160 ° C for PLA and 200 ° C rotation speed was 15 per minute. The extruded wire was cooled in a water bath and then transferred using a knife mill back to granulate the unit Scherr SGS - 50E. On the laboratory blow line TVR - C9S - 7EX (UTB) connected to the extruder single screw unit Brabender OHG Duisburg were prepared from granules blown film. From the prepared granules were pressed plates of dimension 125 x 125 x 2 mm. The temperature for molding the PP and PE was 210 ° C, 150 ° C for PLA 220 ° C. The pressing time was 3 minutes for all the polymers and the cooling period was from 7 to 15 minutes.

The structure was studied using an URD-6 Diffractometer in the reflection mode in the range from 0.8000 to 11.9870 ° 2 θ at a voltage of 40 kV and 30 mA with a step size of 0.0263 °. The dispersion of the clays in polymer matrix and nanostructures were observed through microscopic investigations.

Samples of 40 x 20 mm made from molded plates were sent to the IMC Prague, where it was performed TEM. As samples were used ultrathin sections prepared on special Ultra - cryomikrotomu LEICA at -100 ° C, temperature of the knife - 50 ° C and a thickness of about 50 nm. Transmission electron microscopy was performed on a JEM 200 CX at an accelerated voltage of 100 kV.

Tensile tests were measured at the Faculty of Technology in UTB Demo Room ALPHA Technologies Ltd. On tensile testing machine TENSOMETR 2000. EN ISO 527-3 (64 0604) was used the speed of the tearing 2 - initial speed was 1

mm / min to the module 2%, then the speed was increased to 100 mm / min until rupture. For tensile strength, elongation at break, tensile-Modulus and yield stress were measured and evaluated.

Of all the film samples were prepared test membranes for measuring the gas permeability in the shape of a circle with a diameter of 80 mm and an average thickness of 0.04 mm. Permeability was measured by a gas at a pressure of 1 bar and at a temperature of ± 25 ° C by the CSN 64 01 15 - constant volume method.

III. RESULT AND DISCUSSION

Polymer/clay nanocomposites have been studied for longer period as materials possible used in packaging industry. Therefore, this work is particularly interested in the mechanical properties. Table 1 and 2 presents the mechanical properties of polymers with nanofillers and the inside surface of the polymeric matrix.

TABLE 1. Tensile tests of PP and PE matrix

Composition	Stress at break (MPa)	Elongation at break (%)	Tensile modulus (MPa)
PP/93A	8,601	601,08	307,67
PP/67	8,657	619,08	313,97
PP	28,592	948,48	320,57
PE/10A	13,323	862,04	142,37
PE/30B	13,261	833,74	145,74
PE	15,903	790,30	117,37

TABLE 2. Tensile tests of PLA matrix

Composition	Stress at break (MPa)	Elongation at break (%)	Tensile modulus (MPa)
PLA/10A	49,1	5,5	4522
PLA/30B	54,2	9,3	7770
PLA	54,1	3,5	4029

In the table 2, we can see that the filler material in PLA matrix showed different values as the polyolefins matrix. It is caused by other mechanical properties of the PLA material. PLA is more fragile compared to conventional packaging materials made from polyolefins.

The exfoliation was very successful for PLA 30B as it comes from results of TEM analysis. In Figure 1 and 2 it can be seen comparison of the distribution of nanofiller in a matrix of PLA and PE. Distribution in both cases is about the same, but images suggest that in the case of PLA matrix the exfoliation is worse [17,19 - 22].

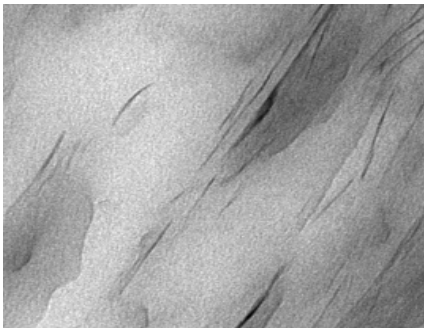


FIGURE 1. TEM Pictures of PLA 5% 30B Nanocomposites

The degree of exfoliation of other PLA matrices was similar to that in Figure 1 TEM. Filler 20A formed after incorporation in the matrix PLA intercalated system. The best reported according to the degree of exfoliation TEM Cloisite 30B. Individual tickets can be observed fillers and aggregates several layers of clay. The particles are thin with regular orientation.

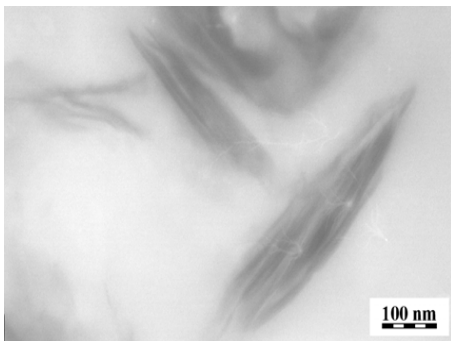


FIGURE 2. TEM Pictures of PE 5% 93A Nanocomposites

Comparing with the scale can be seen that in the system are MMT agglomerates having a thickness of about 50-90 nm for samples PE and PP, but in the case of the sample with Cloisite 93 A and it can be said that the gaps between the plates are slightly larger, therefore, that there is a little better intercalation. Still it is not possible to talk about good exfoliation of montmorillonite, as shown in Figure 2.

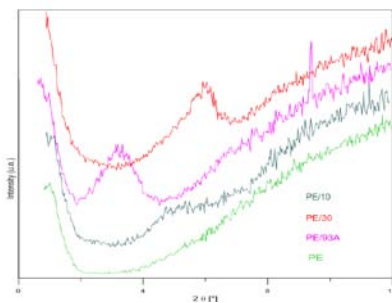


FIGURE 3. XRD PE nanofillers, pure PE, PE +MMT 93A 5%, 30B 5% and 10 5%

In the figure 3 we compare the pure PE and PE with filler. Curves PE samples with Cloisite 93A and 30 show peaks indicating a low degree of exfoliation. Only PE with Cloisitem 10A shows a comparison with pure PE desired degree of exfoliation of the filler in the polymer matrix.

Best results in X-ray diffraction was observed PLA, where curves of both filled materials are compared with pure sample and they are almost identical, with no peaks. It can be stated that only filled PLA probably occurred highest grade of exfoliation when comparing the prepared samples [19-22].

TABLE 3. Barrier properties for O₂

Composition	Thicknes (mm)	Permeation rate (mol / m.s.Pa)
PP/Cloisite 93A	0,0737	9,6384 · 10 ⁻¹⁵
PP/Dellite 67	0,0527	6,7048 · 10 ⁻¹⁵
Pure PP	0,0343	4,7423 · 10 ⁻¹⁵
PE/Cloisite 93A	0,0507	6,6115 · 10 ⁻¹⁵
Pure PE	0,0250	3,3931 · 10 ⁻¹⁵

TABLE 4. Barrier properties for O₂

Composition	Thicknes (mm)	Permeation rate (mol / m.s.Pa)
PLA/10A	0,0509	5,22 · 10-16
PLA/30B	0,0350	1,96 · 10-16
PLA	0,0337	2,53 · 10-16

Samples with PLA show better barrier properties than the samples with O₂ PP and PE. For samples with PP and PE enriched with nanofiller gas permeability significantly deteriorated in Cloisitu 93A is almost 2 times higher. For samples PLA 30B results are better for the pure material. A possible explanation for poorer outcomes for O₂ instability in the measurement of atmospheric O₂ is its small molecular diameter. The results of gas permeability may be influenced by varying the thickness of the films.

IV. CONCLUSION

Comparison of mechanical and barrier properties and exfoliation of the nanofiller in the polymer matrix was observed. Platelets of montmorillonite overlapped and may cause deterioration of the desired properties. The goal of the production of polymer nanocomposites is to achieve the full exfoliation. Important is the observation that nanofillers within the polymer matrix or on the surface of the polymer matrix mechanics affect polymer properties. We can say that good exfoliation of fillers can improve mechanical properties of nanocomposites. Nevertheless, the degree of exfoliation and orientation of the platelets is the most critical parameter.

ACKNOWLEDGMENT

This article (specify by the fact) was written with support of the project FR TI4/623 and by Operational Program Research and Development for Innovations co-funded by the European Regional Development Fund (ERDF) and national budget of Czech Republic, within the framework of project Centre of Polymer Systems (reg. number: CZ.1.05/2.1.00/03.0111). Some of presented data were already published.

Special acknowledgement is dedicated to doc. Ing. Petr Zádřapa PhD. who permeation rate measured and Ing. Miroslav Pastorek for X-ray analysis.

REFERENCES

- [1] G. O. Young, "Synthetic structure of industrial plastics (Book style with paper title and editor)," in *Plastics*, 2nd ed. vol. 3, J. Peters, Ed. New York: McGraw-Hill, 1964, pp. 15–64.
- [2] W.-K. Chen, *Linear Networks and Systems* (Book style). Belmont, CA: Wadsworth, 1993, pp. 123–135.
- [3] Ch. Suchada, Current trends in biodegradable polyhydroxyalkanoates. *Journal of Bioscience and Bioengineering* 2010, n. 6, pp. 621-632
- [4] G. Zehetmeyer, J. M. Scheibel and R. M. D. Soares, et al., *Polymer bulletin*, 70 (8), 2181-2191
- [5] S. Zhu ; J. Chen and H. Li; et al., *Journal of Applied Polymer Science*, 128 (6) , 3876-3884
- [6] D. Merinska, H. Kubisova and A. Kalendova et al., *Journal of Thermal Analysis and Calorimetry*, 25 (1), 115-131
- [7] S. M. A. Dadfar, I. Alemzadeh, S. Dadfar and S. M. Reza; et al., *Materials&Desing*, 32(4), 1806-1813
- [8] J. Ma.; Z. Duan, and CH. Xue.; et al., *Journal of Thermoplastic Composite Materials*, 26 (4) , 555-569 (2013)
- [9] T. Seyidoglu and U. Yilmazer, *Journal of Applied Polymer Science* , 127 (2) 1257-1267 (2013)
- [10] S. Rodriguez-Llamazares, B. L. Rivas and M. Perez, et al., *Journal of Applied Polymer Science*, 122 (3) , 2013-2025 (2011)
- [11] Y. Y. Su, S. P. Rwei and W. J. Gou.; et al, *Journal of Thermoplastic Composite Materials* , 25 (8), 987-1003 (2012)
- [12] R. Klitkou, E.A. Jensen and J de C. Christiansen, *Journal of Applied Polymer Science*, 126, (2) 620-630 (2012)
- [13] Q. P. Ran, H. Y. Hua and Y. Tian, et al., *Polymers & Polymer Composites*, 14 (3) 301-306 (2006)
- [14] M. H. Abdolrasouli, E. Behzadfar and H. Nazockdast, et al., *Journal of Applied Polymer*, 125 (1) E435-E444 (2012)
- [15] A. Sharif-Pakdaman, J. Morshedian and Y. Jahani, *Journal of Applied Polymer*, 125 (1), E305-E313 (2012)
- [16] H. K. F. Cheng, N. G. Sahoo and X Lu; et al., , *Journal of Thermal Analysis and Calorimetry*, 109 (1) 17-25 (2012)
- [17] L. Xie, L. Xia-Yan and Z-J. Han, et al., *Polymer Plastic Technology and Engineering*, 51 (12), 1251-1257 (2012)
- [18] B. Akbari and R. Bagheri, *Journal of Nanocomposites*, 810623
- [19] Auras. *Poly(lactic acid): synthesis, structures, properties, processing, and applications*. Hoboken, N. J.: Wiley, 2010, p 499 .
- [20] V.T Duncan. Applications of nanotechnology in food packaging and food safety: Barrier. *Journal of Colloid and Interface Science* [online]. 2011, n. 363, p. 1-24
- [21] V. Goodarzi, S. H. Jafari, and H. A. Khonakdar, et al., *Journal of Polymer Research*, 18 (6), 1829-1839
- [22] J. Ahmed and S. K. Varshnev. Polylactides — Chemistry, Properties and Green Packaging Technology: a Review. *International Journal of Food Properties* 2011, č. 14, s. 37–58

Optimal model of a masonry building structure with wooden floors

Mariella Diaferio, Dora Foti, Nicola Ivan Giannoccaro, Salvador Ivorra

Abstract The aim of the paper is to present the structural analysis of an important historical building: the San James Theater actually used as the Municipality House in the city of Corfu.

The building is made of carved stones and is located in the centre of Corfu, Greece.

The study deals with the structural identification of such structure through the analysis of its ambient vibrations recorded by means of very accurate accelerometers. A full dynamic testing was developed using ambient vibrations to identify the main modal parameters and to make a non-destructive characterization of this building

The results of these dynamic tests will be used for the model updating of a complex FE simulation of the structure. This analysis may present several problems and uncertainties for this stocky building. Due to the presence of wooden floors, the local modes can be highly excited and, as a consequence, the evaluation of the structural modal parameters presents some difficulties.

The paper discusses the experimental tests and compares the results with those obtained from the analysis of a preliminary FE model obtained using a commercial software.

Keywords Historical building, Non-destructive tests, Operational modal analysis, Dynamic analysis, FEM analysis.

I. INTRODUCTION

The structure of this building was started to build in 1663 but it stopped for a period, probably due to financial problems and continued in 1687. The construction was completed in 1693. Initially, the structure was built as lodge for the nobles and was known with the name *Loggia*, only in 1720 it was renamed as *San Giacomo* like the close

This work was supported in part by the European Territorial Cooperation Programme *Greece-Italy 2007-2013*, under grants of the project *Structural Monitoring of ARTistic and historical BUILDing Testimonies (S.M.ART:BUILD)*.

Mariella Diaferio, Department of Department of Civil Engineering and Architecture, Technical University of Bari, Bari, Italy

Dora Foti, Department of Department of Civil Engineering and Architecture, Technical University of Bari, Bari, Italy. (Corresponding author +39 080596-3771; email: Dora.foti@poliba.it.

Nicola Ivan Giannoccaro, Department of Engineering for Innovation, University of Salento, Lecce, Italy

Salvador Ivorra, Department of Civil Engineering, University of Alicante, Alicante, Spain.

catholic Cathedral and was converted in a theatre. At the end of 1903 it was converted into a City Hall when the insertion at the front part of the building was dismantled and one more floor in the central part was built.

This masonry historical construction is built in a rectangular plant absolutely symmetric, with dimensions 24.75 m (Figure 1) and 14 m (Figure 2). The building has a maximum height of 19 m. Five domed arched windows in a row at the two main sides and two symmetric rectangle windows in each narrow side characterize the structure. In the main façade the central arched window is modified to build the main entrance to the building from the Dimarchiou square.

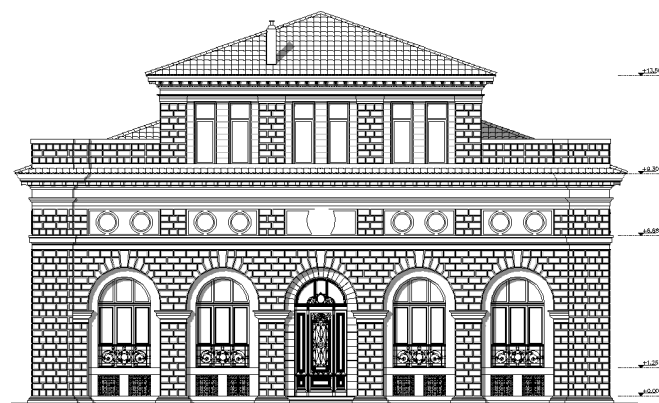


Figure 1. Main façade. South façade. Dimarchiou square

This structure has a semi-basement for the south façade. Figure 2 shows a south-west lateral façade where it is possible to identify this semi-basement for the South façade and the first basement in the North façade.



Figure 2. Lateral façade. North-East (Left). South-West (Right).

Inside the building has three different levels of wooden floors; the third was built some year after the initial building. Some load-bearing walls ensure the stability of this building in its two main orthogonal axes (Figure 3). This configuration presents a particularity in this structure for the dynamic identification analysis because of its shape, which is extremely stocky.



Figure 3. Longitudinal section. North view. Wooden floor location.

II. NUMERICAL MODEL

The numerical analysis of different historical masonry constructions has been studied by many authors [1-3] and they explain the complexity to model the behavior of masonry construction under static and dynamic loads. To obtain a homogeneous numerical model the technique of modal identification is a useful procedure for this structural typology [4-14].

A detailed 3D numerical model was developed to simulate the structural behavior of this historical construction (Figure 4). SAP2000Nonlin commercial software [15] was used considering an initial linear behavior for the masonry and wooden materials. The connection between the soil and the constructions has been considered rigid and the connection for the semi-basement with the perimeter soil has been considered rigid too.

15259 shell elements have been utilized to simulate the different structural elements: resisting walls, cover and floors. 15139 nodes and 162 frames elements have been utilized to simulate the wooden beams supporting the top cover of the building. (Figure 5)

The hypothesis of thick-shell elements has been considered for all the surface elements, defined using 4 nodes and 6 degrees of freedom for each node. Thickness between 0.3 m and 1.05 m has been considered to simulate the real structural

elements. The wooden floor elements have been modeled using a medium thickness of 0.25 m to simulate the wooden beam and the wooden deck platform.

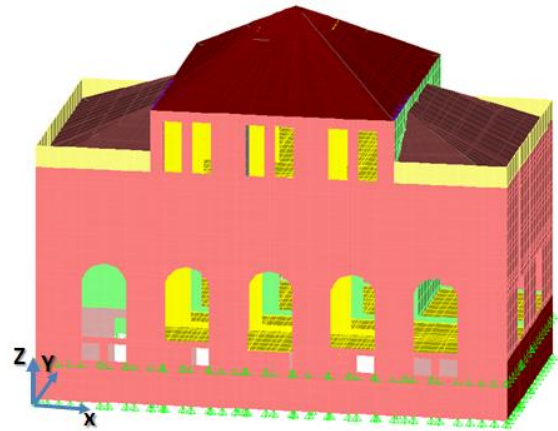


Figure 4. General view of the 3D numerical model.

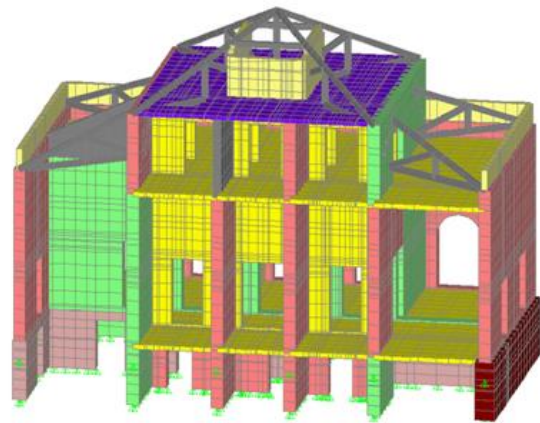


Figure 5. 3D Numerical model. Longitudinal section. South view.

No specific tests have been made to obtain the main characteristics of the structural materials: Masonry and wooden. Table 1 shows some initial values for this materials obtained from reference [1]

Table 1. Characteristics of the materials

	Elastic modulus (MPa)	Density (kg/m ³)
Masonry	5883	1800
Wooden	14709	800

To simulate the live load on each floor a live load of 2 kN/m² has been considered on the floor elements: levels 1 and 2.

An initial static analysis of the main walls of this building indicates that the maximum compression stresses reached at

one of the surface of the shell elements and due to the self-weight and the live load (Figure 6) are lower than 1 MPa, completely admissible for a conventional masonry. This analysis allows to state that the maximum tension stresses reached at the other surface of the shell elements are lower than 1 MPa, a value completely admissible for a conventional masonry (Figure 7).

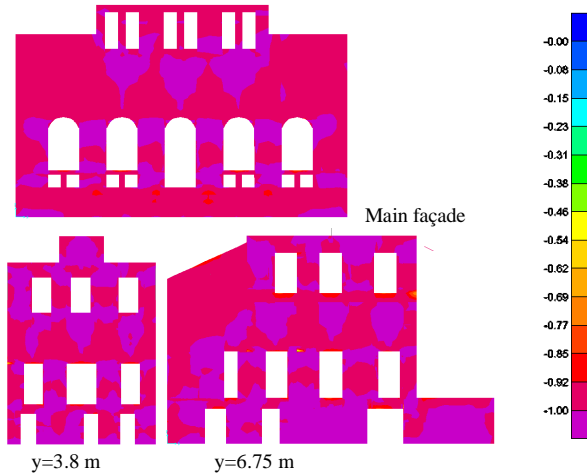


Figure 6. Maximum normal compression stresses in the main walls. (N/mm²)

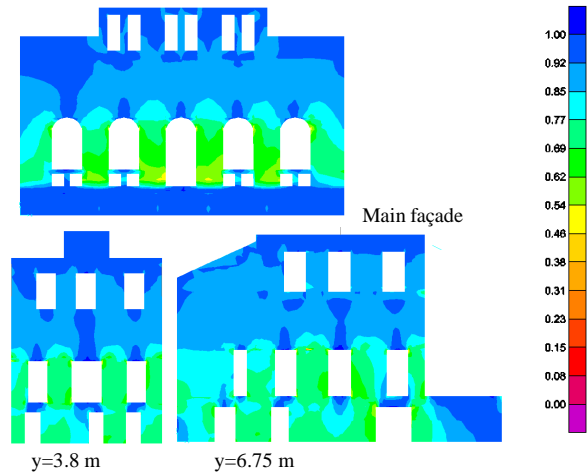


Figure 7. Maximum normal tension stresses in the main walls. (N/mm²)

For this preliminary analysis the stresses on the different floors under the self-weight and the live load of 2 kN/m² have been considered. Figures 8 and 9 present, respectively, the maximum and minimum normal stresses on each floor at h=3 m and h=10.9 m. The results shown here are lower than the maximum admissible values for a conventional wooden structure well preserved.

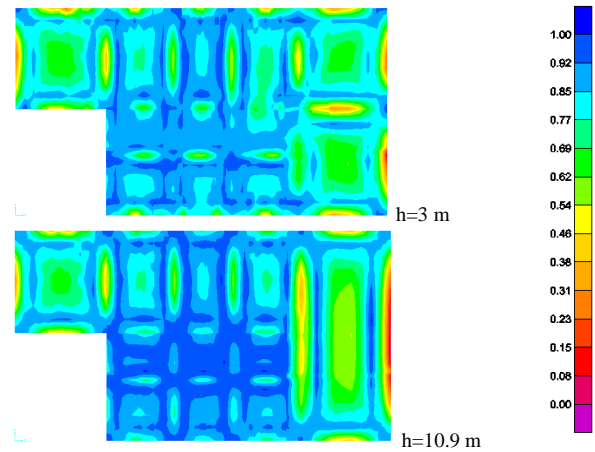


Figure 8. Maximum normal tension stresses in wooden floors. (N/mm²)

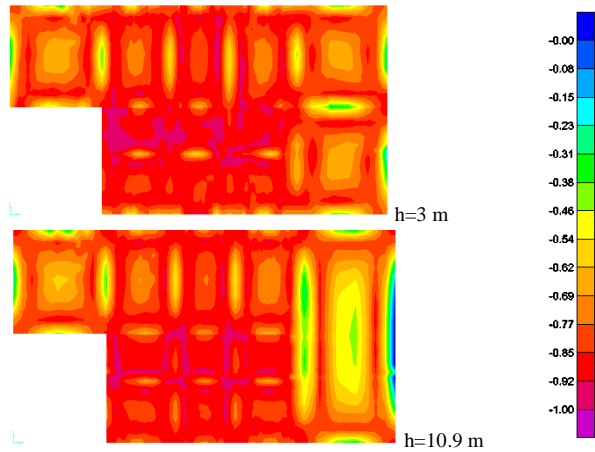


Figure 9. Maximum normal compression stresses in wooden floors. (N/mm²)

A modal analysis has been developed to obtain the identification of the main frequencies of this building. Figure 10 presents a visual identification of these modes. Table 2 indicates the total mobilized mass and the numerical values of the main frequencies.

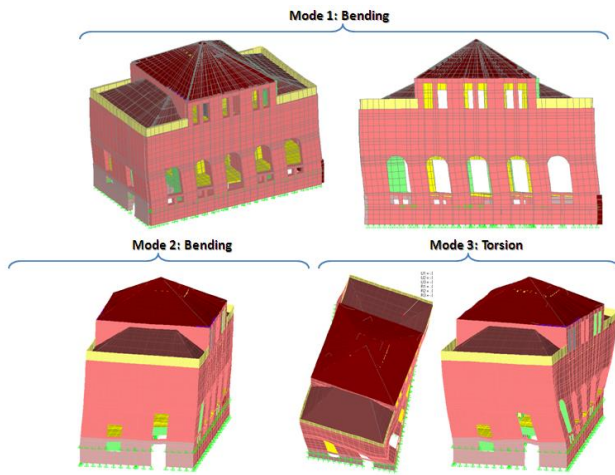


Figure 10. Modal analysis results. Identification.

Table 2. Identified periods and frequencies

Mode	Period (s)	Frequency (Hz)	Sum UX	Sum UY	Sum UZ	Sum RX	Sum RY	Sum RZ
1	0.164	6.09	0.71	0	0	0	0.3	0.12
2	0.131	7.64	0.71	0.65	0	0.6	0.3	0.41
3	0.108	9.24	0.71	0.66	0	0.61	0.3	0.64
4	0.095	10.52	0.71	0.66	0	0.61	0.3	0.65
5	0.094	10.66	0.71	0.66	0	0.61	0.3	0.65

III. DYNAMIC TESTS

Some dynamic tests have been developed to obtain the global main frequencies of the structure. A total of 18 piezoelectric seismic accelerometers have been used to register ambient vibrations.

The monitoring system consisted of several elements properly connected: 18 piezoelectric accelerometers with a sensitivity of about 1000 mV/g have been positioned at different levels and in different rooms, according to the orthogonal directions x and y defined by the orthogonal main façades; a data acquisition system positioned at each monitored level; the laptop with an acquisition software, and the cables.

Figure 11 shows the biaxial configuration of the accelerometers in two different positions on the building walls prepared to register longitudinal and transversal vibrations on this building.



Figure 11. Identification Seismic accelerometers located in different positions on the building.

A preliminary analysis [16] developed with the recorded vibrations by using the classical Operational Modal Analysis (OMA) techniques implemented by means of a commercial software [16] has permitted to identify the first frequencies. In detail, the first identified experimental frequency related to the first bending mode is equal to about 4.6 Hz, while the first identified experimental frequency related to a torsional mode is equal to about 5.7 Hz .

These initial values permit to affirm that the numerical model is less rigid than the real model. To obtain more realistic results for the numerical model it is necessary to define the main parameters to homogenize the total masonry building only using two materials: masonry and wood.

IV. CONCLUSION

In this work an optimized FE model of a masonry building structure with wooden floors has been presented and discussed with the aim of comparing the numerical frequencies with the identified ones. This analysis will permit, in the future researches, to obtain important information about the character of the mode shapes and also the correct values of the material properties.

ACKNOWLEDGMENT

Authors highly acknowledge the work developed by Mr. Francesco Paparella and Mr. Marco Iurilli.

The authors gratefully acknowledge the funding by European Union and by National Funds of Greece and Italy, European Territorial Cooperation Programme "Greece-Italy 2007-2013", under grants of the project Structural Monitoring of ARTistic and historical BUILDing Testimonies (S.M.ART:BUIL.T.).

REFERENCES

- [1] S. Ivorra, F.J. Pallares, Dynamic investigations on a masonry bell tower. *Eng Struct.* Vol 28(5), pp. 660-667, 2006.
- [2] P.B. Lourenço. Computations of historical masonry constructions. *Prog. Struct. Eng.*, 4 (3) (2002), pp. 301-319
- [3] M. Betti, M. Orlando, A. Vignoli. Static Behaviour of an Italian Medieval Castle: Damage Assessment by Numerical Modelling. *Comput. Struct.*, 89 (21-22) (2011), pp. 1956-1970
- [4] M. Lepidi, V. Gattulli, D. Foti, Swinging-bell resonances and their cancellation identified by dynamical testing in a modern bell tower. *Engineering Structures*, Elsevier 31 (2009) 7, 1486-1500.
- [5] D. Foti, S. Ivorra, M.F. Sabbà. Dynamic investigation of an ancient masonry bell tower with operational modal analysis: A non-destructive experimental technique to obtain the dynamic characteristics of a structure. *Open Construction and Building Technology Journal*, 6 (2012) 384-391.
- [6] D. Foti, M. Diaferio, N.I. Giannoccaro, N.I. & Mongelli M., Ambient vibration testing, dynamic identification and model updating of a historic tower. *NDT & E International*, Vol. 47, pp. 88-95, 2012.
- [7] M. Diaferio, D. Foti, M. Mongelli, N.I. Giannoccaro, P. Andersen, Operational Modal Analysis of a Historical Tower in Bari. In: *Conference Proceedings of the Society for Experimental Mechanics Series*, "IMAC XXIX". Vol. 7, pp. 335-342, ISBN: 978-1-4419-9315-1, doi: 10.1007/978-1-4419-9316-8_31, 2011.

- [8] M. Diaferio, D. Foti, V. Sepe, Dynamic Identification of the Tower of the Provincial Administration of Bari, Italy. In: Eleventh International Conference on Civil, Structural and Environmental Engineering Computing. Malta, 18-21 Sept. 2007, paper n. 2 (2007).
- [9] D. Foti, V. Gattulli, F. Potenza, Output-only identification and model updating by dynamic testing in unfavorable conditions of a seismically damaged building. *Computer-Aided Civil and Infrastructure Engineering*, February (2014), Online ISSN: 1467-8667, doi: 10.1111/mice.12071.
- [10] M. Diaferio, D. Foti, N.I. Giannoccaro, Identification of the modal properties of a building of the Greek heritage , *Key Engineering Materials* (2014).
- [11] M. Diaferio, Dynamic analysis of a historical fortified tower, *Key Engineering Materials* (2014)
- [12] D. Foti, "Non-destructive techniques and monitoring for the evolutive damage detection of an ancient masonry structure" in *Key Engineering Materials*, (2014)
- [13] M. Diaferio, D. Foti, N.I. Giannoccaro, "Non-destructive monitoring of an old masonry clock tower with forced and environmental actions" in *Proc. XXII International Forum Le Vie dei Mercanti*, Editor La Scuola di Pitagora, in "Fabbrica della Conoscenza", pp. 815-824 (2014)
- [14] D. Foti, "Identification of the modal properties of a Medieval tower next to a landslide" in: *Proc International Forum "Le Vie dei Mercanti"*, Editor La Scuola di Pitagora, in "Fabbrica della Conoscenza", pp. 1302-1311(2014)
- [15] SAP2000™ CSI Analysis Reference Manual ver. 14.1. Computers and Structures, Inc. Berkeley, California, USA (2009).
- [16] ARTeMIS Extractor Pro software. Issued by Structural Vibration Solutions ApS. NOVI Science Park, Niels Jernes Vej 10, DK 9220 Aalborg East, Denmark; (2013).

TRM strengthening of precast reinforced concrete wall panel with cut-out opening - experimental investigation

C. Todut, D. Dan, and V. Stoian

Abstract—The experimental research presented in this paper aims to investigate the cut-out effect on the behavior of the precast reinforced concrete wall panels under in-plane seismic loading conditions. Wall openings in buildings are provided for architectural reasons or access requirements, while the cut-outs in walls are made due to change of use or simply, architectural reasons. The precast reinforced concrete wall panel presented in this paper was designed according to the 1981 Romanian code, and has an initial small window opening. In order to investigate the cut-out effect, the small window opening was enlarged to a wide window opening. The specimen was first tested in the unstrengthened condition and subsequently was repaired using high strength mortar, rehabilitated, and then tested again. The experimental tests are described and a discussion based on cut-out effect on shear walls is undertaken and future research is suggested. Numerical analysis are further needed in order to simulate the cut-out interventions made in precast reinforced concrete shear walls of different parameters.

Keywords—cut-out, experimental, reinforced concrete, TRM.

I. INTRODUCTION

BETWEEN the 1950s and 1970s, the use of large panel structures was widely used, but then after followed the decay period until the 1990s, which marked the end in Romania. It is known that the system composed of precast reinforced concrete panels can provide a good seismic performance, but after 50 years of existence and interventions some were subjected to, detailed investigation is strongly needed. The investigated experimental specimens meet the requirements of Eurocode 8 for walls designed to medium ductility and are referred as large lightly reinforced walls.

The application of textile reinforced mortar (TRM) was investigated in this study as a rehabilitation manner, in order to restore the load bearing capacity of the specimen first tested in the unstrengthened condition. Research on textile reinforced

mortar strengthening were conducted by Bernat-Maso et al. [1], Triantafillou and Papanicolaou [2], Papanicolaou et al. [3], San-José et al. [4], Bernat et al. [5], Elsanadedy et al. [6], Larrinaga et al. [7]. Other research presented by Mohammed et al. [8], Bing Li and Qin Chen [9], Mosoarca [10], Kitano et al. [11], Demeter et al. [12], Sas et al. [13], Doh and Fragomeni [14], Guan et al. [15], Carrillo and Alcocer [16], investigated reinforced concrete walls with openings. An experimental research on the effect of cut-out made in wall panels to the behavior of the reinforced concrete wall panel was investigated. The tests were performed under in-plane cyclic lateral loads. The specimen was tested unstrengthened, then after it was repaired, rehabilitated and tested again. A few literature on the TRM for RC wall strengthening and cut-outs made in walls is available.

The paper aims to comprehend the influence of the wall cut-out on the seismic performance of the wall without cut-out, and also the performance of the TRM system for the load bearing capacity restoration. Important aspects related to the seismic performance, lateral stiffness, horizontal displacement (drift), ductility and energy dissipation capacity are presented and discussed for the rehabilitated element in comparison with the reference one. The behavior of the tested elements also include: the failure modes, the strain analysis in reinforcement and glass fiber grid (TRM component). Some remarks are also presented for the TRM anchorage system used.

II. EXPERIMENTAL PROGRAM

The experimental program consists of six 1:1.2 scale elements, namely precast reinforced concrete wall panels PRCWP (7–12), designed and casted according to a Romanian Project Type 770-81 [17], [18]. Two specimens were selected for investigation in this paper, namely PRCWP (10-L1/L3-T), specimen having an initial small window opening and enlarged to a wide window opening, and PRCWP (11-L1-T), specimen having a small window opening. On the basis of the two experimental tests in the unstrengthened condition, important aspects related to the cut-out effect can be drawn out. Then after the specimen with cut-out opening was repaired using high strength mortar, rehabilitated and subsequently tested again, to investigate the strengthening effect and the seismic behavior efficiency. The post-damage strengthened specimen was denoted PRCWP (10-L1/L3-T/R). The experimental specimens were: 2150 mm height, 2750 mm

This work was supported in part by the Grant no. 3-002/2011, INSPIRE – Integrated Strategies and Policy Instruments for Retrofitting buildings to reduce primary energy use and GHG emissions, Project type PN II ERA NET, financed by the Executive Agency for Higher Education, Research, Development and Innovation Funding (UEFISCDI), Romania.

C. Todut is with the Politehnica University Timisoara, 300223, Romania (phone: 0040-256-403-950; fax: 0040-256-403-958; e-mail: carla.todut@student.upt.ro).

D. Dan is with the Politehnica University Timisoara, 300223, Romania (e-mail: daniel.dan@upt.ro).

V. Stoian is with the Politehnica University Timisoara, 300223, Romania (e-mail: Valeriu.stoian@upt.ro).

width and 100 mm thickness. The small window opening was 1000 mm height and 750 mm length, while after enlargement the dimensions of the wide window opening were 1000 mm height and 1750 mm length. The wall panels were set between two reinforced steel concrete composite beams, namely a loading beam and a foundation beam. The reinforcement of the precast reinforced concrete (RC) wall panel was made of: horizontal and vertical bars, welded wire mesh in both piers, spatial reinforcement cage in the spandrel, an inclined bar at each corner of the opening, a vertical bar each side of the opening on its height and a wire mesh in the parapet. The configuration of the two specimens selected for the cut-out investigation is presented in Figure 1 (a) and (b).

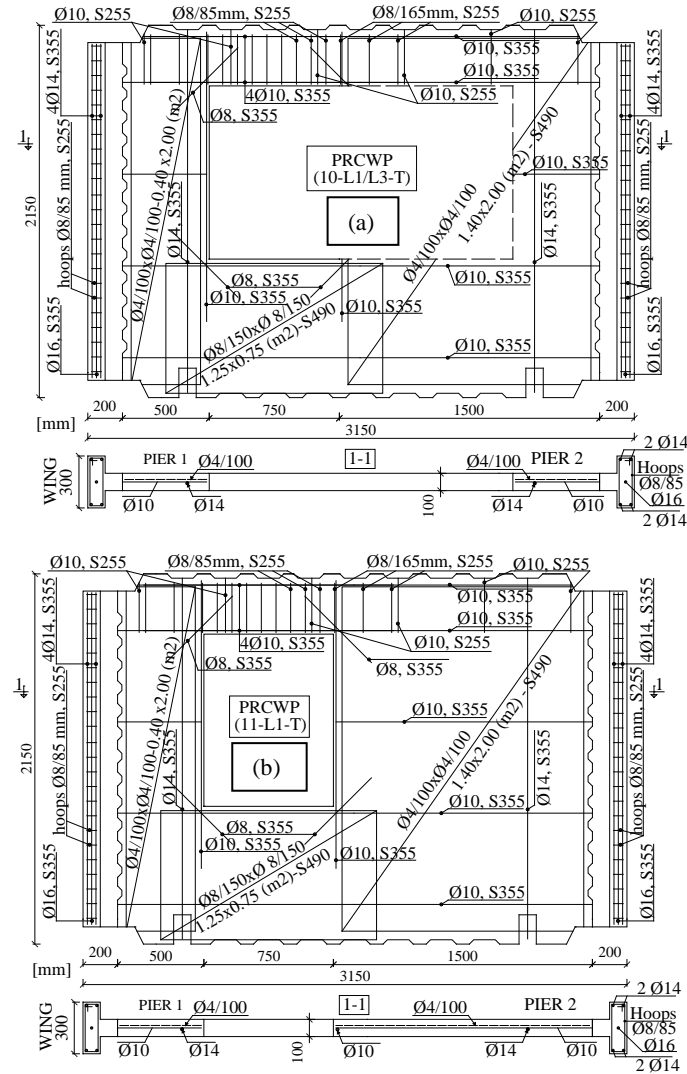


Figure 1 the schematics and reinforcement details of the specimens

Table 1 material properties of steel

Re-bar type	Grade	Φ (mm)	f_y (N/mm ²)	f_u (N/mm ²)	E_s (N/mm ²)
OB37	S255	6	400	550	207
		8	425	507	205
		8	424	553	208
PC52	S355	10	450	564	210
		14	395	584	206
		16	385	613	210
STPB	S490	4	618	667	208

Table 2 Geometrical and mechanical properties of the grid

Component	Areal weight [g/m ²]	Opening size [mm]	Tensile strength [MPa]	Tensile modulus [GPa]	Elongation at break [%]	Component mortar
SikaWrap 350G Grid	280	15.7-10.1	3400	73	3.5	SikaMono Top 722 Mur

A. Material Considerations

The specimen's concrete quality was C16/20 class, the reinforcement S255 for the spatial reinforcement cage, S355 for horizontal, vertical and inclined steel bars, and S490 for the steel wire mesh. The steel reinforcement properties obtained experimentally are given in Table 1. Textile reinforced mortar was used for the rehabilitation of the specimen. The system used was made of glass fiber grid and 1-component, fiber reinforced cementitious mortar with a compressive strength at 7 days of 15 N/mm² according to the product data sheet. Table 2 summarizes the geometrical and mechanical properties of the grid used. The mentioned characteristics are based on manufacturer's data. The mortar, used to replace the heavily damaged concrete, was Sika MonoTop 614, with a compressive strength at 28 days of 55–60 N/mm², according to the product data sheet.

B. Behavior and results of unstrengthened elements

Similar behavior was observed for the two unstrengthened specimens. Cracks appeared in the spandrel, piers, wings, corners of the window opening, cast in place mortar and mostly in the parapet. Failure of the tested specimens are presented in Figure 2 (a) [19] and (b) [20]. The first diagonal crack in the right pier appeared at 0.3% drift ratio, first cycle, loaded from the right for both specimens. Concrete crushing was observed in the left corners of the specimen with window enlargement, while for the specimen with small opening at the bottom left corner of the opening and parapet. Failure of the PRCWP (10-L1/L3-T) was attained at 0.65% drift ratio, while for the PRCWP (11-L1-T) it was recorded at 0.73% drift ratio.

C. Repair and strengthening of the specimen

The rehabilitation strategy adopted here intended to restore the initial load bearing capacity of the element, namely PRCWP (10-L1/L3-T/R), the solution being qualitative and based on the behavior of the reference specimen.

The PRCWP (10-L1/L3-T/R) specimen, having an initial narrow window opening and enlarged to a wide window opening, was repaired after the experimental test of the reference specimen using a repair mortar (Sika MonoTop 614) and then it was rehabilitated using TRM with GF grid and subsequently tested again. After the repair of the specimen, the rehabilitation process started with surface preparation, namely wall panel polishing, 8 mm hole drilling for the anchorage system, 20 mm rounding of the window edges and vacuum-cleaning. Then, the anchorage system composed of threaded rods having 6 cm length were fixed to the panel using resin, in order to provide a mechanical and punctual type of anchoring system (together with the nut and washer) for the transmission of stresses and deformations from the structure substrate to the TRM system. According to the rehabilitation strategy (Figure

3), the GF grid was cut using scissors. A bonding primer, namely Sika Monotop 910 N was applied on the surface of the wall, followed by the first layer of mortar, GF grid and the second layer of mortar (Figure 4). Related to the glass fiber grid application (Figure 5), first were mounted the number 4 grid pieces, each side of the parapet,



Figure 2 Failure of the tested unstrengthened specimens

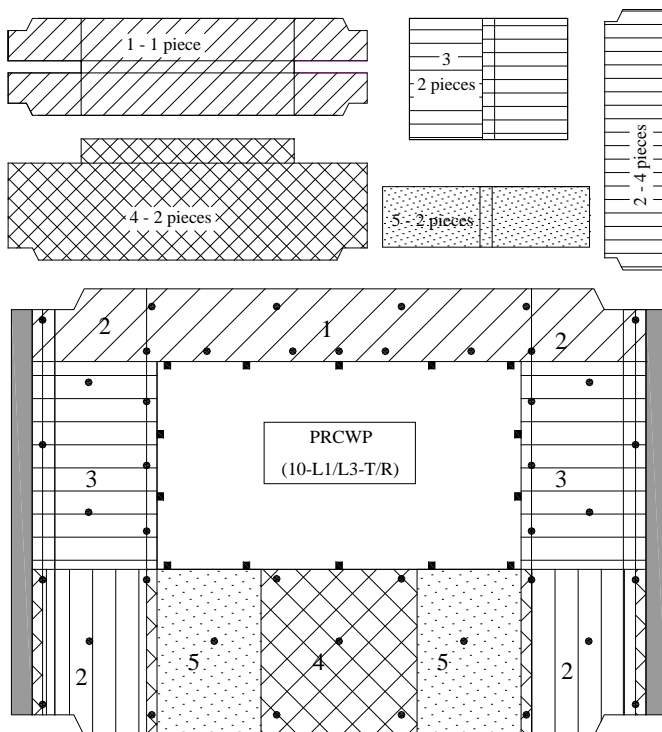


Figure 3 The TRM rehabilitation strategy for the wall with cut-out

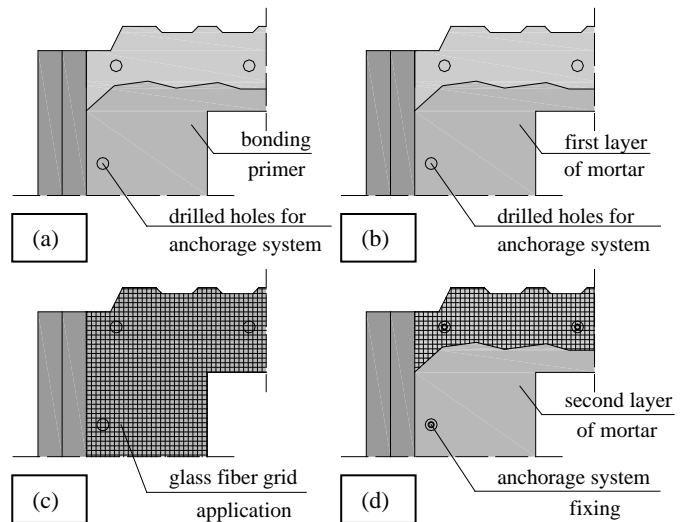


Figure 4 Rehabilitation detail for the TRM use

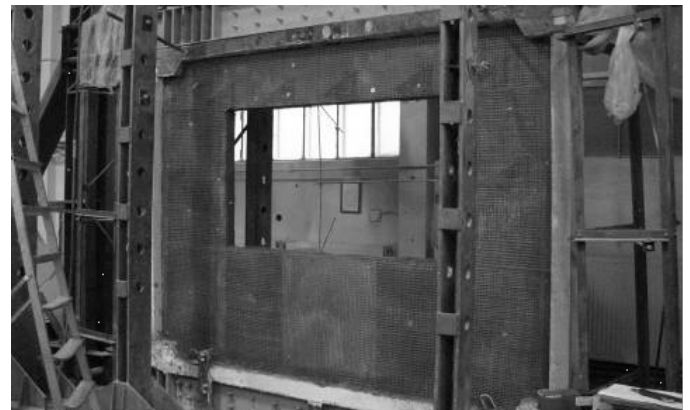


Figure 5 Glass fiber grid application for the wall with cut-out

followed by the number 5 grid pieces, wrapped around the parapet, over the number 4 grid pieces. Then the number two grid pieces were placed each side of the parapet, followed by the number 3 grid pieces which were wrapped over the number 2 grid pieces, each side of the opening. Finally the number 1 glass fiber grid piece was wrapped around the spandrel. Strain gauges were mounted on rebar for the reference element and on the GF grid for the strengthened one.

D. Testing methodology and test set-up

Detailed data related to the tests set up and testing methodology of the precast reinforced concrete wall panel specimens are presented in Demeter [21]. A general view of the test set-up is presented in Figure 6.

The testing procedure of the specimens consisted in quasi-static reversed cyclic lateral loads - displacement controlled (using two cycles per drift), having the measure of 0.1% drift ratio, namely 2.15 mm. Vertical loading was also applied to simulate the gravity loading condition and restrain the rotation of the elements. Pressure transducers (P), displacement transducers (D) and strain gauges placed on rebars and glass fiber grid (G) were used to monitor the behavior of the precast reinforced concrete wall panel specimens (Figure 7). The same displacement transducer position was used for all the experimental specimens.

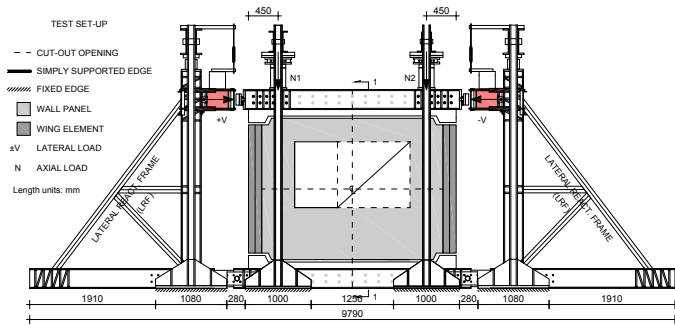


Figure 6 general view of the test set-up

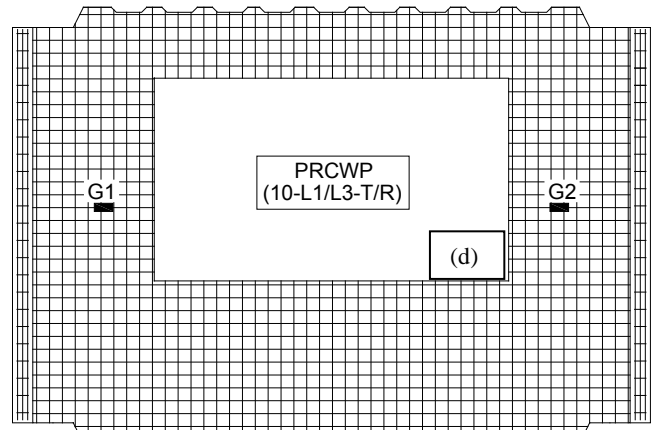


Figure 7 Instrumentation layout of the specimens

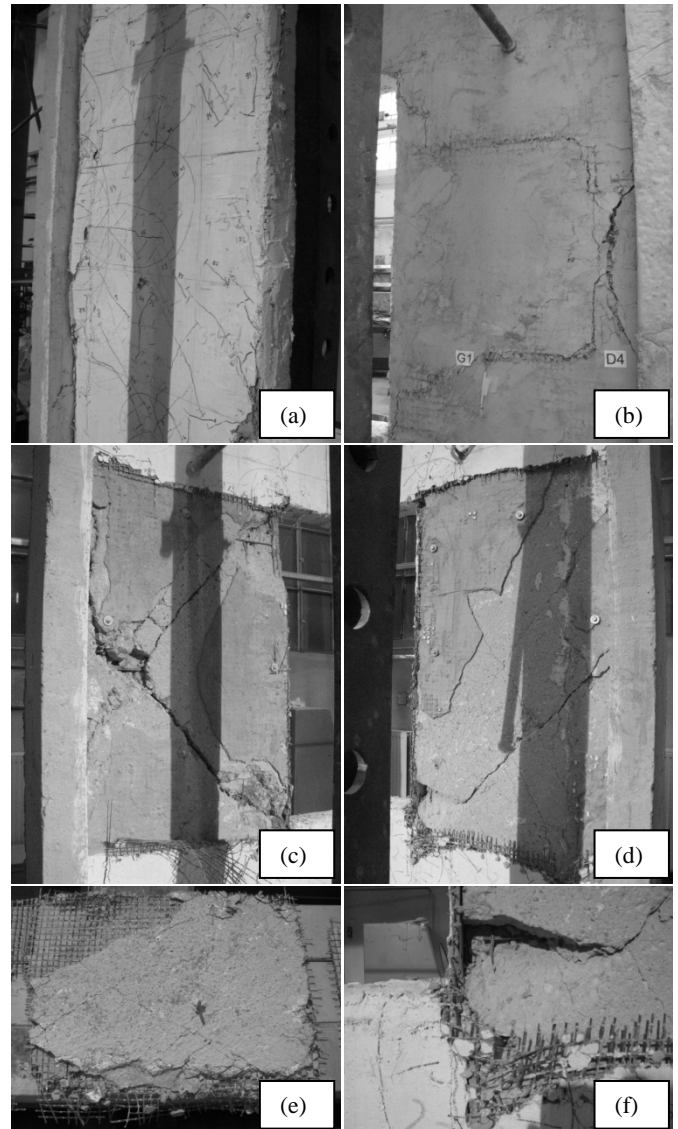
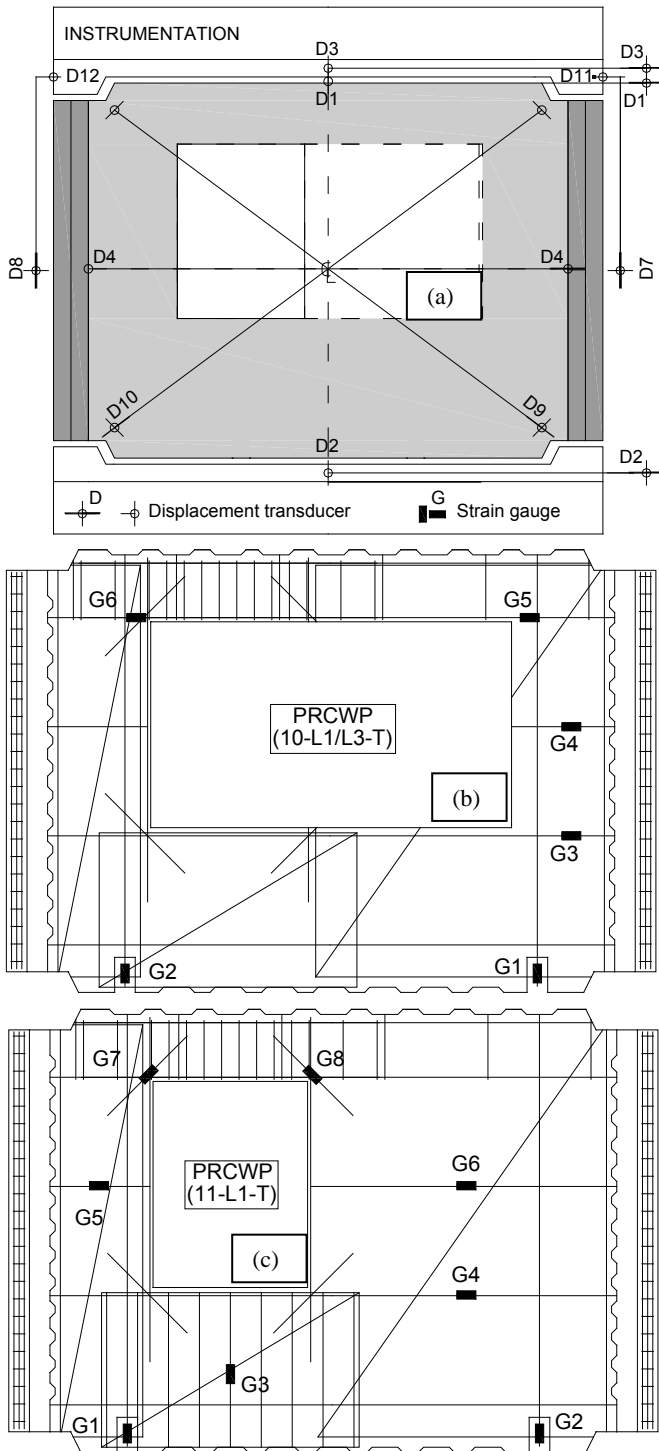


Figure 8 Failure details of the TRM strengthened specimen

III. EXPERIMENTAL RESULTS AND COMPARATIVE STUDY

A. General Behavior and Failure Modes of the TRM post-damage strengthened specimen

The behavior of the strengthened and retested specimen

PRCWP (10-L1/L3-T/R) under reversed cyclic lateral loads, revealed an expected behavior in accordance with the design strategy. During the experimental test, the PRCWP (10-L1/L3-T/R) specimen developed cracks in the spandrel, piers, corners of the opening and parapet. The TRM system exhibited mortar detachment from 0.3% drift ratio, followed by mortar exfoliation and system excessive detachment (about 3 cm between the TRM system and the wall was observed) between 0.4-0.6% drift ratio. Subsequent detachments and mortar crushing appeared between 0.7-0.8% drift ratio. At the end of the experimental test, the TRM system was removed from each side of the opening and thick inclined cracks were observed together with concrete crushing (Figure 8). The load bearing capacity of the initial system was restored even if the anchorage system used turned to be inefficient. It can be concluded that the punctual mechanical type of anchorage is a cheap alternative to the surface type of anchorage [21] but smaller distances between the threaded rods are necessary.

B. Load displacement response diagrams

The obtained lateral loads versus the drift ratio envelopes are presented in Fig. 9a for the cut-out effect investigation and in Fig. 9b for the TRM performance. It can be seen that significant strength reduction ($\approx 50\%$) was induced by the cut-out made in the experimental specimen. The TRM rehabilitation strategy restored the initial load bearing capacity of the specimen with cut-out opening, despite the inefficiency of the anchorage system used.

C. Energy dissipation

The cumulative energy dissipation was obtained by the continuous integration of the load-drift hysteretic response using an iterative equation, as presented in [21].

A comparison between the cumulative dissipated energy (CED) per half-cycle versus drift ratio within each test performed is presented in Fig. 10. It can be concluded that the PRCWP (10-L1/L3-T) specimen with cut-out opening developed a significant lower energy dissipation ($\approx 57\%$) compared to the reference specimen, namely PRCWP (11-L1-T). In the case of the post-damage strengthened specimen using TRM, namely PRCWP (10-L1/L3-T/R), the energy dissipation was higher ($\approx 33\%$) compared to the unstrengthened specimen, PRCWP (10-L1/L3-T).

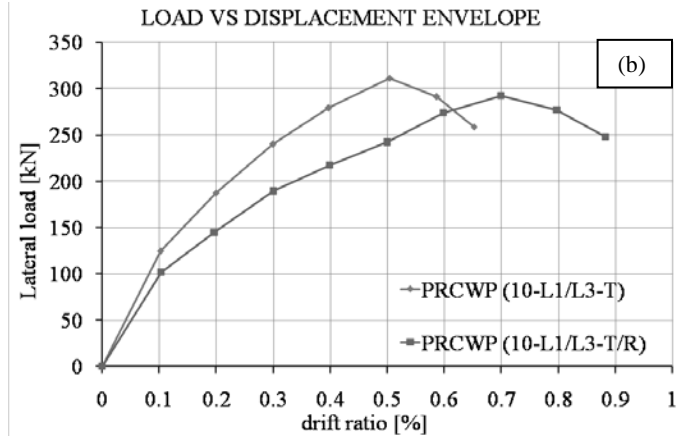


Figure 9 Load-drift ratio response diagrams

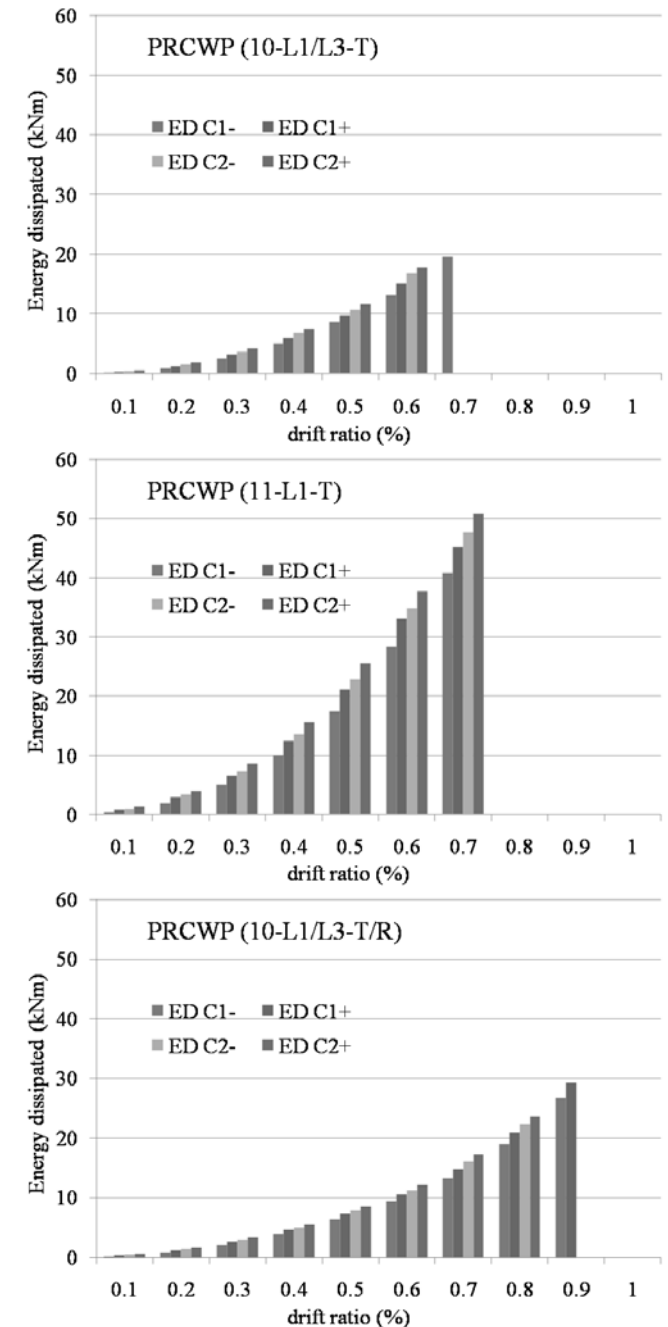
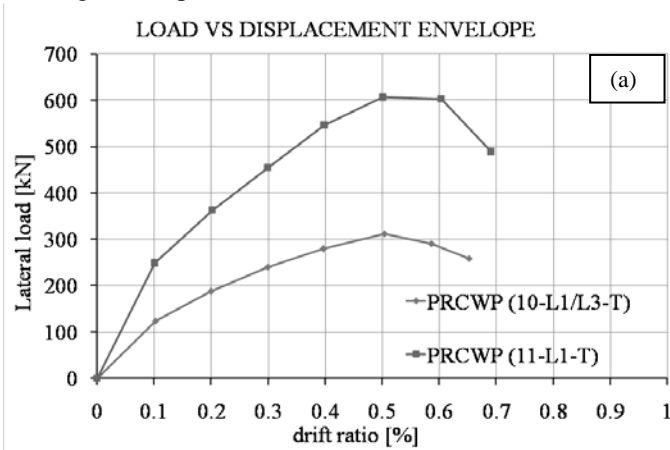


Figure 10 The cumulative energy dissipation of the specimens



D. Strain analysis

During the experimental tests, strain was measured on the vertical, horizontal and inclined reinforcing bars, and horizontal on the glass fiber grid. In Figure 11 are presented the strain ϵ (%) versus drift ratio for the current tested specimens. The position of strain gauges is shown in Fig. 7. It can be seen that, yielding of the reinforcement was attained for the unstrengthened wall panels, in the top left corners of the opening and parapet. In the case of the TRM strengthened specimen, the grid debonded beyond 2 ‰ strain due to the inefficiency of the anchorage system used.

E. Stiffness degradation

According to the stiffness versus drift ratio diagram (Figure 12), the cut-out made in wall produced a significant reduction in the initial stiffness (50%) compared to the reference specimen, PRCWP (11-L1-T). In the case of the wall with cut-out opening the initial stiffness was similar for the unstrengthened and post-damage strengthened condition.

F. Ductility considerations

The ductility of the wall specimens was evaluated using the $\mu_{0.85}$ method, which defines the ductility ($\mu = \Delta u / \Delta y$) as the ratio between the ultimate displacement (Δu - the displacement when the horizontal load falls to 80% of the maximum horizontal force) to the displacement corresponding to 0.85 of the maximum load on the ascending branch of the monotonic envelope (Δy - the displacement at yielding). The ductility coefficient $\mu_{0.85}$ for the tested specimens is presented in Figure 13. It can be concluded that the specimen with cut-out opening, namely PRCWP (10-L1/L3-T) exhibited a lower ductility than the reference one, PRCWP (11-L1-T). The TRM strengthened specimen, PRCWP (10-L1/L3-T/R), exhibited a considerable higher ductility than the reference specimen, PRCWP (10-L1/L3-T).

IV. CONCLUSIONS

The work presented in this paper refers to the experimental results on cut-out effect investigation and post-damage strengthening of a precast reinforced concrete wall panel using textile reinforced mortar.

The following conclusions can be drawn within the limitation of the current research:

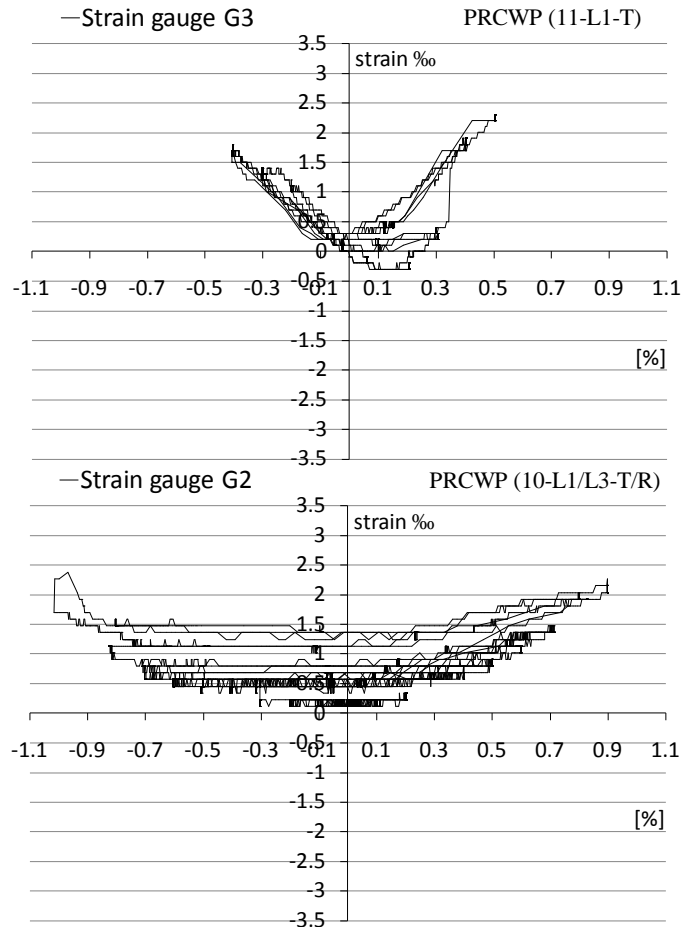


Figure 11 Steel strain (ϵ) versus drift ratio of the specimens

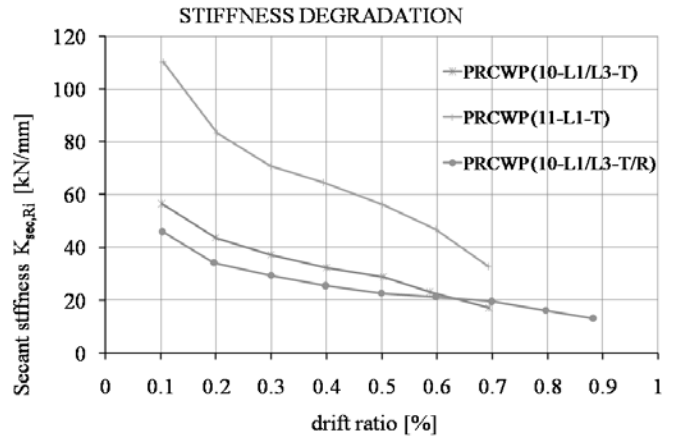


Figure 12 The stiffness versus drift ratio diagram of the specimens

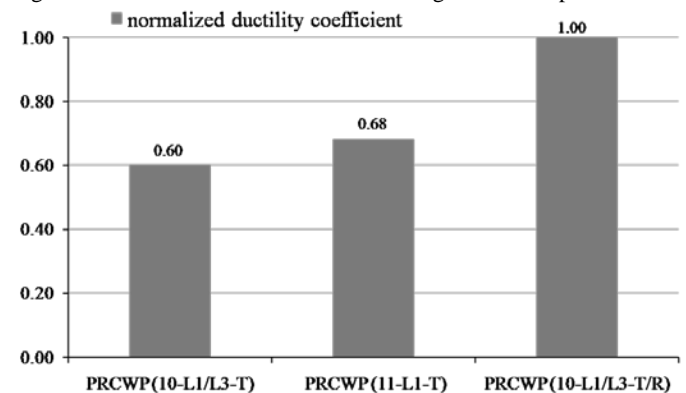
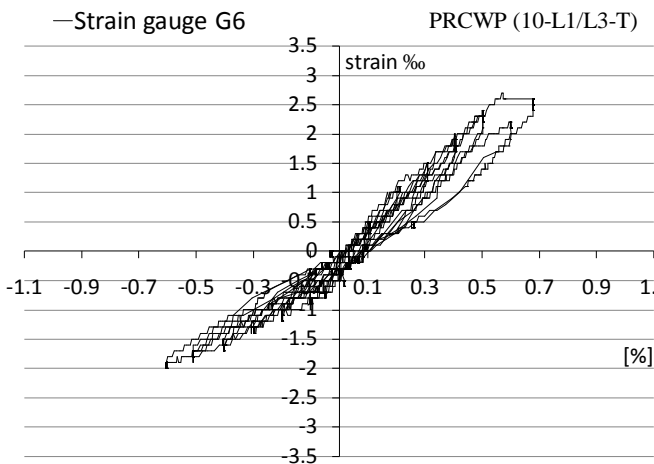


Figure 13 The normalized ductility coefficient for specimens

- the corners of the opening and the parapet exhibited concrete crushing in the case of the reference specimens;
- the dissipated energy was significantly lower for the wall with cut-out compared to the wall without cut-out, while the post-damage strengthened specimen dissipated more energy compared to the unstrengthened one;
- according to the $\mu_0.85$ method, the ductility of the wall with cut-out was inferior to the ductility of the wall without cut-out, while the post-damage strengthened specimen proved to be more ductile compared to the reference specimen;
- vertical wire mesh yielding was recorded in the parapet for the unstrengthened specimen; while in the case of the TRM strengthened specimen, the grid debonded beyond 2 % strain;
- the cut-out made in wall produced a significant reduction in the initial stiffness (50%) compared to the reference specimen, while the TRM strengthened specimen exhibited a comparable initial stiffness to the reference one;
- TRM system can be an effective solution for strengthening elements; the punctual anchorage system used turned to be inefficient, allowing for system local debondings.

Further studies related to the numerical modelling of the tested elements are in progress. The studies aims to establish the seismic performance of PRCWP having different parameters and the most convenient solutions of strengthening.

ACKNOWLEDGMENT

The author acknowledges the following research grant for the support of this study:

1. Grant no. 3-002/2011, INSPIRE – Integrated Strategies and Policy Instruments for Retrofitting buildings to reduce primary energy use and GHG emissions, Project type PN II ERA NET, financed by the Executive Agency for Higher Education, Research, Development and Innovation Funding (UEFISCDI), Romania.

2. This work was partially supported by the strategic grant POSDRU/159/1.5/S/137070 (2014) of the Ministry of National Education, Romania, co-financed by the European Social Fund – Investing in People, within the Sectoral Operational Programme Human Resources Development 2007-2013.

REFERENCES

- [1] E. Bernat-Maso, C. Escrig, C. A. Aranha, L. Gil, "Experimental assessment of Textile Reinforced Sprayed Mortar strengthening system for brickwork wall-panels", *Construction and Building Materials*, 50, (2014), pp. 226–236.
- [2] T. C. Triantafyllou, C. G. Papanicolaou, "Shear strengthening of reinforced concrete members with textile reinforced mortar (TRM) jackets", *Materials and Structures*, 39, (2006), pp. 93–103.
- [3] C. G. Papanicolaou, T. C. Triantafyllou, M. Papatheanasiou, K. Karlos, "Textile reinforced mortar (TRM) versus FRP as strengthening material of URM walls: out-of-plane cyclic loading", *Materials and Structures*, 41, (2008), pp. 143–157.
- [4] J. T. San-José, D. García, T. El Hadid, R. San-Mateos, A. Al Far, I. Marcos, "Novelty FRP and TRM Strengthening Systems Applied to Stone Masonry Walls: Experimental Programme Presentation (I)", *Asia-Pacific Conference on FRP in Structures (APFIS 2007)*, pp. 271–276.
- [5] E. Bernat, L. Gil, P. Roca, C. Escrig, "Experimental and analytical study of TRM strengthened brickwork walls under eccentric compressive loading", *Construction and Building Materials*, 44, (2013), pp.35-47.
- [6] H. M. Elsanadedy, T. H. Almusallam, S.H. Alsayed, Y. A. Al-Salloum, "Flexural strengthening of RC beams using textile reinforced mortar – Experimental and numerical study", *Composite Structures*, 97, (2013), pp. 40-55.
- [7] P. Larrinaga, C. Chastre, J. T. San-José, L. Garmendia, "Non-linear analytical model of composites based on basalt textile reinforced mortar under uniaxial tension", *Composites: Part B*, 55, (2013), pp.518-527.
- [8] B. S. Mohammed, L.W. Ean, M.A. Malek, "One way RC wall panels with openings strengthened with CFRP", *Construction and Building Materials*, 40, (2013), pp. 575-583.
- [9] B. Li, Q. Chen, "Initial stiffness of reinforced concrete structural walls with irregular openings", *Earthquake Engineering and Structural Dynamics*, 39, (2010), pp. 397–417.
- [10] M. Mosoarca, "Seismic Behavior of Reinforced Concrete Shear Walls with Regular and Staggered Openings After the Strong Earthquakes Between 2009 and 2011", *Engineering Failure Analysis*, 34, (2013), pp. 537-565.
- [11] A. Kitano, O. Joh, Y. Goto, "Experimental Study on the Strengthening and Repair of R/C Wall-Frame Structures with an Opening by CF-Sheets or CF-Grids", *FRP Composites in Civil Engineering - CICE*, (2004).
- [12] I. Demeter, T. Nagy-György, V. Stoian, D. Dan, "Seismic Retrofit of Cut-out Weakened Precast RC Walls by Externally Bonded CFRP Composites", 15 WCEE, Lisboa, (2012).
- [13] G. Sas, I. Demeter, A. Carolin, T. Nagy-György, V. Stoian, B. Täljsten, "FRP Strengthened RC Panels With Cut-out Openings", *Challenges for Civil Construction*, Porto, (2008).
- [14] J.H. Doh, S. Fragomeni, "Ultimate Load Formula for Reinforced Concrete Wall Panels with Openings", *Advances in Structural Engineering*, 9 (1), (2006), pp. 103-115
- [15] H. Guan, C. Cooper, D. Lee, "Ultimate strength analysis of normal and high strength concrete wall panels with varying opening configurations", *Engineering Structures*, 32, (2010), pp. 1341-1355.
- [16] J. Carrillo, S. Alcocer, "Degradation Properties of Reinforced Concrete Walls with Openings", *Dyna*, ISSN 0012-7353 (2011), vol. 78, pp. 106-115.
- [17] IPCT: Cladiri de locuit P+4 din panouri mari. Proiect 770-81, Vol. C: Elemente prefabricate, Bucuresti, Romania, (1982). IPCT: Precast reinforced concrete large panel buildings P+4. Project type 770-81, Vol. C: Precast elements, Bucharest, Romania, (1982).
- [18] IPCT: Cladiri de locuit P+4 din panouri mari. Proiect 770-81, Vol. D: Elemente prefabricate - Armari, Bucuresti, Romania, (1982). IPCT: Precast reinforced concrete large panel buildings P+4. Project type 770-81, Vol. D: Precast elements – Reinforcing, Bucharest, Romania, (1982).
- [19] Seismic Strengthening of a Precast Reinforced Concrete Wall Panel using Textile Reinforced Mortar – Todut C., Stoian V., Demeter I., Fofiu M., in Proceedings of the International Conference on Earthquake Engineering, Skopje, Republic of Macedonia, (2013), paper 323.
- [20] Glass Fiber versus Carbon Fiber Grid used in Textile Reinforced Mortar Strengthening of Precast RC Walls – Todut C., Stoian V., and Demeter I., *IACSIT International Journal of Engineering and Technology*, vol.5, no.5, (2013), pp. 622-626.
- [21] Demeter, I. (2011), Seismic retrofit of precast RC walls by externally bonded CFRP composites. PhD Thesis, Politehnica University of Timisoara.

C. Todut was born in Satu Mare, Romania on the 13th of April 1986. She earned the Bachelor's degree in Civil Engineering at the Politehnica University Timisoara, Romania in 2009, the Master of Science degree in Structures at the Politehnica University Timisoara, Romania in 2011. Currently she is a PhD Student at the Civil Engineering Department of the Construction Faculty, Politehnica University Timisoara, Romania.

During Faculty some of the author's achievements are obtaining a scholarship at the University of Edinburgh, Scotland, 3rd place at Carpatemont contest, 1st place in the County Olympics for the Strength of Materials contest, Timisoara and 2nd place in the National Olympics for the Strength of Materials contest, Iasi. Previous publications of her appear in the Proceedings of fib 2013, FRP RCS 2013 and Structural Faults and Repair 2012. Her current research is based on precast reinforced concrete wall panels, seismic performance, weakening induced by cut-outs and strengthening possibilities.

PhD Student Todut was a student member of the American Concrete Institute and the American Society of Civil Engineers.

Evaluation of Concrete Deterioration through Artificial Neural Networks based Systems

Guida Gomes, Henrique Vicente, and José Neves

Abstract—The deterioration of concrete structures is one of the major concerns of our society. Indeed, concrete is a relatively sensitive material, which degrades throughout time. Factors like age, use, periodic maintenance, type of environmental exposure and aggression by biological, chemical, mechanical and physical agents are important to determine the level of degradation of the concrete structures. Logic Programming was used for knowledge representation and reasoning, letting the modeling of the universe of discourse in terms of defective data, information and knowledge. Artificial Neural Networks were used in order to evaluate the deterioration of concrete structures and the degree of confidence that one has on such a happening.

Keywords—Artificial Neuronal Networks, Concrete Degradation, Knowledge Representation and Reasoning, Logic Programming.

I. INTRODUCTION

DESPITE its ancient origin, concrete is considered a modern material used in the majority of today's constructions. Concrete is a composite material formed by coarse granular material (the aggregate or filler) embedded in hard matrix of material (the cement or binder) that fills the space among aggregate particles and glues them together [1]. Concrete exhibits high compressive strength but a low tensile one. To avoid this weakness concrete is usually reinforced with materials like steel, which in turn gives rise to other problems like corrosion. Concrete has a very low coefficient of thermal expansion and shrinks as it matures. All concrete structures will crack to some extent, due to shrinkage and tension [2]. Another fundamental limitation of concrete is that it is very sensitive to the conditions in which it is mixed and applied. There are a large number of variables that affect the concrete quality. The lack of attention given to these variables makes concrete more vulnerable and it has been the reason why the service lifespan of many contemporary concrete structures has

been unexpectedly short [3]. Concrete is a relatively sensitive material that degrades throughout time, i.e. even if it is well made, sooner or later the defects, which define the deterioration, will appear. For this reason, concrete structures suffer a natural aging caused by the environment (e.g. rain, sun, pollution, wind) and by normal use.

The deterioration of concrete structures can be categorized in different ways (e.g. in terms of damage types, causes, mechanisms of attack, frequency of defects, financial loss or cost of repair [4]). The present study adopts a classification based on the causes of attack. Thus, the causes of attack are grouped in four main families, namely chemical, physical, biological and mechanical factors as illustrated in Fig. 1.

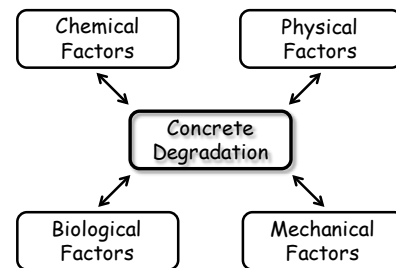


Fig. 1 Origins of the deterioration of concrete structures

The chemical factors include the chemical reactions causing deterioration of concrete structures like carbonation, chloride attack, effects of acids and sulphates and alkali-aggregate reactions. The physical factors include freezing-thawing cycles, shrinkage and cracking and exposure to temperature extremes such as freezing or fire. The biological factors include the effects of biological agents like microorganisms, fungi, algae and moss. Finally the mechanical factors include abrasion, erosion and cavitation.

Carbonation occurs due to the penetration of atmospheric carbon dioxide into the concrete. In contact with the pore water, the carbon dioxide produces carbonic acid that reacts with calcium hydroxide, creating a slightly less alkaline environment for the reinforcement rods. The passivating film is neutralised and the rods are exposed to aggression by the oxygen.

The aggression by chlorides occurs when concrete is in contact with environments with high chloride content like seawater or de-icing salts or if concrete was prepared using contaminated raw materials. Chlorides attack the passivating film and the rods are exposed to aggression by the oxygen.

This work is funded by National Funds through the FCT - Fundação para a Ciência e a Tecnologia (Portuguese Foundation for Science and Technology) within projects PEst-OE/EEI/UI0752/2014 and PEst-OE/QUI/UI0619/2012.

Guida Gomes is with the Department of Informatics, University of Minho, Braga, Portugal (e-mail: mguida.mgomes@gmail.com).

Henrique Vicente is with the Department of Chemistry & Évora Chemistry Centre, School of Science and Technology, University of Évora, Évora, Portugal (corresponding author to provide phone: +351-266745315; fax: +351-266745303; e-mail: hvicente@uevora.pt).

José Neves is with the CCTC/Department of Informatics, University of Minho, Braga, Portugal (e-mail: jneves@di.uminho.pt).

Sulphate ions may be present in water and in the ground, and may also be found directly in the aggregates as impurities. The water-soluble sulphates penetrate into concrete pore water and react with aluminates or calcium hydroxide in cement paste. The reaction products expand remarkably, which causes crack propagation and decreases the strength properties of concrete.

Alkali-aggregates reactions may cause considerable expansion and serious deterioration of concrete structures. Reactive siliceous minerals in the aggregate react with alkaline hydroxides originating usually from cement. Alkali-silicate gel is formed in the voids and cracks of the aggregate or on the surface of the aggregate. In contact with water, the gel can expand about 5% to 20% in volume. Internal pressures are generated and eventually cracking can destroy the concrete structure. Thawing and freezing is the most common weather related physical factor. Freeze-thaw damage is generated by repeated hydraulic pressures caused by volume expansion when water turns to ice (volume increases by 9%). In each successive freeze-thaw cycle, the cumulative effect causes expanding deterioration of concrete. The deterioration is visible in the form of cracking, scaling, and general degradation of the surface paste.

The exposure to temperature extremes like fire causes severe damage on concrete structures. The main harm in fire is caused by a combination of the effects of smoke and gases, which are emitted from burning materials, and the effects of flames and high air temperatures. The most serious form of damage to concrete under fire is explosive spalling, which occurs usually during the first 30 minutes after fire starts. The conventional explanation of explosive spalling is that it is caused by the build-up of water vapor pressure in concrete during fire and thermal stresses. During fire concrete undergoes severe microstructural changes that lead to irreversible structural damage. More details about the effect of fire on concrete and concrete structures can be found in [5].

Mechanical abrasion of concrete surfaces occurs when a material is repeatedly struck by particles from a harder body, due to the friction that the harder powder particles exercise on the surface of the material. This type of deterioration can be caused by different agents like the slid of different materials or wheels. Erosion is a particular form of wear due to wind, water or ice that provokes the removal of material from the concrete surface. Cavitation is caused by flowing water when the pressure changes abruptly. The air bubbles (formed in the water flow downstream) collapse and create a strong impact on the concrete surface. If the speed of the water is particularly high damage may be serious.

Solving problems related to degradation of concrete requires a proactive strategy. Thus, the development of models to evaluate the degradation of concrete may be a way to solve or minimize the problem. This work introduces a computational system to evaluate the degradation of concrete centred on logic programming to knowledge representation and reasoning, complemented with a computational framework based on Artificial Neural Networks.

II. KNOWLEDGE REPRESENTATION AND REASONING

Many approaches for knowledge representation and reasoning have been proposed using the *Logic Programming (LP)* paradigm, namely in the area of Model Theory [6]–[8], and Proof Theory [9], [10]. We follow the proof theoretical approach and an extension to the *LP* language, to knowledge representation and reasoning. An *Extended Logic Program (ELP)* is a finite set of clauses in the form:

$$p \leftarrow p_1, \dots, p_n, \text{not } q_1, \dots, \text{not } q_m \quad (1)$$

$$?(p_1, \dots, p_n, \text{not } q_1, \dots, \text{not } q_m) \quad (n, m \geq 0) \quad (2)$$

where $?$ is a domain atom denoting falsity, the p_i , q_j , and p are classical ground literals, i.e., either positive atoms or atoms preceded by the classical negation sign \neg [10]. Under this representation formalism, every program is associated with a set of abducibles [6], [8], given here in the form of exceptions to the extensions of the predicates that make the program. Once again, LP emerged as an attractive formalism for knowledge representation and reasoning tasks, introducing an efficient search mechanism for problem solving.

Due to the growing need to offer user support in decision making processes some studies have been presented [11], [12], related to the qualitative models and qualitative reasoning in Database Theory and in Artificial Intelligence research. With respect to the problem of knowledge representation and reasoning in Logic Programming (LP), a measure of the *Quality-of-Information (QoI)* of such programs has been object of some work with promising results [13], [14]. The *QoI* with respect to the extension of a predicate i will be given by a truth-value in the interval $[0,1]$, i.e., if the information is *known (positive)* or *false (negative)* the *QoI* for the extension of *predicate_i* is 1. For situations where the information is unknown, the *QoI* is given by:

$$QoI_i = \lim_{N \rightarrow \infty} \frac{1}{N} = 0 \quad (N \gg 0) \quad (3)$$

where N denotes the cardinality of the set of terms or clauses of the extension of *predicate_i* that stand for the incompleteness under consideration. For situations where the extension of *predicate_i* is unknown but can be taken from a set of values, the *QoI* is given by:

$$QoI_i = 1 / \text{Card} \quad (4)$$

where Card denotes the cardinality of the *abducibles* set for i , if the *abducibles* set is disjoint. If the *abducibles* set is not disjoint, the *QoI* is given by:

$$QoI_i = \frac{1}{c_1^{\text{Card}} + \dots + c_{\text{Card}}^{\text{Card}}} \quad (5)$$

where $c_{\text{Card}}^{\text{Card}}$ is a card-combination subset, with Card elements. The next element of the model to be considered is the relative importance that a predicate assigns to each of its attributes

under observation, i.e., w_i^k , which stands for the relevance of attribute k in the extension of $predicate_i$. It is also assumed that the weights of all the attribute predicates are normalized, i.e.:

$$\sum_{1 \leq k \leq n} w_i^k = 1, \forall_i \quad (6)$$

where \forall denotes the universal quantifier. It is now possible to define a predicate's scoring function $V_i(x)$ so that, for a value $x = (x_1, \dots, x_n)$, defined in terms of the attributes of $predicate_i$, one may have:

$$V_i(x) = \sum_{1 \leq k \leq n} w_i^k \times QoI_i(x)/n \quad (7)$$

It is now possible to engender all the possible scenarios of the universe of discourse, according to the information given in the logic programs that endorse the information depicted in Fig. 3, i.e., in terms of the extensions of the predicates *General Information*, *Biological Effects*, *Chemical Effects*, *Mechanical Effects*, *Physical Effects* and *Environmental Exposure*.

It is now feasible to rewrite the extensions of the predicates referred to above, in terms of a set of possible scenarios according to productions of the type:

$$predicate_i((x_1, \dots, x_n)) :: QoI \quad (8)$$

and evaluate the *Degree of Confidence (DoC)* given by $DoC = V_i(x_1, \dots, x_n)/n$, which denotes one's confidence in a particular term of the extension of $predicate_i$. To be more general, let us suppose that the Universe of Discourse is described by the extension of the predicates:

$$a_1(\dots), a_2(\dots), \dots, a_n(\dots) \text{ where } (n \geq 0) \quad (9)$$

Therefore, for a given *scenario*, one may have (where \perp denotes an argument value of the type unknown; the values of the others arguments stand for themselves):

$$\left\{ \begin{array}{l} \neg a_1(x_1, y_1, z_1) \leftarrow not a_1(x_1, y_1, z_1) \\ a_1([7, 8], 15, \perp) :: 0.75 \\ \quad \underline{[5, 10][3, 25][0, 5]} \\ \quad \text{attribute's domains for } x_1, y_1, z_1 \\ \\ \neg a_2(x_2, y_2, z_2) \leftarrow not a_2(x_2, y_2, z_2) \\ a_2([33, 42], [10, 12], \perp) :: 0.6 \\ \quad \underline{[20, 50] [6, 14] [200, 500]} \\ \quad \text{attribute's domains for } x_2, y_2, z_2 \\ \\ \vdots \end{array} \right.$$

↓ 1st interaction: transition to continuous intervals

$$\left\{ \begin{array}{l} \neg a_1(x_1, y_1, z_1) \leftarrow not a_1(x_1, y_1, z_1) \\ a_1([7, 8], [15, 15], [0, 5]) :: 0.75 \\ \quad \underline{[5, 10] [3, 25] [0, 5]} \\ \quad \text{attribute's domains for } x_1, y_1, z_1 \\ \\ \neg a_2(x_2, y_2, z_2) \leftarrow not a_2(x_2, y_2, z_2) \\ a_2([33, 42], [10, 12], [200, 600]) :: 0.6 \\ \quad \underline{[20, 50] [6, 14] [200, 600]} \\ \quad \text{attribute's domains for } x_2, y_2, z_2 \\ \\ \vdots \\ \\ \Downarrow \text{2nd interaction: normalization } \frac{Y - Y_{min}}{Y_{max} - Y_{min}} \\ \\ \left\{ \begin{array}{l} \neg a_1(x_1, y_1, z_1) \leftarrow not a_1(x_1, y_1, z_1) \\ a_1\left(\left[\frac{7-5}{10-5}, \frac{8-5}{10-5}\right], \left[\frac{15-3}{25-3}, \frac{15-3}{25-3}\right], \left[\frac{0-0}{5-0}, \frac{5-0}{5-0}\right]\right) \equiv \\ a_1([0.4, 0.6], [0.545, 0.545], [0, 1]) :: 0.75 \\ \quad \underline{[0, 1] [0, 1] [0, 1]} \\ \quad \text{attribute's domains for } x_1, y_1, z_1 \\ \\ \neg a_2(x_2, y_2, z_2) \leftarrow not a_2(x_2, y_2, z_2) \\ a_2\left(\left[\frac{33-20}{50-20}, \frac{42-20}{50-20}\right], \left[\frac{10-6}{14-6}, \frac{12-6}{14-6}\right], \left[\frac{200-200}{500-200}, \frac{500-200}{500-200}\right]\right) \equiv \\ a_2([0.433, 0.733], [0.5, 0.75], [0, 1]) :: 0.6 \\ \quad \underline{[0, 1] [0, 1] [0, 1]} \\ \quad \text{attribute's domains for } x_2, y_2, z_2 \\ \\ \vdots \end{array} \right. \end{array} \right.$$

The *Degree of Confidence (DoC)* is evaluated using the equation $DoC = \sqrt{1 - \Delta l^2}$, as it is illustrated in Fig. 2. Here Δl stands for the length of the arguments' intervals, once normalized.

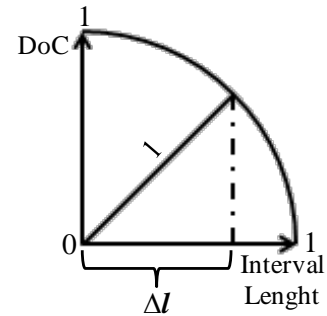


Fig. 2 Degree of Confidence evaluation

Below, one has the expected representation of the universe of discourse, where all the predicates' arguments are nominal. They speak for one's confidence that the unknown values of the arguments fit into the correspondent intervals referred to above.

$$\left. \begin{array}{l}
 \neg a_{1DoC}(x_1, y_1, z_1) \leftarrow \text{not } a_{1DoC}(x_1, y_1, z_1) \\
 a_{1DoC}(0.98, \quad 1, \quad 0) \quad :: \quad 0.75 \\
 \quad \underline{[0.4, 0.6] [0.545, 0.545] [0, 1]} \\
 \quad \text{attribute's values ranges for } x_1, y_1, z_1 \\
 \quad \underline{[0, 1] \quad [0, 1] \quad [0, 1]} \\
 \quad \text{attribute's domains for } x_1, y_1, z_1 \\
 \\
 \neg a_{2DoC}(x_2, y_2, z_2) \leftarrow \text{not } a_{2DoC}(x_2, y_2, z_2) \\
 a_{2DoC}(0.95, \quad 0.97, \quad 0) \quad :: \quad 0.6 \\
 \quad \underline{[0.433, 0.733] [0.5, 0.75] [0, 1]} \\
 \quad \text{attribute's values ranges for } x_2, y_2, z_2 \\
 \quad \underline{[0, 1] \quad [0, 1] \quad [0, 1]} \\
 \quad \text{attribute's domains for } x_2, y_2, z_2 \\
 \\
 \vdots
 \end{array} \right\}$$

III. A CASE STUDY

Therefore, and in order to exemplify the applicability of our model, we will look at the relational database model, since it provides a basic framework that fits into our expectations [15], and is understood as the genesis of the LP approach to knowledge representation and reasoning.

Consider, for instance, the scenario where a relational database is given in terms of the extensions of the relations or predicates depicted in Fig. 3, which stands for a situation where one has to manage information about concrete structures. Under this scenario some incomplete data is also available. For instance, in relation *Biological Effects* the presence/absence of microorganisms for case 2 is unknown, while in relation *General Information* the *Age* value for example 1 ranges in the interval [50,60].

The *Environmental Exposure* database (Fig. 3) is populated according to [16]. Thus, 0 (zero) and 1 (one), in column *Risk of Corrosion* denote, respectively, *absence* and *existence* of corrosion risk. *Corrosion by Carbonation* is classified between 1 (one) and 4 (four). 1 (one) for sub-class XC1, 2 (two) for sub-class XC2, 3 (three) for sub-class XC3 and 4 (four) for sub-class XC4. *Corrosion by Chlorides* (except *seawater*) is categorized between 0 (zero) and 3 (three). 0 (zero) means absence of corrosion by chlorides, 1 (one), 2 (two) and (three) stand, respectively, for sub-classes XD1, XD2 and XD3. Similarly, *Corrosion by Sea Water Chlorides* ranges between 0 (zero) and 3 (three). 0 (zero) means absence of corrosion by seawater chlorides, 1 (one), 2 (two) and (three) denote, respectively, the sub-classes XS1, XS2 and XS3. *Impact of Freeze/Thaw Cycles* is rated between 1(one) and 4 (four), respectively for sub-classes XF1, XF2, XF3 and XF4. The last one, *Chemical Agents*, is classified between 1 (one) and 3 (three), respectively for sub-classes XA1, XA2 and XA3. The value of *Environmental Exposure* in *Concrete Deterioration* database is calculated by:

$$\text{Environmental Exposure} = X0 \times (XC + XD + XS) + XF + XA \quad (10)$$

where $X0$, XC , XD , XS , XF and XA denote the values of the respective column in *Environmental Exposure* database. In this way this value is set between [2,14].

The values of the *Biological*, *Chemical*, *Mechanical* and *Physical Effects* in *Concrete Deterioration* database are the sum of the respective values, ranging between [0,3] for the two first effects and between [0,4] for the remaining ones. In *Biological Effects* database the column *Animals* includes the presence/absence of insects, birds, rodents, termites, worms. The column *Other* encompasses the presence/absence of seeds, roots, moulds, fungi, moss, algae.

Now, we may consider the extensions of the relations given in Fig. 3 to populate the extension of the *concrete* predicate, given in the form:

$$\text{concrete} : \text{Age}, L_{ast} I_{nspection}, U_{sage}, \text{Bio}logical\ Effects, \\
 \text{Chem}ical\ Effects, \text{Mech}anical\ Effects, \text{Phy}sical\ Effects, \\
 \text{Env}ironmental\ Exposure \rightarrow \{0,1\}$$

where 0 (zero) and 1 (one) denote, respectively, the truth-values *false* and *true*. It is now possible to give the extension of the predicate *concrete*, in the form:

$$\left\{ \begin{array}{l}
 \neg \text{concrete} (\text{Age}, LI, U, \text{Bio}, \text{Chem}, \text{Mech}, \text{Phy}, \text{Env}) \\
 \leftarrow \text{not concrete} (\text{Age}, LI, U, \text{Bio}, \text{Chem}, \text{Mech}, \text{Phy}, \text{Env}) \\
 \\
 \text{concrete} ([50,60], 3, \quad 2, \quad 1, \quad 1, \quad 1, \quad 2, \quad 5) :: 1 \\
 \quad \underline{[0,150][0,25][1,3][0,3][0,3][0,4][0,4][2,14]} \\
 \quad \text{attribute's values ranges} \\
 \\
 \text{concrete} (37, \quad \perp, \quad 1, \quad \perp, \quad 1, \quad 1, \quad 1, \quad 11) :: 1 \\
 \quad \underline{[0,150][0,25][1,3][0,3][0,3][0,4][0,4][2,14]} \\
 \quad \text{attribute's values ranges}
 \end{array} \right\}$$

In this program, the first clause denotes the closure of predicate *concrete*. The next clauses correspond to two terms taken from the extension of the *concrete* relation. It is now possible to have the arguments of the predicates extensions normalized to the interval [0, 1], in order to compute one's confidence that the nominal values of the arguments under considerations fit into the intervals depicted previously. One may have:

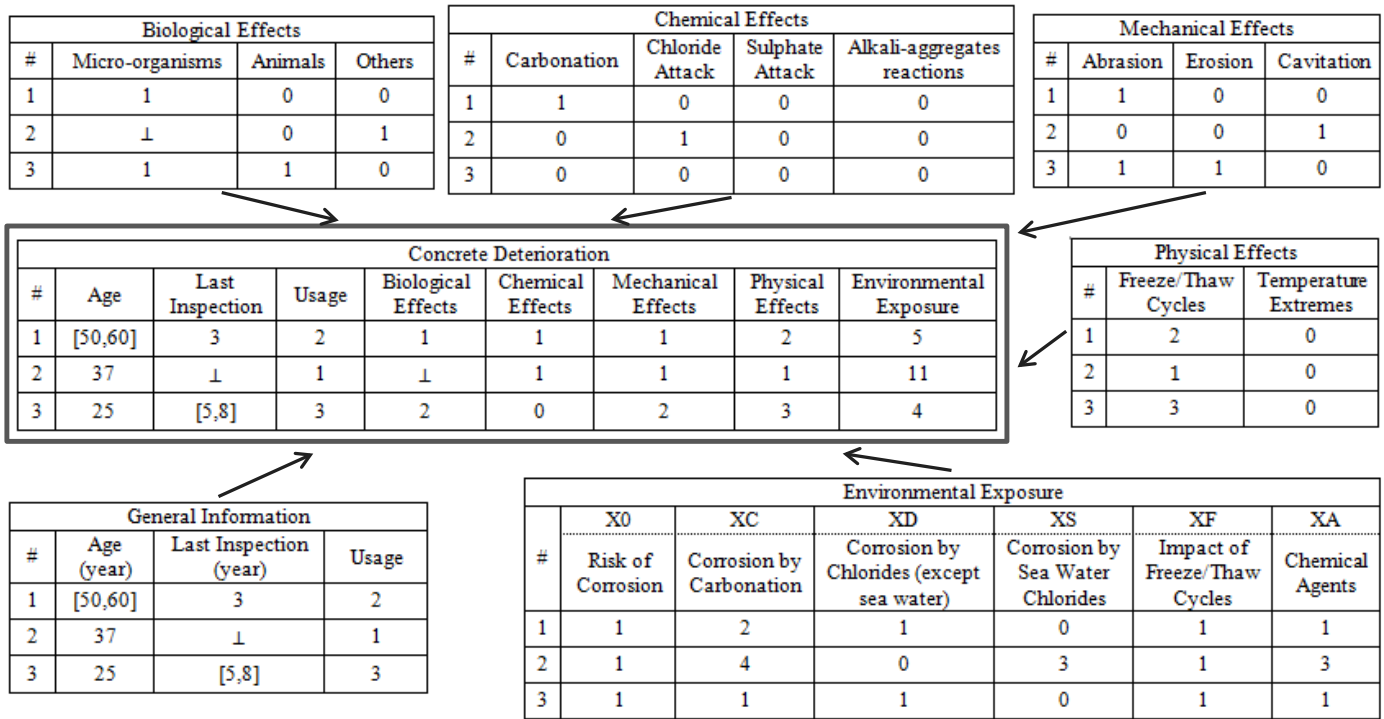


Fig. 3 An extension of the relational database model. In column *Usage* of *General Information* database, 1 (one), 2 (two) and 3 (three) stand, respectively, for *low*, *regular* and *high usage*. In column *Freeze/Thaw Cycles* of *Physical Effects* database, 1 (one), 2 (two) and 3 (three) denote, respectively, *rare*, *frequent* and *very frequent* exposure to freeze/thaw cycles. In the remaining columns of *Biological*, *Chemical*, *Mechanical* and *Physical Effects* 0 (zero) denotes *absence* and 1 (one) denotes *presence*

```

{
  ¬concrete (Age, LI, U, Bio, Chem, Mech, Phy, Env) ← not concrete (Age, LI, U, Bio, Chem, Mech, Phy, Env)

  concrete([0.33,0.4], [0.12,0.12], [0.5,0.5], [0.33,0.33], [0.33,0.33], [0.25,0.25], [0.5,0.5], [0.25,0.25]) :: 1
      [0,1]      [0,1]      [0,1]      [0,1]      [0,1]      [0,1]      [0,1]      [0,1]
      attribute's domains

  concrete([0.247,0.247], [0,1], [0,0], [0,1], [0.33,0.33], [0.25,0.25], [0.25,0.25], [0.75,0.75]) :: 1
      [0,1]      [0,1] [0,1] [0,1]      [0,1]      [0,1]      [0,1]      [0,1]
      attribute's domains
}
    
```

The logic program referred to above, is now presented in the form:

```

{
  ¬concreteDoc(Age, LI, U, Bio, Chem, Mech, Phy, Env) ← not concreteDoc(Age, LI, U, Bio, Chem, Mech, Phy, Env)

  concreteDoc(0.998, 1, 1, 1, 1, 1, 1, 1) :: 1
      [0.33,0.4], [0.12,0.12], [0.5,0.5], [0.33,0.33], [0.33,0.33], [0.25,0.25], [0.5,0.5], [0.25,0.25]
      attribute's values ranges
      [0,1]      [0,1]      [0,1]      [0,1]      [0,1]      [0,1]      [0,1]      [0,1]
      attribute's domains
}
    
```

$$\begin{aligned}
 & \text{concrete}_{DoC} (1, \quad 0, \quad 1, \quad 0, \quad 1, \quad 1, \quad 1, \quad 1) \quad :: \quad 1 \\
 & \quad \underbrace{[0.247,0.247], [0,1], [0,0], [0,1], [0.33,0.33], [0.25,0.25], [0.25,0.25], [0.75,0.75]}_{\text{attribute's values ranges}} \\
 & \quad \underbrace{[0,1] \quad [0,1] \quad [0,1] \quad [0,1] \quad [0,1] \quad [0,1] \quad [0,1] \quad [0,1]}_{\text{attribute's domains}} \\
 &)
 \end{aligned}$$

where its terms make the training and test sets of the Artificial Neural Network given below (Fig. 4).

IV. ARTIFICIAL NEURAL NETWORKS

In [17]–[19] it is shown how Artificial Neural Networks (ANNs) could be successfully used to model data and capture complex relationships between inputs and outputs. ANNs simulate the structure of the human brain being populated by multiple layers of neurons. As an example, let us consider the third case presented in Fig. 3, where one may have a situation that may lead to concrete degradation, which is given in the form:

$$\begin{aligned}
 & \{ \text{concrete attributes (Age, LI, U, Bio, Chem, Mech, Phy, Env)} \\
 & \quad \Downarrow \\
 & \text{concrete (25, \quad [5,8], \quad 3, \quad 2, \quad 0, \quad 2, \quad 3, \quad 4) \quad :: \quad 1} \\
 & \quad \underbrace{[0,150] \quad [0,25] \quad [1,3] \quad [0,3] \quad [0,3] \quad [0,4] \quad [0,4] \quad [2,14]}_{\text{attribute's domains}} \\
 & \quad \Downarrow \text{ 1st interaction: transition to continuous intervals} \\
 & \text{concrete}([25,25], [5,8], [3,3], [2,2], [0,0], [2,2], [3,3], [4,4]) \\
 & \quad \underbrace{[0,150] \quad [0,25] \quad [1,3] \quad [0,3] \quad [0,3] \quad [0,4] \quad [0,4] \quad [2,14]}_{\text{attribute's domains}} \\
 & \quad \Downarrow \text{ 2nd interaction: normalization } \frac{Y - Y_{min}}{Y_{max} - Y_{min}} \\
 & \text{concrete}([0.17,0.17], [0.2,0.32], [1,1], [0.67,0.67], [0,0], [0.5,0.5], [0.75,0.75], [0.17,0.17]) \quad :: \quad 1 \\
 & \quad \underbrace{[0,1] \quad [0,1] \quad [0,1] \quad [0,1] \quad [0,1] \quad [0,1] \quad [0,1] \quad [0,1]}_{\text{attribute's domains}} \\
 & \quad \Downarrow \text{ DoC calculation: } DoC = \sqrt{1 - \Delta I^2} \\
 & \text{concrete}_{DoC} (1, \quad 0.993, \quad 1, \quad 1, \quad 1, \quad 1, \quad 1, \quad 1) \quad :: \quad 1 \\
 & \quad \underbrace{[0.17,0.17], [0.2,0.32], [1,1], [0.67,0.67], [0,0], [0.5,0.5], [0.75,0.75], [0.17,0.17]}_{\text{attribute's values ranges}} \\
 & \quad \underbrace{[0,1] \quad [0,1] \quad [0,1] \quad [0,1] \quad [0,1] \quad [0,1] \quad [0,1] \quad [0,1]}_{\text{attribute's domains}} \\
 & \}
 \end{aligned}$$

In Fig. 4 it is shown how the normalized values of the interval boundaries and their DoC and QoI values work as inputs to the ANN. The output translates the chance of being necessary to go ahead with an intervention, and $concrete_{DoC}$ the confidence that one has on such a happening. In addition, it also contributes to build a database of study cases that may be used to train and test the ANNs.

V. CONCLUSIONS AND FUTURE WORK

To set a timeline to the maintenance of concrete structures is a hard and complex task, which needs to consider many different conditions with intricate relations among them. These characteristics put this problem into the area of problems that may be tackled by AI based methodologies and techniques to problem solving. Despite that, little to no work has been done in that direction. This work presents the founding of a computational framework that uses powerful knowledge representation and reasoning techniques to set the structure of the information and the associate inference mechanisms. This representation is above everything else, very versatile and capable of covering every possible instance by considering incomplete, contradictory, and even unknown data. The main contribution of this work is to be understood in terms of the evaluation of the DoC , and the possibility to address the issue of incomplete information. Indeed, the new paradigm of knowledge representation and reasoning enables the use of the normalized values of the interval boundaries and their DoC values, as inputs to the ANN. The output translates the chance of the deterioration of concrete structures and the degree of confidence that one has on such a happening. Future work may recommend that the same problem must be approached using other computational frameworks like Case Based Reasoning or Particle Swarm, just to name a few.

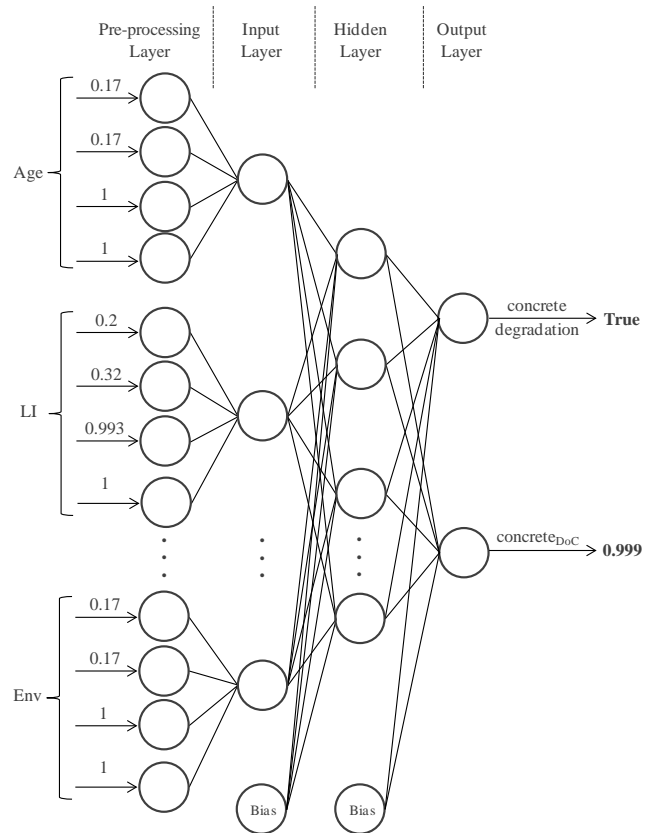


Fig. 4 The Artificial Neural Network topology

REFERENCES

- [1] Z. Li, *Advanced Concrete Technology*. Hoboken, New Jersey: John Wiley & Sons, 2011, ch. 1.
- [2] C. Larosche, "Types and causes of cracking in concrete structures", in *Failure, distress and repair of concrete structures*, N. Delatte, Ed. Cambridge: Woodhead Publishing Limited, 2009, pp. 57-83.
- [3] V. Penttala, "Causes and mechanisms of deterioration in reinforced concrete", in *Failure, distress and repair of concrete structures*, N. Delatte, Ed. Cambridge: Woodhead Publishing Limited, 2009, pp. 3-31.
- [4] K. Kovler and V. Chernov, "Types of damage in concrete structures", in *Failure, distress and repair of concrete structures*, N. Delatte, Ed. Cambridge: Woodhead Publishing Limited, 2009, pp. 32-56.
- [5] G. Khoury, "Effect of fire on concrete and concrete structures", *Progress in Structural Engineering and Materials*, vol. 2, pp. 429-447, October/December 2000.
- [6] A. Kakas, R. Kowalski and F. Toni "The role of abduction in logic programming", in *Handbook of Logic in Artificial Intelligence and Logic Programming*, vol. 5, D. Gabbay, C. Hogger and I. Robinson, Eds., Oxford: Oxford University Press, 1998, pp. 235-324.
- [7] M. Gelfond and V. Lifschitz, "The stable model semantics for logic programming", in *Logic Programming - Proceedings of the Fifth International Conference and Symposium*, R. Kowalski and K. Bowen, Eds. Cambridge: MIT Press, 1988, pp. 1070-1080.
- [8] L. Pereira and H. Anh, "Evolution propection", in *New Advances in Intelligent Decision Technologies - Results of the First KES International Symposium IDT 2009*, K. Nakamatsu, G. Phillips-Wren, L. Jain and R. Howlett Eds. Studies in Computational Intelligence, vol. 199, Berlin: Springer, 2009, pp. 51-64.
- [9] J. Neves, J. Machado, C. Analide, A. Abelha and L. Brito, "The halt condition in genetic programming", in *Progress in Artificial Intelligence - Lecture Notes in Computer Science*, vol 4874, J. Neves, M. F. Santos and J. Machado Eds. Heidelberg: Springer, 2007, pp. 160-169.
- [10] J. Neves, "A logic interpreter to handle time and negation in logic data bases", in *Proceedings of the 1984 annual conference of the ACM on the fifth generation challenge*, R. L. Muller and J. J. Pottmyer Eds. New York: Association for Computing Machinery, 1984, pp. 50-54.

- [11] J. Halpern, *Reasoning about uncertainty*. Massachusetts: MIT Press, 2005.
- [12] B. Kovalerchuck and G. Resconi, "Agent-based uncertainty logic network", in *Proceedings of the IEEE International Conference on Fuzzy Systems – FUZZ-IEEE 2010*, Barcelona, Spain, 2010, pp. 596-603.
- [13] P. Lucas, "Quality checking of medical guidelines through logical abduction", in *Proceedings of AI-2003 (Research and Developments in Intelligent Systems XX)*, F. Coenen, A. Preece and A. Mackintosh, Eds. London: Springer, 2003, pp. 309-321.
- [14] J. Machado, A. Abelha, P. Novais, J. Neves and J. Neves, "Quality of service in healthcare units", *International Journal of Computer Aided Engineering and Technology*, vol. 2, pp. 436-449, 2010.
- [15] Y. Liu and M. Sun, "Fuzzy optimization BP neural network model for pavement performance assessment", in *Proceedings of the 2007 IEEE International Conference on Grey Systems and Intelligent Services*, Nanjing, China, 2007, pp. 18-20.
- [16] *Concrete – Specifications, performance, production and conformity – Complementary instructions for the application of EN 206-1*, UNI Standard 11104:2004.
- [17] A. T. Caldeira, M. R. Martins, M. J. Cabrita, C. Ambrósio, J. M. Arteiro, J. Neves and H. Vicente, "Aroma Compounds Prevision using Artificial Neural Networks Influence of Newly Indigenous *Saccharomyces* SPP in White Wine Produced with *Vitis Vinifera* Cv Siria", in *FOODSIM 2010*, V. Cadavez and D. Thiel Eds. Ghent: Eurosis – ETI Publication, 2010, pp. 33–40.
- [18] H. Vicente, S. Dias, A. Fernandes, A. Abelha, J. Machado, and J. Neves, "Prediction of the Quality of Public Water Supply using Artificial Neural Networks", *Journal of Water Supply: Research and Technology – AQUA*, vol. 61, pp. 446-459, 2012.
- [19] H. Vicente, J. C. Roseiro, J. M. Arteiro, J. Neves and A. T. Caldeira, "Prediction of bioactive compounds activity against wood contaminant fungi using artificial neural networks", *Canadian Journal of Forest Research*, vol. 43, pp. 985-992, 2013.

Non-destructive detection of metal fibres in cementitious composites

Jiří Vala, Leonard Hobst and Vladislav Kozák

Abstract—Development of non-destructive methods for the control of metal fibers in cementitious composites concrete is needed to certify the volume fraction of fibers and their directions, crucial for the mechanical properties of a composite. Based on the research experience of authors, namely on the Brno University of Technology, the paper demonstrates advantages and restriction of several useful classes of methods, namely of i) the planar X-ray imaging, with the discrete fast Fourier transform applied to image processing, ii) the magnetic approach, utilizing the Hall probe and advanced considerations on material homogenization (with certain electromagnetic alternative), iii) the computed tomography, as an unique exact method for the detection of volume fraction without breaking the sample, with an information on (an)isotropy as a benefit.

Index Terms—Cementitious composites, non-destructive testing, electromagnetic measurements, image processing, computational simulation.

I. INTRODUCTION

ADVANCED building structures make frequently use of materials as silicate composites, reinforced by metal particles (e. g. steel-fibre-reinforced concrete), preventing the tension stresses and strains as sources of undesirable micro- and macro-cracking. Mechanical properties of such composites are determined by the choice of fibre properties and their volume fraction, location and orientation in the matrix, sensitive to the technological procedures (as special compaction) and to the early-age treatment – cf. [11], as well as by the bond/slip interface relations – cf. [2]. The employment of the destructive approach relies usually on the separation of particles, taken from the early-age matrix, alternatively obtained from the crushed part of the existing structure, in the laboratory; consequently the volume fraction of particles can be evaluated accurately, whereas any information related to the original orientation of particles is missing. Moreover, such experiments with many structures are not allowed by technical standards. This is a strong motivation for the employment of some reliable non- or (at least) semi-destructive measurement methods, applicable in situ, handling homogeneity and isotropy and detecting the volume fraction of fibres in the material structure.

Regardless of the significant progress in this research area in the last decade (for more historical remarks and references see [7]), no inexpensive, robust and reliable method is available, thus all identification approaches rely on a) some indirect measurements and b) non-trivial numerical analysis, to handle a corresponding inverse problem – typically ill-posed, unstable, etc., forcing artificial regularization. Since a) produce quite

other information than needed volume fractions and directional distributions of fibres, typically digital images in pixels or voxels, or electromagnetic quantities detected on the specimen surface, some calibration relations are needed, motivated by the physical and geometrical similarity. Moreover, some reasonable algorithm for the evaluation of effective material properties, using the properties of matrix and particles and the geometrical configuration, as input data, is needed: from simple arguments from the mixture theory to complicated physical and mathematical homogenization techniques (which will be specified later, in connection with electromagnetic measurements).

In this paper we shall pay attention thanks to the research experience of the authors from BUT (Brno University of Technology), namely to three representative approaches:

- i) the planar X-ray imaging, with the discrete fast Fourier transform applied to image processing,
- ii) the magnetic approach, utilizing the Hall probe and advanced considerations on material homogenization (with certain electromagnetic alternative),
- iii) the computed tomography, as an only exact method for the detection of volume fraction without breaking the sample, with an information on (an)isotropy as a benefit.

II. ANALYSIS OF X-RAY IMAGES

The radiographic approach, developed in [6] for a rather large class of building materials, comes from the gray-scale planar images and some of their post-processing modifications, in particular:

- 1) the reduction of all fibres (whose length and thickness is known) to one-pixel thick black curves, followed by the simplified evaluation of their amount and orientation, by [6],
- 2) the application of the two-dimensional fast Fourier transform by [9], avoiding most artificial image changes, where the same as in 1) can be identified with a special diffraction process: for a the gray level at pixel coordinates $f(x, y)$, related to a square image containing $N \times N$ pixels (with N tending to ∞ theoretically), the direct and inverse Fourier transforms are

$$F(u, v) = \sum_{x=0}^{N-1} \sum_{y=0}^{N-1} f(x, y) \exp(-2\pi i(ux + vy)/N),$$

$$N^2 f(x, y) = \sum_{u=0}^{N-1} \sum_{v=0}^{N-1} F(u, v) \exp(2\pi i(ux + vy)/N)$$

and the power spectrum $P(u, v) = |F(u, v)|^2$ contain the useful information, needed for the derivation of the histograms of fibre directions.

J. Vala and L. Hobst are with the Brno University of Technology, Faculty of Civil Engineering, Czech Republic, 602 00 Brno, Veveří 95.

V. Kozák is with the Institute of Physics of Materials, Academy of Sciences of the Czech Republic, 616 62 Brno, Žitkova 22.

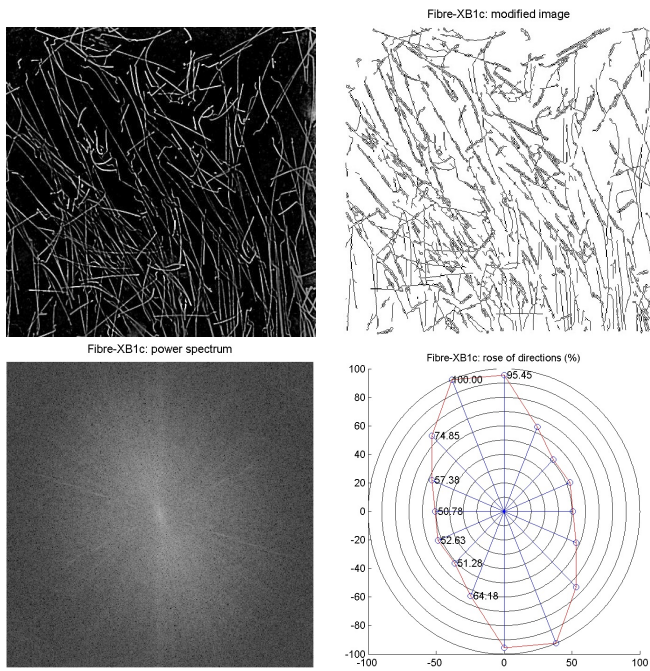


Fig. 1. Evaluation of fibre orientation from the X-ray image: original image (left upper photo), result of fibre localization (right upper image), power spectrum P (left lower graph), resulting rose of fibre directions (right lower graph).



Fig. 2. X-ray machine EcoRay HF 1040 with digital recording to PC equipment (left photo). PeMaSo-01 depth probe for magnetic measurements (right photo).

Figure 1 presents an example of such MATLAB-supported evaluation of fibre orientation in the fibre concrete specimen; the utilized X-ray equipment is shown on Figure 2. In general, the radiographic analysis gets useful results related to preferential orientations of fibres, although limited to data from planar images, even from several views to cubic specimens. The estimate of volume fraction of fibres is not very precise, at least in the comparison with destructive tests.

III. NUMERICAL TREATMENT OF MAGNETIC MEASUREMENTS

Magnetic measurements like [20] and [4] rely on the different values of relative permeability of fibres and a matrix, with possible alternative of electrical measurements and relative permittivity. The special experimental configuration usually tries to force a (nearly) stationary process, whose mathematical description works with a differential operator close to the classical Laplace one, to enable non-expensive software simulation. Figure 3 shows the geometrical configuration of such process numerical simulation of such process in COMSOL: the magnetic field is generated by several permanent magnets,

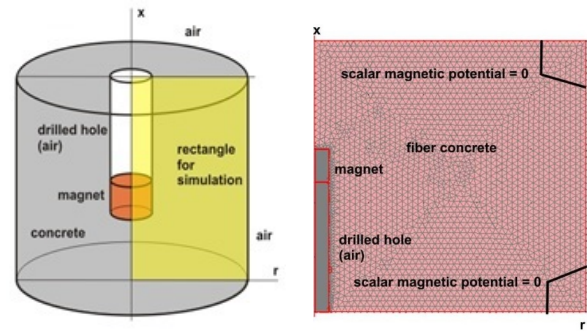


Fig. 3. Radially symmetric geometrical arrangement of the magnetic experiment (left scheme) and computational simplification, including finite/infinite element mesh (right scheme).

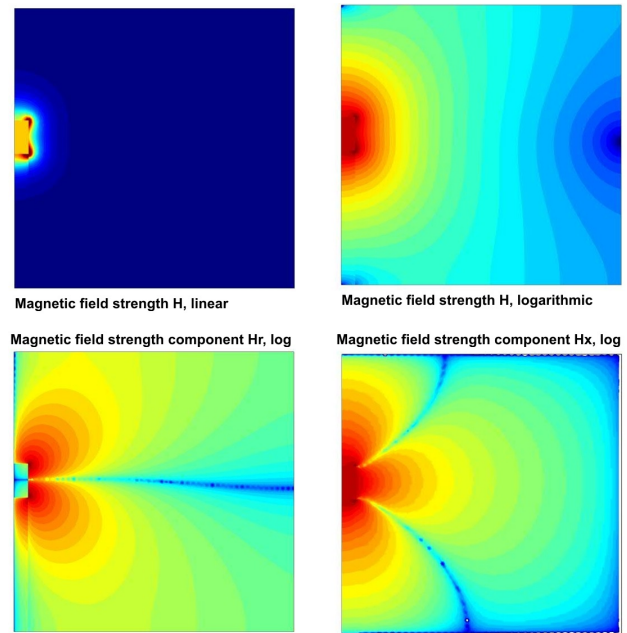


Fig. 4. Results of COMSOL based finite/infinite element simulation of stationary magnetic field strength.

located in the drilled hole (thus this method could be classified as low-invasive, not non-destructive completely), consequently the Hall effect based probe from Figure 2 detects the magnetic field strength. Figure 4 documents the numerical simulation of such experiment, applying the COMSOL supported planar finite/infinite element technique: the influence of the irregularities caused by an artificial hall seems to be not substantial. The comparative simulation, applying only selected functions of *pde* toolbox from MATLAB, leads to the same conclusion.

The crucial problem is now to implement a correct evaluation procedure for an effective relative permeability (or permittivity) using the incomplete data on the material microstructure and on relative permeability of fibres. For spherical particles the classical Maxwell-Garnett mixing formula is available; the generalization of [5] comes from the so-called Bruggemann approach and the repeated usage of similar ellipsoids as reference volume elements, whereas [13] admits the presence of multiple scattering, important for high volume fractions of fibres. No additional physical assumption are needed, again for periodic spheres, in [12]: the auxiliary problem, referring to the mathematical theory of homogenization of elliptic operators,

can be then analyzed (including the existence and uniqueness of solution, the convergence of sequences of approximate solutions, etc.) using the two-scale and similar convergence theorems by [1]; the crucial (seemingly) explicit formula for the evaluation of an effective parameter value, comes from the method of oscillating test functions. In [21] the difficulties with complex particle shapes are handled using the boundary integral approach, thanks to the knowledge of general solutions of the Laplace equation, with Heaviside characteristic functions of particles; [10] admits a priori anisotropic structures. Unfortunately, further generalization of this approach (namely to non-periodic structure, avoiding all mixing tricks), lead to non-trivial (partially still open) problems of mathematical analysis, namely to the convergence using probability measures by [18], thus various alternative statistical approaches, as that with Sobol sensitivity indices and Monte Carlo simulations by [8], have been developed.

The unique material characteristics included here is the magnetic permeability μ [Vs/(Am)]; at least in the case of silicate composites used in civil engineering μ can be set to 1 for the pure matrix, but no relevant constant is guaranteed by the producers of ferromagnetic fibres. In practice, the dimensionless relative permeability $\mu_r = \mu/\mu_0$, using the well-known magnetic constant $\mu_0 = 4\pi \cdot 10^{-7}$ Vs/(Am), is usually considered; similarly the relative permeabilities μ_c for the matrix and μ_s for all fibres can be introduced. Fortunately, for a sufficiently slow volume fraction ξ of fibres ($\xi \leq 0.05$ in real experiments), following [5], under the assumption of random orientation of fibres, we obtain an explicit monotone and continuous dependence between μ and ξ in the form

$$\xi = 1 - M \frac{\mu_s - \mu_r}{\mu_s - \mu_c} \left(\frac{\mu_c}{\mu_s} \right)^{3L(1-2L)(2-3L)}$$

where the factors

$$M = \left(\frac{M_1}{M_2} \right)^{2(3L-1)^2 / ((2-3L)(1+3L))},$$

$$L = \frac{\varsigma}{4\vartheta^3} \left(2\varsigma\vartheta + \ln \frac{\varsigma - \vartheta}{\varsigma + \vartheta} \right)$$

are determined using the ratio ς of lengths of a major and (both) minor axes of ellipsoidal particles (clearly $\varsigma > 1$) for the simplifying notation $\vartheta = \sqrt{\varsigma^2 - 1}$ and $M_1 = (1+3L)\mu_c + (2-3L)\mu_s$, $M_2 = (1+3L)\mu_r + (2-3L)\mu_s$. In particular, for a (theoretically) infinite length and zero diameter of particles we receive $L = 1/3$. Unfortunately, all attempts to generalize this result for more complicated distributions of fibre directions lead to unpleasant non-analytical integrals, with the duty of their non-trivial numerical evaluations.

Figure 6 documents the least squares based identification of μ_r for 3 input data sets with assumed $\mu_r = 1$ for pure concrete and uncertain μ_s in all other cases, using the above sketched formulae for an isotropic medium. the specimens (unlike the situation in situ) were prepared with exact volume fractions of fibres 0.5%, 1% and 1.5%. Other experiments with comparable results have been performed by the authors' team with magnetic field induced by an electric coil. Moreover, [3] presents a totally non-destructive equipment, applicable

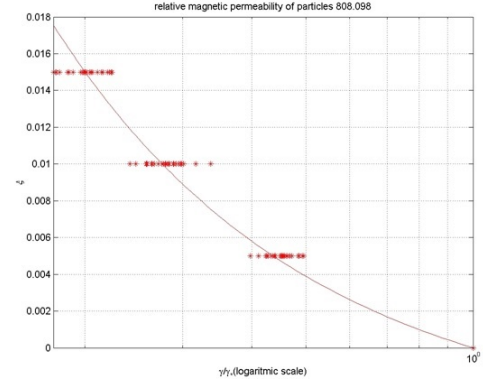


Fig. 5. Application of the least squares technique to the identification of parameters ξ and μ_s from magnetic measurements.

to the surface of a specimen (thus preferring fibres close to such surface). All these result seem to give good estimates of volume fractions (whose improvement using more advanced mathematical analysis is possible), but the differentiating between system and random errors in distributions of fibre directions is difficult.

IV. COMPUTED TOMOGRAPHY

A new approach to non-destructive analysis of structures of cementitious composites, motivated by [14] and [19], has been offered by the computed tomography (X-ray CT), generating 3-dimensional images from large series (slices) of 2-dimensional radiographic images taken around a single axis of rotation. The modern industrial tomograph, presented on Figure 6, has been recently installed in the Central European Institute CEITEC of BUT. Unlike most tomographs for medical applications, an analyzed specimen is fixed on the manipulation table of the tomograph, between the radiation source and the surface radiation detector, compound from a matrix of mini-detectors. During the rotation of the table the surface detector records successive changes of X-ray radiation; consequently the specialized computer software is needed to analyze the inner structure of a specimen.

Several types of fibre concrete specimens have been tested using this equipment: whereas some cylindrical specimen is visible on Figure 6, Figure 7 shows the cubic specimen, similar to that from Figure 1, and demonstrates the ability of the specialized software to recognize all fibres completely unlike all approximate estimates from separate planar images. Consequently various forms of histograms or graphical or 3-dimensional roses of directions similar to 2-dimensional ones from Figure 1 can be created. However, this is rather time consuming, expensive and not applicable to the fibre concrete structures in situ. Nevertheless, this seems to be a useful method to obtain a reliable reference basis for all numerical simulation attempts with random positions and orientation of fibres.

V. CONCLUSION

This paper should be understood as an introductory comparative study to the most promisable non-destructive approaches



Fig. 6. Tomograph GE phoenix.v|tome|xL 240 (left photo) and a cylindrical specimen fixed in its manipulator (right photo).

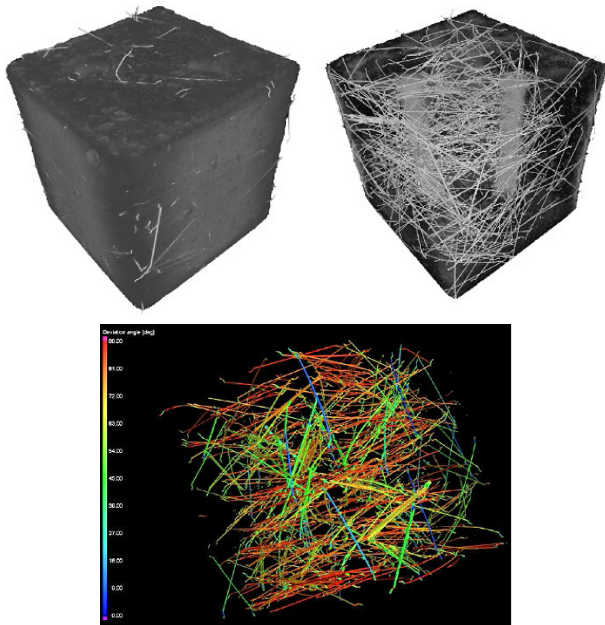


Fig. 7. Cubic fibre concrete specimen, edge length 150 mm, required X-ray tube voltage 300 kV: axonometric view on its surface (left upper image) and inside its structure (right upper image). Axonometric projection of separated fibres in the cube specimen (lower image).

to macroscopic identification of content and random location of fibres in the structure of cementitious composites. However, all introduced approaches have strong restrictions: serious obstacles to get some reasonable estimate of volume fraction of fibres, as the most requested parameter, in the case i), expensive and fastidious experimental setting in the case iii), interpretable as the more sophisticated upgrade of i), both technical and computational difficulties in the case ii).

For the successful computational detection of volume fraction and preferential orientation of fibers, making use of their ferromagnetic properties, both under laboratory and in situ conditions, the crucial point of all considerations is the development of a homogenization procedure, specific to the analyzed class of materials, including its formal verification and its validity range. This leads to non-trivial problems of both physical and mathematical analysis, whose validation seems to be available thanks to the progress in the image processing techniques, consequently their deeper study should belong to the research priorities for the near future.

ACKNOWLEDGMENT

The financial support of the FAST-S-14-2490 research project at BUT is acknowledged.

REFERENCES

- [1] D. Cioranescu and P. Donato, *An Introduction to Homogenization*. Oxford University Press, 1999.
- [2] V. M. C. F. Cunha, J. A. O. Barros and J. M. Sena-Cruz, An integrated approach for modelling the tensile behaviour of steel fibre reinforced self-compacting concrete. *Cement and Concrete Research* 41, 2011, pp. 64–76.
- [3] M. Faifer, L. Ferrara, R. Ottoboni and S. Toscani, Low frequency electrical and magnetic methods for non-destructive analysis of fiber dispersion in fiber reinforced cementitious composites: an overview. *Sensors* 13, 2013, pp. 1300–1318.
- [4] M. Faifer, R. Ottoboni, S. Toscani and L. Ferrara, Nondestructive testing of steel-fiber-reinforced concrete using a magnetic approach. *IEEE Transactions on Instrumentation and Measurement* 60, 2011, pp. 1709–1711.
- [5] S. Giordano, Effective medium theory for dielectric ellipsoids. *Journal of Electrostatics* 58, 2003, pp. 59–76.
- [6] L. Hobst, O. Anton, J. Vodička and J. Ščučka, Homogeneity detection of fibre-concrete structures by using radiographic technique. In: *Nondestructive Testing of Materials and Structures*, Springer 2013, pp. 323–328.
- [7] L. Hobst and P. Bílek, Various control methods developed for fibre concrete structures. *Recent advances in integrity, reliability and failure – 4-th International Conference in Funchal (Madeira)*, 2013, pp. 721–730.
- [8] Z. Kala, Geometrically non-linear finite element reliability analysis of steel plane frames with initial imperfections. *Journal of Civil Engineering and Management* 18, 2012, pp. 81–90.
- [9] S. Kärkkäinen and E. B. Vedel Jensen, Estimation of fibre orientation from digital images. *Image Analysis and Stereology* 20, 2001, pp. 199–202.
- [10] M. Y. Koledintseva, R.E. DuBroff and R.W. Schwartz, Maxwell-Garnett rule for dielectric mixtures with statistically distributed orientations of inclusions. *Progress In Electromagnetics Research* 99, 2009, pp. 131–148.
- [11] A. Krasnikovs, V. Zaharevskis, O. Kononova, V. Lusi, A. Galushchak and E. Zaleskis, Fiber concrete properties control by fibers motion – investigation in fresh concrete during casting. *Industrial Engineering – 8th International DAAAM Baltic Conference* in Tallin, 2012, Part V: Materials Engineering, #10, 6 pp.
- [12] G. Kristensson, Homogenization of spherical inclusions. *Progress in Electromagnetic Research* 42, 2003, pp. 1–25.
- [13] P. Mallet, C. A. Guérin and A. Sentenac, Maxwell-Garnett mixing rule in the presence of multiple scattering: derivation and accuracy. *Physical Review B* 72, 2005, 14205/1–9.
- [14] P. J. M. Monteiro, C. Y. Pichot and K. Belkebir, Computer tomography of reinforced concrete. In: *Materials Science of Concrete*, Chapter 12, American Ceramics Society, 1998.
- [15] G. Nguetseng and N. Svanstedt, σ -convergence. *Banach Journal of Mathematical Analysis* 5, 2011, pp. 101–135.
- [16] M. Pieper and P. Klein, Application of simple, periodic homogenization techniques to non-linear heat conduction problems in non-periodic, porous media. *Heat and Mass Transfer* 48, 2012, pp. 291–300.
- [17] M. Ya. Sushko, Effective permittivity of mixtures of anisotropic particles. *Journal of Physics D: Applied Physics* 42, 2009, 155410: 9 pp.
- [18] N. Svanstedt, Multiscale stochastic homogenization of convection-diffusion equations. *Applications of Mathematics* 53, 2008, pp. 143–155.
- [19] G. Weidemann, R. Stadie, J. Goebels and B. Hillemeier, Computer tomography study of fibre reinforced autoclaved aerated concrete. *Materials Testing* 50, 2008, pp. 278–285.
- [20] H.-J. Wichmann, H. Budelmann and A. Holst, Determination of steel fiber dosage and steel fiber orientation in concrete. In: *Nondestructive Testing of Materials and Structures*, Springer 2013, pp. 239–245.
- [21] K. W. Whites and F. Wu, Effects of particle shape on the effective permittivity of composite materials with measurements for lattices of cubes *IEEE Transactions on Microwave Theory and Techniques* 50, 2002, pp. 1723–1729.

Prof. Leonard Hobst (*1949) is the head of the Institute of Building Testing at the Brno University of Technology, Faculty of Civil Engineering.

Prof. Jiří Vala (*1956) works at the Institute of Mathematics and Descriptive Geometry at the same faculty as Prof. L. Hobst.

Dr. Vladislav Kozák (*1954) is the scientist at the Institute of Physics of Materials in Brno, a part of the Academy of Sciences of the Czech Republic.

Planning the coastal management. The Apulia Region Plan.

Piscitelli C., Rotondo F., Selicato F., Selicato S.

Abstract—The work discuss about the territorial planning methods useful to assure an integrated coastal management. It proposes an integrated method based on a sensitivity analysis of environmental and landscape values, with an hydraulic model of coastal behavior. The method is illustrated in the case of the Apulia Regional Coastal Plan. The Apulia Region is one of the most long coast in Italy, so the coastal management is a relevant need for inhabitants, with many different interests to take in to account simultaneously. The paper is introduced by a presentation of the coast and its problems, illustrating in the second chapter the major coastal policies at national and regional level. In the following five chapters the method proposed is illustrated in the case of the Apulia Regional Coastal Plan, showing tools to pursue an integrated coastal management, while in the last chapter some conclusions are made.

Keywords—territorial planning, coastal management, coastal landscape, multicriteria evaluation.

I. INTRODUCTION

The coast can be defined as the relational element promoting interaction between land and sea, and is considered as a resource not only from the environmental but also from the social and economic standpoints. In the transitional strips between land and water, nature is regulated to an even greater extent than elsewhere by processes with a cyclical sequence, governed by laws that have an intrinsic value, and that can offer opportunities for human lifestyle [1] [2].

However, the spreading man-made processes and invasive land uses for urbanization purposes have contributed to alter, or even to disrupt, these natural cycles. In many cases this has led to a need for new interventions, directed largely to mitigate and foster natural processes rather than to modify their evolution. In fact, the creation of infrastructures and buildings for residential, industrial and recreational settlements, changed agricultural land uses and exploitation of the natural elements;

nowadays, the extraction of groundwater and works carried out to regulate water courses, as well as the extraction of inert materials from rivers and dragging, are just some of the problems facing coastal areas, that are causing the erosion, pollution and destruction of the natural habitats.

In many cases the localization of activities and residential areas on, or near the coast, has given rise to urban sprawl processes, causing the ancient towns built around port to spread out lengthwise in a direction that is emphasized by the tendency to build on the communication systems direction. In addition, the growing tourist demand (for mass tourism) has inspired in most families an increasing desire to possess or make use of holiday homes, preferably by the sea, and so has led to the exploitation of the areas along the coast to institute private beaches, access points, camping sites and tourist reception facilities. These phenomena have caused to occupy large parts of the coastal spaces by settlements that, despite a great variety of aesthetic lines and building quality, are characterized by their nature as residential structures that have little or nothing to do with the pre-existing urban character. Added to this, there is the burden of the waste disposal systems and septic tank systems created to serve these buildings, that often exceed by far the capacity of absorption of the natural environment, thus causing severe harm to many coastal habitats.

Urban sprawl and agricultural and industrial spread are the main causes of coastal erosion. Coastal erosion involves three different types of impact or risks: (i) the loss of areas with an economic, social and ecological value; (ii) the destruction of the natural coastal defences (generally the dunes systems) after just a single catastrophic event, causing flooding of the inland regions; (iii) the weakening or destruction of the artificial coastal defences, causing a potential or real risk of flooding of the land they protected.

An even greater awareness is emerging that a more sustainable concept of the tourist economy needs to be promoted, and the demand of actions and projects emerges to institute integrated management of the seaside, to safeguard the landscape, to improve the quality of the environment and to restore the existing landscape heritage.

II. COASTAL POLICIES IN ITALY AND APULIA REGION

The concentration of populations and human activities along the coasts, that is particularly evident in coastal areas that were

This paper has been elaborated in a shared work by all the authors, also if the chapter III and IV has been written by Claudia Piscitelli, the chapter I and II has been written by Francesco Rotondo, the chapter VII and VIII has been written by Francesco Selicato, the chapter V and VI has been written by Sergio Selicato.

All the authors are with the Civil Engineer and Architecture Department in the Polytechnic University of Bari, via Orabona, 4, 70122, Bari (Italy)(corresponding author to provide phone: 0039-080-5963337; fax:

0039-080-5963348; e-mail: claudia.piscitelli; francesco.rotondo; francesco.selicato@poliba.it).

already heavily populated like those in the Mediterranean, as well as the resulting problems of coastal erosion, have in recent years attracted the attention of different research disciplines and highlighted the need to institute suitable governance measures. The complex natural and man-made phenomena that affect the coast, because of its transitional nature as a land-sea buffer in perennial transformation, need to be closely studied and investigated in the light of their dynamics.

In this scenario, urban territorial and environmental planning has taken on a very important role to make appropriate government policies. Coastal planning, in such circumstances, must therefore target the goal, among many others, of restoring two essential balances, namely the biological and the sedimentological balance, that are at present severely impaired [3] [4] [5].

The issues of coastal governance are closely linked to those of landscape and environment in terms of territorial planning, and have therefore overturned the traditional forms of action for territorial management [6] [7].

The result of this interaction has been the development of a dual attitude to coastal planning that is now being seen as regulatory, of course, but also as strategic and far-seeing. The need for a strategic approach stems from the uncertainties and difficulties in modelling future scenarios for these contexts, and from the need to control cross-scale dynamics, of both an environmental and landscape nature, that are intrinsic to the coastal context. Therefore, with the goal of safeguarding and above all conserving the coastal territory over time, it is important to analyze all those factors now exerting pressure that are disrupting the precarious balances, and to exert more stricter regulation of the different and often conflictual land uses.

In the coastal planning sphere there are in fact some blank areas, where rules are entirely lacking or are inappropriate for coding, planning and managing the coastal territories and their dynamics in an "integrated" fashion. A preliminary investigation of the current scenario in coastal areas highlights the lack of innovative coastal planning methodologies, and demonstrates that those in force are often inadequate to the real needs and so inapplicable to coastal governance at the present time [8]. Starting from the Coastal Zone Management Act approved by the Federal USA Government in 1972, up to more recent schemes for Integrated coastal and marine areas management [9] the planning model that emerges at international level [10] [11] requires coordination among plans of different nature which are drawn up at different levels, by various institutions (ranging from the national government to the local authorities), and it is recognized as necessary to arouse a wide awareness and involvement of both public and private operators in these schemes.

In many nations, this awareness of the critical nature of the issues and the need for a better management of the coastal systems has led to the institution of specific norms, national strategies, regional stability plans, studies, inventories and

research, legislative measures and tools that should contribute to protect the coastline environment. This availability of specific norms is satisfactory but still far from truly effective because there is still a lack of coordination among the tools and subjects that affect the evolution of the coastal zones. This does not only apply to the horizontal relations among the various sectors but also the interactions among the policies and actions instituted at the different levels of territorial responsibility (local, regional, national and European). In fact, too rigid an application of the principle of reciprocal collaboration often leads to divided responsibilities, that are portioned out among the different local authorities without taking into account their many interactions. Owing to this lack of coordination, the complex relations among human activities and the coastal zones are ignored (the single measures often fail to meet the goals or indeed may actually hinder them), as well as the complex nature of these zones, that are affected by number of mutual forces and pressures (this includes the cases of the hydrological, geo-morphological, socio-economic, administrative, institutional and cultural systems).

In Italy the coastal planning system is still extremely contradictory and split among the different State, Regional and Municipality authorities. Law n. 979 of 31 December 1982, that set up a "Piano Mercantile Generale di difesa del mare e delle coste" (General Trade Plan for Defence of the sea and coast), drawn up by the Naval Ministry in agreement with the Regional Governments, should have introduced an important change in the policies for safeguarding the marine and coastal environments. Unfortunately, at the moment we can but deplore the delay in ratifying the plan, that has not become operative yet. The need to safeguard the coast from indiscriminate building as regards quantity and quality was not met in Italy until 1985, the year when a law² appointing more rigorous safeguards of the territory was passed, although this was not always able to halt the abuses, if the local authorities failed to repress them.

Nowadays, in Italy, except for individuating the coastal strip as the first 300 metres of emerged land, subject to landscape constraints established by the Galasso Decree, there are no active safeguarding measures or indications in force that could face the ever increasing demand for transformation of the coastline. Italy did not submit a national report and there is no national Integrated Coastal Zone Management strategy. This was possible because the governance system is highly decentralized, so that Integrated Coastal Zone Management functions are devolved to the regional and/or local governments instead of pertaining to the central, national government. Some regions offer support programmes for training, education and communication for Integrated Coastal Zone Management, but these programmes are few and far between, especially at national level. Positive examples of Integrated Coastal Zone Management can be found in regional and local efforts, as some Regions are elaborating guidelines for integrated coastal management (e.g. the Emilia Romagna Region). Non - governmental organizations play an important

role in environmental safe-guards; among these the Italian branch of the World Wildlife Fund, the “Lega per L’ambiente” and “Italia Nostra” are the most prominent.

The changed legal picture in Italy, since the main responsibilities were shifted from the State to the Regions, has led to the identification of the regional level as the best suited to the implementation of coastal planning and integrated management policies.

In Apulia the first institutional act for coastal management was the D.G.R. n.319/2001, which assigned the Municipalities the task and power to propose, by means of the Piano Comunale delle Coste (PCC: Municipal Coastal Plan), a rational use of seashore public land, in agreement with the other State Boards. The region also has the tasks of programming, planning and general orientation, as well as of overseeing general management and the Administrative Police Force. In this deliberation, it is also pointed out that the PCC are to all effects the foundations on which the “Piano di Utilizzo delle Coste Regionali” (Plan for Use of Regional Coasts) is based. Following this deliberation, many Municipalities have drawn up a Coastal Plan, but none have yet been approved by the Region.

Subsequently, in the context of integrated coastal management, Regional Law n. 17 of 2006 regulated the exercise of administrative functions connected with the management of marine public land and seaside zones, distinguishing the functions of the Region and those pertaining to the Municipalities and Provinces. These functions are carried out in the form of planning, done at Regional and Municipal level. Regional planning is done by drawing up the Piano Regionale delle Coste (PRC): Regional Coastal Plan), that is an essential tool regulating the use of the Apulian coast and imposing a rational management of the coastal resources to guarantee a correct balance between safeguarding the environmental and landscape heritage and promoting the development of tourist and recreational activities. The principles and norms of the PRC must conform all the Municipal coastal plans (PCC).

III. THE APULIA REGIONAL COASTAL PLAN

The morphological and environmental features of the Apulian coastal landscape have been severely disrupted in many tracts, as a result of the man-made transformations that have spread at an ever increasing pace in the last decades. In Apulia, the lack of proper safeguards and regulating norms has caused the complete destruction of dunes¹ system in many areas. The environmental impact of the seaside consumption resulting from widespread building of tourist residences in the last few decades of the 20th century and the furious cement-laying (that is a part of the lawless building spree against the local regulatory plans and protective laws) have, in most cases, been devastating.

Recently, in many towns and seaside localities in Apulia, planning processes to restore the functions of the waterfront have been set in motion. This has occurred not only in

abandoned areas that are open to urban transformations but also in response to the ever greater demand by residents and tourists for environmental, landscape and urban quality. In various areas of the Apulian region attempts are being made to diversify and deseasonalize places by developing new forms of leisure activities that can contribute, if they are adequately supported, to redistribute tourist flows over a wider portion of the territory, not limited just to the coast, as well as over a wider portion of the year. But an analysis of the ongoing planning reveals a series of contradictions and critical aspects that can be summarized in the following three points:

- i) the regional coast is a laboratory of single projects with very little integration among them, directed above all to develop tourism and increase the safety of the territory;
- ii) the plans and financing are still too sectorial;
- iii) an overall strategic regional plan for the coastal landscape is lacking.

Against this background, although the Apulian PRC is essentially aimed at disciplining the use of the strictly public land in Apulia¹, it also offers an important chance to govern the multiple conflicts that arise in the coastal areas in a multidisciplinary way [12]. This could help to overcome the fragmented knowledge and sectorial approaches that have made it so difficult to formulate efficacious integrated policies from the economic, social, landscape and environmental standpoints. The PRC is an important step toward a better knowledge and management of the Apulian coastal public land. In fact, it has led to: a reorganization of the available information and technical–scientific knowledge of the physical dynamics occurring along the Apulian coastline, the drawing up of a clear picture of the sensitive and critical areas in each coastal tract, the definition of the policies for land use along the entire Apulian coastline, in complete conformity with the environmental and urban constraints and the human safety concerns, to avoid promoting tourism in some areas at risk or, vice versa, the use of areas with a strong tourist attraction for industrial purposes, the gain of indications for drawing up the tools establishing norms and regulations at Municipal level, to guarantee the correct management of the territory and measures, and a continually updating to better analyze the environmental heritage.

IV. OBJECTIVES AND SPATIAL UNITS

Using an interdisciplinary approach, as is now normal practice in all planning processes with an environmental scope², to define the most useful strategies for disciplining the land use and interventions the planning projects were conducted using an analytical-methodological approach.

The first step in drawing up the plan was to define the study scope. Owing to the heterogeneity and complexity

¹ Law 8 August 1985, n. 431, named Galasso law, is about urgent measures for the protection of areas of particular environmental interest.

² The Apulia Coast, excluding Tremiti islands (with a coastline of approximately 50 km), extends for 970 km and consists of 33% of sandy beaches, of 33% of rocky shores, of 21% of high cliffs, and 5% of man-made features.

characterizing the entire regional coastal territory, it was not judged advisable to delimit the study area in a constant manner over the whole region (e.g. a width equal to 1 km), nor was it deemed useful to refer to the administrative limits of the coastal municipalities: works carried out at sea (ports, defenses, filling, etc.), respond to precise needs in municipal planning, on the one hand, but on the other, they can have important repercussions on the neighboring municipalities, from both the environmental and the socio-economic standpoints. When dealing with environmental planning any definition of borders, limits or reference areas can have little significance, because the actions exerted in one zone for a particular purpose may have unexpected effects in terms of time and space in other zones (even not bordering ones) and at different intervals. In any case, since it was necessary to define a territorial study area, this had to be expanded so as to gain a fuller comprehension of the environmental phenomena to be analyzed. The reference criteria assigned were those of an environmental nature because only these ones were able to quantify the "transformations" and make the processes defining them readable. For these reasons, the study area with a variable depth was defined, depending on the specific situation present in the given coastline strip, where the shore limit was taken as the coastline³.

The scope was defined using the following environmental criteria:

a) the altimetry and orography: in fact, these two components often have a significant impact on the dynamics of human settlements;

b) the gullies and superficial groundwater: gullies (fossil rivers) and rivers are the main sources of sedimental deposits along the coastal strip, as well as being ecological links between the sea and land;

c) the type of coast: cliff or lowland, rocky or sandy bottom, and other similar aspects – in practice much more complex than the examples we record here – that contribute to define recurrent elements along the coastline;

d) the geological characteristics: these have a significant influence on the elements shaping the coastal morphology;

e) marshy zones and the ones with particular environmental characteristics (protected marine areas, S.I.C., Z.P.S): these are the areas with the greatest environmental value, already assigned by the planning system set for superordinates;

f) the vegetation system: the vegetation often contributes to characterize the coastal environment, giving added value.

Then the physiographic units were defined (Figure 1), that individuate coastal tracts where there is little transport of solid sediments, due to rough seas and strong currents. Both natural physiographic units (generally present on the ends of promontories that hinder the entry and/or exit of sediment) and man-made units, (in other words the tracts between a promontory and works at sea, for a port or for defense, ending at a depth of more than 10 meters) have been taken into account. These works act to all intents and purposes as true

barriers against the longitudinal transport of solids. To study this aspect in more details, inside each physiographic unit some sub-units were identified, delimited by small promontories or works ending at a depth of less than 10 meters⁴.

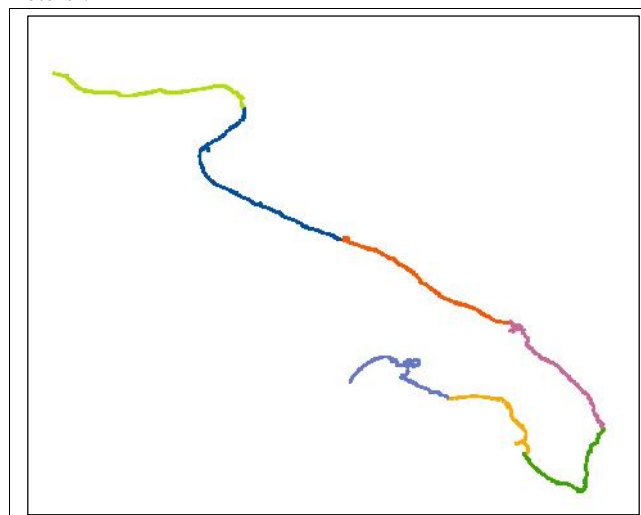


Figure 1: The 7 physiographic units identified

V. DEFINING THE SPATIAL AND LANDSCAPE COMPONENTS

Thus, in this study context, thanks to the contribution of many different research disciplines, it has been possible to analyze the multiple territorial components that combine to shape the structure of a place, and can reveal the profound significance and relational links, intrinsic and extrinsic values that need to be respected when defining possible, environmentally compatible actions [13] [14] [15].

The coastal environment has been interpreted in the light of historical, morphological, sedimentological and geo-hydrological analyses. Its tendency to undergo physical changes, due to natural causes, has been explained by the study of the erosion phenomena and sea forces. In the physiographic units, the physical and topographic features of the coastal strip, running from the shoreline to the first infrastructures inland, have been defined. The coastal type has been identified and the data electronically stored, in terms of the evolution of the sandy tracts, of the breakdown of rocky tracts¹, of the coastal protection works and port areas⁵, the protected areas for geo-morphological reasons, the protected areas for meteoric-marine conditions (areas affected by tidal phenomena, currents in shallow waters), the protected areas for hydrological reasons, and hygiene-health risk factors. Then the land uses and behaviors that have contributed significantly to modify the relations between the natural and anthropological systems have been analyzed, focusing on the man-made pressures generated by urbanization and infrastructural works. In fact, these

⁴ According to this criterion, the Apulian coastal territory has been divided into seven physiographic units which, depending on their physiography, have been divided in sub-units.

⁵ Through the study of the emerged and submerged (trend of depth contours) morphology of the coast, the orientation of the shoreline and the lithological nature of the coast.

³ Identified on the base of orthophotographs map made 2005.

dynamics have often been ignored, both in the planning and executive phases. In particular, the links between tourist development and coastal landscape have been studied in depth, analyzing the myriad tourist and recreational facilities⁶. Coastal settlements were classified in the following categories: (i) residential (centres, residential nuclei and single buildings; occupied homes, unoccupied homes and second homes); (ii) historical cultural heritage (coastal look-out towers, old towns, lighthouses, fortifications, castles, etc.); (iii) productive activities (industries, agriculture, trade); (iv) tourist activities (accommodation: hotels and beds; tourist villages and maximum accommodation; beaches and their full capacity); (v) infrastructures (works and port facilities in terms of type and number of berths, main and minor roads systems, railway lines); (vi) sources of pollution (industrial and non industrial waste, purification plants).

Finally, information on the man-made pressures on the coast was identified and stored in electronic form, in terms of the zones with urban planning and environmental constraints (Areas protected by regional, national and Community norms, hydro geological constraints, Municipal and non Municipal urban planning constraints), zones with constraints for planned works in the context of Municipal, Regional and National projects, particularly vulnerable zones (for which no concessions for land use can be granted and even public use must be regulated), zones where land use has already been granted and those where concessions could be granted⁷.

VI. DEFINING THE CRITICALITY AND SENSITIVITY OF THE COASTAL TERRITORY

After acquiring the data needed to define the state of the coastal territory and the existing relations, the "critical" and "sensitive" points of the area under study were identified. The term "criticality" indicates a greater or lesser tendency of the coastal territory to undergo erosion, as well as the causes generating this phenomenon. The term "sensitivity" indicates the level of fragility associated with the environmental peculiarities of that specific context.

The shoreline was subdivided into elementary lines, each 100 m long.

The environmental sensitivity was defined as a function of a multitude of markers that represent the physical state of the coastal strip (including public land and its territorial reference context), in relation to the safeguarding norms that stress its environmental importance. The sensitivity parameter represents the state of the coastal strip from the historical and environmental standpoint. For this reason, a series of markers have been individuated that, after the assignment of the appropriate weights, contribute to define this parameter. These markers are:

- the hydrographic picture to an established depth of 300 mt on both sides⁸;

This marker was chosen both in conformity with the regional safeguarding tools and in view of the important draining function of the gullies and water courses in coastal dynamics. The main source of sediment in the sea is, in fact, the transportation of fluids down the rivers. These sediments are then remoulded and redistributed by the waves and currents (especially during storms), and ultimately form the seaside.

- "Siti di Importanza Comunitaria" (S.I.C.⁹: Sites of Community Importance); "Zone di Protezione Speciale"(Z.P.S.: Special Protection Zones¹⁰);

These are areas that contribute significantly to maintain or restore habitat types of particular species and species with a particular biological value or at risk of extinction and/ or that contribute significantly to maintain the biodiversity of the region.

- Protected Areas¹¹;

These include "protection oases", "repopulation and capture zones", "marshy zones", special nature reserves, complete nature reserves, biogenetic nature reserves, forest protection nature reserves.

- the territorial ambits indicated in the P.U.T.T./p¹²;

- territorial constraints ex lege 1497/39¹³;

- Galassini areas¹⁴;

- woods;

- archeological constraints and flagged areas¹⁵;

- architectural constraints and flagged areas¹⁶;

- lanes, trulli and historical settlement systems;

These markers were selected to identify cultural heritage not

⁸ The streams are protected by the existing Puglia PUTT / p (Territorial and Landscape Regional Plan) which is the instrument of regional planning approved by the DGR n.1748, 15 December 2000. It includes the list of public waters throughout the Apulia Region.

⁹ Site of Community Importance is a concept defined by EU Directive No 43, 21 May 1992 (92/43), Council Directive on the conservation of natural habitats and flora and fauna, also known as the Habitats Directive, implemented in Italy since 1997.

¹⁰ The ZPS are provided and regulated by the Community Directive 79/409 "Bird" whose goal is "conservation of all birds species living in the wild", which is achieved not only through the protection of populations, but also protecting their natural habitats, with the designation of Special Protection Areas.

¹¹ This indicator was selected in compliance with the Apulia region PUTT / p.

¹² The PUTT / p defines territorial areas with different landscape value, distinguishing between those of exceptional value ("A"), those of significant value ("B"), those of distinguishable value ("C"), those of relative value ("D"), those of normal value ("E").

¹³ This indicator is a constraint of maintaining landscapes marked by the State according to the procedures of Law 1947 of June 29, 1939 named "Protection of natural beauty".

¹⁴ This indicator was selected in compliance with L. n.431/1995 concerning the areas and assets identified by Article 2 of the Decree of the Ministry of Culture and Environment in September 21, 1984.

¹⁵ This indicator was selected in accordance with the PUTT / p which defines and protects the "archaeological zones".

¹⁶ This indicator was selected in accordance with the PUTT / p Puglia Region which defines and protects "architectural suburban assets", recognized significant for historical, architectural and landscape point of view.

⁶ Identifying ports, river mouths armed, longitudinal and transverse defense works.

⁷ According to this criterion, the Apulian coastal territory has been divided into seven physiographic units which, depending on their physiography, have been divided in sub-units.

actually regulated by law, but in any case representative of the characteristic features of the regional landscape.

- the use of agricultural soil.

The soil, cultivated or not, is a sensitive element of the territory because if it is subject to the use of harmful substances it can damage the final recipient (the sea), and if it is abandoned to decaying processes it will not foster tourist-recreational use of the coastal strip¹⁷.

The critical exposure to erosion of sandy coastlines has been defined according to three markers:

- the historical tendency to evolve of the coastline;

This marker was populated with the data reported in the executive monitoring project: "Progetto Esecutivo del Monitoraggio P.O.R. Puglia 2000 - 2006". If the coastline under study has a historical tendency to evolve in the sense of undergoing erosion, a value of 1 is assigned, otherwise a value of 0.

- the recent tendency to evolve;

This marker was populated using the data on the extent to which the coastline receded between 1992 and 2005, where the range was defined as 10 m. In particular, the ratio between the length of the receding sandy coast tracts as opposed to the length of the intact sandy coast was calculated .

- the state of conservation of dunes systems.

This marker was populated with the data obtained with the "P.O.R. Puglia 2000 - 2006", assigning a value of 1 to receding dunes tracts, otherwise 0.

To assign weights to the markers, the AHP¹⁸ method was applied using Expert Choice applicative software. With the AHP method each marker element is assigned a weight according to its greater or lesser contribution to determining the element it is subordinate to (map of Sensitivity, map of Criticality). For all the markers subordinated to the same criterion (sensitivity or criticality) pairwise comparisons are made.

Levels of judgement in Saaty's fundamental scale	
(m/n)=1/9=0.111	Very much less
(m/n)=1/7=0.143	Much less
(m/n)=1/5=0.2	Less
(m/n)=1/3=0.333	Moderately less
(m/n)=1/1=1	Indifferent
(m/n)=3/1	Moderately more
(m/n)=5/1	More
(m/n)=7/1	Much more
(m/n)=9/1	Very much more

¹⁷ The protection of ancient olive trees, which represent the history of the Apulian countryside, is important in order to avoid uprooting abuses, especially along the coast for aesthetic purposes (beautifying parks and private gardens).

¹⁸ The Analytic Hierarchy Process (AHP) is a method of multi-criteria decision developed by Thomas Lorie Saaty [16]. The AHP is a method of qualitative analysis in which the assessment is determined by aggregating the opinions expressed in ordinal scale: the decision problem is formulated in a hierarchical structure and defines the priority of its elements by comparing their mutual importance.

Tab. 1 Saaty's fundamental scale

The elements in each pair are compared to establish which one is more important with respect to the super-ordinate element, and to what extent. For example, as regards the criterion Sensitivity [17], a box matrix is built, expressing by element *aij* the level of preference between marker *Ai* and marker *Aj* with respect to the same criterion. To determine the values of the coefficients *aij*, Saaty's¹⁹ semantic scale is used, that associates the first nine whole numbers with the same number of judgements, that express the possible results of the pairwise comparison in qualitative terms.

The paired comparison made it possible to build the following comparison matrix among *n* elements, semi-symmetrically to the diagonal.

Elements	A	B	C	...	N
A	1	m_{AB}/n_{AB}	m_{AC}/n_{AC}	...	m_{AN}/n_{AN}
B	n_{AB}/m_{AB}	1	m_{BC}/n_{BC}	...	
C	n_{AC}/m_{AC}	n_{BC}/m_{BC}	1	...	m_{CN}/n_{CN}
.....
N	n_{AN}/m_{AN}	n_{BN}/m_{BN}	n_{CN}/m_{CN}	...	1

Tab.2 The paired comparison matrix

The weight of each criterion is obtained by checking the matrix auto-values that, thanks to its semi-symmetrical shape, give a round sum.

Applying the above methodology, the Sensitivity²⁰ marker weights values were obtained.

The weights for the criticality markers are assigned as follows: 20 for a historical tendency to evolve, 50 for recent evolution and 30 for the state of the dunes.

To obtain the maps of sensitivity and criticality, after establishing the weights of the markers, an overlay process of the territorial issues (maps) was done to transfer the information about the territory onto the corresponding linear coastal element. In this way, a Boolean matrix was built of the markers, where the rows are elementary lines (*i*) and the columns are the markers (*j*); if in the *i*-th line there is the *j*-th marker, the identifying element (*ij*) is equal to 1, otherwise it is equal to 0.

Thus, for each coastal strip a score was given equal to the:

¹⁹ The latter is articulated on judgements like unimportant, moderately important, more important, much more important, extremely important. At the judgment as "The criterion A is more important than criterion B" will be associated the ratio *m / n*, with *m* > *n* to the extent that the importance assessment will be accompanied by attributes such as "moderately", "very much", "extremely", etc.

²⁰ In order to assign weights to the indicators in this case priorities arising from the Regional Law n.17 of 2006 were used, which deals primarily the tourist use regulating the use of state property particularly in relation to concessions, and thus , the sandy coastline. Title III, art.16, paragraph 1) and 2) of that Act, refers to the absolute prohibition of issue, renewal and variation of granting state property in the following areas and their buffer zones: mouths of rivers or streams or watercourses, flood channels, areas with risk erosion near cliffs, archaeological zones and historical and environmental assets.

i -the value = j (i -th score x j -th criterion weight)

where the i -th weight is attributed on the basis of the Boolean method:

presence of criterion: i -th score = 1
 absence of criterion: i -th score = 0

The results of this operation allowed each coastal strip to be classified according to one of the criticality and sensitivity class values: high environmental sensitivity, medium environmental sensitivity, low environmental sensitivity (Table 3), high criticality, medium criticality, low criticality (Table 4).

SENSITIVITY CLASS	VALUES
Low Sensitivity	0 – 0.155
Medium Sensitivity	0.156 – 0.285
High Sensitivity	0.286 – 0.56

Tab.3 The sensitivity classes

CRITICALITY CLASS	VALUES
Low Criticality	0 – 0.061
Medium Criticality	0.062 – 0.237
High Criticality	0.238 – 0.545

Tab.4 The criticality classes

VII. THE NORMATIVE DISCIPLINE

The different levels of criticality and sensitivity to erosion and environmental damage were then cross-referenced, giving rise to a scoring system with 9 levels (Table 5), that can provide reference information for drawing up the "Piani Comunali delle Coste" (P.C.C.: Municipal Coastal Plans).

C1.S1	Low Criticality	High Sensitivity
C2.S2	Medium Criticality	Medium Sensitivity
C3.S3	Low Criticality	Low Sensitivity
C1.S2	High Criticality	Medium Sensitivity
C1.S3	High Criticality	Low Sensitivity
C2.S1	Medium Criticality	High Sensitivity
C2.S3	Medium Criticality	Low Sensitivity
C3.S1	Low Criticality	High Sensitivity
C3.S2	Low Criticality	Medium Sensitivity

Tab.5 The Scoring System

This system is linked to the actions to be adopted in all nine cases, that are included in a document named "Norme Tecniche di Attuazione e Indirizzi Generali per la Redazione dei Piani Comunale delle Coste" (Technical Norms for Enacting, and General Indication for Drawing Up the Municipal Coastal Plan) of the PRC.

In the context of the norms, the critical classes scoring system serves to regulate grants of concessions for public land use, while the environmental sensitivity classes regulate the type of public land concessions and the methods to be adopted to contain their relative impact. In each coastal municipality

the concessions public land use (whether for a renewal or a new concession) must first of all be granted for areas belonging to the lower levels of criticality and environmental sensitivity. In general, concessions should not be granted at all in highly critical zones and in any case - unless it is impossible to fall back on low or medium criticality zones inside the municipal territory - these must be instituted gradually over time to allow stabilization of the erosion processes to take place. In zones with medium scores for criticality - if no low criticality zones are available in the municipal territory - the granting of concessions is subordinate to assessment that the erosion phenomena have stabilized. By contrast, in zones with a low criticality score, concessions for public land use should normally be granted without any problems.

Similarly, in zones with high sensitivity, concessions are normally prohibited and in any case, if no zones with low or medium sensitivity are available in the territory, should they be granted, priority must be given to "Spiagge Libere con Servizi" (S.L.S.: Free Beaches with Facilities) and only secondarily, to "Stabilimenti Balneari" (S.B.: Private Beaches). In any case, the minimum beach facilities only should be offered, limited to a bar-kiosk-management desk and public conveniences. Even these ones are subject to a prior environmental survey. In zones with medium sensitivity, if no low sensitivity area is available, concessions may be granted only after a full environmental survey, again giving priority to free beaches with facilities (S.L.S.) and only secondarily to private beaches (S.B.). In both cases the facilities must be defined after proper surveys. By contrast, in areas with low environmental sensitivity public land use concessions are normally granted without any problems.

VIII. CONCLUSION

The PRC of the Apulian Region is not just a tool regulating the use of strictly public land, i.e. State property areas, but also defines the "state of the conditions" of the entire coastal strip, highlighting its "critical nature" and "potential" in relation to multiple factors, both endogenous (natural phenomena) and exogenous (pressures exerted from outside).

With the support of this analysis, methods have been defined to attempt to satisfy the tourist demand while avoiding damage to the natural and historical-cultural qualities, that are important resources in the region. Indeed, they constitute a large part of the tourist attractions, and so have an important economic and social weight as resources for the local populations and operators in the sector. In this sense, rather than endeavouring to identify suitable forms of use for those areas that are still free (apart from reconsidering those for which authorizations had already been granted) the potential is assessed in the light of a desirable overall process of reclaiming and restoring the coastal territory. In practice, the study has provided a significant contribution to draw up norms that may guarantee a correct territorial management, as well as providing an overall picture of the current scenario, that needs to be continually updated. Thanks to this research, policies

have been identified for the use of the seaside while respecting the environmental constraints and consequent urban choices, that take into account the problems revealed, as well as the essential safety issues. These policies aim to enhance use of the coastal areas for purposes best suited to their peculiarities: on one hand they aim to limit the use of vulnerable areas - in practice by prohibiting "tourist exploitation" - and the use of areas posing a hygiene-health risk, while on the other, they point out the need for urban planning to prevent land uses for industrial type productive purposes being instituted in these areas characterized by a strong tourist vocation.

It is also thanks to these tools providing a better knowledge of the coastal territory that it is now possible to develop a regional territorial plan with far-reaching consequences, in other words a strategic plan that is able to integrate provisions among programs, tools and projects for safeguarding, enhancing and reclaiming coastal landscapes in a coherent future scenario. This has the purpose of combining environmental, cultural, landscape and urban quality, infrastructural and, last but not least, economic-tourist interests. It is up to the Municipalities to enforce respect of the rules established in the PRC, and above all to mediate these Municipal Coastal Plans as an opportunity to associate public land uses with suitable environmental reclaiming and restoration processes. In particular, this involves extending the long term options to make the actions more environmentally sustainable and more financially rewarding in the long term; recognizing the uncertainty of the future and so promoting systemic, flexible approaches; including all interested parties in the reclaiming and planning processes by instituting forms of involvement that promote shared responsibilities and tasks, exploit local knowledge and contribute to identify the real issues at stake, leading to feasible solutions arrived at by agreement and participation among all the stakeholders.

The management and protection of the coastal zones in a sustainable framework can be successful only thanks to a strong reliance on a set of legal and economic tools, voluntary agreements, ample information stores, technological solutions, optimization techniques for integrated monitoring [18], research, education and training. A better coordination among the stakeholders can, in fact, contribute to identify the synergies or conflicts among actions based on different policies and facilitate the acceptance of the necessary arbitration, imbuing all the stakeholders with a sense of their responsibilities. This kind of concerted action can only develop if all stakeholders are in possession of complete, comprehensible information about the state of the environment, the causes of the changes it is undergoing, the implications of the policies and measures at the various levels, and the available options.

In Apulia, this experience of the "Piano Regionale delle Coste" (PRC) has constituted the first attempt to build a knowledge base that can help to promote a fruitful dialogue among the stakeholders in the different sectors. It will be continually updated thanks to constant data exchange at the

various levels of territorial authority.

REFERENCES

- [1] I.L. McHarg, *Design with the Nature*, Natural History Press, New York, 1969.
- [2] J. M. Klopatek, R. H. Gardner, (eds.), *Landscape ecological analysis: Issues and applications*, Springer-Verlag, New York, 1999.
- [3] R.M.V. Russo, *Le coste tra tutela e progettazione*, Jason, Reggio Calabria, 1996.
- [4] E. Pranzini, *La forma delle coste. Geomorfologia costiera, impatto antropico e difesa dei litorali*, Zanichelli, Bologna, 2004.
- [5] A. D. Short, *Handbook of beach and shoreface morphodynamics*, John Wiley & Sons, New York, 2001.
- [6] R. Gambino, *Conservare - innovare. Paesaggio, ambiente e territorio*, UTET Università, Novara, 1997.
- [7] F. Rotondo, F. Selicato, *Progettazione Urbanistica. Metodi e Tecniche*, McGraw Hill, Milano-New York, 2010.
- [8] GNRAC (Gruppo Nazionale per la Ricerca sull'Ambiente Costiero), "Lo stato dei litorali italiani", in *Studi costieri. Dinamica e difesa dei litorali - Gestione integrata della fascia costiera*, n.10, 2006.
- [9] UNEP (1995), Guidelines for Integrated Management of Coastal and Marine Areas. UNEP Regional Seas Reports and Studies No. 161, p. 80.
- [10] Taussik J., The opportunities of spatial planning for integrated coastal management, *Marine Policy*, vol.31, pp.611-618, 2007.
- [11] L.C.C. Pereira, J.A. Jiménez, C. Medeiros, R.M. Da Costa, Use and Occupation of Olinda Littoral (NE Brazil): Guidelines for Integrated Coastal Management, *Environmental Management*, vol.40, pp. 210-218, 2007.
- [12] A. F. Petrillo, F. Selicato, M. F. Bruno, A. Giordano, G. Maggio, "La gestione integrata della fascia costiera nel Piano Regionale delle Coste in Puglia", in *VII Congresso Regionale dell'INU Territori costieri: Quali politiche per un governo integrato*, Palermo, 29-30 novembre 2007, Franco Angeli, Milano, 2009.
- [13] G. Maciocco, *Le dimensioni ambientali della pianificazione urbana*, Franco Angeli, Milano, 1991
- [14] F. Rotondo, P. Perchinunno, M.C. Torre, The Evidence of Links between Landscape and Economy in a Rural Park. *International Journal of Agricultural and Environmental Information Systems (IJAEIS)*, 3(2), 72-85, 2012.
- [15] S. Serreli, *Dimensioni plurali della città ambientale. Prospettive di integrazione ambientale nel progetto del territorio*, Franco Angeli, Milano, 2004.
- [16] T. L. Saaty, *The Analytic Hierarchy Process*, Wiley, New York, 1980.
- [17] T.L. Saaty, *Multicriteria Decision Making: The Analysis Hierarchy Process*, RWS Publications, 1990.
- [18] E. Pranzini, L. Wetzel, *Beach erosion monitoring*, Nuova Grafica Fiorentina, Firenze, 2008.

ABOUT THE PLACE OF INSTALLATION OF A GAS COOKER IN THE KITCHEN

Iu. H. Polandov, M. A. Barg, V. A. Babankov

Abstract. Hypothesis of the possible influence on the place of ignition of town gas, which fills up the room, on the explosion pressure, was put forward in the results of physical experiments on the model using the change of place with the ejection window (which plays the safety window role). On the model experiment, it was established that approximation of the window towards the place of ignition under certain conditions reduces by more than order of the explosion pressure. Applied to our task, it is reasonable to expect, that approximation of gas cooker towards the window, must contribute the reduction of the pressure of gas explosions in the kitchen.

Hypothesis was checked during holding the numerical experiment. Mathematical model consists of the system of known CFDs (Computational Fluid Dynamics), expressing conservation laws in relation to ideal inviscid gas. This system is complemented by the equation, describing the original mechanism of flame spread. System was solved by the Large-particle method (Belotzerkovskii and Davidov) by the explicit scheme. The convergence accounts deteriorated due to the commissioning of combustion, because of that the step account of time had reduced to $5 \cdot 10^{-7} \text{c}$.

Acceptable model adequacy is confirmed by comparing the results of numerical and physical experiments, on which not only the dynamics of the basic parameters, but secondary effects, such as amplitude, phase and frequency of the acoustic vibrations, turned out to be similar. The results of the calculations are visualized on the computer with the help of extra program.

Explosions in the kitchen are most frequently associated with the gas leak in the room and followed by an attempt of ignition of the gas cooker that is why we have a right to assume that the place of ignition of the gas from explosions is the gas cooker.

The results of an experiment shows us that the pressure of the gas explosion stoichiometric composition in a small room 3 m x 4 m x 2.5 m with one window whose size 1 m x 1.2 m, depends on the place of the ignition and it can change in 6 times: near the window – 0.8 kPa, near the far wall of the window- 4.8 kPa. This result has confirmation of the hypothesis.

Also, it is obtained that after the explosion comes the implosion with the pressure of 40 Pa lower then atmospheric pressure that causes at the end of explosion the cold airflow outside and sharp decline of the temperature in the room, beginning from the window.

The time of the increased pressure of the room lasts 1 second in case of explosion at the far wall and 3.5 – near the window.

Iu. H. Polandov is with the State University – Education-Science-Production Complex, CO 302020 Russia (corresponding author to provide e-mail: polandov@yandex.ru).

M. A. Barg, was with the State University – Education-Science-Production Complex, CO 302020 Russia (corresponding author to provide e-mail: mikemvpi@yandex.ru).

V. A. Babankov is with the State University – Education-Science-Production Complex, CO 302020 Russia (corresponding author to provide e-mail: xenosv@mail.ru).

Conclusion: approximation of the gas cooker to the window significantly reduces the explosion pressure in the kitchen, but increases the thermal influence on the elements of kitchen furnishing.

Keywords: explosion, gas cooker, gas indoors, numerical experiment, pressure of the explosion.

I. INTRODUCTION

Gas as a domestic fuel in Russia is very common and, perhaps even more than in other European countries [1]. However, the high level of gasification in the country has led to a significant increase in the incidence of explosions and fires, calculated for one person, and in this respect, Russia has become one of the most disadvantaged. We also know that the vast majority (over 90%) of these cases were in hazardous non-manufacturing sector, where the gas is used in boilers and domestic premises. Should be highlighted the danger of explosions, as they firstly characterized by high pressure and a powerful thermal pulse, and, secondly, the process of explosion is very fleeting and uncontrollable. This problem is most acute for high-rise buildings.

Judging by the fact that the gas equipment in all the countries is approximately the same, but in Russia explosions happen more often than in the others, the high frequency of occurrence of explosions and fires can be explained most likely mentality of the population, and this feature, as is known, changes sufficiently slowly. Notable measures in solving the problem of gas explosions are generally reduced to attempts to educate inhabitants' safe receptions of introduction of gas equipment, excluding gas leakage and device windows with a specific area of glazing. To move "the parity" between the gasification of life and value of the frequency in the right direction, can be done by the elaboration and implementation of technical solutions which, on the one hand, would help to reduce the risk of explosion, if it happens, and, on the other hand, has a low dependence on the human factor. In this situation, it is clear that the existing ideas about the process of gas explosion and the corresponding technical solutions cannot correct the situation, as they have exhausted their ability, but because we need new ideas, experiments and solutions to meet the current state of science and technology.

In particular, the transition to the calculation of the parameters of the gas explosion in view of their distribution in terms of volume, in which an explosion occurs, provides a new look at the mechanics of the process, the formulation of new ideas and a selection of new technical solutions aimed at

reducing the risk and, above all, the explosion pressure. But, it is known that the modeling of such processes called numerical, encounters the complexity of the calculations, but the rapid development of computer technology with each passing year more and more fully satisfy the request.

II. THE WORKING HYPOTHESIS

The working hypothesis stems from the findings of a physical experiment, which researched the development of a gas explosion in the chamber ($d = 200$ mm, $L = 1500$ mm). Experiments on the camera (Fig. 1) was filled with a stoichiometric propane- air mixture, which produced inflammation of the electric pulse and always in the same place at the end of the chamber adopted for its beginning. The explosions gas mixture discharged into the atmosphere in one of the three valves placed on the cylindrical part of the chamber in the beginning the camera in the middle length of the chamber and at the end.

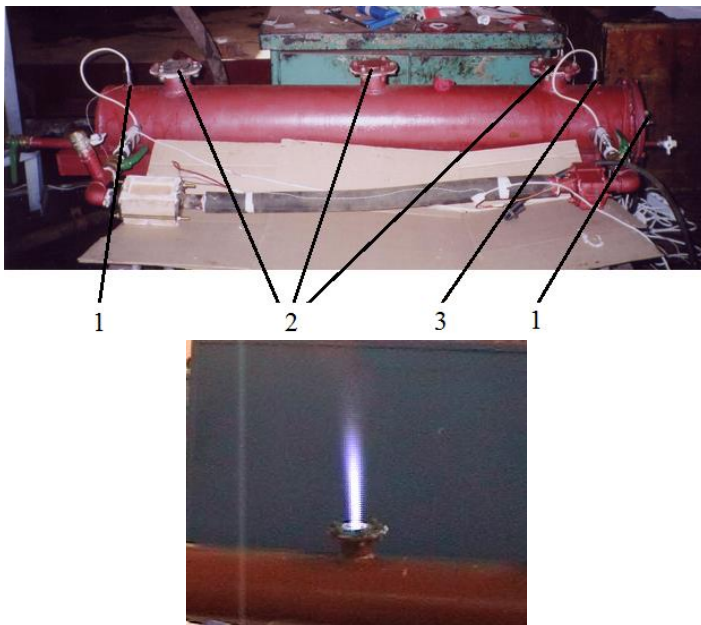


Fig. 1 a general view of "Sergeant" and experienced an explosion
1 - pressure sensors, 2 - place of the bombing valve 3 - ignition device
Fitting Position

Initial valve position - muffled, when it is initialized plug removed, and orifice baffle glued sheet of paper, varying valve, which removed the cap and the other muffled, as if we moved it has been installed. Experimentally varied by two factors: firstly, there was a change of the bombing of the valve, and secondly - the changing diameter of the flow cross section of the valve (20 mm to 70 mm). The experimental setup is equipped with a purge chamber systems, preparation and filing of the gas mixture, as well as computerized systems of automatic control and measurement process.

Found out, that the removal from the place of explosion vent ignition explosion pressure increases and this dependence becomes stronger with increasing diameter of the valve, which

can be seen from these figures (Fig. 2 and Fig. 3). On each of these figures combined results of 10 repeated experiments, it is made to demonstrate the reproducibility of the results and conclusions of non-randomness. It may be noted that the small size of the valve ($d < 25$ mm) change siting little effect on the pressure of the explosion. In contrast, for sufficiently large diameters explosion vent ($d > 65$ mm) as a result of the displacement of the valve position explosive, the explosion pressure changes by more than an order of magnitude.

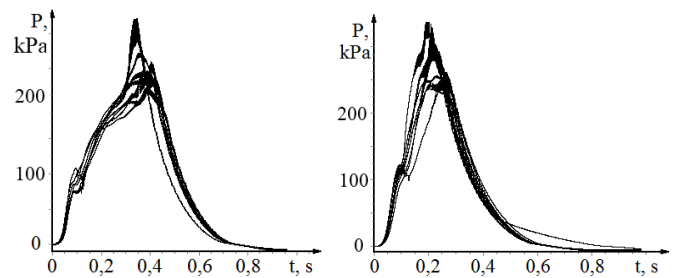


Fig. 2 stroke of pressure at explosions with a diameter of 20 mm valve

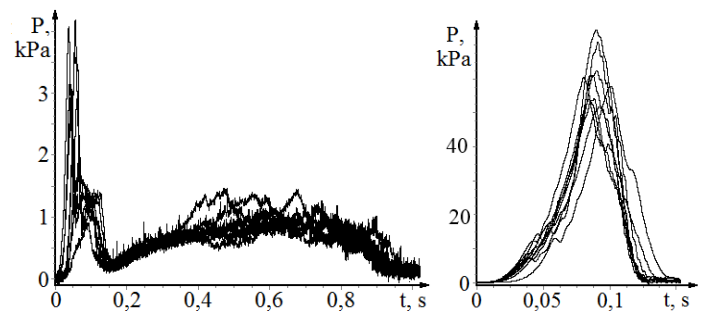


Fig. 3 stroke of pressure at explosions with a diameter of 70 mm valve

Projecting the effect on the gas explosion in a room where there is a window in which the ratio of glass area to the volume of the room is close to what it was in the experiment, one can expect that the place of ignition of gas in this case will play a significant role in shaping the explosion pressure.

In everyday life, this question concerns primarily gasified boiler rooms and kitchens. If we assume that the source of the open fire in domestic premises are likely to be a gas boiler or gas stove, the search for the variant of the risk reduction can be dimensioned to choosing the most secure place to install them. Thus, the hypothesis is formulated as follows: approximation space installation of a stove to the window should reduce the pressure of the explosion. And this in turn should lead to a reduction in the risk of collapse of the building in a gas explosion inside it.

III. THE METHOD AND THE MEANS OF TESTING THE HYPOTHESIS

Hypothesis testing carried out numerical simulations. The notion of numerical experiment involves drawing up a

mathematical model of the gas explosion in the room, the selection of the approximation method for solving equations and systems, demonstrating the adequacy of the model and conducting numerical simulations of gas explosion in a small kitchen.

The basis of the mathematical model is based on three points: the initial system of equations with initial and boundary conditions, the method of solution of the system model and flame propagation.

1) The original system of equations

In the initial system of equations included known in gas dynamics partial differential equations expressing the basic laws of conservation (continuity equation, momentum and energy) with respect to an ideal compressible inviscid environment in the form of so-called Euler's formula (momentum conservation equation , in turn, given as three scalar equations):

$$\begin{aligned} \partial\rho/\partial t + \operatorname{div}(\rho\bar{U}) &= 0 \\ \partial\rho U_x/\partial t + \operatorname{div}(U_x\rho\bar{U}) + \partial p/\partial x &= 0 \\ \partial\rho U_y/\partial t + \operatorname{div}(U_y\rho\bar{U}) + \partial p/\partial y &= 0 \\ \partial\rho U_z/\partial t + \operatorname{div}(U_z\rho\bar{U}) + \partial p/\partial z &= 0 \\ \partial\rho E/\partial t + \operatorname{div}(E\rho\bar{U}) + \operatorname{div}(p\bar{U}) &= 0 \end{aligned} \quad (1)$$

$$p = \rho I (\gamma - 1) \quad (2)$$

where ρ – gas density, kg/m³; \bar{U} – velocity vector, m/s; E – is the specific total energy, J/kg; p – pressure, Pa; γ – the adiabatic index of the medium; I – specific internal energy, J/kg; U_x, U_y, U_z – velocity components respectively along the axes x, y, z , m/s.

2) The initial and boundary conditions

Assumed that all space is filled with a stoichiometric composition of methane-air mixtures, the initial pressure and temperature of the mixture are normal value. Boundaries of the room impermeable, gas emission in the explosion occurs through the window. The gas composition is not changed in the process is the same combustion and air. Window is a weightless partition collapsing at the initial moment of the explosion.

3) The system of equations

The system is solved by a numerical method developed by O. M. Belotserkovskii and Yu. M. Davydov [4], called the method of large particles. The idea is to calculate the following formulation. Estimated volume was divided into cells, called also calculated and represents cubes 10 cm x 10 cm x 10 cm number about 13,200 pieces. Leak proof border sections constructed in a different cell type - the border and escape of gas going through the third type of cells called expendable.

In computational cells are conserved, approximated difference equations. In the border cells of the condition of impermeability by introducing them fictitious speed, direction normal to the interface inside volume and equal modulo speed computational cell, is also normal and oppositely directed to

the border. On the outside of cells through which the outflow of medium pressure from the equivalent pressure values calculated in the short cell and the atmosphere. The magnitude of the time step is chosen based on the size of cells, and in accordance with the criterion of stability of solutions of Courant - Friedrichs -Levy (in our case $\Delta t = 5 \cdot 10^{-7}$ s) . As is known, the solution is sought in three stages, called Euler's form, Lagrange and final. Despite the fact that the system of linear equations can be solved explicitly, the solution is stable.

4) Model of flame propagation

For simulation of flame propagation introduced a new variable - the mass fraction of combustion products in a cell that is equivalent to applying a fourth type of cells in which the line moves separating the products of combustion and the initial mixture. This technique has allowed not only to monitor the combustion process for the line section, but use the difference in the calculation of heat in the general algorithm. Movement is carried out inside the cell lines at a rate equal to the normal combustion rate, which depends on the temperature and pressure in the starting mixture. We consider separately the issue of transition line section through the cell border. More detail the movement of the line described in the software product "VulcanM" [9] . Using additional cell type affects the stability of the solution, it degrades, so as experience has shown [10], it became necessary to carry out calculations with increased reserves by sustainability.

5) Taking into account the losses on the borders volume

Studies conducted previously by us revealed a fairly noticeable effect of heat loss on the borders of the volume on the parameters of explosion. Are taken into account, according to [8] amended to incorporate these heat losses.

6) Visualization of the calculations

A data base is being calculated allowed to visualize the process of the explosion, to follow the condition of parameters at each step of the account. To facilitate the monitoring of the development of the explosion, the cells are painted in different colors. Since the velocity vectors are known in each cell, it has been possible to see the vector lines (trajectories), on which moves the gas medium.

According to the calculation the dynamics graphs of the individual parameters are plotted.

IV. DEMONSTRATION OF ADEQUACY OF MODEL

For assessing the adequacy of the model, a series of numerical experiments with regard to conditions of physical experiments. Fig. 4 shows how the computational domain, the shape and dimensions of which are repeated construction of a physical model. Ignition of the mixture produced at the tip of the left as well as on the physical experiment. Comparison of the explosion dynamics received at the physical experiment and during the calculation is carried out in Fig. 5. Visible to the proximity of the results.

Additional confirmation the adequacy of the numerical model is the registration for these experiments (physical and its corresponding numerical) unplanned secondary effect - of

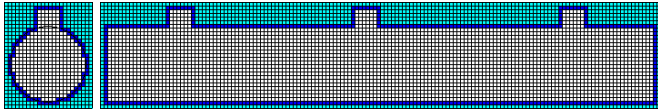


Fig. 4 the computational domain of the experimental setup "Sergeant" (white cells - calculated, blue - the border (the boundary of the computational domain))

periodic oscillations of pressure - with the same frequency and amplitude. In the fig. 6 by the center and on the right shows callouts entries that increase in scale of pressure values for the each of the sensors. Committed in the opposite phase periodic pressure fluctuations can be explained by the presence of an acoustic wave, of moving from one face end of the chamber to the other and back as in physical experience, and in the settlement. It can be seen that the frequency of the acoustic oscillations and their amplitude are identical during both types of experiments (frequency - about 160 Hz, amplitude - a little less than 1 kPa, which correspond to the sound level of 140 dB

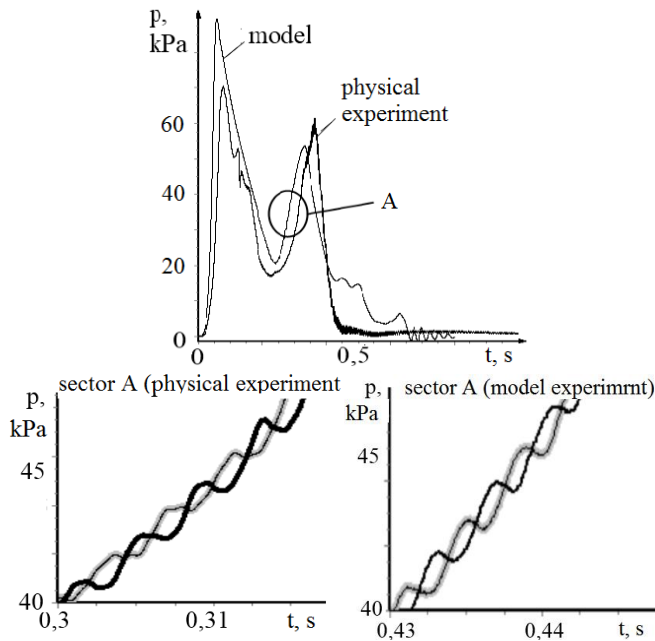


Fig. 5 a general picture of the process

SPL for half a second).

V. OBJECT OF THE RESEARCH

The numerical experiment is carried out to the extent typical for a small kitchen space the size of 4 m x 3 m and a height of 2.2 m, which has a window of 1 m x 1.2 m in the kitchen for the " revival" of the premises placed household items, such as wardrobe, fridge, table and gas cooker represented as parallelepipeds (Fig. 6). Also shown 5 points located along the axis of the room at a height of 1 meter, these points of choice in each individual experiment "installed" a source of ignition. "Sensor" pressure on all the experiments was fixed in

the central part of the room. "Sensor" temperature is placed in the center of the plane window.

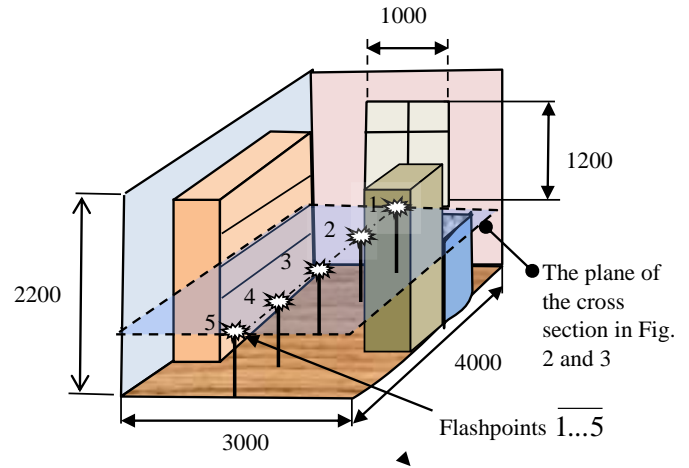


Fig. 6 scheme of the kitchen facilities

Physical and thermal properties of gases and their dependence on pressure and temperature are taken from known directories. The speed of normal combustion and its dependence on pressure and temperature taken in the form in which they are defined V.S. Babkin [6] V.V. Molkov [7].

VI. RESULTS OF EXPERIMENT

Fig. 7 shows the development of explosion footage visualization, which is visible on the front of the flame and the trajectories of moving gas stream. Vector lines create the illusion of the experiment, and the picture has, as expressed by programmers multipliers, verisimilitude.

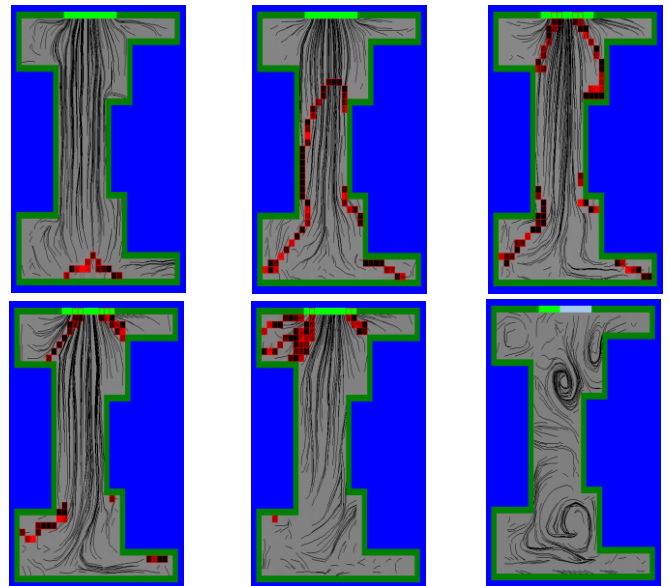


Fig. 7 separate frames rendered picture of the gas explosion ignited when the window on the far wall

Footage taken from the spatial pattern of development of the explosion at the location of the ignition source at the opposite wall from the window according to the cross section shown in Fig. 6 (point 5). Asymmetrical arrangement of windows and furniture with respect to the longitudinal axis of the room made the motion picture of the combustion front is quite different in the right and left side of the axis of the room. Furniture is available in the kitchen helped establish vortices. The footage shows the individual stages of the explosion. About the time when the flame front reaches the window, you can try and schedule changes in temperature in the cell located at the center plane of the window (Fig. 7), where the sharp rise in temperature can estimate the approach of the flame front to the window in each variant of ignition.

Combustion time approaches the window, of course, depends on the place of ignition, it is located farther from the window, the later flame front approaches it. Temperature can be seen in the window and on the duration of the explosion process. Explosion if ignited by the far wall four times less time explosion if ignited by the window. Perhaps the most important result of this experiment is to obtain the dependence of the pressure from the place of explosion ignition gas (fig.8).

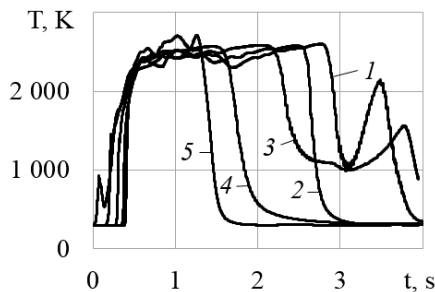


Fig. 8 temperature dynamics on the center plane of the windows

The experiment showed that the closer to the window, the ignition source, the less the pressure of the explosion: The difference reaches 6 times the value for the experiment 4.8 kPa when ignited from the window on the far wall and 0.8 kPa when ignited by the window. In the kitchen the most likely sources of ignition in the gas stove when ignited burner, so the result can be interpreted as follows: approximation gas stove to the window with a high probability will reduce the pressure of the explosion in the kitchen. Note that a reduction in the temperature of the gas should not directly from the fact that the end of combustion. It appears that the drop in temperature due to the fact that the end of the dynamic burning process finishes ejection of gas space which is then replaced by the implosion process, which can be seen in the graph of pressure (Fig. 9). Implosion pressure than the pressure of the explosion is small, a total of 40 Units, but it is sufficient to cool the room air is rushed from the atmosphere at a speed of about 8m/s. Clearly seen fading oscillations with a frequency of about 5 Hz, very similar to those observed in the Helmholtz resonator, referred to as the first frequency. Accompany the process of explosion sound vibrations frequency of about 90 Hz and them, he ends

up with gradually decreasing amplitude from 4 to 1 Units, i.e. from loud noise to gradually abating.

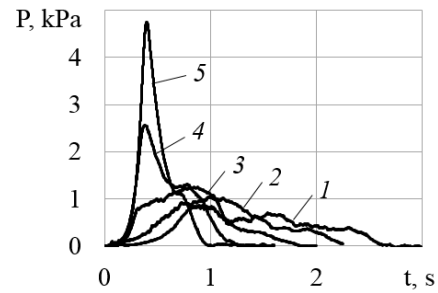


Fig. 9 dynamics of pressure in the explosions at different distances of the flashpoints from the window

An interesting question is about the factors contributing to this difference in pressure of the explosion: whether this difference is size of the area of the flame front at different experiments, whether it is the temperature of the combustion products, approached the window and provide a high rate of flow? The dynamics of the flame front is shown in fig 10, which shows in comparison with fig. 9, that increasing combustion area is increased and the pressure of explosion, but the maximum area ratio is not more than 1.4, while the pressure ratio, as can be seen - considerably more. It is also known that these two process parameter proportional to each other, which implies that the pressure increase cannot be explained only by an increase in the area of the flame front. The main reason for the increase of pressure at a remote location from the ignition box lies in the fact that when ignited the far wall all the released energy is consumed during combustion to increase the capacity of the gas is in the room, including increasing the pressure. When ignited, the same window of the energy would be moved from out flowing gas from the premises, so the potential for gas indoor environment less, and with it the pressure is less than in the first case

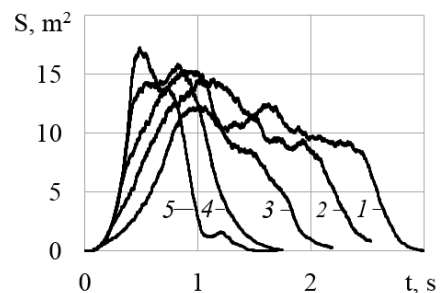


Fig. 10 dynamics of the flame front at different distances of the flashpoints from the window

Fig. 11 shows an enlarged version of the graph of temperature dynamics in the cell window, shown in Fig. 4, extract taken early in the process. "Irresolute" pressure increase in temperature early in the process, most likely due to the fact that the temperature sensor is located in a different cell

than a source of ignition, even though both cells are arranged in the plane of the window.

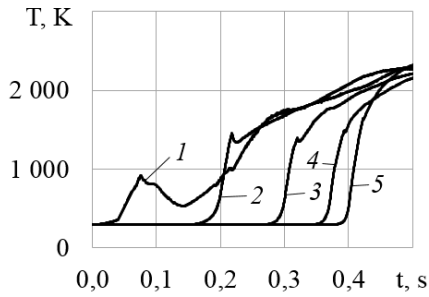


Fig. 11 first time of temperature dynamics on the center plane of the windows

It is understood that as a result of explosion in all embodiments of the combustion space to occupy a density less 5 times than the original mixture. It turns out that the difference in weight between the original mixture and the combustion products is 80 % of the original, has been thrown out the window. Thrown in different ways: in the ignition at the far wall a significant part of the initial mixture was ejected unburned, and when ignited by the window - of him all the time expired explosion combustion products. Unburned portion of the original mixture, presumably, had burned outside, outdoors.

We remark that the reduction in the temperature of the gas should not directly from the fact that the end of combustion. Appears that temperature decrease due to the fact that the end of the dynamic burning process finishes the ejection of gas space which is then replaced by the implosion process, which can be seen in the graph of pressure (Fig. 12). Implosion pressure compared with the pressure of the explosion is small, only 20 Pa below atmospheric pressure, but as can be seen, it is sufficient to cool rushed to the room air atmosphere with a rate of about 6 m / s. Clearly seen fading oscillations with a frequency of about 5 Hz, very similar to those observed in the Helmholtz resonator, referred to as the first frequency.

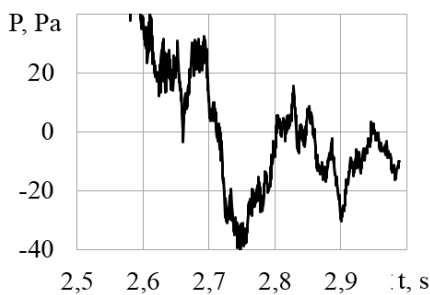


Fig. 12 dynamics of pressure in the explosions at ignition near the window for $t > 2.5$ (fragment fig. 9)

Accompany the processes of the explosion sound oscillations frequency of about 90 Hz and them, he ends up with gradually decreasing amplitude from 4 to 1 Pa, i.e. from

loud noise to gradually abating.

VII. CONCLUSION

Pressure gas explosion in a room largely depends on the location of ignition, the closer to the window is the flash point, the lower explosion pressure, and the pressure ratio can be 6 times. Duration explosion contrary, in this case reduced in triplicate, in the above calculation 1 second of gas when ignited, and the far wall to 3 seconds - the window when ignited.

REFERENCES

- [1] Pozhari I vzrivi v proizvodstvennih pomeseniah v stranah Evropi. Hronika 2003-2005 gg. RIA Novosti. El.Resysr. <http://ria.ru/spravka/20051212/42448122.html>
- [2] Iurii H. Polandov, Mikhail A. Barg and Vitaly A. Babankov (2009), "On the decreasing of the burnout time for a gas-air mixture in a closed volume", Proceedings of the 7th International Congress on Computational Mechanics (GRACM 07), Athens, 30 June – 2 July 2011.
- [3] Iurii H. Polandov, Mikhail A. Barg and Vitaly A. Babankov, "On the effectiveness of the bypass explosion valve", Proceedings of 6th European Congress on Computational Methods in Applied Sciences and Engineering (ECCOMAS-2012), September 10-14, 2012, Vienna
- [4] Davydov, Yu. M. (1990) Large-particle method. In: Encyclopaedia of Mathematics. Vol. 5, Kluwer academic publishers, London.

Effect of carburizing on fatigue life of high-strength steel specimen under push-pull loading

Štěpán Major, Vladimír Jakl and Štěpán Hubálovský

Abstract— Many articles are dedicated to effect of surface layer on fatigue life. However, most of these articles are dedicated to the steels with nitride layer and only small number of papers is dedicated to the carburizing. Results of extended experimental investigation of fatigue resistance of plasma-carburized specimens made of the low-alloy high-strength steel are presented. The specimens were subjected to push-pull loading of different R -ratios. The application of plasma carburizing can lead to about 25% increase in the fatigue resistance in the high cycle region (over 10^5 cycles). On the contrary, in the case of low cycle fatigue often has a negative effect on the service life.

Keywords—Carburizing, fatigue life, sub-surface crack, high-strength steel, push-pull, bending-torsion..

I. INTRODUCTION

NOWADAYS, gas and plasma nitriding, carburizing and nitrocarburizing are widely used surface treatments in applications where mechanical properties, such as wear and fatigue resistance, are in major concern [1-8]. Their comparatively low cost in combination with their wide applicability of steel grades explains the success of these techniques. Several investigations have been carried out to determine the influence of nitriding treatments on mechanical properties but, the influence of carburization is much less studied.

A. Role of Surface Layer

Under the high-cycle fatigue loadings, the fatigue crack of a smooth metal specimen initiates from the inclusion formed during cyclic loading and became a source of local stress concentration [3,4]. Therefore, by improving surface hardness, the initiation of a fatigue crack can be retarded by restraining the dislocation movement on the surface [3,4]. If it is hard enough to prevent slip deformation on the specimen surface due to the relatively less applied stress, the fatigue crack should be made at other position. Therefore, it is possible that a fatigue crack may occur due to stress concentration at a void

This work was supported in part by the Czech Science Foundation in the frame of the Project No. SVV-2011-262901.

Š. Major is working at the Institute of Theoretical and Applied Mechanics, Academy of Science, Prague 190 00, Prosecká 809/76, Czech Republic (e-mail: s.major@seznam.cz).

V. Jakl is studying at University of Pardubice, Jan Perner Transport Faculty, Pardubice 532 10, Studentská 95 and he works in Metel s.r.o., Česká Skalice 552 03, Žižkův kopec 617, Czech Republic (e-mail: vladimir.jakl@metel.cz).

Š. Hubálovský is Institute of Informatics, Faculty of Natural Science, University of Hradec Králové, Hradec Králové 500 03, Rokitsanského 62, Czech Republic (e-mail: stepan.hubalovsky@uhk.cz).

or an inclusion that exists at a position close to the specimen surface but not hardened [2,3].

B. Role of Inclusions in Fracture Process

Long life fractures usually reveal two remarkable features: a) crack nucleation on the nonmetallic or mixed inclusion, b) propagation of a crack inside the specimen. The subsurface crack usually occurs on the inclusion located at the interface of cemented layers and core of material. In the case of nitridation or in the case of ultralong life ($N_f > 10^7$) this subsurface crack have typical form, known as “fish-eye crack”. This type of subsurface cracks has been extensively studied on samples with nitrided layer [6-8]. The creation of subsurface cracks on inclusion can be explained as the result of the presence of residual stress in the surface layer. Residual stress prevents cracks on the surface of the sample. The value $K_{I,max}$ of the stress intensity factor on the surface of an ellipsoidal inclusion can be expressed as:

$$K_{I,max} \approx 0.65\sigma\sqrt{\pi\sqrt{S_{incl,ef}}} \approx \sqrt{\pi d_{incl,ef}} \quad (1)$$

where S_{incl} is the area of a cross-section of the inclusion and $d_{incl,ef}$ is the effective diameter of nonmetallic inclusion [3]:

$$S_{incl} = \frac{1}{4}\pi d_{incl}^2 \quad (2)$$

The fatigue limit σ_C can then be assessed as follows:

$$\sigma_C = \frac{K_{critical}}{0.65\sqrt{\pi \cdot d_{incl,ef}}} \quad (3)$$

where $K_{critical}$ is the critical threshold value of stress intensity factor. The residual compressive stresses in the carbon rich surface layer change the loading asymmetry [3]. Thus the critical threshold value varies depending on the depth from specimens surface. The relationship between critical threshold value of stress intensity factor and the loading asymmetry can be described as:

$$K_{critical(R)} = \frac{1.8K_{critical(R=0)}}{\left\{ \frac{1+R}{1-R} + \left[\left(\frac{1+R}{1-R} \right)^2 + 4 \right]^{1/2} \right\}^{a/2}} \quad (4)$$

where $K_{critical(R=0)} = 2.58 \text{ MPa}\cdot\text{m}^{1/2}$ is the critical threshold value for $R = 0$, position $R = 0$ in the surface layer corresponds to the tempered steel in the core of specimen. Calculated relation between critical threshold value $K_{critical}$ and the depth inside the carburized surface (calculation is made from the surface up to the tempered core) is plotted in Fig. 1(a). Based on this knowledge, a critical inclusion dimension, $d_{incl,ef} = d_{critical}$, necessary for the crack initiation, can be assessed by using (3). The result is presented in Fig. 1(b). The critical dimension inside the carburized layer exceeds hundredfold the inclusion size of tens of microns as commonly found in commercial steels. This is also the reason why the crack initiates on inclusions inside the tempered core of specimen and cracking is not observed on inclusions in carbon-rich layers (in the case of high-cycle fatigue). On the other hand, the diameter $d_{incl,ef}$ of an sulfide inclusion in the core (in the distance of about 0.5 mm from the surface) fully corresponds to a real dimension of inclusions.

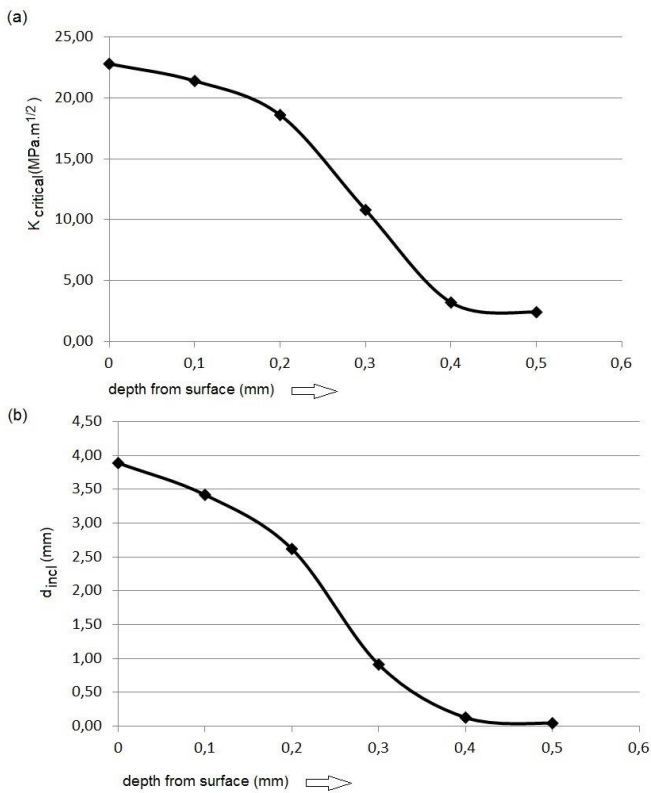


Fig. 1 (a) Distribution $K_{critical}$ in surface layer, (b) Critical dimension of inclusion.

In the center of the “fish-eye” crack, an inclusion is found and in the case sufficiently long fatigue process (over $5 \cdot 10^5$ cycles in the case of surface-refined material and in the case of specimen without coating/surface layer over 10^7 cycles, thus in the case of ultralong fatigue) there is the optically different region in vicinity of initiation inclusion [2,9].

A. Material Composition

The cylindrical specimens were made of the steel DIN 17210 (equivalent to 20NiCrMo2-2 EN 10084-94). The chemical composition of the materials is (weight %): C 0.015, Si 0.43, 0.04 P, 0.035 S, 0.65 Cr, 0.28 Mo, 0.48 Ni, 0.013 Al. The basic mechanical properties of the material are minimal yield strength $\sigma_{y,min} = 930 \text{ MPa}$ and ultimate strength $S_u = 1170 \text{ MPa}$. One of the surface treatment methods improving the some materials properties is carburizing. Carburizing is a heat treatment process in which steel is heated in the presence of another material (in the range of 880 to 980 °C) which liberates carbon as it decomposes. Depending on the amount of time and temperature, the affected area can vary in carbon content. Longer carburizing times and higher temperatures lead to greater carbon diffusion into the part as well as increased depth of carbon diffusion. When the iron or steel is cooled rapidly by quenching, the higher carbon content on the outer surface becomes hard via the transformation from austenite to martensite, while the core remains soft and tough as a ferritic or pearlite microstructure.

B. Details of Carburizing Process

In gas carburizing, commercially the most important variant of carburizing, the source of carbon is a carbon-rich furnace atmosphere produced either from gaseous hydrocarbons, for example, methane (CH_4), propane (C_3H_8), and butane (C_4H_{10}), or from vaporized hydrocarbon liquids. Parameters of gas-carburizing process are: carburizing temperature $T_C = 880 \text{ °C}$, time of carburizing $t_{TC} = 4$ hours for first group of samples and for second group is $T_C = 920 \text{ °C}$ and time $t_{TC} = 2.2$ hours, time of cooling $t_{cool} = 2.5$ hours for both type of specimen. In this case the application of the atmosphere composed of 23% CO , 36% H_2 , 40% N_2 , 2% CH_4 and 2% ($\text{CO}_2 + \text{H}_2\text{O}$). In the role of carburizing agents are in this case CO and CH_4 . The obtained depth of hardened layer was $h_{CS} = 0.65 \text{ mm}$. After carburizing the samples were twice hardened, first at 900 °C and again at 780 °C . In both cases were endurance time at hardening temperature $t_H = 35 \text{ min}$ and time of cooling $t_{cool} = 30 \text{ min}$. As a cooling medium was used water solution with 10% NaOH . The specimens were tempered at 180 °C (2 hours).

III. FATIGUE EXPERIMENTS

Fatigue tests of steel 20NiCrMo2-2 EN 10084-94 in tempered and carburized states were performed by means of the resonance testing machine Rumul – Mikrotron 20 kN using cylindrical specimens with diameter 6 mm. Two stress ratios were used: $R_{SRA} = 0.1$ for tension – tension loading and $R_{SRA} = -0.053$. The latter asymmetry was set up with respect to the total load capacity of the testing machine. Frequency of loading was 80 Hz. These experiments fall in high-cycle region.

The low-cycle experiments were performed only for stress ratio $R_{SRA} = 0.1$. The fatigue experiments were made at the room temperature. The specimens were loaded to final rapture.

IV. EXPERIMENTAL RESULTS AND DISCUSSION

A. Push-Pull Loading and Effect of Stress Asymmetry

The effect of carburizing technology on the sensitivity to the loading asymmetry is expressed by means of the Smiths diagram constructed for both tempered and carburized specimens (Fig. 2) by using fatigue limits presented in Table 1.

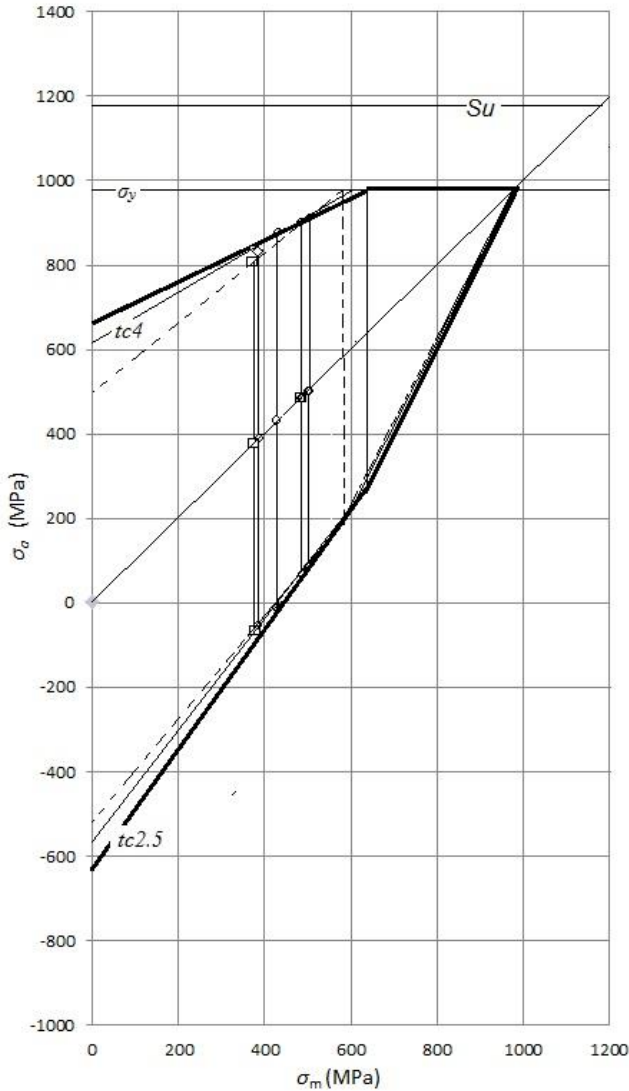


Fig. 2 Smiths diagram designed for the tempered state (dash line) of steel and the carburized state: time of carburizing $t_{CT} = 4$ hours (thick line) and $t_{CT} = 2.5$ hours (thin line).

From the diagram, the fatigue limit for $R_{SrA} = -1$ can be deduced. Presented values indicate a sensitivity of the carburized steel to the loading asymmetry. The application of carburizing increases the fatigue limit in case of $R_{SrA} = .1$ ($\sigma_m = 0$). When pull loading prevails ($R_{SrA} = 0.053$), the increase in the fatigue limit amplitude is only moderate and, for the fully pull loading ($R_{SrA} = 0.1$), the contribution of carburizing to fatigue resistance becomes negligible. In the case of low-cycle fatigue, the fatigue resistance decreases with the thickness of the carbon-rich layer. Carbide particles in the surface layer are

cracking under cyclic loading and become the point of crack initiation, and the effect of carburizing on the fatigue resistance become negative.

Table 1. Comparison of fatigue limits for different stress asymmetry ratios R_{SrA} . h is depth of surface layer, t_{CT} time of carburizing

R_{SrA}		-0.053		0.1		-1
Stress [MPa]		σ_m	σ_a	σ_m	σ_a	σ_m
Treatment/ t_{CT} [hours]	h [mm]					
tempering	0	370	± 440	500	± 400	± 500
$t_{CT} 2.5$	0.25	440	± 440	520	± 400	± 680
$t_{CT} 4$	0.55	390	± 430	540	± 420	± 600

B. Effect of carburized layer depth

The effect of layer depth on the fatigue life was measured for the asymmetry $R_{SrA} = -0.053$, and the results are shown in Fig. 3. It seems that the optimal layer depth ranges from 0.2 to 0.4 mm. The optimum depth of about 0.35 mm corresponds to the carburizing time of 2.5 hours. For the case of $R_{SrA} = 0.1$, the fatigue life even decreases with increasing depth of the carburized layer. It means that thicker carburized layer needs not always lead to a longer fatigue life; there is an optimal layer depth for each type of steel and loading.

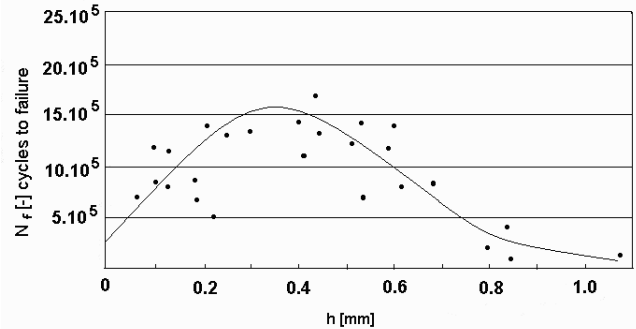


Fig. 3 Dependence of the fatigue life on the layer depth for the asymmetry $R_{SrA} = -0,053$

C. Effect of annealing of surface layer

A very important factor, influencing the fatigue resistance of specimen, is the depth of surface film of carbids (compound layer) deposited onto the carburized layer. A heterogeneous compound layer is often a site of an early fracture initiation. This fact has been confirmed, as well as was in experiments, where the compound layer was mechanically removed by fine grinding [1]. This type of sample modification completely changed the type of fracture initiation particularly at high levels of loadings. Before this operation, fracture started from the specimen surface inside the compound layer. After the

process of grinding, the epicentre of fracture transferred out of the diffusion layer into the specimen core. This alteration in fracture mode was accompanied by a significant increase in the fatigue life.

A reduction of the compound layer depth can also be achieved by the annealing treatment after carburizing. It removes the carbide film, increases the depth of diffusion layer and reduces the gradient of carbon concentration throughout the layer. On the other hand, the annealing treatment decreases the level of residual stresses in the diffusion layer. To evaluate the efficiency of such treatment, three sets of specimens were prepared:

- 1) depth of carburized layer 0.25 mm, compound layer of about 0.002 mm
- 2) depth of carburized layer 0.25 mm, compound layer of about 0.004 mm.
- 3) Annealing 565°C, without compound layer, carburized layer of about 0.6 mm.

Experimental results are shown in Fig. 4 in the form of Wöhler curves, plotted for the maximum stress in the loading cycle. The lines marked with the symbol (a) show levels of fatigue limit and endurance in the tempered state. Lines marked by symbols (b), (c) and (d) correspond to the above mentioned carburizing treatment. Also, levels of the yield stress, σ_y , are marked out in this diagram. It is clear from the graph, that the fatigue limits of carburized specimens (b) and (c) are higher than the fatigue limit of only tempered specimens. A reduced thickness of the compound layer increased the fatigue limit (of nearly 5 %). Moreover, the annealing strongly reduces both the fatigue limit and the fatigue endurance despite of an increased depth of the diffusion layer. The reason lies, most probably, in the release of compressive residual stresses since prevailing tension internal stresses were found on the surface of annealed specimens.

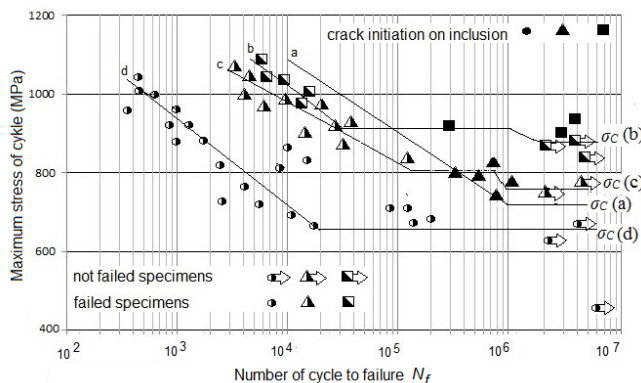


Fig.4 Wöhler curves of the steel 20NiCrMo2-2 (a) quenched and tempered, (b) carburized, depth of the compound layer of 0.002 mm, (c) carburized, depth of the compound layer of 0.004 mm, (d) carburized and annealed at 565 C.

V. CONCLUSION

The main results of investigations can be summarized into

the following points:

- 1) The application of plasma carburizing can lead to about 25% increase in the fatigue resistance in both the low- and the high cycle region. It holds for a wide range of loading types as symmetrical push-pull loading. However, the fatigue strength dramatically drops when the peak stress in the cycle reaches the strength of the carburized compound layer. This is typical for highly asymmetric push-pull loadings
- 2) The elimination of the compound carbide film by annealing after carburizing led to a significant reduction of fatigue limit even in comparison to only tempered (virgin) specimens. The reason lies in inducing tensile residual stresses on the surface.
- 3) In case of sufficiently homogeneous carburized layers, the crack initiation in the high cycle region starts near the inclusions outside the layer, close to the layer-core interface. It leads to the fish-eye fracture morphology. This phenomenon can be explained by the concept of the threshold stress intensity factor with respect to the existence of residual stresses in the carburized layer.

ACKNOWLEDGMENT

This work was supported in part by the Czech Science Foundation in the frame of the Project No. SVV-2011-262901 and by the institutional research project of Institute of Theoretical and Applied Mechanics, AS ČR.

REFERENCES

- [1] Š. Major, J. Papuga, J. Horníková, J. Pokluda, Comparison of Fatigue Criteria for Combined Bending-torsion Loading of Nitrided and Virgin Specimens. *Strength of Materials*, Vol. 40, No. 1 (2008), 64-66.
- [2] Y. Murakami: *Metal Fatigue: Effects of Small Defects and Nonmetallic Inclusions*, Elsevier, 2002.
- [3] K. Slámečka; J. Pokluda; M. Kianicová, Š. Major, I. Dvořák, *International Journal of Fatigue*, 2010, vol. 32, No. 6, s. 921-928.
- [4] J. Pokluda, I. Dvořák, Š. Major, H. Horáková: Influence of Plasma-Nitriding surface layer on fatigue life of steel specimens under push-pull and bending-torsion. *Fatigue Congress 2006, Atlanta, USA*
- [5] Shao Mei Zheng et al., 2011, *Advanced Materials Research*, 214, 564-568
- [6] Li Na Guo, Jin Chen, Jun De Pan, 2012, *Applied Mechanics and Materials*, 217-219, 1257-1260
- [7] Gao Hui Zhang, Ping Ze Zhang, Ming Zhou Yu, Zhong Xu, 2008, *Advanced Materials Research*, 47-50, 1197-1200
- [8] Hassan A. Wahab, M.Y. Noordin, S. Izman, Z. Kamdi, Denni Kurniawan 2013, *Advanced Materials Research*, 845, 378-381
- [9] K. Shiozova, L. Lu, S. Ishihara, *Fatigue Fract. Eng. Mater. Struct.* 24, 2001, pp. 781-790.

PERPETUATE project: guidelines for the seismic performance-based assessment of cultural heritage assets

Sergio Lagomarsino

Abstract—The paper describes the methodology proposed in the PERPETUATE Project (funded by the Seventh Framework Program of the European Commission – Theme ENV.2009.3.2.1.1). The methodology proposed in PERPETUATE uses a displacement-based approach for the vulnerability assessment evaluation and design of interventions. The use of safety verification in terms of displacement, rather than strength, orients to new strengthening techniques and helps in the comprehension of interaction between structural elements and unmovable artistic assets. A full methodological path for the assessment of cultural heritage assets is proposed, which is based on three main steps. In the first one, the building is investigated and the seismic input is defined in accordance with specific safety and conservation requirements. In the second one, the seismic response of the asset is described through mechanical model and its capability to satisfy the defined requirements is assessed. Finally, in the third step, rehabilitation decisions are taken and, if necessary, the second step is repeated for the design of strengthening interventions. A general overview of the research tools adopted in the project is provided; in particular, experimental tests and case studies useful to validate the reliability of the proposed procedure are presented.

Keywords—Cultural heritage, Masonry buildings, Performance-Based Assessment, Pushover analysis.

I. INTRODUCTION

The damage assessment to cultural heritage assets after recent earthquakes, in particular in Italy (Umbria and Marche, 1997; L’Aquila 2009 and Emilia 2012), showed the high vulnerability of some types of historical structures (churches, towers). Earthquakes also proved that strengthening interventions adopted in the last decades are invasive, not effective and even increase the vulnerability. Thus, there is an urgent need for disseminating these discoveries and promoting a new and really effective strategy for the risk mitigation of cultural heritage.

The preservation of cultural heritage assets must guarantee their capacity of lasting over time against decay, natural hazards and extreme events, without losing their authenticity and usability. This means that the need of guaranteeing an “acceptable level” of structural safety for building’s occupants should be always related to the principle of “minimum intervention” on the building itself. The definition of “acceptable” safety levels, as well as the concept of “safety”,

still represents an open issue for monumental buildings. Furthermore, it should be considered that the intangible value of these buildings depends, besides their social and historical meaning, on both architectural and artistic factors. Thus, their risk assessment is a challenge regarding not only structural and architectural components, but also movable (paintings, statues, libraries...) and unmovable (frescos, stucco-works, pinnacles, battlements, banisters, balconies) artistic assets contained in it.

Within this context, the project has intended to develop a methodology for the assessment of seismic risk to cultural heritage assets and design of interventions. PERPETUATE [1] (www.perpetuate.eu) is a project funded by the Seventh Framework Programme (Theme ENV.2009.3.2.1.1 – 2010-2012) developed by a consortium which includes 6 Universities, 2 Public Institutions and 3 SMEs. In particular, 5 European Countries (France, Greece, Italy, Slovenia, United Kingdom) and 1 International Cooperation Partner Country (Algeria) are represented.

In particular, the methodology developed is based on the following principia.

The protection of cultural heritage needs an *improvement in methods of analysis and assessment procedures* rather than improvement of intervention techniques. A reliable assessment procedure is the main tool to respect the principle of “minimum intervention” under the constraint of structural safety.

If, by reliable methods of analysis and assessment procedures, *it is demonstrated that the monument is not safe and that its retrofitting is unavoidable*, an effective improvement of the intervention techniques does not necessarily need new materials and technologies. In many cases, traditional techniques, improved by the results of new methods of analysis, represent a sustainable, effective, cost-efficient and reversible solution.

The *displacement-based approach* for vulnerability assessment of cultural heritage assets and design of interventions is adopted as standard method of analysis. The mechanical models available for the analysis of ancient masonry buildings or elements usually consider a verification approach in terms of strength, because in the past strengthening techniques were based on the concept of increasing stiffness and strength. This approach is correct in static conditions. However, earthquake is a dynamic

S. Lagomarsino is with Department of Civil, Chemical and Environmental Engineering, University of Genoa, Via Montallegro 1, 16145 Genova, Italy (phone: +39 3487985456; e-mail: sergio.lagomarsino@unige.it).

phenomenon that induces deformations and dynamic amplification. The seismic response of the structure depends on its dynamic properties. Usually much more the construction is stiffer much higher are the equivalent static actions, which is subjected to: thus, flexibility is a first positive characteristic for a good seismic behaviour. Moreover, since inertial actions are proportional to the weight of the construction, the lightness is a second fundamental aspect. Finally, in the case of rare destructive earthquakes, it is impossible to bear the seismic actions without significant damage. Hence, the building must be ductile enough and be able to sustain vertical loads without collapse, even if large horizontal displacements are induced by the earthquake.

Despite the complex nature of heritage buildings and artistic assets, the DBA (Displacement Based Assessment) calls for *nonlinear models*. Nonlinear static (pushover) analyses are considered as main tool for the application of the assessment procedure. Nonlinear dynamic analyses are considered as an alternative tool only for certain types of assets.

A reliable assessment procedure of heritage buildings requires that both *architectonic and artistic assets* contained in them are considered.

The procedure is oriented to the assessment of single cultural assets. The concept of “single cultural asset” has been extended to different scales, *going from the single monument to the historic centre*, intended as a complex asset that, although made of many buildings, has a cultural relevance in its systemic unity.

A full methodological path for the assessment of cultural heritage assets is proposed based on three main steps. In the first one, the building is known and the seismic input is defined in accordance with specific safety and conservation requirements. In the second one, the seismic response of the asset is described through mechanical model and its capability to satisfy the defined requirements is assessed. Finally, the results are discussed and rehabilitation decisions are taken.

According to the general framework aforementioned, in the paper a general overview of the complete path proposed for the seismic assessment in PERPETUATE project is described (§2), paying attention also on some of the main tools that supported the research developed, like as experimental campaigns (§3) and application to several case studies (§4).

II. BASIC PRINCIPLES OF THE PERPETUATE PROCEDURE

Seismic performance-based assessment (PBA) of an existing building checks if the construction is able to fulfil some selected performance levels (PLs) in case of occurrence of properly defined earthquake hazard levels, in terms of annual rate of exceedance (or return period T_R).

Target performance levels are properly defined by PERPETUATE for cultural heritage assets, which consider not only the use and safety of people but also the conservation of the architectonic and artistic value of the monument.

Nonlinear analyses, both static and dynamic, are necessary for evaluating the seismic behavior of masonry structures after damage occurs, till to near collapse conditions. A classification of architectonic and artistic assets is proposed

and typical damage modes are described in order to address the possible modeling strategies. Four alternative types of models have been identified and developed with the aim of analyzing the wide variety of historical masonry constructions. Nonlinear static (pushover) analysis is considered the main tool for the PBA and detailed acceptance criteria are proposed for the identification of PLs on the pushover curve, related to the different targets of performance (Fig. 1).

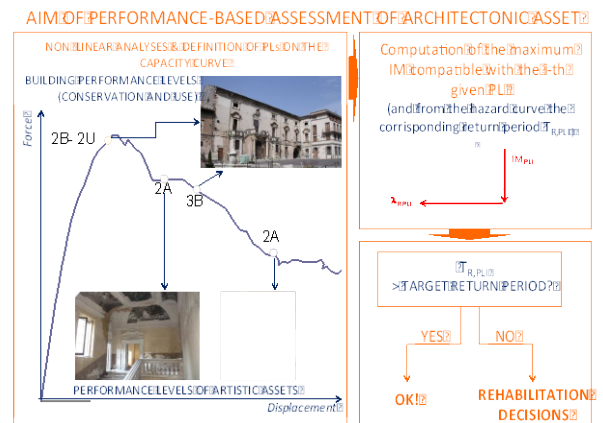


Fig. 1 The performance-based assessment of architectonic and artistic assets: pushover curve, performance levels and return periods of the seismic input compatible with target performance

Nonlinear dynamic analyses represent an alternative tool, suitable for some types of architectonic assets and useful in some specific conditions. Rarely it is necessary to restrict to linear elastic analysis, due to the complexity of the model if the building is huge; hints are given for the definition of a simplified capacity curve and the PLs, in order to perform also in this case a displacement-based assessment.

The seismic input is represented by an Acceleration-Displacement Response Spectrum (ADRS), completely defined for the specific site of the building under investigation as a function of one parameter assumed as Intensity Measure (IM) of the earthquake. Possible IMs are: peak ground acceleration, spectral acceleration for a given period, maximum spectral displacement, Arias intensity, Housner intensity. A Probabilistic Seismic Hazard Analysis (PSHA) is necessary in order to evaluate the annual probability of occurrence (or the return period) of earthquakes of different values of IM (hazard curve). In some cases a Vector-Valued PSHA may be used, in order to better describe the characteristics of the seismic input (hazard surface).

The outcome of the assessment is the maximum IM compatible with the fulfilment of each performance level that has to be considered for the asset; through the hazard curve, it is possible to evaluate the annual rate of exceedance λ (or the earthquake return period $T_{R,PL}=1/\lambda$) correspondent to this performance. These values may be compared with the target return period assumed for the assessment, as a function of the characteristics of the asset.

The format of the assessment proposed by PERPETUATE guidelines is deterministic, except for the occurrence of the earthquake, as well as in all codes and recommendations

worldwide adopted at present. However, it is well known many uncertainties, aleatory and epistemic, affect the assessment of an existing masonry building, with reference to: a) the relevant characteristics of seismic input (duration, frequency content, etc.); b) the reliability of mechanical models; c) the material parameters; d) the incomplete knowledge of the construction. PERPETUATE takes into account of probabilistic aspects in some steps of the procedure: acceptance criteria for the definition of PLs; sensitivity analysis for drawing the protocol of in-situ investigations.

A full methodological path for the assessment of cultural heritage assets is proposed, which is based on three main steps (Fig. 2) [2].

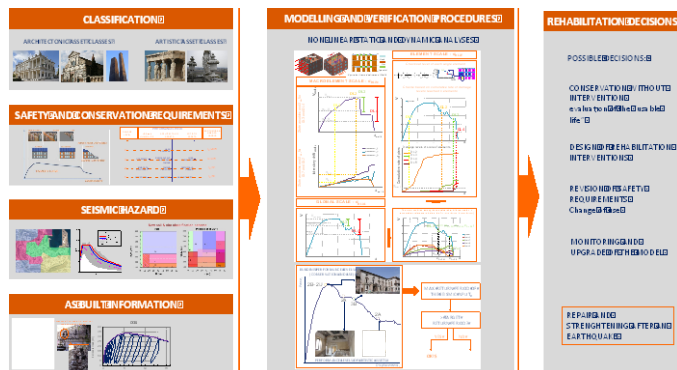


Fig. 2 Overall scheme of the PERPETUATE procedure

The first one includes: 1) classification of the architectonic asset and contained artistic assets; 2) definition of performance limit states (specific for the cultural heritage assets); 3) evaluation of seismic hazard and soil-foundation interaction; 4) construction knowledge (non-destructive testing, material parameters, structural identification). The second step is related to: 1) the definition of structural models for the seismic analysis of the masonry building and the contained artistic assets; 2) verification procedures. Finally, in the third step, rehabilitation decisions are taken and, if necessary, the second step is repeated for the design of strengthening interventions.

A. Classification of the architectonic asset and the artistic asset contained and preliminary modeling choices

The seismic assessment of a cultural heritage asset requires a deep preliminary knowledge of the construction from the historical point of view, in order to single out the main elements of authenticity and architectural value, as well as the transformations occurred along the past centuries. It is necessary to be aware of the relevance of the different parts of the construction, establishing a hierarchy among architectural elements with the aim of choosing, among possible alternatives, the less invasive strengthening solution.

After a preliminary phase in which the asset is studied, its historical and architectural relevance is analyzed and its use is identified, the monument is classified according to PERPETUATE classes: from A to F (Fig. 3) [3]. The classification is based on the prevailing seismic damage modes of assets (identified at the scale of “macroelements” in

Deliverable 4 [3] and Deliverable 5 [4]) and on the assumption that their occurrence is closely related to building morphology (architectural form, proportions) and technology (type of masonry, nature of horizontal diaphragms, effectiveness of wall-to-wall and floor-to-walls connections). It should be not intended in a strict way because of complexity of buildings and variety of related macroelements. It is clear that each class and related sub-class collect a wide variety of buildings and a single building may belong to different classes depending on its specific features (e.g. even if two buildings have the same function they may differ for the morphology or for the constructive and technological details/solutions). In this sense, as an example, it is important pointing out it is the prevailing seismic behavior and not the use that plays the fundamental role in the assignment of a certain class. The assignment to a class is functional to drive modeling choices and identify proper limit states on the capacity curve.

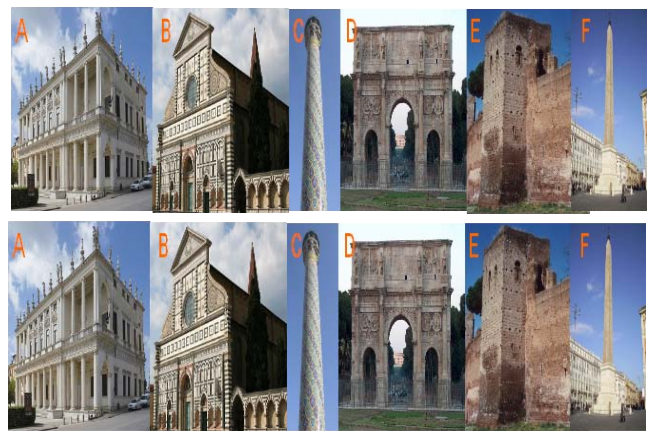


Fig. 3 Overview of the architectonic asset examined and classified in PERPETUATE project

In particular models are classified with reference to the modelling scale (masonry material or structural elements) and the type of discretization (continuous or discrete):

- CCLM (Continuous Constitutive Law Models): finite element modelling with phenomenological or micromechanical homogenized constitutive laws;
- SEM (Structural Elements Models): equivalent frame modelling by discretization in terms of piers, spandrels and other linear and nonlinear elements;
- DIM (Discrete Interface Models): discrete modelling of blocks and interfaces;
- MBM (Macro-Blocks Models): application of limit analysis (upper and lower bound theorem) to a predefined collapse mechanism of rigid blocks.

The correlation between classes and suggested modelling approaches is summarized in Fig. 4.

The type of models proposed have been analyzed in Deliverable 7 [5], while in Deliverable 26 [6] the specific problems of each approach in relation to different building classes are discussed.

Architectonic asset class		Model type			
		CCLM	SEM	DIM	MEM
A	Assets subjected to prevailing in-plane damage Palaces, castles, religious houses, caravansaries, collective buildings	Standard	Global	Possible	Local
B	Assets subjected to prevailing out-of-plane damage Churches, mosques, modern theatres, markets, industrial buildings	Possible	Possible	Possible	Local
C	Assets characterized by monodimensional masonry elements Towers, bell towers, minarets, lighthouses, chimneys	Possible	Global	Possible	Possible
D	Arched structures subject to in-plane damage Triumphal arches, aqueducts, bridges, cloisters	Possible	Possible	Possible	Local
E	Massive structures with prevailing local failure of masonry Fortresses, defensive city walls, Roman and Greek theatres	Possible	Possible	Global	Possible
F	Blocky structures subjected to overturning Columns, obelisks, trilithes, archaeological ruins, Greek temples	Possible	Possible	Possible	Local
G	Built systems subjected to complex damage Historical centers	Possible	Global	Possible	Local

Standard Possible Rare

Fig. 4 Classes of buildings and related types of models

B. Safety and conservation requirements

It is a shared opinion that it is not possible to define strict safety levels for cultural assets, since the “case by case” approach is always preferable. The definition of “acceptable” safety levels may be intended as a compromise: on the one side, they must prevent the damage deriving from environmental actions (earthquake, flood, aging); on the other side, they must prevent from invasive interventions, designed in order to avoid future damage from environmental actions but unwillingly producing immediate and significant loss in terms of conservation. To conciliate these issues is of fundamental relevance. “Acceptable” safety levels for cultural heritage assets aimed to be based on the concept of performance limit states (PLs). For ordinary buildings, PLs mainly refers to safety and economic issues. If the occurrence of damage may be acceptable for monumental buildings, it may be debatable for artistic assets due to their intrinsically “irrecoverable” nature. Thus, in cultural heritage assets, conservation and safety of people should be considered in an integrated approach. According to this, in PERPETUATE project, the following targets have been considered: *Use and human life* (U), *Building conservation* (B); *Artistic asset conservation* (A) (Fig. 5).

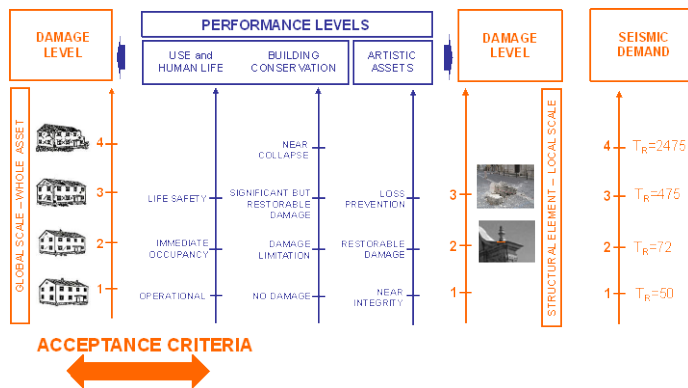


Fig. 5 PERPETUATE performance levels and damage levels

Proper acceptance criteria (to verify whether the asset is able to satisfy the required PLs for the considered hazard levels or not) are defined on the basis of *Damage Levels* (DLs), as illustrated in Deliverable 17 [7].

Moreover, PLs for each targets are identified and the related earthquake hazard levels, expressed in terms of return period ($T_{RD,PLi}$), are indicated. The return periods may be modified by importance coefficients (γ_k , where $k=U,B,A$), which take into account the use and the architectonic and artistic relevance of the examined building [3].

C. Seismic hazard

The evaluation of the seismic hazard plays a fundamental role in the seismic risk assessment of heritage buildings, since they are sensitive to: particular characteristics of the seismic input (earthquake duration, frequency content in the long period range, vertical component of the motion); soil amplification effects; soil-structure interaction phenomena (in the case of big, heavy and stiff masonry structures). In fact, many differences with modern buildings considered in building codes may be highlighted. As an example, historical buildings are sometimes built at locations where strong local site effects occur due to steep topography (e.g. hilltops), basin effects or foundations built on the remains from previous structures. Moreover, the long period of vibration of some classes of asset (consider the case of rocking behaviour in single stone columns) requires a reliable definition of the acceleration-displacement response spectrum also in this range.

PERPETUATE, after a detailed probabilistic analysis of available intensity measures, has intended to obtain proper Acceleration-Displacement Response Spectra (ADRS) and proper time-histories for cultural heritage assets (Deliverable 10 [8], Deliverable 13 [9], Deliverable 24 [10]). Furthermore, the project developed an improved foundation model for the vulnerability assessment of massive masonry structures, taking into account the role of the foundation compliance, associated soil-foundation interaction (SFI) and soil-foundation-structure interaction (SFSI) effects (Deliverable 14 [11] and Deliverable 25 [12]). The role of the foundation and SFSI effects was supposed to be studied both for seismic ground shaking and induced permanent ground deformations (Deliverable 21 [13]).

D. As built information

The minimization of interventions on cultural heritage assets requires a comprehensive knowledge on the assets themselves. In order to guarantee a shared and uniform approach at a European level, the project defined both standards concerning the survey of the asset (structural and technological survey, material characterization, etc.) on the basis of traditional and innovative techniques (Deliverable 6 [14]) and proper criteria to optimize the investigation plan (in order to minimize its invasiveness and impact on building).

In particular, according to the PERPETUATE procedure, the idea is that investigation program should be based on preliminary sensitivity analyses aimed to: identify the main parameters to be investigated; define proper Confidence Factors (CFs) of the model (Deliverable 22 [15]). Such an approach is motivated by two observations: in the seismic safety assessment of an existing building epistemic

uncertainties due to the incomplete knowledge of the asset add up to statistical ones; in cultural heritage assets, the primary conservation objective should be guaranteed and thus the impact of investigations should be minimized. The identification of main parameters influencing the structural response of the asset allows to finalize the investigation to few important points (thus reducing costs and time) and to reduce the number of destructive tests. The calibration of CFs on the basis of sensitivity analyses instead of a-priori assumptions (as usually done for standard buildings) provides more reliable models and results. In fact, in sensitivity analyses both statistical uncertainties, treated by proper random variables, and epistemic uncertainties, treated by a logic tree approach, are considered.

Moreover, on the basis of a review of techniques for the knowledge of cultural assets developed in Deliverable 6 [14], sets of information related to principles and scopes of testing, figures of test set-up, test procedures and measurements, interpretation of results, together with code provisions, are summarized in tables that may represent an useful tools for professionals. Reference values for the main mechanical parameters of masonry (elastic modulus, shear and compressive strength, panel drift) are provided, based on literature and codes review and experimental tests. Besides methods to identify mechanical parameters of materials and structural elements, also the methods to identify the overall dynamic behavior of heritage buildings (through the ambient vibration techniques, Deliverable 16 [16]) or the presence of permanent displacements (through remote sensing techniques, Deliverable 11 [17]) have been investigated.

E. Modelling and safety verifications

In order to perform displacement-based verifications, models capable to describe the nonlinear behaviour of the assets under the external actions, up to their collapse, are required. After a review of the tools available in the literature, PERPETUATE aimed to define a logical path to select the most reliable, accurate and computationally sustainable model and define proper seismic safety verification procedures for each class of asset (Deliverable 35 [18]), according to various categories as illustrated in Fig. 3.

The outcome of the PBA proposed in PERPETUATE [2] is the maximum seismic Intensity Measure compatible with the fulfilment of each performance level (IM_{PLi}), which are identified in the second step (safety and conservation requirements). To this aim, the following methods of analysis and verification procedures are considered:

- *Nonlinear Static Analysis* (pushover) and *Capacity Spectrum Method* (CSM), based on the comparison between the displacement demand, obtained by reduced acceleration-displacement response spectrum, and the displacement capacity.
- *Incremental Dynamic Analysis* (IDA) or *Nonlinear Dynamic Analyses* with a large amount of records (cloud method), based on the statistical evaluation of IM_{PLi} from the results of nonlinear dynamic analyses with properly selected time histories.

The first method (CSM) is assumed as the standard one. It

can be used for all classes of architectonic assets and also for the assessment of artistic assets. The pushover curve is obtained according to well known procedures (definition of load pattern, mixed force-displacement incremental analysis), widely applied for modern structures; the application to irregular structures with flexible horizontal diaphragms poses some questions and some specific hints for the different classes of cultural heritage assets have been examined in depth (Deliverable 26 [6]). The second one (by IDA or cloud method), even if more accurate, is suggested only for some classes of assets (e.g. Class F), for which it is applicable with a reasonable computational effort; it can be used also as validation of CSM results, in order to improve the reliability of the assessment.

As regard the safety verification path and the model to be adopted, it is useful to make a distinction between simple assets made by a single macroelement and complex assets made by a set of macroelements (Fig. 6). For assets of the first type, the single macroelement is modelled, the assessment being performed on its capacity curve. For complex assets, it is necessary to distinguish the following two sub-cases:

- Buildings characterized by box behaviour. In this case, a 3D model of the whole building is required (*global scale* approach), the assessment being performed on its overall capacity curve.
- Buildings made by a set of N macroelements, which exhibit an almost independent behaviour. In this case, each macroelement is modelled independently (*macroelement scale* approach) and N capacity curves are calculated, the seismic load being assigned by a proper redistribution. The assessment of whole asset is then made through proper combination criteria.

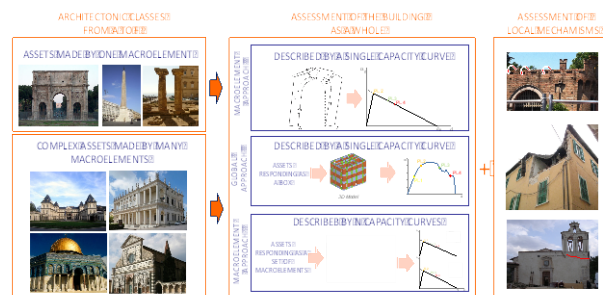


Fig. 6 Seismic assessment scales for different types of asset

All previous issues implicitly refer to the assessment of the building as a whole, with seismic loads due to the total mass of the structure. However, it is worth noting that an exhaustive seismic assessment would require also the verification of possible local mechanisms (mainly out-of-plane ones).

One of the crucial steps of the verification is the reliable definition of PLs through mechanical models. To this aim, a multi-scale approach have been proposed (Deliverable 17[7]) aimed to take into account the response of asset at different scales: structural elements scale (local damage), architectonic elements scale (damage in macroelements) and global scale (pushover curve). The basic idea is the assessment of a certain DLi at global scale comes out from a set of checks

carried out at different scales, based on: a heuristic approach related to the attainment of conventional limits on the capacity curve (fixed by expert judgment or parametric analyses), either of the whole building or of “relevant” macroelements; systematic checks on elements and macroelements, aimed to avoid the occurrence of local damage levels incompatible with the fulfillment of the considered DLi.

Finally, in order to practically model the structure, whether by the *global scale* approach or the *macroelement scale* approach, many critical observations and operative tools are provided by PERPETUATE. In particular, a new tool has been specifically developed for the macro-block modeling of collapse mechanisms (MB-PERPETUATE, Deliverable 29 [19]) and an existing software TREMURI [20] for the global analysis of masonry buildings was significantly improved.

F. Rehabilitation decisions

By mean of the hazard curve, the calculated values of IM compatible with the required PLs (IM_{PLi}) are converted in corresponding return periods $T_{R,PLi}$ in order to be compared with $T_{R,PLi}^*$, the return period of the target earthquake level requested for the given PLi. Starting from these data, results of assessment are summarized in terms of proper safety index or by introducing the concept of nominal life aimed to address the rehabilitation decisions [2].

In case safety verification highlights the need of improving the seismic capacity of the building, different rehabilitation alternatives may be considered. The design of strengthening interventions is not the only possible choice. Conservation without interventions may be also considered, if strengthening actions would be too invasive. In this case, the usable life of the building is evaluated and further decisions are postponed. Another alternative is the revision of safety requirements that, in practice, means the change of use of the building. Finally, the building may be monitored and models upgraded. Also in this case the choice is forecast in the future, when more accurate and validated tools will be available for sure, due to the improvements of applied research in the field.

G. Artistic assets

As introduced in §1 and §2.2, the safety assessment procedure developed include also the presence of immovable artistic assets contained in the building. Once identified and once assessed their cultural relevance, they are assigned to a class. In this case, the classification is based on two main criteria [21]. The first one concerns the role of the asset in the building (if structural or not). The second one is related to the interaction with the architectural asset, which they are linked to (in some cases they are strictly connected to structural elements, in others they show an own independent seismic response), and on the type of damage. In particular, according to these latter principles, three main classes have been identified (P, Q and R as indicated in Figure 7). The assignment to a class drives again modeling choices (Deliverable 23 [22]). In Figure 7, the classes of artistic assets and related modeling approaches are summarized. Besides the model type, the relation with the building structures is also

indicated, since in certain cases the seismic behavior of assets is strictly related to that of the structure, while in other cases it is not. Finally the application of the safety verification in case has been discussed as well (Deliverable 36 [23]).

Class	Str. Relation	Model type					
		Dep.	Ind.	CCLM	SEM	DIM	MBM
P Artistic assets which are structural elements by themselves Carved, carved stone columns, decorated wooden beams...	X			Standard	Possible		
Q Artistic assets which are not structural elements (strictly connected to structural elements) Carved stone plates, frescos, mosaics, stuccoes, decorated tiles...	X			Possible			
R Artistic assets which are not structural elements (with own seismic response) Altars, sculptures, pulpits, balconies, shelves, gargoyles, bells...		X		Possible		Standard	Possible

■ Standard ■ Possible ■ Rare

Fig. 7 Artistic assets classes and related modelling strategies

H. Building aggregates

When undertaking the seismic vulnerability assessment for building aggregates of a historic city centre (that may be included in class G of PERPETUATE classification) or for the portfolio of historic monumental assets of a Conservation Authority, the level of detail and the extension to which such an assessment can be performed are conditioned on one hand by the availability of economic resources and time and by the level of technical expertise of the staff appointed, on the other by the level of access to and number and types of buildings within the urban context that can be surveyed to create a realistic inventory profile. Within PERPETUATE project, a procedure for the vulnerability assessment of historic centres, methodologically similar to that proposed for single assets, have been developed.

In particular, two methodologies for the analysis of buildings in aggregate have been adopted and/or specifically developed in PERPETUATE project (Deliverable 27 [24]): the intuitive procedure LOG-IDEAH (LOGic trees for Identification of Damage due to Earthquakes for Architectural Heritage, Deliverable 30 [25]) and the numerical procedure FaMIVE (Failure Mechanism Identification and Vulnerability Evaluation) [26]. The FaMIVE procedure has been selected as reference after a detailed review of several methods proposed in literature (Deliverable 8 [27]). The two methodologies have been designed to identify the possible collapse mechanisms on a large sample of buildings by using few parameters, which can be easily collected on site or by pictures. The difference between them consists in the fact that LOG-IDEAH is based on intuitive logic that uses seismic damage to identify the failure modes of the architectural asset under inspection, while FaMIVE is a numerical approach that uses geometric and mechanical properties to identify the performance of historical buildings. Thus, the first one is particularly suitable for post-earthquake assessment, while the second one is oriented to preventive actions.

III. EXPERIMENTAL TESTS

Laboratory experimental tests performed in PERPETUATE project (Fig. 8) were aimed to various objectives.



Fig. 8 Experimental tests performed within PERPETUATE project

Shaking table tests performed in the laboratories of NTUA in Greece (Deliverable 33 [28]) and ENEA in Italy (Deliverable 12 [29]) were mainly oriented to: analyse the dynamic behaviour of multi-blocks systems (a multi-drum column, an arch-pier system and a 3-block obelisk), stress their displacement capacity under different seismic inputs, evaluate limit states and validate numerical models typically adopted for this type of structures (belonging to class F); analyse the shear behaviour of cross vaults (real scale masonry vault) under asymmetric boundary conditions; evaluate the effectiveness of retrofitting interventions, such as the introduction of rigid or flexible tie-rods in masonry arches (such as in the case of the arch-pier system) and the insertion of base isolation systems for artistic assets (such as in the case of statues). Shear tests on masonry walls (Deliverable 15 [30] and Deliverable 23 [22]) were oriented to two main objectives. On the one side, the mechanical properties of ancient-like brick and stone walls were measured and the reliability of strength criteria were stressed. On the other side, the interaction between the structural behaviour of the wall and the mechanical behaviour of coverings (plasters) was analysed. This latter point was linked to the will to consider the problem of artistic assets strictly connected to structural elements (class Q according to PERPETUATE classification). Finally, many in situ tests were performed in Slovenia by UL and ZRMK (Deliverable 15 [30] and Deliverable 34 [31]). Such tests mainly aimed to evaluate the effectiveness of different techniques of interventions (CFRP diagonal or perpendicular stripes and GFRP meshes).

IV. APPLICATION TO CASE STUDIES

The application to several case studies in different countries (Deliverable 28 [32] and Deliverable 40 [33]) has been fundamental for the validation of the new assessment procedure proposed by PERPETUATE (Figure 9). The problem of seismic protection of cultural heritage was faced at different scales and conditions of damage: on the one hand, both single monuments and historic centres have been considered; on the other, both undamaged and recently damaged buildings have been considered (in the first case, the objective was the prevention, in the second, the reparation/reconstruction). The analysis of case studies recently damage by an earthquake has been mainly addressed

to simulate the actual seismic response shown by the structure and validate the models adopted. In many cases, relevant artistic assets were present, allowing to test the capability of the procedure to consider their interaction with damage in structural elements.

Table 1. Overview of the PERPETUATE case studies

Case Study	Site	Partner	Class	Seismic Damage	Model type				Num.Sim. of interventions
					CCLM	SEM	DI	MBM	
Ardinghelli Palace	L'Agula	UNIGE	A	Yes		X		X	Yes
Santa Maria Paganica church	L'Agula	UNIGE	B	Yes	X			X	Yes
St. Pardo Cathedral	Larino	UNIGE	B	Yes	X			X	No
Neoclassical School	Rhodes	UL AUTH	A	No		X			Yes
Arsenal de Milly	Rhodes	AUTH UNIGE BRGM	B	No	X	X		X	No
Hassan Bey Mansion	Rhodes	UNIGE AUTH	A	No		X			Yes
Great Mosque	Algiers	UNIGE	B	No	X	X		X	Yes
Casbah of Algiers	Algiers	UBATH USTHB	G*	No				FAMVE LOG-IDEAH	Yes
Kolzej Palace	Ljubljana	UL ZRMK	A	No		X			No
Rural buildings in Posojeje region	Posojeje Region	UBATH UL	A*	Yes				FAMVE	No
Historic centre of Ljubljana	Ljubljana	UBATH UL	G*	No				FAMVE	Yes

* application at urban scale

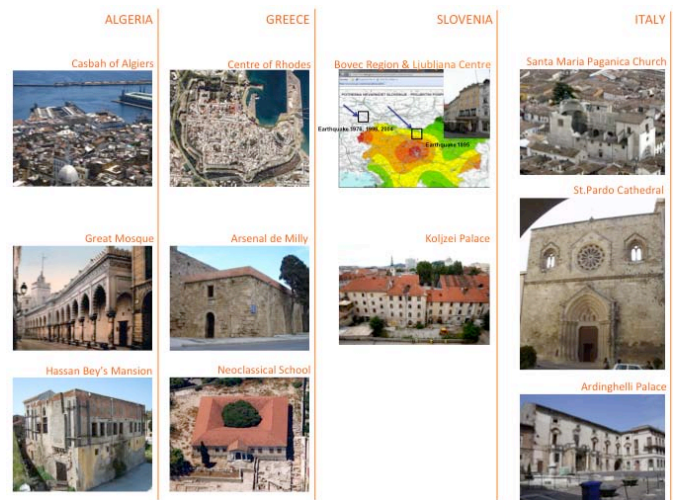


Fig. 9 Case studies examined in PERPETUATE project

Table 1 summarizes the case studies considered and their main features. As evident from it, assets examined belong to Classes A and B (for single asset) and G (for historic centers); despite the prevalence of these classes, it is worth noting that the response of others ones has been in-depth analyzed within the shaking table experimental tests (focused on mock-up of assets covering also Classes D and F). An accurate probabilistic seismic hazard characterization, supported by in-situ micro-tremors survey and array measurements for the soil characterization (Deliverable 18 [34]) has been provided for most of the considered sites (in particular for those of Rhodes and Algiers). Moreover, for each case study, data related to the

as built information have been collected, including in some cases also ambient vibration measurements for the structural identification (Deliverable 16 [16]).

V. FINAL REMARKS

Last earthquakes in Italy have shown the high vulnerability of cultural heritage assets. Invasive interventions adopted in the last century results to worsen the seismic capacity and, according to the principle of minimum intervention, it is important to consider the original behavior of the construction, by eliminating specific vulnerabilities. However, it is not possible to trust only on qualitative interpretations and a really effective strategy for the risk mitigation of cultural heritage has to be based on reliable mechanical models. The preservation of cultural heritage assets must consider both safety and conservation, by guaranteeing their capacity of lasting over time against decay, natural hazards and extreme events, without losing their authenticity and usability. Thus, in the case of historic buildings, the safety of the people and the conservation of the cultural heritage should be considered in an integrated approach. PERPETUATE has proposed models for the nonlinear analysis of ancient masonry structures and a well-defined procedure for the displacement-based assessment. In particular, it has shown it is possible to preserve monuments from ultimate limit states without invasive interventions, by improving the displacement capacity rather than stiffness and strength.

ACKNOWLEDGMENT

The project PERPETUATE (www.perpetuate.eu), funded by the European Commission in the Seventh Framework Program (FP7/2007-2013), under grant agreement n° 244229.

REFERENCES

- [1] S. Lagomarsino, H. Modaressi, K. Ptilakis, V. Bosjlikov, C. Calderini, D. D'Ayala, D. Benouar and S. Cattari, "PERPETUATE Project: the proposal of a performance-based approach to earthquake protection of cultural heritage", *Advanced Materials Research*, Vols. 133-134: 1119-1124, Trans Tech Publications, 2010, Switzerland, doi:10.4028/www.scientific.net/AMR.133-134.1119
- [2] S. Lagomarsino and S. Cattari, "PERPETUATE guidelines for seismic performance-based assessment of cultural heritage masonry structures", *Bulletin of Earthquake Engineering*, to be published
- [3] Deliverable D4, "Classification of the cultural heritage assets and description of the limit states and identification of damage measures". PERPETUATE Project, 2010 (www.perpetuate.eu/d4/)
- [4] Deliverable D5, "Abacus of the most common seismic damage". PERPETUATE Project, 2010 (<http://www.perpetuate.eu/d5/>)
- [5] Deliverable D7, "Review of existing models for global response and local mechanisms". PERPETUATE Project, 2010 (<http://www.perpetuate.eu/d7/>)
- [6] Deliverable D26, "Modelling strategies for seismic global response of building and local mechanisms". PERPETUATE Project, 2012 (<http://www.perpetuate.eu/d26/>)
- [7] Deliverable D17, "Correlation of limit states and damage levels for types of buildings". PERPETUATE Project, 2012 (<http://www.perpetuate.eu/d17/>)
- [8] Deliverable D10, "Characterization of the seismic hazard scenario for historical buildings". PERPETUATE Project, 2010 (<http://www.perpetuate.eu/d10/>)
- [9] Deliverable D13, "Definition of demand spectra and other intensity measures for different soil categories and site condition", PERPETUATE Project, 2011 (<http://www.perpetuate.eu/d13/>)
- [10] Deliverable D24, "Report on vector-valued characterisation of seismic hazard with respect to strong-motion parameters". PERPETUATE Project, 2011 (www.perpetuate.eu/d24/)
- [11] Deliverable D14, "Report on the SFI effects for ground shaking". PERPETUATE Project, 2011 (www.perpetuate.eu/d14/)
- [12] Deliverable D25, "Report on the development of the simplified soil-foundation model". PERPETUATE Project, 2011 (www.perpetuate.eu/d25/)
- [13] Deliverable D21, "Report on the SFSI, foundation performance and vulnerability assessment for permanent ground displacement". PERPETUATE Project, 2011 (www.perpetuate.eu/d21/)
- [14] Deliverable D6, "Review of innovative techniques for the knowledge of cultural assets (geometry, technologies, decay,...)". PERPETUATE Project, 2010 (www.perpetuate.eu/d6/)
- [15] Deliverable D22, "Definition of confidence factors for the safety verification". PERPETUATE Project, 2012 (www.perpetuate.eu/d22/)
- [16] Deliverable D16, "Report on microtremor measurement for structural identification". PERPETUATE Project, 2011 (www.perpetuate.eu/d16/)
- [17] Deliverable D11, "Report on permanent displacement analysis of the building through remote sensing techniques". PERPETUATE Project, 2011 (www.perpetuate.eu/d11/)
- [18] Deliverable D35, "Definition of seismic safety verification procedures for historical buildings". PERPETUATE Project, 2012 (www.perpetuate.eu/d35/)
- [19] Deliverable D29, "MB_PERPETUATE - A Macro-Block program for the seismic assessment (Freeware software for the safety verification of seismic local mechanisms)". PERPETUATE Project, 2012 (www.perpetuate.eu/mb/)
- [20] S. Lagomarsino, A. Penna, A. Galasco and S. Cattari, "TREMURI Program: An equivalent frame model for the nonlinear seismic analysis of masonry buildings". *Engineering Structures*, 56: 1787-1799, 2013.
- [21] S. Lagomarsino, N. Abbas, C. Calderini, S. Cattari, M. Rossi, R. GinanniCorradini, G. Marghella, F. Mattolin and V. Piovanello, "Classification of cultural heritage assets and seismic damage variables for the identification of performance levels". *WIT Transactions on the Built Environment*, vol. 118: 697-708, 2011, doi:10.2495/STR110581
- [22] Deliverable D23, "Proposal of modelling strategies for artistic assets". PERPETUATE Project, 2012 (www.perpetuate.eu/d23/)
- [23] Deliverable D36, "Definition of modelling and seismic safety verification procedures for artistic assets". PERPETUATE Project, 2012
- [24] Deliverable D27, "Formulation of vulnerability models including the survey form to collect the data required by the adopted models". PERPETUATE Project, 2012 (www.perpetuate.eu/d27/)
- [25] Deliverable D30, "Freeware software with the implementation of the vulnerability models". PERPETUATE Project, 2012 (www.perpetuate.eu/d30/)
- [26] D. D'Ayala and E. Speranza, "Definition of CollapseMechanisms and Seismic Vulnerability of HistoricMasonryBuildings", *EarthquakeSpectra*, 19: 479-509, 2003.
- [27] Deliverable D8, "Review and validation of existing vulnerability displacement-based models". PERPETUATE Project, 2010 (www.perpetuate.eu/d8/)
- [28] Deliverable D33, "Results of the shaking table and imposed displacements tests". PERPETUATE Project, 2012 (www.perpetuate.eu/d33/)
- [29] Deliverable D12, "Results of experimental test on damage measures and reference values to be considered". PERPETUATE Project, 2011 (www.perpetuate.eu/d12/)
- [30] Deliverable D15, "Results of laboratory and in-situ tests on masonry properties and table with mechanical parameters to be adopted in numerical modeling". PERPETUATE Project, 2012 (www.perpetuate.eu/d15/)
- [31] Deliverable D34, "Results of experimental tests on strengthening techniques and guidelines for the design". PERPETUATE Project, 2012 (www.perpetuate.eu/d34/)
- [32] Deliverable D28, "Intermediate report on the application of the proposed methodology to the case studies selected", PERPETUATE Project, 2011 (www.perpetuate.eu/d28/)
- [33] Deliverable D40, "Final report on the application of the proposed methodology to the case studies selected". PERPETUATE Project, 2012 (www.perpetuate.eu/d40/)
- [34] Deliverable D18, "Results of in-situ microtremors surveys and array measurements at selected sites". PERPETUATE Project, 2011 (www.perpetuate.eu/d18/)

Anchoring Influence in RC Beams Flexural Strengthening Using CFRP Fabric

D. Diaconu, V. Stoian, T. Nagy-Gyorgy and S.C. Florut

Abstract—Since there is a real bond issue between the support layer (concrete) and the epoxy resin used to bond the CFRP fabrics, in most situations the failure of the strengthened element occurs due to debonding mechanism, long before the capacity of the fabric is reached. This phenomenon usually arises because of the lack of attention paid to the preparation of the support layer by neglecting the concrete's quality, by poor knowledge of technological requirements or by poor qualification of the workers who apply this strengthening technique. In order to overcome this bond issue that could lead to important faults and reduced effect of strengthening intervention, a series of anchoring solutions (mechanisms) were proposed and experimentally investigated in the laboratory. Proposed anchoring solutions are anchor spikes and metallic anchors (using recycled diamond abrasive grinding wheels).

Keywords—strengthening, RC beams, fabric, CFRP, anchoring, composite materials, seismic areas.

I. INTRODUCTION

A lot of buildings in Romania (both civil, industrial ones, along with the works of art like bridges, passages, pedestrian bridges) have reached and maybe even exceeded their designed life period.

In the same time, some structures no longer correspond to present demands required by the new codes.

In all of the above mentioned cases, these structures require some rehabilitation/repairing and/or strengthening interventions. These interventions have to be carefully analyzed in terms of: time efficiency, robustness, ease of application, impact on the existing structure and financial effectiveness. The solutions proposed in this paper also try to achieve an optimum balance between structural effectiveness and cost efficiency, taking into account also the reversibility of each solution.

Even though previous studies were carried out in order to discover new technological solutions and to develop theoretical models and guidelines, there are still a lot of unknowns in this field.

Thus, the target of the experimental program conducted at

This work was supported in part by the "Politehnica" University of Timisoara, Laboratory for Reinforced Concrete within the Department of Civil Engineering.

D. DIACONU is with the Civil Engineering Department, "Politehnica" University of Timisoara, Romania (e-mail: dan.diaconu@upt.ro).

V. STOIAN is with the Civil Engineering Department, "Politehnica" University of Timisoara, Romania (e-mail: valeriu.stoian@upt.ro).

S.C. FLORUT is with the Civil Engineering Department, "Politehnica" University of Timisoara, Romania (e-mail: codrut.florut@upt.ro).

the Laboratory for Reinforced Concrete within the Department of Civil Engineering at "Politehnica" University of Timisoara, was to develop viable anchoring systems and to study their behavior once they are applied on RC beams in order to strengthen such members.

II. TESTING PROCEDURE. EXPERIMENTAL ELEMENTS

The tests started with two reference elements that were loaded up to failure without being strengthened.

The first beam (RB) was reinforced with three 16 mm diameter steel rebar ($f_{l,med}=781$ N/mm²), while the second one (RB2) had only two 16 mm diameter steel rebar. Both beams were cast using commercially available concrete with a strength class of C30/37.

The stirrups were designed so to resist an oversize shear forces (using steel stirrups of 8 mm placed at every 15 cm) because the purpose of the tests was to studied efficiency of flexural strengthening (i.e. the beams had to fail due to flexure prior to shear failure phenomena initiation).

The length of the entire beam was 4200 mm, leading to an effective span of 4000 mm. The cross section of the beam was rectangular, of 200x400 mm (Fig. 1).

The other tested beams had the same characteristics as beam RB2, the strengthening systems being design so that these beams reach the ultimate capacity of 160 kN.

For better understanding anchoring influence we consider as a reference element the one strengthened only with CFRP fabric (R-2W).

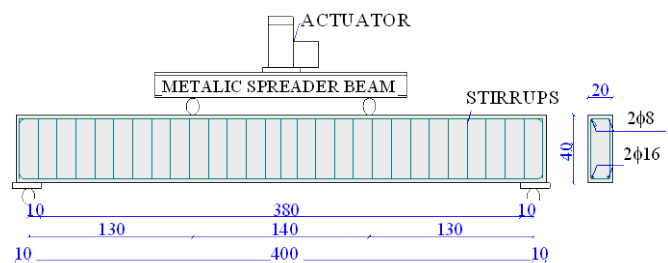


Fig.1. Test setup and characteristics for RB2 beam (cm)

The experimental elements were subjected to a monotonic increasing vertical force, applied in steps of 10 kN, by a hydraulic jack. The jack was placed on a steel beam that passed on the load to the RC beam in two points, 1400 mm one from another, equally distanced from the middle cross section (i.e. the beam was subjected to four point bending).

The two reference elements behaved in the expected manner:

- RB reaching an ultimate displacement of 120.94 mm and withstanding a load of 196 kN;
- RB2 element reached an ultimate displacement of almost 99.72 mm, withstanding a load of 134 kN.

The reference element strengthened only with 2 layers of CFRP fabric on backface (R-2W) reached an ultimate displacement of almost 49.9 mm, withstanding a load of 166 kN.

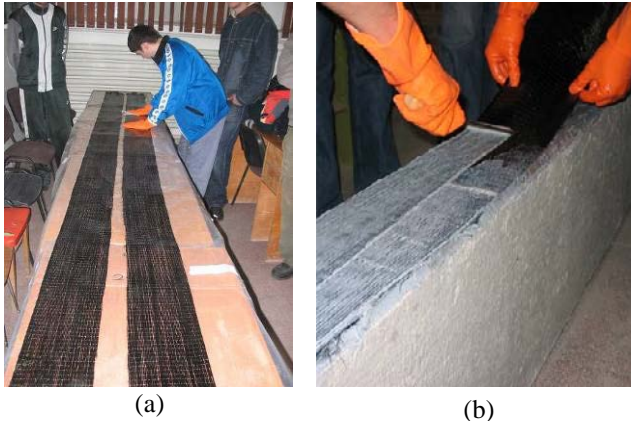


Fig.2. Reference element strengthened with 2 layers of CFRP fabric on backface (R-2W)

III. STRNGTHENING SOLUTIONS

The paper presents three strengthening solutions, with two different anchoring systems:

- anchoring the CFRP fabric at both ends using anchor spikes chemically anchored in the concrete (one beam had been strengthened by laterally placed CFRP fabric while the second beam was strengthened CFRP sheets of fabric placed along its bottom face - these elements were named RL-2W-A and R-2W-A);

- anchoring the CFRP fabric at both ends using recycled diamond abrasive grinding wheels connected to the concrete element by sleeve anchors - the element was named R-2W-MA.

A. The Element RL-2W-A

In this case, the strengthening method involves 2 layers of CFRP fabric on both lateral faces, with a cross section of 2x0.12x90 mm, bonded onto the concrete by epoxy resin. At both ends, for a better anchoring, anchor spikes chemically anchored in the concrete was used, illustrated in Figure 3.

For strengthening the beam, the following technological stages were considered:

- grinding of concrete surface
- drilling of 14 mm diameter bores for attaching anchor spikes to the concrete
- cleaning the dust and all other residues by vacuuming and using compressed air
- applying epoxy resin on the concrete surface
- lay up the fabric (first layer) and applying pressure with special roller
- lay up the fabric (first layer on longitudinal direction) and applying pressure with special roller
- filling of the bores with anchoring resin

- inserting the anchor spikes into the resin filled bores
- applying epoxy resin on the first fabric layer
- lay up the fabric (second layer on longitudinal direction) and applying pressure with special roller.

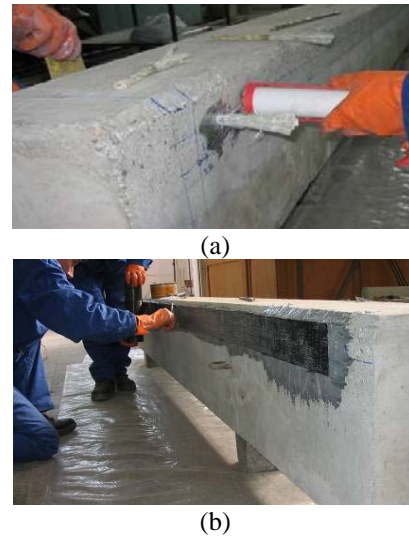


Fig.3. Anchoring system using anchor spikes - element RL-2W-A

The strengthened element was tested after seven days, time needed for the resin to cure. Were used four displacement transducers for measuring the deflection of the beam (Figures 4 and 5). The strain in de CFRP was measured using three strain gauges glued on the same tow of fibres.



Fig.4. RL-2W-A element prior testing



Fig.5. RL-2W-A element after testing

The failure of the element started with debonding of CFRP fabric on the entire length between the anchorages, followed by delamination at the interface between the two layers of the composite (Figure 6). This phenomenon appears because the

anchorages have penetrated only the first layer of fabric not both. Knowing this, all anchorages used from now on have penetrated all fabric layers.



Fig.6. Failure mode for RL-2W-A element

The RL-2W-A beam reached an ultimate displacement of 53 mm and withstood a load of 161 kN.

B. The Element R-2W-A

In this case, the strengthening method involves 2 layers of CFRP fabric applied on backface, with a cross section of 2x0.12x180 mm, bonded onto the concrete by epoxy resin. At both ends, for a better anchoring, anchor spikes chemically anchored in the concrete were used, illustrated in Figure 7.



(a)



(b)



(c)

Fig.7. Anchoring system using anchor spikes
- element R-2W-A

For strengthening the beam, the following technological stages were considered:

- grinding of concrete surface
- drilling of 14 mm diameter bores for attaching anchor spikes to the concrete

- cleaning the dust and all other residues by vacuuming and using compressed air
- applying epoxy resin on the concrete surface
- lay up the fabric (on transversal direction) and applying pressure with special roller
- lay up the fabric (first layer on longitudinal direction) and applying pressure with special roller
- applying epoxy resin on the first fabric layer
- lay up another layer of fabric (on transversal direction) and applying pressure with special roller
- lay up the fabric (second layer on longitudinal direction) and applying pressure with special roller
- filling of the bores with anchoring resin
- inserting the anchor spikes into the resin filled bores.

The strengthened element was tested in the same manner as previous element RL-2W-A.



Fig.8. R-2W-A element prior testing



Fig.9. R-2W-A element after testing

The failure of the element started with debonding of CFRP fabric on the entire length between the anchorages, followed by rupture near the anchorage (Figure 10).



(a)



(b)

Fig.10. Failure mode for R-2W-A element

The R-2W-A beam reached an ultimate displacement of 69.32 mm and withstood a load of 191 kN.

C. The Element R-2W-MA

In this case, the strengthening method involves 2 layers of CFRP fabric applied on backface, with a cross section of 2x0.12x180 mm, bonded onto the concrete by epoxy resin. At both ends, for a better anchoring, recycled diamond abrasive grinding wheels was used, connected to the concrete element by sleeve anchors, illustrated in Figure 11.



Fig.11. Anchoring system using recycled diamond abrasive grinding wheels - element R-2W-MA

The steps that need to be carried out for this solution are:

- grinding of concrete surface
- drilling of 12 mm diameter bores for sleeve anchors
- cleaning the dust and all other residues by vacuuming and using compressed air
- applying epoxy resin on the concrete surface
- lay up the fabric (on transversal direction) and applying pressure with special roller
- lay up the fabric (first layer on longitudinal direction) and applying pressure with special roller
- applying epoxy resin on the first fabric layer
- lay up second layer of fabric (on transversal direction) and applying pressure with special roller
- lay up the fabric (second layer on longitudinal direction) and applying pressure with special roller
- lay up third layer of fabric (on transversal direction) and applying pressure with special roller
- grinding recycled metallic disks for better adhesion
- inserting sleeve anchors.

The strengthened element was tested in the same manner as previous elements.



Fig.12. R-2W-MA element prior testing



Fig.13. R-2W-MA element after testing

The failure of the element started with debonding of CFRP fabric on the entire length between the anchorages, followed by rupture between anchorages and concrete crushing in the compressed zone at the mid span (Figure 14).



(a)



(b)

Fig.14. Failure mode for R-2W-MA element

The R-2W-MA beam reached an ultimate displacement of almost 71.42 mm and withstood a load of 176 kN.

IV. CONCLUSION

The beams strengthened by the above mentioned methods (R-2W, RL-2W-A, R-2W-A, R-2W-MA) have resisted to loads higher than the designed one of 160 kN, as it can be seen in Figure 15.

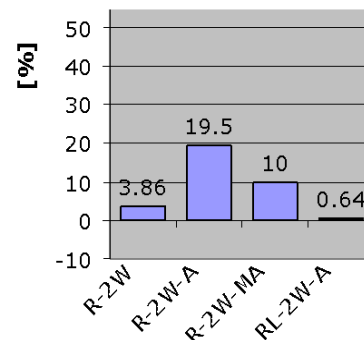


Fig. 15 – Efficiency of all strengthened elements

Comparing strengthened element using different anchors types (RL-2W-A, R-2W-A, R-2W-MA) with the element strengthened without anchors (R-2W) the efficiency anchoring systems can be determined. By analyzing Figure 16 it is revealed that the anchoring solution chosen for RL-2W-A beam is ineffective. This phenomenon appears because the anchorages used in this case have penetrated only the first layer of fabric not both.

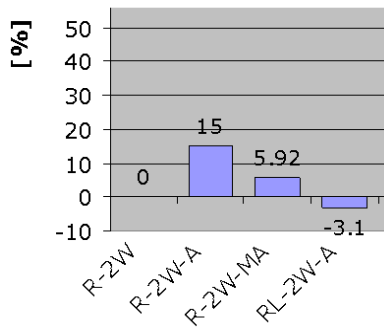


Fig. 16 – Efficiency of anchoring systems

In conclusion, the anchorage must penetrate all fabric layers used for strengthening.

REFERENCES

- [1] Huang P.C., Myers J.J., Nanni A., *Dapped-End Strengthening in Precast Prestressed Concrete Double Tee Beams with FRP Composites*, 3rd International Conference on Advanced Composite Materials in Bridges and Structures, Ottawa, Canada, 2000, pp. 545-552.
- [2] Nagy-György T., Stoian V., Dan D., Dăescu C., Diaconu D., Sas G., Moșoarcă M., *Research Results on RC Walls and Dapped Beam Ends Strengthened with FRP Composites*, FRPRCS-8, Patras, Greece, 2007.
- [3] Stoian V., Nagy-György T., Dăescu C., Diaconu, D., *Theoretical and experimental study of prestressed concrete beam support zone strengthened with composite materials*, Proceedings of the Second fib Congress, Naples, Italy, 2006.
- [4] Diaconu D., Stoian V., Floruț S.C., *Anchoring Influence in RC Beams Flexural Strengthening Using CFRP Lamellas*, Latest Trends on Engineering Mechanics, Structures, Engineering Geology - Corfu Island, Greece, July 2010.

D. Diaconu was born in Timisoara, Romania on June 24, 1979. In 2003 he finished profile economic engineering, specializing Production Systems Engineering in Construction at the Faculty of Management in Production and Transportation, "Politehnica" University of Timisoara, Romania. In 2004 he obtained his Master Science Degree in Structural Rehabilitation at the "Politehnica" University of Timisoara, Romania with theme: "Strengthening reinforced concrete beams using FRP composite materials at Arhidiecezana Printing House from Timisoara". In 2011 he obtained his Ph. D. Degree in Construction Engineering at the "Politehnica" University of Timisoara, Romania with theme: "RC beams flexural strengthening using polymeric composite materials and different anchoring systems".

Rotor Blade Stress and Vibration Amplitudes Monitoring During Operation Condition in One-Pass Jet Engine

Ryszard Szczepanik

Abstract—This paper considers 1st stage compressor blade dynamics in the one-pass jet engines of trainer aircraft. Research was carried out on an engine test bench using the SAD system and its results were compared with those obtained using the tensometric approach. In this paper presented basic dynamic properties of rotor blades, bench test of rotor blade dynamics, Bench tests of the dynamic behaviour of blades subjected to external impacts and then Comparison of strain gauge and SAD tip-timing results. Then discusses the results of tests assessing the accuracy of the 1987 ITWL device by comparing strain gauge signals with those recorded by SAD apparatus in a running engine. It also presented simultaneous vibration readings of all the rotor blades at selected rotation speeds. Also shows that increased stress in these blades may be due to repeated engine surges, normal and hot engine surges, entry into the engine of a foreign object.

Among others selection and layout of rotor blades in the 1st stage of a one-pass engine compressor, stress amplitudes for rotor blade, stress in rotor blade, stress amplitudes, free inlet flow and smooth engine acceleration, vibration amplitudes, asynchronous vibrations are presented in the paper.

Keywords—*Diagnostics of aircraft engines, compressor blade dynamics.*

I. INTRODUCTION

In the years 1985-1987 one-pass turbojet engine failures occurred as a result of compressor 1st stage blade breakage. The nature of these failures (two cases of a number of blades breaking off simultaneously) with no discernible material or manufacturing defects led to investigations conducted by the ITWL. Two main lines of investigation were considered. The first involved tensometric studies of 1st stage of compressor rotor blade vibration amplitudes and stress taking into account operation factors that could lead to momentary or periodical growth of stress [7][6]. The second approach involved developing apparatus that would be able to measure vibration amplitudes in-flight using the tip-timing method [6]. In 1986 ITWL also researched the rate of crack propagation in blades. Research was carried out on an engine test bench using the SAD system (based on tip-timing technology presented in chapter 5) and its results were compared with those obtained using the tensometric approach.

II. BASIC DYNAMIC PROPERTIES OF ROTOR BLADES

Experimental studies established that the average fatigue strength for the oscillatory cycle Z_{-1} [2], p. 13] of 15 new randomly selected 1st stage compressor rotor blades was $Z_{-1} = 693$ MPa. In the case of four blades from the same batch used in an engine where the rotor blades broke off during operation the fatigue strength was $Z_{-1} = 700$ MPa, whilst in the case of rotor blades after 1,200 hours of operation it was $Z_{-1} = 636$ MPa.

On this basis it possible to state that the difference between the average fatigue strength Z_{-1} of new blades and those that had operated for 1,200 hours is 9%.

Extensive experimental analyses of titanium and steel rotor blade fatigue strength in various operating conditions are presented in [3]. These analyses show that under various operating conditions, over various periods of time and depending on the blade material machining procedure, deviations in fatigue strength may reach up to 30%.

Experimental studies of 1,350 1st compressor stage rotor blades revealed that natural frequencies ranged from 318 to 385 Hz [7].

It should be stressed that 1st and 2nd mode shapes predominate in the 1st stage of compressor blades of a one-pass engine. The 2nd mode shape only predominates in a narrow range of rotation speeds (10,500-11,500 rpm).

In order to study rotor behaviour, the blades were arranged so as to obtain maximal mistuning.

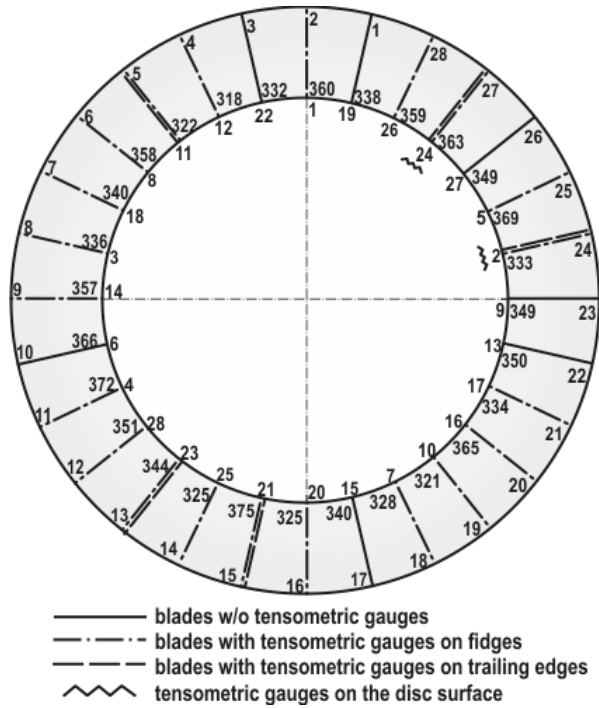


Fig. 1. Selection and layout of rotor blades in the 1st stage of a one-pass engine compressor

The layout of the compressor 1st stage blades with their specific free vibration frequencies is shown in **Blad! Nie można odnaleźć źródła odwołania..** Here one can see that the frequencies were within the 318 to 385 Hz range. An engine that had had confirmed 1st compressor stage blade break-offs was selected for the strain gauging and further tests. Out of a total of 28 blades, 21 had strain gauges. These were installed on the suction base near the base, where blade vibration causes maximum bending stresses of the 1st and 2nd mode Fig. 2. Three blades, 11, 21 and 23, had additional strain gauges installed near their trailing edge bases Fig. 1. Moreover, two gauges were installed on the 1st compressor stage disc surface to confirm the occurrence of any coupling between the disc and the rotor blades.

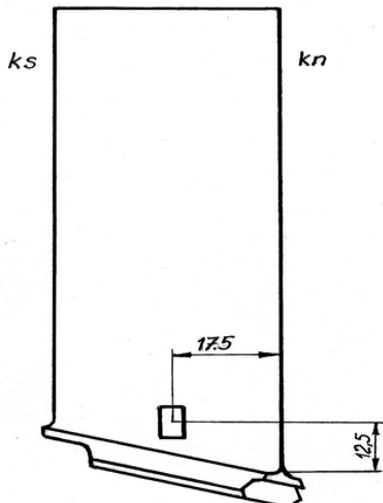


Fig. 2. Location of tensometric gauge on a 1st compressor stage rotor blade

III. BENCH TEST OF ROTOR BLADE DYNAMICS

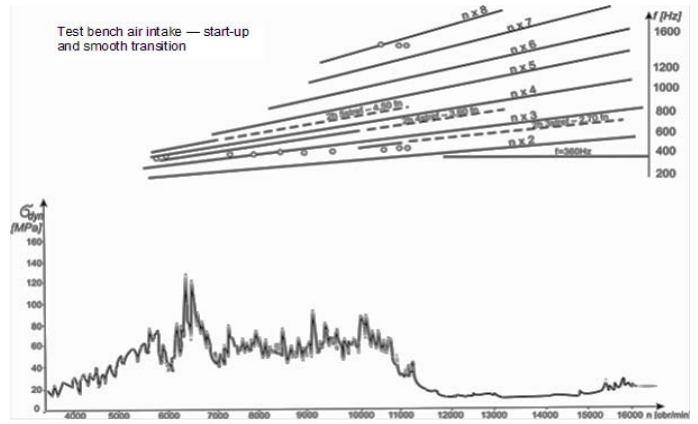


Fig. 3. Stress amplitudes for rotor blade 1 installed in the 1st stage of a one-pass engine

The highest levels of rotor blade stress occur at resonance frequencies and during unsteady compressor operating conditions. There are several kinds of unsteady aircraft engine operation conditions: ones associated with combustion, aero-elastic unsteadiness such as rotor blade flutter [4] as well as aerodynamic instability caused by rotating stall zones and compressor surges [1]. Rotating separation zones are a disruption of flow through the compressor involving its detachment from rotor or stator blades. This process expands, causing the detachment of flow from individual blades to merge into separation zones partially or fully encompassing the compressor flow channel. Their speed is dictated by and slightly lower than the rotation speed of the blades.

Compressor stalls involve periodic axial pressure pulsations in the compressor's flow duct. They are associated with higher amplitudes of pressure oscillation than in the case of rotating separation zones but with a much lower frequency. Engine stalls are almost always preceded by the occurrence of separation zones. Unlike the rotating separation zone, stalling occurs axis-symmetrically and uniformly around the compressor perimeter. Literature [1] distinguishes between the ordinary stall with large, low frequency pressure fluctuations and the modified stall, which combines a deep, expanded ordinary stall with a reverse flow through the compressor.

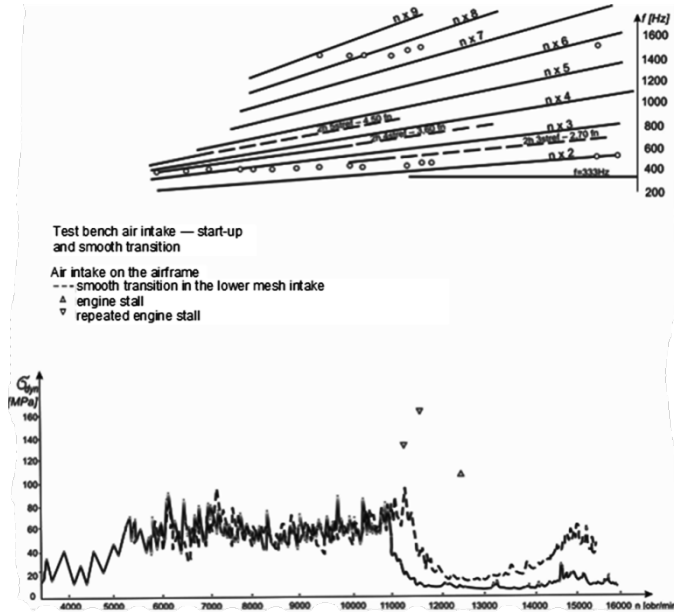


Fig. 4. Stress in rotor blade 2 of 1st stage of a one-pass engine compressor

Deep surges are most dangerous as far as stress on blades is concerned.

Figure 3 shows the time-varying stress amplitudes in blade 1 (360 Hz, Fig. 1, blade numbering on the inner circle), in the test bench inlet, with rotation speed smoothly increased from 6,000 rpm to 16,070 rpm. The Campbell graph ‘circles’ denote the blades’ measured free vibration frequencies of the 1st and 2nd mode. This shows that in the 1st stage three stall zones occur at 9,500 rpm and 400 Hz and four zones at 6,600 rpm and 410 Hz. Fig. 4 presents time-related variations of stress in blade 2 (333 Hz, Fig. 1). The presented test bench measurements concern a single engine inlet (continuous line) and a two-channel/aeroplane engine inlet (dashed line). The latter causes asymmetric circumferential pressure on the guide vanes, forcing low-frequency excitations [5], thus maximum stress in the blade occurs at different and slightly higher rotation speeds than at the airframe inlet. Fig. 5.3 also presents the measured stress amplitude values in the case of a deep stall and repeated stalls at certain rotation speeds.

IV. BENCH TESTS OF THE DYNAMIC BEHAVIOUR OF BLADES SUBJECTED TO EXTERNAL IMPACTS

These studies showed the largest stress amplitudes occur during repeated stalls in blade 4 at 372 Hz ($\sigma_8 \cong 280$ MPa at 11300 rpm) (Fig. 5), during ordinary, high-temperature engine stalls with 1/3 of inlet covered in blade 4 ($\sigma_8 \cong 300$ MPa at 11300 rpm) as well as after the intake of epoxy resin fragments (inlet failure) in blade 14 at 325 Hz (461 MPa at 14900 rpm). It should be remembered that cold stalls cause aircraft engine unsteadiness without a temperature rise downstream of T_4 turbine, whilst hot (high temperature) engine stalls cause unsteadiness with substantial temperature growth downstream of T_4 turbine. In the case of inlet failure the highest stress amplitude, 461 MPa, occurred in a blade with a free vibration frequency of 325 Hz. When the inlet was

partly covered, the highest stress amplitude, 378 MPa, was recorded for a blade with a recorded vibration frequency of 351 Hz.

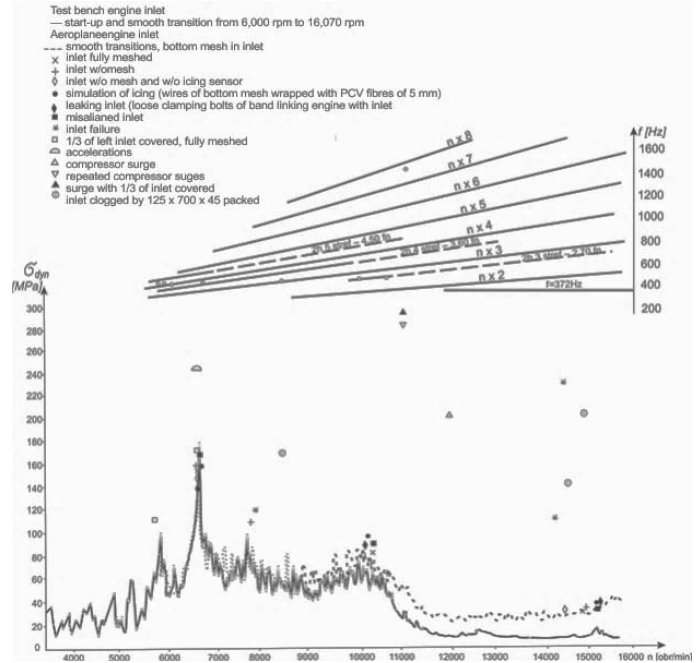


Fig. 5. Stress amplitudes in 1st stage rotor blade 4 of one-pass engine compressor

It should be noted that with 1/3 of one of the inlets covered stress increases by as much as 50-60% when experiencing a conventional surge (from n_{mg} to n_{max}) in comparison with conditions when there is no surge (Fig. 5-7).

Assuming a similar rate of stress increase occurs during repeated stalling, its level would reach ca. 420-450 MPa. This could be very hazardous to blades, all the more so because on account of their low temperature, repeated stalling is not usually recorded.

Stress amplitude variations resulting from rotation speed are different in the case of each blade. Figure 8 presents the stress amplitude variations of all the blades in their consecutive order (as numbered on the outer circle in Fig. 1).

The maximum stress amplitude for rotor blade 1 (on the inner circle and 2 on the outer circle in Fig. 1) is 128 MPa at 6,500 rpm (Fig. 3), for rotor blade 2 (24 on outer circle) it is 96 MPa at 6,300 rpm (Fig. 4), and so on. These deviations result from differences in the geometrical dimensions of the blades and the nature of the flow, which is associated with rotating stall zones.

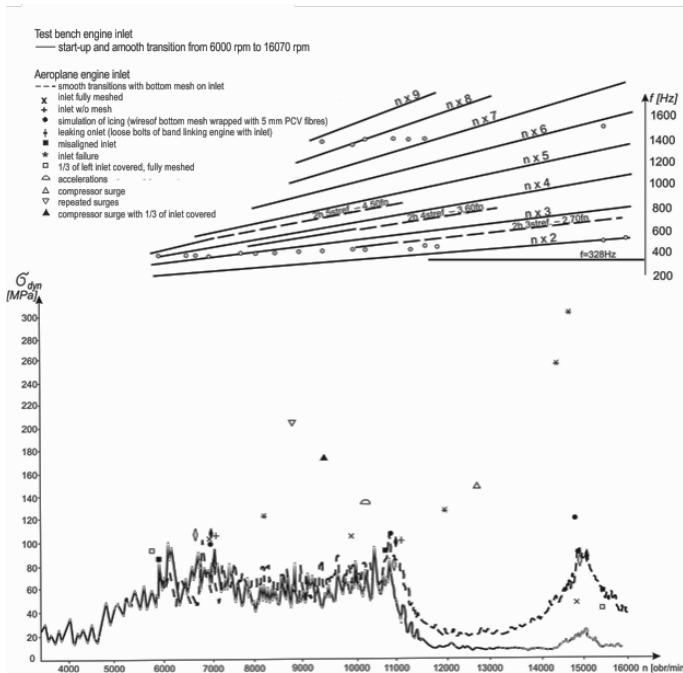


Fig. 6. Stress amplitudes in 1st stage rotor blade 7 of one-pass engine compressor

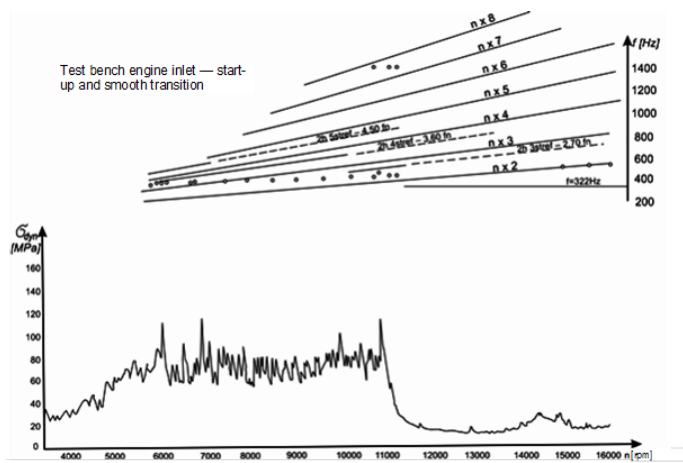


Fig. 7. Stress amplitudes in 1st stage rotor blade 28 of one-pass engine compressor

V. COMPARISON OF STRAIN GAUGE AND SAD TIP-TIMING RESULTS

The first series of tests confirmed good correspondence between strain gauge and SAD signals as well as the nature of the fluctuations as seen on an oscilloscope display (Fig. 9).

Figure 10 shows SAD registered vibration amplitudes of all the rotor blade tips in the 1st stage of a prior to modernisation one-pass engine compressor at various rotation speeds.

At $n = 10\,300$ rpm rotating stall zones occur, thus the blade vibration amplitudes are higher than $n = 7100$ rpm. At 12,000 rpm vibration amplitudes diminish as there are no major excitations in the flow.

Figure 9 demonstrates that each rotor blade vibrates with different amplitude around a different equilibrium. This results from differences in the geometrical dimensions of blades, the

precision of how blades are mounted onto the disc and the way in the bladed disc vibrates. The figures reveal the complexity of individual blade movement in a real turbine and the advantages of SAD measurements over those of strain gauges.

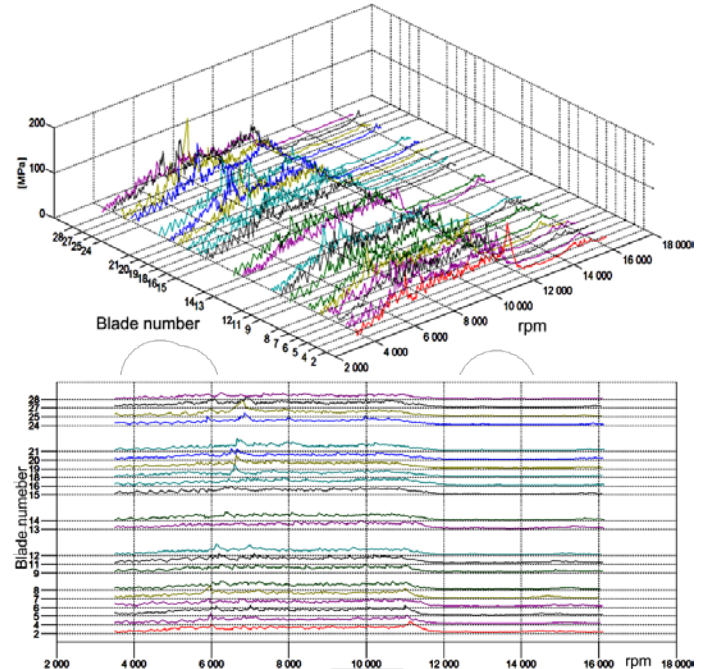


Fig. 8. Stress amplitudes of 1st stage rotor blade in one-pass engine compressor with varying rotation speeds, free inlet flow and smooth engine acceleration

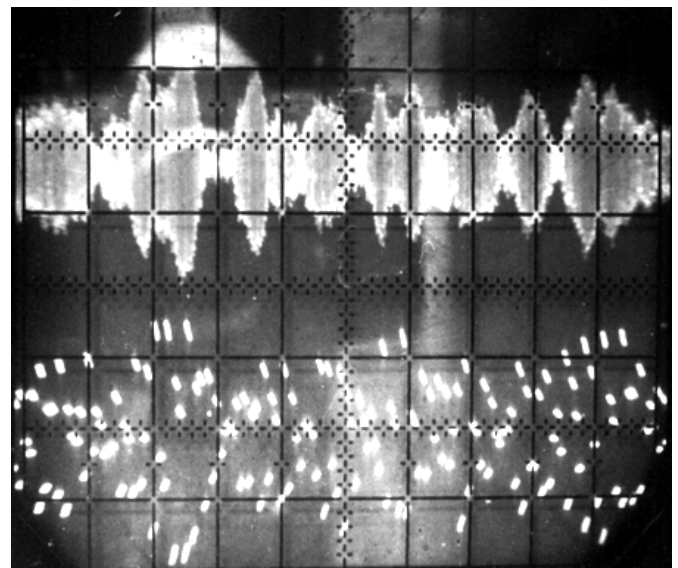


Fig. 9. Comparison of strain gauge analogue signals with digital SAD signals regarding the 1st stage rotor blades of a one-pass engine

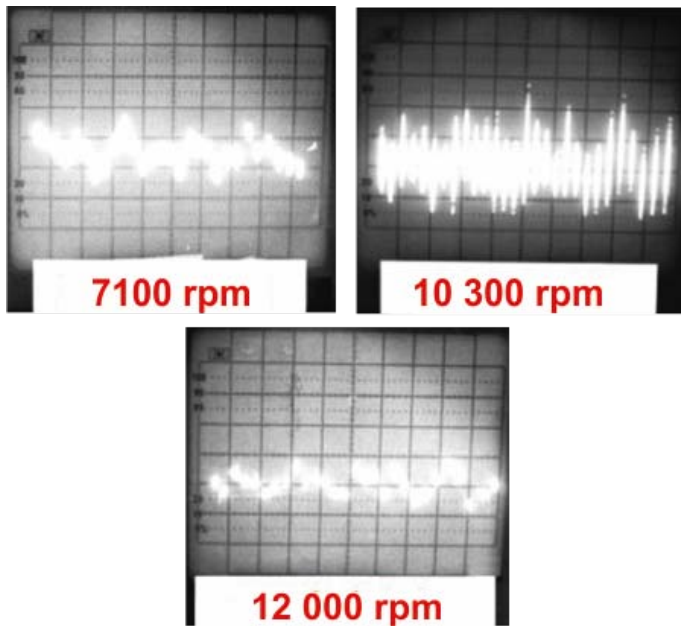


Fig. 10. Vibration amplitudes of 1st stage blade tips in a one-pass engine compressor prior to modernisation and at various rotation speeds. Asynchronous vibrations appear at $n = 7,100$ rpm; $10\ 300$ rpm and blade vibration amplitudes are substantially reduced at $n = 12,000$ rpm

VI. CONCLUSIONS

The conducted research into the dynamic behaviour 1st stage rotor blades in a one-pass engine compressor, before and after modernisation, shows that increased stress in these blades may be due to the following:

- repeated engine surges with no temperature increase downstream of turbine T_4 , considered harmless and not even recorded in aircraft operating documents. Stress (bending) amplitudes up to $\sigma_d = 280$ MPa,
- normal (hot) engine surges with rotation acceleration stopped and a rapid increase of temperature in T_4 , occurring when 1/3 of one of the two inlets is covered. The (bending) stress amplitudes up to $\sigma_d = 300$ MPa,
- entry into the engine of a foreign object (e.g. rag, piece of paper, bird or glove) partly covering the compressor guide vanes and therefore causing strong forced vibrations with stress amplitudes of up to 700 MPa.

Other operating conditions including meshes in aeroplane engine inlets, with full meshes, without meshes or an icing sensor, imitation of icing (wires in bottom meshes wrapped with plasticized PVC fibres up to $g = 5$ mm thick), leaking inlet (loosened band in front of engine inlet), misaligned inlet, left inlet partly covered (1/3 of inlet + full meshes), steady operating conditions with 1/3 of left inlet covered area, did not cause a significant increase of stress. One should note that the selected free vibration frequencies of the blades where within the free vibration range ($f = 318$ - 385 Hz) and did not result in a significant increase of stress. Approximately 180 MPa was recorded for a blade with a free vibration frequency of $f = 372$ Hz (Fig. 5). This blade had resonance vibrations forced by the first harmonic component of the four-zoned configuration with

rotating stalls.

It is probable that stress levels resulting from conditions prepared in the bench tests may be considerably higher in certain phases of flight, especially in cases where the intake of air is substantially disturbed. This is suggested by the examined effect of hot surges on level of stress in the blades. The maximum stress recorded during such surges did not actually exceed $\sigma_d \approx 200$ MPa. However, when 1/3 of the inlet was covered, the same surges increased stress by about 50-60% of the initial value to reach $\sigma_d \approx 300$ MPa. Assuming that overlapping a wind tunnel on the ground corresponds to diminished inlet size during certain phases of flight, and supposing that blade stress increase in repeated surges is proportional to blade stress increases in hot surges, its amplitudes may even reach 420-450 MPa. Such stress may seriously affect blade durability, especially engines with a tendency to have surges (e.g. on account of badly adjusted or faulty automatic engine acceleration (APS).

It was therefore decided that further tests needed to be carried out, both on the ground and in flight, during regular operation and under surge conditions with a lateral engine inlet (ground tests) and an air intake reduction during typical aircraft manoeuvres, high angles of attack and sideslip.

REFERENCES

- [1] Gravidahl, J. Y., *Modeling and Control of Surge and Rotating Stall in Compressors*, Doctor Thesis, Report 98-6-W, Department of Engineering Cybernetics, Norwegian University of Science and Technology, Trondheim, Norway 1998.
- [2] Kocańda, S., Szala, J., *Podstawy obliczeń zmęczeniowych, (Fundamentals for Fatigue Computations)*, PWN, Warszawa 1985.
- [3] Петухов, А., Сопротивление усталости деталей ГТД, *Машиностроение* 1993, (*Fatigue Strength of Components in Gas Turbine Engines*, Mashinostroyene, 1993).
- [4] Rządkowski, R., *Flutter of Turbine Rotor Blades in Inviscid Flow*, Wydawnictwo Akademii Marynarki Wojennej, Gdynia 2004.
- [5] Rządkowski, R., Gnesin, V., Soliński, M., Szczepanik, R., *Analysis of Low-Frequency Forces Affecting Rotor Blades of Gas Turbines*, ITWL Publishing House, 2012.
- [6] Szczepanik, R., Kudelski, R., *Report from the Project 'Engineering and Construction of SAD Instruments for Studies on Vibrations of Blades Rotors in Turbine Engines'*, Study of ITWL, No. 9121/I, 1988.
- [7] Szczepanik, R., *Experimental studies on Dynamic Properties Demonstrated by Rotor Blades under Various Operating Conditions*, Scientific Journal No. 26, ITWL, Warsaw 2010.

Prof. Ryszard Szczepanik, D.Sc. Ph.D. Eng.
Air Force Institute of Technology
KsieciaBoleslawaa Street 6, 01-494 Warsaw, Poland
tel.: +48 22 6851101, fax: +48 22 8364471
e-mail: ryszard.szczepanik@itwl.pl

Profile of heat transfer between two different materials

K.Gherfi^{a,b}, S.Boukroune^a, H.Bendjama^a, D.Idiou^a

^aWelding and NDT Research Centre (CSC) BP 64 CHERAGA-ALGERIA

^bUniversité Badji Mokhtar-ANNABA, BP 12 Annaba, 23000 Algeria

kaddour.gherfi@gmail.com, k.gherfi@csc.dz, sofiane25000dz@yahoo.fr,
hocine_bendjama@yahoo.fr, ddidiou@yahoo.com

Abstract—In this article we made a study on the transfer of heat in two different materials such as steel and copper. Initially we present the profile of heat transfer in each material alone, after we present the profile of the same phenomena in the two materials in contacts, and to see how the temperature is propagated when we have a variation of thermal conductivity. The simulation is made by ANSYS software which permits us to solve the energy equation by finite element method.

Keywords— Simulation; material; heat transfer.

Nomenclature

T : temperature (C°)

t : Time (S)

$\alpha = \lambda / \rho C_p$

ρ : Material density ($kg.m^3$)

λ : Thermal conductivity ($W/m K$)

C_p : specific heat ($j/kg.K$)

I. INTRODUCTION

STUDIES of heat and mass transfers involved research areas as diverse as mechanical, construction, nuclear,... and particularly involved in various applications such as car motors, solar sensors, nuclear reactors, heat exchangers, thermal insulation, drying foodstuffs, etc.. In addition, thorough mastery of knowledge such transfer allows to achieve a better energy optimization of many systems (cars, thermal power, building materials, chemical and petrochemical units, processes agro-food, paper, textile, etc ...) [1].

Heat transfer is a process by which energy is exchanged in the heat form between the body or environments at different temperatures. Heat may be transferred by conduction, convection or radiation. Currently we can see that the heat transfer is one of the most studied physical phenomena [2].

According to the second laws of thermodynamics, the temperature difference in a closed system, as time goes by, will gradually be homogenizing. The process of

homogenization temperature and heat flux is accompanied from the hot point to the low point. The speed rate of the heat flux movement between two points will accelerate as the temperature difference increment [3].

This paper is structured as follows: in Sec. II a sample of material with dimensional boundary conditions is presented. Sec III describes an equation of heat transfer with several parameters. In Sec. IV we presented a short definition of finite element method. In Sec. V the Simulation results and discussion of obtained results are presented. Sec. VI concludes this article.

II. GEOMETRICAL CONFIGURATION

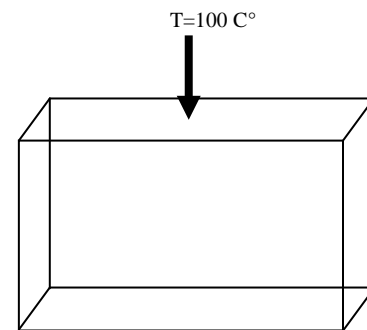


Fig. 1. Sample geometry

The materials considered are: steel for conductivity ($\lambda = 50$ W/m K), and copper for ($\lambda = 380$ W/m K)

III. THE TEMPERATURE OF HEAT TRANSFER EQUATION

Base on heat transfer theory, the heat-transfer differential equation reveals the continuous temperature distribution, the spatial coordinates and time coordinates internal communication, makes the problem to solve the heat conduction possible.

The formula called the heat transfer equation is shown below (in one dimensional case) [4].

$$\frac{\partial T}{\partial t} - \alpha \left[\frac{\partial^2 T}{\partial X^2} \right] = 0 \tag{1}$$

In our case we have three dimensional the heat transfer equation becomes:

$$\frac{\partial T}{\partial t} - \alpha \left[\frac{\partial^2 T}{\partial X^2} + \frac{\partial^2 T}{\partial Y^2} + \frac{\partial^2 T}{\partial Z^2} \right] = 0 \tag{2}$$

We apply a constant temperature (T=100C°) on the upper surface, we suppose that all others face is exposed to the air with an ambient temperature (T=30C°), these conditions are apply on the two materials (cooper and steel), and we see how this temperature diffused in the sample.

The governing equation is discretized by the finite element method by using the ANSYS software.

IV. SOLUTION METHOD

A. Finite element method

The finite element system of equations is obtained by applying Galerkin's procedure [5], [6]. The finite element method is widely used for the structural modeling of physical systems. In the finite element model, an object can be viewed as a finite element graph, which is a connected and undirected graph that consists of a number of finite elements.

Each finite element is composed of a number of nodes. The number of nodes of a finite element is determined by an application. Due to the properties of computation-intensiveness and computation-locality, it is very attractive to implement the finite element method on distributed memory multi-computers [7], [8], [9], [10], [11].

V. RESULTS AND ANALYSIS

The objective of our numerical simulations is for studying the temperature profiles of samples from different materials (conductivity is different) and the temperature profile compared with each other, and as compared with a mixed sample (containing two different materials).

A. Steel sample

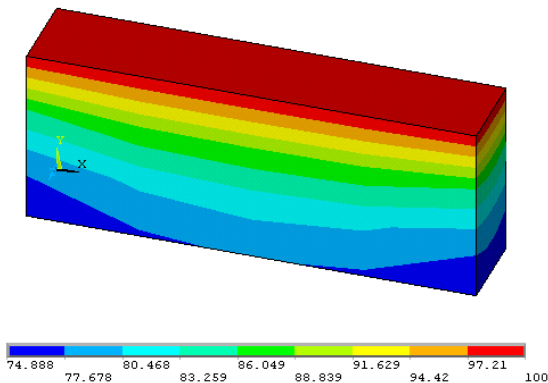


Fig. 2. Temperature profile in steel sample (3D)

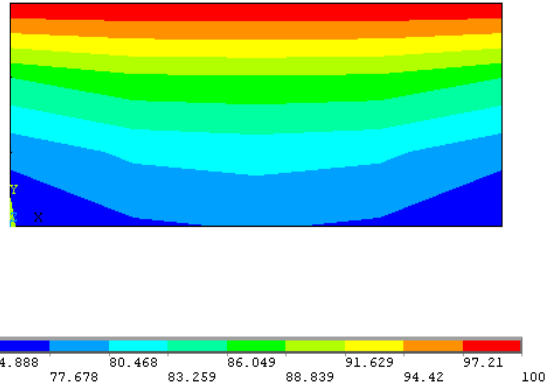


Fig. 3. Temperature profile in steel sample (2D XY plane)

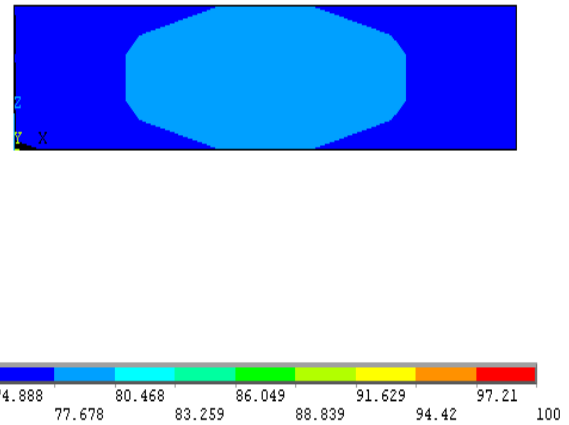


Fig. 4. Temperature profile in steel sample (2D XZ plane)

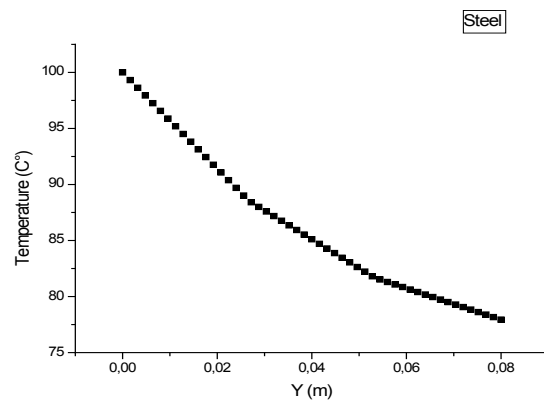


Fig. 5. Temperature evolution according to the steel sample thickness

We presented in Fig. 2, 3 and 4 the temperature contours in different planes, from these figures and Fig. 5 which shows the temperature as function of the thickness, we see that the temperature gradually decreases from 100 C° until to have a temperature of the outer wall of 74,888 C°.

B. Copper sample

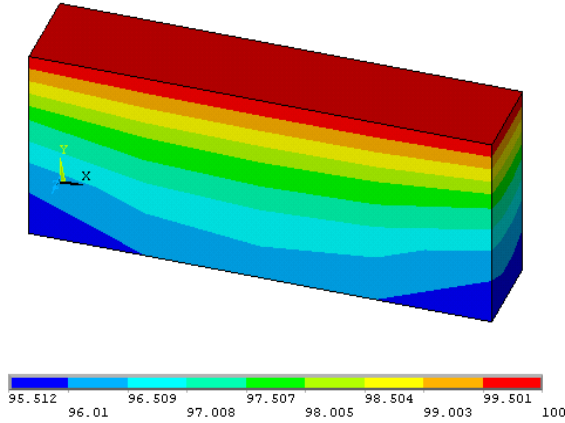


Fig. 6. Temperature profile in copper sample (3D)

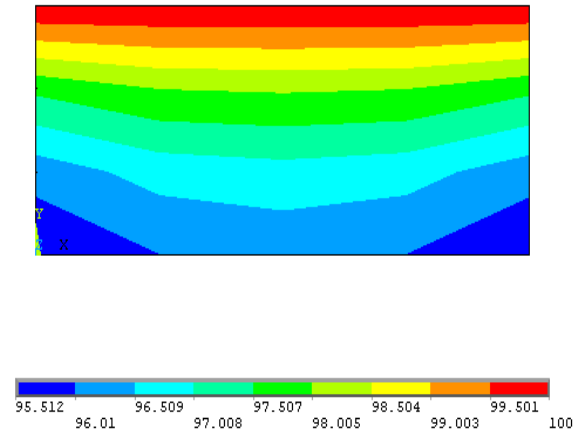


Fig. 7. Temperature profile in copper sample (2D XY plane)

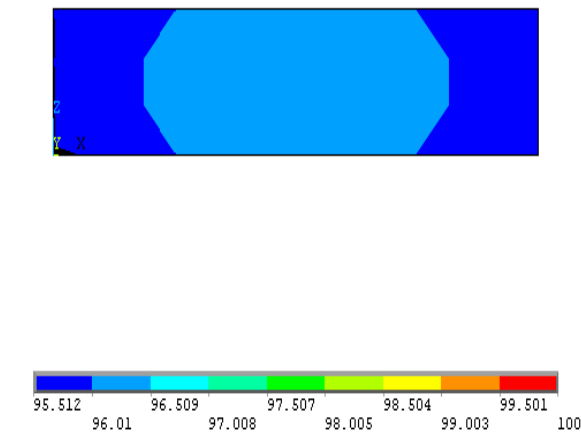


Fig. 8. Temperature profile in copper sample (2D XZ plane)

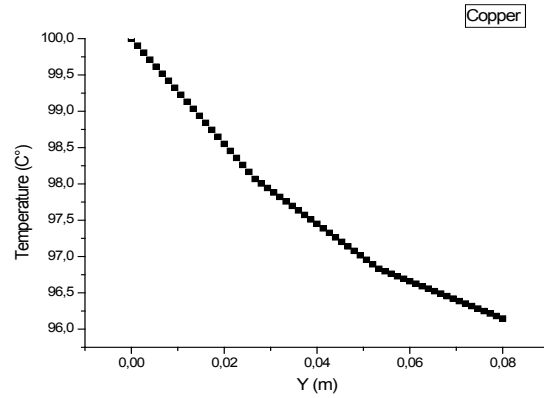


Fig. 9. Temperature evolution according to the copper sample thickness

We presented in Fig. 6, 7 and 8 the temperature contours in different planes, from these figures and Fig. 9 which shows the temperature as function of the thickness, we see that the temperature gradually decreases from 100 C° until to have a temperature of the outer wall of 95,512 C°.

C. Steel-Copper sample

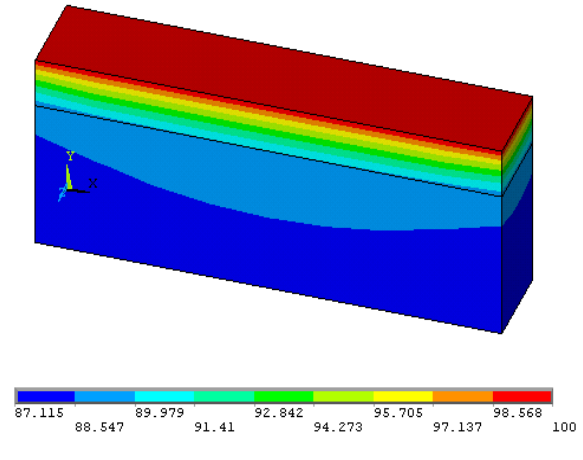


Fig. 10. Temperature profile in steel-copper sample (3D)

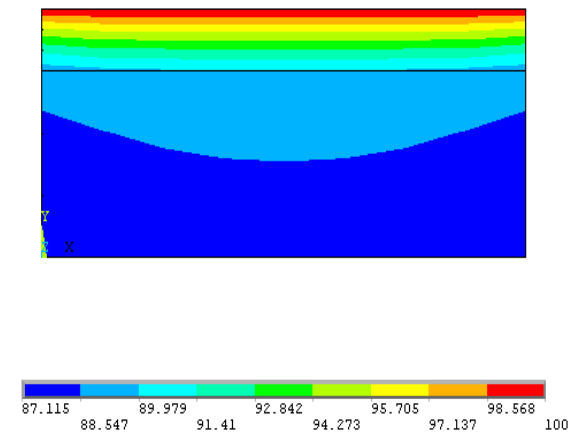


Fig. 11. Temperature profile in steel-copper sample (2D XY plane)

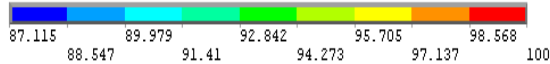


Fig. 12. Temperature profile in steel-copper sample (2D XZ plane)

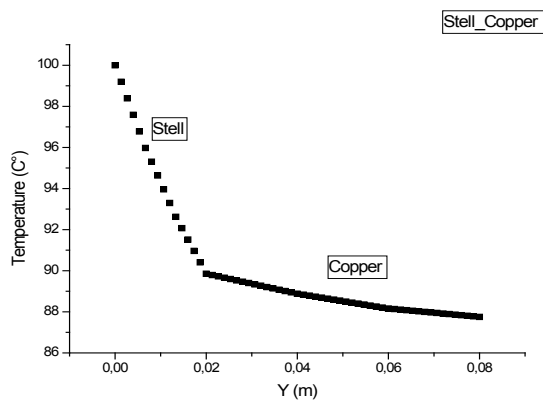


Fig. 13. Temperature evolution according to the steel-copper sample thickness

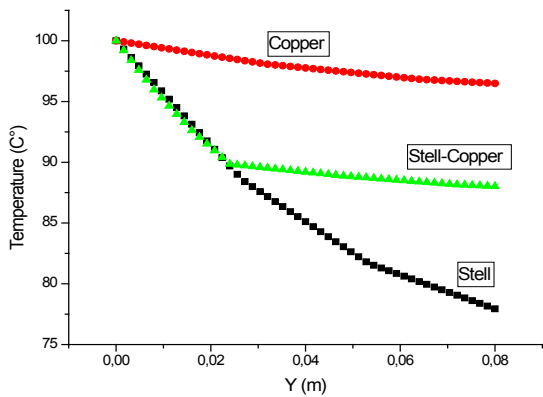


Fig. 14. Heat transfer comparison between steel, copper and steel-copper

In this case we have mixture material (steel-copper), we presented in Fig. 10, 11 and 12 the temperature contours in different planes, from these figures and Fig. 13 which shows the temperature as function of the thickness, we see that the temperature gradually decreases from 100 C° until to have a temperature of the outer wall of 87,115 C°.

According to Fig. 14, we notice that the heat transfer in the copper is larger than in the steel, but the heat transfer to the case of steel-copper mixture is between steel and copper.

VI. CONCLUSION

Our simulation results show that the heat transfer in the material is directly related to the thermal conductivity, when the thermal conductivity increases heat transfer also increases, for this in the case when we need to slow down the heat transfer in a material which exhibits a fast heat transfer, such as in the machines or engines domain, we use a second material which has a slow heat transfer, in our case we use steel as a first material to slow the heat transfer.

REFERENCES

- [1] Y. Tamene, S. Abboudi, C. Bougriou, "Etude numérique des transferts de chaleur et d'humidité en régime transitoire dans une paroi bicouche", 20ème congrès français de mécanique [CFM2011], Besançon, France.
- [2] S. Boulkroune, M. Chaour, O. Kholai "Simulation du transfert de chaleur dans un mur multicouche application à un four cubilot", La 2ème Conférence International sur la Maintenance et la Sécurité Industrielle CIMST'2013 Université 20 Août Skikda.
- [3] Xu Yihong, "Numerical simulation of heat-transfer in fracture rock based on fluid-solid coupling", DOI 10.1109/ICDMA.2013.202, 2013 Fourth International Conference on Digital Manufacturing & Automation IEEE.
- [4] Pawet Kopyt, Malgorzata Celuch-Marcysiak, "On the influence of mesh refinement and non-uniformity on the solution of the heat transfer equation in coupled EM-thermal analysis", vol. 2, N P. 578-581, Product Type: Conference Publication Date of Conference: 17-19 May 2004 IEEE.
- [5] I. Guven and E. Madenci, "Transient conduction analysis of regions with dissimilar materials via coupled finite and boundary element methods," Tech. Rep., Report to Semiconductor Research Corporation in Fulfillment of Grant 96-pp-086#1, 1997.
- [6] L. J. Segerlind, *Applied Finite Element Analysis*. New York: Wiley, 1984.
- [7] I.G. Angus, G.C. Fox, J.S. Kim, and D.W. Walker, *Solving Problems on Concurrent Processors*, vol. 2. Englewood Cliffs, N.J.: Prentice Hall, 1990.
- [8] C. Fox, M. Johnson, G. Lyzenga, S. Otto, J. Salman, and D.W. Walker, *Solving Problems on Concurrent Processors*, vol. 1. Englewood Cliffs, N.J.: Prentice Hall, 1988.
- [9] H.D. Simon, "Partitioning of Unstructured Problems for Parallel Processing," *Computing Systems in Eng.*, vol. 2, nos. 2/3, pp. 135-148, 1991.
- [10] R.D. Williams, "Performance of Dynamic Load Balancing Algorithms for Unstructured Mesh Calculations," *Currency : Practice and Experience*, vol. 3, no. 5, pp. 457-481, Oct. 1991.
- [11] R.D. Williams, *DIME: Distributed Irregular Mesh Environment*. California Inst. of Technology, 1990.

Axial compression resistance of cold-formed steel lipped channel at elevated temperature

A.A.S.C.Neto, P.D.A. Neto, A.A.R. Costa, R.B.Caldas, F.C. Rodrigues

Abstract—In the present study, it was analyzed analytically and numerically the variation of the yield strength reduction factor for sections subject to local buckling at high temperatures, $k_{\sigma,\theta}$, as a function of the relative slenderness λ_p for U lipped channel profiles. The analytical models used are based on the european standard EN 1993-1-2:2005 and the Brazilian Standard ABNT NBR 14323:2013. The numerical model is based on the Finite Element Method. It was verified that these numerical results differed from standard analytical results. Theoretical values of an adjusted reduction factor showed a correlation with the relative slenderness of the cross section.

Keywords—local buckling, elevated temperature, cold-formed, lipped channel.

I. INTRODUCTION

THE cold-formed sections, being made of thin plates, are subject to phenomena of local instability, such as local and distortional buckling. In a fire situation, the knowledge of the behavior of these profiles, especially in relation to the instabilities, is still early and therefore further studies are needed.

Because of these instabilities phenomena, the light gauge steel profiles reach the critical load before yielding, preventing the use of the reduction factor for the yield strength of steel at elevated temperature, $k_{y,\theta}$, which is defined at total strain of 2% in the steel stress-strain curve at high temperatures.

Nowadays, the european standard EN 1993-1-2:2005 [1] and Brazilian Standard ABNT NBR 14323:2013 [2] propose to use the reduction factor $k_{\sigma,\theta}$ for design profiles subject to local buckling, defined to a residual strain of 0.2%. Fig. 1 shows the variation of this factor, as well as the reduction factor $k_{y,\theta}$ and the reduction of elastic modulus, $k_{E,\theta}$, as a function of the steel temperature.

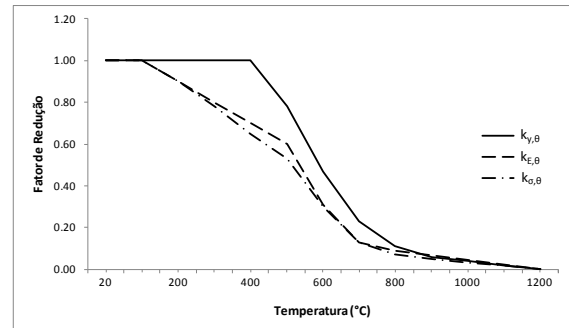


Figure 1: Variation of reduction factors $k_{y,\theta}$, $k_{\sigma,\theta}$ and $k_{E,\theta}$ as a function of steel temperature

In that way, for profiles subjected to local buckling, i.e., with critical local buckling stress below the yield stress, we use the reduction factor $k_{\sigma,\theta}$; otherwise we use $k_{y,\theta}$. The $k_{\sigma,\theta}$ and $k_{y,\theta}$ ratio can reach values of 0.65 and, according to EN 1993-1-2:2005 [1] and ABNT NBR 14323:2013 [2], the reduction factor $k_{\sigma,\theta}$ should be used even when the critical local buckling stress is slightly lower than the yield strength.

It is easily noted, as stated by these normative specifications, a discontinuity in the treatment of local buckling phenomenon in fire situation, since it uses the reduction factor $k_{\sigma,\theta}$ in profiles where local buckling occurs before the material reaches its yield strength and the reduction factor $k_{y,\theta}$ otherwise. It is important to note that the reduction factor $k_{\sigma,\theta}$ is used even if the local buckling occurs at the limit of yielding.

The aim of this study is to analyze the theoretical variation of the reduction factor $k_{\sigma,\theta}$ in relation to the relative slenderness for U lipped channel profiles. To conduct this study, many of these profiles, provided in Brazilian Standard ABNT NBR 6355:2003 [3], were analyzed numerically for temperatures of 20°, 400°, 550° and 700° C.

II. ANALYTICAL MODEL

There are three methods in Brazilian Standard ABNT NBR 14762:2010 [4] to calculate the design resistance at room temperature: Effective Width Method (EWM), the Effective Section Method (ESM) and the Direct Strength Method (DSM) [1],[5].

The EWM consider the elements of the cross-section as isolated plates, calculating the effective width for each element separately. In another way, the ESM and the DSM consider the behavior of the whole section, through a relative slenderness

A.A.S.C.Neto is a MSc student at the Universidade Federal de Minas Gerais; e-mail: armandoeng@yahoo.com.br

P.D.A. Neto is a graduation student at Universidade Federal de Minas Gerais; e-mail: possidoniodantas@gmail.com

A.A.R. Costa is a MSc engineer formed at Universidade Federal de Minas Gerais

R.B.Caldas is a Professor Doctor at Universidade Federal de Minas Gerais; e-mail: caldas@dees.ufmg.br

F.C. Rodrigues is a Professor Doctor at Universidade Federal de Minas Gerais; e-mail: francisco@dees.ufmg.br

associated to the profile cross-section,

$$\lambda_p = \sqrt{\frac{\chi A f_y}{N_l}} \quad (1)$$

where: χ is the reduction factor for global buckling; A is the gross cross-sectional area; f_y is the yield strength; N_l is the critical axial load for local buckling.

In the DSM, the critical local buckling load, N_l is normally obtained by a analysis based on the elastic stability theory, which can be accomplished via computer programs. Using the ESM, for U lipped channel profiles, the critical load can be determined by the equation

$$N_l = k_l \frac{\pi^2 E}{12(1-\nu^2) (b_w/t)^2} \quad (2)$$

where

$$k_l = 6.8 - 5.8(b_f/b_w) + 9.2(b_f/b_w)^2 - 6.0(b_f/b_w)^3 \quad (3)$$

k_l is a coefficient associated to local buckling of the cross-section. In the above equations: b_w is the nominal web width; b_f is the nominal flange width; t is the plate thickness.

In a fire situation, the EN 1993-1-2:2005 [1] and the ABNT NBR 14323:2013 [2] allow to perform the calculations of the effective area in the same way as it is done at room temperature, with material properties at 20° C. As shown in Fig. 1, the ratio value between the reduction factors $k_{\sigma,\theta}$ and $k_{E,\theta}$ is close to 1, which justifies the approach adopted by the standards. The design resistance to axial forces of the cross-section for uniform compression at elevated temperature is given by:

$$N_{c,Rd} = \chi_{fi} k_{\sigma,\theta} A_{ef} f_y \quad (4)$$

where: χ_{fi} is the reduction factor for global buckling in the fire design situation; A_{ef} is the effective area; f_y is the yield strength.

Since the goal of this work is just to study the phenomenon of local buckling, global buckling-related effects were eliminated by taking χ_{fi} equal to unity.

III. NUMERICAL MODEL

The profiles were modeled by Finite Element Method (FEM) on the computer program Abaqus [6], using quadrilateral shell elements of 4 nodes with reduced integration. The mesh was refined until they reach an appropriate convergence results. The use of reduced integration did not lead to convergence problems and achieved adequate results, beyond the fact that reduces processing time.

The boundary conditions used for these models were doubly pinned supported with a rigid body in the ends.

Firstly, it is necessary to determine the cross-section critical load for local buckling subjected to a concentrated load applied on its geometric center. Afterward, the displacements of the local buckling mode configuration, Fig. 2, was applied as a small initial imperfection to the profile with a maximum value equal to $b_w/1000$, as b_w being the nominal web width.

To determine the ultimate load, it is performed a non-linear analysis with increments of load and displacement. With the intention to minimize the effects of the global buckling was adopted a profile length equal to twice the nominal web width.

The nonlinearity of the material was implemented by means of a steel stress-strain curve, varying with the temperature according to EN 1993-1-2:2005.

To validate the numerical model, the results were compared with the experiments performed by Hanya and Kanno [7], who analyzed the cold-formed profiles with different types of steel. The characteristics of these profiles and the ultimate loads obtained experimentally by Hanya and Kanno [7] for various temperatures, $N_{u,e}$, and the numerical results obtained in the present work, $N_{u,n}$, are shown in Table 1. In the first column of Table 1, the profiles are named as follows: b_w (nominal web width) x b_f (nominal flange width) x c (width of the flat portion of the lip) x t (nominal plate thickness).

It is observed that the ratio between the experimental and numerical results, $N_{u,e}/N_{u,n}$, varies from 0.87 to 1.16, proving the efficiency of the numerical model used in this work.

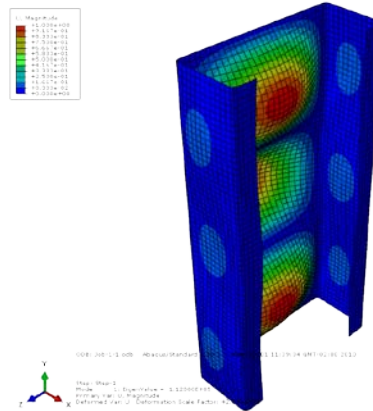


Figure 2: Local Buckling Mode

Table 1: Experimental and numerical results at ambient temperature

Perfis	20°C		
	$N_{u,e}$	$N_{u,n}$	$N_{u,e}/N_{u,n}$
89x44.5x12x1.0	43.2	46.8	0.92
50x44.5x12x1.0	42.2	47.3	0.89
150x75x12x1.0	40.9	46.6	0.88
89x44x12x1.58	73.3	80.4	0.91
89x44x12x1.57	74.1	85.2	0.87

mm to 140 mm, as presented by ABNT NBR 6355:2003 [3]. There is a good approximation of the results, noting that the analytical values obtained via MLE are slightly lower than the numerical values. The same profiles were used in the study at elevated temperature as described below.

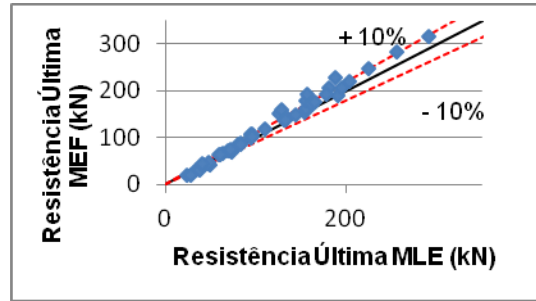


Figure 3: Comparison for the ultimate resistance results obtained via MLE and MEF at 20°

Table 2: Experimental and numerical results at 350°

Perfis	350°C		
	$N_{u,e}$	$N_{u,n}$	$N_{u,e}/N_{u,n}$
89x44.5x12x1.0	29.7	25.6	1.16
50x44.5x12x1.0	30	25.8	1.16
150x75x12x1.0	31.3	28.7	1.09
89x44x12x1.58	56.2	48.2	1.17
89x44x12x1.57	64.7	61.8	1.05

IV. RESULTS

With the validated numerical model, the studied profiles were chosen with web width ranging from 75 mm to 140 mm, provided by ABNT NBR 6355:2003 [3]. These profiles are consistent with the specifications of ABNT NBR 14762:2010 [4], aiming to not present any distortional or global buckling, as shown in the previous sections. It was found that the numerical results differed from results obtained with the analytical models prescribed by EN 1993-1-2:2005 [1] and the ABNT NBR 14323:2013 [2], who consider $k_{\sigma,\theta}$ varying only with temperature. Based on this observation, theoretical values were determined for the yield strength reduction factor of sections subject to local buckling, $k'_{\sigma,\theta}$, which turns the analytical results closer to the numerical results, using the expression

Table 3: Experimental and numerical results at 550

Perfis	550°C		
	$N_{u,e}$	$N_{u,n}$	$N_{u,e}/N_{u,n}$
89x44.5x12x1.0	19.2	19.8	0.97
50x44.5x12x1.0	21.1	19.3	1.09
150x75x12x1.0	22.1	23.9	0.92
89x44x12x1.58	36.7	33.2	1.1
89x44x12x1.57	45.5	44.9	1.01

$$k'_{\sigma,\theta} = \frac{N_{u,n}}{A_{ef} f_y} \tag{5}$$

where $N_{u,n}$ are the ultimate loads obtained numerically via FEM, and A_{ef} is the effective area calculated at room temperature, as proposed by the design rules in fire condition [8].

Fig. 4, Fig. 5 and Fig. 6 show the theoretical variation of $k'_{\sigma,\theta}$ as a function of the cross-section relative slenderness for profiles analyzed according to the methodology presented at temperatures of 400° C, 550° C and 700° C respectively.

The relative slenderness was calculated with Equations 1, 2 and 3. Also it was found that, although not shown in this paper, the numerical values for the critical local buckling load results are very close to analytical results.

The coefficient values, $k_{\sigma,\theta}$ and $k_{y,\theta}$, according to EN 1993-1-2:2005 [1] and the ABNT NBR 14323:2013 [2], equal in both standards, are indicated in the graphs (Fig. 4, Fig. 5 and Fig. 6) by continuous and dashed horizontal lines, respectively.

Additionally, the results at room temperature, obtained by the Effective Width Method (EWM), according to ABNT NBR 14762:2010 [4], were compared with numerical results obtained by Finite Element Methods (FEM). The results, shown in Fig. 3, were obtained ranging the web width from 75

As shown in Fig. 4, Fig. 5 and Fig. 6, it is noted a variation for the reduction factor $k'_{\sigma,\theta}$ differently than proposed by the EN 1993-1-2:2005 [1] and ABNT NBR 14323:2013 [2], which is constant and only dependent of temperature.

The theoretical reduction factor $k'_{\sigma,\theta}$ tends to the value of $k_{y,\theta}$ as smaller is the section relative slenderness, and decays for larger slenderness values, apparently tending to a constant value on average, which is lesser than $k_{\sigma,\theta}$.

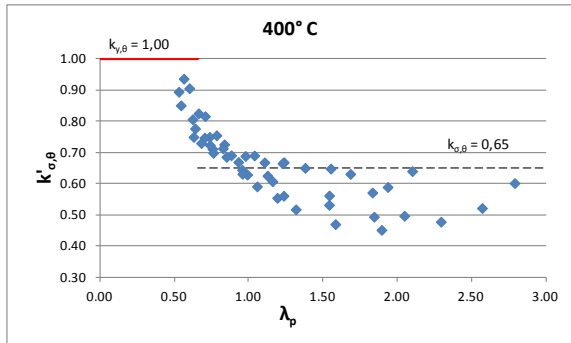


Figure 4: Variation of the theoretical $k'_{\sigma,\theta}$ reduction as a function to the cross-section relative slenderness at 400°C

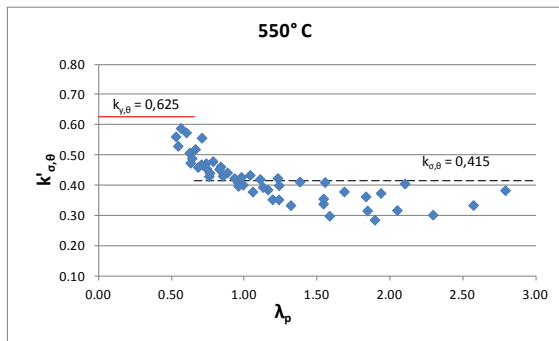


Figure 5: Variation of the theoretical $k'_{\sigma,\theta}$ reduction as a function to the cross-section relative slenderness at 550°C

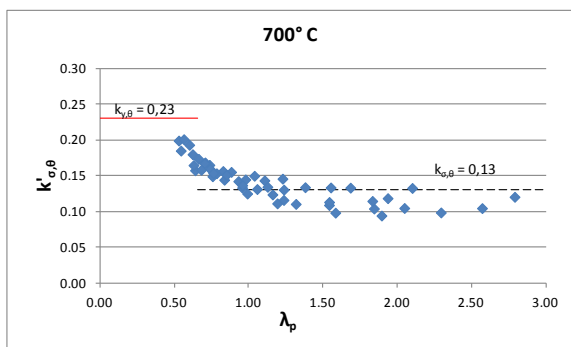


Figure 6: Variation of the theoretical $k'_{\sigma,\theta}$ reduction as a function to the cross-section relative slenderness at 700°C

It is noted that the reduction factor $k'_{\sigma,\theta}$ has a greater dispersion of the results when slenderness increases. To better model this equation, it was analyzed separately in groups of profiles with the same b_w / b_f relationship, where b_f is the nominal flange width and b_w is the nominal web width.

As shown in Fig. 7, the variation of $k'_{\sigma,\theta}$, analyzed separately in groups of profiles, becomes more standardized,

i.e., with lesser dispersions. It may be noted that the profiles with b_w / b_f ratio closer to 1.00 have a more pronounced decrease of the $k'_{\sigma,\theta}$ value as slenderness increase, while the profiles with higher b_w / b_f ratio tends to remain constant, more close to the value proposed by EN 1993-1-2:2005 and ABNT NBR 14323:2013 [2]. The same behavior occurs in the other temperatures.

Values of b_w / b_f ranging from 1 to 3.5 corresponds to values of b_f / b_w ranging from 1 to 0.28. With a parametric analysis using the Finite Element Method, when only local mode is triggered, it is possible to prove that, for U lipped channels sections subjected to uniform compression varies from a lower (at $b_f / b_w = 1$) to a higher value (at $b_f / b_w = 0.28$), thereby resulting in, respectively, lower and higher values for critical local buckling load, N_l , according to Rodrigues [9].

Approaching the theoretical reduction factor as an exponential function (Equation 6) dependent of the cross-section relative slenderness λ_p , for each profile group separately, it is possible to have a very similar behavior.

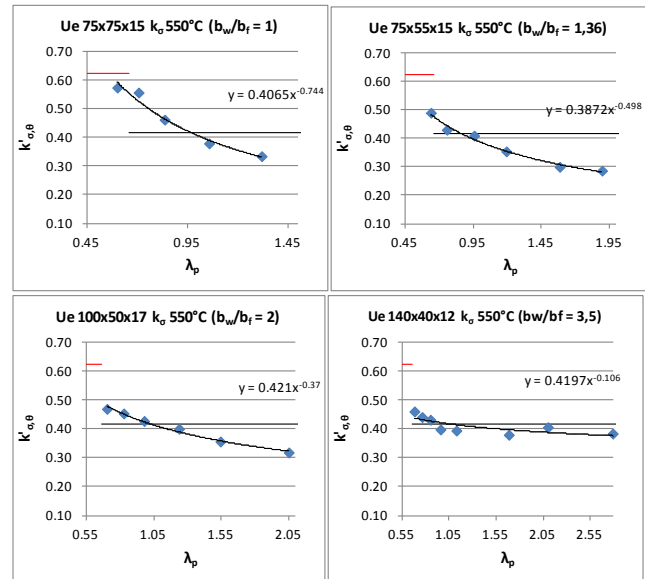


Figure 7: $k'_{\sigma,\theta}$ coefficient variation to the relative slenderness separated in b_w / b_f ratio groups at a temperature of 500°C

$$k''_{\sigma,\theta} = a\lambda_p^b \quad (6)$$

It was conducted a regression analysis with Excel Office 2007 package. In each group is noted that the coefficient "a" of Equation 6 has a value close to $k_{\sigma,\theta}$ proposed by EN 1993-1-2:2005 [1], and the value of the coefficient "b" varies with b_w / b_f (Fig. 8).

After these analysis, it was proposed the equation 6 to calculate the yield strength reduction factor for U lipped channel profiles subjected to local buckling in fire condition ($k''_{\sigma,\theta}$) as a function of the relative slenderness of the profile:

$$k''_{\sigma,\theta} = k_{\sigma,\theta} \lambda_p^b \quad (7)$$

where: $k''_{\sigma,\theta}$ is the adjusted yield strength reduction factor for profiles subjected to local buckling at elevated temperature, as proposed in this work; $k_{\sigma,\theta}$ is the yield strength reduction factor for profiles subjected to local buckling at elevated temperature presented by EN 1993-1-2:2005 [1]; λ_p is the relative slenderness ratio of a U lipped channel profile; b is a coefficient given by Equation (8) and dependent of b_w / b_f ratio.

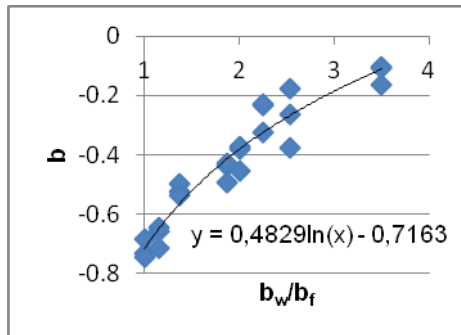


Figure 8: Variation of b coefficient in relation to the b_w / b_f ratio

$$b = 0.4829 \ln(b_w / b_f) - 0.7163 \leq 0 \quad (8)$$

Additionally, due to the possibility that this formulation can be used for other types of cross-section, it was suggested a second formulation for the calculation of the coefficient "b" based on the coefficient for local buckling of cold formed steel profiles, k_l , shown in Figure 9.

$$b = 0.092k_l^3 - 1.0593k_l^2 + 4.0424k_l - 5.8261 \quad (9)$$

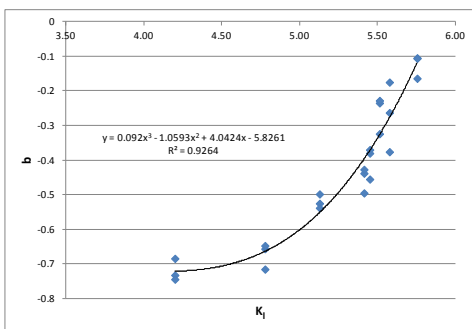


Figure 9: Variation of b coefficient in relation to the k_l coefficient

V. CONCLUSIONS

In the present study, it was analyzed analytically and numerically the variation of the yield strength reduction factor for sections subject to local buckling at high temperatures, $k_{\sigma,\theta}$, as a function of the relative slenderness λ_p for U lipped channel profiles. The analytical models used are based on the

European Prestandard EN 1993-1-2:2005 [1] and the Brazilian Standard ABNT NBR 14323:2013 [2]. The numerical model is based on the Finite Element Method. With the numerical results, it was verified that these numerical results differed from standard analytical results, considering $k_{\sigma,\theta}$ varying only with temperature. Theoretical values of an adjusted reduction factor, named $k'_{\sigma,\theta}$, showed a correlation with the relative slenderness of the cross section, as well as the b_w / b_f ratio.

For λ_p values close to 0.5, it is observed that $k'_{\sigma,\theta}$ becomes very close to $k_{y,\theta}$. It is observed that this slenderness value is below the threshold that defines the profiles subjected to local buckling at ambient temperature, which is around 0.776. The value 0.5 is still well below even when the limit is 0.776 multiplied by 0.85, as provided by the design rules for fire condition, leading to a limit value of 0.66. For relative slenderness values between 0.5 and 1.0, the theoretical reduction factor is higher than the reduction factor provided by the standards. As for λ_p values greater than 1.0, the $k'_{\sigma,\theta}$ values are generally smaller than those proposed by EN 1993-1-2:2005 [1] and ABNT NBR 14323:2013 [2] and tending to a constant value on average.

ACKNOWLEDGMENT

To FAPEMIG, CAPES, CNPq and Programa Institucional de Auxílio à Pesquisa de Doutores Recém-Contratados da PRÓ-REITORIA DE PESQUISA DA UNIVERSIDADE FEDERAL DE MINAS GERAIS, which make possible the elaboration and presentation of this work.

REFERENCES

- [1] EN 1993-1-2:2005. Eurocode 3: Design of Steel Structures, Part 1.2: General Rules, Structural Fire Design. European Committee for Standardization.
- [2] ABNT NBR 14323:2013. Brazilian Association for Technical Standards. Design of Steel Structures and Composite Steel and Concrete Structures in Fire Situation.
- [3] ABNT NBR 6355:2003. Brazilian Association for Technical Standards. Profiles of Structural Cold-Formed Steel – Standardization.
- [4] ABNT NBR 14762:2010. Brazilian Association for Technical Standards. Design of Cold-Formed Steel Structures.
- [5] AISI S100-2007. North American Specification for the Design of Cold-Formed Steel Structural Members. American Iron and Steel Institute.
- [6] Simulia (2010). Software ABAQUS/CAE, 6.10 version. Dessault Systemes Simulia Corp., USA.
- [7] Hanya, K; Kanno, R. "Material Properties and Buckling Behavior of Cold-Formed Thin - Walled Steel Members Under Elevated Temperatures Due to Fire." Euro Steel 2005, 5.1–77.
- [8] COSTA, A.A.R. (2012) Estudo da Flambagem Local de Perfis U Enrijecidos em Situação de Incêndio. PostGraduation Program in Structural Engineering – Engineering School – Federal University of Minas Gerais. 120p. 2012.
- [9] Rodrigues, F. C. (2004), Design of Cold-Formed Steel Structural Profiles in Fire Situation. Federal University of Minas Gerais, 03/05/2004 version.

Forging by rocket driven hammer: Dynamics and experiments

Dimitar N. Karastoyanov, Vladimir K. Kotev and Todor N. Penchev

Abstract—Technological processes such as forging, die forging, and pile driving are realized as a result of a collision between two bodies. After the impact the bodies' energy transforms to plastic or elastic deformations of the colliding bodies. This paper studies the influence of impact parameters such as forces, accelerations, velocities, time and energy on shape forming of parts achieved by rocket driven hammer. A laboratory set up for control of impact utilizing a cold rocket engine working with compressed air was created. This experimental set up allows for the generation of an additional force on a body during the impact period. In order to control the working conditions in forging the dynamics of the impact process is analyzed. Also, experiments on plastic deformation of specimens were conducted on this set up using *controlled impact*. An increase of the specimen deformation was obtained compared to the common *free-fall impact* deformation as well as a decrease of the rebound to zero (we called that a sticking impact). The obtained theoretical and experimental results show that *controlled impact* enhanced forging process.

Keywords—Deformations, forging, impact, impact machines.

I. INTRODUCTION

FORGING is a bulk deformation process in which the workpiece is compressed between two opposing dies so that the die shapes are imparted to the workpiece. Bulk deformation processes involve large amount of plastic deformation [1], [2]. The cross-section of workpiece changes without volume change [1], [2]. The temperature in forging has significant influence on metal forming processes [1]-[3]. Cold working is metal forming performed at room temperature [1]. The cold working forging processes has the following advantages better accuracy, better surface finish, high strength and hardness of the part, no heating is required [1], [2]. The main disadvantages are higher forces and power, limitations to the amount of forming, additional annealing for some material is required, and some material are not capable of cold working [1], [2]. In order to manufacture parts with high geometrical accuracy by forging and pile driving hammers a cold working

process can be used [1]-[6]. The speed of the falling parts of these machines is 5-7 m/s. For forging of special alloy forgings and forgings of complex shape, high-speed gas forging hammers are used with speed of the falling parts of 16–20 m/s [1]-[6].

Today, forging is a major world-wide industry that has significantly contributed to humanity's development. Typical parts manufactured by forging are bolts, rivets, connecting rods, tube shafts, coins, gears, hand tools, structural components of machinery and aircraft and ect [1]-[4]. Forging processes are achieved by the following machines: hydraulic press, mechanical press with an eccentric or pneumatic drive, the eccentric shaft can be replaced by a crankshaft to give the up-and-down motion to the ram, knuckle-joint press, screw press, and gravity drop hammer [1], [2]. These machines have some mechanical restrictions like energy, load and stroke limitation [1], [2].

To extend energy and load limitation in forging in the early 90-ties the first licensed industrial rocket engine (IRE), and a hammer propelled by that engine were produced in Bulgaria [2]-[6]. Several hundred conical gears were manufactured by it [2], [3]. Also, many experiments have been made by proposed technology [2]-[6]. Moreover, in the article [2] the rebound force in 3D hot die forging is obtained empirically. This type of impact machines allow to add and control the addition force during the impact between collided bodies. A laboratory set up was developed in order to explore the *controlled impact* [3]-[6]. The obtained results make clear that the use of IRE propelled production machines for plastic deformation technologies improve those processes and decrease the production drain [4], [5]. Furthermore it was found out that the use of a jet engine for the application of additional force at impact significantly reduces the size of the rebound in the elastic shock [4]-[6]. With increase of the additional force we can achieve value at which to obtain impact without rebound, which is called in [4], [5] *sticking impact*. The possibility for altering the parameters of the impact at the beginning of impact between colliding bodies gives us grounds to confirm the term *controlled impact* [5], [6]. Further studies are needed to explore the possibility of reducing the rebound in the technological impact processes such as forging, die forging, pile driving and high velocity briquetting of waste and powder materials.

The aim of this paper is to study the dynamics of the metal forming processes achieved by rocket driven hammer in order

This work was supported by the project AComIn - *Advanced Computing for Innovation*, Grant 316087, funded by the FP7 Capacity Program (Research Potential of Convergence Regions initials).

D. N. Karastoyanov is with IICT-BAS, Sofia, Bulgaria, (phone: +359-2-979-27-23; e-mail: dkarast@iinf.bas.bg).

Vl. K. Kotev was with the Institute of Mechanics – BAS, Sofia, Bulgaria. He is now with the Institute of Information and Communication Technologies (IICT) - BAS, Sofia, Bulgaria; e-mail: kotev@imbm.bas.bg.

T. N. Penchev is with the Materials Processing Department, Technical University of Sofia, Sofia, Bulgaria, (e-mail: tzpenchevi@abv.bg).

to control the impact processes and parts manufacturing properly. Particularity in this research we studied the influence of force, velocity, energy transformation and time of impact on deformation of parts achieved by addition force by IRE. We try to control and optimize the forging process conditions.

II. ROCKET DRIVEN HAMMER

A. Experimental Set-up

The free impact is an uncontrolled process [2]-[6], [11]. It generates a rebound of the colliding bodies. The rebound energy E_{rb} is part of the impact energy E_i . The decrease of rebound and rebound energy E_{rb} lead to increase of the efficiency of the impact machines and increase the tool's life [1,2]-[6]. A laboratory set up for exploration of controlled impact was created in a laboratory at the Technical University of Sofia, Bulgaria [4]-[6]. In Fig.1 a laboratory set up with cold rocket engine is shown [4]-[6]. It works on pressurized air that can be continuously changed in the limits of 5 to 30 bar. The maximum drop height is 1.1 m, and the impact speed is between 1 and 8,2 m/s. A Casio Exlim EX-F1, 1200 fps camera was used to film the collision and rebound.

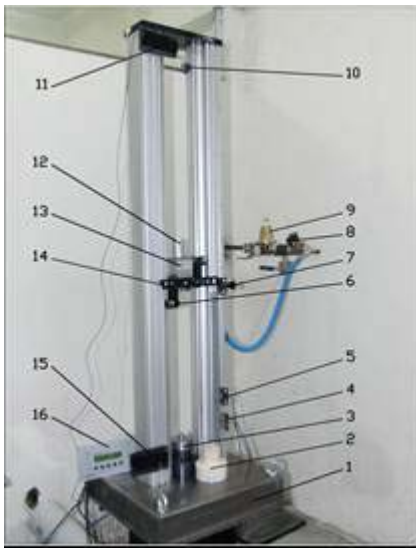


Fig.1 The laboratory set up for studying of collision processes.

The components of the depicted on fig1 set-up are: 1 – base plate with a mass of 235 kg; 2 – lower fixed body for elastic impact; 3 – lower fixed tool for plastic impact; 4 – induction speed sensors; 5 – air on/off induction sensor; 6 – guides for the falling part; 7 – trigger mechanism; 8 electro-magnetic valve; 9 – air pressure control valve; 10 - air 'On' sensor; 11 – receiver of the light sensor for speed; 12 – cold rocket engine; 13 – 6,17 kg mass falling part; 14 – plate for activation of sensors 4, 5 and 11; 15 – light speed sensor emitter; 16 – electronic control board.

B. Impact and Deformations

In impact phenomenon the velocities of the colliding bodies

are changed very fast for a very short period of time about few milli seconds or nano seconds [2], [8-10]. During the impact period a very high forces are acting on the colliding bodies. These forces lead to body's deformations and energy transformation [2], [8-10]. To control the impact between bodies the dynamics of impact has to be studied [5]-[11]. The main problems in impact dynamics are to find bodies accelerations and velocities after impact with given ones before impact as well as the hit impulses during the impact [8-10]. In this paper we study the dynamics of controlled impact and the parts deformation. In our theoretical and experimental study (fig.2a) the following four cases of impact are considered:

- Free fall of the ram and additional force (F_{ad}) at the time of impact (fig.2.b). In this case of the controlled impact the maximum speed is $V_I=4.5$ m/s;
- Fall with acceleration by a rocket engine (fig.2.c), without additional force in the time of impact (free fall with maximum $V_I = 8.5$ m/s;
- Fall with acceleration -a generated by rocket engine and additional force (F_{ad}) in the time of impact (controlled impact with maximum speed $V_I = 8.5$ m/s) fig.2.d.;
- Free fall with maximum speed $V_I = 4.5$ m/s (fig.2e).

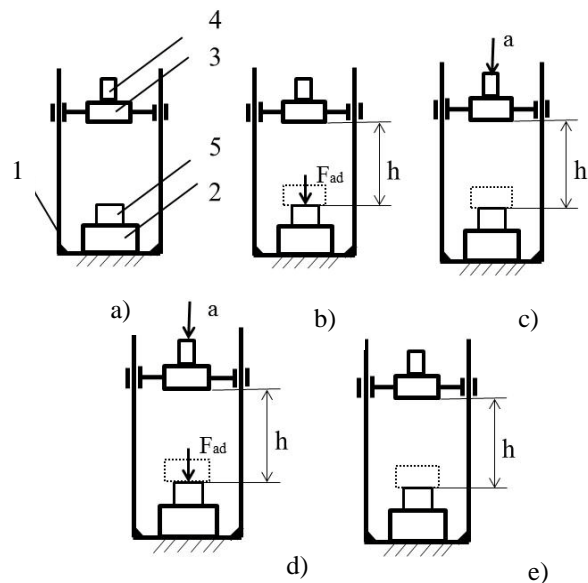


Fig.2 the studied cases of impact in forging.

III. DYNAMICS

Dynamics of forging by hammer

We consider the dynamics of two colliding bodies which have a common normal passing through their mass centers (fig.1 and 2). These two bodies represent the workpiece and hammer's ram respectively. A straight line perpendicular to the plane of contact of two colliding bodies is called the line of impact. If the centers of gravity of the two bodies lie on the line of contact, the impact is called *central* or *direct impact*, in

any other case, eccentric impact [8], [9]. We assume that the mass of base plate is larger than the mass of the ram. The dynamics of this phenomenon can be described by equation (1) and (2).

$$mu - mv = S \tag{1}$$

$$S = \int_t^{t_0+\tau} F dt.$$

where:
 $m = 6,17$ kg is a mass of the ram,
 u is the speed after impact,
 v is the speed before impact,
 S is the impact impulse. This integral represents the forces acting during the impact.

After collision, the bodies continue to move with changed velocities of v_1 and v_2 . Since the contact forces on one body are equal to and opposite the contact forces on the other, the sum of the linear momenta of the two bodies is conserved. In collinear impact the equation (1) can be written in the following form

$$m_1u_1 + m_2u_2 = m_1v_1 + m_2v_2 \tag{2}$$

$$u_1 - u_2 = -k(v_1 - v_2).$$

where: k is the coefficient of restitution after a collision.
 The value of k will depend on the shape and material properties of the colliding bodies [4], [7], [8]. In *elastic impact*, the coefficient of restitution is *unity* and there is *no energy loss*. A coefficient of restitution of *zero* indicates perfectly inelastic or *plastic impact*, where there is no separation of the bodies after collision and the energy loss is a maximum. In oblique impact, the coefficient of restitution applies only to those components of velocity along the line of impact or normal to the plane of impact. The velocity of base plate m_2 is unchanged for all practical purposes during impact and $k = u_1/v_1$. Moreover k could be express like

$$k = \sqrt{\frac{h_{reb}}{h}}. \tag{3}$$

where: h is a ram dropped from a height h upon the workpiece or a base plate and rebounding to a height h_{reb} .

The both colliding bodies the ram and plate base respectively, interact each other by internal impulse

$$S_1 = -S_2 = -(1+k) \frac{m_1m_2}{m_1+m_2} v_1. \tag{4}$$

The waste of the kinetic energy $-T$ during the impact is

$$T_2 - T_1 = -\frac{1}{2} \frac{m_1m_2}{m_1+m_2} (1-k^2)(v_1 - v_2)^2. \tag{5}$$

Generally, the equations from (1) to (5) describe dynamics of plastic working of metals achieved by hammers.

IV. EXPERIMENTS

Lead specimens (Pb = 99.99 %) with equal volume K ($K = 4.786 \text{ sm}^3$) and $H_0/D_0 = 1.2; 1.5; 1.8$, where H_0, D_0 are the initial height and diameter of the specimens, are used for the experiments. The falling part mass $m = 6.17$ kg, and its impact velocity $V_i = (2,90 - 8,80) \pm 2 \%$, m/s . The upsetting is realized by maximum friction on contact surfaces.

The height $H \pm 0.01$ mm of the specimens is measured after the experiments. The specific impact energy E_s and difference $\Delta\varepsilon$ are calculated by the formulae

$$E_s = \frac{E_i}{K} \quad J/sm^3, \tag{6}$$

$$\Delta\varepsilon = \varepsilon_{ci} - \varepsilon_{fi} \quad \% . \tag{7}$$

where: $\varepsilon_{ci}, \varepsilon_{fi}$ are the relative deformations by *controlled impact* and *free impact*.

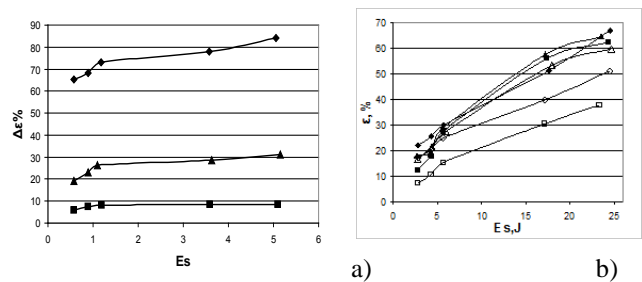


Fig. 3 Variation of $\Delta\varepsilon$ and ε .

On fig.3a: *free impact* —□— $H_0/D_0 = 1.2$; —△— $H_0/D_0 = 1.5$; —◇— $H_0/D_0 = 1.8$; *controlled impact* - —■— $H_0/D_0=1.2$; —▲— $H_0/D_0 = 1.5$; —◆— $H_0/D_0 = 1.8$. On fig.3b: —◆— $H_0/D_0 = 1.2$; —■— $H_0/D_0 = 1.5$; —▲— $H_0/D_0 = 1.8$.

From the high speed camera pictures the rebound height h_{reb} , m, is given and coefficient of restitution k is calculated [4]. In this paper we study the deformation by reverse extrusion of the specimen. The lead specimens shown on fig.4 are used with $H_0 = 20$ mm, $D_0 = 20$ mm and 6.28 sm^3 volume. The die diameter is 20 mm and punch diameter is 16 mm.



Fig.4 Slit specimens extruded by different impact energy.

The left side specimen in fig.4 of each two is deformed by *controlled impact* and the right side specimen is deformed by *free impact*. The weight of the free dropped ram is 11.46 kg and falling height $h = 0.965$ m, 0.82 m, 0.74 m, 0.67 m, 0.47 m. The oil lubricant is used by deformation. After deformation the whole height ± 0.01 mm of the specimens is measured. Because of irregular extrusion heights s_{max}, s_{min} are measured and average height $h_{av} = (s_{max} + s_{min})/2$ is calculated. After that the specimens are slit – Fig.4. In Fig.5 the $V_i - h_{av}, E_s - h_{av}$ are given in graphical form.

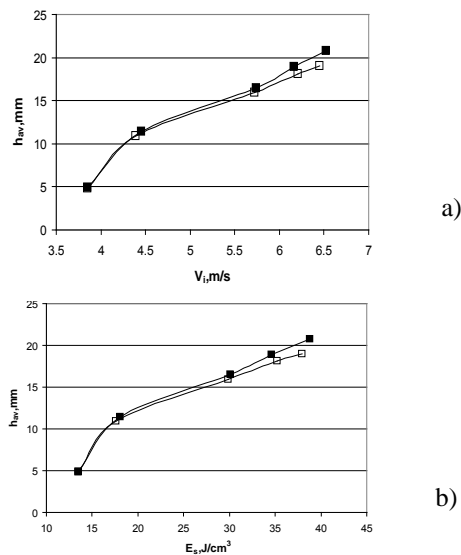


Fig. 5 Variation of h_{av} and E_s .

Fig.5. Variation of average whole height h_{av} with impact speed V_i (a) and specific energy E_s (b): *free impact* and *controlled impact* by reverse extrusion.

V. CONCLUSION

We study theoretically and experimentally two cases of forging by hammer. The first case is called *free impact* and the second is called *controlled impact*. The obtained results show that *controlled impact* enhanced forging process. Lead specimens were used because of the relatively small cold rocket engine thrust $R=22$ kg. It is seen on Fig.3 that in both kinds of impact the relative deformation ϵ is in great dependence on the H_0/D_0 ratio. The maximum difference $\Delta\epsilon$ defined from (7) is at $H_0/D_0 = 1.2$ and minimum difference $\Delta\epsilon$ is at $H_0/D_0 = 1.5$ - Fig.3b. The rebound height h_{reb} and coefficient of restitution k by impact upsetting depends on both H_0/D_0 ratio and impact velocity V_i . With increase of V_i h_{reb} and k decrease. By *controlled impact* upsetting at $V_i \geq 7.5$ m/s h_{reb} and k are equal zero (sticking impact), irrespective of H_0/D_0 value. By comparing the impact specific energy E_s of upsetting and reverse extrusion in the case of *free impact* it can be pointed out that by reverse extrusion with greater energy E_s a smaller deformation ϵ is reached. This means that by reverse extrusion more impact energy is needed than by upsetting for the same relative deformation ϵ .

The derived mathematical model of the forging by hammer will help us to design experiments theoretically and to set working conditions properly. In order to establish a proper set of working conditions in forging we will study the impact energy transformation and piece deformation by thermo camera and 3D tomograph. To get structural information and impact influence 3D will be used.

REFERENCES

- [1] V. Marinov, "Manufacturing Processes for Metal Products", Kendall Hunt Publishing Company, 2010 - Technology & Engineering.

- [2] T. Penchev and D. Karastoyanov, "High Speed Industrial Hammer Using Rocket Engine", XX-th ADP Conference, Sosopol, Bulgaria, 2011.
- [3] Penchev T., Karastoyanov D., New Industrial Engine: Priority and Field of Application., International Conference ICMAS 2012, November 8-9 2012, Bucharest, Romania, published in JOURNAL PROCEEDINGS IN MANUFACTURING SYSTEMS, VOL. 7, ISSUE 4, 2012, ISSN 2067-9238, PP 241-244
- [4] T. Penchev, I. Altaparmakov and D. Karastoyanov, "Experimental study on the possibilities to decrease the coefficient of restitution after impact". Applied Mechanics and Materials Vols. 217-219 (2012) pp. 1659-1662.
- [5] T. Penchev, D. Karastoyanov and V. Monov., Control System For "Controlled Impact" Laboratory Device., Third IEEE International Conference on Information Science and Technology ICIST 2013, March 23-25, 2013; Yangzhou, Jiangsu, China., 978-1-4673-2764-0/13/ ©2013 IEEE., pp 215-219
- [6] T. Penchev, D. Karastoyanov, and I. Altaparmakov, "Experimental Study on *Controlled Impact* Effect in Plastic Deformation Process, Advanced Materials Research Vol. 772 (2013) pp 3-8.
- [7] D. Karastoyanov, Control of Robots and other Mechatronic Systems, Academy Publ. House "Prof. Marin Drinov", Sofia 2010, ISBN 987-954-322-415-9 (in Bulgarian)
- [8] F. Beer, E. Russell, E. Eisenberg, and Ph. Cornwell, Vector Mechanics for Engineers: Dynamics, McGraw-Hill Science/Engineering/Math; 9 edition, 2009.
- [9] F. Beer, Jr. Johnston, J. De Wolf, and D. Mazurek, Mechanics of Materials, McGraw-Hill Science/Engineering/Math; 6 edition, 2011.
- [10] A. Avallone, T. Baumeister, A. Sadegh, MARK's Standard Handbook for Mechanical Engineers, 11th ed. New York: McGraw-Hill, 2007.
- [11] Wang Zhong-jin, Cheng Li-dong, Effect of material parameters on stress wave propagation during fast upsetting, Transactions of Nonferrous Materials Society of China, 2008, 18, 1189-1195. R. W. Lucky, "Automatic equalization for digital communication," *Bell Syst. Tech. J.*, vol. 44, no. 4, pp. 547-588, Apr. 1965.

Dimitar N. Karastoyanov is a member of the Bulgarian Scientists Association. He was born in Stara Zagora, Bulgaria in 1952. He has a master degree in Electrical engineering. He graduated Technical University Sofia in 1977. The author received a doctoral degree in 1982, Robotics from the Institute of engineering cybernetics and robotics (BAS). Dr. Karastoyanov is a professor in Institute of Information and Communication Technologies (BAS). Prof. Dr. Karastoyanov is a key professor under AcomIn project at the IICT - BAS. He is conducting research on design, dynamics and intelligent control of robots and mechatronic systems. His professional interests refer to real time systems, adaptive control, industrial engineering and robotics.

Vladimir K. Kotev is a member of the Bulgarian Scientists Association. He was born in Sliven, Bulgaria in 1976. He has a master degree in Mechanical engineering. He graduated Technical University Sofia in 2002. After that he worked in a private machine building company for 2 years. Next, the author received a doctoral degree in 2008, Biomechanics from the Institute of mechanics at the Bulgarian Academy of Sciences (BAS). Dr. Kotev is an assistant professor in Institute of Mechanics. He has been a postdoctoral researcher in medical robotics at the Kawasaki and Mori laboratory at Gifu University - Japan from 2011 to 2013. Dr. Kotev is a postdoctoral fellow under AcomIn project at the IICT - BAS. He is conducting research on design, dynamics and intelligent control of robots and mechatronic systems. His professional interests refer to mechanics and biomechanics, industrial engineering and robotics.

Todor N. Penchev is a member of the Bulgarian Scientists Association. He was born in Sofia, Bulgaria in 1941. He has a master degree in Mechanical engineering. He graduated Technical University Sofia in 1967. The author received a doctoral degree in 1979, Machine Technology from the Technical University Sofia. Dr. Penchev is an assoc. professor in Institute of Information and Communication Technologies (BAS). Dr. Penchev is an assoc. professor under AcomIn project at the IICT - BAS. He is conducting research on design, dynamics and mechanics of mechatronic systems and industrial processes. His professional interests refer to forging systems, rocket engines, industrial engineering and technology.

Turbulence Models Comparison for the Numerical Study of the Air Flow, an Internal Combustion Engine

Ioannis Pantokratoras, Charalampos Arapatsakos

Abstract—Numerical flow studies of air flowing into the cylinder of an internal combustion, four stroke, two valve engine have been undertaken. The studies relating to the phase of intake stroke, when the piston movement of the engine creates pressure lower than the atmospheric in the cylinder. Results were obtained with the following turbulent models provided by commercial CFD code ANSYS v15.0: a) Standard k- ϵ , b) Standard k- ω , c) RNG k- ϵ , d) Sst k- ω . Three dimensional, steady state flow conditions considered, for valve opening and piston position at 90° degrees of crankshaft revolution after top dead center.

Key-Words—Turbulence, Four Stroke Engine, Intake Stroke, Computational Fluid Dynamics

I. INTRODUCTION

It is very important for the efficiency, fuel economy and ideal working characteristics of an internal combustion engine, to be able to predict and model the air/fuel mixture and exhaust gases flow dynamics. Throughout the years of engine development, various experimental techniques have been developed for this reason. But the cost and time needed and also the limited potential that experiments provided, made these techniques obsolete for engine design and development[6]. The evolution and increase of the computational capabilities resulted to the use of Computational Fluid Dynamics (CFD) codes. CFD codes define a solution to a set of equations of fluid flow by advancing the solution through space and time and provide a numerical description of the flow field. CFD nowadays has applications in almost all fields of engineering. Very complicated phenomena can be accurately simulated, while cost and time are saved without the need of prototyping. It is not difficult to understand why CFD became so popular for modern engine design. Various intake manifolds and exhaust geometries can be accurately simulated fast and with comparatively low cost[4,5,7,9]. CFD workflow consists of: a) Geometry design, b) Grid generation, c) Setup the model, d) Solution, e) Results evaluation. CFD codes use the finite volume method (FVM) to discretize the geometry of the flow. This discretization is created upon an integral form of the partial differential equations (conservation of mass, momentum and energy) to be

This work developed in the Laboratory of Thermodynamics and Thermic machines of Democritus University of Thrace-Greece, under the supervision of Prof. Charalampos Arapatsakos.

Dr C. Arapatsakos is Professor on Democritus University of Thrace-Greece. Tel. 00302541079362, Fax. 00302541079362, email: xarapat@pme.duth.gr

solved. The geometry is divided into cells as small control volumes and the governing equations are solved for each control volume.

II. TURBULENCE

During intake of the air into the engine cylinder and also during the exhaust of the gases to the atmosphere, highly turbulent flows are developed. Also, when the mixture enters the engine cylinder, jet, swirl and tumble motions are generated[8][10].

In turbulent flows the species which constitute the fluid, follow random streamlines, creating vortices and the velocity fields are fluctuating. As a result the transported quantities such as momentum and energy fluctuate as well. The vortices created enhance the momentum exchange in all 3 directions.

These fluctuations can be of small scale and high frequency and they are highly computational expensive to be precisely simulated. A very effective way to reduce computational cost and maintain reliable and usable results is Reynolds Averaged Navier-Stokes (RANS) approach.

In this method additional terms are incorporated in the governing equations that need to be modeled in order to reach the solution. The RANS equations govern the transport of the averaged flow quantities, with the whole range of the scales of turbulence being modeled. This approach reduces the required computational effort and resources, and is effective for practical engineering applications, where there is no need of highly detailed modeling of the flow. The modified equations contain additional unknown variables, and turbulence models are needed to determine these variables. The governing equations that ANSYS code uses to compute the flow quantities are the continuity equation for the conservation of mass and the conservation of momentum. The general form of the mass conservation equation (continuity equation) is given by:

$$\frac{\partial \rho}{\partial t} + \nabla \cdot (\rho \vec{v}) = S_m$$

The source S_m is the mass added to the continuous phase from the dispersed second phase and user defined sources.

The conservation of momentum equation:

$$\frac{\partial}{\partial t}(\rho \bar{v}) + \nabla \cdot (\rho \bar{v} \bar{v}) = -\nabla p + \nabla \cdot (\bar{\tau}) + \rho \bar{g} + \bar{F}$$

Where P is the static pressure, $\bar{\tau}$ is the stress tensor, $\rho \bar{g}$ is the gravitational body forces and \bar{F} the external body forces.

As said, in turbulent flows additional terms are added to these equations. These terms are calculated by the different turbulence model techniques.

III. TURBULENCE MODELS

Many turbulence models have been developed in order to solve the RANS governing equations. At the beginning were one equation models (Spalart-Allmaras) and subsequently more effective two-equation models. No one of them, unfortunately, is widely accepted as being superior to others for all cases. The choice of turbulence model depends on considerations such as the geometry of the field, physics in the flow, the level of accuracy required, the available computational resources and the amount of time available for the simulation. Two-equation models are considered nowadays the best way to calculate the unknown variables emerging from the RANS approach. In these models the solution of two separate transport equations allows the turbulent velocity and length scales to be independently determined. Two of the most important of them are the k-ε model and the k-ω model. Later, optimized versions of these models, like RNG k-ε and Sst k-ω, were developed[2,3].

Standard k-ε model:

The standard k-ε model was proposed by Launder and Spalding. It became very popular because it provides robust results, computational economy, and acceptable accuracy for a wide range of turbulent flows.

The standard k-ε model is characterized as a semi-empirical model based on model transport equations for the turbulence kinetic energy (k) and its dissipation rate (ε). In the derivation of the k-ε model, the acceptance is that the flow is fully turbulent, and the effects of molecular viscosity are negligible. It is considered very accurate for free stream flows

Transport Equations:

The turbulence kinetic energy, k, and the dissipation rate, ε, arising from the following transport equations[1]:

$$\frac{\partial}{\partial t}(\rho k) + \frac{\partial}{\partial x_i}(\rho k u_i) = \frac{\partial}{\partial x_j} \left[\left(\mu + \frac{\mu_t}{\sigma_k} \right) \frac{\partial k}{\partial x_j} \right] + G_k + G_b - \rho \epsilon - Y_M + S_k$$

$$\frac{\partial}{\partial t}(\rho \epsilon) + \frac{\partial}{\partial x_i}(\rho \epsilon u_i) = \frac{\partial}{\partial x_j} \left[\left(\mu + \frac{\mu_t}{\sigma_\epsilon} \right) \frac{\partial \epsilon}{\partial x_j} \right] + C_{1\epsilon} \frac{\epsilon}{k} (G_k + C_{3\epsilon} G_b) - C_{2\epsilon} \rho \frac{\epsilon^2}{k} + S_\epsilon$$

where:

$$\mu_t = \rho C_\mu \frac{k^2}{\epsilon} \quad G_k = -\overline{\rho u_i' u_j'} \frac{\partial u_j}{\partial x_i}$$

$$G_b = \beta g_t \frac{\mu_t}{Pr_t} \frac{\partial T}{\partial x_i} \quad \beta = -\frac{1}{\rho} \left(\frac{\partial \rho}{\partial T} \right)_p$$

Pr_t is equal to 0,85.

$$Y_M = 2\rho \epsilon M_t^2$$

$$M_t = \sqrt{\frac{k}{a^2}}$$

Where a is the speed of sound.

$$C_{1\epsilon} = 1.44, \quad C_2 = 1.9, \quad \sigma_k = 1.0, \quad \sigma_\epsilon = 1.2$$

are constants.

RNG k-ε model:

The RNG k-ε model is identical to the Standard k-ε model but includes specific refinements. It was formed using renormalization group methods. That resulted in constants different than those in the Standard k-ε model and also additional terms and functions[1].

Transport Equations:

$$\frac{\partial}{\partial t}(\rho k) + \frac{\partial}{\partial x_i}(\rho k u_i) = \frac{\partial}{\partial x_j} \left(\alpha_k \mu_{eff} \frac{\partial k}{\partial x_j} \right) + G_k + G_b - \rho \epsilon - Y_M + S_k$$

$$\frac{\partial}{\partial t}(\rho \epsilon) + \frac{\partial}{\partial x_i}(\rho \epsilon u_i) = \frac{\partial}{\partial x_j} \left(\alpha_\epsilon \mu_{eff} \frac{\partial \epsilon}{\partial x_j} \right) + C_{1\epsilon} \frac{\epsilon}{k} (G_k + C_{3\epsilon} G_b) - C_{2\epsilon} \rho \frac{\epsilon^2}{k} - R_\epsilon + S_\epsilon$$

where:

$$C_\mu = 0.0845, \quad C_{1\epsilon} = 1.42, \quad C_{2\epsilon} = 1.68$$

$$Pr_t = 1/\alpha$$

$$\alpha_k, \quad \alpha_\epsilon$$

are the inverse effective Prandtl numbers for k and ε.

$$\left| \frac{\alpha - 1.3929}{\alpha_0 - 1.3929} \right|^{0.6321} \left| \frac{\alpha + 2.3929}{\alpha_0 + 2.3929} \right|^{0.3679} = \frac{\mu_{mol}}{\mu_{eff}}$$

$$\alpha_0 = 1.0.$$

At first it has an additional term in the ϵ equation that makes the model more efficient for strained flows. Moreover it is more accurate predicting swirling flows, as it includes the effect of swirl and it gives the user a detailed form of turbulent Prandtl numbers. Finally, the RNG k- ϵ model is more reliable at low-Reynolds number situations, because it offers an enhanced differential formula for effective viscosity. These characteristics result in more accurate and reliable results for a wider class of flows.

Standard k- ω model:

The standard k- ω model in ANSYS is based on the Wilcox model and includes modifications for low-Reynolds-number effects, compressibility, and shear flow spreading. It can estimate free shear flow spreading rates, mixing layers, different type of jets and is thus applicable to wall-bounded flows and free shear flows. The standard k- ω model is an empirical model based on model transport equations for the turbulence kinetic energy (k) and the specific dissipation rate (ω).

Transport Equations:

The turbulence kinetic energy, k, and the specific dissipation rate, ω , are arising from the following transport equations[1]:

$$\frac{\partial}{\partial t}(\rho k) + \frac{\partial}{\partial x_i}(\rho k u_i) = \frac{\partial}{\partial x_j} \left(\Gamma_k \frac{\partial k}{\partial x_j} \right) + G_k - Y_k + S_k$$

$$\frac{\partial}{\partial t}(\rho \omega) + \frac{\partial}{\partial x_i}(\rho \omega u_i) = \frac{\partial}{\partial x_j} \left(\Gamma_\omega \frac{\partial \omega}{\partial x_j} \right) + G_\omega - Y_\omega + S_\omega$$

where:

$$G_k = -\overline{\rho u'_i u'_j} \frac{\partial u_j}{\partial x_i}, \quad G_\omega = \alpha \frac{\omega}{k} G_k$$

$$\alpha = \frac{\alpha_\infty}{\alpha^*} \left(\frac{\alpha_0 + Re_t/R_\omega}{1 + Re_t/R_\omega} \right),$$

$$\alpha^* = \alpha_\infty^* \left(\frac{\alpha_0^* + Re_t/R_k}{1 + Re_t/R_k} \right)$$

$$R_\omega = 2.95,$$

$$Re_t = \frac{\rho k}{\mu \omega}$$

$$\Gamma_k = \mu + \frac{\mu_t}{\sigma_k}, \quad \Gamma_\omega = \mu + \frac{\mu_t}{\sigma_\omega}$$

$$\mu_t = \alpha^* \frac{\rho k}{\omega}$$

$$Y_k = \rho \beta^* f_{\beta^*} k \omega$$

$$f_{\beta^*} = \begin{cases} 1 & \chi_k \leq 0 \\ \frac{1+680\chi_k^2}{1+400\chi_k^2} & \chi_k > 0 \end{cases},$$

$$\chi_k \equiv \frac{1}{\omega^3} \frac{\partial k}{\partial x_j} \frac{\partial \omega}{\partial x_j} \quad \begin{matrix} R_\beta = 8 \\ \beta_\infty^* = 0.09 \end{matrix}$$

$$\beta^* = \beta_t^* [1 + \zeta^* F(M_t)]$$

$$\beta_t^* = \beta_\infty^* \left(\frac{4/15 + (Re_t/R_\beta)^4}{1 + (Re_t/R_\beta)^4} \right)$$

$$\zeta^* = 1.5$$

$$Y_\omega = \rho \beta f_\beta \omega^2$$

$$f_\beta = \frac{1 + 70\chi_\omega}{1 + 80\chi_\omega}, \quad \chi_\omega = \left| \frac{\Omega_{ij} \Omega_{jk} S_{kt}}{(\beta_\infty^* \omega)^3} \right|,$$

$$\Omega_{ij} = \frac{1}{2} \left(\frac{\partial u_i}{\partial x_j} - \frac{\partial u_j}{\partial x_i} \right)$$

$$\beta = \beta_t \left[1 - \frac{\beta_t^* \zeta^* F(M_t)}{\beta_t} \right],$$

$$\beta_t^* = \beta_\infty^* \left(\frac{4/15 + (Re_t/R_\beta)^4}{1 + (Re_t/R_\beta)^4} \right)$$

Compressibility correction:

$$F(M_t) = \begin{cases} 0 & M_t \leq M_{t0} \\ M_t^2 - M_{t0}^2 & M_t > M_{t0} \end{cases}$$

$$M_t^2 \equiv \frac{2k}{a^2}$$

$$M_{t0} = 0.25$$

$$a = \sqrt{\gamma RT}$$

$$\alpha_\infty^* = 1, \quad \alpha_\infty = 0.52, \quad \alpha_0 = \frac{1}{9}, \quad \beta_\infty^* = 0.09, \quad \beta_t = 0.072, \quad R_\beta = 8$$

$$R_k = 6, \quad R_\omega = 2.95, \quad \zeta^* = 1.5, \quad M_{t0} = 0.25, \quad \sigma_k = 2.0, \quad \sigma_\omega = 2.0$$

are constants.

σ_k and σ_ω

are the turbulent Prandtl numbers

S_k, S_ω

are user defined.

The k- ω model is considered to provide high accuracy in the near wall region and it is recommended for wall bounded flows.

Shear stress transport (SST) k- ω model:

The shear-stress transport k- ω model was developed by Menter in order to combine the accuracy of the Standard k- ω model in the near wall region with the effectiveness of the k- ϵ model in the free stream region of the flow. It is based on the Standard k- ω model including refinements[1]:

Transport equations:

$$\frac{\partial}{\partial t}(\rho k) + \frac{\partial}{\partial x_i}(\rho k u_i) = \frac{\partial}{\partial x_j} \left(\Gamma_k \frac{\partial k}{\partial x_j} \right) + \tilde{G}_k - Y_k + S_k$$

$$\frac{\partial}{\partial t}(\rho \omega) + \frac{\partial}{\partial x_i}(\rho \omega u_i) = \frac{\partial}{\partial x_i} \left(\Gamma_\omega \frac{\partial \omega}{\partial x_i} \right) + G_\omega - Y_\omega + D_\omega + S_\omega$$

where:

$$\Gamma_k = \mu + \frac{\mu_t}{\sigma_k}$$

$$\Gamma_\omega = \mu + \frac{\mu_t}{\sigma_\omega}$$

$$\mu_t = \frac{\rho k}{\omega} \frac{1}{\max \left[\frac{1}{\alpha^*}, \frac{SF_2}{a_1 \omega} \right]}$$

$$\tilde{G}_k = \min(G_k, 10\rho\beta^*k\omega)$$

$$G_\omega = \frac{\alpha}{\nu_t} \tilde{G}_k$$

$$\alpha_\infty = F_1 \alpha_{\infty,1} + (1 - F_1) \alpha_{\infty,2}$$

$$\alpha_{\infty,1} = \frac{\beta_{t,1}}{\beta_\infty^*} - \frac{\kappa^2}{\sigma_{w,1} \sqrt{\beta_\infty^*}}$$

$$\alpha_{\infty,2} = \frac{\beta_{t,2}}{\beta_\infty^*} - \frac{\kappa^2}{\sigma_{w,2} \sqrt{\beta_\infty^*}}$$

$$Y_k = \rho\beta^*k\omega$$

$$Y_\omega = \rho\beta\omega^2$$

$$\beta_t = F_1\beta_{t,1} + (1 - F_1)\beta_{t,2}$$

$$F_1 = \tanh(\Phi_1^4)$$

$$\Phi_1 = \min \left[\max \left(\frac{\sqrt{k}}{0.09\omega y}, \frac{500\mu}{\rho y^2 \omega} \right), \frac{4\rho k}{\sigma_{\omega,2} D_\omega^+ y^2} \right]$$

$$D_\omega^+ = \max \left[2\rho \frac{1}{\sigma_{\omega,2}} \frac{1}{\omega} \frac{\partial k}{\partial x_j} \frac{\partial \omega}{\partial x_j}, 10^{-10} \right]$$

$$\sigma_{k,1} = 1.176, \quad \sigma_{\omega,1} = 2.0, \quad \sigma_{k,2} = 1.0, \quad \sigma_{\omega,2} = 1.168$$

$$a_1 = 0.31, \quad \beta_{t,1} = 0.075, \quad \beta_{t,2} = 0.0828$$

are constants.

The standard k- ω model is used in the near wall region, while the Standard k- ϵ is used in the free stream. This is achieved by multiplying the model by a blending factor which takes the values “0” away from the boundary and “1” close to it. Also the SST model uses a cross diffusion derivative term in the ω equation and the constants are different. These features result in a more accurate and reliable model for more flow cases such as airfoils, shock waves etc, than the standard k- ω model.

IV. SOLUTION METHODS-RESULTS

The computational grid consists of an unstructured mesh of 1.034.000 tetrahedron and hexahedron elements. Five layer inflation was created at all boundaries. This particular grid was used because it consists of high quality elements and after evaluation it was proved to provide grid independent results.

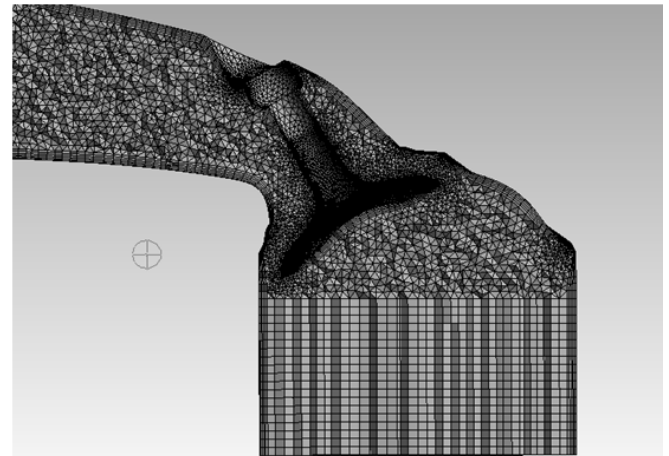


Figure 1. Section view of the computational grid

The geometry boundary conditions consist of Pressure Inlet, Walls and Pressure Outlet. Atmospheric pressure considered at the inlet and 90.000 Pascal in the cylinder. Standard wall functions were used in the k- ϵ models and compressibility effect was activated in all cases, because at certain areas (such as the valve opening region) the flow becomes compressible. COUPLED algorithm was used for pressure-velocity coupling. The COUPLED algorithm is a pressure-based solver that solves the

momentum and pressure-based continuity equations at the same time. Coupling is achieved through an implicit discretization of pressure gradient terms in the momentum equations, and an implicit discretization of the face mass flux. It is considered more effective comparing to SIMPLE or SIMPLEC solvers. Second-order upwind spatial discretization schemes were used for momentum and density, providing high accuracy.

The four different turbulence models were used in order to compute the flow quantities. Velocity streamlines, surface velocity distribution, pressure values and also velocity profile results for critical areas, such as the valve body, after valve area and runner, are demonstrated.

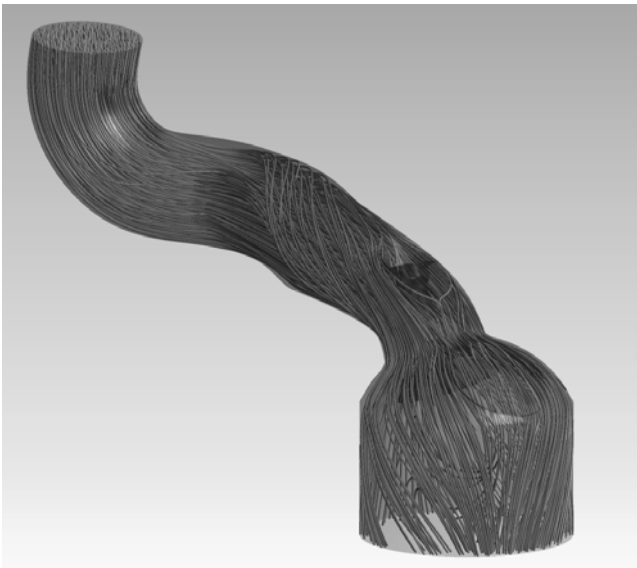


Figure 2. Flow streamlines

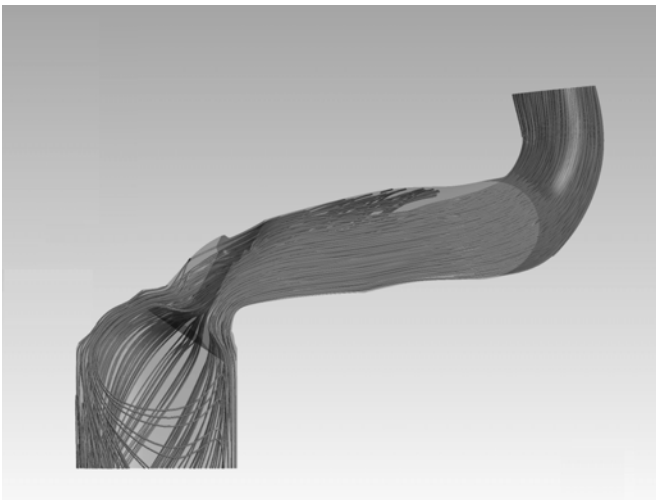


Figure 3. Section view of the velocity streamlines, tumble motion created in the cylinder

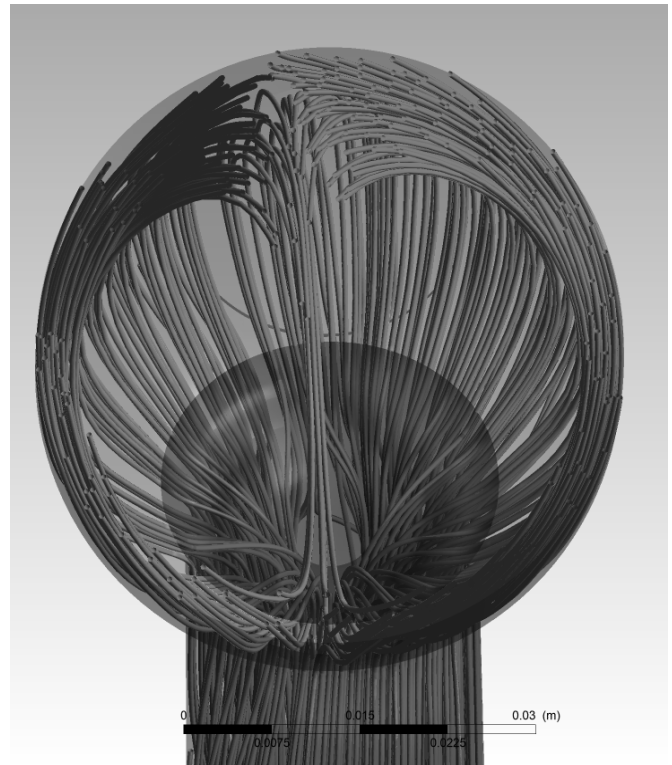


Figure 4. Bottom view of the velocity streamlines. Swirl motion created in the cylinder

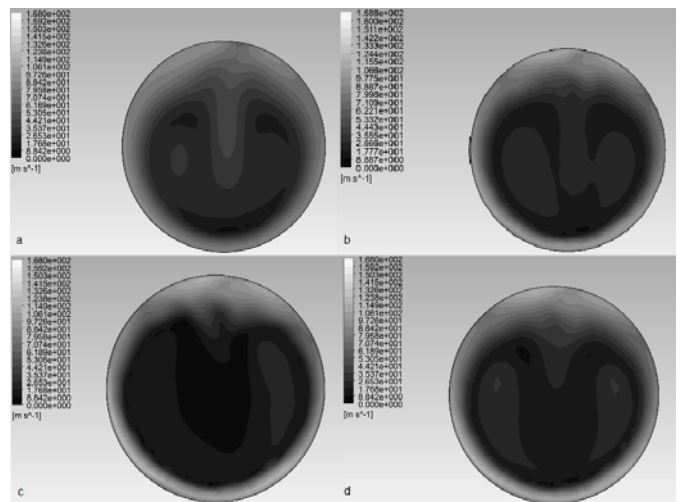


Figure 5. Top view of Velocity contours in the engine cylinder, for a) $k-\epsilon$, b) $k-\omega$, c) RNG $k-\epsilon$, d) Sst $k-\omega$.

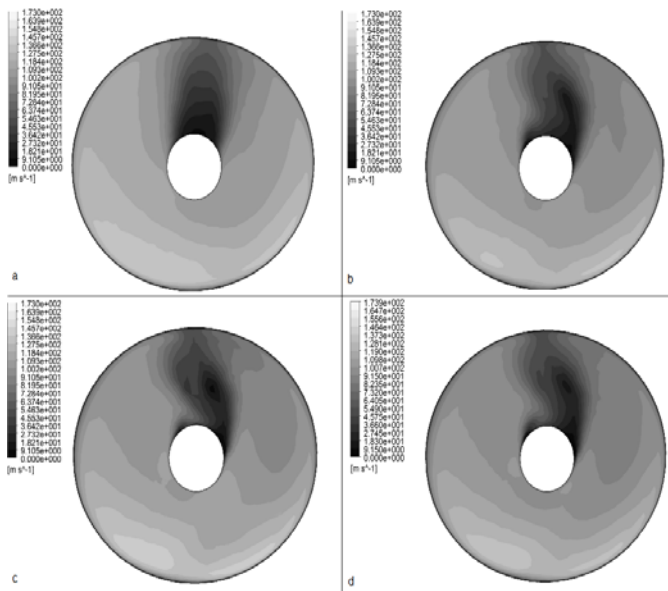


Figure 6. Top view of Velocity contours around the valve body for a) $k-\epsilon$, b) $k-\omega$, c) RNG $k-\epsilon$, d) Sst $k-\omega$

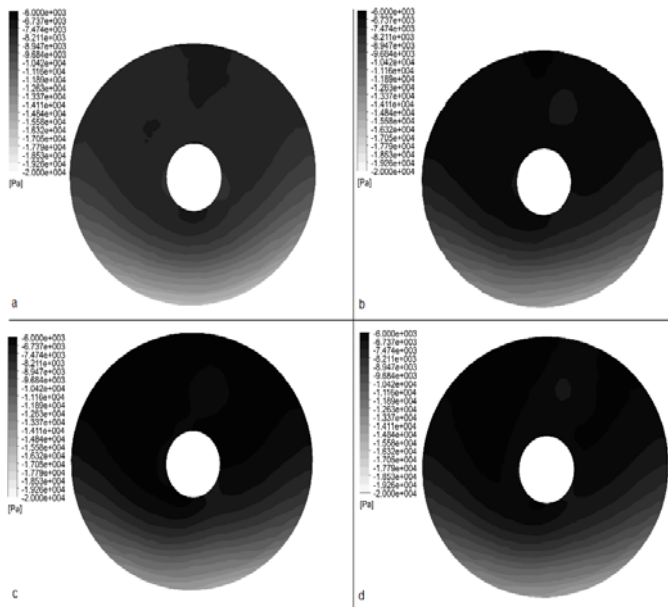


Figure 7. Top view of Pressure contours around the valve body for a) $k-\epsilon$, b) $k-\omega$, c) RNG $k-\epsilon$, d) Sst $k-\omega$ (the values are negative from the atmospheric pressure).

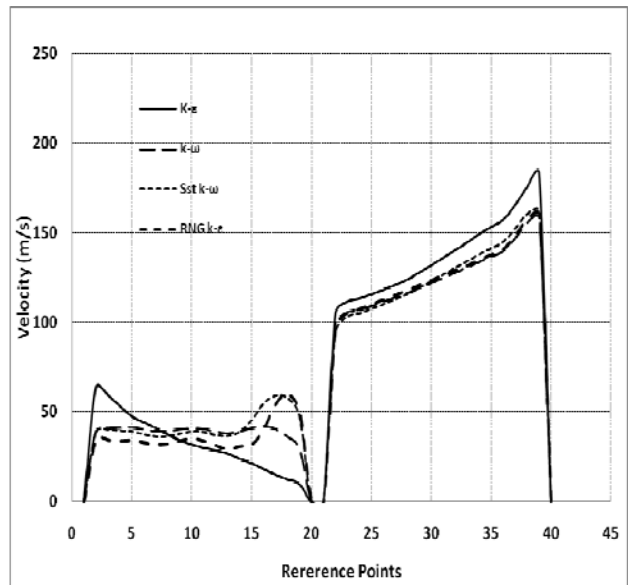


Figure 8. Velocity profiles at the valve body, for different turbulence models

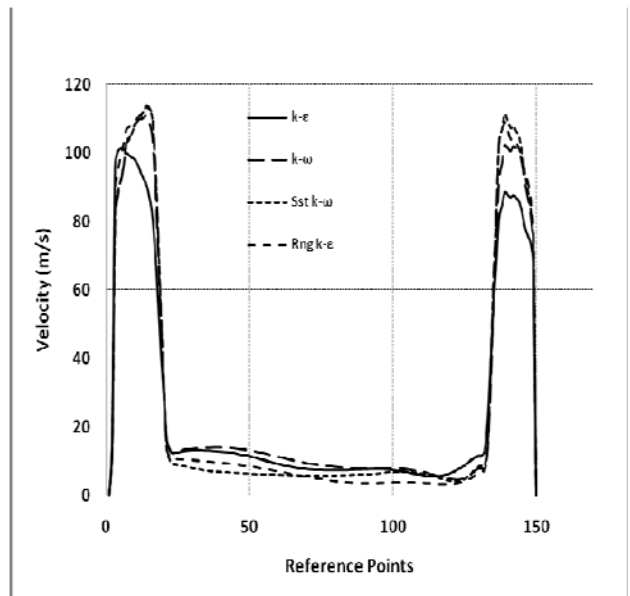


Figure 9. Velocity profiles after the valve, for different turbulence models

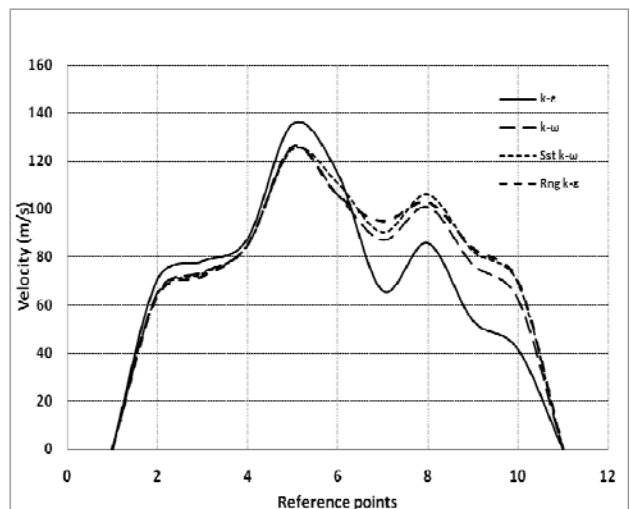


Figure 10. Velocities at the centerline of the inlet

manifold, through the valve opening and until the surface of the piston

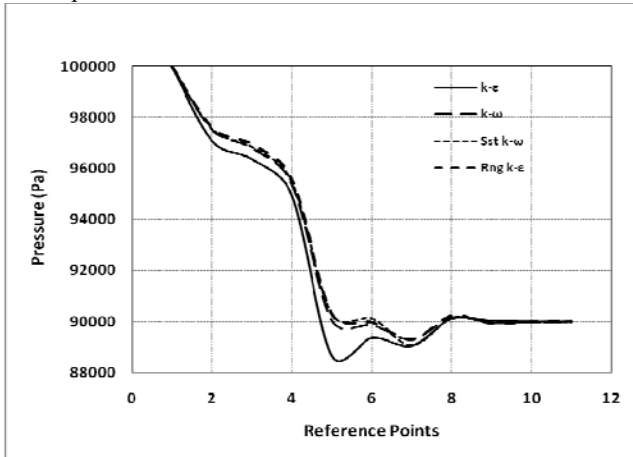


Figure 11. Pressure drop from the inlet of the manifold, through the valve opening and until the surface of the piston

V. CONCLUSION

The turbulent flow through the intake runner and inside the cylinder of a four stroke engine, two valve engine was investigated numerically using the commercial CFD code FLUENT v15.0. The RANS method was used and the performance of four different turbulence models is compared.

The turbulence models $k-\epsilon$, $k-\omega$, RNG $k-\epsilon$ and Sst $k-\omega$ provide results that have some rate of divergence between them. It is obvious that the $k-\epsilon$ model differ more than the other three. It is important to notice also that the $k-\epsilon$ model was the less computational expensive between them. The theory and factors that every model use, can guide the user to choose between them for the purpose being sought. Also the computational cost along with the accuracy searched for, could be factors of choice. The detailed evaluation of these results would be possible if experimental values had been taken and compared with these results.

REFERENCES

- [1]Ansys Fluent 12, Theory Guide. Ansys Inc. 2009
- [2]Ismail B. Celik, Introductory Turbulence Modeling, West Virginia University Mechanical & Aerospace Engineering Dept.1999
- [3]Wilcox D. C., Turbulence Modeling for CFD, DCW Industries, La Canada, California, 1998.
- [4]N. Trigui, V. Griaznov, H. Affes and D. Smith, CFD Based Shape Optimization of IC Engine, *Oil & Gas Science and Technology – Rev. IFP*, Vol. 54 (1999), No. 2, pp. 297-307.
- [5]Drie, P. and Zellat, M. (1994) Simulation of Flow Field Generated by Intake Port-Valve-Cylinder Configurations-Comparison with Measurements and Applications. *SAE, Paper No. 940521*.
- [6]Damian E. Ramajo and Norberto M. Nigro, Numerical and experimental in-cylinder flow study in 4-valve spark ignition engine, *Mecánica Computacional Vol XXVII*, pages. 181-205.
- [7]Mahrous A, Wysznski M, Xu H and Tsolakis A, A CFD Investigation into the Effects of Intake Valves Events on Airflow Characteristics in a Motored 4-Valve Engine Cylinder with Negative Valve Overlapping, *07-NAPLES-74*, 2007.

[8]Priscilla , Meena. P, A Comprehensive Study On In-Cylinder Ic Engine Due To Swirl Flow, *International Journal of Engineering Research & Technology (IJERT)*, Vol. 2 Issue 7, July – 2013, ISSN: 2278-0181.

[9]Benny Paul, V. Ganesan, Flow field development in a direct injection diesel engine with different manifolds, *International Journal of Engineering, Science and Technology* Vol. 2, No. 1, 2010.

[10]H.Sushma, Jagadeesha.K.B, CFD modeling of the in-cylinder flow in Direct-injection Diesel engine, *International Journal of Scientific and Research Publications*, Volume 3, Issue 12, December 2013 1 ISSN 2250-3153.

Implementing knowledge based PCB Design Support System

A. Pataki, G. Horváth

Abstract— Printed circuit boards (PCB) are indispensable parts of today's electronic equipments. Due to the customer demands the size of PCBs has been shrinking, while the number of components to be mounted on these boards is still increasing. Because of highly competitive environment, it is necessary to deliver products on time and within budget. In automotive industry these factors are even more in focus so, that reliability and quality are the most important project objectives. As a result of extremely high volumes (~1Mio pieces/year) the appropriate choosing of printed board technology can yield significant savings and profit caused by the cost reduction of PCB. Design engineers are forced to find an optimal solution at given constraints and within time, which satisfies all the requirements. These trends make the design and the manufacturing of PCBs even more complex and difficult. There are many different models to estimate the project complexity and board density respectively. This article gives firstly a brief summary on the versatile design objectives and trade-offs. Secondly we investigate the possibilities creating an effective PCB Design Support System (PCB-DSS). The model wants to incorporate both PCB metrics, experiences of design engineers in the past and results of simulations and tests.

Keywords—Implementing Knowledge base, Java, Printed Circuit Board complexity, statistical analysis using PCB metrics

I. INTRODUCTION

DESIGNING Electronic Control Unit (ECU) is always a very challenging task. It is especially challenging in automotive industry. The customers (for instance car manufacturers) are choosing the OEMs who are able to provide the best quality and the cheapest product, which have to comply even with the strictest standards. OEMs also have to pay attention to their internal processes. Due to the higher customer expectations, the number of functions to be integrated into an ECU is increasing while board size is shrinking. This results in more and more complex schematic circuits and denser printed board layouts. Because of the numerous requirements such as desired layout area, placement restrictions (high current or high frequency components), mechanic constraints, electromagnetic emission limits and immunity levels (commonly EMC) the routing becomes time consuming and very difficult. Unfortunately some of the rules are excluding the others making impossible the optimization of every parameter. [1] Usually a trade-off analysis is done to define which requirements are more important and which one is less, so the routing paths and topology can be accordingly prioritized. It must be investigated, whether the layout is feasible or it is possible to

reduce PCB fabrication cost by using less demanding technology. At extremely high volumes the development costs content in unit price -compared to the manufacturing costs- are very low. Every achievement for example wiring in 6 layers instead of 8 layers or replacing blind and buried vias by their through-hole counter parts causes significant unit price reduction. Unit price must cover the profit and the following main costs:

- Schematic design
- Layout design
- Mechanic design and tooling
- Design validation and simulations
- PCB Manufacturing and Assembly

These points represent different activities, most of them were earlier independent from the others, but it has changed principally. Today they are mutually influencing each other. The aspiration for reducing the overall project costs imposes the optimization at different stages.

- Schematic designers are optimizing by evaluating the different circuit solutions on the part from cost and performance. This leads to choose generally the cheaper solution, which uses discrete components instead of integrated circuits. In turn the board will be more complex.
- Layout designers are trying to minimize net lengths and use as simple structures as possible. To be competitive they must reduce the layout time too. For example an ECU with 1500-2000 parts on 4 layers without blind vias on a 160mm×160mm board takes normally 10-12 weeks. About 60% of board space is populated with high current ICs (in sum 100-200A) and conductive areas; the remaining area is used by high frequency components and sensitive analog circuits.
- Mechanic designers must simplify the construction and reduce the amount of material needed (metal or plastic case). The mechanical stability may affect the routing channels.
- Manufacturing wants to increase the productivity

It can be seen in Fig. 1 that the design process is strongly iterative. At last all the results of tests and simulations will be incorporated in the layout. The main problem is: Several parameters can be only modified at the beginning of the project. That time the mechanical construction gives the main restrictions: placement of drillings, keepout areas or height limits. Without having listed all the parameters it can be seen that finding an optimal solution so that 30-40 different types of mechanical and electrical constraints are to be taken into

A. Pataki is with the Robert BOSCH Ltd, Budapest, Hungary. E-mail: andras.pataki@hu.bosch.com.

G. Horváth is with Budapest University of Technology and Economics, Dept. of Measurement and Information systems, Budapest, Hungary. Email:horvath@mit.bme.hu.

account requires creativity and discipline. The improvement of some parameters causes the degradation of others. [1] If the assumption was wrong, it affects later the whole design.

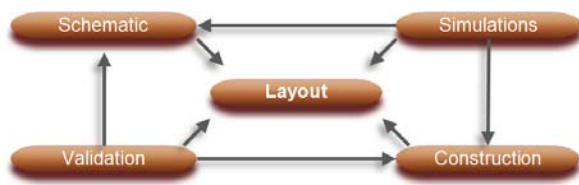


Figure 1. Relations between design processes

II. RELATED WORK

It was seen that increasing complexity makes it hard to reach the project objectives. Utilizing designer's experience along with computer aided technologies would be a powerful method in exploring the hidden difficulties and in decision making. Keeping in mind that there is no perfect solution just an optimal one, the following questions are to be answered:

- How can be determined the appropriate PCB technology?
- Is the PCB routable?
- If not, which constraints are to be changed?
- How much time is needed for routing?
- Is it possible to generate design rules automatically based on project priorities (EMC, Thermo, High Current etc.)?

To answer the questions the following topics must be examined: data mining techniques, autorouting, wire length prediction and layout effort analyze or PCB fabrication cost estimation respectively. In our work we are focusing on PCB design, so PCB assembly is out of scope. We mention that during the component placement the goal is to minimize the total movement path of the head of SMT machine to increase the productivity. Among the different concepts genetic algorithms offer an effective solution to this problem. [2], [3] PCB fabrication costs are determined by the technology and the fabrication yield. In [5] an activity based cost estimation model (ABC) is described. It takes into account each individual factor (board shape, material costs, added materials, tool costs) that are driving the fabrication costs. Our aim is to integrate this approach later into the model.

In practice PCB complexity estimation was done as follows:

- Experienced designers get a feel for layout feasibility; a more experienced designer can help obviously more than a less experienced one.
- Autorouting the board is also an alternative to check the layout concept. The settings of autorouter basically determine the routing efficiency. [10] If the router completes at least 80-90% of the routes with no tweaking, it is a sign that the selected placement and stack-up is routable. There may be a number of reasons why a board will not be routed to completion. Poor placement is often the cause.
- Placement study: placing all the components to the board to see if enough space remains for the routing.

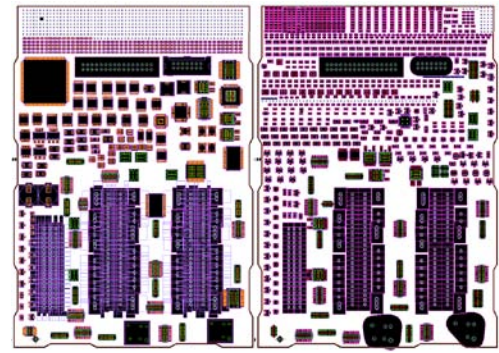


Figure 2. Placement study of a new design

These methods are heuristic and have their limits: The success of estimation depends on the designer's experience. Autorouting is time consuming and the result represents always one scenario and because of variety of products it is almost impossible to define a uniform rule base for it. The human factor is in turn very important in routing automotive mixed signal circuits. Analytic approaches are also known. The two main groups are: qualitative and quantitative. [4], [6], [7], [8]. These groups can be further divided into subgroups. Qualitative approach says that the similarities between the new project data and the existing experience in the past give the basics of prediction of layout design time, PCB cost or design complexity. Niazi et al. compare, classify and discuss the different models in [4]. It is common to all the approaches that they create design metrics, try to find similarities between recent project data and historic designs. They give some details on regression analysis, which assumes linear relationship. Back-Propagation neural networks (BPNN) on the other hand can be used to overcome the disadvantages of regression analysis. These methods are analogical. Intuitive methods like expert systems, fuzzy systems are trying to store the knowledge of expert in form of rule bases. On the other hand qualitative methods like analytical cost estimation techniques are keeping in focus that both design process and manufacturing are made of different activities. The previously mentioned ABC method belongs to this group. In [6] Kastner et al. set up a model which takes into account the number of components and connection and the technology parameters. This capacity-demand method then predicts if the layout is feasible. Their approach is more likely a statistic based one, but unfortunately there is no information in the article which model has been used. It must be a trade secret. Bazeghi et al. in their paper [8] explain an extended version of a statistical model. Kwon et al. are using data mining techniques in [7]. An adaptive support vector regression (ASVR) was applied. Bashir and Thomson are using parametric effort estimation model. [9] Wire length prediction is also an interesting approach that focuses on post placement and pre routing analysis. In [17] statistical modeling has been applied for the characterization of nets and designs.

III. PCB DESIGN PROCESS

Before extracting the concept let us take a look at the design processes. There are many different models. Which one is used depends on the project and market. Some companies are proposing virtual prototyping. [15] In many cases the project scheduling does not allow that. Others suggest the use of

around-the-clock or around-the-world design schedule. [11] These models have advantages but limitations as well. The design process in the automotive industry is often a multi-location development, but according the high complexity it is iterative. Furthermore, it is a development partnership between the customer and the OEM from the beginning of the project.

IV. EXPERIMENTAL RESULTS AND THEIR LIMITATIONS

The technology rules are based on the minimum pitch of the SMT components employed. Technology of 0.1/0.1 mm (trace/clearance) and vias of 0.5/0.2mm (pad/hole) are generally required for complex high speed design incorporating ball grid arrays (BGA). To get an insight how complex a project can be, we have firstly interviewed our layout team. They had to classify every objective of several projects in the past from 1 to 5. (1: easy to fulfill, 2: moderate difficult, 3: difficult, 4: very difficult, 5: extreme difficult) The textural comments like on design problems were also taken into account. (TABLE I) Although [9] proposes a scale of 1, 2 and 3 for functional complexity we are convinced that according to the experience of design engineer in our case better is. It was recognized for example at BCM1_4 and BCM2_4 that the schematics were 80% identical, the changing of connector concept (Mechanic) by the customer has significantly made difficult to meet the other objectives. MCU1_4, MCU2_6 and MCU3_8 are showing that the construction of schematic along with routing area (using BGA footprint instead of TQFP or disadvantageous pin outs at high lead count ICs, high limits on the PCB) may also affect the feasibility of the PCB. The total number of layers required for a given design is partly dependent on the complexity of the design. Factors include: the number of signal nets that must break out from a BGA; the number of

power supplies required by the BGA's; component density and package types. However, using of less demanding dimensions will reduce cost and improve the fabrication yield. DCD1_4 and PPC1_6 are differing from the other projects while the others (BCM and MCU etc.) must control 50-60 different functions; they are special DCDC converters. The mechanical constrains are not so complex. The thermal and layout requirements due to the high currents (100-1000A) cause very complex layout. Some basic PCB Metrics were derived in TABLE II to extract additional relationships. This approach has an assumption that the PCB is homogenous. Real projects consist of analog, digital, high frequency and high current circuits, which results in inhomogeneous layout. These have led us to the decision that we shall to cluster the projects according their electric and other properties to predict difficulties during the design phase. We must generate location dependent metrics for better understanding.

TABLE I. SUBJECTIVE COMPLEXITY OF SOME PROJECTS

#Layers	Project	Subjective complexity				
		EMC	High-Currents	Thermal	Mech	Sch.
4	BCM1_4	2	3	2	3	4
4	BCM2_4	3	4	3	5	4
4	MCU1_4	3	2	2	2	3
6	MCU2_6	3	2	2	2	3
8	MCU3_8	3	2	2	5	5
6	PCU1_6	3	5	5	3	2
4	DCD1_4	3	4	5	2	2
4	PPC1_4	4	1	1	2	2

TABLE II. PCB METRICS OF DIFFERENT PROJECTS

	BCM1_4	BCM2_4	PCU1_6	MCU2_6	MCU3_8	MCU1_4	DCD1_4	PPC1_4
Width[mm]×Height[mm]	175×134	175×134	200×177	200×190	164×87	164×132	140×110	156×64
Area[cm ²]	234,5	234,5	354	380	142,68	216,48	154	99,84
#TRACKS	12295	17998	10296	19725	10311	10576	2914	1312
#PADS	5990	5612	5315	10241	7759	10228	5365	2573
#VIAS	2330	2865	2850	4437	1755	2321	556	315
Vias/cm ²	9,9	12,2	8,1	11,7	12,3	10,7	3,6	3,2
Components/cm ²	2,3	3,3	1,3	2,4	3,7	3,1	1,1	0,9
Pins/cm ²	6,5	8,7	3,1	5,9	9,5	7,0	2,9	2,3
Testpoints/cm ²	1,3	1,7	0,6	0,9	1,3	1,2	0,6	0,4
Pads/cm ²	12,8	12,0	7,5	13,5	27,2	23,6	17,4	12,9
Tracks/cm ² layer	13,1	19,2	7,3	13,0	18,1	12,2	4,7	3,3

V. DENSITY MAPS AND DETECTING ROUTING CHANNELS

Via density maps were generated with 10mm×10mm moving window with an offset of 0.25mm. In Figure 3 at the right side the critical regions were marked with red. Figure 4 shows a little bit more: the vias and the routing channels together. There are many other types of maps (Trace direction change density, wiring capacity). It would be interesting to know which patterns can be detected most frequently.

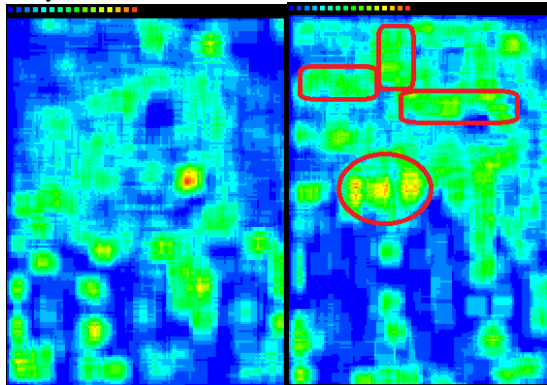


Figure 3. 2D View of Via density of BCM2_4 project

Recognizing regular geometries is always a hint that either the designer had to implement something special or this object is probably a footprint which can not be modified. Then partitioning to sub modules as design template would be also possible.

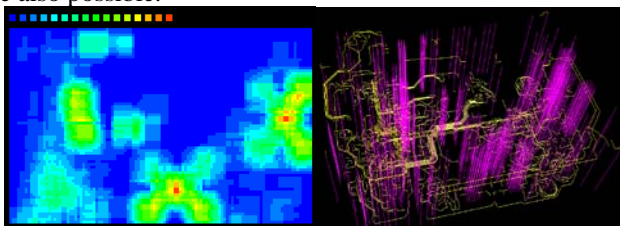


Figure 4. 2D and 3D Views of Via density of DCD1_4 project

VI. PROCESSING THE NETLIST

Previously we have analyzed several PCBs in the past and evaluated the experience of designers. Analyzing the schematic (netlist) based on its electrical modules would be a powerful method to find further similarities between projects:

- Identifying known schematic modules (CAN, LIN, Flexray, Ethernet, DCDC converter, analog peripherals)
- Identifying graph structures

An essential part is the netlist parser. The software must be able to detect supply and ground nets. This can be easily done since normally the supply nets have the most nodes. On the other hand every net with high node count can be handled like the GND and supply nets, routing them in a dedicated layer if it is allowed. After having detected they will be removed from graph. The next step is to remove test points from the remaining graph. Layout data may be processed so,

and then we can compare the different projects with each other. There are building blocks like low pass filter and high pass filter which are identical from view of routing complexity. Figure 5 shows a node-net distribution. Y-axis represents the different nets while x-axis the corresponding number of nodes. We found that GND and VCC have the most nodes. Care must be taken to handle this, since the high number just indicates the possibility of supply net. Additional methods are required to validate it. [16]

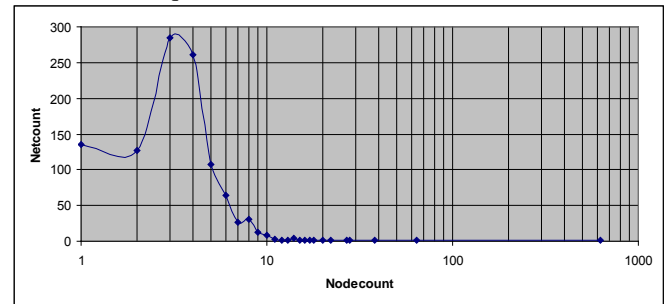


Figure 5. Distribution of different nets

VII. IMPLEMENTING THE KNOWLEDGEBASE

There are many articles dealing with project complexity, layout feasibility and design time but a combined method which incorporates all the advantages of these models is needed. We found that the fuzzy relationships between PCB metrics of different projects making necessary the use of a multi criterion design support system (DSS). It means that the user can define the project objectives then the software seeks similarities and tries to estimate the layout performance. This model should be modular to improve the accuracy of the estimation according to the achievements in the future.

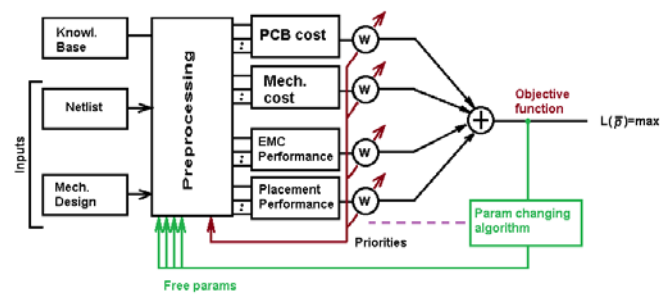


Figure 6. Concept of PCB-DSS

Figure 7 shows that diverse competences are distributed over many countries at multinational corporations. We had to analyze how could be possible to collect data from many different locations. It is very complicated to unify the versatile data into one knowledge base without distributed systems. We implemented a multi agent concept which utilizing the advantages parallel computing. So it will not be necessary to poll the sources whether new raw data are ready. The agents are software acting autonomously whenever new information is to be transferred into the central knowledgebase. So the results of design validation (results of EMC, environment tests, mechanical tests etc.) will be uploaded as they are ready.

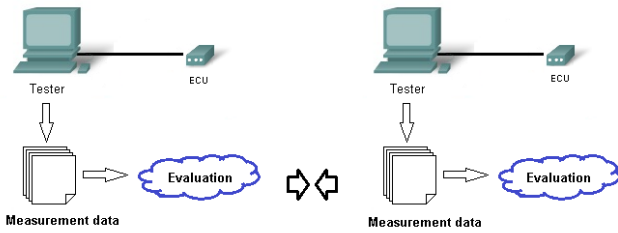


Figure 7. Distributed tests and simulations over multiple locations

For the central software the JAVA technology was chosen since it is suitable for internet based distributed systems. It can be integrated with MYSQL database over JDBC. It has also Remote Method Invocation (RMI) interface and is a powerful tool for visualizing in 3D. For data mining MAHUT from APACHE was chosen. With a little programming effort high quality graphic views can be achieved. We have developed an SQL based application to store data effectively. The database in Figure 9 has already been implemented and is being used to collect and analyze data during the EMC tests.

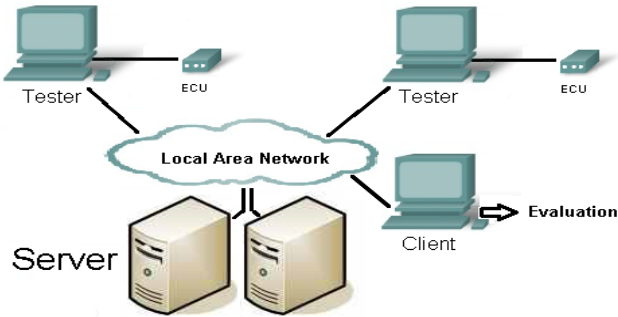


Figure 8. Construction of the knowledgebase

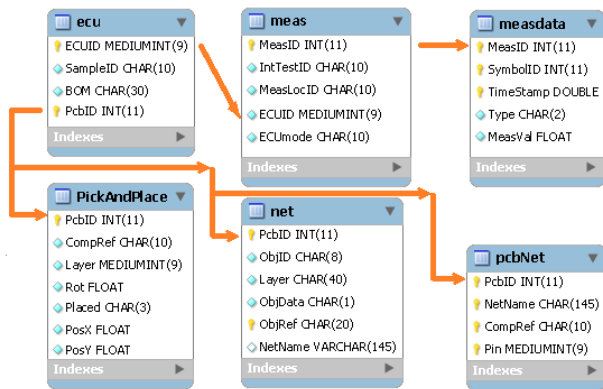


Figure 9. Structure of the relational database

VIII. PROCESSING MEASUREMENTS

During the validation the signals will be exposed to electromagnetic disturbance. To verify that no function is affected by EM-field many parameter will be monitored. It can be done since the ECU software has a diagnostic module. In turn there will be eventually more than 200 internal variables sampled. This time the EMC module is ready to be

used. It has already proved to be very useful. During the EMC tests a huge amount of data are arising, which can be filtered by the application. The filters are capable to classify results of ECU intern variables. Each periphery has a current sense output, which sampled regularly by the microcontroller’s ADC. Some of the signals will be filtered others will not. The preprocessed values are stored in the RAM and are accessible over a CAN (Controlled Area Network) diagnostic protocol. Our aim is to find correlation between particular layout structures and EMC patterns.

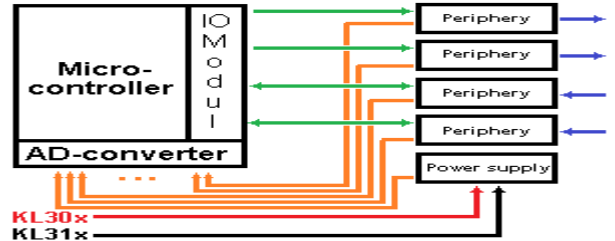


Figure 10. Concept of selfdiagnostic

The testing effort proportional increases with the customer requirements. TABLE III shows the amount of measurement results which have to be processed to find the relevant data. The following equation helps to determine the amount of data

$$DM \approx \sum_i \sum_j^{Number\ of\ Variable\ i} Variable_{ij} * Samplerate_{ij} \tag{1}$$

TABLE III. COMPARISON OF DATA AMOUNT OF DIFFERENT TESTS

Test	Number of records [Millions]	HDD-demand	Number of tests
EMC	~50	1.2GB	~400
Endurance	~500	12GB	~500
Electrical Test	~100	2.5GB	~600

The graphical user interface can be seen below. It is multi-purpose software and can be configured according project requirements. Until the new modules are integrated, its main task is to parse EMC results and to create test reports automatically.



Figure 11. Graphical user interface

IX. SOME REAL EMC PROBLEMS IN THE PAST

Figure 12 shows an EMC issue in the range of [100MHz-150MHz]. This occurs at bulk current injection (BCI) test. (The detailed description of this method exceeds the possibilities of this paper.) The ECU harness is exposed to high frequency disturbances by an inductive coupling clamp. The HF currents are trying to find a return path causing potential shift on the PCB. It was found that too high via density along with HF currents cause significant local ground shift. This eventually results in erroneous operation, since the ADC measures a corrupted current. The root cause was identified and the layout revised. The following diagram shows a high frequency decoupling problem. The third example shows the problematic frequencies at emission measurements. Peaks at 375 kHz, 700 kHz and 1.1 MHz were caused by the DCDC converter circuit of BCM2_4 project and the layout at that point has also been revised.

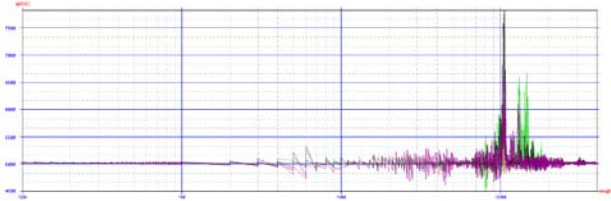


Figure 12. Visualization of an immunity problem

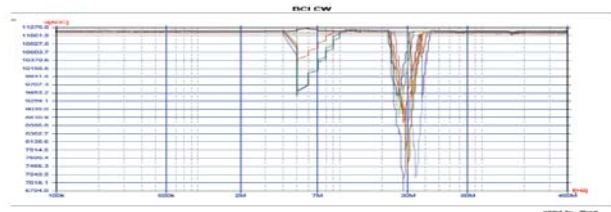


Figure 13. Visualization of an immunity problem

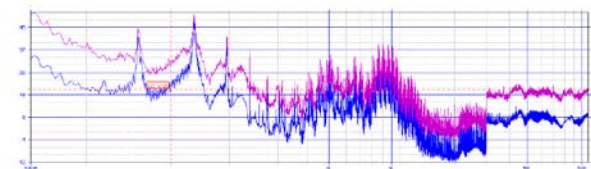


Figure 14. Visualization of an emission problem by a DCDC converter

X. CONCLUSION

This paper was dealing with the aspects of the complexity analysis of printed circuit boards. There are different methods which are capable to estimate some aspect of a new design using design metrics. Software was developed. It makes possible the excessive analysis and mining of PCB related data. We proposed that the results of tests and simulation are also taken into account. Some examples were shown to highlight the problems of highly complex mechanic design and EMC issues.

The topic was divided into four sections:

- Manufacturer's and printed board technology features must be identified

- Based on priorities and preliminary netlist information tried to find similarities and predicting how complex the layout would be.
- By post processing the layout we would like to collect experience related to that what in the past good or wrong was.
- The test results can be used as objective functions

The potential design risks can be estimated by trying to find similarities between knowledge and schematic. Artificial intelligence based methods are being tested to extract useful information. We are convinced that this approach helps to exploit better out PCB technology.

REFERENCES

- [1] IPC-2226 "Design Standard for High Density Interconnect (HDI) Printed Boards" 10-2000, pp. 6-9.
- [2] C. S. Hardas, T. L. Doolen, D. H. Jensen, "Development of a genetic algorithm for component placement sequence optimization in printed circuit board assembly" *Computers & Industrial Engineering*, Jan. 2008, pp. 165-182
- [3] L. P. Khoo, T. K. Ng, "A genetic algorithm-based planning system for PCB component placement" *International Journal of Production Economics*, Vol. 54, Jan. 1998, pp. 321-332
- [4] A. Niazi, J. S. Dai, S. Balabani, L. Seneviratne "Product Cost Estimation: Technique Classification and Methodology Review" *Journal of Manufacturing Science and Engineering*, Vol. 128, May 2006, pp. 563-575
- [5] R. E. Giachetti, J. Arango, "A Design-Centric Activity-Based Cost Estimation Model for PCB Fabrication" *Concurrent Engineering*, Nov. 2003, <http://cer.sagepub.com/cgi/content/abstract/11/2/139>
- [6] R. Kastner, E. Moshe, "Predictability for PCB Layout Density" <http://www.ipcoutcome.org/mart/49710.shtml>, Apr. 2012
- [7] Y. Kwon, O. A. Omitaomu, G. N. Wang, "Data mining approaches for modeling complex electronic circuit design activities" *Computers & Industrial Engineering*, Vol. 54, July. 2007, pp. 229-241
- [8] C. Bazeghi, J. Renau, "Printed Circuit Board Time Estimation" *Workshop on Complexity-Effective Design*, June. 2006, pp. 4-10
- [9] H. A. Bashir, V. Thomson, "Estimating Design Complexity" *Journal of Engineering Design*, Vol. 10, 1999, pp. 247-257
- [10] T. Yan, M. D. F. Wong, "Recent Research Development in PCB Layout" *International Conference on Computer-Aided Design (ICCAD)*, Nov. 2010, pp. 398-403
- [11] J. Isaac, D. Wiens, "The Future of PCB Design" Mentor Graphics Co. pp. 6-7.
- [12] S. Gupta, "Innovations in EM Simulation for High Speed Digital Design" Agilent Technologies
- [13] H. Holden, "The HDI Handbook" BR Publishing, Inc., 2009, ch. 3.
- [14] IPC-2226 "Design Standard for High Density Interconnect (HDI) Printed Boards" 10-2000, pp. 20-21.
- [15] C. Gozzi, "EMI-EMC Analysis and Noise Reduction on Printed Circuit Board" ANSOFT corporation
- [16] A. Rajaraman, J. Leskovec, J. D. Ullman, "Mining of Massive Datasets", Cambridge University Press, 2012, pp. 71-125.
- [17] J.L. Wong, A. Davoodi, V. Khandelwal, A. Srivastava, M. Potkonjak, "A Statistical Methodology for Wire-Length Prediction", *IEEE Transactions on Computer-Aided Design of Integrated Circuits and Systems*, Vol. 25, NO. 7, pp. 1327-1336, July 2006

Stability Analysis of Nonparallel Unsteady Flows by a Symmetry-Based Method

GEORGY I. BURDE¹, ILDAR SH. NASIBULLAYEV^{1,2} and ALEXANDER ZHALIJ³

¹ Jacob Blaustein Institute for Desert Research, Ben-Gurion University,
Sede-Boker Campus, 84990, ISRAEL

² Ufa State Aviation Technical University, 12, K.Marx str, Ufa, 450000, RUSSIA

³ Institute of Mathematics of the Academy of Sciences of Ukraine,
Tereshchenkivska Street 3, 01601 Kyiv-4, UKRAINE

Abstract: -

The problem of variables separation in the linear stability equations, which govern the disturbance behavior in viscous incompressible fluid flows, is treated using a symmetry-based approach. In the symmetry approach to the separations of variables in linear PDEs, a possibility of variable separation in a given PDE is intimately related to its symmetry properties. In the so-called direct approach to separation of variables in linear PDEs, which formalizes the main features of the symmetry approach, a form of the 'ansatz' for a solution with separated variables as well as a form of reduced ODEs, that should be obtained as a result of the variable separation, are postulated from the beginning. In the present study, such a direct approach is applied to the equations of the linear stability theory. The results of application of the method are the new coordinate systems and the most general forms of basic flows, which permit the postulated form of separation of variables. Thus, the stability analysis of nonparallel unsteady flows is reduced to the eigenvalue problems of ordinary differential equations. This method involves very complicated analytical calculations which can be implemented only using symbolic manipulating programs. The resulting eigenvalue problems are solved numerically with the help of the spectral collocation method based on Chebyshev polynomials. For some classes of perturbations, the eigenvalue problems can be solved analytically. Those unique examples of exact (explicit) solution of the nonparallel unsteady flow stability problems provide a very useful test for numerical methods of solution of eigenvalue problems, and for methods used in the hydrodynamic stability theory, in general.

Key- Words: - hydrodynamic stability, separation of variables, nonparallel flows, direct method, symbolic manipulating programs, spectral collocation method

1 Introduction

Problems of hydrodynamic stability are of great theoretical and practical interest, as evidenced by the number of publications devoted to this subject. The linear stability theory (see, e.g., [1]) for a particular flow starts with a solution of the equations of motion representing this basic flow. One then considers this solution with a small perturbation superimposed. Substituting the perturbed solution into the equations of motion and neglecting all terms that involve the square of the perturbation amplitude yield the linear stability equations which govern the behavior of the perturbation. The linearization provides a means of allowing for the many different forms that the disturbance can take. In the method of normal modes, small disturbances are resolved into modes, which may be treated separately because each satisfies the linear equations and there are no interactions between different modes.

Thus, the mathematical problem of the determination of stability of a given flow involves

deriving a set of perturbation equations obtained from the Navier-Stokes equations by linearization around this basic flow and finding a set of possible solutions which would permit splitting a perturbation into normal modes. For a steady-state basic flow, normal modes depending on time exponentially, with a complex exponent λ , are permissible - the sign of the real part of λ indicates whether the disturbance grows or decays in time. If further separation of variables is possible, it makes the stability problem amenable to the normal mode analysis in its common form when the problem reduces to that of solving a set of ordinary differential equations. It can be done, however, only for basic flows of specific forms - mostly those are the parallel flows or their axial symmetric counterparts.

For nonparallel basic flows, when the coefficients in the equations for disturbance flow are dependent not only on the normal to the flow coordinate but also on the other coordinates, the corresponding operator does not separate unless certain terms are ignored. If, in addition, the

basic flow is non-steady, this brings about great difficulties in theoretical studies of the instability since the normal modes containing an exponential time factor $\exp(\lambda t)$ are not applicable here. Therefore stability of viscous incompressible flows developing both in space and time is a little studied topic in the theory of hydrodynamic stability.

All the above said shows that the method of separation of variables is of a fundamental importance for the hydrodynamic stability problems. Till now, the method of separation of variables has been used for stability analysis in an intuitive way which makes it generally applicable only to the stability problems of the steady-state parallel flows.

Recently, the so-called direct approach to separation of variables in linear PDEs has been developed by a proper formalizing the features of the notion of separation of variables (see, e.g., [2], [3]). This method involves very complicated analytical calculations which can be implemented only using symbolic manipulating programs. Till recently, computer capabilities were insufficient to apply this method to such complicated systems as linear stability equations – only single equations of mathematical physics have been treated. The first attempt of applying this method to the linear stability problem has been done in Ref. [4]. The success has been achieved not only due to the increase of computer capability but also at the expense of modifying the method based on physics of the problem. Solutions obtained has been used in Ref. [5] to implement the stability analysis of some viscous incompressible unsteady nonparallel flows, exact solutions of the continuity and Navier-Stokes equations in cylindrical coordinates.

In this paper, we present both some earlier results and the results obtained by further development of the stability analysis based on separation of variables in the linearized equations for the flow perturbations. Stability analysis of the three-dimensional unsteady nonparallel flows includes two stages. First, analytical calculations using the symbolic manipulating *Mathematica* package are made to determine classes of separable solutions for basic flows and separable solutions of the equations for perturbations – both in Cartesian and cylindrical coordinates. Next, the ODE eigenvalue problems to which the original stability problems reduce via separation of variables are solved numerically with the help of the spectral collocation method based on Chebyshev polynomials. The results obtained show dependence of the flow stability properties on the perturbation

wave numbers and parameters of the problems. This includes neutral curves, perturbation spectra, unstable perturbation modes and others.

In some cases, the eigenvalue problems can be solved analytically. Those unique examples of exact (even explicit) solution of the nonparallel unsteady flow stability problems provide a very useful test for numerical methods of solution of eigenvalue problems, and for methods used in the hydrodynamic stability theory, in general.

2 Variable separation using the direct method

2.1 Formulation

The Navier-Stokes equations governing flows of incompressible Newtonian fluids are

$$\frac{\partial \hat{\mathbf{v}}}{\partial t} + (\hat{\mathbf{v}} \nabla) \hat{\mathbf{v}} = -\frac{1}{\rho} \nabla \hat{p} + \nu \nabla^2 \hat{\mathbf{v}} \text{ and } \nabla \hat{\mathbf{v}} = 0, \quad (1)$$

where ρ is the constant density and ν is the constant kinematic viscosity of the fluid.

As usual in stability analysis, we split the velocity and pressure fields $(\hat{v}_x, \hat{v}_y, \hat{v}_z, \hat{p})$ into two problems: the basic flow problem (V_x, V_y, V_z, P) and a perturbation one (v_x, v_y, v_z, p) ,

$$\hat{v}_x = V_x + v_x, \quad \hat{v}_y = V_y + v_y, \quad \hat{v}_z = V_z + v_z, \quad \hat{p} = P + p \quad (2)$$

Introducing (2) into the Navier-Stokes equations (1) and neglecting all terms that involve the square of the perturbation amplitude, while imposing the requirement that the basic flow variables (V_x, V_y, V_z, P) themselves satisfy the Navier-Stokes equations, one arrives at the following set of linear stability equations in the Cartesian coordinates:

$$\begin{aligned} \frac{\partial v_x}{\partial t} + V_x \frac{\partial v_x}{\partial x} + v_x \frac{\partial V_x}{\partial x} + V_y \frac{\partial v_x}{\partial y} + v_y \frac{\partial V_x}{\partial y} + V_z \frac{\partial v_x}{\partial z} + \\ v_z \frac{\partial V_x}{\partial z} = -\frac{1}{\rho} \frac{\partial p}{\partial x} + \nu \left(\frac{\partial^2 v_x}{\partial x^2} + \frac{\partial^2 v_x}{\partial y^2} + \frac{\partial^2 v_x}{\partial z^2} \right), \\ \frac{\partial v_y}{\partial t} + V_x \frac{\partial v_y}{\partial x} + v_x \frac{\partial V_y}{\partial x} + V_y \frac{\partial v_y}{\partial y} + v_y \frac{\partial V_y}{\partial y} + V_z \frac{\partial v_y}{\partial z} + \\ v_z \frac{\partial V_y}{\partial z} = -\frac{1}{\rho} \frac{\partial p}{\partial y} + \nu \left(\frac{\partial^2 v_y}{\partial x^2} + \frac{\partial^2 v_y}{\partial y^2} + \frac{\partial^2 v_y}{\partial z^2} \right), \\ \frac{\partial v_z}{\partial t} + V_x \frac{\partial v_z}{\partial x} + v_x \frac{\partial V_z}{\partial x} + V_y \frac{\partial v_z}{\partial y} + v_y \frac{\partial V_z}{\partial y} + V_z \frac{\partial v_z}{\partial z} + \\ v_z \frac{\partial V_z}{\partial z} = -\frac{1}{\rho} \frac{\partial p}{\partial z} + \nu \left(\frac{\partial^2 v_z}{\partial x^2} + \frac{\partial^2 v_z}{\partial y^2} + \frac{\partial^2 v_z}{\partial z^2} \right), \\ \frac{\partial v_x}{\partial x} + \frac{\partial v_y}{\partial y} + \frac{\partial v_z}{\partial z} = 0, \end{aligned} \quad (3)$$

2.2 Outline of the direct method

Let us introduce a new coordinate system t , $\xi = \xi(t, x)$, $\eta = \eta(t, y)$, $\gamma = \gamma(t, z)$

We choose the Ansatz for a solution $\mathbf{u} = (v_x, v_y, v_z)$ and p to be found

$$\begin{aligned} \mathbf{u} &= T(t) \exp(a\xi + s\gamma + mS(t))\mathbf{f}(\eta), \\ p &= T_1(t) \exp(a\xi + s\gamma + mS(t))k(\eta) \end{aligned} \quad (4)$$

where $\mathbf{f} = (h, f, g)$ and functions $T(t)$, $T_1(t)$, $S(t)$, $\xi(t, x)$, $\eta(t, y)$, $\gamma(t, z)$ are not fixed *a priori* but chosen in such a way that inserting the expressions (4) into system of PDEs (3) yields a system of three second-order and one first order ordinary differential equations for four functions $h(\eta)$, $f(\eta)$, $g(\eta)$, $k(\eta)$. To get constraints on functions T , T_1 , S , ξ , η , γ we formalize a reduction procedure as follows.

First, we postulate the form of the resulting system of ordinary differential equations as follows

$$\begin{aligned} h''(\eta) &= U_{11}g'(\eta) + U_{12}h'(\eta) + U_{13}k'(\eta) + \\ &U_{14}f(\eta) + U_{15}g(\eta) + U_{16}h(\eta) + U_{17}k(\eta), \\ f''(\eta) &= U_{21}g'(\eta) + U_{22}h'(\eta) + U_{23}k'(\eta) + \\ &U_{24}f(\eta) + U_{25}g(\eta) + U_{26}h(\eta) + U_{27}k(\eta), \\ g''(\eta) &= U_{31}g'(\eta) + U_{32}h'(\eta) + U_{33}k'(\eta) + \\ &+ U_{34}f(\eta) + U_{35}g(\eta) + U_{36}h(\eta) + U_{37}k(\eta), \\ f'(\eta) &= U_{41}f(\eta) + U_{42}g(\eta) + U_{43}h(\eta) + U_{44}k(\eta). \end{aligned} \quad (5)$$

Here U_{ij} are second order polynomials with respect to spectral parameters a, s, m with coefficients, which are some smooth functions on η and should be determined on the next steps of the algorithm. Next, we insert the expressions (4) into (3) which yields a system of PDEs containing the functions ξ, η, γ and their first- and second-order partial derivatives, and the functions $f(\eta)$, $g(\eta)$, $k(\eta)$ and their derivatives. Further we replace the derivatives $h''(\eta)$, $f''(\eta)$, $g''(\eta)$, $f'(\eta)$ by the corresponding expressions from the right-hand sides of (5).

Now we regard $h'(\eta)$, $g'(\eta)$, $k'(\eta)$, $h(\eta)$, $f(\eta)$, $g(\eta)$, $k(\eta)$ as the new independent variables. As the functions $\xi(x, t)$, $\eta(y, t)$, $\gamma(z, t)$, $T(t)$, $T_1(t)$, $S(t)$, basic flows V_x, V_y, V_z and coefficients of the polynomials U_{ij} (which are functions of η) are independent on these variables, we can require that the obtained equality is transformed into identity under arbitrary $h'(\eta)$, $g'(\eta)$, $k'(\eta)$, $h(\eta)$, $f(\eta)$, $g(\eta)$, $k(\eta)$. In other words, we should split the equality with respect to these variables. After splitting we get an overdetermined system of nonlinear partial differential equations for unknown

functions $\xi(x, t)$, $\eta(y, t)$, $\gamma(z, t)$, $T(t)$, $T_1(t)$, $S(t)$, basic flows V_x, V_y, V_z and coefficients of the polynomials U_{ij} . At the last step we solve the above system to get an exhaustive description of coordinate systems providing separability of equations (3), as well as all possible basic flows V_x, V_y, V_z such that the system (3) is solvable by the method of separation of variables.

Thus, the problem of variable separation in equation (3) reduces to integrating the overdetermined system of PDEs for unknown functions $\xi(x, t)$, $\eta(y, t)$, $\gamma(z, t)$, $T(t)$, $T_1(t)$, $S(t)$, basic flows V_x, V_y, V_z and coefficients of the polynomials U_{ij} . This have been done with the aid of *Mathematica* package.

2.3 Results for equations in Cartesian coordinates

The most general form of the basic flow is:

$$\begin{aligned} V_x &= \nu A(\eta)T(t) - \frac{c'_1(t) + xT'(t)}{T(t)}, \\ V_y &= \nu B(\eta)T(t) - \frac{c'_2(t) + yT'(t)}{T(t)}, \\ V_z &= \nu C(\eta)T(t) - \frac{c'_3(t) + zT'(t)}{T(t)}, \end{aligned}$$

The forms of the perturbations v_x, v_y, v_z and p are:

$$\begin{aligned} \mathbf{u} &= T(t) \exp\left(a\xi + s\gamma + m \int T(t)^2 dt\right) \mathbf{f}(\eta), \\ p &= \rho T(t)^2 \exp\left(a\xi + s\gamma + m \int T(t)^2 dt\right) k(\eta), \end{aligned}$$

where $\xi = T(t)x + c_1(t)$, $\eta = T(t)y + c_2(t)$, $\gamma = T(t)z + c_3(t)$.

The equations with separated variables are

$$\begin{aligned} (m - a^2\nu - s^2\nu + a\nu A(\eta) + s\nu C(\eta))h(\eta) + \\ ak(\eta) + \nu(f(\eta)A'(\eta) + B(\eta)h'(\eta) - h''(\eta)) = 0, \\ f(\eta)(m - a^2\nu - s^2\nu + a\nu A(\eta) + s\nu C(\eta) + \\ \nu B'(\eta)) + \nu B(\eta)f'(\eta) + k'(\eta) - \nu f''(\eta) = 0, \\ (m - a^2\nu - s^2\nu + a\nu A(\eta) + s\nu C(\eta))g(\eta) + \\ sk(\eta) + \nu(f(\eta)C'(\eta) + B(\eta)g'(\eta) - g''(\eta)) = 0, \\ sg(\eta) + ah(\eta) + f'(\eta) = 0. \end{aligned} \quad (6)$$

The restrictions on the forms of the basic flows following from the requirement that they themselves satisfy the Navier-Stokes equations lead to the two following cases:

Case I:

$$\xi = \frac{1}{\sqrt{t}}x + c_1(t); \quad \eta = \frac{1}{\sqrt{t}}y + c_2(t); \quad \gamma = \frac{1}{\sqrt{t}}z + c_3(t).$$

$$\begin{aligned} V_x &= \frac{x}{2t} + \nu A(\eta) \frac{1}{\sqrt{t}} - c'_1(t)\sqrt{t}, \\ V_y &= -\frac{y}{t} - \frac{1}{\sqrt{t}} \left(t c'_2(t) + \frac{3}{2} c_2(t) \right), \\ V_z &= \frac{z}{2t} + \nu C(\eta) \frac{1}{\sqrt{t}} - c'_3(t)\sqrt{t}, \end{aligned} \quad (7)$$

and the functions $A(x)$ and $C(x)$ satisfy the equations

$$3A'(\eta) + 3\eta A''(\eta) + 2\nu A'''(\eta) = 0, \quad (8)$$

$$3C'(\eta) + 3\eta C''(\eta) + 2\nu C'''(\eta) = 0. \quad (9)$$

which can be solved in terms of the error functions and the generalized hypergeometric functions. The separation Ansatz takes the form

$$\mathbf{u} = t^s e^{a\xi + m\gamma} \mathbf{f}(\eta), \quad p = \rho t^{s-1/2} e^{a\xi + m\gamma} \pi(\eta). \quad (10)$$

For the *Case II* we have $\xi = x + c_1(t)$; $\eta = y + c_2(t)$; $\gamma = z + c_3(t)$; $V_x = A_1\eta^2 + A_2\eta - c'_1(t)$, $V_y = -c'_2(t)$, $V_z = C_1\eta^2 + C_2\eta - c'_3(t)$ and the separation Ansatz is

$$\mathbf{u} = e^{a\xi + s\gamma + mt} \mathbf{f}(\eta), \quad p = \rho e^{a\xi + s\gamma + mt} \pi(\eta).$$

2.4 Results for equations in cylindrical coordinates

The Navier-Stokes equations are written in cylindrical coordinates (r, φ, z) and then the velocity and pressure fields $\hat{v}_r, \hat{v}_\varphi, \hat{v}_z, \hat{p}$ are splitted into the basic flow and perturbation parts

$$\hat{v}_r = V_r + v_r, \quad \hat{v}_\varphi = V_\varphi + v_\varphi, \quad \hat{v}_z = V_z + v_z, \quad \hat{p} = P + p \quad (11)$$

where V_r, V_φ, V_z, P are the basic flow fields and v_r, v_φ, v_z, p are the perturbations.

Application of the direct method defines the forms of the basic flows allowing separation of variables in the stability equations as well as the solutions of the stability equations with separated variables.

The most general form of the basic flow is:

$$\begin{aligned} V_z &= A(\xi)T(t) - \frac{c'(t) + zT'(t)}{T(t)}, \\ V_r &= B(\xi)T(t) - r \frac{T'(t)}{T(t)}, \quad V_\varphi = C(\xi)T(t), \end{aligned} \quad (12)$$

where $\xi = T(t)r$, $\eta = T(t)z + c(t)$.

The forms of the perturbations $\mathbf{u} = (v_r, v_\varphi, v_z)$ and p and with the trial functions $\mathbf{f} = (f, g, h)$ and π we have:

$$\begin{aligned} \mathbf{u} &= T(t) \exp \left(a\eta + m\varphi + s \int T(t)^2 dt \right) \mathbf{f}(\xi), \\ p &= \rho T(t)^2 \exp \left(a\eta + m\varphi + s \int T(t)^2 dt \right) \pi(\xi). \end{aligned} \quad (13)$$

The restrictions on the forms of the basic flows following from the requirement that they satisfy Navier-Stokes equations lead to the two cases similar to those obtained for equations in Cartesian coordinates.

3 Stability properties of some flows

3.1 Basic flow

Considering the class of solutions in Cartesian coordinates identified in Section 2 as Case I, we will specify the solutions by setting $c_1(t) = c_2(t) = c_3(t) = 0$ but will use a possibility to enrich the solutions by a shift of the time variable. Making change of variables $t = t' - 1/b$, where b is a constant, and omitting primes in what follows, we will have the solution of the Navier-Stokes equations in Cartesian coordinates in the form

$$\begin{aligned} V_x &= \frac{1}{\sqrt{1-bt}} \left(-\frac{b\xi}{2} + \nu A(\eta) \right), \quad V_y = \frac{b\eta}{\sqrt{1-bt}}, \\ V_z &= \frac{1}{\sqrt{1-bt}} \left(-\frac{b\zeta}{2} + \nu C(\eta) \right), \\ \frac{P}{\rho} &= \frac{1}{1-bt} \times \\ &\times \left(\frac{b^2}{8} (\xi^2 + \zeta^2 - 8\eta^2) - 2\nu^2 (A_3\xi + C_3\zeta) \right), \end{aligned}$$

where

$$\xi = \frac{x}{\sqrt{1-bt}}, \quad \eta = \frac{y}{\sqrt{1-bt}}, \quad \zeta = \frac{z}{\sqrt{1-bt}} \quad (14)$$

and b can be both positive and negative. The functions $A(\eta)$ and $C(\eta)$ are given in terms of the error $\text{erf}(z)$ and generalized hypergeometric ${}_2F_2(z)$ functions. The perturbations (10) must be correspondingly specified.

The above formulas remain valid if we introduce the nondimensional variables, with the time scale $1/|b|$ and the correspondingly defined velocity scale. In the dimensionless equations (we will retain the same notation for the nondimensional variables), the parameter b takes one of the two values: $b = 1$ or $b = -1$, and ν is replaced by

$1/\text{Re}$ where Re is the Reynolds number. (if we mark the dimensional variables with stars, the Reynolds number will be $\text{Re} = L^{*2}|b^*|/\nu^*$ where L^* is the length scale.)

We will consider the solution for the case of $b = -1$ which allows interpretations corresponding to unsteady flows near stretching (impermeable or permeable) surfaces or the flows that develop within a channel possessing permeable, moving walls. It is worth remarking that the considered flows are essentially nonparallel – the flow fields include all three velocity components dependent on all coordinates.

There exists a class of solutions of the Navier-Stokes equations in cylindrical coordinates, which is similar in many features to the class of solutions in Cartesian coordinates considered above. The basic flow solution in cylindrical coordinates permits interpretations similar to those considered above for the solution in Cartesian coordinates. However, the cylindrical geometry and presence of the additional free parameters allow one to find more problem formulations and enrich the problem definitions. The basic flow might be again an unsteady axially symmetrical stagnation-point type flow, with the flow velocity decreasing with time as $(1+t)^{-1}$, but, as distinct from the flows considered in the previous section, here fluid flows radially from infinity approaching the axis and spreading along it. The basic flow might also be an unsteady flow inside an expanding stretching cylinder, which may also rotate, and there is an injection of fluid through the porous pipe surface.

3.2 Criterion for stability

We choose as a criterion for stability that the ratio of the magnitude of a perturbation to that of a basic flow decreases with time, which for the solutions leads to

$$\Re\left(s + \frac{1}{2}\right) < 0 \quad \text{or} \quad \Re(s) < -\frac{1}{2} \quad (15)$$

where $\Re(s)$ denotes a real part of the eigenvalue s (the imaginary part $\Im(s)$, if nonzero, determines the oscillation frequency). In particular, for the decelerating flow ($b = -1$) the meaning of instability implies that even any disturbance is damped ($\Re(s) < 0$ for the velocity perturbations and $\Re(s) < 1/2$ for the pressure perturbations) yet it may dominate the decelerating flow after sufficient time if $\Re(s) > -1/2$. It is also seen that the condition (15) unifies the stability criterion for the velocity and pressure perturbations.

3.3 Solution of the eigenvalue problems

The eigenvalue problems were solved numerically with the help of the spectral collocation method based on Chebyshev polynomials [6, 7]. For some classes of perturbations, the eigenvalue problems can be solved analytically (see below) which provides an additional, probably the most important, testing the numerical results.

It can be shown that there exists a transformation (similar in a sense to Squire's transformation [1]) such that the three-dimensional problem defined by equations (6) can be reduced to an equivalent two-dimensional problem. Then equations for the perturbation amplitudes can be reduced to a system of two equations for two functions $g(\eta)$ and $h(\eta)$ of the form

$$\alpha(ab - abs + \alpha^3\nu + i\nu(\alpha^2A(\eta) + A''(\eta)))g(\eta) + \frac{3}{2}ba^2\eta g'(\eta) - (b - bs + 2\alpha^2\nu + i\alpha\nu A(\eta))g''(\eta) - \frac{3}{2}b\eta g'''(\eta) + \nu g^{(IV)}(\eta) = 0, \quad (16)$$

$$\nu C'(\eta)g(\eta) + \left(-\frac{1}{2}b - bs + \alpha^2\nu + i\alpha\nu A(\eta)\right)h(\eta) + \frac{3}{2}b\eta h'(\eta) - \nu h''(\eta) = 0 \quad (17)$$

It is seen that for $C(\eta) = 0$ the system of equations (16) and (17) decouples into two separate equations for $g(\eta)$ and $h(\eta)$. Thus, in this case two separate branches exist, first of which corresponds to the disturbances with one z -component of the velocity vector changing with x and y , while the second branch corresponds to the two-dimensional disturbances with velocity vector lying in the (x, y) plane and not dependent on z .

In the case where both $A(\eta) = 0$ and $C(\eta) = 0$ equations (16) and (17) can be reduced to Kummer's equation [8] and can be solved in quadratures in terms of confluent hypergeometric functions.

There is an important point in which the stability problems in cylindrical coordinates differ from those in Cartesian coordinates: a transformation, similar to Squire's transformation, which reduces the three-dimensional perturbation problem to an equivalent two-dimensional problem, does not exist. Therefore, in general, one has to consider the three-dimensional perturbations to assess the flow stability. Below we present the results of numerical solution of the eigenvalue problems for the most general three-dimensional perturbations of the unsteady nonparallel flows developing within expanding pipe.

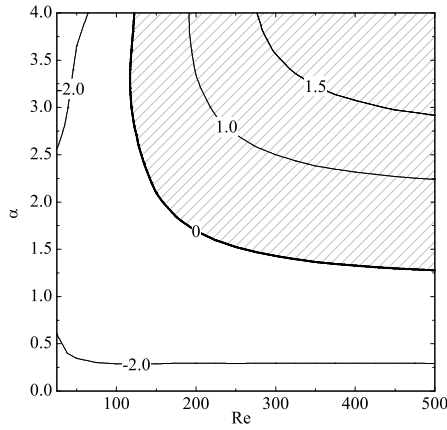


Figure 1: Neutral curve and contours of constant growth rate S for $U_0 = 30$ and $n = 2$. The shaded area represents the region in parameter space where unstable solutions exist.

First, the analysis shows that the flow within not rotating cylinder and in the absence of the axial pressure gradient is stable ($S < 0$) in all the parameter space. All the eigenvalues are real so that the disturbances decay monotonically.

If the basic flow includes the part due to the axial pressure gradient ($U_0 \neq 0$), positive values of S appear (see Fig. 1). The neutral curve $S = 0$ in Fig. 1 separates the regions of stability and instability. It is seen that for any Reynolds number larger than some critical value Re_* (for $U_0 = 30$, $Re_* \approx 120$) there exists a range of wave numbers α corresponding to unstable solutions. Thus, the flow including the part due to the axial pressure gradient is unstable for $Re > Re_*$. The critical Reynolds number Re_* decreases while U_0 increases. Another example of application of the method is the flow in a gap between rotating expanding cylinders. An unstable mode for this flow is given in Fig. 2.

4 Concluding remarks

To conclude, in this paper we present a unified, computational synthesis of analytical and numerical calculations to study stability of viscous unsteady nonparallel flows. The combination of analytical and numerical solutions may provide a basis for a well-grounded discussion of some problematic points of hydrodynamic stability analysis and a very useful test for methods used in the hydrodynamic stability theory, in general. It is also worth remarking that the basic flows whose stability is studied in the paper are themselves of interest for fluid dynamics and have received considerable attention in the literature due to their

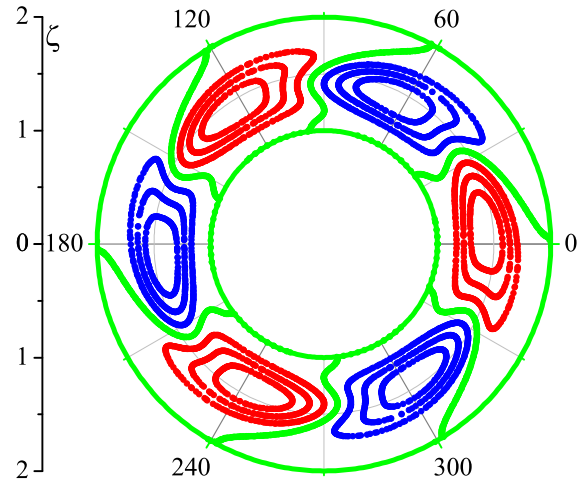


Figure 2: Flow in a gap. The unstable mode. Red, blue and green lines correspond to negative, positive and zero values of stream function.

relevance in a number of engineering applications.

References

- [1] P. G. Drazin and W. H. Reid *Hydrodynamic stability*, Cambridge University Press, 1981
- [2] R. Zhdanov and A. Zhalij, On separable Schrödinger equations, *J. Math. Phys.*, Vol. 40, 1999, pp. 6319–6338
- [3] R. Zhdanov and A. Zhalij, Separation of variables in the Kramers equation, *J. Phys. A: Math. Gen.*, Vol. 32, 1999, pp. 3851–3863
- [4] A. Zhalij, G. I. Burde, and I. Sh. Nasibullayev, Separation of variables in the hydrodynamic stability equations, *J. Phys. A: Math. Gen.* Vol. 39, 2006, pp. 7141–7160
- [5] G. I. Burde, I. Sh. Nasibullayev and A. Zhalij, Stability analysis of a class of unsteady non-parallel incompressible flows via separation of variables, *Phys. Fluids*, Vol. 19, 2007, pp. 114110-1–14
- [6] M. Khorrami, M. R. Malik and R. L. Ash, Application of spectral collocation techniques to the stability of swirling flows, *J. Comp. Phys.*, Vol. 81, 1989, pp. 206–229
- [7] P. J. Schmid and D. S. Henningson, *Stability and transition in shear flows*, New York: Springer, 2001
- [8] M. Abramowitz and I. Stegun *Handbook of mathematical functions*, New York: Dover publications, 1965

Feasibility of power flow control on LV distribution systems

Dario De Santis, Gaetano Abbatantuono, Sergio Bruno, Massimo La Scala, Roberto Sbrizzai

Abstract- The electric distribution systems of the 21st century are characterized by the huge diffusion of distributed generations (DG) units. Their always increasing number, however, asks for new and advanced technical solutions for management and optimization of low voltage grids, whose design and efficiency is still strictly dependent to old operative conditions and schemes. In this paper, a methodology aimed to achieve power flow control and optimization on low voltage distribution systems by means of an Unified Power Flow Controller (UPFC) is presented. Tests have been made on three different operating conditions and their numerical results demonstrate how this device can be positively applied even to electric distribution networks in order to solve some typical issues such as loss reduction, power flows inversion and so on.

Keywords- flow optimization, low voltage distribution grids, power loss reduction, unified power flow controller.

I. INTRODUCTION

MODERN Smart Grids are characterized by an always increasing quantity of distributed generation (DG) units. Thanks to their limited power generation capability, these devices (PV panels, micro wind generators and so on) have turned what was seen just as an ordinary electric user into a “prosumer” who can fully satisfy his needs for electric energy by himself and also inject the exceeding power generation straight on the low voltage distribution grids. Unfortunately, this radical transformation is also causing many challenges that these aging networks are still not technologically ready to face [1-8].

DG units are also good options to enhance power quality, which include keeping voltage level and power factor corrections. On the other hand, large-scale introduction of decentralized power generating units may lead to instability of the voltage profile due to the bi-directional power flows and the complicated reactive power equilibrium, thus making voltage control difficult. Another problem is that intervention of electric power equipments will release higher harmonics to the grid.

Power quality and stability, for example, could be compromised by the fact that DG units are not restricted by the regulations of the grid operator to maintain system frequency, so they have to increase or reduce their effort. This leads to an impact not only on frequency but also on efficiency and emissions levels.

Power usually flows from higher to lower voltage levels, from transmission to distribution grid. But the increased DG units may induce power flows from low-voltage grid into medium-voltage grid. The value of the power flow is also changed. That collapses the original relay protection calculation scheme with the intervention of electronic equipments which may reduce the short current during fault. The protection system has to be sufficiently selective in order to optimize reliability and availability of supplied power [9].

These issues are mostly solved by hardware application and control: using DC converters in load side can improve power quality, because even when fault occurs in the load side, other loads would not be influenced.

The islanding detection, aimed to protect the grid from reverse power flow can't be realized changing completely the original protection relays in distributed network lines, so the best way is to use original relays but with different schemes to different network configuration. In each scheme the settings of relays are calculated respectively, but this may change the maximal and minimal operation modes, branch coefficient. Another way of using fault location is to trip the relative relays and avoid the mistake trip of other relays.

In this paper, the authors present a methodology aimed to achieve power flow control and optimization on low voltage distribution systems by means of unified power flow controllers (UPFC). The UPFC consists of a combination of a series inverter, a shunt inverter, and a dc-link capacitor: The series inverter controls an active and reactive power flow of the distribution line while the shunt inverter controls an input line voltage and a dc-link voltage [10].

Unified power flow controllers (UPFC) are normally used to control the power flow in the transmission systems by controlling the impedance, voltage magnitude and phase angle. [11-13]

Within the framework of traditional power system concepts, the UPFC is able to control, simultaneously or selectively, all the parameters affecting power flow in the transmission line (i.e. voltage, impedance and phase angle), and this unique capability is signified by the adjective “unified” in its name. Alternatively, it can also independently control both the real and reactive power flows in the line.

The UPFC can perform the functions of the STATCOM, SSSC and the phase angle regulator, and also provide additional flexibility by combining some of the classic functions of these controllers [14].

II LV DISTRIBUTION CONTROL BY UPFC

The UPFC device is normally connected in order to control active and reactive power flowing through two different lines. It includes two different voltage source converters (VSC): the first one has a shunt connection with the terminal of a L1 line, while the second is connected to L1 and the other line (L2) and is able to impress a certain phase and magnitude voltage level between them, in order to perform the flow control.

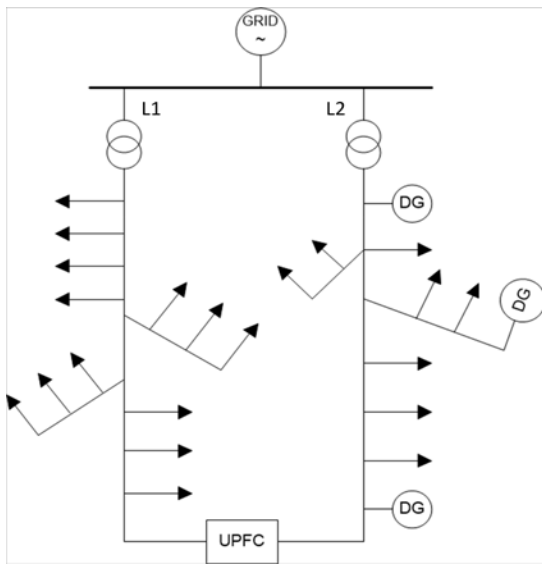


Fig.1 LV systems connected by UPFC

This is possible because the active power injected by VSC2 is balanced by the active power withdrawn by VSC1 and viceversa, while reactive power surged by the phase shifter is always nought.

The converters are three-phase bridges built with IGBT transistors at 10kHz frequency level; the DC link has a voltage level of 800 V and capacity equal to 0,8 mF.

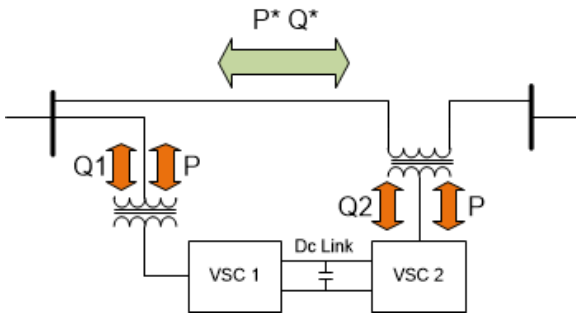


Fig.2 UPFC internal scheme

The converters have two different operating and control schemes.

VSC 1 is current-controlled by I_{ca} , I_{cb} , I_{cc} , which are drained from the L1 terminal. We consider a d,q rotating coordinate system; the d axis of the chosen coordinate system is aligned with the grid voltage vector, according voltage oriented control technique (VOC). E_{ga} , E_{gb} and E_{gc} are referred to the Thevenin equivalent model of the grid calculated in respect to the connection point of VSC1.

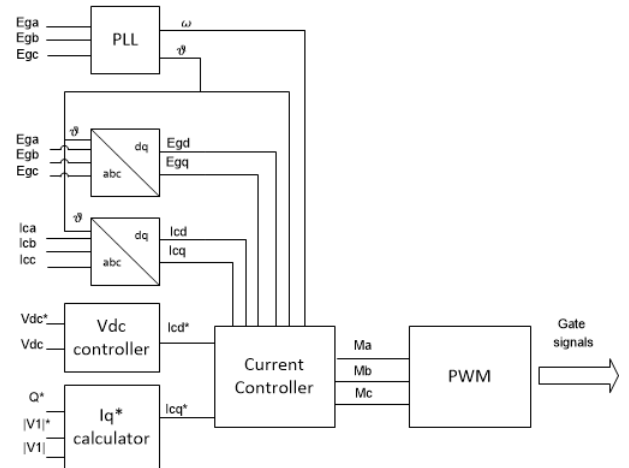


Fig.3 VSC1 control architecture

Figure 4 shows the plant to which the current controller refers to; it's been conceived like an average single phase circuitual model where L and R indicate the total inductance and resistance of Tf1, the internal filter of VSC1 and the Thevenin model of the grid.

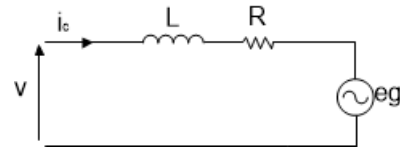


Fig. 4 VSC1 plant

Plant equations used for designing the PIs current controllers are:

$$V_d = RI_{cd} + L \frac{dI_{cd}}{dt} - \omega LI_{cq} + E_{gd} \quad (1)$$

$$V_q = RI_{cq} + L \frac{dI_{cq}}{dt} + \omega LI_{cd} + E_{gq} \quad (2)$$

where V_d, V_q are the values of voltages of the converter.

The relations between active and reactive power and I_{cd} and I_{cq} currents can be written as follows:

$$P = \frac{3}{2} E_d I_{cd} \quad (3)$$

$$Q_1 = -\frac{3}{2} E_d I_{cq} \quad (4)$$

In order to determinate current set point on d axis, it's necessary to control the DC link voltage level V_{dc} .

There are two external decoupled control loops, that calculate the current set-points for I_{cd}^* and I_{cq}^* . The first loop manages the voltage level of the capacitor and determines the active power that the converter exchanges

with L1. The second loop determines I_{cq}^* according two different processes: by equation (4) if the Q_1 value is known or measuring V on L1, comparing it with the voltage set point and finally calculating the I_{cq}^* set point with a PI controller.

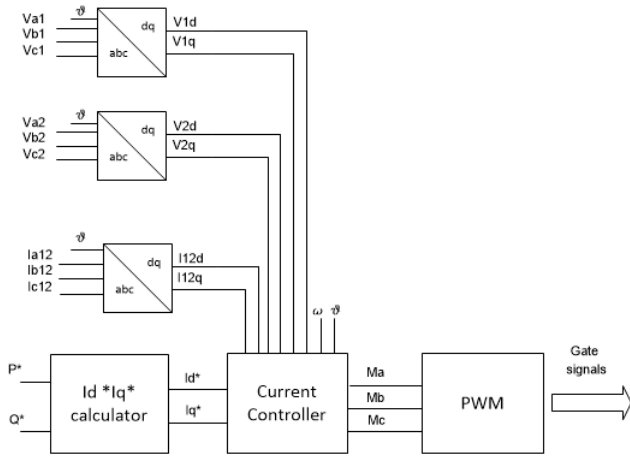


Fig.5 VSC2 control architecture

Similarly to VSC1, VSC2 too is current-controlled but in this case the currents are directly depending to the ones flowing between LINE1 and LINE2 (I_{a12} , I_{b12} , I_{c12}). The internal current loop needs the voltage values on L1 and L2 terminals (V_{a1} , V_{b1} , V_{c1} and V_{a2} , V_{b2} , V_{c2}).

Figure 6 shows the VSC2 plant. In this case L and R indicate the total inductance and resistance of the internal filter of VSC2; V1 and V2 are the voltage levels on L1 and L2 terminals and V is the voltage provided by VSC2.

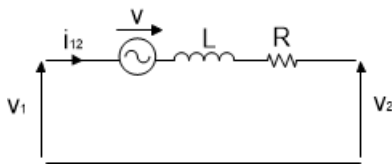


Fig. 6 VSC2 plant

The plant equations are now:

$$V_d = RI_{12d} + L \frac{dI_{12d}}{dt} - \omega LI_{12q} + V_{2d} - V_{1d} \quad (5)$$

$$V_q = RI_{12q} + L \frac{dI_{12q}}{dt} + \omega LI_{12d} + V_{2q} - V_{1q} \quad (6)$$

I_{12d}^* and I_{12q}^* are calculated by (7) equation:

$$\begin{bmatrix} I_{12d}^* \\ I_{12q}^* \end{bmatrix} = \frac{2}{3} \frac{1}{V_{1d}^2 + V_{1q}^2} \begin{bmatrix} +V_{1d} + V_{1q} \\ +V_{1q} - V_{1d} \end{bmatrix} \begin{bmatrix} P^* \\ Q^* \end{bmatrix} \quad (7)$$

P^* and Q^* star represent the active and reactive power levels that should flow through LINE1 and LINE2; the ω pulse and φ angle values are calculated by the PLL controller. The Q_1 level is always supposed to be equal to zero because our target is not to exchange reactive power through the VSC1 but manage P and Q flows between LINE1 and LINE2.

III NUMERICAL RESULTS

We consider a low voltage grid linked to a 20 kV distribution line (figure 7).

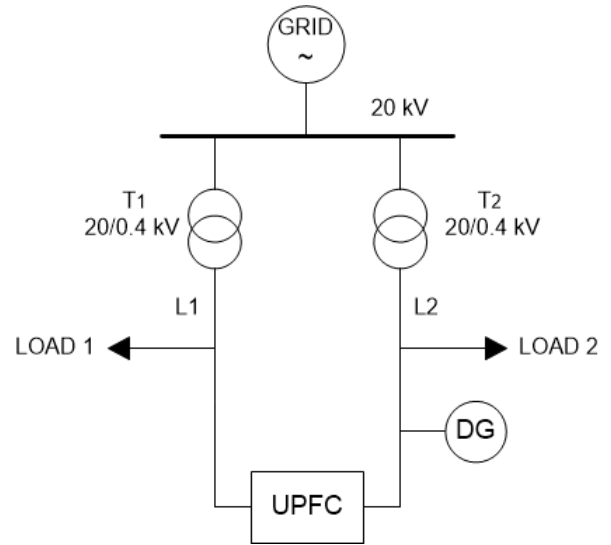


Fig.7 Grid topology

The MV bus feeds two different transformers, T1 and T2, and their respective lines called LINE 1 and LINE 2, which are both connected to a phase shift transformer. Each line supplies power to its own loads. LINE 1 has mostly tertiary and commercial users; LINE 2 has residential loads and one distributed generation point who can inject power and cause flow inversion. The parameters of transformers and lines are reported in Table I and Table II.

	LINE 1	LINE 2
Length (m)	500	1000
Cables	2x3x150+150	3x63+50
R (w/km)	0,063	0,278
X (w/km)	0,074	0,35
I_r (A)	688	260

Table I

	Tf1	Tf2
Voltage ratio (kV)	20/0,4	20/0,4
Connections	Delta-wye	Delta-wye
U_{cc} %	4	6
P_{Cu} %	1,8	1,8
An (kVA)	400	160

Table II

Our study it's been focused on three different test scenario. Case 1 it's concerned about loss reductions and optimal distribution of P and Q through LINE 1 and LINE 2; case 2 simulates the possible control of flow inversion caused by the distributed generation located on LINE 2; case 3 analyses possible reduction of line congestion due to elevate power demand on LINE 1.

A. Case 1

The starting grid conditions for Case 1 are reported in Table III; SPS is set so that P^* and Q^* flows are equal to zero: it's like if there is no connection between the two lines. Active power loss is equal to 8,87 kW. The active and reactive power through Tf1 and Tf2 are equal to what is reported as "Load 1" and "Load 2".

Load / DG	P (kW)	Q (kVAR)	A (kVA)
Load 1	30	10	31,62
Load 2	60	30	60,83
DG	10	0	10,00

Table III

Our goal is to balance power flows distribution and reduce power losses on the lines; next figures show how this is possible.

At $T=0$, the UPFC starts to shift 10 kW from LINE 2 to LINE 1 (figure 8). Consequently, P flowing through Tf2 decreases from almost 60 to 45 kW, while the active power through Tf1 increases from 30 to almost 40 kW (figure 9–10). These optimization causes a relevant decrement of power losses on LINE 2 and a total loss reduction of 37% , going from more than 8 to 4.7 kW (figure 11).

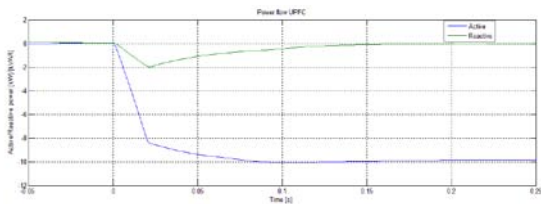


Fig. 8 UPFC power flow – case 1

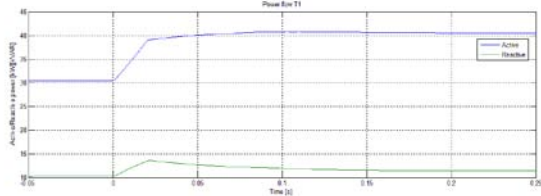


Fig. 9 T1 power flow - case 1

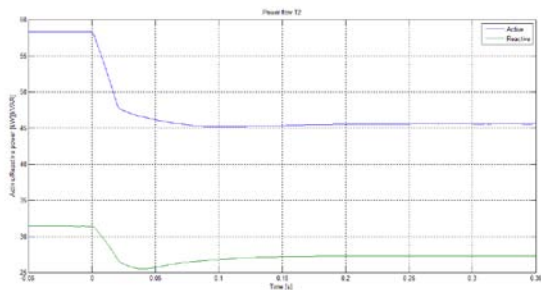


Fig. 10 T2 power flow - case 1

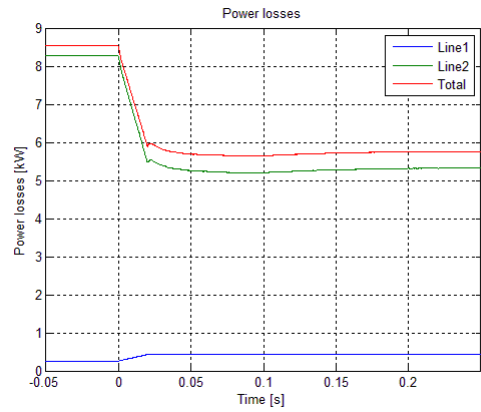


Fig. 11 Total power losses - case 1

B. Case 2

In this case the DG unit on LINE 2 is injecting 60 kW on the grid and causing flow inversion through T2, where active power is equal to -30 kW (we consider as negative the power flowing back from low voltage to medium voltage system). So, in order to balance this situation, at $T=0$ SPS starts to transfer $P^* = 30$ kW from LINE 2 to LINE 1 (figure 12). Grid configuration is reported in Table IV.

Load / DG	P (kW)	Q (kVAR)	A (kVA)
Load 1	150	40	155,24
Load 2	30	10	31,62
DG	60	0	60,00

Table IV

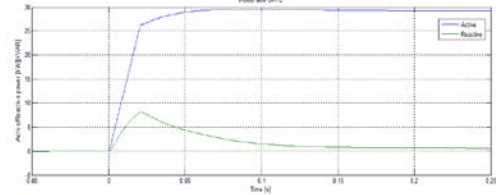


Fig. 12 UPFC power flow – case 2

In figure 13 it's possible to see how I_{a12} oscillates between -60 and +60 A after $T=0$:

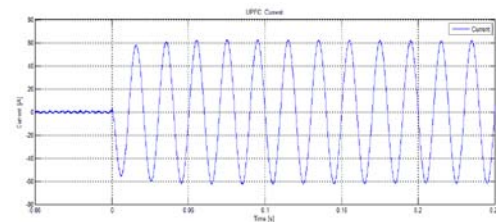


Fig. 13 UPFC current – case 2

In figure 14 and 15 are reported the active and reactive power flows through the transformers. At $T=0$, the SPS starts to transfer P^* from LINE 2 to LINE 1; consequently, P provided by T1 decreases of almost 30 kW and the while T2 end to inject the same quantity back to the MV grid.

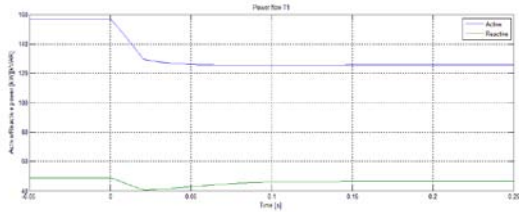


Fig. 14 T1 power flow - case 2

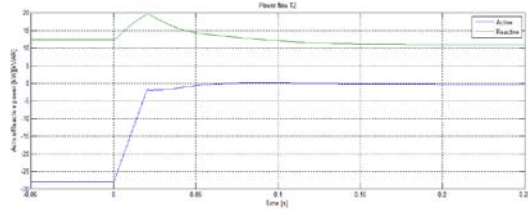


Fig. 15 T2 power flow - case 2

Figure 16 shows how total power losses on lines and transformers are almost reduced to half.

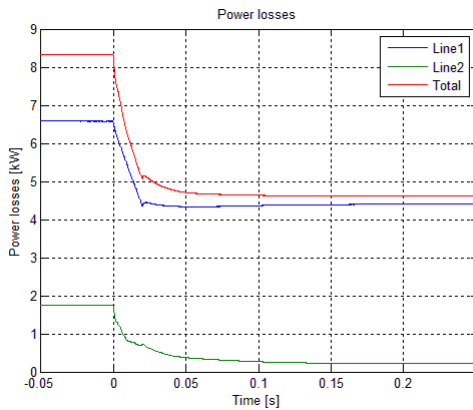


Fig. 16 Total power losses - case 2

C. Case 3

The starting conditions for this last case are reported in Table V. There is a very high power demand from loads on LINE 1, so the UPFC is used to distribute some power on LINE 2 in order to prevent possible overloads.

Load / DG	P (kW)	Q (kVAR)	A (kVA)
Load 1	260	50	264,76
Load 2	30	5	30,41
DG	20	0	20,00

Table V

In the following figures we can see as, for T=0, the static phase shifter begins to shift 60 kW from LINE 2 to LINE 1. The active power on LINE 1 decreases from almost 280 to 210 kW, with a reduction of 25%, while LINE 2 is rising from 10 kW (we consider the total P obtained subtracting distributed generation from load) up to more than 75 kW.

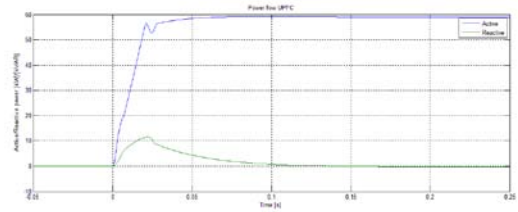


Fig. 17 UPFC power flow – case 3

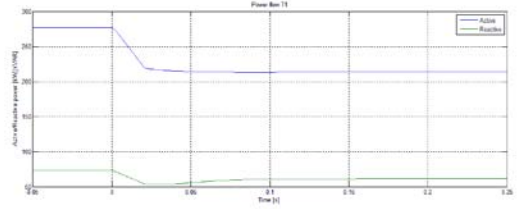


Fig. 18 T1 power flow - case 3

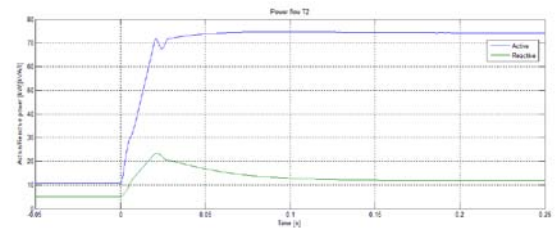


Fig. 19 T2 power flow - case 3

IV CONCLUSIONS

In this paper, present a methodology aimed to achieve power flow control and optimization on low voltage distribution systems by means of an unified power flow controller (UPFC) was presented. Test cases have been developed to show how this devices can be adopted to solve some typical eventualities of modern low voltage grids such as power flow inversions, line losses excess and possible load demand overloads.

Further studies will be focused on the implementation of advanced mathematical methodologies and efficient algorithms in order to automatically calculate the best set-points of P* and Q* for UPFC implemented on low voltage systems and avoid these kind of technical problems

REFERENCES

[1] G. Caprinelli, G. Celli, F. Pilo, A. Russo, “Embedded generation planning under uncertainty including power quality issues”, *Euro. Trans. Electr. Power*, vol.13, no.6, pp. 381-389, Nov. 2003.
 [2] D. Zhu, R.P. Broadwater, K.S. Tam, R. Seguin, H. Asgeirsson, “Impact of DG placement on reliability and efficiency with time-varying loads”, *IEE Transactions on Power Systems*, vol. 21, no.1, pp. 419-427, Feb. 2006.
 [3] N. Acharya, P. Mahat, N. Mithulananthan, “An analytical approach for DG allocation in primary distribution network”, *Int. Journal of Electric Power Energy System*, vol. 28, no.10, pp. 669-678, Dec. 2006
 [4] M.R. Haghifam, H. Falaghi, O.P.Malik, “Risk-based distributed generation placement”, *IET Gener. Transm. Distrib.*, vol. 2, no.2, pp.252-260, Mar. 2008
 [5] S. Kotamarty, S. Khushalani, N. Schulz, “Impact of distributed generation on distribution contingency analysis”, *Elect. Power Systems Res.*, vol.78, no.9, pp. 1537-1545, Sep. 2008

- [6] L.F. Ochoa, G.P. Harrison, "Minimizing energy losses: Optimal accommodation and smart operation of renewable distributed generation", *IEEE Transactions on Power Systems*, vol. 26, no.1, pp. 198-205, Feb. 2011.
- [7] N.G.A. Hemdan, M. Kurrat, "Efficient integration of distributed generation for meeting the increased load demand", *Int. J. Electric Power Energy Syst.*, vol. 33, no.9, pp. 1572-1583, Nov. 2011.
- [8] D.Q. Hung, N. Mithulananthan, "Multiple distributed generators placement in primary distribution networks for loss reduction", *IEEE Trans. Ind. Electron.*, vol. 60, no. 4, pp. 1700-1708, Apr. 2013.
- [9] C.X. Wu, F.S. Wen, Y.L. Lou, "The existed problems and possible solutions of micro-grid based on distributed generation", *3rd International Conference on Deregulation and Restructuring and Power Technologies DRPT 2008*, 6th-9th Apr 2008, Nanjing, China.
- [10] D.G. Cho, E. Ho. Song, "A simple UPFC control algorithm and simulation on stationary reference frame", *International Symposium on Industrial Electronics ISIE 2001*, 12th - 16th June 2001, Pusan, Korea
- [11] J. Joglekar, Y. Nerkar, "Application of UPFC for improving micro-grid voltage profile", *IEEE International Conference on Sustainable Energy Technologies ICSET 2010*, 6th - 9th Dec. 2010, Kandy, Sri-Lanka
- [12] Y.M. Alharbi, A.M. Shiddiq Yunus, A. Abu Siada, "Application of UPFC to improve the LVRT Capability of wind turbine generator", *22nd Australasian Universities Power Engineering Conference AUSPEC*, 26th - 29th Sept. 21012, Bali
- [13] M.A. Sayed, T. Takeshita, "Line loss minimization in isolated substations and multiple loop distribution systems using UPFC", *IEEE Transactions on Power Electronics*, Volume PP, Issue 99, Jan. 2014
- [14] T. Nireekshana, G. Kesava Rao, S. Siva Naga Raju, "Modelling and control design of unified power flow controller for various control strategies", *International Journal of Engineering Science and Technology*, vol. 2, pp. 6293-6307, 2010

Efficient Management Methods of Project Transfers

Florina-Cristina Filip, Vladimir Mărăscu-Klein

Abstract—The present paper describes the transfer of products, product series and the associated production resources across plants and locations, as well as the reorganization of plants. Due to the complexity and scope of production transfers, these are planned with the aid of project management. In the case of production transfers, planning of manufacturing locations creates an appropriate project organization depending on the tasks involved. The composition of the core team and expanded team will vary according to the scope of transfer projects. The project team is generally composed of employees from the same departments in the delivering and receiving plant and is supported by central functions. The general product coordinator selects the team and defines the sub-projects which are not relevant based on organizational aspects and with regard to content. Transfers in the sense of production transfers are carried out by means of project management in accordance with the gateway principle. Transfers extending over a longer period can be divided into several transfer stages. In the case of transfers, an audit is to be planned at the delivering plant prior to moving machinery and at the receiving plant once the move is complete.

Keywords—machine, product, production, project transfer.

I. INTRODUCTION

IN the past decades, competition has intensified and customers are more demanding than ever before [1]. The automotive industry is notoriously exposed to the risk of low capacity utilization, and a variety of measures have been taken to improve flexibility [1], [2]. The recent change in Renault's manufacturing strategy demonstrates the new paradigm, away from inflexible one-plant/one-vehicle policies towards highly flexible machines and manufacturing platforms that are capable of producing multiple products [1], [3].

Companies feel ever-increasing pressure to get new products to market faster. As new products are developed, successful new product transfer from research and development to manufacturing is a common problem for companies of all sizes. The best internal transfer process integrates all departments at the same time into the process yielding a gap-free transfer, builds on solid tools and techniques that streamline execution and produce effective results, and is developed and implemented such that the whole

company embraces the transfer process [4].

The basis for economic success in the world today is knowledge. The challenge for any nation seeking economic success can therefore be thought of as twofold: first, to facilitate the acquisition of knowledge from within (or without) its borders and second, to facilitate the conversion of that knowledge into benefits for its citizens by the most efficient means available. This is the essence of technology transfer [5]. Technology transfer as a separate field did not appear until the 1970s. It emerged as a result of accelerating awareness of the key role of technology in economic development and its study has essentially been driven by the need to better understand the process, its determinants, its effects on transferor and transferee and factors affecting its control [6]. Companies follow different technology transfer strategies. Several factors determine technology-transfer strategies in the presence of potential imitation, including variable-cost-saving potential, fixed transfer and imitation costs, market potential, and product differentiation [7].

A product is designed to meet certain functional requirements, and to satisfy the customer's needs. New technology and new materials currently available will also be explored during the product design stage. A product consists of assemblies, sub-assemblies and component parts [8]. Product transfer is a key activity in the complex process of new product development. Purposeful management of the product transfer process leads to more effective transfers in terms of timeliness, cost, functional performance, and competence building. Better management of product transfer gives firms access to a greater variety of new technology options, improves a firm's ability to offer significantly differentiated products, deepens the firm's competitive competencies, and positively influences sustained product development success [9].

Companies often incorporate new product technologies in their product designs to help achieve distinctive new products. Companies rarely rely solely on internal research and development for the initial development of all the new product technologies they will employ in a new product system [9], [10]. Accordingly, careful integration of product technologies from external organizations, called the "product technology transfer process" here, is an essential competence for new product development organizations. Companies skilled in the product technology transfer process have access to a vastly greater array of technological options and can ration their

F.C. Filip is with the Engineering and Industrial Management Department, Transilvania University of Brasov, Romania (e-mail: florina-cristina.filip@unitbv.ro).

V. Mărăscu-Klein is with the Engineering and Industrial Management Department, Transilvania University of Brasov, Romania (e-mail: klein@unitbv.ro).

scarce research and development resources better [9], [11], [12]. This process often is fraught with unanticipated problems and excessive risk, leading to product development efforts that are unsuccessful due to time delays in market introduction, cost overruns, and technical functionality problems. It is acknowledged that product technology transfer is conducted regularly in an ad-hoc manner [9], [13].

There are differences in the elaborateness of transfers, which seem to be determined based on anticipated degree of difficulty. A transfer corresponds primarily to novelty of the product and process, and secondarily to process capability for the most difficult manufacturing processes [14].

II. TYPES OF TRANSFERS

A. Production and Product Transfer

A production transfer is defined as a change or localization in the production location for existing products, where all necessary production resources are transferred or sourced as new (e.g. machinery, plant facilities, assembly and measurement equipment etc.).

A product transfer is a change of the production location or a change from in-house to external production (purchase) or vice versa, if only the tooling, devices and documents for production of the affected products are transferred. In a product transfer, machinery is not transferred and no training will be performed (Fig. 1 described the main steps of transfer).

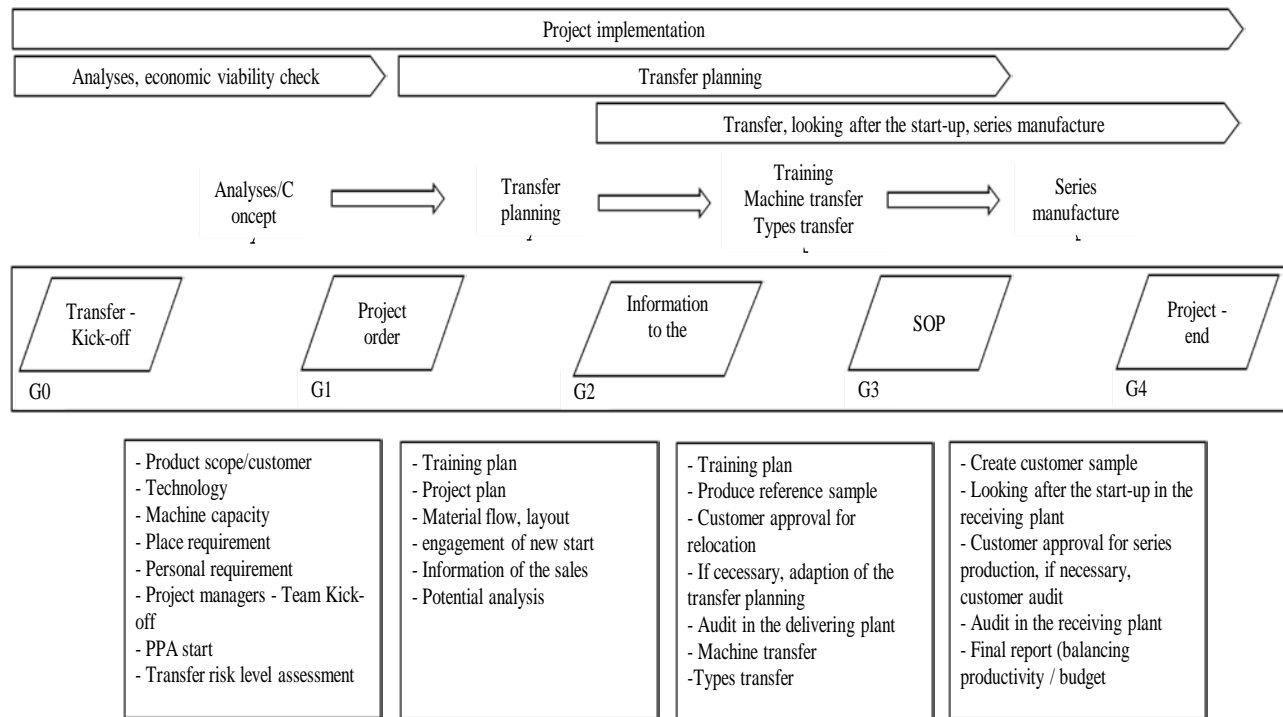


Fig. 1. Steps of transfer

B. Machine Transfers

A machine transfer is part of a production transfer or is a local transfer of machines within a plant. The transfer of machines within a plant is carried out by the plant itself and not ruled by central procedures.

III. PROJECT TRANSFERS

A. Project Order and Basic Conditions

The project coordinator in planning of manufacturing locations documents the fact that the transfer has been approved. This is carried out in writing by means of an approved project order. The project order must always be signed by a member of executive management board. For transfer projects which are included in the approved transfer budget list, the project order is also valid if it bears the

signature of a member of the relevant business unit.

B. Project Manager Kick-off

The project manager kick-off represents the official start of a transfer. Possible participants: general project coordinator, project manager at delivering plant, head of planning of manufacturing locations, plant managers, project manager at receiving plant, other participants are possible.

C. Project Team Kick-off

The project team kick-off takes place after or together with the project manager kick-off and constitutes the start point for the sub-projects. The core team is defined during this stage, at the latest. Main subjects/targets of the meeting: presentation of the project targets (e.g. start-up curve, production figures, key data etc.) and basic conditions, presentation of rough project timetable, presentation of project roles, presentation of tasks

and sub-project targets for defined sub-project managers, information about the project, clarify course of action for project work (e.g. status meetings, information channels, project plan, checklist), disclosure of critical project points.

D. Project Organization

The project organization is composed of the following:

- 1) Steering committee – is composed of executive management board, product line management, plant management, the business unit and the head of planning of manufacturing locations, and supports the transfer projects.
- 2) General project coordinator – coordinates the activities of the project manager’s project management at delivering plant (PL-A) and project management at receiving plant (PL-E) and the team members with each other. He coordinates the documents which are relevant to the project (e.g. project plan, checklists) and the sub-projects or work packages with regard to arranging deadlines. He actively and continually monitors the timing targets and reports on their status to the steering committee by means of intermediate reports/status reports. The general project coordinator supports the project team with reporting and documentation. He reports to and receives his instructions from the steering committee. He is the contact person for the steering committee, the supporting central departments and for the project managers. The general project coordinator can call on the support team to assist with monitoring deadlines and costs and documenting the project.
- 3) Support from central departments (support team) – this support is composed of cross-plant central departments (quality management, process/production development, product development, business management, controlling, personnel management, legal department). Support from central departments can be requested as required by any individual team member.
- 4) Project managers (PL-A and PL-E) – tasks of the project managers refers to: responsibility for the overall project, suggest project team members, prepare and maintain the detailed project plan (based on the basic project plan), reporting and target monitoring for the sub-projects, ensure internal communication (identical information for all team members), disclose problems and critical activities to the general project coordinator, responsible for the achievement of the project targets, processing checklist points of the project manager, responsible for the processing and quality of the checklists, granting approval of deviations / conditions on gateway releases.
- 5) Core team – is composed of PK, PL-A, PL-E and the sub-project managers that are essential for a transfer project and have responsibility for the most important and most extensive sub-projects. The composition of the core team can be freely selected and is formed at the project start-up meeting (project manager kick-off or project team kick-off) by PK, PL-A and PL-E.
- 6) Expanded team – is composed of sub-project managers who are necessary for achieving the project target but not for the regular status meetings. These are smaller work packages covering a limited period of time. The composition of the expanded team is formed at the project start-up meeting (project manager kick-off or project team kick-off) by PK, PL-A and PL-E.
- 7) Sub-project manager – the general project coordinator selects the team and defines the sub-projects which are relevant based on organizational aspects and with regard to content. For the specific transfer projects, the scope of the sub-projects is defined by PK, PL-A and PL-E.

IV. PROJECT PLANNING AND DOCUMENTATION

Transfers in the sense of production transfers are carried out by means of project management in accordance with the gateway principle. Transfers extending over a longer period can be divided into several transfer stages. Gates 2 to 4 may be passed several times in this case (refer with: Fig. 2). Gate 4, which is planned as the last in the sequence, constitutes the end of the transfer. If gates 2 to 4 are passed several times, it is the responsibility of the general project coordinator to decide which checklist points should be processed. In the case of transfers, an audit is to be planned at the delivering plant prior to moving machinery and at the receiving plant once the move is complete.

A. Internal Transfer Announcement

The internal transfer announcement stating all products to be transferred is passed to sales at an early stage and by no later than gate 2. Sales are responsible for notifying customers and obtaining the customer’s consent for approval of volume deliveries. The transfer timetable and the required product lead stock must be agreed with the customer as necessary. If this is rejected by the customer, sales have the task of obtaining approval for volume delivery by further measures. Sales must inform the general project coordinator of the current status of approval so that he can introduce the implementation steps.

Components of the internal transfer announcement: reason for transfer and background information, name of general project coordinator, project manager at delivering plant and project manager at receiving plant, planned transfer date, possible sample delivery date, product list, brief description of the receiving plant, customer letter, and checklist from legal department.

B. Project Plan

The project manager with main responsibility (generally PL-A) prepares a project plan with support from the general project coordinator and the project manager at the receiving plant. This project plan contains the most important milestones and transfer steps, the summarized sub-projects, the degree of completion, the persons responsible and the start and end dates. The sub-project managers of the delivering and receiving plant create sub-project plans/activity plans by request of the general project coordinator. The software tool

used to prepare the sub-project plans and activity plans can be freely selected on the basis of availability and capability.

Continuous monitoring of activities should help to improve the consistent realization of planning. Changes and deviations of the planned activities must be included in the project plan in a timely manner in order so that an overview of the large number of individual stages and details can be obtained at any time. It is advisable to enter an appropriate note in the project plan when changes occur. Continuous monitoring of activities should help to improve the consistent realization of planning.

C. Checklist

Checklists are specifically allocated to the sub-projects that are also assigned in timing terms to the gates. If the project is divided into several transfer stages, the checklist must be processed several times as necessary indicating the associated stage in the headline. The checklist points are obligatory and prove that a project phase has been completed. Responsibility in the specific sub-project (naming of a specific person) for processing of checklists is indicated in the general checklist under the checklist overview. The status must be recorded for each checklist point.

Approval of a transfer gateway is granted by the general project coordinator following completion of the individual checklist items for this gateway. If individual items have not yet been completed or are critical, the general project coordinator can decline approval of the gate. In the event of gateway deviations, approval must be granted by the PL-A, PL-E, PK and a representative from the steering committee. The general project coordinator is responsible for monitoring the gateway date deviations. Documentation/monitoring takes place in accordance with the project plan or minutes of the status meeting.

D. Status Meetings

The status meetings are to be held regular or demand-oriented in order to maintain a uniform level of knowledge in the project team. They are an important instrument for discussing the progress of a project progress, activities, problems and possible solutions. Invitations are issued by the general project coordinator and the participants are defined by the general project coordinator.

E. Training and Monitoring of Training

In production transfers, employees of the receiving plants are to be trained usually before machinery is moved. The training serves to communicate theoretical and practical knowledge of products, machinery and processes. The

delivering plant notifies the receiving plant of the training times and the required qualifications at an early stage in the transfer planning phase so that personnel selection or the appointment strategy can be defined. The training requirements for direct and indirect areas are to be defined from the project team.

In order to define the scope of training must be prepared a training plan for each individual employee that records all knowledge and activities. The success of training is discussed in regular meetings between the trainers and their line managers in order that any further or special training can be derived from this. The trainee receives feedback on the status of his training on one or more occasions, depending on the length of the training. At the end of his training period, the trainee receives his instruction evidence of training, including the targets achieved, by means of a copy to his line manager. In each case, instruction evidence of training, including the targets achieved, must be prepared by the trainer at the delivering plant and by the trainee. If he has not completed all of the training content, a decision is made on whether to extend the training measure or carry out further training at the receiving plant.

F. Intermediate Reports for the Steering Committee

If the project status is critical, an intermediate report must be prepared for the steering committee. The intermediate report is a brief overview of the transfer project and informs the steering committee of the project status. The intermediate report content: current project status, highlight deviations from the plan, indicate countermeasures and reasons, reference to potential risks.

G. End of the Project

As soon as all of the relevant transfer activities in the project plan/activity plan are completed and the audit measures have been implemented, the general project coordinator must prepare a final report. The final report content: status of activities, checklist points and targets, planning (nominal), transfer process, project results (actual), other activities, including responsibilities, conclusion/ empirical values, findings for other projects.

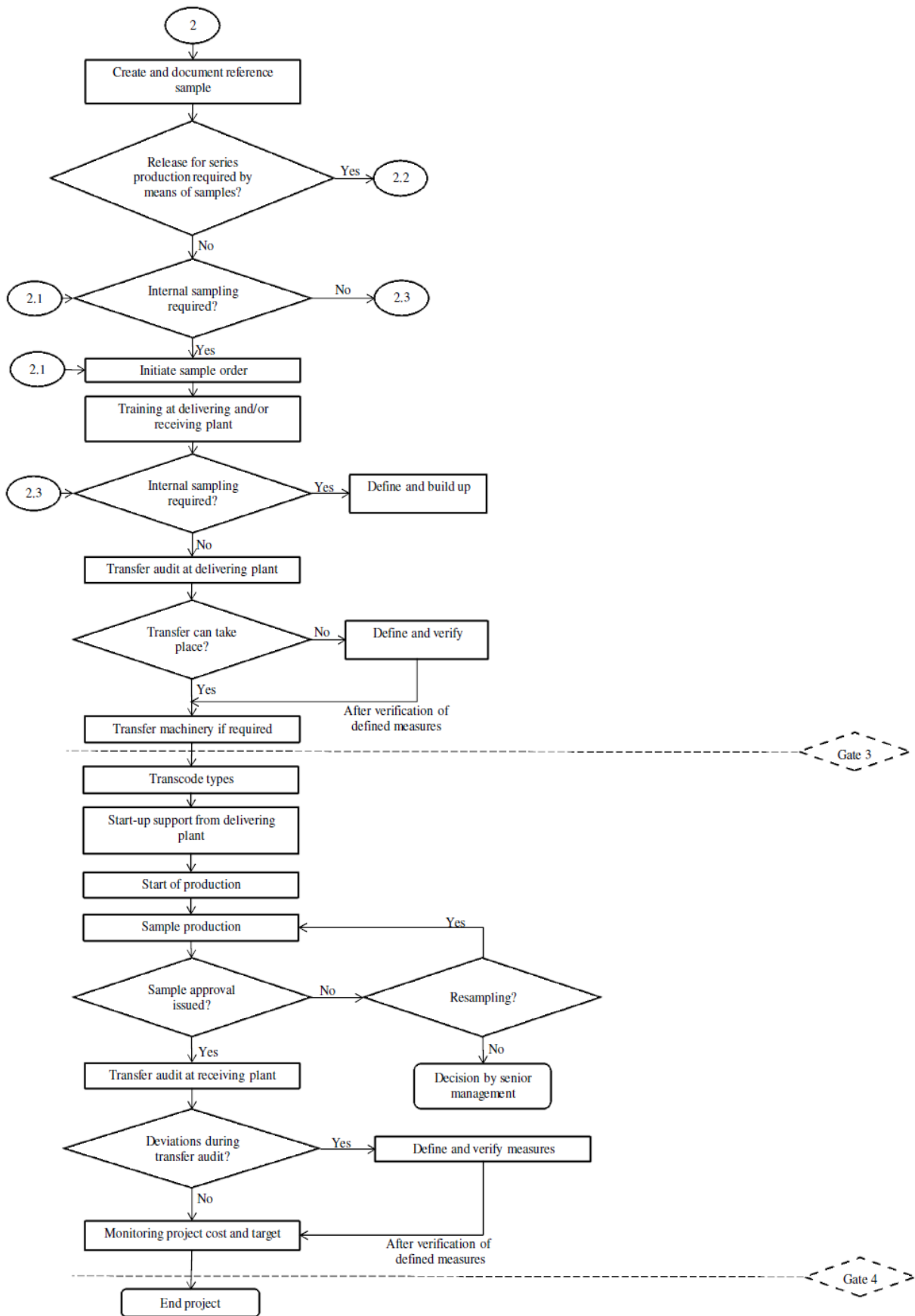


Fig. 2. Project Transfer

V. CASE STUDY

The case study presented in this paper, was conducted in 2013 in an automotive company “X”.

The study followed the steps needed for a project transfer of four different products made on the same production machine. All costs of project transfer are described in table 1.

Table 1. Costs of project transfer

Project Transfer							
Cost of labor							
Actual situation				Proposed situation			
	2013	2014	2015		2013	2014	2015
Annual volume	30600	24250	11000	Kapacitate	30600	24250	11000
Time of processing [min/pcs]	0.285	0.285	0.285	Time of processing [min/pcs]	0.688	0.688	0.688
Total time of production [min]	8721	6911	3135	Total time of production [min]	21053	16684	7568
Time of adjustment / shift [min]	30	30	30	Time of adjustment / shift [min]	10	10	10
MPH (labour cost per min)	0.06	0.06	0.06	MPH (labour cost per min)	0.06	0.06	0.06
Total MPH saving	523	415	188	Total MPH saving	1263	1001	454
Total until end of project	1,126.04 €			Total until end of project	2,718.29 €		
Cost of material							
	2013	2014	2015		2013	2014	2015
Annual volume	30600	24250	11000	Annual volume	30600	24250	11000
Material consumption (brushes)	3	3	3	Material consumption (perii)	2	2	2
Total material	91800	72750	33000	Total material	61200	48500	22000
Stain cost [Euro/buc]	1184220	938475	425700	Stain cost [Euro/buc]	1646280	1304650	591800
Total until end of project	2,548,395 €			Total until end of project	3,542,730 €		
	2013	2014	2015		2013	2014	2015
Annual volume	30600	24250	11000	Annual volume	30600	24250	11000
Material consumption (paste)	112	112	112	Material consumption (pasta)	10	10	10
Total material	3427200	2716000	1232000	Total material	306000	242500	110000
Stain cost [Euro/kg]	2776032	2199960	997920	Stain cost [Euro/kg]	474300	375875	170500
Total until end of project	5,973,912 €			Total until end of project	1,020,675 €		
Total costs MPH			1,126 €	Total costs MPH			2,718 €
Total costs for material			8,522,307 €	Total costs for material			4,563,405 €
Total saving form costs diferece and MPH savings/year				1,319,103 €			
Total saving form costs diferece and MPH savings				3,957,310 €			

Fig. 3 describes the layout of the company, where it can see the production flow of the four products transferred, and the location of the machine transferred.

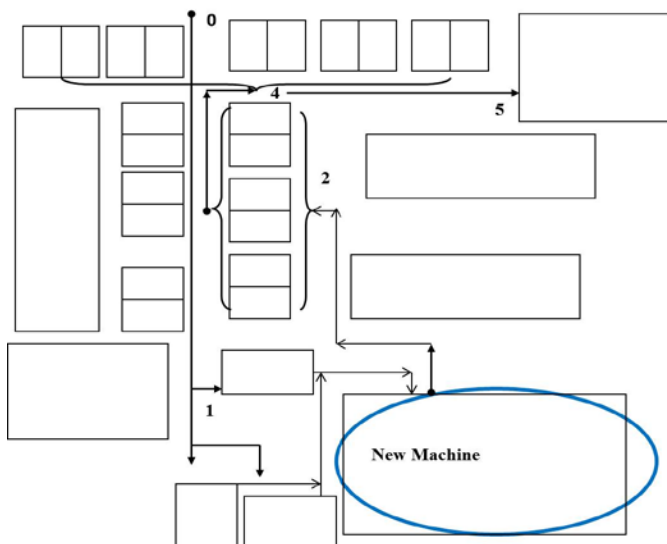


Fig. 3. Production flow of product transfer

Benefits of project transfer refers to:

- 1) Easy programming of machine (defining trajectory based on the parts geometry).
- 2) Machine ability to process complex geometries (3D – 5 axis = 3 vertical axis (roll) + 2 horizontal axes).
- 3) Minimum intervention of operator to the machine parameters, so simplicity in operation.
- 4) Minimum adjustment time.
- 5) Automatic selection of the program and working parameters by placing lock couplers with program number.

VI. CONCLUSION

Production transfers include the following conditions: change in the production location for existing products, technology in the receiving plant not available, training is required, and machinery/facilities are being transferred. Restriction of production transfers: if the risk level assessment for the production transfer indicates a significantly reduced training requirement in conjunction with the movement of machinery for identical or strongly related processes, the particular case can be processed in low-risk cases as a product

transfer. This applies under the following conditions: all four assessment categories in the risk level assessment are classified as green, commercial risk and/or application risk classified as yellow. The decision on a possible product transfer is made in consultation with the product line and planning of manufacturing locations and documented. Even if the conditions for a production transfer are not fulfilled, the particular case can be processed with project Management and planning of manufacturing locations. The decision is made in consultation with the product line and location planning and has to be documented.

The responsible project managers at the delivering plant and receiving plant are equally responsible for the success of a project (tandem concept). The overall responsibility for the transfer and start up production of the transferred products lies with the project manager at the delivering plant, except for when the receiving plant is technologically more advanced than the delivering plant. Responsibility for updating the project plan lies with the project manager at the delivering plant with main responsibility, whereas responsibility for updating the sub-projects lies with the sub-project managers. The general project coordinator must be informed of any serious status changes.

The activities for the project plan / activity plan are derived from the checklists. They represent a minimum requirement for a transfer project and contain the most important transfer items. Deviations from the checklists are documented in the gateway release with activities and dates. If a sub-project is not opened, the general project coordinator must check the checklists for these sub-projects and derive any activities, appoint the persons responsible and document these as necessary. If a checklist item is not valid for the transfer, this must be recorded in the field "comments". Furthermore, reference must be made to documents and paperwork in the "comments" field. If a checklist item cannot be processed by the submission date, the person with responsibility must define an appropriate activity and obtain a deviation approval.

In the event of deviations from targets, checklist points, audits and outstanding long-term activities, these are divided up into critical and non-critical deviations by planning of manufacturing locations and the project managers. In the event of critical deviations, the project is not closed out and a new project final date is defined between planning of manufacturing locations and the project managers. In the event of non-critical deviations, an action plan is prepared with the responsible persons. Reference is made to this action plan in the final report and a copy is then attached to the final report. After presentation of this project final report, the general project coordinator must dissolve the project team. The general project coordinator closes the project number and archives and deletes the project drive.

ACKNOWLEDGMENT

This paper is supported by the Sectoral Operational Programme Human Resources Development (SOP HRD),

financed from the European Social Fund and by the Romanian Government under the project number POSDRU/159/1.5/S/134378.

REFERENCES

- [1] D. Francasa, N. Löhdorfb and S. Minner, "Machine and labor flexibility in manufacturing networks", *International Journal of Production Economics*, vol. 131, no. 1, pp. 165–174, 2011.
- [2] D. Francas, M. Kremer, S. Minner and M. Friese, "Strategic process flexibility under lifecycle demand", *International Journal of Production Economics*, vol. 121, no. 2, pp. 427–440, 2009.
- [3] S. De Saint-Seine, "Renault steers away from one-platform, one-model plant", *Automotive News Europe*, vol. 12, no. 12, p. 17, 2007.
- [4] D. M., Brethauer, *New Product Development and Delivery: Ensuring Successful Products Through Integrated Process Management*, Saranac Lake, NY, USA, 2002.
- [5] J.S. Butler and D.V. Gibson, *Global Perspectives on Technology Transfer and Commercialization. Building Innovative Ecosystems*, Edward Elgar Publishing Limited, Cheltenham, UK, 2011.
- [6] M. Saad, *Development through Technology Transfer: Creating New Cultural Understanding*, Intellect Ltd., Bristol, GBR, 2000.
- [7] J. Sun, L.G. Debo, S. Kekre and J. Xie, "Component-Based Technology Transfer in the Presence of Potential Imitators", *Management science*, vol. 56, no. 3, pp. 536–552, 2010.
- [8] M. Adithan, *Process Planning and Cost Estimation*, New Age International, Daryaganj, Delhi, IND, 2007.
- [9] M.V. Tatikonda and G.N. Stock, "Product Technology Transfer in the Upstream Supply Chain", *The Journal of Product Innovation Management*, vol. 20, pp. 444–467, 2003.
- [10] S.C. Wheelwright and K.B. Clark, "Creating Project Plans to Focus Product Development", *Harvard Business Review*, vol. 70, no. 2, pp. 70–82, 1992.
- [11] J.A. Miller, "Changes Ahead – Prepare Now", *Research Technology Management*, vol. 38, no. 5, pp. 9–10, 1995.
- [12] H. Noori, *Managing the Dynamics of New Technology*, Englewood Cliffs, NJ: Prentice-Hall, 1990.
- [13] J.H. Sheridan, "Managing the Chain", *Industry Week*, vol. 248, no. 16, pp. 50–54, 1999.
- [14] C. Terwiesch, K. S. Chea and R. E. Bohn, *An Exploratory Study of International Product Transfer and Production Ramp-Up in the Data Storage Industry*, International Transfer and Ramp-up, 1999.

Research on the intelligent adaptive hybrid control system for an autonomous mobile robot

I. Kobersy, V. Finaev, D. Beloglazov, I. Shapovalov, J. Zargaryan, and V. Soloviev

Abstract — Here we present the results of research on the intelligent adaptive hybrid control system of the autonomous mobile robot. Modules and genetic training algorithms of the control system were also considered in this paper. The modules are neuro-fuzzy networks. Research on the training algorithms allows obtaining information about the time of optimal system parameters search, the accuracy of obtained results. For this purpose the software system was developed.

Keywords — Adaptation, genetic algorithms, neuro-fuzzy networks, uncertainty, vehicles.

I. INTRODUCTION

Control systems of autonomous mobile robots (vehicles) can be implemented by different approaches on the basis of classical control theory [1] – [6] methods or artificial intelligence [7], etc. We consider the features of the second approach practical application in this paper.

The adaptive hybrid control system (AHCS) of vehicle consists of three interrelated operating modules: the motion direction control (steering) module; the velocity control module; the module of obstacle parameters identification. The modules are three neuro-fuzzy networks (NFN₁, NFN₂, and NFN₃). To train the modules of AHCS, genetic algorithms were developed.

Efficiency of the AHCS training should be proved experimentally [8] – [11]. To conduct objective experiments, we referred to the known control tasks of autonomous mobile robots motion along the desired path with obstacle avoidance [10] – [14]. We ran the sets of experiments for the purpose of conclusions credibility [9], [15] – [18].

This work was supported by the Russian Scientific Foundation Grant 14-19-01533 and made at the Southern Federal University, Russia.

I. Kobersy is with the Southern Federal University, Rostov-on-Don, Russia (+7(8634)37-16-89; fax: +7(8634) 37-16-89; e-mail: iskobersi@gmail.com).

V. Finaev, is with the Southern Federal University, Rostov-on-Don, Russia (+7(8634)37-17-73; e-mail: finaev_val_iv@tgn.sfedu.ru).

D. Beloglazov is with the Southern Federal University, Rostov-on-Don, Russia (e-mail: d.beloglazov@gmail.com).

I. Shapovalov is with the Southern Federal University, Rostov-on-Don, Russia (+7(8634)37-16-89; e-mail: shapovalovio@gmail.com).

J. Zargaryan is with the Southern Federal University, Rostov-on-Don, Russia (+7(8634)37-16-89; e-mail: kosenko@titi.sfedu.ru).

V. Soloviev is with the Southern Federal University, Rostov-on-Don, Russia (+7(8634)37-16-89; e-mail: soloviev-tti@mail.ru).

II. EXPERIMENTAL DESIGN

The schedule of experiments was developed for the research. The set of experiments includes three experiments. For the first experiment input parameters and desired values (control actions) of the vehicle control system outputs are shown in table 1, where φ_v is the vehicle direction, V_v is the vehicle velocity and L_v is the distance to obstacle.

In fig. 1 the input parameters and the desired control system output values of ten trials (see table 1) for the first experiment are shown. We showed the schedule of the second experiment in table 2 and in fig. 2.

Table 1
Input and desired output values of vehicle control system in the first experiment

Input parameters			Desired output parameters		
φ [degree]	V [km/h]	L [m]	φ_v [degree]	V_v [km/h]	L_v [m]
10	20	40	20	20	40
15	30	60	25	25	50
20	40	80	35	25	50
25	50	100	10	40	80
30	60	120	5	45	90
35	70	140	5	50	110
40	80	160	10	70	140
45	90	180	5	80	160
5	100	200	5	85	200
10	110	165	5	80	120

Table 2
Input and desired output values of vehicle control system in the second experiment

Input parameters			Assumed output parameters		
φ [degree]	V [km/h]	L [m]	φ_v [degree]	V_v [km/h]	L_v [m]
15	120	180	10	90	135
20	20	30	25	20	35
25	30	45	45	20	35
30	40	60	35	30	45
35	50	75	25	30	45
40	60	90	15	40	65
45	70	115	10	60	75
0	80	120	10	65	80
5	90	135	5	80	95
10	100	150	5	90	135

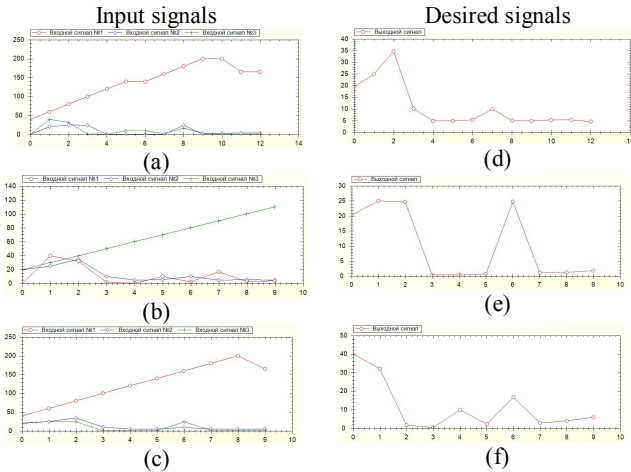


Fig. 1 Input parameters and desired output values of control system in the first experiment

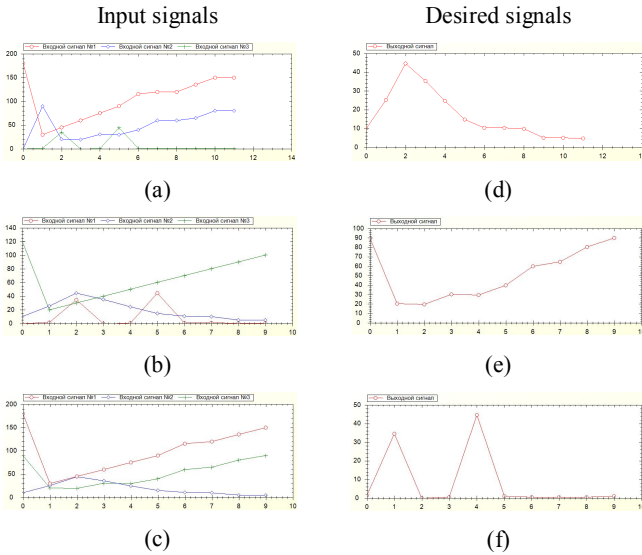


Fig. 2 Input parameters and desired output values of control system in the second experiment

The results of the third experiment are shown in table 3 and in fig. 3.

Table 3 Input and desired output values of vehicle control system in the third experiment

Input parameters			Assumed output parameters		
φ [degree]	V [km/h]	L [m]	φ_v [degree]	V_v [km/h]	L_v [m]
10	100	150	5	85	50
15	110	110	5	85	50
20	120	120	2	90	45
25	20	20	45	20	45
30	30	30	45	20	60
35	40	40	35	20	65
40	50	50	35	30	75
45	60	60	25	40	85
0	70	70	15	60	85
5	80	80	15	80	90

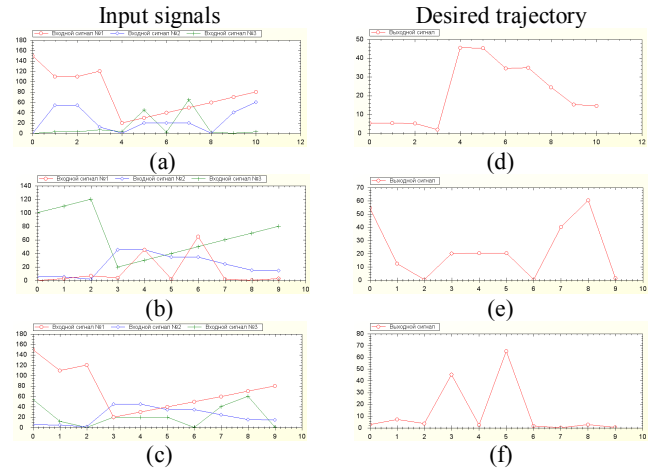


Fig. 3 Input parameters and desired output values of control system in the third experiment

In fig. 1, fig. 2, fig. 3 (a), (d) show input signals and output signal of the first module; (b), (e) show input signal and output signals of the second module; (c), (f) show input signal and output signals of the third module.

III. FEATURES OF DEVELOPED SOFTWARE

We created NeuroAndFuzzy software system for research purposes by means of the high-level language C# in the programming environment Microsoft Visual Studio. The structure of NeuroAndFuzzy system is presented in fig. 4.

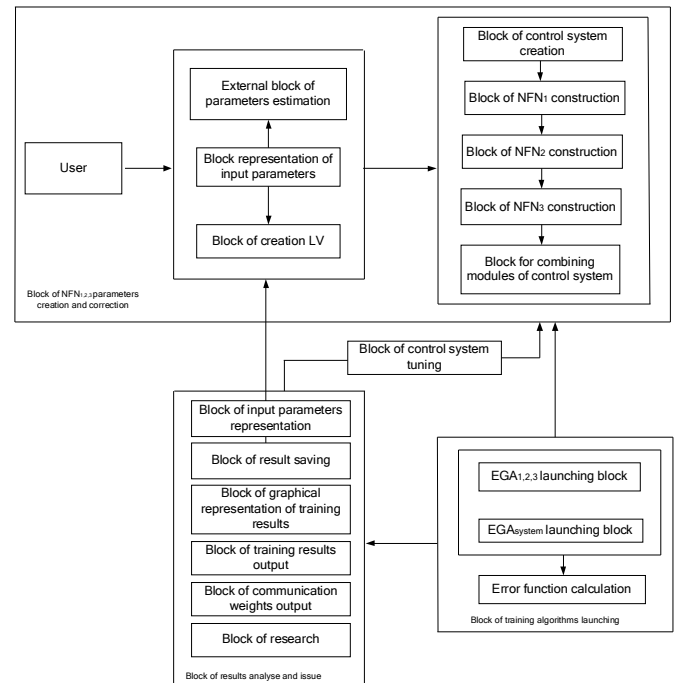


Fig. 4 Structure of NeuroAndFuzzy software application

The software system is composed of four blocks: the block of NFN_{1,2,3} parameters creation and correction; the block of training algorithms launching; the block of control system

tuning; the block of analysis and issue results. Each of these blocks contains auxiliary subblocks.

The external block of parameters estimation is the interface that allows connecting the external procedures to estimate the control system parameters and the parameters of training algorithms. The parameters are formed as a result of interaction between the external block and a user on the basis of user's preferences and experience.

The block of NFN_1 construction is the first control system module for the vehicle steering control. In this block the construction of fuzzy rules and the tuning of fuzzy inference defuzzification algorithm takes place with using a learning neural network.

The block of NFN_2 construction is the module for the vehicle velocity control. In this block the construction of fuzzy rules and the tuning fuzzy of inference defuzzification algorithm takes place on the basis of the centroid method.

The block of NFN_3 construction is the module classifying obstacles on the vehicle path. In this block the construction of fuzzy rules and the tuning of fuzzy inference defuzzification algorithm take place also on the basis of the centroid method.

The block for launching of training algorithms is assigned to implement the NFN training procedure with a learning sample formed by the user. I.e. the user inputs the parameters of motion paths $x_1, x_2, x_3, \dots, x_n$ with the information about obstacles. The user selects training method: whether to train the system by modules or in general. For training by modules three individual training algorithms for each module were developed and described in $EGA_{1,2,3}$ launching block. $EGA_{1,2,3}$ block is the subsystem for individual launching of each module. EGA_{system} block is the subsystem for launching of training algorithm of the control system in general.

The block for analyse and issue of results is assigned to gather information about the training process, the control system operation, and the system modules. Experiments with the given parameters are carried out in the research block. The weights issue block allows visualisation the intermediary and final values of weight coefficients from each module and from the whole system.

The training results block visualizes information about intermediary and final control values formed by the individual modules and the whole control system at each training step. The error output block visualizes the intermediary and final values of the objective function of the whole control system and each module.

The block of graphical representation of results shows the training results: control error, number of iterations, input and output signals of modules and control system.

The user works with the human-engineered interface allowing modifications of training algorithms, control system, modules, and reviewing of simulation results. In fig. 5 the main form of program is shown. The number of fuzzy variables can be increased, decreased, or edited in the dialogue window.

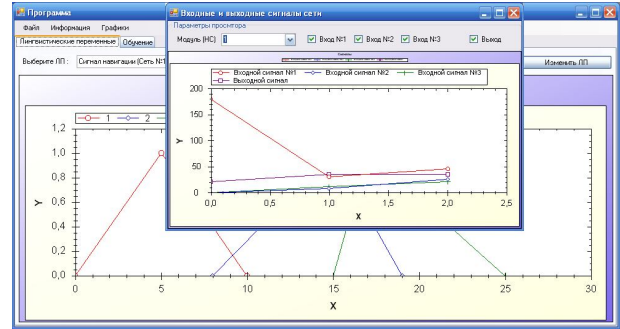


Fig. 5 Main form of NeuroAndFuzzy software application

We showed the window where the user can input motion path description in fig. 6. The windows displaying the NFN training results in a numerical and graphical form are also shown in fig. 6.

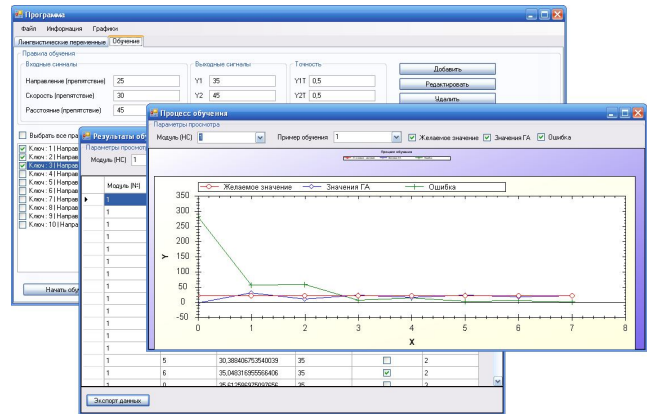


Fig. 6 Input of motion path description and training results

IV. EXPERIMENTAL RESULTS

A. Experiment 1.

We launched the our program 40 times for each of 10 test examples. Each launch was independent. Output parameters with relation to desired values were determined (see table 4) for data at the system input. These output parameters are the results of control system training.

The average iteration number for the first module is equal to 7, for the second module it is equal to 10 and for the third module it is equal to 15 iterations. Results of the first module training for the vehicle steering control (NFN_1) is shown in fig. 7. We implemented training of the NFN_2 and the NFN_3 module in the similar way.

The values of squared deviation of made decision from a desired value are shown in table 5 [19].

We showed the process of changing in the mean square error of control system per one motion path sector in fig. 8. The error is within the interval from 0 to 14×10^{-3} for the first module, the error is within the interval from 0 to 45×10^{-3} for the second module, and the error is within the interval from 0 to 0,3612 for the third module.

Table 4

Output parameters and desired values for the first experiment

Desired (Des) and output (Out) parameters of system								
φ [degree]			V [km/h]			L [m]		
It. numb.	Des	Out	It. numb.	Des	Out.	It. numb.	Des	Out
5	20	19,8	20	20	0	7	40	0
4	25	24,9	16	25	24,9	40	50	49,7
3	35	34,9	9	25	25,2	4	50	50,3
13	10	10,1	6	40	39,9	10	80	79,8
5	5	4,9	13	45	44,7	16	90	90,3
10	5	5	8	50	49,8	20	100	98,6
1	10	10,1	7	70	79,8	10	140	140
9	5	5,0	6	80	80,2	25	160	160
9	5	0	9	85	84,8	8	200	199
10	5	0	8	80	80,1	8	80	79,9

Table 5

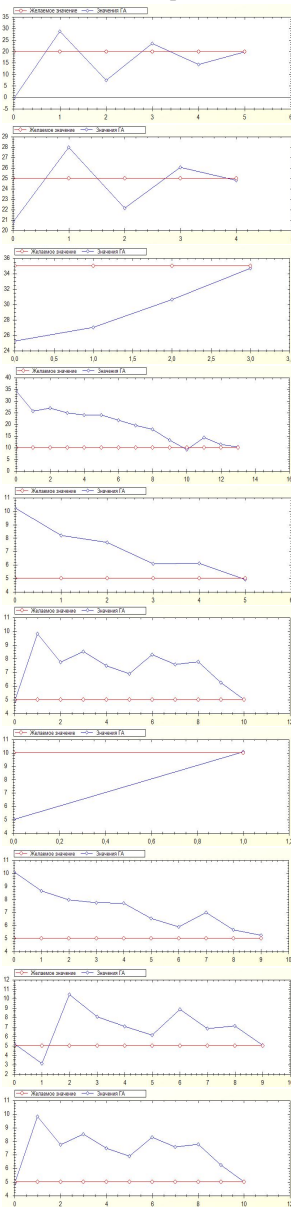
Squared deviation of made decision

Example	1	2	3	4	5
$E_1(x)$	0,014	0,01	0,004	0,003	0,005
$E_2(x)$	0	0,005	0,01	0,002	0,045
$E_3(x)$	0	0,09	0,05	0,020	0,045
Example	6	7	8	9	10
$E_1(x)$	0	0,003	0,001	0	0
$E_2(x)$	0,028	0,020	0,014	0,0288	0,008
$E_3(x)$	0,080	0,088	0,057	0,3612	0,008

B. Experiment 2

We showed the output parameters with relation to desired values for data at the system input in table 6. The average iteration number for the first module is equal to 9, for the second module it's equal to 12 and for the third module it's equal to 10 iterations. Our program allows observing the training process of each system module.

Desired value and value at module output



Average training error

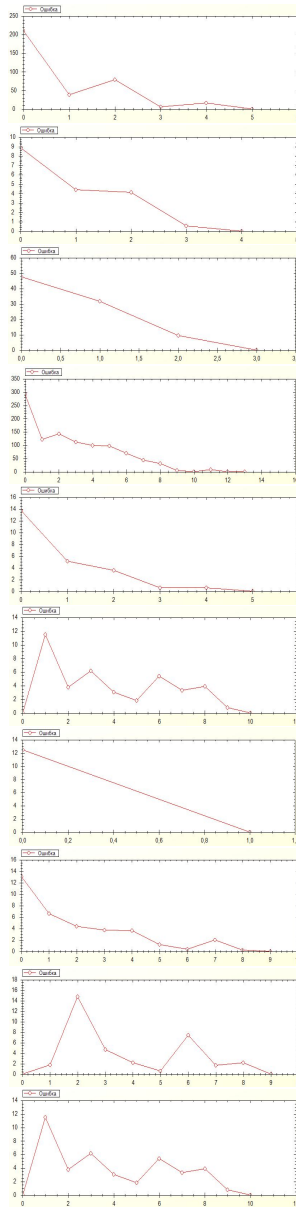


Fig. 7 Training process of the first module

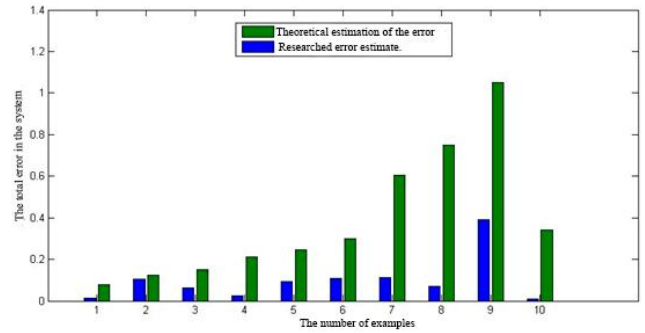


Fig. 8 Mean square error of control system per one motion path sector in the first experiment

Table 6

Output parameters and desired values for the second experiment

Desired (Des) and output (Out) parameters of system								
φ [degree]			V [km/h]			L [m]		
It. numb.	Des	Out	It. numb.	Des	Out.	It. numb.	Des	Out
15	10	10	31	90	89,3	17	135	134
8	25	24,9	7	20	20	8	35	35
2	45	44,7	8	20	30,0	2	35	34,9
7	35	35,1	7	30	29,9	4	45	45,0
12	25	24,1	5	30	30	12	45	44,9
6	15	14,3	5	40	40	12	65	65
7	10	10,3	4	60	60,1	3	75	75,0
6	10	9,85	12	65	60,0	13	80	80
16	5	5	30	80	79,9	8	95	94,8
7	5	5,23	7	90	89,1	17	135	134

Fig. 9 shows the changing of mean square error of the control system per one motion path sector in the second experiment. The error is within the interval from 0 to 0,245 for the first module, the error is within the interval from 0 to 0,378 for the second module, and the error is within the interval from 0 to 0,016 for the third module [19].

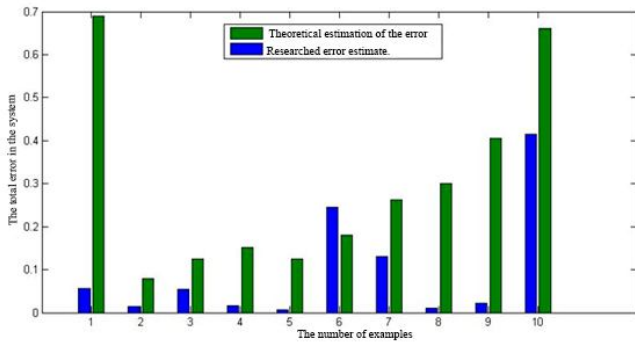


Fig. 9 The mean square error of the control system per one motion path sector in the second experiment

C. Experiment 3

We gave the experimental results of the adaptive control system operation in table 7. The average iteration number is equal to 7 for the first module, it's equal to 10 for the second module and it's equal to 10 iterations for the third module.

We showed the changing of mean square error of the control system per one motion path sector in fig. 10. The error is within the interval from 0 to 0,016 for the first module, the error is within the interval from 0 to 0,01 for the second module, and the error is within the interval from 0 to 0,02 for the third module.

Table 7

Output parameters and desired values for the third experiment

Desired (Des) and output (Out) parameters of system								
φ [degree]			V [km/h]			L [m]		
It. numb.	Des	Out	It. numb.	Des	Out.	It. numb.	Des	Out
12	5	5.02	8	85	85	8	50	50
5	5	5	25	85	85,0	11	50	50,6
4	2	1,93	12	90	90	2	45	45,2
11	45	45	16	20	20,0	4	45	45,0
7	45	45,1	3	20	19,8	10	60	60
5	35	34,8	2	20	19,0	14	65	65,0
4	35	34,9	3	30	30,2	15	75	75,0
13	25	24,9	13	40	40	11	85	85,0
4	15	15,1	13	60	60	22	85	85
9	15	14,9	9	80	80	6	90	90,1

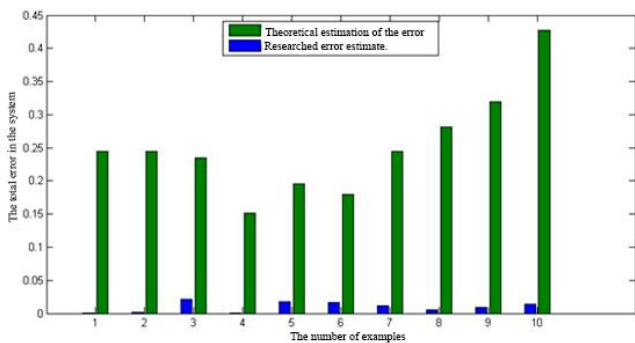


Fig. 10 Mean square error of control system per one motion path sector in the third experiment

The best results of the intelligent AHCS operation are shown in tables 1 - 7. We ran experiments for each test path 40 times.

V. CONCLUSIONS

We developed NeuroAndFuzzy program as the information support system. This information support system allows researching the training algorithms and the operation of intelligent adaptive hybrid control system for the vehicle motion control. We scheduled experiments on the developed software system simulating the control system with a training algorithm of the system.

We carried out some experiments and processed statistical data. The results of the system and genetic training algorithm operation were received in graphical form.

Developed software can be applied for design and research on the vehicle control by the AHCS with genetic tuning. The research has revealed that the intelligent learning AHCS gets the desired results with the permissible tolerance of not more than 0,5 %.

REFERENCES

- [1] Pshikhopov V.Kh., Medvedev M.Yu., Gaiduk A.R., Gurenko B.V Control system design for autonomous underwater vehicle // 2013, Latin American Robotics Symposium, pp. 77-82
- [2] Pshikhopov V., Sergeev N., Medvedev M., Kulchenko A. The design of helicopter autopilot // 2012, SAE Technical Papers
- [3] Pshikhopov V., Medvedev M., Kostjukov V., Fedorenko R. et al. Airship Autopilot Design // 2011, SAE Technical Paper.
- [4] Pshikhopov V.Kh., Ali A.S. Hybrid motion control of a mobile robot in dynamic environments // 2011, International Conference on Mechatronics, ICM 2011, pp. 540-545
- [5] Pshikhopov V.K., Medvedev M.Yu., Gurenko B.V. Homing and Docking Autopilot Design for Autonomous Underwater Vehicle // 2014, Applied Mechanics and Materials, pp. 490-491.
- [6] Pshikhopov, V.Kh., Krukhmalev V.A., Medvedev M.Yu, Fedorenko R.V., Kopylov S.A., Budko A.Yu., Chufistov V.M. Adaptive control system design for robotic aircrafts // 2013, IEEE Latin American Robotics Symposium, pp. 67-70.
- [7] Рутковская Д., Пилиньский М., Рутковский Л. Нейронные сети, генетические алгоритмы и нечеткие системы: Пер. с польск. И.Д. Рудинского. – М.: Горячая линия – Телеком. 2004. - С. 452.
- [8] Cheng J.L., Yong J.X. Design of Neuro-Fuzzy systems using a hybrid evolutionary learning algorithm // 2007, Journal of information science and engineering 23, 463-477.
- [9] Ridwan M. A parallel genetic algorithm-based tsf-fuzzy system for dynamic car-following modeling // 2009, European Journal of Scientific Research. N.4. - pp. 627-641.
- [10] Pshikhopov V.K., Medvedev M.Yu., Gurenko B.V. Homing and Docking Autopilot Design for Autonomous Underwater Vehicle // 2014, Applied Mechanics and Materials, 490-491, 700.
- [11] Pshikhopov V.Kh., Ali A.S. Hybrid control of a mobile robot in dynamic environments // Proceedings of 2011 IEEE International Conference on Mechatronics, 2011. P. 540-545.
- [12] Neydorf R., Krukhmalev V., Kudinov N., Pshikhopov V. Methods of statistical processing of meteorological data for the tasks of trajectory planning of MAAT feeders // 2013, SAE Technical Papers.
- [13] Pshikhopov V., Medvedev M., Neydorf R., Krukhmalev V. et al. Impact of the feeder aerodynamics characteristics on the power of control actions in steady and transient regimes // 2012, SAE Technical Papers.
- [14] Pshikhopov V., Krukhmalev V., Medvedev M., Neydorf R. Estimation of energy potential for control of feeder of novel cruise/feeder MAAT // 2012, SAE Technical Papers.
- [15] Коберси И.С. Оценка погрешности адаптивной гибридной обучаемой системы управления транспортными средствами // 2011, Международный семинар «Системный анализ, управление и

- обработка информации». - Ростов-на-Дону: Изд. центр Донск. гос. техн. ун-та. - С. 212 - 216.
- [16] Коберси И.С. Скубилин М.Д., Нелина С.Н., Бублей С.Е., Балабаев Р.И. Элементы и устройства систем управления. - Таганрог, изд-во ТТИ ЮФУ, 2010 г. – 397 с.
- [17] Pshikhov V.Kh., Medvedev M.Yu. Document Block design of robust control systems by direct Lyapunov method // 2011, IFAC Proceedings Volumes (IFAC-PapersOnline), pp. 10875-10880.
- [18] Pshikhov V.Kh., Medvedev M.Yu. Robust control of nonlinear dynamic systems // 2010, IEEE ANDESCON Conference Proceedings, ANDESCON
- [19] Коберси И.С. Разработка интеллектуальной гибридной адаптивной обучаемой системы управления транспортным средством с генетической настройкой // 2010, XI всероссийская научно-техническая конференция и школа молодых ученых, аспирантов и студентов «Научные исследования и разработки в области авиационных, космических и транспортных систем», АКТ. Москва
- [20] Gang L., Thomas M. Design for self-organizing fuzzy neural networks based on genetic algorithms // 2006, IEEE Transactions on fuzzy systems, Vol. 14, N. 6, December. - pp. 755-776.

Fuzzy MCDM approach to evaluate wastewater treatment alternatives

Mehtap Dursun

Abstract—Wastewater is composed of liquid or water-carried wastes originating in the sanitary conveniences of dwellings, commercial or industrial facilities. Untreated wastewater has serious effects on human health and natural environment. For this reason, selection of the appropriate wastewater treatment alternative is vital for sustainable development. In this paper, a fuzzy multi-criteria decision making approach integrating DEAMATEL method and fuzzy TOPSIS is proposed for identifying the most suitable wastewater treatment alternative.

Keywords—DEMATEL, Fuzzy MCDM, TOPSIS, Wastewater treatment

I. INTRODUCTION

TODAY, wastewater management is considered as one of the most important environmental problem faced by the developing countries [1]. The main objective of wastewater treatment (WWT) is generally to allow human and industrial effluents to be disposed of without danger to human health or natural environment [2]. Selection of appropriate WWT technologies that enable sustainable development presents a challenge to national, regional and local policy makers [3].

Recent developments provide many WWT technology options. The most widely used WWT technology is the conventional activated sludge process (ASP). Other technologies have also been developed that use various treatment processes (aerobic or anaerobic, highly mechanized or not highly mechanized, etc) such as trickling filters and biotowers, upflow anaerobic sludge blanket reactors, rotating biological contactors (RBC), aerated lagoons, sequential batch reactor (SBR) [4]. Apart from these, natural WWT systems including stabilization ponds, duckweed ponds, constructed wetlands, are also employed [5]. The treatment of wastewater is usually based on a multiple stage approach as shown in Tale 1 [6]. Generally, wastewater treatment plants (WWTPs) have common preliminary and primary treatment stages. Secondary stages are more divers and they are usually the focus of alternative methods.

TABLE I
LEVELS OF WASTEWATER TREATMENT [6]

Treatment Level	Description
Preliminary	Removal of wastewater constituents such as rags, sticks, floatables, grit, and grease that may cause maintenance or operational problems with the treatment operations, processes, and ancillary systems
Primary	Removal of a portion of the suspended solids and organic matter from the wastewater
Advanced primary	Enhanced removal of suspended solids and organic matter from the wastewater. Typically accomplished by chemical addition or filtration
Secondary	Removal of biodegradable organic matter (in solution or suspension) and suspended solids. Disinfection is also typically included in the definition of conventional secondary treatment
Secondary with nutrient removal	Removal of biodegradable organics, suspended solids, and nutrients (nitrogen, phosphorus, or both nitrogen and phosphorus)
Tertiary	Removal of residual suspended solids (after secondary treatment), usually by granular medium filtration or microscreens. Disinfection is also typically a part of tertiary treatment. Nutrient removal is often included in this definition
Advanced	Removal of dissolved and suspended materials remaining after normal biological treatment when required for various water reuse applications

This work was supported by Galatasaray University Research Fund.

M. Dursun is with the Industrial Engineering Department, Galatasaray University, Istanbul 34349, Turkey (corresponding author to provide fax: +90-212-2595557; e-mail: mdursun@gsu.edu.tr).

This paper focuses on the detailed evaluation of WWT alternatives to determine the most suitable. WWT alternative selection problem involves the consideration of conflicting criteria incorporating vagueness and imprecision. The objective of this study is to propose a fuzzy multi-criteria decision making approach that integrates making trial and evaluation laboratory (DEMATEL) method and fuzzy TOPSIS (technique for order preference by similarity to ideal solution) for identifying the most suitable WWT alternative.

In the literature, there are few papers that employ different multi-criteria decision making (MCDM) approaches to evaluate WWT alternatives. Aragonés-Beltrán et al. [7] used analytic hierarchy process (AHP) and PROMETHEE methods for the selection of WWT alternative. Bottera et al. [8] considered AHP and analytic network process (ANP) for prioritizing different WWT technologies. Karimi et al. [9] presented the applications of AHP and fuzzy AHP for selecting the most appropriate WWT process. Sala-Garrido et al. [10] employed data envelopment analysis (DEA) for techno-economic efficiency comparison of different WWT technologies. Kalbar et al. [3] ranked WWT technologies used for the treatment of municipal wastewater in India by applying TOPSIS method. Srdjevic et al. [11] evaluated WWT methods for the metal industry in Serbia using AHP. Lately, Kalbar et al. [12] developed an MCDM approach that considered both qualitative and quantitative criteria for ranking WWT technologies.

The rest of the paper is organized as follows. Section 2 and Section 3 delineate DEMATEL method and fuzzy TOPSIS, respectively. Section 4 presents the application of the proposed methodology to WWT technology selection problem. The concluding remarks are given in the final section.

II. DEMATEL METHOD

The DEMATEL method was intended to study and resolve the complicated and intertwined problem group. This method could improve understanding of the specific problem, the cluster of intertwined problems, and contribute to identification of workable solutions by a hierarchical structure. Four major steps of DEMATEL method can be summarized as follows [13].

Step 1. Compute the average matrix.

Respondents are asked to indicate the direct influence that they believe each factor j exerts on each factor k of the others, as indicated by a_{kj} . From any group of direct matrices of respondents, it is possible to derive an average matrix A .

Step 2. Calculate the normalized initial direct-relation matrix.

The normalized initial direct-relation matrix D can be obtained as $D=s.A$, where

$$s = \min \left[\frac{1}{\max_{1 \leq j \leq n} \sum_{j=1}^n |a_{jk}|}, \frac{1}{\max_{1 \leq j \leq n} \sum_{j=1}^n |a_{jk}|} \right] \quad (1)$$

Step 3. Calculate the total relation matrix.

The total relation matrix T is defined as $T = D(I - D)^{-1}$, where I is the identity matrix. Define r and c be $n \times 1$ and $1 \times n$ vectors representing the sum of rows and sum of columns of the total relation matrix T , respectively. Suppose r_j be the sum of j th row in matrix T , then r_j summarizes both direct and indirect effects given by factor j to the other factors. If c_k denotes the sum of k th column in matrix T , then c_k shows both direct and indirect effects by factor k from the other factors. When $j = k$, the sum $(r_j + c_k)$ shows the total effects given and received by factor j . Thus, $(r_j + c_k)$ indicates the degree of importance for factor j in the entire system. On the contrary, the difference $(r_j - c_k)$ represents the net effect that factor j contributes to the system. Specifically, if $(r_j - c_k)$ is positive, factor j is a net cause, while factor j is a net receiver or result if $(r_j - c_k)$ is negative.

Step 4. Set up a threshold value to obtain the digraph.

III. FUZZY TOPSIS

TOPSIS, which was proposed by Hwang and Yoon [14], is a widely accepted multi-attribute decision making technique. It is based on the intuitive principle that the preferred alternative should have the shortest distance from the ideal solution and the farthest distance from the anti-ideal solution [15].

In the following, fuzzy TOPSIS method that is apt to handle fuzzy data as well as crisp data is presented.

Step 1. Identify the alternatives ($A_i, i=1,2,\dots,m$) and required selection criteria ($C_j, j=1,2,\dots,n$), and construct the decision matrix that denote the fuzzy assessments corresponding to qualitative criteria and the crisp values corresponding to quantitative criteria for the considered alternatives.

Step 2. Normalize the decision matrix to obtain the unit-free and comparable criteria values. If there exist crisp data x_{ij} , it can be represented as $\tilde{x}_{ij} = (x_{ij}^1, x_{ij}^2, x_{ij}^3)$ in triangular fuzzy number format, where $x_{ij} = x_{ij}^1 = x_{ij}^2 = x_{ij}^3$. The normalized values regarding benefit ($j \in B$) as well as cost criteria ($j \in C$) are calculated employing linear scale transformation as

$$\tilde{r}_{ij} = \begin{cases} \left(\frac{x_{ij}^1 - x_j^-}{x_j^* - x_j^-}, \frac{x_{ij}^2 - x_j^-}{x_j^* - x_j^-}, \frac{x_{ij}^3 - x_j^-}{x_j^* - x_j^-} \right), & j \in B \\ \left(\frac{x_j^* - x_{ij}^3}{x_j^* - x_j^-}, \frac{x_j^* - x_{ij}^2}{x_j^* - x_j^-}, \frac{x_j^* - x_{ij}^1}{x_j^* - x_j^-} \right), & j \in C \end{cases} \quad (2)$$

where $x_j^* = \max_i x_{ij}^3$, $x_j^- = \min_i x_{ij}^1$.

Step 3. Compute the weights of criteria, $\tilde{w}_j, j=1,2,\dots,n$, using DEMATEL method.

Step 4. Calculate the weighted normalized fuzzy decision matrix as

$$\tilde{v}_{ij} = \tilde{w}_j \otimes \tilde{r}_{ij} \quad (3)$$

Step 5. Define the ideal solution $\tilde{A}^* = (\tilde{v}_1^*, \tilde{v}_2^*, \dots, \tilde{v}_n^*)$ and the anti-ideal solution $\tilde{A}^- = (\tilde{v}_1^-, \tilde{v}_2^-, \dots, \tilde{v}_n^-)$, where $\tilde{v}_j^* = (1, 1, 1)$ and $\tilde{v}_j^- = (0, 0, 0)$ for $j = 1, 2, \dots, n$.

Step 6. Calculate the distances from the ideal and the anti-ideal solutions (D_i^* and D_i^- , respectively) for each alternative A_i as

$$D_i^* = \sum_{j=1}^n d(\tilde{v}_{ij}, \tilde{v}_j^*) \quad (4)$$

$$D_i^- = \sum_{j=1}^n d(\tilde{v}_{ij}, \tilde{v}_j^-) \quad (5)$$

where distance between two triangular fuzzy numbers $\tilde{A} = (a_1, a_2, a_3)$ and $\tilde{B} = (b_1, b_2, b_3)$ can be calculated as

$$d_v(\tilde{A}, \tilde{B}) = \sqrt{\frac{1}{3} [(a_1 - b_1)^2 + (a_2 - b_2)^2 + (a_3 - b_3)^2]} \quad (6)$$

Step 7. Calculate the proximity of the alternatives to the ideal solution, P_i^* , by considering the distances from ideal and anti-ideal solutions as

$$P_i^* = \frac{D_i^-}{(D_i^* + D_i^-)} \quad (7)$$

Step 8. Rank the alternatives according to P_i^* values in descending order. Identify the alternative with the highest P_i^* as the best alternative.

IV. APPLICATION OF THE MCDM FRAMEWORK TO WASTEWATER TREATMENT ALTERNATIVE SELECTION PROBLEM

As a result of discussions with experts, four WWT alternatives are determined as

- A_1 : Activated sludge (AS),
- A_2 : Aerated lagoon (AL),
- A_3 : Sequential batch reactor (SBR),
- A_4 : Constructed wetlands (CWs).

Nine criteria relevant to WWT alternative selection are identified as

- C_1 : Cost,
- C_2 : Global warming,
- C_3 : Eutrophication potential,
- C_4 : Land requirement,
- C_5 : Manpower requirement,
- C_6 : Reliability,
- C_7 : Sustainability,
- C_8 : Flexibility.

TABLE II
LINGUISTIC SCALE FOR DETERMINING THE DIRECT INFLUENCE MATRIX AMONG CRITERIA

No influence	0
Low influence	1
Moderate influence	2
Strong influence	3
Extreme strong influence	4

The decision-maker used the linguistic scale given in Table 2, to determine the direct influence matrix among criteria, whereas they utilized the linguistic term set depicted in Figure 1 to denote the ratings of alternatives with respect to qualitative criteria.

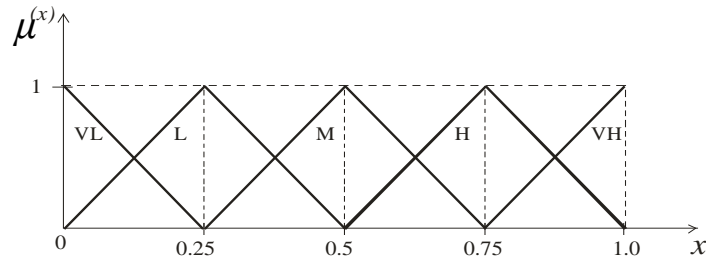


Figure 1: A linguistic term set where VL = (0, 0, 0.25), L = (0, 0.25, 0.5), M = (0.25, 0.5, 0.75), H = (0.5, 0.75, 1), VH = (0.75, 1, 1)

The average matrix A is determined as in Table 3.

TABLE III
AVERAGE MATRIX

	C_1	C_2	C_3	C_4	C_5	C_6	C_7	C_8
C_1	0	1	1	4	4	3	2	2
C_2	4	0	4	1	1	3	4	3
C_3	4	3	0	1	1	4	4	3
C_4	4	1	1	0	2	2	2	2
C_5	4	1	1	2	0	2	2	2
C_6	3	4	3	3	3	0	4	3
C_7	3	4	3	3	3	4	0	4
C_8	3	3	3	2	2	3	3	0

By employing DEMATEL method, the weights of the criteria are determined as $C_1=0.15$, $C_2=0.13$, $C_3=0.12$, $C_4=0.08$, $C_5=0.08$, $C_6=0.16$, $C_7=0.16$, $C_8=0.12$.

$C_1, C_2, C_4,$ and C_5 are considered as cost criteria, whereas $C_3, C_6, C_7,$ and C_8 are considered as benefit criteria. Normalized ratings of alternatives are computed via Eq. (2). Then, employing Eq. (3), weighted normalized fuzzy decision matrix is constructed. The distances from the ideal and the anti-ideal solutions for each alternative are computed using Eqs. (4-6). Finally, the ranking index for each alternative is computed using Eq. (7). Table 3 summarizes the results obtained using the fuzzy decision framework. According to the

results of the analysis aerated lagoon is determined as the most suitable WWT alternative, which is followed by aerated lagoon. Sequential batch reactor is ranked at the bottom due to high global warming effect and low eutrophication potential.

TABLE IV
RANKING OF WWT ALTERNATIVES

Alternatives	D_i^*	D_i^-	P_i^*	Rank
A_1	7.441	0.594	0.074	2
A_2	7.352	0.685	0.085	1
A_3	7.528	0.505	0.063	4
A_4	7.513	0.532	0.066	3

V. CONCLUDING REMARKS

Untreated wastewater has serious environmental and health hazards effects. Thus, wastewater must immediately be conveyed away from its generation sources and treated appropriately before final disposal [16]. WWT alternative selection problem, which considers several individual attributes exhibiting vagueness and imprecision, may be regarded as a highly important decision-making problem. The classical MCDM methods that consider deterministic or random processes cannot effectively handle decision-making problems including imprecise and linguistic information. In this paper, a fuzzy multi-criteria decision making algorithm, which combine DEMATEL method and fuzzy TOPSIS, is proposed to rectify the problems encountered when using classical decision making methods in decision making problems. Future research might focus on applying the decision frameworks presented in here to real-world group decision making problems in diverse disciplines.

REFERENCES

- [1] The Post 2015 Water Thematic Consultation – Wastewater Management & Water Quality.
- [2] K. Gomes, *Wastewater Management*, Jaipur, IND: Global Media, 2009.
- [3] P. P. Kalbar, S. Karmakan, S. R. Asolekar, "Selection of an appropriate wastewater treatment technology: A scenario-based multiple-attribute decision-making approach", *Journal of Environmental Management*, vol. 113, pp. 158-169, 2012.
- [4] Metcalf and Eddy, Inc., *Wastewater Engineering: Treatment, Disposal, and Reuse*, fourth ed. McGraw Hill Inc., 2003.
- [5] S. J. Arceivala, S. L. Asolekar, *Wastewater treatment for pollution control and reuse*, McGraw Hill, New Delhi, 2007.
- [6] Wastewater engineering: an overview, www.mhhe.com/engcs/civil/metcalf/information/chapter1.pdf
- [7] P. Aragonés-Beltrán, J. A. Mendoza-Roca, A. Bes-Piá, M. García-Melón, E. Parra-Ruiz, "Application of multicriteria decision analysis to jar-test results for chemicals selection in the physical-chemical treatment of textile wastewater", *Journal of Hazardous Materials*, vol. 164, pp. 288-29, 2009.
- [8] M. Bottero, E. Comino, V. Riggio, "Application of the analytic hierarchy process and the analytic network process for the assessment of different wastewater treatment systems", *Environmental Modelling & Software*, vol. 26, pp. 1211-1224, 2011.
- [9] A. R. Karimi, N. Mehrdadi, S. J. Hashemian, G. R. Nabi Bidhendi, R. Tavakkoli Moghaddam, "Selection of wastewater treatment process based on the analytical hierarchy process and fuzzy analytical hierarchy

- process methods", *Int. J. Environ. Sci. Tech.*, vol. 8 (2), pp. 267-280, 2011.
- [10] R. Sala-Garridoa, M. Molinos-Senante, F. Hernández-Sancho, "Comparing the efficiency of wastewater treatment technologies through a DEA metafrontier model", *Chemical Engineering Journal*, vol. 173, pp. 766– 772, 2011.
- [11] Z. Srdjevic, M. Samardzic, B. Srdjevic, "Robustness of AHP in selecting wastewater treatment method for the coloured metal industry: Serbian case study", *Civil Engineering and Environmental Systems*, vol. 29 (2), pp. 147-161, 2012.
- [12] P. P. Kalbar, S. Karmakan, S. R. Asolekar, "The influence of expert opinions on the selection of wastewater treatment alternatives: A group decision-making approach", *Journal of Environmental Management*, vol. 128, pp. 844-851, 2013.
- [13] G. H. Tzeng, W. H. Chen, R. Yu, M. L. Shih, "Fuzzy decision maps: a generalization of the DEMATEL methods," *Soft Comput*, Vol. 14, pp. 1141-1150, 2010.
- [14] C. L. Hwang, K. Yoon, *Multiple Attribute Decision Making: Methods and Applications*, Springer, Heidelberg, 1981.
- [15] K. P. Yoon, C. L. Hwang, *Multiple attribute decision making: An introduction. Sage University Papers series on Quantitative Applications*, 07-104, Thousand Oaks, 1995.
- [16] *Wastewater treatment technologies: a general review*, United Nations, New York, 2003.

Mehtap Dursun is an assistant professor of Industrial Engineering at Galatasaray University, Turkey. She holds BS, MS, and PhD degrees in Industrial Engineering from Galatasaray University. Her areas of interest include quality function deployment, fuzzy optimization, and multi-criteria decision making with special focus on waste management, personnel selection, and supplier selection. She has coauthored articles that appeared in *Expert Systems with Applications*, *Resources Conservation and Recycling*, *International Journal of Production Research*, and *Applied Mathematical Modelling*.

Magnetic Hysteresis under an Applied Continuous External Magnetic Field

Hamza HOUASSINE¹ Djelloul MOUSSAOUI² Samir MOULAHOU¹

¹Electrical and Automatic Research Laboratory (L.R.E.A) University of Medea Algeria

²Laboratory Of Electromagnetic Systems, Emp, Bordj El Bahri, Algiers, Algeria

Abstract: Electromagnetic systems such as AC machines have to support supply voltages containing a DC component which induces both an increase of the total magnetic losses and the premature saturation of the magnetic core. In the present paper, we present an approach for predicting the hysteresis loop of a magnetic material such as non oriented FeSi 3% which is subjected to a DC bias. The measurements are carried out with a bench test built around an Epstein frame. The material is excited with a damped sinusoidal flux density superimposed to a known continuous field. We obtain superimposed asymmetrical hysteresis loops. The cycles are modeled via the Preisach Model (PM) [1], which provides both a mathematical model for the B(H) curve and an analytical approach which identifies and predicts the parameter behavior needed by the PM.

Key words: *Hysteresis, Preisach Model, continuous field, magnetic material.*

1. Introduction

The magnetic properties of soft material such as Fesi 3% are very sensitive to both applied mechanical and thermal stresses as well as the external electromagnetic field. Magnetic materials such as Fesi 3% are commonly used in the manufacturing of electromagnetic devices which are supplied by a sinusoidal electrical network. The flux density is symmetrical, a very important property for the good functioning of this type of device.

Many devices operating in the low- and medium-frequency range, ranging from rotating machinery (dc machines, permanent magnet motor) to magnetic cores in electronic drives, are employed under special supply conditions, which may include dc bias and generally non-sinusoidal induction with local minima. The prediction of the core losses under such conditions, which are far removed from the standard conditions required for conventional magnetic testing of materials [1], may present special difficulties, inherent to the general features of hysteresis (e.g. Non-local memory effects) and their evolution with the magnetizing frequency [2].

This work attempts to investigate the function $b(h)$ take account the continue component of the excitation. The pm model is chosen because, on one hand, it merely accounts for all the parameters involved in process of magnetization of magnetic materials such as saturation, minor cycles, etc, and on the other hand, the simplicity of its implementation.

In order to validate the simulations, we

carried out tests on two types of sheets: Fesi 3% with oriented-grains 0.5mm thickness on the Epstein bench.

2. Preisach Model

The classical Preisach model together with quite a few generalizations has been efficiently applied to describe hysteresis phenomena under various conditions [1,2]. It consists in a set of hysteresis operators (ideal switches with rectangular characteristics) and features some very favourable properties: fast and memory sparing numerical implementation based on the everett integrals, well defined and reliable experimental identification procedure based on measurement of first order reversal curves. It can adequately describe the static magnetic behavior of various ferromagnetic materials. Combined with eddy current computation, the dynamic operation of homogeneous materials or thick parts having randomly oriented, tiny domains can be simulated with acceptable accuracy [3]. This method fails however to encompass the effects of domain wall displacement [5], important in the case of electrical steel sheets and it is also costly—in terms of computing time and memory requirement. Preisach represented the magnetic state of magnetic material, at any time, has two possible states of magnetization ($m=1$ and $m=-1$), defined by a rectangular elementary cycle on the input-output diagram. The latter is characterized by the inversion fields of α and β (with $\alpha \geq \beta$) for which

there is an irreversible transition from the high state ($m=1$) to the low state $m=-1$ and vice versa; that is, α and β correspond to up and down switching values of the input, respectively. The calculation of total magnetization requires knowledge of the statistical distribution of the elementary cycles. This function is called Preisach function [1], [2][4]. Assuming the input and output variables as function of time, the Preisach function of magnetization resulting from the application of an $h(t)$ field is given by:

$$M(t) = \iint \rho(\alpha, \beta) \Phi_{\alpha, \beta}[H(t)] d\alpha d\beta \quad (1)$$

With: (the value is $(+1)$ if $h=\alpha$ and (-1) if $h=\beta$)

$\rho(\alpha, \beta)$: Density function—also referred as Preisach measure-. It depends on the nature of the material [1].

$\Phi_{\alpha, \beta}[H(t)]$: Operator associated to the magnetic entities referred to as elementary Preisach hysteron operator.

1.1. Geometrical Interpretation of the Model

There is a known one-to-one correspondence between the operator $\Phi_{\alpha, \beta}[H(t)]$ and the points (α, β) located in the half plan $\alpha \geq \beta$. Geometrically, S can be subdivided into two parts, which are separated by the border $l(t)$, which is itself time dependent. The surface $S_+(t)$ represents all the entities whose state of magnetization is $(+1)$, while $S_-(t)$ represents those with state of magnetization (-1) . Model (1) can then be written in the following form:

$$M(t) = \iint_{S_+} \rho(\alpha, \beta) d\alpha d\beta - \iint_{S_-} \rho(\alpha, \beta) d\alpha d\beta \quad (2)$$

1.2. The Distribution Function

The complete determination of the Preisach model requires the knowledge of the density function $\rho(\alpha, \beta)$, which is the basis for the calculation of the total magnetization. For this purpose and at a given time, intuitively two approaches contrast.

The first method relies on extensive experimental hysteric loops while the second method consists of approximating real loops by means of some analytical function. In our study, we consider the second approach.

1.3. Analytical Approach

Several analytical expressions can be used. One of these approximations is the Lorentz function given by [1], [2]:

$$\rho(\alpha, \beta) = \frac{K}{\left[1 + \left(\frac{\alpha}{H_c} - 0.5\right)^2\right] \left[1 + \left(\frac{\beta}{H_c} + 0.5\right)^2\right]} \quad (3)$$

With

K : constant of standardization adjusted to have $M(H_s(t))=M_s$,

H_c : the coercitive field.

For a better approximation of the experimental loop, the Lorentzian function is modified by adding parameters and takes the form:

$$\rho(\alpha, \beta) = \frac{Ka}{\left[a + \left(\frac{\alpha}{H_c} + b\right)^2\right] \left[a + \left(\frac{\alpha}{H_c} - b\right)^2\right]} \quad (4)$$

Experimental measurements show that the two parameters a and b depend on the the nature of the material, i.e. remanent induction, coercitive field and permeability of the material. On the other hand, the area of $B(H)$ increases with the frequency [3]. An adjustment of the parameters a and b is necessary to have a correct modelling of the $B(H)$ behaviour. The parameters a and b are defined as follow: $a \in \mathbb{R}_+^*$ and $b \in \left[1, \frac{H_s}{H_c}\right]$

1.4. Mathematical Modified Formulation

With the PM model and the modified Lorentz function, we obtain the following expression.

$$M(t) = M_{i-1}(t) \pm 2 \iint_D \rho(\alpha, \beta) d\alpha d\beta \quad (5)$$

M_{i-1} stands for the previous magnetization moment. This formulation makes the calculation easier. Figure 1 shows the influence of the continuous component of the magnetic field on the hysteresis loop of the ferromagnetic material.

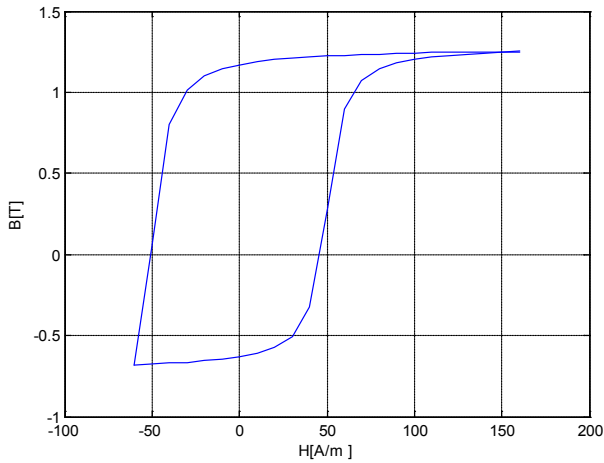


Fig.1: Hysteresis loop under the continuous component of magnetic field

This figure shows that the hysteresis loop is asymmetrical. Hence, the magnetic properties of the material are modified under the sollicitation field with constant component.

2. Simulation of the Hysteresis Loops under Sollicitation with Constant Component

The sollicitation considered is a combination of dc bias and ac magnetization with linearly diminishing amplitude. In order to modelize the hysteresis, we subdivide the considered signal into other periodical signal, and we use the Preisach Model for the simulation.

The combined signal from dc bias and ac magnetization as well as the linearly diminishing amplitude and the hysteresis loops obtained using PM are shown in Fig.2 and Fig.3 respectively.

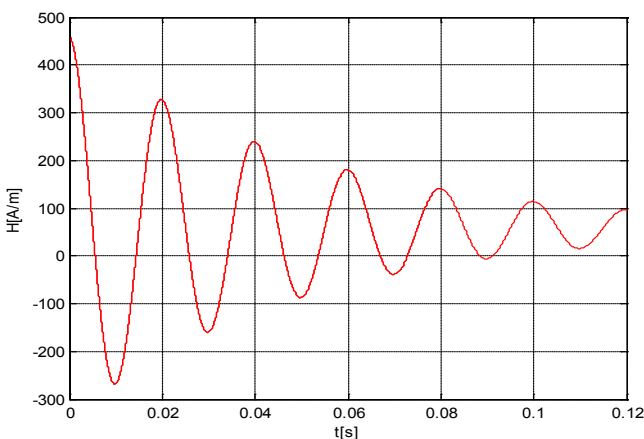


Fig.2. DC bias combined whit AC magnetization field excitation

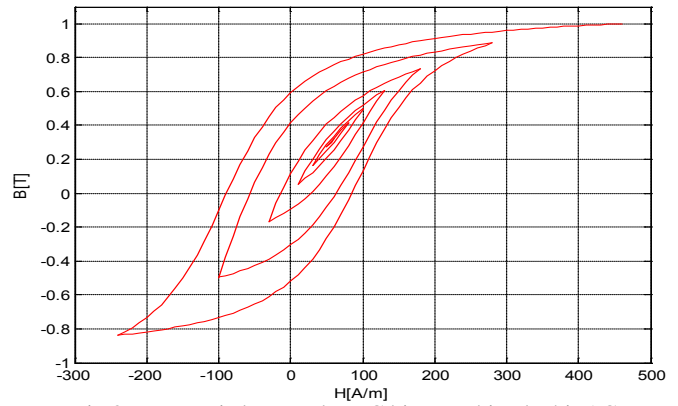


Fig.3. Hysteresis loop under DC bias combined whit AC magnetization field excitation

The figure 4 shows the anysteretic curve obtained by varying the amplitude of the dc bias magnetization.

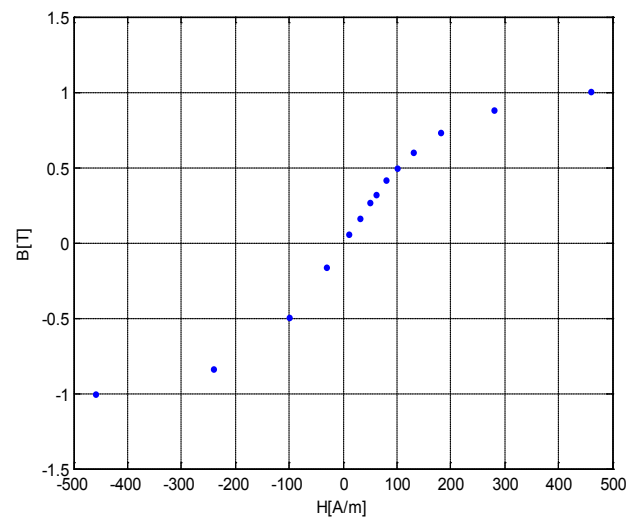


Fig.4. the Anysteretic curve obtained by varying the amplitude of the dc bias magnetization

3. Experimental Bench

The Figure 5 illustrates the experimental measurement setup composed from:

- An Epstein frame standardized
- A power amplifier KEPCO
- A numerical generator programmable WAVETEK 39.
- A digital scope (MXOX2000) for the visualisation and for data acquisition.
- A PC for data acquisition and processing.
- A current sensor.

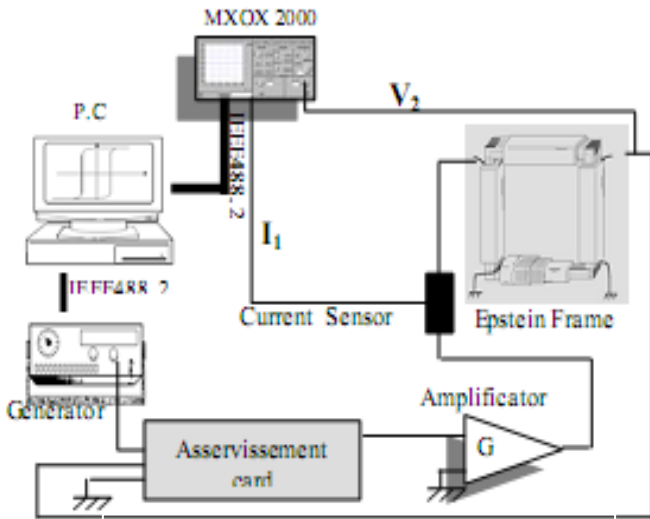


Fig.5. Experimental bench

4. Experimental validation

The Epstein test method is used to perform measurements for an FeSi 3% sheet. The primary winding is supplied with a sinusoidal voltage superimposed to a known DC voltage component. The amplitude of the maximum alternating voltage is decreasing linearly (Figure 4). We keep constant the parameter b in the Lorentz distribution function while the parameter a is adjusted to draw hysteresis loops as is described in Fig.6. We obtain a linear evolution for the parameter a as a function of the magnetisation and the loops are converging to the magnetic state determined by the dc field, as shown in Figure 7.

The same process is reproduced by considering an exponential decrease of the maximum amplitude of the alternating voltage. Figures 8 and 9 show the comparison between predicted and experimental hysteresis loops and the dependence of parameter a with maximal induction B_{max} .

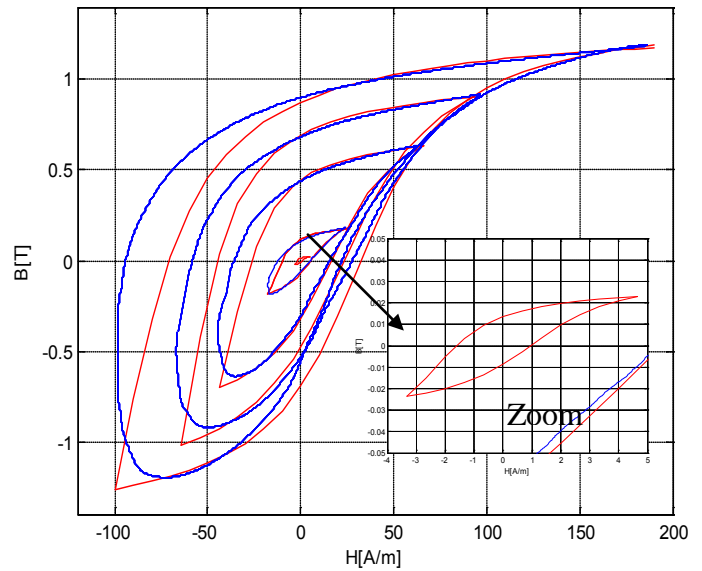


Fig.6. Experimental and modeled loops under sinusoidal field superposed to a known DC voltage component

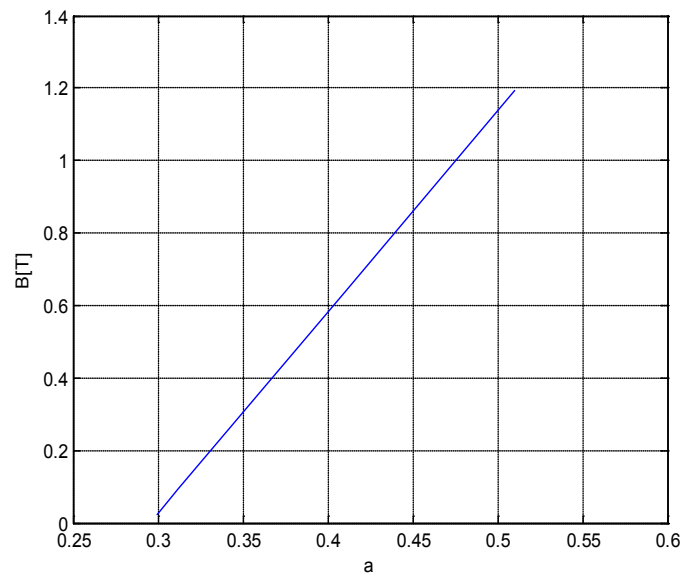


Fig.7. Dependence of "a" parameter of the Lorentz function with the magnetic induction

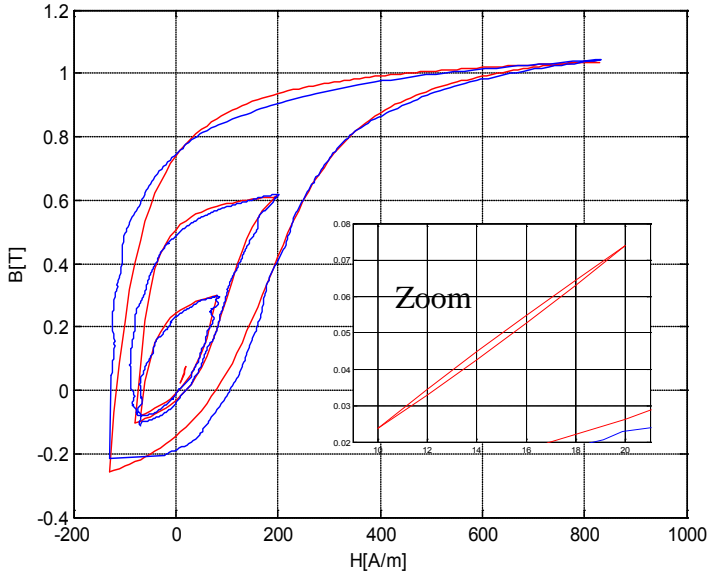


Fig.8. Experimental and modeled loops an exponential decrease of the maximum amplitude of the alternating voltage

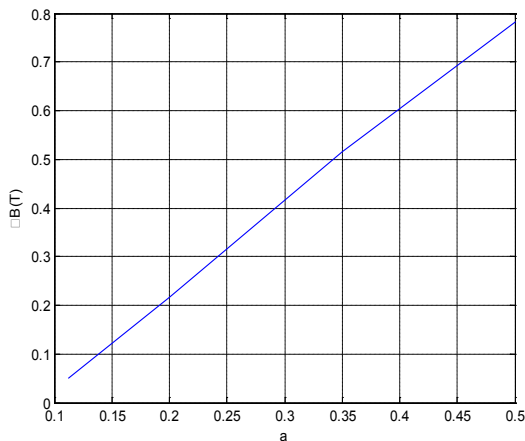


Fig.9. Dependence of “a” parameter of the Lorentz function with the magnetic induction

By repeating the process for different DC voltage values corresponding to the different DC magnetization, the table 1 illustrates the comparison between the experimental and predicted values of the DC magnetization state. We notice that there is no significant difference between the two.

DC component of the Experimental magnetization	DC component of the predicted magnetization
0.2587	0.22
0.3235	0.35
0.4038	0.45
0.5265	0.55
0.6612	0.7

Table 1 : Comparison between DC magnetization values (experimental and predicted)

Conclusion

Measurements have been carried out in 0.5mm thick non-oriented FeSi 3% laminations. The material is excited with a deadened sinusoidal field superimposed on a continuous component. The obtained asymmetric loops are modeled through the proposed approach based on the Preisach Model (PM) combined with a mathematical model which predicts the parameters that the PM needs. The experiment validation results are in agreement with several experiments. As a perspective for this work, the study of the modeling of the B(H) curve through the new approach could be extended to predict magnetic losses.

References

- [1] G. Bertotti “Dynamic Generalization of the Scalar Preisach Model of Hysteresis ” IEEE Trans. Magn., vol 28, pp. 2599-2601, September 1992
- [2] D. Moussaoui, A. Bendjerad, M.Oussalah and H. Houassine “A Neural Network approach for Determination of Preisach Model parameters Under a Sinusoidal Induction at Various Frequencies”, Physica B, 372, pp. 106-110, Oct. 2006.
- [3] E. Barbisio, O. Bottausciob, M. Chiampi, F. Fiorillo, C. Ragusa “Prediction of magnetic power losses in soft laminations under DC-biased supply”, Journal of Magnetism and Magnetic Materials 290–291 (2005) 1476–1479.
- [4] J.Füzi, “Experimental verification of a dynamic hysteresis model”, Physica B: Condensed Matter, Volume 343, Issues 1–4, 1 January 2004, pp. 80–84
- [5] O. Bottauscio, G. Pellegrino, P. Guglielmi, M. Chiampi, and A. Vagati “Rotor Loss Estimation in Permanent Magnet Machines With Concentrated Windings” IEEE Transactions On Magnetics, Vol. 41, pp. 3913-3915 N°. 10, Oct. 2005.

A branching variables rule for the B & B algorithm based on the flatness of the polyhedron

Improving the efficiency of the B&B algorithm

Iván Sergio Derpich Contreras
 Department of Industrial Engineering
 Universidad de Santiago de Chile, USACH
 Santiago, Chile
Ivan.derpich@usach.cl

Claudio Javier Macuada Silva
 Department of Industrial Engineering
 Universidad de Santiago de Chile, USACH
 Santiago, Chile
claudio.macuada@usach.cl

Abstract— This work presents two rules of branching variables for the Branch and Bound algorithm; one is based on the flatness polyhedron and the other one is an hybrid rule that uses this rule in combination with the pseudocost rule. The flatness rule is more time consuming because it requires solving two linear programming problems for each fractional variable, but the search tree displayed is about 50% smaller. The hybrid rule proposed uses the flatness rule on the first iterations of the algorithm and then uses pseudocost rule until it finds the optimum solution. Time savings are about 30% of the CPU time and about 50% from the total number of nodes.

Keywords— Branch and Bound, Variable selection, Pseudocost branching, Hybrid branching rules.

I. INTRODUCTION

In this paper we are going to work with the binary integer programming (BIP) problem, in the following format:

$$c^* = \min \{c^T x : Ax \leq b, x \in (0,1)^n\}$$

with, $A \in \mathbb{R}^{m \times n}$, $b \in \mathbb{R}^m$, $c \in \mathbb{R}^n$

The binary integer programming (BIP) offers a huge variety of tools for variable modelation and with them we are able to model a variety of scientific, engineering and management problems, such as system design, operations planning, task scheduling, logistics, inventory models, design and control networks, etc. Integer programming allows us to represent decisions through the use of binary variable and/or integer general variables.

To get solve a binary integer problem is generally difficult. And if the matrix A is not unimodular, it has been proved that these are problems belonging to NP-hard class. The most commonly used algorithm to solve this type of linear mixed integer programming (MIP) is Branch and Bound algorithm (B & B). This algorithm explicitly enumerates the set of values that the integer variables can take. This numbering scheme drifts from the idea dividing for conquering and its performance is strongly influenced by the way the search space is divided iteratively.

In this paper we develop new techniques for partitioning the search space using the concept of flatness polyhedron in combination with the classic pseudocost approach. The purpose of this branching rule is to improve the Branch and Bound algorithm performance. The idea of flatness is inspired by the Kinchine's flatness theorem, it indicates that the polyhedron in either direction is thinner than in others;

therefore the maximum number of partitioning respect to the coordinate axis is minimal.

Some studies indicate that it would be better to branch first in those directions in which the polyhedron is thinner. However, this idea would be perfect if the polyhedron were coinciding with the coordinate axis, which is not always the case. Another factor that disturbs this idea is the existence of integer points very near to restrictions or optimum integer points that are too far from these. So, we could have two polyhedron equal in shape, but one in which the optimum is very close to the edge while other is very far to the edge, and that fact would make the solving time using the B&B algorithm very different. These "accidents" complicate the development of a general theory of B&B algorithm. Despite these drawbacks, the concept of flatness polyhedron suggests that is better to branch in the thinnest direction.

II. STRATEGIES BRANCHING VARIABLES IN THE BRANCH AND BOUND ALGORITHM

Let P be the polyhedron corresponding to the relaxed linear programming problem (LP) associated to the problem (1), then:

$$P = \{x : Ax \leq b\}$$

and let $S^0 = P \cap (0,1)^n$ be the set of feasible points of (1). Let Z_{BIP} be the optimal value of BIP. The B&B algorithm starts by solving the LP relaxation from the BIP problem. The value of the LP relaxation Z_{LP} provides a lower bound for Z_{BIP} . Any solution of BIP provides an upper bound of Z_{BIP} . The B&B algorithm iteratively increases the lower bound and the upper bound decreases until these are equal, at which point the algorithm ends. If the solution of the LP relaxation is also feasible for the BIP problem, then it is the optimum solution for the BIP and the algorithm finish. Otherwise the search region is divided into some direction in which the optimum solution of the LP relaxation is not integer. Steps to use the Branch and Bound algorithm are described below:

1. Initialization: Let $z_{LB} = -\infty$ and $z_{UB} = \infty$. $k = 0$. Let L be the list of candidate problems, $L = \{P^0\}$, where $P^0 = P$.
2. If $L = \emptyset$, then x^0 is the optimal solution and the optimum value is z_{UB} . If there is not such solution the problem is declared infeasible.

3. Choose a problem P^i and erase it from L . Solve the LP relaxation of P^i to obtain the optimum value z_{LP}^i . Let x_{LP}^i be the optimal solution.
4. If the LP relaxation is infeasible, or if $z_{LP}^i \geq z_{UB}$, go to step 2. If the solution LP of P is feasible and $z_{LP}^i < z_{UB}$, then $z_{UB} = z_{LP}^i$. Erase from L all the problems P^i such that $z_{LP}^i \geq z_{UB}$ and go to step 2. Otherwise go to step 5.
5. To branch: Create 2 sub problems (adding linear restrictions). Each one corresponds to the chosen problem P^i adding an inequality of the type $x_k \leq [x_k^*]$ or $x_k \geq [x_k^*]$ in which x_k^* is the component K of the optimal solution from the problem P^i . These sub problems are added to the list L .

Update $z_{LB} = \min \{z_{LP}^i: P^i \in L\}$. If $z_{LP} \geq z_{UB}$, stop by. If not, go to step 2.

The B&B algorithm must answer the two following questions on each iteration: What problem to choose from the set L in step 2? and What child-node branch first after choosing the variable to use, this is, the right child or the left child? It is often convenient to represent the evolution of the B&B algorithm graphically through a B&B tree. In such representation, each sub problem P^i is associated with a node of the tree, which is connected to the k nodes, each one denoting a resulting sub problem from the imposition of a branch on P^i . Therefore, each node also corresponds to an associated LP relaxation that is solved for a particular sub problem. The first question is typically known as the problem of branching variables and it is the problem addressed at this paper. There are several known strategies to answer this question, let's review the main strategies available in the literature.

A. Pseudocost strategy

Dribeek [1] suggested to select the variable that produces the maximum increase on the lower bound of the sub problem after branching. He proposed to use a few dual simplex iterations to estimate this change. Later, this technique came to be known as strong branching. Subsequently, Bénichou et al. [2] introduced the idea of pseudocost to estimate the change in the lower bound. More specifically, let's suppose that \tilde{x}^k is the optimal solution for the LP relaxation from the sub problem k and that \tilde{x}_i^k has a fractional value for any $i=1, \dots$. Let's suppose the value of the objective function from the LP relaxation of the k -th sub problem is z^k and this value changes to z^{k+1} and z^{k+2} after branching on the variable i (i.e. imposing the disjunction $x_i \leq [\tilde{x}_i] \vee x_i \geq [\tilde{x}_i]$). Then the upper and lower bound of pseudocost for the variable i is defined as:

$$PCL_i = \frac{z^{k+1} - z^k}{f_i^k} \quad PCU_i = \frac{z^{k+1} - z^k}{1 - f_i^k}$$

$$\text{Where } f_i^k = \tilde{x}_i^k - [\tilde{x}_i^k]$$

Bénichou et al. [2] observed that the pseudocost of a variable usually do not change more than one order of magnitude during the execution of the B&B algorithm and this information could be used to quickly estimate the changes on the values of the objective function. Thus, if the value of the objective function of the LP relaxation of the current sub

problem k , then the objective value after branching on variable i can be estimated as:

For example:

$$\begin{aligned} \hat{z}_i^{k+1} &= (PCL_i)f_i^k + z^k, \\ \hat{z}_i^{k+2} &= (PCU_i)(1 - f_i^k) + z^k \end{aligned} \quad (3)$$

The pseudocosts are initially unavailable and can not be used when it has not been initialized. Eckstein [3] suggested that when only the pseudocosts of a few variables are available, the average of these could be used as an estimate.

B. Strong Branching

In the 90's Applegate et al. [4] proposed the concept of strong branching. In this approach the selection of variable is made tentatively selecting each one of the variables in the set C of potential candidates to be branched and observing the value of relaxation after running a certain fixed amount of dual simplex operations. This rule has proven to be an effective rule for many MIP problems and has been incorporated into many commercial solvers. Linderoth & Savelsbergh [5] carried out extensive experiments to show that using the selection of variable strategy strong branching leads to trees of B&B algorithm much smaller than occurring when pseudocost is used. Besides CPU times are also lower.

C. Strategies based on minimum integer width

These strategies are based on the "integer width" of the feasible region associated to the LP relaxation. Given the polytope \mathcal{P} and a direction $\mu \in \mathbb{Z}^n$, the width of \mathcal{P} through direction μ we will name it $w(\mu, \mathcal{P})$.

$$w(\mu, \mathcal{P}) = \max_{x, y \in \mathcal{P}} \mu^T(x - y) \quad (4)$$

Then, the integer width is:

$$w(\mathcal{P}) = \min_{\mu \in \mathbb{Z}^n, \mu \neq 0} w(\mu, \mathcal{P}) \quad (5)$$

Aardal & Esisenbrand [6] discussed the fact that when the dimension is fixed, it might obtain polynomial time algorithms to solve integer programming problems, branching on called thin directions of the feasible region, i.e. branches where the integer width of the feasible region is thin. These polynomial time algorithms are derived from Lenstra's work Lenstra [7] and mainly vary in the way to approximate the direction of the LP relaxation. For example, Krishnamoorthy & Pataki [8] showed that certain specific problems can be easily solved if it branches on particular disjunctions. Derpich & Vera [9] obtained the direction of minimum width and give a score to each variable; the score is higher if the branch direction is closer to the minimum width. Then, the branch direction is selected using this score. Two commonly found special structures were exploited by Beale & Tomlin [10] to generate branching rules called SOS-1 and SOS-2. SOS-1 is used when only one variable of a given set of binary variables can take a non-zero value, while SOS-2 can be used when only two adjacent variables of a given set of binary variables can be non-zero.

D. Hybrid strategy

The combining strategies idea is not new, there are several cases in the literature with good results, particularly Achterberg et al. [11] combined the ideas of strong branching and pseudocost to generate a new rule which they termed *reliability-branching*. They suggest to use strong branching on each variable to branch a fixed number of times, defining a parameter called reliability parameter. Then, they use pseudocost for the rest of the branches. Their approach showed that it is much better than using only pseudocost in terms of the size of the search tree and the time taken to solve the problem.

III. IMPLEMENTATION OF BRANCHING RULES

After having exposed the branching and generating of inequalities techniques more known in the literature and commercial software, is presented implementation of flatness rule and hybrid rule flatness/pseudocost. By x_1

A. Flatness rule

As said before, the flatness polyhedron can strongly influence the number of visited nodes by the B&B algorithm if the branching direction is conveniently chosen. Let us illustrate this with an example.

$$\begin{aligned} & \max x_1 + x_2 \\ & \text{s. t.} \\ & 2x_1 + 5x_2 \leq 16, 6x_1 + 5x_2 \leq 30 \\ & x_1, x_2 \geq 0, x_1, x_2 \in \mathbb{Z}^+ \end{aligned}$$

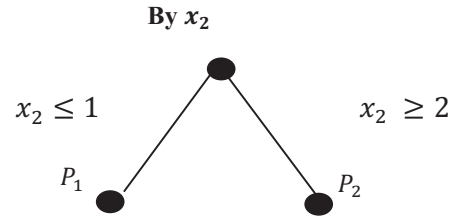
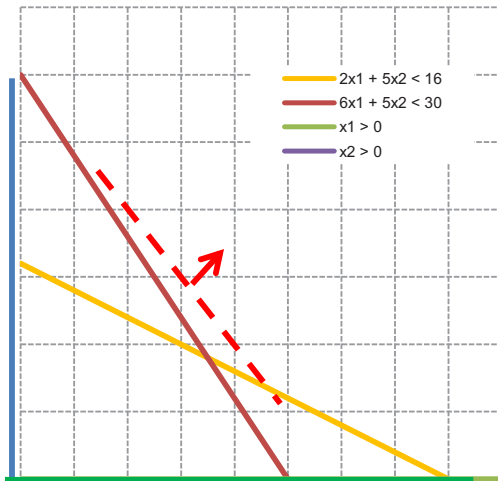


TABLE I. BRANCHING BY x_2 : 3 NODES, 0 INFEASIBLE

	x^*	p^*
P_0	(3.50, 1.80)	5.30
P_1	(4.00, 1.00)	5.00
P_2	(3.00, 2.00)	5.00

We can notice that branching by x_2 are less nodes than branching by x_1 . On the other hand, the integer width on the direction x_1 is lower than in the direction x_2 as shown the variable Δ_{x_i} .

$$\Delta_{x_1} = (5.0 - 0.0) = 5.0, \Delta_{x_2} = (3.2 - 0.0) = 3.2$$

As $\Delta_{x_1} > \Delta_{x_2}$. This shows that in this case it would be more convenient to branch first by direction x_2 because a smaller branching tree is obtained. While this result corresponds to a particular case, the analysis can be generalized to more variables and to other restrictions types.

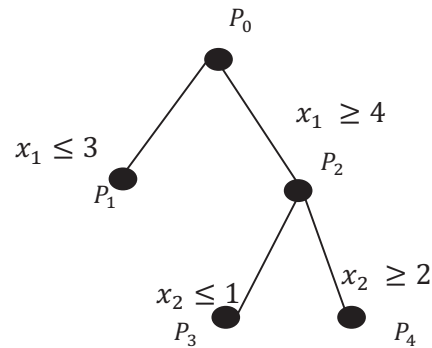


TABLE II. BRANCHING BY x_1 : 5 NODES, 1 INFEASIBLE

	x^*	p^*
P_0	(3.50, 1.80)	5.30
P_1	(3.00, 2.00)	5.00
P_2	(4.00, 1.20)	5.20
P_3	(4.00, 1.00)	5.00
P_4		$+\infty$

B. Hybrid rule

The hybrid rule combines two or more branching rules, in this case branches first a γ number of times using the flatness rule and then pseudocosts is used to find the optimal

solution. Through experimentation with the studied problems, the value 20 for the γ parameter was found.

IV. COMPUTATIONAL RESULTS

A. Experimental design

The used problems correspond to 3 sets of multidimensional knapsack problems, mknap1, mknap2 and mknapcb1 taken from the Internet public library OR-library. The first set contains 7 test problems that correspond to Petersen [12]. The second set of problems corresponds to 48 problems taken from literature, while the third set corresponds to 30 problems with 5-100 restrictions-variable respectively. This last was approached in Chu & Beasley [13] and their work includes the best value found for the objective function. At this work we programmed using Matlab R2011a, since it is a program that allows us to realize "pure" codes, i.e., codes without being subject to improvement implementations that contain some commercial software. It was used to run the presented models an Intel Core i5 3.2 GHz computer with 8Gb RAM under Windows 7 environment.

B. Results

This section shows the obtained results by solving the three problems set taken from OR-library. Below, different results tables presented, consider on each column:

TABLE III. FOR THE PROBLEMS SET MKNAP1

1.	P	Problem
2.	OP-OR	Optimum from the OR-library.
3.	t-01	Time to solve the problem using the pseudocost method (on seconds).
4.	Nodes-01	Number of explored nodes by B&B algorithm using pseudocost method.
5.	t-02	Time to solve the problem using the flatness method (on seconds).
6.	Nodes-02	Number of explored nodes by B&B algorithm using thinnes method.
7.	t-03	Time to solve the problem using the hybrid method fl/ps (on seconds).
8.	Nodes-03	Number of explored nodes by B&B algorithm using hybrid method fl/ps.

TABLE IV. TIME RESULTS FOR THE PROBLEMS SET MKNAP1

P	OP-OR	t-01(sec)	t-02(sec)	t-03(sec)
1 (6 x 10)	3800	1	1	1
2 (10 x 10)	8706,1	1	1	1
3 (15 x 10)	4015	9	10	8
4 (20 x 10)	6120	3	3	3
5 (28 x 10)	12400	14	13	12
6 (39 x 5)	10618	10	12	10
7 (50 x 5)	16537	12	16	11
Average		7	8	6

This first part shows the results obtained together with the optimal value published in the OR-library. It also shows the time to solve each one of the three methodologies: pseudocost, flatness and the hybrid method fl/ps. It can be note that the times to solve this set of problems are not very large and the average time to solve is higher than in the hybrid

method fl/ps. Besides, all the optimums published in the OR-library (OP-OR) matches with optimum integer found. It can be observed that the computational process times are lower when the flatness rule is used to branch (t-03 versus t-01 y t-02).

TABLE V. : RESULTS OF NODES FOR THE SET OF PROBLEMS MKNAP1

P	OP-OR	Nodes-01	Nodes-02	Nodes-03
1 (6 x 10)	3800	26	16	19
2 (10 x 10)	8706,1	22	19	20
3 (15 x 10)	4015	240	217	249
4 (20 x 10)	6120	127	62	84
5 (28 x 10)	12400	2425	1002	1357
6 (39 x 5)	10618	246	153	152
7 (50 x 5)	16537	2825	1536	1745
Average		844	429	518

In Table VIII it can be advice that the time to solve the problems has significantly increased compared to the problems reported in Table V. In every case the values published by OR-library were obtained. It can see that on average, the values for the hybrid rule are lower than for another tested rules, for example, compared to pseudocost rule 24% savings are obtained on average. CPU time values using flatness rule are, on average, greater than in other cases. This is explainable because this rule on each iteration requires solving 2^n linear programming problems.

TABLE VI. : RESULTS OF NODES FOR THE SET OF PROBLEMS MKNAP2

P	OP-OR	Nodes-01	Nodes-02	Nodes-03
SENT01.DAT (30 x 60)	7772	94847	34585	48693
SENT02.DAT (30 x 60)	8722	96362	32598	47515
WEING1.DAT (2x28)	141278	14615	11523	12710
WEING2.DAT (2x28)	130883	3844	3117	3220
WEING3.DAT (2x28)	95667	8844	6367	6544
WEING4.DAT (2x28)	119337	11708	9651	9113
WEING5.DAT (2x28)	98796	3888	3154	3249
WEING6.DAT (2x28)	130623	7890	6556	5909
WEING7.DAT (2x105)	1095445	8890	6452	6214
WEING8.DAT (2x105)	624319	9934	6582	7937
WEISH01.DAT (5 x 30)	4554	3243	2435	2410
WEISH02.DAT (5 x 30)	4536	668	397	408
WEISH03.DAT (5 x 30)	4115	5890	3265	3775
WEISH04.DAT (5 x 30)	4561	1588	1237	1524
WEISH05.DAT (5 x 30)	4514	1944	1075	1250
WEISH06.DAT (5 x 40)	5557	3765	2402	3130
WEISH07.DAT (5 x 40)	5567	1924	1202	1314
WEISH08.DAT (5 x 40)	5605	1274	875	1044
WEISH09.DAT (5 x 40)	5246	5644	4373	5097
WEISH10.DAT (5 x 50)	6339	9190	6618	7656
WEISH11.DAT (5 x 50)	5643	4278	3463	3489
WEISH12.DAT (5 x 50)	6339	4952	4061	4273
WEISH13.DAT (5 x 50)	6159	3965	2840	2977
WEISH14.DAT (5 x 60)	6954	5198	3760	4340
WEISH15.DAT (5 x 60)	7486	3324	2265	2775
WEISH16.DAT (5 x 60)	7289	8698	4972	5509
WEISH17.DAT (5 x 60)	8633	4224	2296	2708
WEISH18.DAT (5 x 70)	9580	34708	20494	22987
WEISH19.DAT (5 x 70)	7698	13191	7936	8886
WEISH20.DAT (5 x 70)	9450	14985	8589	10010
WEISH21.DAT (5 x 70)	9074	26474	14961	17830
WEISH22.DAT (5 x 80)	8947	28418	16154	19048
WEISH23.DAT (5 x 80)	8344	21218	11599	13913
WEISH24.DAT (5 x 80)	10220	22747	12280	14244
WEISH25.DAT (5 x 80)	9939	39138	27261	30805
WEISH26.DAT (5 x 90)	9584	30015	16440	18795
WEISH27.DAT (5 x 90)	9819	27844	13917	16411
WEISH28.DAT (5 x 90)	9492	20620	9950	12912

WEISH29.DAT (5 x 90)	9410	24538	13031	16174
WEISH30.DAT (5 x 90)	11191	14847	8416	9923
PB1.DAT (4 x 27)	3090	3335	1342	2455
PB2.DAT (4 x 34)	3186	2247	2152	2210
PB4.DAT (2 x 29)	95168	2008	1583	1600
PB5.DAT (10 x 20)	2139	6423	5255	5660
PB6.DAT (30 x 40)	776	50687	20607	25478
PB7.DAT (30 x 37)	1035	56991	24080	28931
HP1.DAT (4 x 28)	3418	2846	1890	2228
HP2.DAT (4 x 35)	3186	3945	3142	2470
Average		16204	8525	10162

WEISH29.DAT (5 x 90)	9410	196	224	186
WEISH30.DAT (5 x 90)	11191	58	67	42
PB1.DAT (4 x 27)	3090	22	26	21
PB2.DAT (4 x 34)	3186	13	17	13
PB4.DAT (2 x 29)	95168	29	34	29
PB5.DAT (10 x 20)	2139	7	9	6
PB6.DAT (30 x 40)	776	522	650	368
PB7.DAT (30 x 37)	1035	496	612	340
HP1.DAT (4 x 28)	3418	12	13	10
HP2.DAT (4 x 35)	3186	16	18	14
Average		133	154	106

Table VI and VII shows the results obtained together with the optimum value published in the OR-library. It also shows the results of the number of nodes for the three methodologies: pseudocosts, flatness and the hybrid method fl/ps. It can be note that the number of nodes in the case of the flatness method is lower than with other methods. The average difference is almost the double than using pseudocosts (429 against 844). This is consistent with the idea expressed in section III.A where it was developed the idea of branching first in the direction that the polyhedron is flat because fewer nodes are generated in the search tree.

TABLE VII. : TIME RESULTS FOR THE SET OF PROBLEMS MKNAP2

P	OP-OR	t-01(sec)	t-02(sec)	t-03(sec)
SENT01.DAT (30 x 60)	7772	601	719	449
SENT02.DAT (30 x 60)	8722	1132	1413	828
WEING1.DAT (2x28)	141278	21	23	18
WEING2.DAT (2x28)	130883	8	10	8
WEING3.DAT (2x28)	95667	15	16	13
WEING4.DAT (2x28)	119337	23	27	21
WEING5.DAT (2x28)	98796	8	9	6
WEING6.DAT (2x28)	130623	9	11	9
WEING7.DAT (2x105)	1095445	109	130	107
WEING8.DAT (2x105)	624319	110	123	102
WEISH01.DAT (5 x 30)	4554	20	23	20
WEISH02.DAT (5 x 30)	4536	6	7	5
WEISH03.DAT (5 x 30)	4115	5	5	4
WEISH04.DAT (5 x 30)	4561	3	3	2
WEISH05.DAT (5 x 30)	4514	2	2	1
WEISH06.DAT (5 x 40)	5557	9	10	8
WEISH07.DAT (5 x 40)	5567	41	50	34
WEISH08.DAT (5 x 40)	5605	10	11	8
WEISH09.DAT (5 x 40)	5246	12	12	10
WEISH10.DAT (5 x 50)	6339	92	113	89
WEISH11.DAT (5 x 50)	5643	40	43	32
WEISH12.DAT (5 x 50)	6339	54	51	40
WEISH13.DAT (5 x 50)	6159	36	42	31
WEISH14.DAT (5 x 60)	6954	41	49	36
WEISH15.DAT (5 x 60)	7486	20	22	17
WEISH16.DAT (5 x 60)	7289	18	22	15
WEISH17.DAT (5 x 60)	8633	17	21	15
WEISH18.DAT (5 x 70)	9580	259	272	229
WEISH19.DAT (5 x 70)	7698	90	105	81
WEISH20.DAT (5 x 70)	9450	133	146	117
WEISH21.DAT (5 x 70)	9074	241	253	216
WEISH22.DAT (5 x 80)	8947	297	307	245
WEISH23.DAT (5 x 80)	8344	251	255	208
WEISH24.DAT (5 x 80)	10220	264	271	210
WEISH25.DAT (5 x 80)	9939	328	338	260
WEISH26.DAT (5 x 90)	9584	308	339	251
WEISH27.DAT (5 x 90)	9819	287	338	240
WEISH28.DAT (5 x 90)	9492	109	135	87

In Table X of results, it can be noted that the number of nodes has considerably increased with some high values, as an example, the case of the SENT01.DAT problem (30x60) and the SENT002.DAT problem (30x60). As in Table X the trend indicates that using the pseudocost method more nodes are generated than using the hybrid method fl/ps, while using the flatness method fewer nodes are generated. About the optimal values published by the OR-library, they are all equal to the optimum. It is noted that the number of nodes visited using the flatness rule is 47% lower than the number of nodes using the pseudocost rule.

TABLE VIII. TIME RESULTS FOR THE SET OF PROBLEMS MKNAPCB1

P	OP-OR	t-01(sec)	t-02(sec)	t-03(sec)
5.100-01	24381	317	332	221
5.100-02	24274	166	209	149
5.100-03	23551	263	338	224
5.100-04	23534	164	171	112
5.100-05	23991	230	286	165
5.100-06	24613	94	114	66
5.100-07	25591	31	39	27
5.100-08	23410	117	151	87
5.100-09	24216	92	119	78
5.100-010	24411	112	145	84
5.100-011	42757	33	40	23
5.100-012	42545	85	107	76
5.100-013	41968	323	428	214
5.100-014	45090	163	211	138
5.100-015	42218	83	108	62
5.100-016	42927	22	27	15
5.100-017	42009	16	20	14
5.100-018	45020	177	202	96
5.100-019	43441	18	24	15
5.100-020	44554	68	88	51
5.100-021	59822	16	20	11
5.100-022	62081	8	10	7
5.100-023	59802	50	64	37
5.100-024	60479	49	64	42
5.100-025	61091	39	50	29
5.100-026	58959	107	130	75
5.100-027	61538	46	59	42
5.100-028	61520	27	35	20
5.100-029	59453	10	13	8
5.100-030	59965	110	140	82
Average		101	125	76

For this set of problems, taken from the file mknapcb1, the time to solve decreased from the previous set (Table IX), reaching a maximum of CPU time on Problem 13, which reached 7.13 minutes. About the results published in the OR-library, the objective functions for the three methods gave the same optimum value. In Table IX it can be noted that the

hybrid rule (flatness/pseudocost) gives a shorter time by 25% than the pseudocost rule.

Finally, in Table IX, it can be noted that the time to solve has increased from the previous set (Table VIII), reaching a maximum of CPU nodes at problem 13 that reaches 38325 nodes. About the results published in the OR-library, the objective functions for the three methods were equal. It can be observed that the number of nodes generated with flatness strategy is significantly lower than the number of nodes produced using pseudocost strategy.

TABLE IX. RESULTS OF NODES FOR THE SET OF PROBLEMS PROBLEMS MKNAPCB1

P	Nodes-01	Nodes-02	Nodes-03
5.100-01	36652	12852	16852
5.100-02	22139	10496	12694
5.100-03	34055	12307	16444
5.100-04	26867	16019	17884
5.100-05	32062	18530	19079
5.100-06	24613	12066	15811
5.100-07	25591	8067	8891
5.100-08	23410	14484	17066
5.100-09	24216	11672	15733
5.100-10	24411	12666	16916
5.100-11	42757	7162	8149
5.100-12	42545	10524	13169
5.100-13	41968	18246	21777
5.100-14	45090	8040	10018
5.100-15	42218	10655	12349
5.100-16	42927	8014	9802
5.100-17	42009	4203	5302
5.100-18	45020	14872	15450
5.100-19	43441	9137	11014
5.100-20	44554	9266	11293
5.100-21	59822	6879	8922
5.100-22	62081	3375	3710
5.100-23	59802	9078	10939
5.100-24	60479	8632	9763
5.100-25	61091	7999	9138
5.100-26	58959	12727	16377
5.100-27	61538	4731	5793
5.100-28	61520	6634	7772
5.100-29	59453	6978	7753
5.100-30	59965	12209	16422
Average		10284	12409

V. CONCLUSIONS

The target of this research was to study the branching variables in the B&B algorithm and to develop a branching rule based on the geometry of the polyhedron associated to the linear problem. The idea was to branch into the direction that the polyhedron is thinner; in order to obtain a branching rule that achieves lower resolution time of the algorithm. Consequently, the flatness rules were designed and hybrid rule flatness/pseudocost (fl/ps) was constructed, which works the first iterations using flatness rule and for the rest iterations uses the pseudocost method. These three rules were tested in 85 multidimensional knapsack problems taken from the

Internet Public Library OR-library generating interesting results.

The most important result of this work is that the number of nodes generated using the hybrid rule (fl/ps) yielded to these test problems, a 43% less nodes than the produced when using the pseudocost rule. This saving is generated from the use of the flatness rule in the first iterations, since it was able to observe that the flatness rule generated a 52% fewer nodes than using pseudocost.

These results are consistent to Kinchine's flatness theorem that indicates that in any direction the polyhedron is thinner, therefore the maximum number of slices with the coordinates axis is minimum. This benefits the developed method, since it positions the partitioning so that his initiation will be efficient, generating fewer nodes than using the pseudocost rule. Comparing the number of nodes generated by different methods, it shows that the percentage difference from the hybrid method increases as the number of constraints and number of variables grow.

Another important result of this work is that it is related to computational algorithms efficiency using different branching rules. CPU times using hybrid rule for this set of test problems, were 22% lower than the times consumed by using the pseudocost rule. As result of the work done, it has been develop a rule named flatness rule and another called hybrid rule (flatness/pseudocost (fl/ps)), which allow us to solve in less time mixed linear programming problems of multidimensional knapsack type. As future work, it is proposed to solve larger problems to check the trend mentioned above is met. It would also be interesting to use the information provided by the objective function, in the flatness rule, since the flatness of a polyhedron is measured in regards to a vector and its associated hyperplane. Then, it would be intuitive thinking that if the hyperplane corresponding to the objective function has a similar orientation to the flatness hyperplane, the number of nodes in the B&B tree will be lower and their directions could be used for branching.

ACKNOWLEDGMENT

The authors acknowledge with thanks the financial support of this research by DICYT-USACH, of the Universidad de Santiago de Chile.

REFERENCES

- [1] Dribeek, Norman J. (1966). An algorithm for the solution of mixed integer programming problems. *Management Science, Volumen 12, Issue 7*, 576-587.
- [2] Bénichou, M., Gauthier, J. M., Girodet, P., Hentges, G., Ribiére, G., & Vincen, O. (1971). Experiments in mixed interger linear programming. *Math Program*, 76-94.
- [3] Eckstein, Jonathan. (1994). Control strategies for parallel mixed integer branch and bound. *Proceedings of the 1994 ACM/IEEE conference on Supercomputing* (págs. 41-48). California: IEEE Computer Society Press Los Alamitos.
- [4] Applegate, David, Bixty, Robert, Chvátal, Vašek, & Cook, William. (1998). On the solution od traveling salesman problems. *Documenta Mathematica Journal der Deutschen Mathematiker-Vereinigung. International Congress of Mathematicians*, 645-656.
- [5] Linderoth, Jeffrey T., & Savelsberg, Martin W. (1999). A computational study of search strategies for mixed integer programming. *INFORMS J. Comput.*, 173-187.

- [6] Aardal, Karen, & Eisenbrand, Friedich. (2005). Integer programming, lattices and results in fixed dimension. *Handbooks in Operations Research and Management Science*, 171–243.
- [7] Lenstra, Hendrik W. (1983). Integer programming with a fixed number of variable. *Mathematics of Operations Research*, 538-548.
- [8] Krishnamoorthy, Bala, & Pakati, Gábor. (2006). *Column basis reduction and decomposable knapsack problems*. Submitted, available at <http://www.optimizationonline.org/DB>.
- [9] Derpich, Iván, & Vera, Jorge R. (2006). Improving the efficiency of the Branch and Bound algorithm for integer programming based on “flatness” information. *European Journal of Operational Research*, Volume 174, Issue 1, 92-101.
- [10] Beale, Evelyn M., & Tomlin, John A. (1970). Special facilities in a general mathematical programming system for nonconvex problems using ordered sets of variables. *Proceedings of the Fifth International Conference on Operational Research*, Volume 55, 447–454.
- [11] Achterberg, Tobias, Koch, Thorsten, & Martin, Alexander. (2005). Branching rules revisited. *Operations Research Letters*, Volume 33, 42-54.
- [12] Petersen, Clifford C. (1967). Computational experience with variants of the Balas algorithm applied to the selection of R&D projects. *Management Science*, Volume 13, Issue 9., 736-750.
- [13] Chu, Pai-cheng, & Beasley, John E. (1998). A genetic algorithm for the multidimensional knapsack problem. *Journal of Heuristics*, Volume 4, Issue 1., 63-86

Modern company maintenance management based on the principle computerized maintenance management system (CMMS) implementation

Peter Poór, Michal Šimon

Abstract—Good working maintenance of machinery can rapidly improve production and economic performance of the company. With the implementation of computerized maintenance management system, keeping maintenance should be easier and more convenient. This contribution describes the role of machinery maintenance in a company, development of maintenance from “traditional” to modern maintenance management via implementation of Computerized Maintenance Management Systems. Implementation of CMMS used nowadays is described in the final part of the article, which also summarizes benefits and disadvantages of using it. The final part also describes all problems, that can be encountered while implementing computerized maintenance management system.

Keywords—CMMS, engineering, machinery, maintenance.

I. FEATURES OF MACHINERY MAINTENANCE IN MANUFACTURING PLANTS

Basic activities of companies management include care about basic resources. Each manufacturing plant wants its production systems and equipment to operate and manage in a reliable manner. The fact is that in today's competitive environment when producers want to maintain their position on market, they have to exploit every possible advantage. One mean, through which companies seek to gain a competitive advantage is lean manufacturing. Many firms develop an initiative to achieve what the best results in the field of maintenance and reliability is. Unfortunately, only a few companies attach the importance of synergy, i.e. the strength of the combination of a lean manufacturing and maintenance .

The best approach seems to focus on lean manufacturing ,

In conclusion, we would like to express thanks for the support of the projects SGS-2012-063 titled “Integrated design of manufacturing system as metaproduct with a multidisciplinary approach and with using elements of virtual reality“ and project NEXLIZ – CZ.1.07/2.3.00/30.0038, which is cofinanced by the European Social Fund and the state budget of the Czech Republic.

Ing. Peter Poór, PhD. is with Department of Industrial Engineering and Management, University of West Bohemia, Univerzitní 8, 306 14 Plzeň, Czech Republic, E-mail: poorpeter@gmail.com, Phone: +420 377 638 401 Fax: +420 377 638 402

Doc. Ing. Michal Šimon, Phd. is with Department of Industrial Engineering and Management, University of West Bohemia, Univerzitní 8, 306 14 Plzeň, Czech Republic, E-mail: simon@kpv.zcu.cz, Phone: +420 377 638 400 Fax: +420 377 638 402

maintenance and improvement of reliability at the same time . Simply put, through increasing and improving the reliability of equipment and processes we need to stabilize the production process. Applying lean manufacturing tools for maintenance will strengthen their mutual synergy.

Each manufacturing plant wants operate their production systems and devices in a reliable manner. What organization does not want, are manufacturing systems or processes collapsed, what leads to production of defective or malfunctioning products. Unfortunately, we do not live in the ideal world, and physical assets won't last forever. In most organizations, therefore, failures are part of everyday life.

They will be reflected, for example. in losses of quality and productivity. Most of these deficiencies are manifested in form of problems associated with devices, such as failure or problems related to maintenance of corrective actions, the right to maintenance, which is all too often regarded as the cause of all problems that plague most of factories, establishments and corporations.

When the machine does what it is and when it is, productivity and business profitability is maximized. One of the most important aspects of well-organized production is machinery maintenance. The term maintenance shall mean the “*combination of all technical, administrative and managerial actions during item life cycle in order to maintain or restore such a state in which it can perform a required function*”[7].

Maintenance job is no longer limited only by immediate response to special events, overcoming problems of using multiple organs and excessive overtime. If there are processes and maintenance procedures appropriately chosen and subsequently adopted actions done well, we can minimize the loss and production becomes stable again. Production capacity will be fully and consistently high quality products will become the norm. This condition you say, "excellent care"

But maintenance of machinery can often be quite costly. It will be appreciated that the actual cost savings and profitability can be achieved only by combining the reliability,

security and availability in a cost-saving process management facilities. Activities and responsibilities of machinery and equipment maintenance in the company are divided into two categories, which are defined as a function of the maintenance transformed into daily operation with regard on solving everyday problems associated with the maintenance of physical facilities (company, machinery, buildings, services) in proper operation.

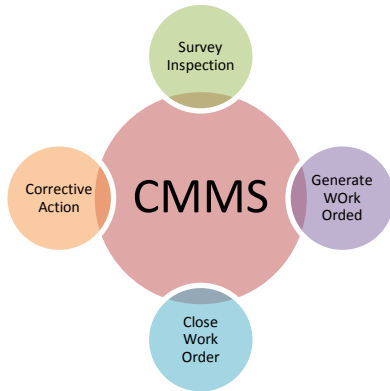


Figure 1 CMMS functionalities

II. PRIMARY AND SECONDARY MAINTENANCE FUNCTIONS

Activities and responsibilities can be divided into two categories :

- The primary functions
 - Maintenance of existing facilities
 - Maintenance of existing facilities, buildings and land.
 - Inspection of equipment and lubrication.
 - Production and distribution of energy.
 - Alterations and installation of new equipment.
- are functions that require daily work and
- Secondary functions
 - Storage
 - Plant protection
 - Waste disposal
 - Insurance Administration
 - other services....

assigned to functions for reasons of expediency, know- how or other .

Secondary functions are maintenance, for example, repair of equipment (large or small) and conducting technical and economic records of the state machinery and equipment [1].

Basicly, CMMS takes its function from 3 big areas (Fig. 2).

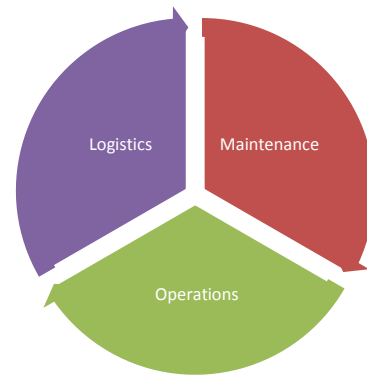


Figure 2 Effective CMMS

III. MAINTENANCE DEVELOPMENTAL STAGES

In the last century, various approaches have been developed such as to perform maintenance in order to ensure attainment or overrun product life. To prevent product failure (reactive maintenance), we can utilize methods of preventive maintenance (switching device until it goes wrong), predictive maintenance or reliability centered maintenance (RCM) and total productive maintenance (TPM). Maintenance strategy is a set of rules under which various maintenance activities and plans are carried out with their time evolution.

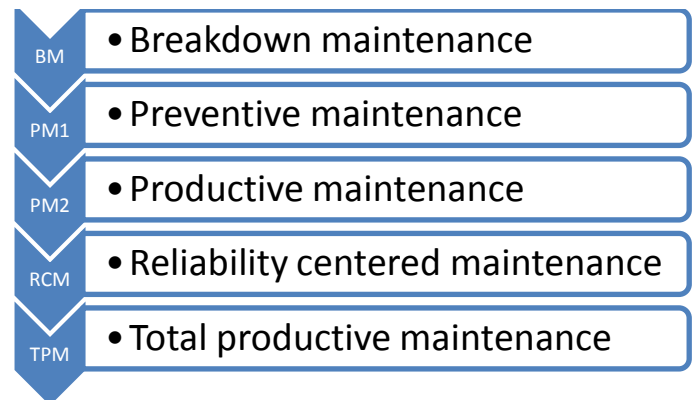


Figure 3 Machinery maintenance evolution [1]

Nowadays two basic strategies of maintenance are distinguished:

- Proactive maintenance - represents a strategy to prevent the emergence of disorders utilizing corrective action, where the action is directed to the source of the fault. Also includes preventative method for predictive maintenance.
- Subsequent maintenance - includes actions that correspond with fault condition of the device. Executing in case where it is not possible respectively appropriate select another form of maintenance [2].

The maintenance activities were not once considered as "necessary evil". Only high costs of maintenance in the range of 15 to 40% of production costs compelled managers to increase the attention on maintenance issues. Development of

maintenance can be observed after World War II.

Reactive maintenance can be considered as first targeted strategy of maintenance management. Maintenance itself was carried out according to the rules "run the device until it goes wrong" and was mainly directed to the damaged parts of the machine. Preventive maintenance is executed at predetermined intervals or in accordance with prescribed criteria and intended to reduce the likelihood of fault or limitation of functionality element.

Predictive maintenance is a special case of preventive strategies and is directed to detecting warning signs of damage which has already begun. Periodic inspection of equipment is expected. Maintenance is performed only on parts, which state is defined as impaired. Reliability centered maintenance (RCM) discusses causes and methods of disorders, according to their expression and the possibility of anticipating, possibly preventing their inception. Total Productive Maintenance (TPM) emphasizes awareness raising and knowledge levels of operators, but also maintenance staff being properly applied motivational tools for enhancing a sense of co-responsibility of all involved.

Modern era of the information society and computers affect all aspects of everyday life and even in societies. Maintenance and repair processes are currently a complex phenomenon. In many production sites well performed maintenance of machinery and equipment may encounter many problems. By introduction of maintenance management with support of IT (CMMS) companies (nearly a half of monitored companies are using CMMS systems – graph below) are able to make effective use of resources (human resources, inventory ...) and ensure average 8% reduction of maintenance costs in first year of CMMS deployment [9].

Most of these systems focus on the basic functions of maintenance, which is primarily used to reduce the number of defects of the production facility. Upgrade of these systems have become systems known as EAM (Enterprise Asset Management), where the function of CMMS is expanded to inventory management of spare parts, spare parts sales and brokering service or tool for predictive maintenance. The highest level modules are then built maintenance control within advanced ERP systems.

The integration processes of maintenance in company information system allows realizing strategic decision on basis of precise figures for help of clear managerial outputs and analysis tools [10]. This results in more efficient operations conduct and the subsequent performance optimization [4].

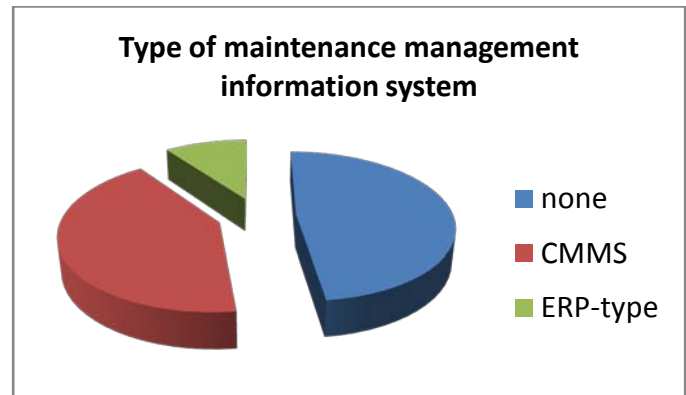


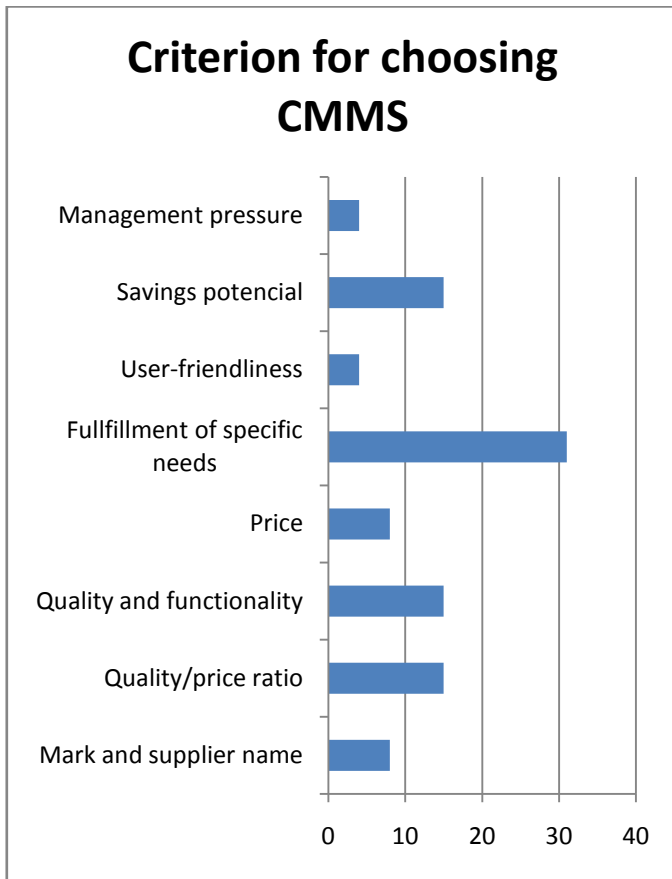
Figure 4 Type of maintenance management IS

IV. COMPUTERIZED MAINTENANCE MANAGEMENT SYSTEM (CMMS)

Computer Maintenance Management System (CMMS) is a type of software for management functions as support management and monitoring operations and maintenance. Computerized maintenance management systems automate most of the functions of logistics provided by maintenance [3].

They come with many options and have many advantages over manual maintenance of the systems. Depending on the complexity of the chosen system, typical functions of computerized maintenance management systems can include the following:

- Work process, priorities generating and monitoring devices
- Historical tracking of all created job orders, which can be aligned, by date, person, answers, and so on.
- Monitor planned and non-planned maintenance.
- Storage of maintenance procedures, as well as all information on a guarantee of items.
- Storage of technical documentation
- Real-time management of ongoing working activity.
- Calendar of preventive maintenance.
- Capital and labor costs monitored by item.
- Complete inventory control of parts of materials, inventory management, with the possibility of automatic configuration of ranks.
- PDA interface for easier entry and job streamlining.
- Other services [5].



Based on the evaluation results of our research, which took place in the form of an extensive survey, it is evident that the incorporation of a system for computer-aided maintenance sector finds its justification not only for easier monitoring and data archiving. Among the greatest benefits from the use of specialized systems, according to respondents affects the level of inventory of spare parts. Further, the positive effect of reliability increasing of final products and reducing total cost of production are important.

Also, fulfillment of customer specific needs is an important criterion. It is caused by a fact, that every production system is specific. Most companies choose between implementation of an existing CMMS system or developing a new one, specific for their needs. Main criterion for CMMS system choosing are shown in the graph below:

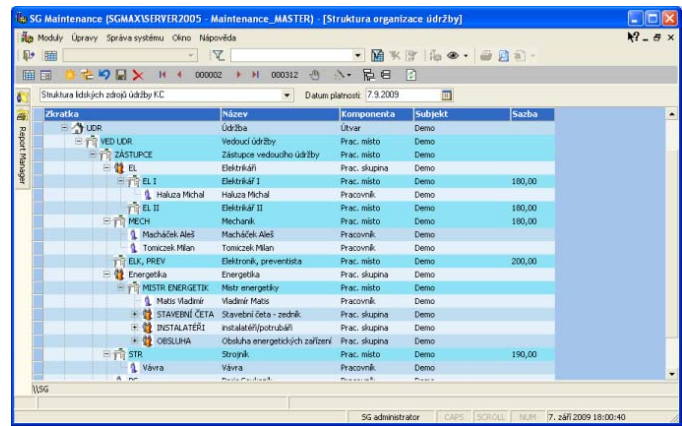


Figure 5 CMMS system SG maintenance

V. ADVANTAGES OF USING CMMS

Using a computerized maintenance management system in a company means a lot of advantages. One of the greatest benefits of a computer maintenance management system is to remove manual paper work and monitoring activities, which lead to greater productivity. It should be noted that the functionality of CMMS is the ability collect and store information in the form researchable easily. Computerized maintenance management system does not do maintenance decisions, rather provides best information for manager of operations and maintenance to adequately affect service and efficient run of the apparatus.

The advantages of the implementation of computerized maintenance management system includes the following picture: [6]

- Maintaining optimum device performance by reducing downtime and resulting in a longer lifetime of the device.
- Detection of imminent problems rather than occurs an error, whereby it is less failures and customer complaints.
- Achieve a higher level of planned maintenance activities that allow more efficient use of personal resources.
- Influencing enables better inventory management anticipation and purchase of spare parts for remove the deficiency and minimize existing stocks.
- Maintaining optimum performance of the device by reducing downtime and resulting in a longer lifetime of the device.

Of course, the functions are different for different kinds of CMMS as each new system are changed and they conform to the needs and requirements of customers.

VII. CHOOSING A GOOD CMMS

A good CMMS software should provide :

- Organization of all maintenance information in a clear database
- Comfortable calendar scheduling preventive maintenance with possibility of manual intervention and accessories
- Print work orders and their easy conversion into finished maintenance events , alarms
- Complete overview of carried work upkeep (ISO audit), repairs and costs
- Capacity utilization statistics and other publications for improving the management and maintenance planning
- Operate in local or network version. Installation is simple and does not necessarily require implementation assistance.
- Access protected by passwords and access rights for each user, defined by the administrator. Access rights extend to the individual machines.
- Interconnecting the states of spare parts in your ERP system and programmed specific functions and add data to your specifications

rescheduling maintained. The plan can be printed in different forms and each action can be printed work order. Stepped maintenance is that the higher level in itself always involves a degree lower. What to do during maintenance can be written as free formatted text. Each type of maintenance can be assigned to professions such as the capacity to participate therein (and possibly write even more workers) and what stock items (spare parts) need to be prepared. Repair means action without repetition.

In a good CMMS, you can define the individual cost centers, enterprise and then watch them on overall maintenance costs. Each machine card machine can be assigned to one cost center. Definition of cost centers is hierarchical, ie starting from the highest point of the hierarchy (the company), and it is subordinated to define cost centers.

Similarly, as cost centers can be defined hierarchical dial placement machines. By placing the machine easy to find when you know at least in which the hall is located in the business.

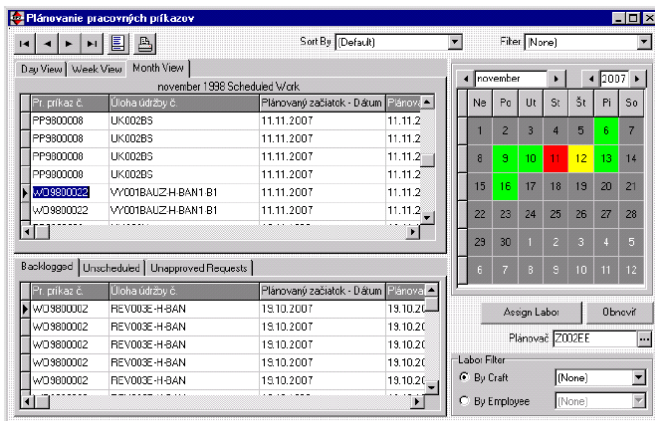


Figure 8 CMMS called EAM2 with scheduled maintenance

The machine is a base on database maintenance. Machines card includes everything you need to know. Outside the predefined data you can take advantage of unlimited text note, assign photos and even instructions for use. These cards access the plan as well as the history of maintenance and repairs.

Planning is essential for the maintenance period, a tolerance period last performed maintenance. Scheduled events can be manually moved to other data and transfer of remains when

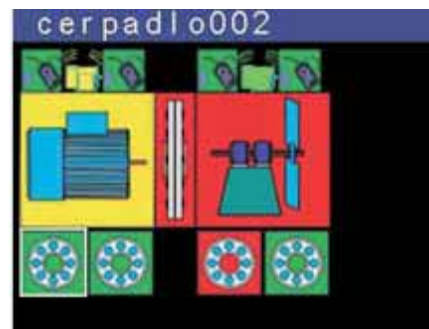


Figure 9 Immediate system diagnostics

It is also important to see how the machine follows intervals of preventive maintenances, what were the machine repaired failure to check, you can find out. who conducted the previous maintenance etc. This simply is accompanied by a maintenance status for ISO audit. Writing in maintenances performed is very simple, usually there is a transfer of work order in the form of maintenance done in one click.

Spare parts and other materials for the maintenance are also assigned to maintenance. When planning status is checked, when writing of maintenance is confirmed consumption. Stock maintenance usually results in the central stock holding. When writing maintenance is then automatically creates a material issue slip material consumed assigned to maintenance.

If there is a machine failure, it is entered in the list of messages to request repair. Janitors have immediate insight and action prioritization can handle. Reports can be executed either by writing to registers repair costs, or simply a description of what was done.

Printing module can filter required printouts according to the time limits and according to other conditions. Filters can be

preset and save the next time you select just the right one, you do not need to write again!

Software solution for maintenance management finds application in wide range of industrial fields. These are mainly automotive manufacturing, engineering, food, electronics and consumer goods production, which produces small series, bulk and custom.

This is mostly represented by chemical, metallurgical, machinery and vehicle traffic. In purchase of these systems show interest especially large companies, where processes are complex and their management and maintenance needs to be carried out by a large number of employees.

VIII. CONCLUSION

There are many advantages of using a predictive maintenance program. A well managed program of predictive maintenance would eliminate catastrophic equipment failure. Staff then will be able to schedule maintenance activities, minimize or eliminate overtime costs. Inventory parts or equipment can be minimized, because there is no need to order parts in advance to support the anticipated claims on maintenance. The equipment will be operated at optimal levels, thus it also saves energy costs and increased measurement device reliability.

Our studies have estimated that a properly functioning predictive maintenance program can provide savings of 8% to 12% during the actual use of the program strategy of preventive maintenance. Depending on the device, depending on the approach of reactive maintenance and material conditions, could easily achieve savings of 30% to 40%.

functional predictive maintenance program:

- savings of 8% to 12%. Depending on the type of device to access reactive maintenance and material conditions can achieve savings of 30% to 40%. Average savings in the industry after the start of term predictive maintenance program using:
- Return on investment: up to 10 times,
- reduced maintenance costs: 25% to 30%
- reduce the number of errors: 70% to 75%
- reduce downtime: 35% to 45%
- increase production 20% to 25%.
- provides increased service life and availability of components.
- provides preventive remedies.
- reflected in a reduction in equipment downtime or process.
- reduces the cost of parts and labor.
- integrates technical diagnostics in maintenance management
- provides improved product quality.
- improves the safety of workers and the environment.
- increases employee morale.
- increases energy savings.
- it is reflected in the estimated 8% to 12% cost savings that may result from a predictive maintenance program.

Another side of using predictive maintenance are initial costs. The initial costs of implementing this type of program can be expensive. Great piece of equipment requires expenditures in excess of \$ 50,000. And training personnel for efficient use of technology and predictive maintenance procedures would involve another financial resources.

Start of a predictive maintenance program requires understanding the needs of enterprise predictive maintenance and steps to be taken. To make this work, it is also necessary to have committed both management and whole personnel and company organization.

Disadvantages:

- provides preventive remedies.
- increase of investment on diagnostic equipment
- increased of investment on staff training
- easy sees potential savings

By introduction of maintenance management using CMMS, the company improves its ability to effectively utilize available resources. The inclusion of maintenance processes in the business information system enables managers to make strategic decisions based on explicit data and analytical tools.

Thanks to such management system for maintenance company to get a complete overview of the functioning of maintenance. Maintenance costs are reduced and the apparatus is always ready at the right time. The efficiency of utilization of the apparatus is improved and the same is true for the use of

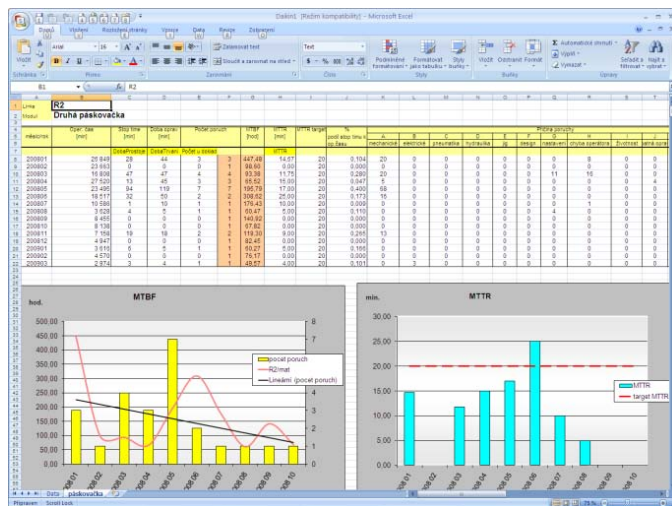


Figure 10 Cost evaluation in CMMS

In fact, independent surveys indicate the following industrial average savings result from the initiation of a

human and material resources for maintenance.

To sum up, for a successfully operating project of CMMS implementation several things need to be resolved:

- Human factors characterized by suitable education, salary, suitable personality, commitment...
- Technology - appropriate methods, devices, networking features, price, reports, graphical interface(HMI).
- Processes - integration into the maintenance process, automation of transmission and data collection.
- News - comprehensive evaluation of state, identification of causes, recommended actions, network availability...

A very important success factor is automation of data linking of preventive maintenance, autonomous (TPM) and predictive maintenance using industrial handheld diagnostic tools and new generation which are intended for operators and maintenance staff, as shown in Figure 8.

Another important step for the success are operators involved in process of collecting inspection, operational and diagnostic data (Operator Driven Maintenance).



Figure 11 PDA-type device for online maintenance checking

ACKNOWLEDGMENT

In conclusion, we would like to express thanks for the support of the projects SGS-2012-063 titled "Integrated design of manufacturing system as metaproduct with a multidisciplinary approach and with using elements of virtual reality" and project NEXLIZ – CZ.1.07/2.3.00/30.0038, which is co-financed by the European Social Fund and the state budget of the Czech Republic.

REFERENCES

- [1] MOBLEY, R. Keith - HIGGINS, Lindley R. - WIKOFF, Darrin J.: Maintenance Engineering Handbook. McGraw-Hill Professional, 2008. 1200 s. ISBN 00-7154-646-4.

- [2] RASCHMAN, P., PAČAIOVÁ, H: Špecifický Modul II (Spôľahlivosť, Riziko a Stratégia údržby), Košice, 2002.
- [3] FEDORČÁKOVÁ, M. ŠEBO, D.: Logistické plánovanie a riadenie výroby. In: Trendy v systémoch riadenia podnikov, 11. medzinárodná vedecká konferencia, Vysoké Tatry, Stará Lesná, 09.-11. december 2008, Zborník príspevkov, TU Košice, 2008, str. 365-370, ISBN 978-80-553-0115-0.
- [4] MATHER, D.: CMMS A Timesaving Implementation Process. CRC Press, 2002. 160 s. ISBN: 08-4931-359-7
- [5] BAGADIA, K: How to turn maintenance into a profit center using CMMS. <http://www.plantservices.com/articles/2005/525.html>.
- [6] BAGADIA, K.: Computerized maintenance management systems made easy: how to evaluate, select, and manage CMMS. McGraw-Hill Professional, 2006. ISBN 0071469850, 9780071469852
- [7] BLOCH, Heinz P. - GEITNER, Fred K.: Machinery component maintenance and repair Volume 3 of Practical machinery management for process plants. Elsevier, 2005. ISBN 0750677260, 9780750677264.
- [8] CAMPBELL, J.: Maintenance excellence: optimizing equipment life-cycle decisions. CRC Press, 2001. ISBN 0824704975, 9780824704971.
- [9] DANN, NR and CANTELL, T. (2005) Maintenance: from philosophy to practice. Journal of Architectural Conservation, 11 (1). pp. 42-54. ISSN 1355 6207
- [10] DUFFUAA, Salih - RAOUF, Abdul - CAMPBELL, John Dixon: Planning and control of maintenance systems: modeling and analysis. John Wiley and Sons, 1999. ISBN 0471179817, 9780471179818
- [11] EDWARDS, David J. - HARRIS, Frank - MCCAFFER, Ronald: Management of off-highway plant and equipment. Taylor & Francis, 2003. ISBN 0415251273, 9780415251273
- [12] EDWARDS, David J. - HOLT, Gary D. HARRIS, F.C.: Predictive maintenance techniques and their relevance to construction plant. Journal of Quality in Maintenance Engineering, 1998 Volume: 4 pp.:25 - 37. ISSN: 1355-2511
- [13] GREGOR, M. - KOŠTURIK, J. - RAKYTA, M. - VRÁB, F. : Totálna neproduktívna údržba (TPM), knižná publikácia, 28 strán, IPI, ISBN 80-88948-037
- [14] JARDINE, A. K. S. , The Use of Mathematical Models in Industrial Maintenance, The Institute of Mathematics and its Applications. U.K., August/September 1976, Page 232-235.
- [15] KYOKAI, Nihon Puranto Mentensu: TPM for every operator. Japan Institute of Plant Maintenance. Productivity Press, 1996. ISBN 1563270803, 9781563270802
- [16] UNIVERSITY OF STRATHCLYDE: Operational research in maintenance: papers presented at the Symposium on Operational Research in Maintenance held at Strathclyde University, December 1968. Manchester U.P., 1970
- [17] ZHANG, Z. - Li, Z. - Huo, Z.: CMMS and its application in power systems. IEEE International Conference on Systems, Man and Cybernetics, 2003. s. 4607- 4612 vol.5 ISSN: 1062-922X ISBN: 0-7803-7952-7
- [18] STN EN13306: Maintenance terminology
- [19] DPSI 1994. Uptime for Windows Product Guide, Version 2.1. DPSI, Greensboro, North Carolina
- [20] <http://www.gartner.com>
- [21] <http://www.rasax.sk>
- [22] <http://www.maintenanceassistant.com>.
- [23] <http://www.sgmaintenance.cz>

Physical modeling of flow characteristic in dissolved air flotation tank with chitosan and bentonite as coagulant

Mohd Remy Rozainy M.A.Z., Hasif M., Syafalny S., and Puganeshwary P.

Abstract— The modeling was carried out to study dissolved air flotation process in a tank involving mainly velocity distribution and turbidity removal. Chitosan and Bentonite were known as coagulant agents thus were used in the modeling. Measurements were carried out on four cases with different inlet velocities of 0.3m/s, 0.6m/s, 0.9m/s and 1.2m/s, each with 75 measurements. Laboratory tests were conducted to test the water quality based on turbidity values and basic drinking water parameters. From the test results, it was found that the liquid inlet velocity gave impacts on the distribution of flow in the tank and thus affects the efficiency of the flotation process. Chitosan and Bentonite can be applied to the flotation tank resulting in an average of 97% turbidity removal.

Keywords—Dissolved air flotation (DAF), physical modeling, chitosan, bentonite.

I. INTRODUCTION

DISSOLVED air flotation (DAF) was first applied to drinking water treatment in the late 1960's in Scandinavia and South Africa. The process is principally efficient in removing low density particles and flocs. Dissolved Air Flotation (DAF) in Malaysia; In recent years, the government's policy to upgrade services and technology development in Malaysia for water treatment processes becoming the main agenda to ensure that clean and adequate water can be supplied to all parts in Malaysia [1]. In conjunction with that, various technologies have been brought, including the DAF technology. Most industries and companies continue to use this method without a detailed study of the mechanism, optimum setting for efficient and high removal. As a result,

This research was carried out with financial support from the School of Civil Engineering, Universiti Sains Malaysia and Short Term Grant, Universiti Sains Malaysia (304/PAWAM/60313007).

Mohd Remy Rozainy M.A.Z. is with the School of Civil Engineering, Universiti Sains Malaysia, Penang, 14300 MALAYSIA (+604-599-6231; fax: +604-594-1009; e-mail: remyrozainy@yahoo.com).

Hasif M., was with School of Civil Engineering, Universiti Sains Malaysia, Penang, 14300 MALAYSIA. He is now with the Department of Renewable Energy, University of Manchester, Oxford Rd, Manchester M13 9PL, UNITED KINGDOM (e-mail: engr.hasif@yahoo.com).

Syafalny is with the Civil Engineering Department, Bina Nusantara University, Palmerah, Jakarta 11480, INDONESIA (e-mail: syafalni@gmail.com).

Puganeshwary P. is with School of Civil Engineering, Universiti Sains Malaysia, Penang, 14300 MALAYSIA (e-mail: cepuganeshwary@eng.usm.my)

there will be more cost of services which lead to very high maintenance. Although this method has been used worldwide in the treatment of surface water, but the DAF tank design standards are flexible and optimal chemical treatment processes are still not receive much attention [2].

Most of DAF application uses conventional coagulation such as Polyaluminium Chloride or Alum as a flocculation agent which can lead to some problems. Reference [3] reported that conventional coagulant (metal salts, such as aluminum or iron salts) lead to some problems such as may produce large amounts of sludge and consequently, abundance of sludge lead to treatment and disposal problems. In addition, Aluminium will possibly link to Alzheimer disease in the long term time frame [3]. So, the question is, is it possible to use the natural coagulant such as Chitosan and Bentonite for alum substitution? If it is possible, the suitability and the removal efficiency must be investigated.

The use of monocoagulants, such as Chitosan, may not be a good solution for highly turbid water purification because of its high cost. The possibility to reduce the amount of the primary coagulant at the same time keeping the removal to be in optimum may be a good strategy to reduce the operation cost. There might be another coagulant aid for example the natural clay of Bentonite to reduce the cost. The initial stage is to determine the Bentonite dosage and mixture ratio to be used with Chitosan. The in-tank flow behavior also must be investigated. For this reason, CFD have been used extensively to understand the contact and flow behavior of coagulant in the tank.

Another problem is, the mechanism of bubble-floc interaction in a DAF contact zone is poorly understood and usually described by conceptual models i.e Computational Fluid Dynamic [4]. Reference [5] reported that there was insufficient method and programs to design the DAF tank. Most of the researcher built up the tank based on the basic design guide. The basic design guidelines are only applicable in a very common water treatment, not in advance water treatment Thus, to get better performance of the tank they need to rebuild a new tank and this will cost them a longer time to be spent.

II. MATERIALS AND METHODS

The experimental work of this research is to validate the

dimensions, geometry proposed in the modeling procedures. The DAF tank is constructed in the laboratory and the flow velocity within the tank is conducted. This will provide data for the validation of the CFD model and identify any unknown outcomes in the DAF tank.

A. DAF Pilot Plant

In order to assess the applicability of CFD in comparison with the physical model, the DAF pilot plant is scaled and fabricated. The pilot plant is built and placed in the USM Environmental Lab 2. The saturator, an air compressor is designed based on the typical DAF guideline for drinking water treatment.

Fig. 1 shows the DAF pilot plant model. The detailed plan and views are illustrated in this figure. In previous research by [2], the DAF pilot plant was designed with rectangular shape with 1400 mm length, 700 mm width and 800 mm height. For this research, the DAF tank is downscaled to half of the tank of what [2] used. So, the new dimension of the new DAF pilot plant was designed with rectangular shape with 700 mm length, 350 mm width and 400 mm height. It is also equipped with baffles (70° inclined) which located in reaction zone. The baffle will help the collision between the particles and the bubbles where it will bring the particle to the surface and will be separated in separation zone.

B. Data Collections

In this research, the measurement was focused on the flow velocity in the tank. For a concrete validation, a visual test that involves the dry tracing method was also carried out to determine the flow characteristics in the DAF pilot plant. The measurement data will be used as a validation value when carrying out the CFD.

A. Velocity Measurement

The principle of the ADV (Acoustic Doppler Velocimeter) is based on the Doppler Effect. The Doppler Effect, which is an acoustical pulse that scattered on a moving object, experiences a frequency shift that is related to the speed of the objects or particles [6]. The ADV is constructed with a central transmitter and three receivers located in a circle around the transmitter (Fig. 2). The receivers are slanted towards a measuring point approximately 5-6 cm from the transmitter. Reference [7] had reported that the instrument is capable of measuring velocities down to 0.4mm/s and maximum was determined at 2.5m/s. Other measurements, [8] and [9] showed, in water with a high concentration of micro-bubbles of about 40-120mm, the measured velocity was reduced up to 70% depending on the air content and probe orientation. In this study, however, there were some points that the measuring point was not located 5 cm from the probe transmitter as stated by the manufacturer but only about 1-2 cm due to space restriction. The measurements of this study were hence assumed to be displaced 3-4 cm upwards, which is of little significance to the overall flow structure considering the size of the contact zone.

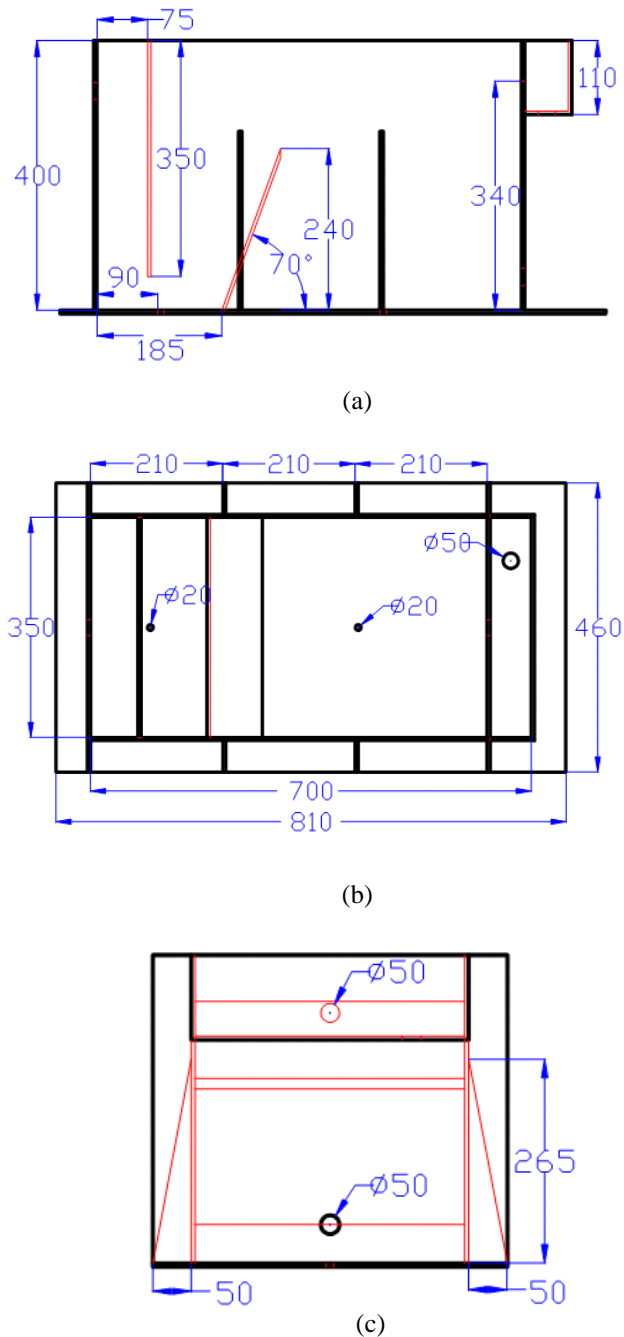


Fig. 1(a) side (b) plan and (c) front view of DAF tank (mm)

The velocity was measured at 0.2, 0.6, 0.8 and lowest of water surface. Velocity node distance is about 70mm from each other. There are 75 nodes of velocity measurement for a single run of the experiment. Fig. 3 and 4 show the location where the velocity data were obtained (front and plan view). From this number of points, 30 points are at between the entrance and first baffle, 18 points are in the contact zone, 42 points are at separation zone and 3 points at the outlet zone.

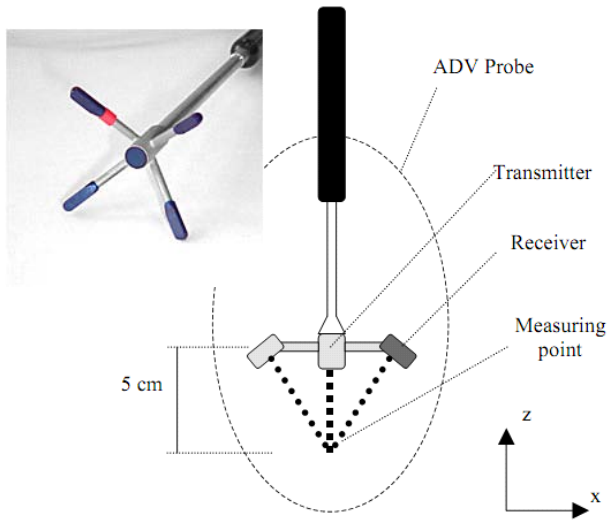


Fig. 2 vectrino™ ADV 3D velocity sensor

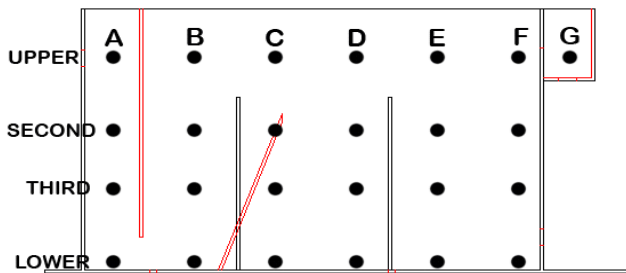


Fig. 3 side view of measurement points

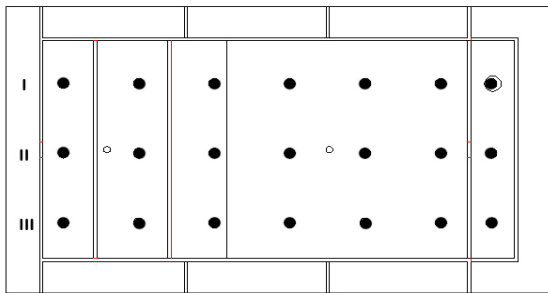


Fig. 4 plan view of measurement points

B. Flow Visualisations

The final assessment of the DAF pilot plant involves the observation of flow distribution in the reaction and separation zone. This is done with water dye tracer, which can give a clear visualization of the flow in the tank. Dyes were mixed with some water and the mixture then was poured into the inlet zone. The flow distribution that occurred in the reaction and separation zone was captured.

C. Turbidity Measurement of Treated Water

In order to check the effectiveness of the model, the sample of raw water and treated water will be taken and the water

quality will be determined based on the water turbidity and typical drinking water parameters. The turbidity of raw water samples was measured using HACH 2100P Portable Turbidimeter while for basic drinking water parameter was measured by using YSI Multiparameter Probe.

III. RESULTS AND DISCUSSION

A. Inlet Velocity of 0.3m/s (Case A)

Fig. 5 shows the velocity distribution inside the flotation tank with inlet velocity 0.3m/s. The highest velocity was occurring in the inlet velocity zone (Point A) for inlet level and in the contact zone area (Point C) for lower level which are 0.3m/s and 0.1m/s respectively. The lower level had this significant value because in contact zone it was located near to the nozzles. So, when the air is released with high pressure it will cause the increment of velocity distribution in that area. Besides, the dead flow region was detected in the separation zone (Point E and F) where the flow is too slow and the velocity is approximately to zero velocity. For separation zone, the water from upper level will move downward. As it's moving down, the velocity will slowly decrease and because Point D and E third level are considered located in the middle of the tank so there is no pressure to force the flow to move faster. At a lower level, the flow will have a backflow and going up and form a circulation flow pattern. Point D at third level somehow becomes the center of the circulation flow and this is probably the reason why the dead region is detected at that point.

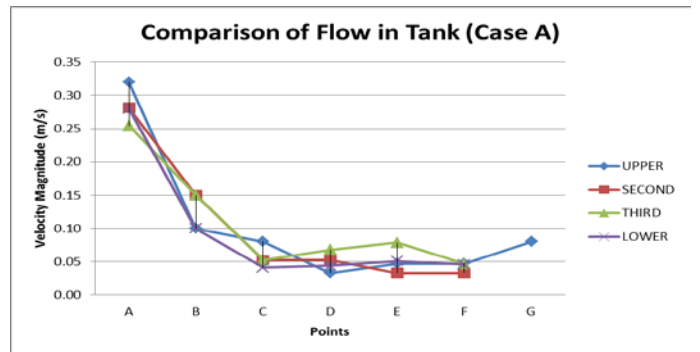


Fig. 5 graph of experimental velocity distribution in DAF tank for Case A (0.3m/s)

For Point A and Point B, the higher velocity is consistently distributed at upper level while the velocities for other levels are decreased. This is due to in contact zone; the water is forced to move to the surface of water by the high pressure from the nozzles. So, when it passes the inclined baffle the flow of the upper level is higher compared to the other levels below it. However, the velocity distribution for all levels is increased at the outlet pipe (Point G) due to suction effect.

B. Inlet Velocity of 0.6m/s (Case B)

Fig. 6 shows the graph of the velocity distribution of water inside the DAF tank with an inlet velocity of 0.6m/s. From the

graph, it shows that the velocity value is higher at the upper level of the tank (Point A) because of its location that's near to the inlet pipe. Point B to point D is an area that located in the contact zone, where the nozzles is placed. The results show that the velocity value is significantly increased at Point C especially for lower level because it is located near to the nozzle.

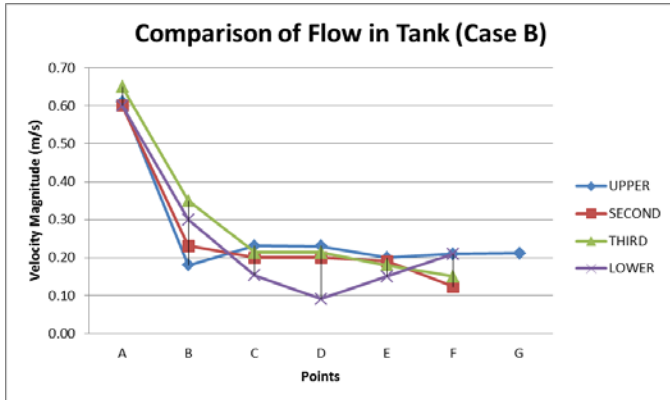


Fig. 6 graph of experimental velocity distribution in DAF tank for Case B (0.6m/s)

Point E and F are areas where the separation process takes place. The velocity distribution for upper level is slightly increased compared to other level which are significantly decreased. This is probably because of the water is flowing from the upper to the lower level in the separation zone. But for Point F at second and third level, the velocity distribution is increased due to the suction effect of the outlet pipe. The same goes to Point G at upper level because it's located on outlet pipe.

C. Inlet Velocity of 0.9m/s (Case C)

Fig. 7 shows the graph of the velocity distribution of water inside the DAF tank with an inlet velocity of 0.9m/s which is can considerably a high velocity for a flotation tank. From the graph, it shows that the velocity value is higher at the upper level of the tank (Point A) because of its location that's near to the inlet pipe. Point B to point D are areas that located in the contact zone, where the nozzles is placed. The results show that the velocity value is significantly increased at Point C especially for lower level because it is located near to the nozzle.

Point E and F are areas where the separation process takes place. The velocity distribution for upper level is slightly increased compared to other level which are significantly decreased. This is because of the water is flowing from the upper to the lower level in the separation zone and in the outlet pipe. But for Point F at second and third level, the velocity distribution is increased due to the suction effect of the outlet pipe. The same goes to Point G at upper level because it's located on outlet pipe.

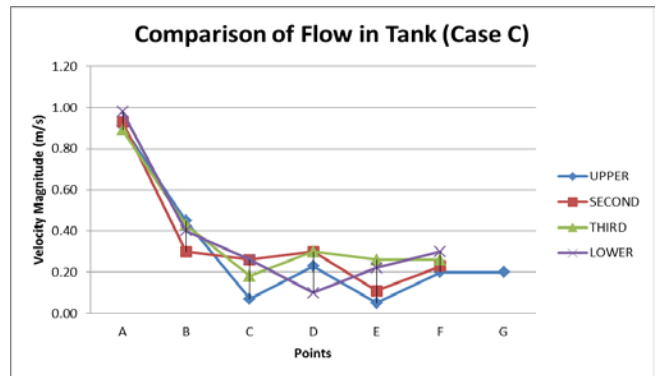


Fig. 7 graph of experimental velocity distribution in DAF tank for Case C (0.9m/s)

D. Inlet Velocity of 1.2m/s (Case D)

Fig. 8 shows the velocity distribution of water inside the flotation tank using three nozzles with inlet velocity 1.2m/s. This case was operated with highest inlet velocity among other cases. A cross-sectional velocity profile was taken at four different water depth levels to verify the velocity of the flow within the tank and the results show that the velocity of water that entering the tank (Point A) is detected the highest which is, 1.21m/s. However, the value is decreasing as it moves from second level to lower level. Amongst all of the cases, the velocity value in the contact zone for lower level had achieved 0.75m/s which are the largest value of this study. Then, the velocity has been rapidly decreased to the Point F and G. Point C and D is detected as high velocity because it located in the contact zone.

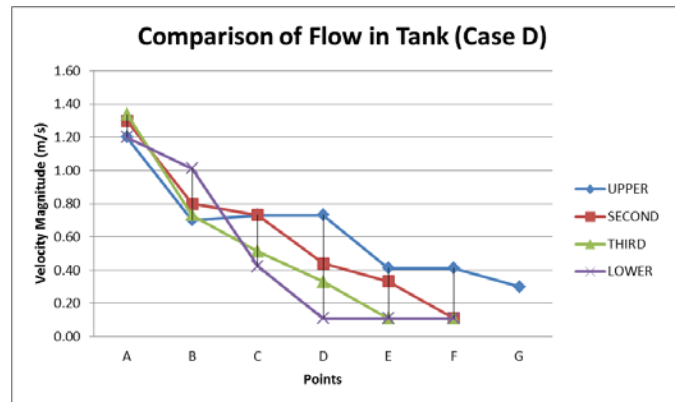


Fig. 8 graph of experimental velocity distribution in DAF tank for Case D (1.2m/s)

In addition, the velocity distribution was found higher in Point F to Point G for upper level compared to the velocity distribution at lower levels. This is due to the flow movement. Contradict to flow movement in contact zone, in separation zone the water is moved downward from upper level to lower level. The upper level will have higher velocity compared to lower level. The suction effect of the outlet pipe can be considered the cause why the velocity distribution is rising at

the end of the DAF tank.

E. Water Quality Test

The water quality test for raw water (before) and treated water (after treatment) are reported in Table I. The water quality test for this experiment is mainly focused on the removal of turbidity in raw water. Additionally, the basic drinking water parameters had being checked for any potential improvement. From the table, it is clear that DAF is very efficient in removing turbidity in the low velocity of water. Case A reported the highest which is 97% of removal efficiency compared to other cases with treated turbidity of 1.82 NTU from the raw water turbidity of 52.3 NTU. Also, for Dissolved Oxygen (DO) reading, it shows the significant decrease with the higher inlet velocity. This is due to, slower the inlet velocity, the more contact time, the more water can be oxygenized.

F. Visual Observation Using Dye

In order to make clear of the characteristics of flow in the flotation tank, a dye tracer is used to give a clear visual of the flow. The dye was injected at the inlet zone and the movement of the dye is observed. For this investigation, Case A with inlet 0.3m/s is chosen. The results show, for contact zone the flow can be classified as turbulent flow due to the existence of air nozzle in that area. Although the inlet velocity is low which is only 0.3m/s, the pressure effect of the nozzle will create a turbulent region in that area. While for separation zone, the flow can be considered as laminar flow where the flow is evenly moving downward.

It is observed that, starting in the inlet zone till the contact zone, it takes a short time for the dye to disperse. That is the proof of the turbulent flow of water in that area. Furthermore, the pressure from the nozzle makes the mixing flow of the water.

For separation zone, it requires more time for dye to cover the entire zone because of the slow movement of water and the volume of separation zone is bigger than in the contact zone and inlet zone. Fig. 9, 10, and 11 show the sequences of the flow from the visual observation. For Fig. 9, the photo was taken before the dye is injected into the tank. The white color of pressurized water with air bubbles (red circle) starting to be released from the nozzle with high pressure. After that, dye tracer is injected for clear visualization which is shown in Fig. 10(a). As soon as the dye tracer is injected into the inlet zone, it will pass down the first baffle and enter the contact zone. Here, the dye is forced to move upward by the high pressure that produces from the nozzles. Then, the flow will move passing the second baffle into the separation zone which shown in Fig. 5.10(b). In separation zone, it shows that the flow will move downward and it tends to flow to the outlet pipe (red circle) due to suction effect. Lastly, Fig. 11 shows the complete process of visual observation where the dye is covered in the entire tank.

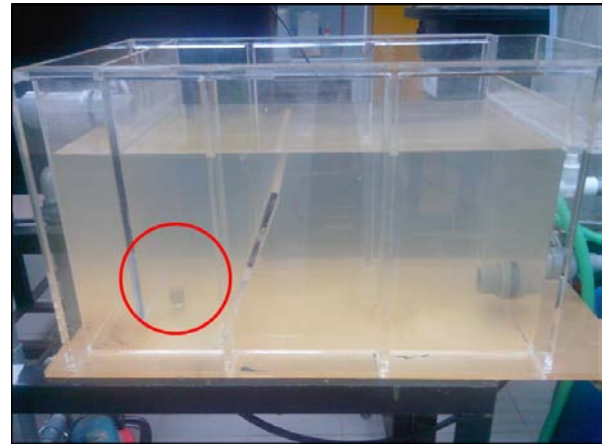
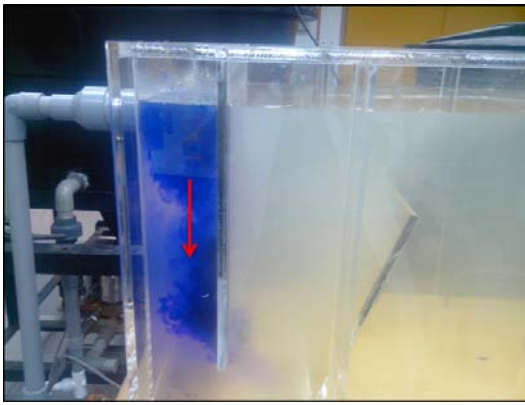


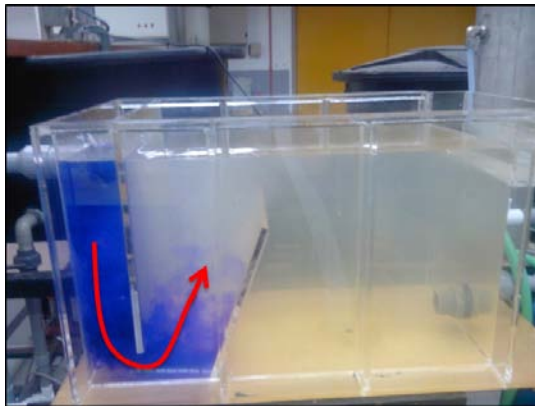
Fig. 9 visual observation before dye injection

Table I: water quality test for before and after DAF treatment with different inlet velocity

Parameters	Before	After Treatment			
		Case			
		A (0.3m/s)	B (0.6m/s)	C (0.9m/s)	D (1.2m/s)
Turbidity (NTU)	52.3	1.82	2.14	3.96	7.89
DO (mg/l)	2.22	3.77	3.72	3.3	2.81
Conductivity (us/cm)	84.50	92.3	90.3	92.3	89.1
TDS (mg/l)	58.3	50.3	50.3	49.8	51.2
pH	7.3	7.3	7.3	7.3	7.3
Salinity	0.03	0.04	0.04	0.03	0.03



(a)



(b)

Fig. 10(a) and (b) visual observation after dye injection from inlet to contact zone

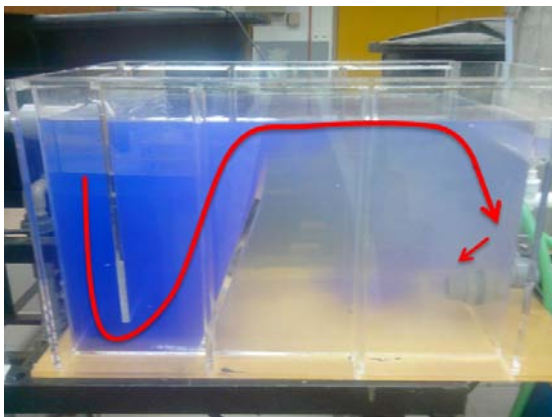


Fig. 11 dye movement in the separation zone

IV. CONCLUSION

This study successfully proved the effectiveness of the combination of Chitosan and Bentonite as a coagulating agent in a DAF tank for raw water treatment process. The optimal conditions were determined on the basis of turbidity removal. From the study, the efficiency achieved 97% of turbidity removal. In all cases, the outcomes show that in inlet zone the velocity distribution is higher at upper level because it is in the vicinity of inlet pipe where the water is flowing into the tank. And as it's moving down, the velocity is slowly decreased. In contrary, the velocity in the contact zone at lower levels is

higher compared to upper level because of the pressure effect of the nozzle. For separation zone the velocity is constant higher in upper level compared to a lower level because the flow is moving downward in separation zone. However the velocity is higher in the vicinity of outlet pipe due to the suction effect caused by the water flowing out. The physical model can justify the fluid flow characteristic in the DAF tank by showing the velocity distribution between the variations of the data. The tracking of coagulant in the DAF tank can be understood when the flow characteristic of fluid is predicted.

ACKNOWLEDGMENT

Authors would like to say thanks to Prof Nordin Adlan and Mr. Afifi Akhbar for their advice and support throughout this study.

REFERENCES

- [1] KeTTHA (2009) *Objectives of Water Sector*. Retrieved May 18, 2013 from Kementerian Tenaga, Teknologi Hijau dan Air Web site: <http://www.kettha.gov.my/en/content/objectives-water-sector.htm>.
- [2] M. F. Murshed, Azalina, M. N. Adlan, and S. Syafalni, "Flow Characteristics in Dissolved Air Flotation using Computational Fluid Dynamic," *Water Science and Technology*, no. 81, pp. 265–271, 2009.
- [3] C. Y. Hu, H. L. Lo, and, C. L. Chang, "Treatment of Highly Turbid Water Using Chitosan and Aluminium Salts," *Separation and Purification Technologies* no. 104, pp. 322-328, 2013.
- [4] L. S. Chow, *Performance Study on Dissolved Air Flotation Unit Process and Performance Improvement Study in the Physico-Chemical Treatment of Wastewater*, Master thesis, Universiti Teknologi Malaysia, 2007.
- [5] R.B.Moruzzi, and M.A.P. Reali, "Characterization of micro-bubble size distribution and flow configuration in DAF contact zone by a non-intrusive image analysis system and tracer tests," *Water Science and Technology*, no. 61, pp. 253–262, 2010.
- [6] M. Lundh, M. Jonsson, and J. Dahlquist, "The Influence of Contact Zone Configuration on the Flow Structure in a Dissolved Air Flotation Pilot Plant," *Ijfat. Res.* vol. 36, no. 6, pp. 1585-1595, 2002
- [7] A. Lohrmann, R. Cabrera, and N.C. Kraus "Acoustic Doppler Velocimeter (ADV) for laboratory use. In: Proceedings of Fundamental and Advancements in Hydraulic Measurements and Experimentation" ASCE, 1994.
- [8] M. Lundh, , M.Jonsson, and J.Dahlquist, "Experimental Studies of the Fluid Dynamics in the Separation Zone in Dissolved Air Flotation," *Water. Resources* vol. 34, no. 1, pp. 21-30, 2000.
- [9] M. Lundh, , M. Jonsson, and J. Dahlquist, "The Flow Structure in the Separation Zone of a DAF Pilot Plant and the Relation with Bubble Concentration" *Water Science and Technology*, Vol. 43 no. 8, pp. 185-194, 2001.



Mohd Remy Rozainy M.A.Z is a senior lecturer in School of Civil Engineering, Universiti Sains Malaysia (USM). This author had join USM from 2012. He was born in Penang Island, Malaysia on 24 September 1980. He got his degree (Bachelor of Civil Engineering) from Universiti Sains Malaysia (2000-2004) and continues his master (urban drainage) from the same university (2004-2008). Then in 2008 he join Prof. Takara Laboratory as graduate student before he pursue his PhD (Water Resources Engineering) in Kyoto University (2009-2012) under supervision of Prof. Kaoru Takara and Associate Prof. Yosuke Yamashiki.

Dr. Remy had joined Japanese Society of Civil Engineer from 2009 until present. Dr. Remy has very vast experiences in hydraulic physical model study and computational modeling of pump sump by using computational fluid dynamic (FLUENT) software. Until now, he had involved more than 15 projects related to physical model of pump sump.

Cyclic in-plane testing for evaluation of shear capacity for ceramic block walls

Eva. Partene, Andrei. Bindean, Mihai. Fofiu, Valeriu. Stoian, Luminita. Fekete-Nagy

Abstract—This experimental research aims to provide valuable informations regarding the behavior and shear capacity of ceramic block structural walls, subjected to in-plane horizontal loads. A number of six shear walls are subjected to cyclic horizontal loading in order to observe the response of this type of structural walls. The experimental specimens are built up using brick with vertical hollows which represents a very common system for low-rise buildings (up to 4 stories, depending on the seismic acceleration of the site). Two Fiber Reinforced Polymers (FRP) based strengthening solutions are applied on the six walls specimens, after testing them in bear state (only as brick masonry walls without any FRP components). The main objective of the strengthening solutions is to obtain increased shear capacity for the strengthened elements. However, the efficiency of the provided strengthening techniques is assessed through several parameters that are of outmost importance for applications in seismic areas, such as ductility, stiffness and energy dissipation.

Keywords—ceramic block with hollows, shear walls, FRP materials, strengthening.

I. INTRODUCTION

Masonry structures are a significant portion of the world's heritage buildings and a significant component of the modern residential building stock. Particularly this type of structures are susceptible to damage from seismic horizontal loading [1]. In Romania, many of these structures, located in seismic area are built without any reference to seismic design rules. Therefore the need for new strengthening technologies is essential [2].

The traditional strengthening methods available today, such as steel plate bonding, steel frame works, welded mesh, shotcrete jacketing, have disadvantages such as adding considerable mass to the structure, are labor intensive, need creating work space and access limitations, and the most important disadvantage is the aesthetics of the building. Therefore, the use of fiber reinforced polymers (FRP) has gained much attention [1].

The advantages of FRP retrofitting solutions are high strength at low weights, ease of application, requires minor preparation, preserves the material integrity and has high resistance to corrosion over existing conventional techniques [3]. However, external chemically bonding involves complex mechanical and

strength phenomena, such as: the possible peeling off of the brick surface, the brittle behavior of FRP both in shear and tension, the effective resisting response of the reinforcement with respect to its theoretical capacity, the influence of friction and dilatancy in the brick-mortar interface on the response of the strengthening and the coupling difference strength mechanisms activated by the reinforcing, which include an increase friction due to the generation of normal anchoring forces and the contribution of the shear strength of the laminates [4].

The present experimental study is focused on masonry walls built with ceramic blocks with hollows, which is a very common system in our country for low-rise buildings, up to 4 stories, depending on the seismic ground acceleration. The strengthening was made using FRP solutions, after testing the masonry walls in bear state.

II. EXPERIMENTAL PROGRAM

A. Test plan

The experimental tests were performed on two masonry walls subjected to a constant vertical load and horizontal cyclic loading. Each wall had the length and height of 1,50 m and the thickness of 25 cm. The horizontal load was increased until the collapse mechanism was activated, then the applied load was removed and each wall was strengthened with FRP materials. The strengthening solutions were applied on the damaged structures and the results allow us to evaluate the enhancement of the structural response of the masonry walls due to the application of the FRP [5].

The test frame considered, is built of three main parts: a reaction frame for the horizontal load, a reaction frame for the vertical load and a sliding frame as seen in Fig. 1. The horizontal load was transferred through the sliding frame to the test units. A dynamic actuator was used to carry out displacement control tests.

Instrumentation consisted in 12 displacement traducers and 2 pressure traducers in order to determine the drift of the wall, the forces applied and to determine if there is any out of plane displacement, as seen in Fig. 1.

This work was partially supported by the strategic grant POSDRU/159/1.5/S/137070 (2014) of the Ministry of National Education, Romania, co-financed by the European Social Fund – Investing in People, within the Sectoral Operational Programme Human Resources Development 2007-2013.

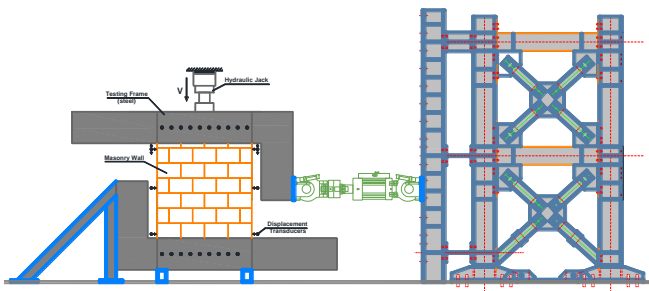


Fig. 1 Experimental stand and loading scheme

B. Test specimens

The masonry wall specimens, where built using ceramic blocks with hollows and as seen in Fig. 2. the first specimen was unreinforced masonry (URM1), the second was reinforced masonry with two concrete columns on sides (RM1) and the third was reinforced masonry with one central concrete column (RM2). The position of the reinforcement can be seen in Fig. 4. The FRP mesh and the FRP carbon plate, were applied in diagonal sections. The URM1 specimen was strengthened using FRP carbon plates and for the RM1 and RM2 specimens was used a FRP carbon mesh material. The strengthening configurations were applied on both faces of the walls. The FRP materials were applied only after the surface of the masonry walls was levelled with a thixotropic epoxy resin as seen in Fig. 3.

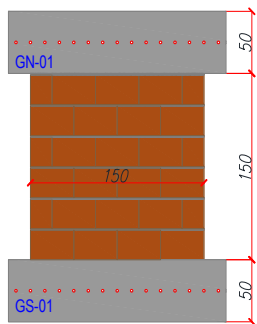


Fig. 2 (a) Test specimen URM1-unreinforced masonry wall

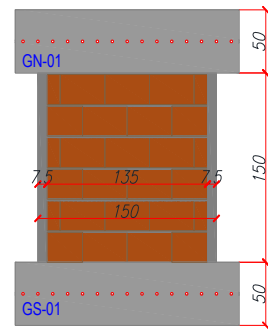


Fig. 2 (b) Test specimen RM1-reinforced masonry

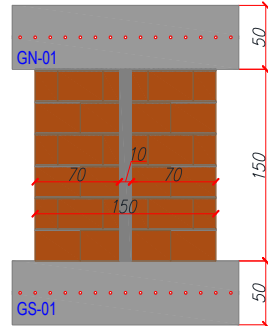


Fig. 2 (c) Test specimen RM2-reinforced masonry

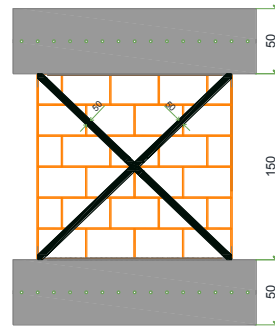


Fig. 3 (a) Strengthened test specimen URM

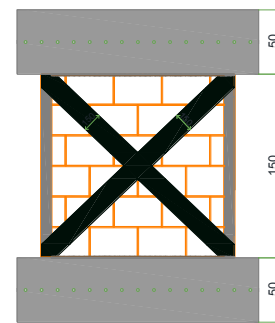


Fig. 3 (b) Strengthened test specimen RM1

C. Material properties

The material properties for masonry walls and CFRP mesh and the carbon plate are given in Table 1. The masonry properties were determined from material tests conducted. The walls were constructed by a qualified brick layer using brick hollowed units and general purpose mortar, consisting of cement, hydrated lime and sand. The FRP material properties shown in Table 1 were obtained from the manufacturer’s data sheets.

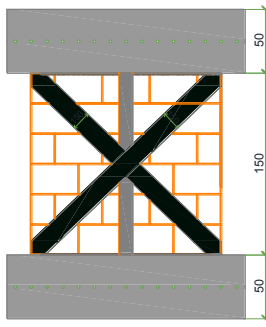


Fig. 3 (c) Strengthened test specimen RM2

III. EXPERIMENTAL RESULTS

As mentioned before, the specimens were subjected to a lateral horizontal load. The vertical load applied was constant.

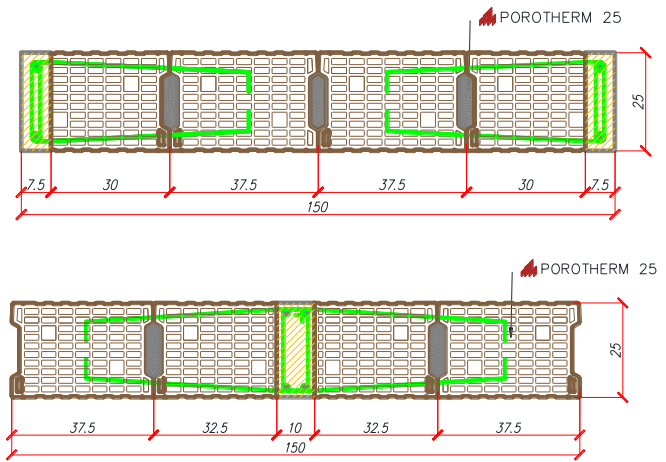


Fig. 4 Reinforcement position for the masonry walls RM1 and RM2

Table 1 – Material properties for wall test specimens

Parameter	Thickness mm	Density g/cm ³	Tensile strength N/mm ²	Viscosity MPas	Shear strength N/mm ²	Compressive strength N/mm ²
Primer	-	1.1	-	300	-	-
Thixotropic epoxy	-	1.70	-	800000	-	-
Medium viscosity epoxy resin	-	1.06	40	7000	-	70
Carbon plates	1.4	0.00161	3100	-	77	-
Carbon mesh	0.166	1.8	4830	-	-	-
Parameter	Flexural tensile strength N/mm ²	Compressive strength N/mm ²	Elastic modulus masonry N/mm ²			
Masonry	0.14	3.98	2350			

As mentioned before, the specimens were subjected to a lateral horizontal load. The vertical load applied was constant. The two masonry specimens failed in the classical failure mode: diagonal cracking. Due to the great irregularity in the masonry texture, the strengthening of the panels was carried out only after spreading a layer of thixotropic epoxy resin, to create a sufficiently plane, uniform surface on which the FRP material was then applied. The maximum load increased with 15% at the reinforced wall RM1, compared with the unreinforced wall URM1, and the maximum displacement also increased with 10%. The difference is not very important, but RM1 supported much more loading cycles, therefore has a higher ductility.

The first retrofitting solution, using FRP carbon plates, even though involves higher costs, had a very good result. The maximum load increased with 85%. The failure mode was very fragile, the disadvantage been the splitting of the carbon plates with the peeling of the ceramic blocks, as seen in Fig. 5.

For the second masonry wall RM1, the retrofitting solution was with CFRP mesh. The surface was uniformed also a thixotropic epoxy resin and after drying, the mesh was applied using a glued resin. The results were not so spectacular, but the wall was able so support a horizontal maximum load similar

with the initial wall, which proves the efficiency of this type of retrofitting solution. The failure mode was also fragile, with the splitting of the CFRP mesh with the peeling of the ceramic block as seen in Fig. 6 [6].

For the third masonry wall RM2, the retrofitting solution was also with CFRP mesh. The results were very good due to the fact that the strengthened wall regained the capacity to support the same horizontal force with the wall in bear state. The failure mode was also with the splitting of the CFRP mesh with the peeling of the ceramic block as seen in Fig.7.

The Displacement-Load diagrams for the 3 walls can be seen in Fig. 8.

IV. CONCLUSIONS

The experimental program was conducted to identify the effectiveness of retrofitting damaged URM and RM shear walls with FRP carbon plates and CFRP mesh. The following conclusions can be drawn from this experimental study:



Fig. 5 Failure mode for URM1-C (URM1-strengthened)

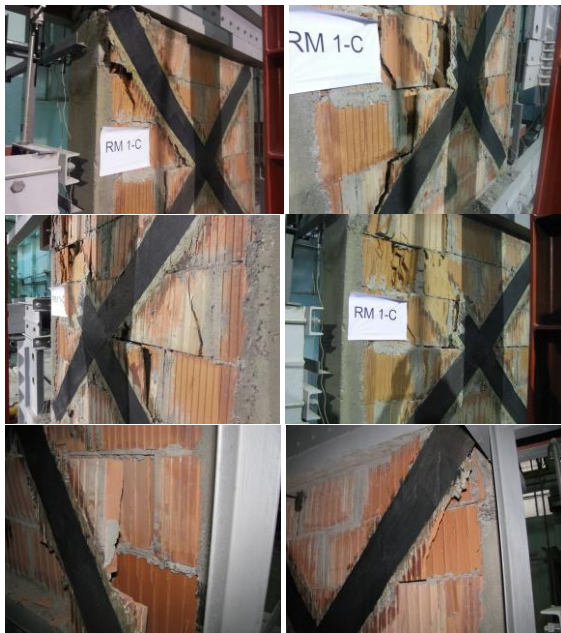


Fig. 6 Failure mode for RM1-C (RM1-strengthened)

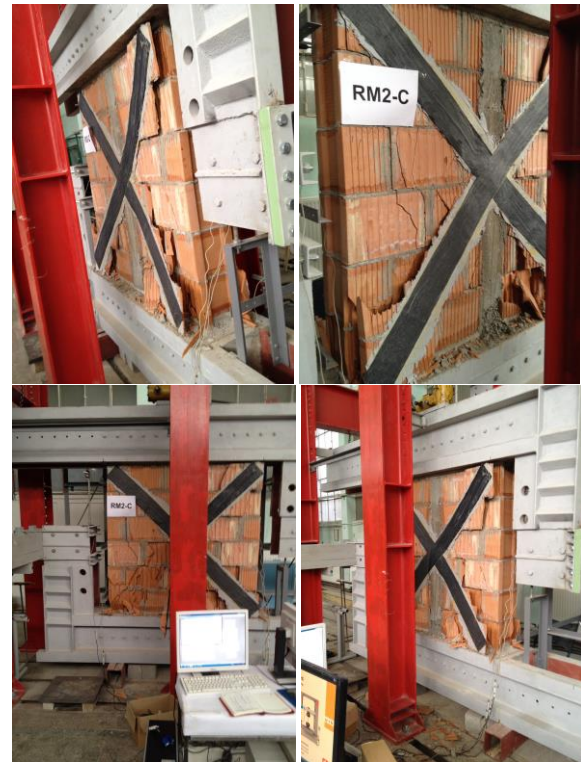


Fig. 7 Failure mode for RM2-C (RM2-strengthened)

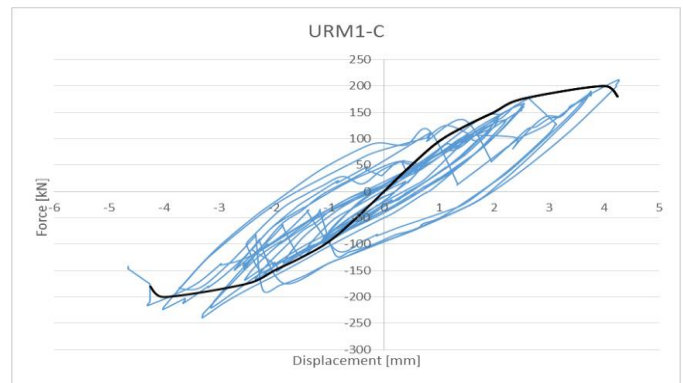


Fig. 8 (a) Force-Displacement Diagrams for URM1-C

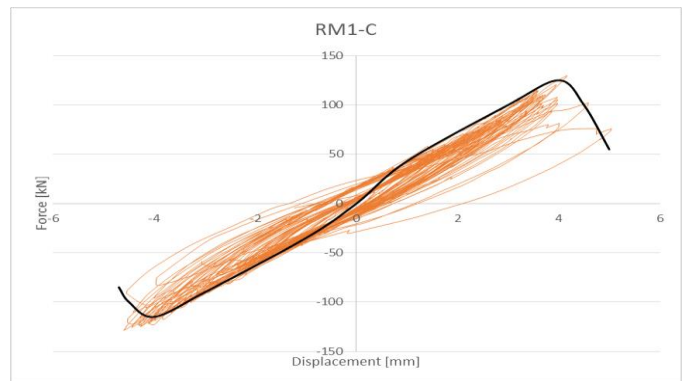


Fig. 8 (b) Force-Displacement Diagrams for RM1-C

- The displacement capacities of the walls increased once due to the reinforcement of masonry and second due to the retrofitting solutions applied.
- The maximum load was significant increased in the first retrofitting solution with FRP carbon plates, but in the second retrofitting solution the load was at 90% from the initial load and for the third wall the load was at 100% from the initial load. However, the retrofitting was successful in restoring the maximum load and even increasing it substantially during the test and allowing a larger maximum displacement for all the walls tested until now.
- The retrofitted walls displayed greater energy dissipation ability compared with the walls in bear state [7].
- If we compare the experimental tests of the walls in bear state with the strengthened walls we can observe the following differences, as seen in Fig. 9.

The results highlight the effectiveness of the FRP carbon plate and CFRP mesh in improving the performance of masonry walls under cyclic in-plane shear loading. Future

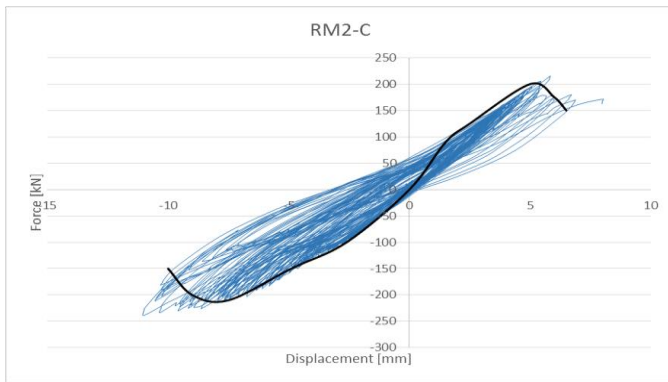


Fig. 8 (c) Force-Displacement Diagrams for RM2-C

Future work will focus on further experiments of this type of wall, with this type and other retrofitting solutions.

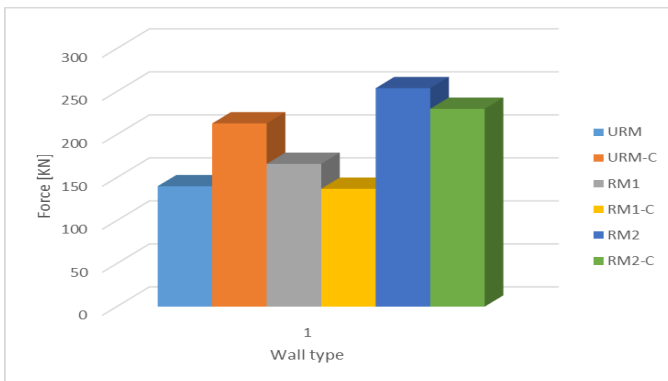


Fig. 9 Maximum horizontal load applied for the six experimental tests

ACKNOWLEDGMENT

The authors would like to express their appreciation and thanks to Politehnica University Timisoara, Department of Civil Engineering, for the technical and partially the financial support. Also, the strengthening materials were funded by MAPEI ROMANIA Company.

REFERENCES

- [1] M. Griffith, "Flexural displacement response of NSM FRP retrofitted masonry walls," in *Constructions and Building Materials*, 2012.
- [2] A. Dogariu, "Seismic retrofitting techniques based in metallic materials of RC and/or masonry buildings," in *PhD Thesis Volumes*, Politehnica University Timisoara, 2009.
- [3] M. Elgawady, "Shear strength of URM walls retrofitted using FRP," in *Engineering Structures*, Vol. 26, 2006, pg. 1658-1670.
- [4] P. Roca, "Shear response of brick masonry small assemblages strengthened with bonded FRP laminates for in-plane reinforcement," in *Constructions and Building Materials*, vol. 24, 2010, pg. 1372-1384.
- [5] I. Cancelliere, "Experimental tests and numerical modelling of reinforced masonry arches," in *Engineering Structures*, Vol. 32, 2010, pg. 776-792.
- [6] C. Lanivski, "State of the art for strengthening masonry with fiber reinforced polymers," in *Buletinul Institutului Politehnic din Iasi*, Vol. 58, 2012., pg. 97-114.
- [7] K.M.C. Konthesingha, "Static cyclic in-plane shear response of damaged masonry walls retrofitted with NSM FRP strips – An experimental evaluation," in *Engineering Structures*, Vol. 50, 2012., pg. 126-136.

AUV Localization Using a Single Transponder Acoustic Positioning System

Igor N. Burdinsky, Semen A. Otcheskiy
 Department of Computer Science
 Pacific National University
 Khabarovsk, Russia
 igor_burdinsky@mail.ru, semgog@mail.ru

Abstract—The article considers the problem of autonomous underwater vehicle navigation using a single transponder and proposes a new method for calculating the underwater vehicle coordinates based on the particle filter. A comparison of the new method with the known method of underwater vehicle's positioning based on the Kalman filter is given in the article.

Keywords—navigation, underwater acoustic positioning systems, autonomous underwater vehicle, Kalman filter, particle filter.

I. INTRODUCTION

Hardware and software for positioning in the marine environment are of great importance for autonomous underwater vehicles (AUV) as a successful execution of the vehicle mission depends on the reliability and accuracy of its navigation system [1,2].

Today long base-line (LBL) acoustic positioning systems are considered to be the best means of determining the AUV coordinates because of a wide range of operation (from hundreds of meters to tens of kilometers) and high accuracy [3,4]. In these systems the object position is determined in real time on the basis of measured distances to a set of reference beacons-transponders with known coordinates [5]. Despite their reliability and accuracy, the classic LBL systems have significant drawbacks:

- Low mobility. Installing the positioning system implies deploying at least three transponders around the area, in which underwater works will be carried out. Since the distance between the beacons can be up to tens of kilometers, it can take a lot of time and must be done in advance before the launch of an AUV. A similar situation is with LBL system dismounting. Due to low mobility, such systems are usually installed once and for a long-term operation in a given area.
- High cost. The acoustic transponders used in LBL systems are complex autonomous technical aggregates, which cost tens and hundreds of thousands of dollars. It is impossible to deploy positioning system beacons without vessels, the operation of which also requires considerable financial expenses.
- Restricted use. There can be such conditions, when it is difficult or impossible to deploy a navigation system

consisting of several transponders, separated by long distances. For example, when using AUV in ice conditions [6].

These drawbacks can be eliminated if a single reference transponder is used. However, in this LBL system configuration the position of the object cannot be determined with a single range measurement. There are two approaches to solving this problem.

The first approach is the use of classical LBL system algorithms under special conditions: a series of range measurements to the reference beacon is carried out from different AUV positions; the AUV movement trajectory between these positions is tracked with maximum precision. This solution is presented in [7] and is based on the use of a high-precision dead reckoning system. This approach has the following drawbacks:

- Providing high precision AUV motion parameters is a difficult task, and solving this task leads to a substantial increase in the cost of onboard systems.
- Since it is impossible to achieve an absolute measurement precision, there still remains an unsolved problem of the error accumulation in dead reckoning systems, because of which it is necessary to periodically correct the AUV position using other navigation tools (the position can be determined using satellite navigation after the surfacing of the AUV).

The second approach to the problem of providing navigation using a single transponder is to develop new algorithms [8-10]. The main advantage of this approach is that it is universal, i.e. the obtained solution can be applied to most existing AUVs and LBL systems.

The purpose of this paper is the research and development of algorithms for calculating the AUV position using a single LBL system transponder.

II. THE KALMAN FILTER

Most algorithms for computing the AUV position with a single transponder are based on the idea of correction of the coordinates obtained by an onboard dead reckoning system according to the measured ranges between the AUV and the transponder. Typically, these algorithms are based on the

Kalman filter [10-12] due to its precision and low computational complexity. Now we will consider a simplified version of the algorithm proposed in [10].

Step 1. Initialization of the Kalman filter.

Setting statistical filter parameters E_1 , E_2 (set once before launching the AUV):

$$E_1 = \begin{bmatrix} \delta v_s^2 & 0 \\ 0 & \delta v_s^2 \end{bmatrix}, \quad E_2 = \delta \tau \quad (1)$$

where δv_s is the expected standard deviation of the sound velocity in the marine environment from the real value; $\delta \tau$ is the expected standard deviation of the measured navigation signal propagation time (time during which a sound wave of the signal covers the distance between the AUV and the transponder).

The following steps of the algorithm focus on calculating the AUV position and they are executed each time the navigation signal from the reference transponder is received by the AUV.

Step 2. Measurement of the AUV motion parameters by means of onboard sensors.

The following parameters are measured: the duration of the navigation interval dt (the time interval between the current and the previous registration of the navigation signal by the AUV); the average speed of the AUV in relation to the seabed during the navigation interval v_{AUV} ; the resultant displacement vector α .

Step 3. Calculating the current AUV position by the onboard dead reckoning system.

$$\left. \begin{aligned} x_i &= x_{i-1} + \Delta_x \\ y_i &= y_{i-1} + \Delta_y \end{aligned} \right\}, \quad (2)$$

where x_{i-1} , y_{i-1} are the AUV coordinates at the end of the previous navigation interval; Δ is a resultant displacement, which is calculated by the formula:

$$\left. \begin{aligned} \Delta_x &= v_{AUV} dt \cos(\alpha) \\ \Delta_y &= v_{AUV} dt \sin(\alpha) \end{aligned} \right\}, \quad (3)$$

Step 4. Calculation of the filtration parameters.

a) Calculation of the expected value of covariance matrix

$$E_{cov} = E_{cov} + E_1, \quad (4)$$

for the first navigation interval E_{cov} equals 0.

b) Calculation of the filtration vector V_k

$$V_k = \frac{P_{AUV} - P_b}{\|P_{AUV} - P\|_{v_s}}, \quad (5)$$

where P_{AUV} is a vector containing the AUV coordinates, taken by the onboard dead reckoning system; P_b is a vector containing the coordinates of the reference transponder; v_s is a mean value of sound velocity in the marine environment.

c) Calculation of the Kalman gain vector C_k :

$$C_k = \frac{1}{C} E_{cov} V_k^T, \quad (6)$$

where C is a coefficient, calculated by the following formula:

$$C = V_k E_{cov} V_k^T + E_2. \quad (7)$$

d) Calculation of the difference Err between the measured (τ) values and the calculated (τ_{est}) in relation to the obtained by the dead reckoning system position values of the sound wave propagation time between the AUV and the reference transponder.

$$Err = \tau - \tau_{est}. \quad (8)$$

Step 5. Calculation of the AUV position:

a) Correction of the coordinates, obtained in Step 2.

$$\left. \begin{aligned} kx_i &= x_i + C_k(1)Err \\ ky_i &= y_i + C_k(2)Err \end{aligned} \right\}, \quad (9)$$

where kx_i , ky_i is the algorithm result, final AUV coordinates.

b) Recalculation of the covariance matrix for calculation of the coordinates of the next navigation signal registration:

$$E_{cov} = (I - C_k V_k) E_{cov}, \quad (10)$$

where I is a 2x2 identity matrix.

In the given algorithm the calculation of the current AUV coordinates is done by correcting the data of the dead reckoning system using the Kalman filter. Thus precise coordinates of the starting point are required for the correct operation of the algorithm. This is due to the fact that dead-reckoning systems accumulate error and if there is an error in the initial stage it will increase in the course of the mission. The Kalman filter restrains the error accumulation and allows preserving navigation precision for quite a long time, but it cannot eliminate the error of the first initialization.

The drawback of the algorithm is that in case of the loss of navigation, which can be caused by the accumulation of errors as well as by impulse noise, the starting position coordinates must be calculated again for the further AUV functioning. Precise initialization usually requires: the AUV's surfacing for determination of the coordinates using satellite navigation systems; usage of specialized acoustic positioning systems installed on the support vessel; bringing the AUV to the point

with known coordinates (for example, to a reference transponder [13]). The first two variants are difficult to implement in ice conditions, where the possibilities of AUV's surfacing and of the ship movement are limited. Therefore, the necessity of precise starting position coordinates can be the cause of mission cancellation and it can expose the AUV to danger when operating in extreme conditions.

III. THE PARTICLE FILTER

To eliminate the described drawback, a new method for calculating the AUV coordinates on the basis of the particle filter was developed. Below is the description of the method algorithm:

Step 1. The particle filter initialization. Setting the filter (set once before launching the AUV):

a) Creation of two arrays $xp [xp_1..xp_{npart}]$, $yp [yp_1..yp_{npart}]$ containing the coordinates of the possible AUV positions ($npart$ is the number of positions) in the local coordinate system of the AUV.

b) Initialization of the created arrays with the coordinates of the points uniformly distributed in a given area (for example, the area of AUV deploying or the area of supposed underwater work).

c) Creation of an array of probability of possible positions $p [p_1..p_{npart}]$.

d) At the initial time all possible positions can be the AUV real position with equal probability. Therefore, the array of probability of possible positions p is filled with $1/npart$ values.

e) Calculation of the vector $c [c_1..c_{npart}]$ which contains the cumulative probability function p .

f) Calculation of the starting position as the mathematical expectation of all possible positions.

The following steps of the algorithm focus on calculating the AUV coordinates and are executed each time the AUV receives the navigation signal from the reference transponder.

Step 2. Resampling. Each possible position $1..npart$ is replaced by a new one.

a) A random number r is generated in the range $[0..1]$ according to a uniform probability distribution law.

b) The first element $c [c_1..c_{npart}]$ satisfying the following condition is found:

$$\left. \begin{array}{l} c_i < r \\ i - > \min \end{array} \right\}, \quad (11)$$

c) the pair of coordinates $(xp(i), yp(i))$ is taken as the new possible position.

Step 3. Displacement of possible positions:

a) A determined displacement of possible positions takes place:

$$\left. \begin{array}{l} xp(i)_j = xp(i)_{j-1} + \Delta_x \\ yp(i)_j = yp(i)_{j-1} + \Delta_y \\ i = 1..npart \end{array} \right\}, \quad (12)$$

where $xp(i)_{j-1}$, $yp(i)_{j-1}$ are the coordinates of i -th possible position; Δ is the displacement, which is calculated by the following formula:

$$\left. \begin{array}{l} \Delta_x = v_{AUV} dt \cos(\alpha) \\ \Delta_y = v_{AUV} dt \sin(\alpha) \end{array} \right\}, \quad (13)$$

where v_{AUV} is the average speed of the AUV in relation to the seabed during the navigation interval; dt is the duration of the navigation interval; α is the resultant displacement vector.

b) A random displacement of the possible positions is added:

$$\left. \begin{array}{l} xp(i) = xp(i) + wxp(i) \\ yp(i) = yp(i) + wyp(i) \\ i = 1..npart \end{array} \right\}, \quad (14)$$

where $wxp(i)$ is a random variable generated under the normal law with the expectation value $xp(i)$ and standard deviation σ (chosen depending on the predicted errors of course measurement and the AUV speed); $wyp(i)$ is a random variable generated under the normal law with the expectation value $yp(i)$ and standard deviation σ (chosen depending on the predicted errors of course measurement and the AUV speed).

Step 4. The formation of AUV coordinates estimation.

a) Recalculation of the array of probability of possible positions $p [p_1..p_{npart}]$. The probability is calculated relative to the following parameters.

$$\left. \begin{array}{l} p\tau(i) = \frac{1}{\sqrt{2\pi}\sigma\tau} e^{-\frac{d(i)-\tau v_s}{2\sigma\tau}} \\ pd\tau(i) = \frac{1}{\sqrt{2\pi}\sigma d\tau} e^{-\frac{d\tau-d\tau_{est}}{2\sigma d\tau}} \\ p\alpha(i) = \frac{1}{\sqrt{2\pi}\sigma\alpha} e^{-\frac{d\alpha-d\alpha_{est}}{2\sigma\alpha}} \\ i = 1..npart \end{array} \right\}, \quad (15)$$

where $p\tau(i)$ is probability relative to the measured propagation time for the i -th possible position; $pd\tau(i)$ is probability relative to propagation time change for the i -th possible position; $p\alpha(i)$ is probability relative to the change of course for the i -th possible position; $d(i)$ is the distance between the i -th possible position and the reference transponder; v_s is the sound velocity in water; τ is the measured propagation time; $\sigma\tau$ is the coefficient of the standard deviation in τ ; $d\tau$ is the change of the measured propagation time relative to the previous event; $d\tau_{est}$ is the change of the calculated propagation time relative to the previous event; $\sigma d\tau$ is the coefficient of the standard deviation in $d\tau$; $d\alpha$ is the change of the measured propagation time relative to the previous event; $d\alpha_{est}$ is the change of the

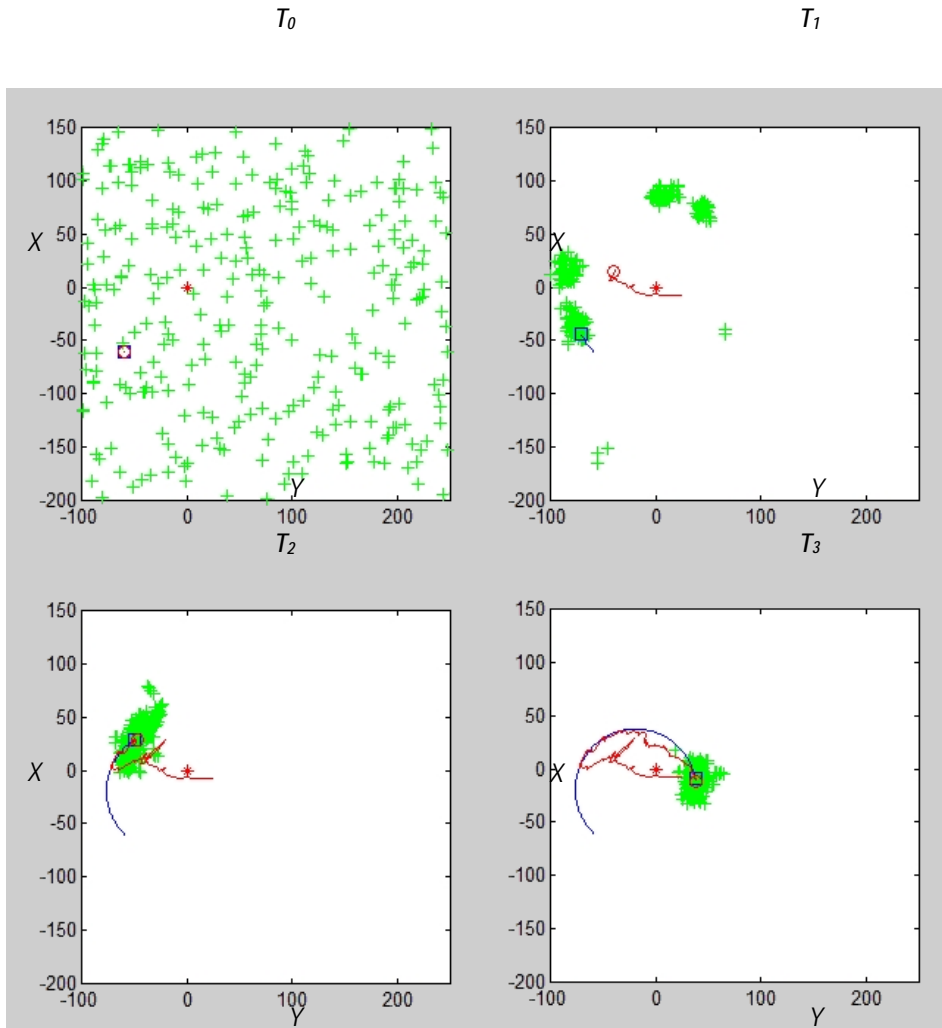


Figure 1. Solving the AUV positioning task.

calculated propagation time relative to the previous event; $\sigma_{d\alpha}$ is the coefficient of the standard deviation in $d\alpha$;

$$p(i) = \frac{(p\tau(i) + pd\tau(i) + p\alpha(i))}{\sum_{i=1}^{npart} p(i)} \quad (16)$$

b) Estimation of the AUV coordinates is calculated as a mathematical expectation of all possible positions:

$$\left. \begin{aligned} x(i) &= \sum_{i=1}^{npart} p(i)xp(i) \\ y(i) &= \sum_{i=1}^{npart} p(i)yp(i) \\ i &= 1..npart \end{aligned} \right\} \quad (17)$$

c) Recalculation of the vector $c [c_1..c_{npart}]$.

A software model was developed and a series of numerical experiments was carried out to test the effectiveness of the presented method and to compare it with the method of the coordinates calculation based on the Kalman filter. The simulation was performed taking into account the instrumental errors of the measuring equipment, with which the modern AUVs and LBL systems made by the Institute of Marine Technology Problems FEB RAS are equipped [14,15].

IV. THE SIMULATION RESULTS

The main advantage of the particle filter is that, thanks to its properties, it can solve the problem of positioning, i.e. it allows determining the object position in the given area.

Figure 1 shows the solution of the AUV positioning task using the developed method for calculating coordinates.

The following symbols are used in the figure: asterisk (the position of the reference acoustic transponder); square (the real position of the AUV); circle (the calculated position of the AUV); plus (one of the possible positions). The real and the calculated tracks of the AUV are also shown in the figure.

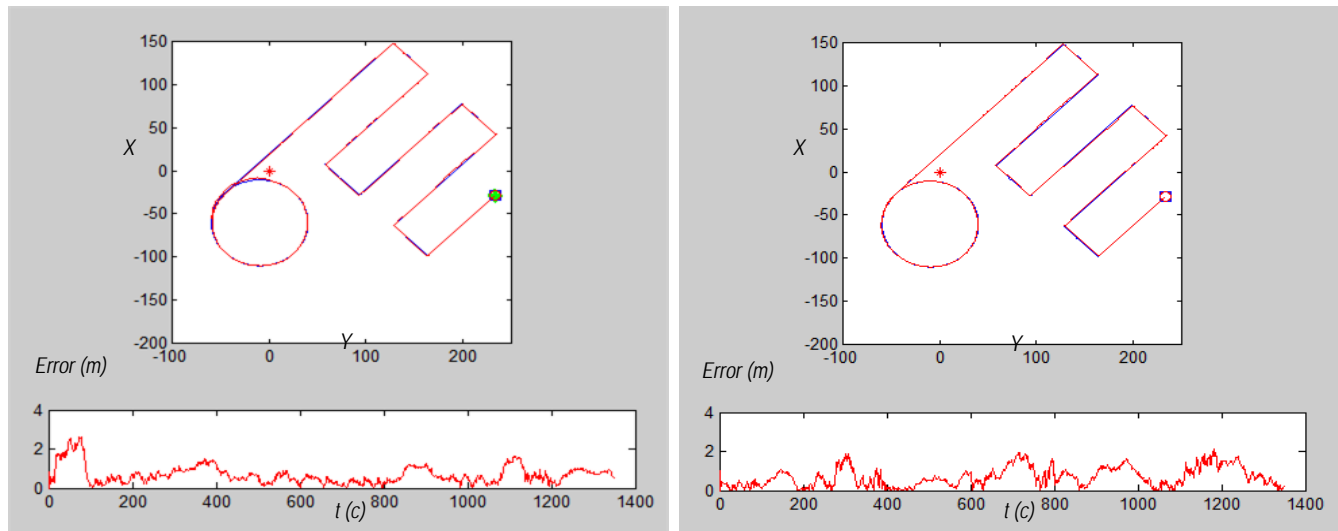


Figure 2. Comparison of single transponder navigation methods.

At the moment of time T_0 the possible positions (particles) are uniformly distributed in the area of AUV functioning. The AUV starts circular motion. On their way particles gather in clouds (areas where the AUV is more likely to be positioned). At the moment of time T_1 four such clouds were formed. Later the clouds merge into one. This resultant cloud concentrates around the real AUV position at T_2 . Since the estimation of the AUV coordinates is the mathematical expectation of all possible positions, the calculated position can be considered correct as soon as the particles form a single cloud around the real position T_3 . Along with the further AUV movement the cloud continues to concentrate around the real position and the accuracy of the calculated coordinates also increases.

The developed method of the AUV position calculation using a single transponder does not require initial initialization. The starting position can be determined with the help of a setup movement. Thus, in case of navigation loss, there is no need to interrupt the execution of the mission, to perform an emergency surfacing or to involve the support vessel.

Figure 2 shows the simulation results of the developed AUV coordinates calculation method based the particle filter (on the left) and the method of calculating the AUV coordinates based on the Kalman filter (on the right). The upper graphs show the real and the calculated tracks of the AUV. The lower graphs show the distribution of time errors for each method (deviation from the real AUV position in meters). A preliminary circular setup movement followed by track consists of parallel legs was used as a model of motion.

Analysis of the results shows that the developed method excels the position calculation method based on the Kalman filter in accuracy. The developed method has the following statistical error parameters: the mean value is 0.8 m, the standard deviation is 0.1 m; for the method based on the Kalman filter the parameters are 1 m and 0.15 m, respectively.

It is worth mentioning that to accelerate the particle filter setting the possible positions were placed uniformly in the area around the point of AUV submergence within a radius of 20 meters. It means that initially a cloud of particles was created, within which there was an AUV. The cloud concentrated on its way, increasing the accuracy of the calculated coordinates.

The drawback of this method is its high computational complexity. Processing of each possible position (one particle) requires twice as much operations with the floating point as it is used in the Kalman filter for each iteration. Fluctuations of accuracy of the values obtained by using the particle filter depend on the number of particles. 150 possible positions were used in the simulation. Thus, to compute one pair of coordinates the developed method required 300 times more floating point operations than the method based on the Kalman filter.

This complexity can become a serious obstacle to the introduction of this method into the existing AUV models, as their computational powers are often severely limited. However, the structure of the developed method algorithms shows that almost all operations with particles (step 3, step 4 (a)) do not influence each other's results and can be executed in a parallel way. Today the development of microprocessor technology allows to effectively organize parallel computing to rationalize the particle filter.

V. CONCLUSION

The developed method of AUV positioning by a single transponder based on the particle filter has the following advantages:

- High reliability. The method does not require the initial position data on board the AUV that allows the AUV to operate without emergency surfacing caused by the loss of navigation.

- Maintenance of the positioning accuracy level throughout the AUV's mission. The method does not use the dead reckoning system, the main drawback of which is the accumulation of errors.
- Universality. The method can be used to navigate any underwater vehicle equipped with acoustic transceiver equipment by software (if AUV computing resources are sufficient) and hardware upgrade.

At present we work on testing and improvement of the developed method taking into account the dynamic motion of an underwater vehicle.

REFERENCES

- [1] I.N. Burdinsky, D.S. Chmeris "The guidance and positioning system based on the video processing" The First Russia and Pacific Conference on Computer Technology and Applications (Russia Pacific Computer 2010) Russian Academy of Sciences, Far Eastern Branch, Vladivostok, Russia, 2010, pp. 300-302, 6 – 9 September 2010.
- [2] I.N. Burdinsky, A.V. Myagotin, "AUV positioning model employing acoustic and visual data processing" OCEANS'10 IEEE Sydney, 2010, pp. 1-6, 24-27 May 2010.
- [3] J.C. Kinsey, R.M. Eustice, L.L. Whitcomb "A survey of underwater vehicle navigation: Recent advances and new challenges" IFAC Conference of Manoeuvring and Control of Marine Craft, 2006.
- [4] J.J. Leonard, A.A. Bennett, C.M. Smith, H. Feder "Autonomous underwater vehicle navigation" IEEE ICRA Workshop on Navigation of Outdoor Autonomous Vehicles, January 1998.
- [5] I.N. Burdinsky, A.V. Myagotin "A framework of an acoustic navigation network servicing multiple autonomous underwater vehicles" Proceedings of the IASTED International Conference on Automation, Control, and Information Technology – Information and Communication Technology, ACIT-ICT2010, pp. 261 -266.
- [6] A.V. Inzartsev, A.V. Kamorny, L.V. Kiselev, Y.V. Matvienko, A.M. Pavin, N.I. Rylov, et al. "The integrated navigation system of an autonomous underwater vehicle and the experience from its application in high arctic latitudes" Gyroscopy and Navigation, 2010. Vol.1., № 2. pp. 107-112.
- [7] M.B. Larsen "Synthetic long baseline navigation of underwater vehicles" OCEANS 2000 MTS, IEEE Conference and Exhibition. IEEE, 2000., Vol. 3., pp. 2043-2050, 11-14 September 2000.
- [8] A.P. Scherbatyuk "The AUV positioning using ranges from one transponder LBL" OCEANS'95. MTS, IEEE. Challenges of Our Changing Global Environment. Conference Proceedings. 1995, Vol. 3. pp. 1620-1623, 9-12 October 1995.
- [9] I.N. Burdinsky "Guidance algorithm for an autonomous unmanned underwater vehicle to a given target" Optoelectronics, Instrumentation and Data Processing. 2012. Vol. 48. – №. 1. – pp. 69-74.
- [10] P. Baccou, B. Jouvencel "Homing and navigation using one transponder for AUV, postprocessing comparisons results with long base-line navigation" Robotics and Automation, 2002. Proceedings. ICRA'02. IEEE International Conference, 2002., Vol. 4. pp. 4004-4009, 11-15 May 2002.
- [11] S.E. Webster, R.M. Eustice, H. Singh, L.L. Whitcomb "Advances in single-beacon one-way-travel-time acoustic navigation for underwater vehicles" The International Journal of Robotics Research, №31(8), pp. 935-950.
- [12] J.A. Saude, A.P. Aguiar "Single Beacon Acoustic Navigation for an AUV in the presence of unknown ocean currents" In Proc. of MCMC09 - 8th IFAC Conference on Manoeuvring and Control of Marine Craft. Guarujá (SP), Brazil., 2009, pp. 298-303.
- [13] F.V. Bezruchko, I.V. Burdinsky, A.V. Myagotin "Global extremum searching algorithm for the auv guidance toward an acoustic buoy" OCEANS, 2011 IEEE-Spain. IEEE, 2011, pp. 1-7, 6-9 June 2011.
- [14] V.E. Gornak, A.V. Inzartsev, O.YU. Lvov, Y.V. Matvienko, A.P.H. Scherbatyuk "MMT 3000 - small AUV of new series of IMTP FEB RAS" OCEANS 2006 Boston, MA, 18-21 September 2006.
- [15] I.V. Karabanov, M.A. Linnik, I.N. Burdinskiy "Threshold Methods of Sonar Pseudonoise Phase-shift Signal Detection" The First Russia and Pacific Conference on Computer Technology and Applications (Russia Pacific Computer 2010) Russian Academy of Sciences, Far Eastern Branch, Vladivostok, Russia, 2010, pp. 404-408, 6 – 9 September 2010.

Novel Aortic Cannula with Spiral Flow Inducing Design

Nadia S. Shafii, N. Darlis, Jeswant Dillon, Kahar Osman, Ahmad Zahran Md Khudzari, and E. Supriyanto

Abstract—Aortic cannula is one of the medical parts used in cardiopulmonary bypass (CPB) during medical operation, or used in conjunction with extracorporeal membrane oxygenator (ECMO) operation during patient support in intensive care unit. The existing stock designs produce jet flow or dispersed flow out of the cannula tip. Thus leading to few complications caused by the non – physiological flow. To reduce adverse effect on the aorta, as well as on red blood cells (RBC), a novel approach to induce spiral flow is proposed. The aim of this study to compare between internal helical curve tip aortic cannula designs comprised of three groove and three ribs, and standard curve tip aortic cannula design. Computational fluid dynamics (CFD) simulation between three cannula designs were carried out in steady state condition. Spiral flow was successfully induced by the proposed internal helical design. The pressure drop across the cannulae designs recorded below the safe limit, outflow velocity was reduced by 34.5%, while wall shear stress was also acceptable (30.8 Pa – 61.59 Pa – 215.6 Pa) which is below critical wall shear stress value.

Keywords—spiral flow, aortic cannula design, heart lung machine, internal helical design, computational fluid dynamics.

I. INTRODUCTION

Aortic cannula is a special catheter device inserted in the aorta during open heart surgery and supply oxygenated blood to the aorta from heart lung machine (HLM) [1]. However, previous study discussing the use of aortic cannula reported that aortic cannula has its fair share of problem; there had been reported cases of haemolytic damage, sand blasting effect, and cerebral haemorrhage due to the non-physiological outflow condition [2]. One of the known limitations of the current cannula in use is the inability to induce the natural spiral blood

This work was supported in part using grant from the Ministry of Education of Malaysia, 00G71. The authors would like to offer their gratitude to Institut Jantung Negara (IJN) for their support in providing clinical support.

N. S. Shafii is with the Faculty of Biosciences & Medical Engineering, Universiti Teknologi Malaysia, 81310, Johor, Malaysia (naddyshaira@yahoo.com)

N. Darlis is with the Faculty Mechanical Engineering, Universiti Teknologi Malaysia, 81310, Johor, Malaysia (nofrizalidris@yahoo.com)

K. Osman. is with the Faculty Mechanical Engineering, Universiti Teknologi Malaysia, 81310, Johor, Malaysia (kahar@fkm.utm.my)

J. Dillon is with the Institut Jantung Negara (IJN), Kuala Lumpur Malaysia, (jeswant@ijn.com.my)

A. Z Md Khudzari and E. Supriyanto are with IJN-UTM Cardiovascular Engineering Centre, Faculty of Biosciences & Medical Engineering, Universiti Teknologi Malaysia, 81310, Johor, Malaysia. (corresponding author phone: +607-555 8462, fax : +607-555 8553; e-mail: zahran.kl@utm.my).

flow patterns which may create adverse effect on blood vessel [4].

The design of the cannula affects the hydrodynamics of the outflow where a typical stock cannula design produces high velocity flow upon exiting the tip into the aorta. High velocity outflow is highly influential to the formation of plaque rupture or ‘sand blasting effect’ induces by the single stream jetting or even multiple jets outflow from the aortic cannula [3, 5]. There are a few examples of cannula designs such as pattern soft-type flow cannula and dispersion-type cannula [5] aiming to reduce outflow velocity, but still introduce varieties of non-physiological flow. Despite producing low velocities, large vortices are present among the flow stream pattern induced located at the thoracic aorta [5]. Another design that is widely used is the end-hole curve cannula which disperses high forces and velocities outflow [3, 5].

The multiple cannula structures, cannula jet flow relates to the event of thromboembolism and also different hemodynamic effects [5]. It is hypothesized that by introducing a helical spiral profile within the cannula internal wall will help to reduce the unstable hemodynamic and sandblasting effects by inducing spiral flow which corresponds to lower velocity, low exit force and also stable wall shear stress [2]. The spiral outflow induced may contribute a positive impact to the pressure – flow condition especially during the operation of the cardiopulmonary bypass (CPB) as well as extra corporeal membrane oxygenator (ECMO) in the cardiac care intensive unit to maintain the physiological flow profile [9].

In this paper, a helical internal spiral cannula design is proposed which serve the purpose of inducing a spiral flow from the tip cannula to the aorta. Comparison between the spiral design and the stock design is made to determine any improvements of inducing spiral flow. Numerical analysis was conducted to compare and evaluate the merits of the spiral and design in a steady state flow condition. Attention was given to the flow characteristics by virtue of the spiral flow inducing design feature such as pressure difference in the proposed design, out flow velocity at the test rig, flow pattern and also the helicity density in order to confirm that the proposed internal helical designs managed to induce the physiological flow profile of blood in aorta.

II. METHODOLOGY

A. Geometry: Characteristics of Models

The cannula were modeled into 3 designs; straight cannula (stock design), a spiral profiled cannula with 3 groove and a spiral profiled cannula with 3 ribs as illustrated in Figure 1. The parameters of the proposed designed are listed in Table 1.

Each models was connected to a simple rigid tube wall vessel which represents the outflow to the aorta (inner diameter 24mm and length is 250mm) [10]. The parameters of the proposed design are listed in the Table 1.

Table 1: The parameters of proposed internal spiral aortic cannula design.

Geometrical properties	Curve standard cannula
Cannula length	250mm
Internal diameter	8mm [24 Fr]
External diameter	10mm
Spiral length	90mm
Spiral pitch, revolution	30,3

To ensure that the existence of spiral flow induced by the proposed designs, a detailed numerical simulation was done to analyze the output flow structure and profile. Attention is given at the tip of the curved cannula where different types of internal profile design will affect the outflow. As shown in Figure 1 and 2, all of the curved cannula designs are intended for adult physiology. The stock cannula was used as control design where the general dimension setup of the proposed design profile was based upon.

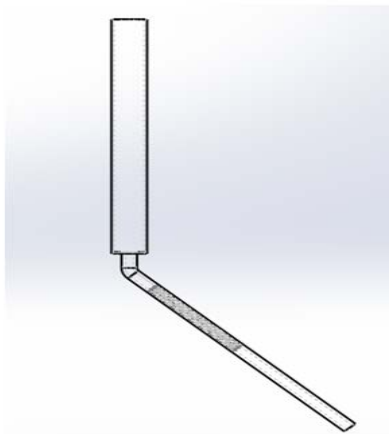


Figure 1: Simple rigid tube wall vessel connected with proposed cannula

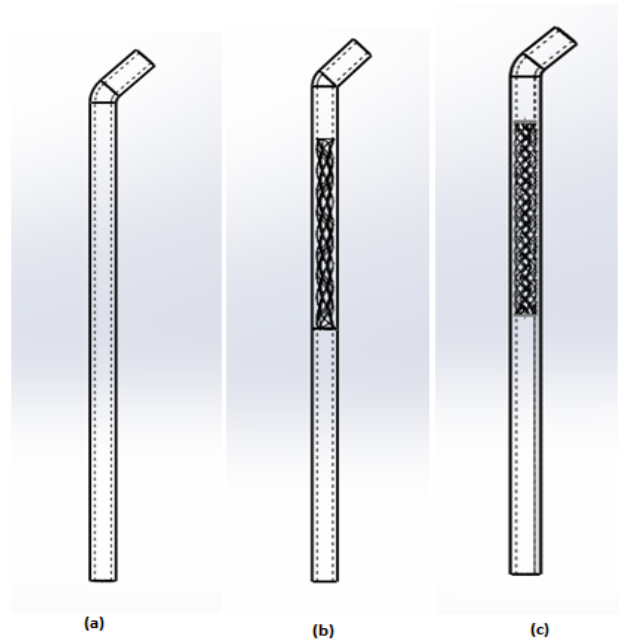


Figure 2: (a) straight cannula (stock design), (b) a spiral profiled cannula with 3 grooves, (c) a spiral profiled cannula with 3 ribs.

properties such as density of the blood = 1050kg/m³, viscosity = 0.00345 Pa s, and it was assumed with non-slip and steady state boundary conditions [11]. The wall boundary condition of the models was assumed to be a rigid body at the cannula wall and also the outflow tube body while neglecting the gravitational effects [11].

The selection of boundary conditions was based on the physiological blood flow distribution in the aorta. The flow rate in the aorta used from the previous study stated that the net flow ranged is between 4.5 and 5.5L/min [11]. It is based on the condition of each patient such as their weight and age. The velocity inlet of the models was set at normal value of 4.5L/min and the outlet pressure was set 120mmhg to simulate physiological condition at aorta [7].

The flow simulated in this study was modeled using 3D incompressible Navier-Stokes equations [11]. A suitable turbulence model K – epsilon RNG was chosen while setting up the simulation process in the ANSYS FLUENT 14.0 (Ansys. Inc., Canonburg, PA, USA), a general flow computational fluid dynamics (CFD) software. The turbulence model was selected due to the suitability of the model for the swirl flow simulation [17]. Computational simulation continues after completing the meshing process with 800k to 950k nodes as below Figure 3 for all designs.

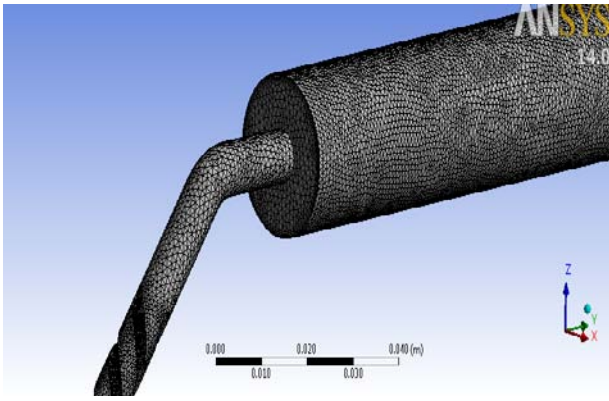


Figure 3: Simple completed meshing

C. Output Measurement

There are several performances and parameters of the hemodynamics observed and measured according to the inlet and outlet set up at the boundary conditions [11]. Comparison between the results of the stock design and the proposed designs discussed further based on few characteristics such as velocity of the profile flow, pressure difference, effect of wall shear stress and the helicity flow profile formation. Area-weighted average helicity density H_a will be calculated to determine the existence of spiral flow induced. The formula used is [18]:

$$H_a = \frac{1}{S} \int H_d dS \quad (1)$$

S is the cross sectional area, H_d is helicity density which is defined by scalar product equation as below:

$$H_d = \vec{V} \cdot (\nabla \times \vec{V}) \quad (2)$$

From the simulated results, visualization of streamlines was done to improve detection of stagnation area and the blood clotting formation tendency [11]. From this result data, the velocity streamlines from the inlet of the curve cannula into the test rig tube was deemed to be important and used to qualitatively determine the extent of spiral flow intensity. The pressure difference was measured along the cannula. Other flow characteristic parameters measured were the outflow velocity in the rig test, and wall shear stress. It is important that the level of wall shear stress from the induced spiral helical flow is kept at a reasonable level, since high wall shear stress leads to hemolysis formation [11].

III. RESULTS

Figure 4 and 5 below illustrate the streamline of the flow patterns after completing the CFD simulation. In Figure 5, the right part shows the spiral flow pattern induced from the internal helical design of curve tip cannula, while Figure 4 shows the flow pattern of the stock design. The graph in Figure 6 shows the area-weighted helicity density, H_a , along the test rig tube for all cannula type tested. The maximum value of

helicity density for the 3 groove designs is $20 \text{ m}^2/\text{s}^2$, while the 3 rib cannula is recording a maximum value of $19.5 \text{ m}^2/\text{s}^2$; however, there was no value recorded from the stock cannula design. The helicity density for both spiral and groove design declines gradually along the test rig tube as the distance gets farther from the tip.

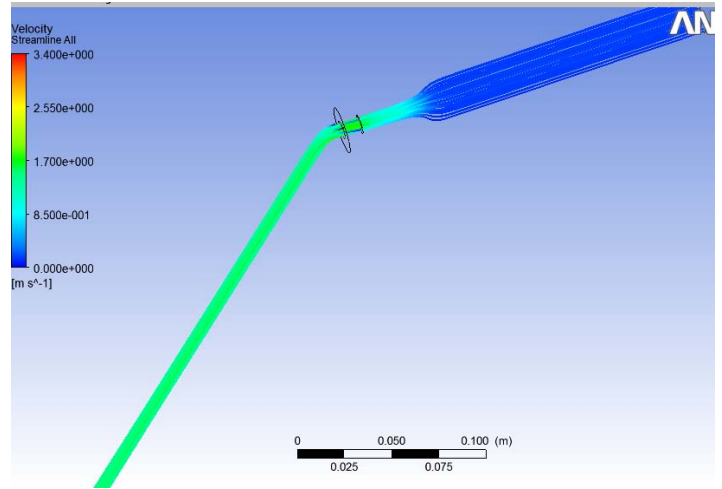


Figure 4: Standard curve cannula (stock design) Velocity streamline

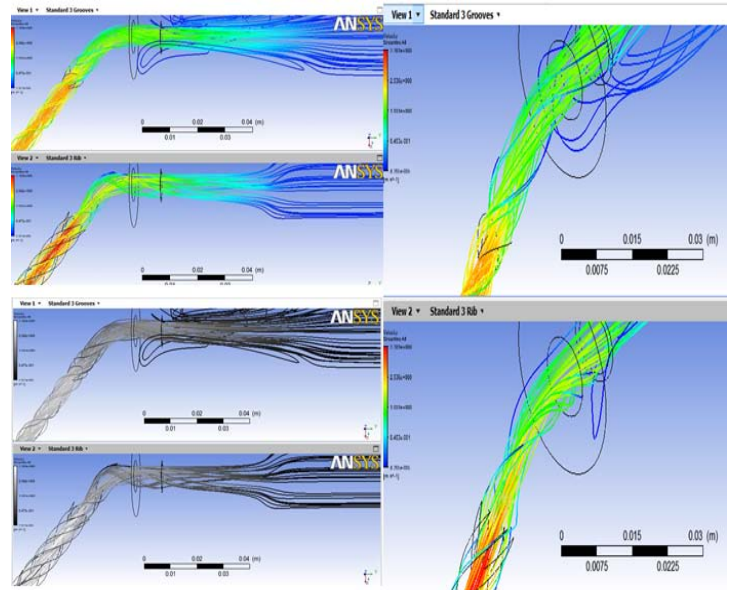


Figure 5: 3 Groove internal curve cannula design and 3 Rib (lower part) internal curve cannula velocity streamline

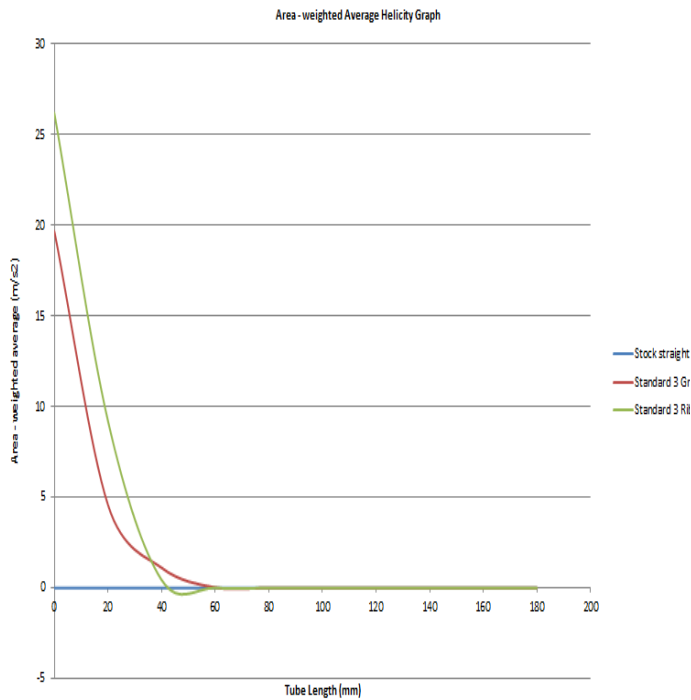


Figure 6: Velocity Helicity Graph

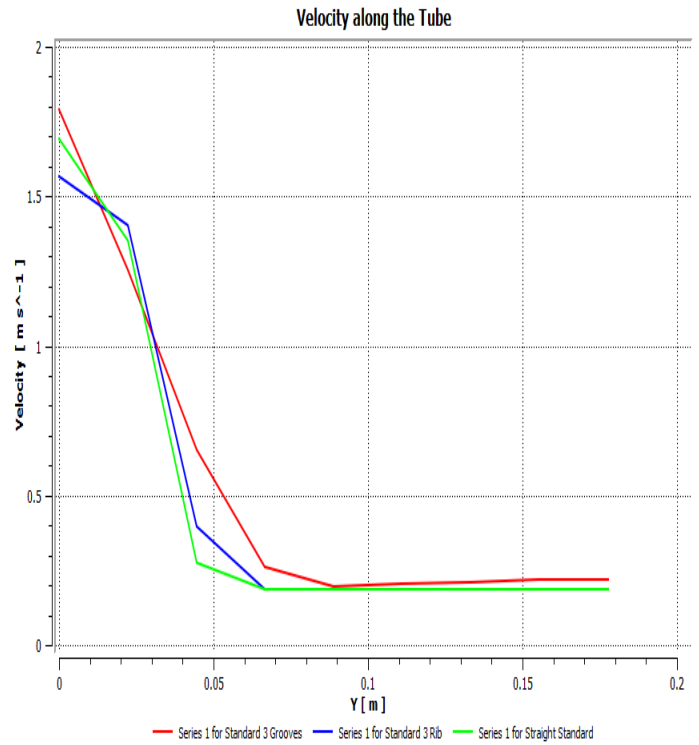


Figure 8: Flow Velocity in tube Rig Test from all three cannulae designs

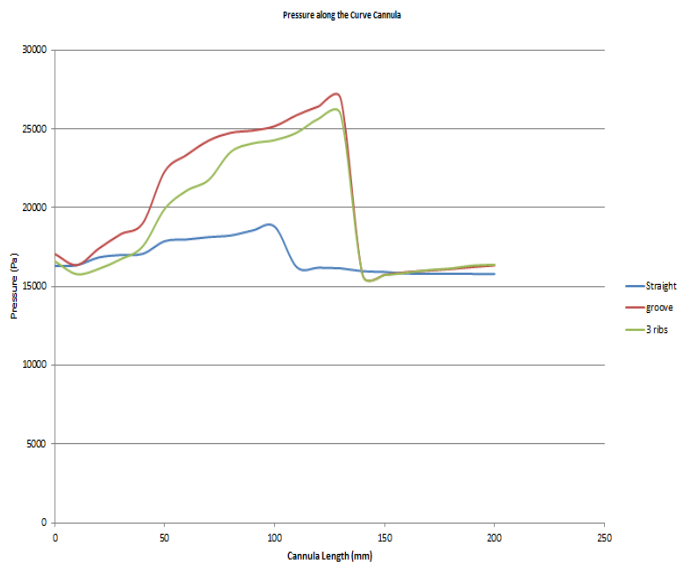


Figure 7: Pressure Differences at Cannula between Standard 3 Groove And 3 Rib Designs Graph

Figure 7 illustrates the total pressure measured along the cannula. There was slightly pressure difference occurred in standard cannula compare to the pressure reduction along the internal helical profiled cannula. Pressure along the stock design curve cannula shows the lowest pressure recorder about below 25000 pascal compared to the others optimized curve cannula.

Next, an outflow measurement on the velocity output is shown in Figure 8. The measurement was taken along the rig test tube to find the flow of each cannula’s outflow other than comparing the outflow velocities. The results showed that the highest outflow velocity was by groove cannula followed by standard cannula design and lastly rib cannula design.

Higher outflow jets of standard cannula tip produce single stream provoke plaque rupture or sand blasting [2]. The outflow velocity recorded along the rig test tube for the 3 groove cannula was 1.8m/s which is the highest velocity compared to the standard and 3 rib cannula velocity which are 1.65m/s and 1.55 m/s respectively. Previous study reported that spiral flow help in lowering the velocity outflow, and reduce the effect of high jetting to the aorta wall [15].

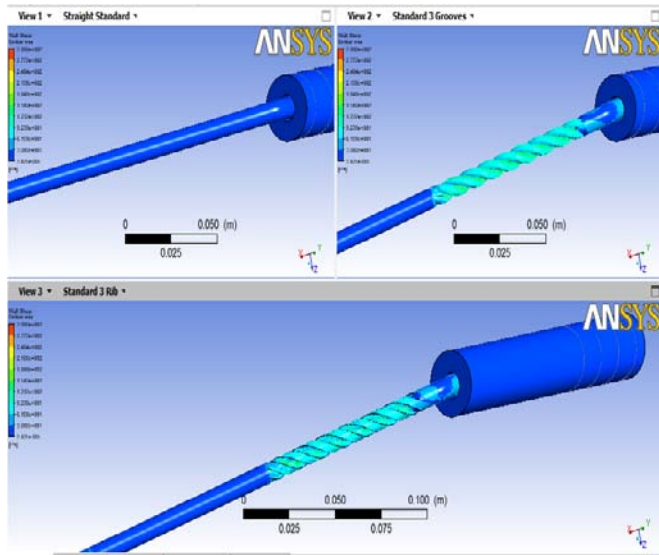


Figure 9: Shear Stress at all Cannula

Creating and inducing high exit velocities and also straight jet flow profile is the possible cause of adverse effects including the cerebral hemorrhage, rupture of the aorta wall side effects while using the cannula during open heart surgery or cardiopulmonary bypass.

In Figure 9, the shear stress of each cannula measured as table below It was reported that the critical value of shear stress that can cause hemolysis of blood cells is 450 Pa (4500 dyne/cm²)[13]. Both proposed designs (3 grooves and 3 ribs) show that the maximum value of wall shear stress is well below the critical level as shown in Table 2.

Table 2: The shear stress measured

Cannula Design	Shear stress Pa (dyn/cm ²)
Standard	3.425 ⁻⁰⁰⁵ –30.800 Pa (0.000342- 308.0 dyn/cm ²)
3 Groove	61.59 – 215.6 Pa (615.9 – 2156.0 dyn/cm ²)
3 Rib	61.59– 154.0 Pa (615.9 -1540.0 dyn/cm ²)

Thrombosis formation also relates to the flow pattern; as mentioned in earlier studies, the formation of spiral flow could prevent adverse effects to blood damage especially on the platelets activation [16]. By introducing an internal helical profile in the cannula, the induced spiral flow has the potential to lower acute thrombus [16].

IV. CONCLUSION

This paper focused on investigating possibility of inducing spiral flow with the use of novel cannula design for medical operations. The use of computational fluid dynamics provides a clear visualization of swirl flow with the use of K-e turbulence model. The proposed design; 3 grooves and 3 rib designs proved to be capable of inducing a spiral flow which is the physiological flow pattern to the aorta. Compared to the stock design of curved-tip cannula, there were improvements in wall shear stress level, pressure drop within the cannula body, as well as reduced outflow velocity. Future development of this design would proceed to experimental verification to further validate the spiral flow formation.

ACKNOWLEDGMENT

This research was supported by Grants from the IJN – UTM Cardiovascular Engineering, Faculty of Biosciences & Medical Engineering, Universiti Teknologi Malaysia, 81310 Skudai Johor (Vote no : G0071).

REFERENCES

- [1] Salama, F.D. and A. Blesovsky, Complications of cannulation of the ascending aorta for open heart surgery. *Thorax*, 25(5), pp. 604-7, 1970.
- [2] Gerdes, A., T. Hanke, and H.H. Sievers, Hydrodynamics of the new Medos aortic cannula. *Perfusion*, 17(3), pp. 217-20, 2002.
- [3] Scharfschwerdt, M., Ritcher A, Boehmer K, Repenning D, Sievers HH., Improved hydrodynamics of a new aortic cannula with a novel tip design. *Perfusion*, 19(3), pp. 193-7, 2004.
- [4] Caballero, A.D. and S. Lafn, A Review on Computational Fluid Dynamics Modelling in Human Thoracic Aorta. *Cardiovascular Engineering and Technology*, 4(2), pp. 103-130, 2013,.
- [5] Minakawa, M., Fukda I, Igarashi T, Fukui K, Yanaoka H, Inamura T, Hydrodynamics of aortic cannulae during extracorporeal circulation in a mock aortic arch aneurysm model. *Artif Organs*, 34(2), pp. 105-12, 2010.
- [6] Stonebridge, Spiral laminar flow in arteries, *The Lancet*, 38, pp. 1360-61, 1991.
- [7] Kira, Y., Kochel PJ, Gordon EE, Morgan HE, Aortic perfusion pressure as a determinant of cardiac protein synthesis. *Am J Physiol*, 246(3 Pt 1), pp. C247-58, 1984
- [8] Coppola, G. and C. Caro, Arterial geometry, flow pattern, wall shear and mass transport: potential physiological significance. *J R Soc Interface*, 6(35), pp. 519-28, 2009
- [9] Grigioni, M., Daniele C, Morbiducci U, D’ Avenio G, Di Benedetto G, Del Gaudio C, Barbaro V, Computational model of the fluid dynamics of a cannula inserted in a vessel: incidence of the presence of side holes in blood flow. *J Biomech*, 35(12), pp. 1599-612, 2002.
- [10] Avrahami, I., Dilmoney B, Hirshorn O, Brand M, Cohen O, Shani L, Nir RR, Bolotin G, Numerical investigation of a novel aortic cannula aimed at reducing cerebral embolism during cardiovascular bypass surgery. *J Biomech*, 46(2), pp. 354-61, 2013
- [11] Menon, P.G., ANtaki JF, Undar A, Pekkan K., Aortic outflow cannula tip design and orientation impacts cerebral perfusion during pediatric cardiopulmonary bypass procedures. *Ann Biomed Eng*, 41(12), pp. 2588-602, 2013
- [12] Jegger, D., Sundaram S, Shah K, Mallabiabarrena I, Mucciolo G, von Seqesser LK, Using computational fluid dynamics to evaluate a novel venous cannula (Smart canula (R)) for use in cardiopulmonary bypass operating procedures. *Perfusion*, 22(4), pp. 257-265.2007
- [13] Paul, M.C. and A. Larman, Investigation of spiral blood flow in a model of arterial stenosis. *Med Eng Phys*, 31(9), pp. 1195-203, 2009.

- [14] Linch and Brown, *Manual of Clinical Perfusion*, A Perfusion.Com Publication, 2004
- [15] Tanaka, M., Sakamoto T, Sugawara S, Nakajima H, Kameyama T, Katahira Y, Ohtsuki S, Kanai H, Spiral systolic blood flow in the ascending aorta and aortic arch analyzed by echo-dynamography. *J Cardiol*, 56(1), pp. 97-110, 2010.
- [16] Stonebridge, P.A., Vermassen F, Dick J, Belch JJ, and Houston G, Spiral laminar flow prosthetic bypass graft: medium-term results from a first-in-man structured registry study. *Ann Vasc Surg*, 26(8), pp. 1093-9, 2012.
- [17] Gupta, Amit, Three- dimensional turbulent swirling flow in cylinder : Experiments and computation, *International Journal of Heat and Fluid Flow*, 28,pp. 249-261, 2007.
- [18] Xiao Liu, Effect of Spiral Flow on the Transport of oxygen in the Aorta : A Numerical Study, *Annuals of Biomedical Engineering*, 3(38), pp. 917-926, 2010

Diagnostics of existing steel roof structure of winter sports stadium

Marcela Karmazínová, Jindrich Melcher, Lubomír Vítek, Petr Cikrle and Jaromír Láník

Abstract—The paper deals with the diagnostics of steel roof structure of the winter sports stadiums built in 1970 year. The necessity of the diagnostics has been given by the requirement to the evaluation design of this structure, which has been caused by the new situation in the field of the loadings given by the validity of the European Standards in the Czech Republic from 2010 year. Due to these changes in the normative rules, in practice existing structures are gradually subjected to the evaluation design and depending on its results to the strengthening or reconstruction, respectively. Steel roof is composed of plane truss main girders, purlins and bracings and the roof structure is supported by two arch main girders with the span of $L = 84$ m. The in situ diagnostics of the roof structure was oriented to the following parts: (i) determination and evaluation of the actual material properties of used steel and (ii) verification of the actual dimensions of the structural members. For the solution the non-destructive methods have been used for in situ measurement. For the indicative determination of steel strengths the modified method based on the determination of Rockwell's hardness has been used. For the verification of the member's dimensions (thickness of hollow sections) the ultrasound method has been used. This paper presents the results obtained using these testing methods and their evaluation, from the viewpoint of the usage for the subsequent static assessment and design evaluation of the existing structure.

Keywords—Diagnostics, existing structure, steel, roof, sport stadium, in situ measurement, non-destructive method, Rockwell's hardness, ultrasound, ultimate strength, yield strength, actual dimensions, verification, determination, evaluation.

I. INTRODUCTION

THE workplaces of the paper authors (Division of Metal and Timber Structures and Division of Structural Testing of the Faculty of Civil Engineering at the Brno University of

This work was supported in part by the Czech Ministry of Education, Youth and Sports under reserach projects CZ.1.05/2.1.00/03.0097 and FAST-S-14-2544.

Marcela Karmazínová is the head of the Division of Metal and Timber Structure of the Faculty of Civil Engineering at the Brno University of Technology, Veveri St. 331/95, 602 00 Brno, Czech Republic (corresponding author to provide phone: +420 541 147 310; fax: +420 549 245 212; e-mail: karmazinova.m@fce.vutbr.cz).

Jindrich Melcher is the head of the Common Testing Room of Load-Carrying Structures of the Division of Metal and Timber Structure, Faculty of Civil Engineering, Brno University of Technology (e-mail: melcher.j@fce.vutbr.cz).

Lubomír Vítek is with the Division of Structural Testing, Faculty of Civil Engineering, Brno University of Technology (e-mail: vitek.l@fce.vutbr.cz).

Petr Cikrle is with the Division of Structural Testing, Faculty of Civil Engineering, Brno University of Technology (e-mail: cikrle.p@fce.vutbr.cz).

Jaromír Láník is with the Division of Structural Testing, Faculty of Civil Engineering, Brno University of Technology (e-mail: lanik.j@fce.vutbr.cz).

Technology) co-operate with ACIERCON, Ltd. Company on the evaluation of existing structures, in the long term.

Within the diagnostics of steel roof structural system, several constructions of sport stadiums in the Czech Republic have already been investigated. The first ones were the winter stadiums in the cities of Olomouc, Jihlava and Znojmo, for example. The main aims of the diagnostics of steel roof structures of these constructions were to verify the dimensions of roof structure members and to determine actual physical-mechanical properties of structural steel, to use these ones in the subsequent static assessment and evaluation of existing structure. Regarding the possibilities given by the different structural configurations and real structural conditions, the different diagnostic methods are needed to use. In the case of the winter sport stadium at Znojmo city mentioned above, non-destructive diagnostics in-situ only has been used. It was given by the fact that, because of static reasons, no structural member or structural part could be taken from the existing roof construction.

II. DESCRIPTION OF INVESTIGATED STEEL ROOF STRUCTURE

The basic configuration and composition of load-carrying system is evident from the orientation schemes in Figs. 1 to 3 provided by the contracting authority.

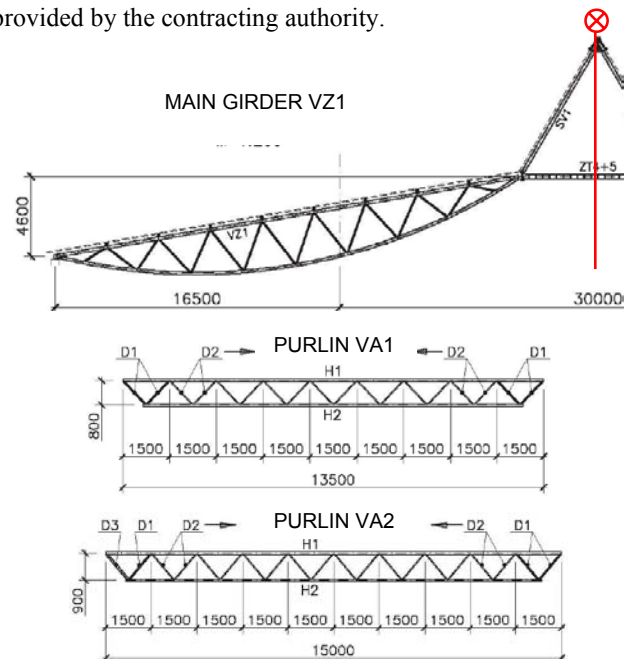


Fig. 1 main roof girder VZ1 (top) and purlins VA1, VA2

The roof structure is composed of plane truss main girders, purlins and bracings (see Figs. 1 and 2) and the structure as a whole is supported by longitudinal arch main girders (Fig. 3).

The typical cross-sections (including their dimensions) of the main structural members, that means main roof girders, purlins and arch girders, are shown in Fig. 4.

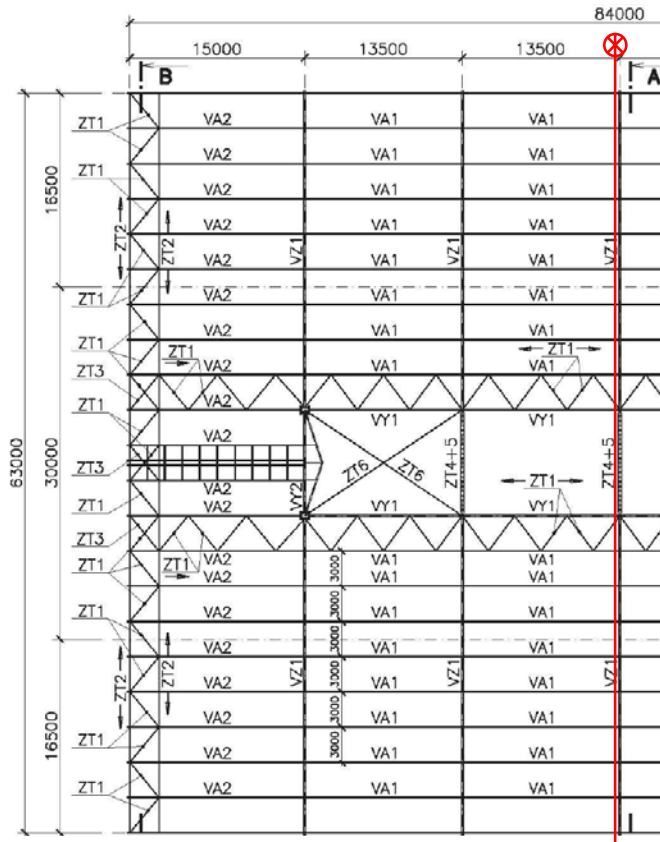


Fig. 2 roof structural system – plan

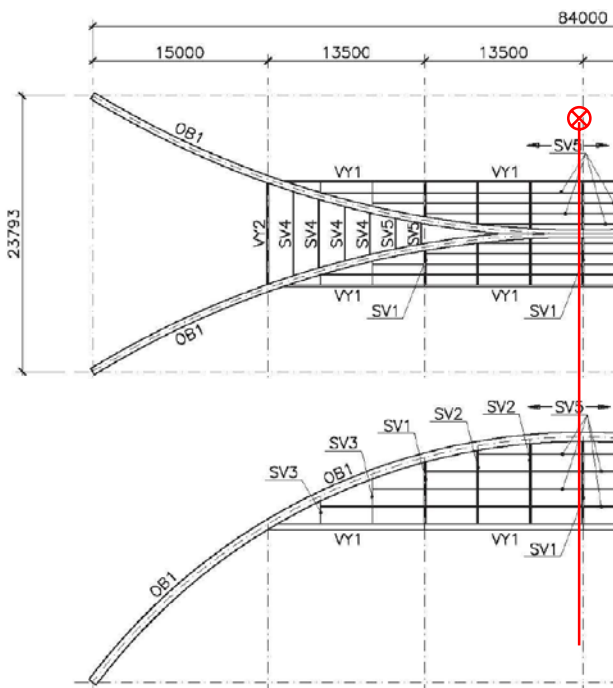


Fig. 3 arch main girders – plan and side view

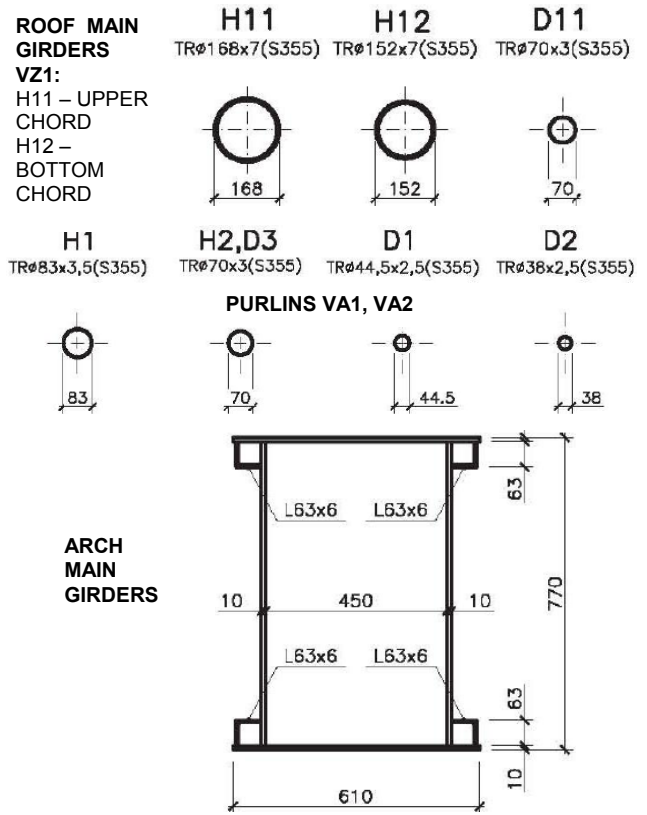


Fig. 4 cross-sections of main structural members

The measurements mentioned below have been realized in the conjunction with the representatives of the company, both from the viewpoint of the selection of measured members of steel structure, and from the viewpoint of the provision of the lifting platforms and security mechanisms for access to the members of the structural system.

III. NON-DESTRUCTIVE DIAGNOSTICS IN SITU – STEEL ULTIMATE STRENGTH DETERMINATION AND EVALUATION

The destructive methods could not be used because of the impossibility to take specimens from existing structure for tensile testing, that the non-destructive diagnostics oriented to the indicative evaluation of strength has been used.

A. Evaluation of Existing Structures

The standard ISO 13822 Basis of Structural Design – Evaluation of Existing Structures [10] can be applied for steel structures mentioned.

Because in this case the origin material statements containing the specification of their quality were available, then the actual values of steel yield and ultimate strengths can be assumed. For the basic verification of these properties, the indirect methods not requiring the problematic sampling from the structure loaded can be used (tests according to Brinell,

Vickers or Rockwell, for example). To verify properties and indicatively to determine steel strength, the suitable method for the hardness measurement can be used; the standard ISO 13822 recommends the method using “POLDI hammer” or some method ensuring sufficient correlation between hardness and strength.

B. Selection of Testing Method

The “POLDI hammer” method recommended in [10] allows the fast assessment of the quality of metal materials inbuilt in the construction because of easily portable testing apparatus. The test is based on the comparison of the deformation caused by hammer in the known hardness specimen with deformation caused in unknown hardness tested material. However, from current viewpoint, this method is somewhat out of date, namely because of the fiddly and not too precise measurement of deformation size. It is especially difficult at high positions and, in addition, testing slender and hollow sections is problematic, too.

The next useable method is the dynamic impact method by D Leeb. The measurement is carried out by the toughened ball catapulted in the direction to the tested element. The ball strikes the surface by the defined speed or kinetic energy, respectively. The ball loses the part of its energy as a result of the surface deformation occurred. The loss of energy is greater, if the deformation is greater, i.e. the material hardness is smaller. The ball affects by the great force in the short duration of the impact. Slender and light-weight components can deform (vibrate) and then cause erroneous measurement. It can be solved by supporting back parts of the measured object, if smaller parts of the simple shape are tested. However, in the case of truss girders the vibration of the members can be difficulty corrected.

According to the structure type and the experiences of the elaborators, the universal portable apparatus for the measurement of hardness “COMPUTEST SC” (Switzerland Company “Ernst Härteprüfer SA”) using the modified Rockwell method has been chosen for testing the roof structure mentioned. The measurement is based on the exact static method enabling accurate and reliable routing of diamond edge in the measuring probe. In the measuring head the moveable sensor is placed enabling the measurement of the depth of the deformation in the range of 0-100 μm. The apparatus shows either the values of the hardness in the usual hardness units or directly tensile strength. This method is standardized by the German Standard DIN 50 157.

C. Displacement and Treatment of Tested Locations

The aim of tests performed was to verify tensile ultimate strength of steel in various members of the roof structure. The number of measured locations has been given and specified directly in situ. Because of the limited range of the lifting platform the roof bracing could not be verified. The displacement of tested locations on the roof structure and on the arches is schematically shown in Figs. 5 and 6. The

composition and configuration of the load-carrying structural members is evident from Fig. 7.

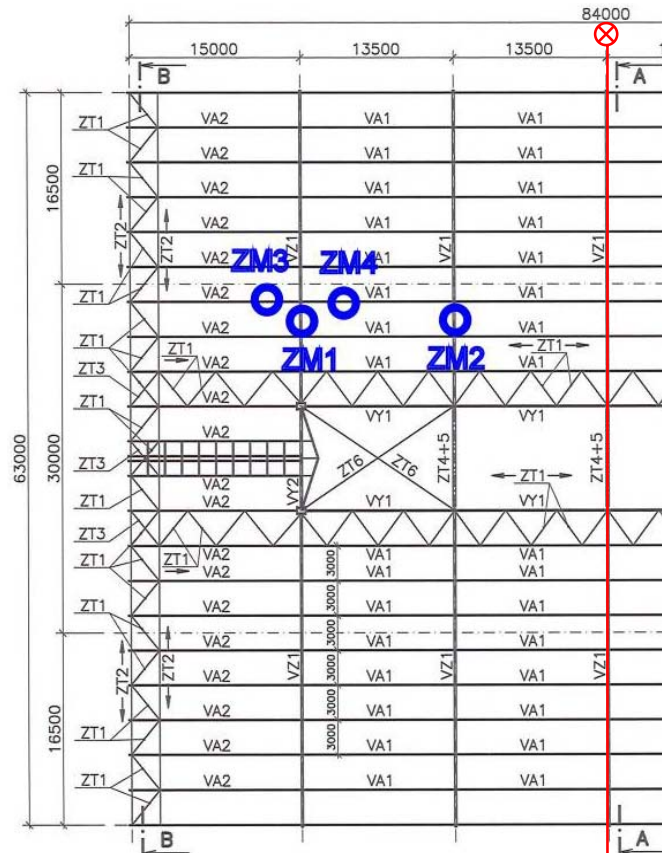


Fig. 5 tested locations: roof girders – ZM1, ZM2, purlins – ZM3, ZM4

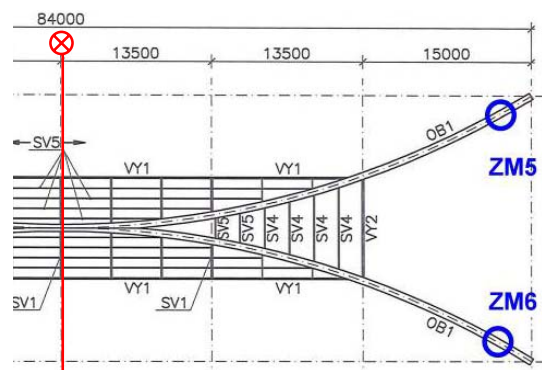


Fig. 6 tested locations: arch main girders – ZM5, ZM6

Before the measurement by “COMPUTEST SC” apparatus it was necessary to remove paint layers and to prepare surface (see Fig. 8 left). The distance of the measuring tip has always been calibrated using the special dipstick (see Fig. 8 right). For measuring on the rounded surface the V-shaped product (see Fig. 9) has been used; on the flat surface the three-point magnetic product (see Fig. 10) has been applied.



Fig. 7 part of the tested structure – truss roof main girders, purlins, bracings, arch main girders



Fig. 8 prepared tested location on rounded surface (left), calibration of measuring tip distance on rounded surface (right)



Fig. 9 measurement by ‘COMPUTEST SC’ apparatus on rounded surface using V-shaped product



Fig. 10 measurement by ‘COMPUTEST SC’ apparatus on flat surface using three-point magnetic product

D. Tests of Steel Tensile Strength

The tests of steel tensile strength have been verified in the different members of the roof structure and arches. Based on the documentation, all tested members should be made of the same material – steel of the grade S 355, in accordance to the standard ČSN EN 10027 [11], [12]. The members of the horizontal bracings only should be made of the different material, but these members have not been tested because of the limited range of the lifting platform (see above).

In total 22 tested locations have been verified on the upper chords PH, lower chords PD and diagonals D: 8 measured locations on 2 main roof girders – upper chord, lower chord, 2 diagonals; 8 measured locations on 2 roof purlins – upper chord, lower chord, 2 diagonals; 6 measured locations on 2 arches – upper flange, lower flange, 2 webs. Individual tested locations are documented in Figs. 11 to 13.

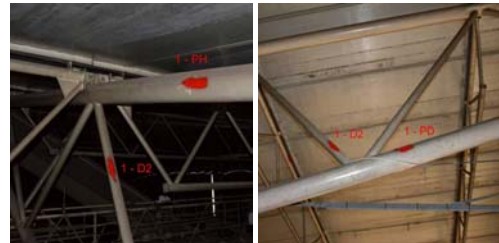


Fig. 11 tested locations on main roof girders



Fig. 12 tested locations on main roof girders



Fig. 13 tested locations on arch main girders

E. Test Results and Evaluation of Steel Tensile Strength

Test results obtained directly from the tests as particular values of steel ultimate tensile strength, have been statistically evaluated, that means characteristic values of tensile strength have been determined.

According to the statistical principles, mean values of the ultimate strength m_{fu} and standard deviations have been determined by statistical procedures from the test data. Respecting the recommendation of EN 1990 (Annex D) [15], the variation coefficients have been considered as “unknown” and the values have been statistically determined from the test data (see Table 1 below). The characteristic ultimate strength has been calculated according to the formula:

$$f_{uk} = m_{fu} (1 - k_n \cdot v_{fu}), f_{ud} = m_{fu} (1 - k_{d,n} \cdot v_{fu}) \quad (1)$$

where $k_n = 1.74$ for 8 tests and $k_n = 1.77$ for 6 tests (in the case of arches) and “unknown” variation coefficient (see Annex D of EN 1990). The results have been separated to three individual sets. The characteristic values of ultimate strengths based on the principles above are listed in Table 1.

Table 1 characteristic steel ultimate strengths f_{uk}

Tested members	Mean value [MPa]	Standard deviation [MPa]	Variation coefficient t [---]	Charact. Value [MPa]
Roof girders	567	21.1	0.037	530
Roof purlins	586	30.7	0.052	533
Arches	535	28.3	0.053	485

The results of the tests in situ shown the assumed material quality of steels used for the members of the roof structure of winter sports stadium in the city of Znojmo: material of all members of main roof girders and purlins is steel S 355 (with nominal ultimate strength of 510 MPa). Ultimate strengths of the material steel arches were a little lower. The results can be influenced by the higher dispersion of the values and by the lower number of tested locations. The combination of both these factors caused decreasing in the characteristic value of the tensile strength compared to the mean value by 50 MPa (the mean ultimate strength is 535 MPa and the characteristic ultimate strength is 485 MPa).

IV. NON-DESTRUCTIVE DIAGNOSTICS IN SITU – VERIFICATION OF STRUCTURAL MEMBERS ACTUAL DIMENSIONS

Based on the client requirements, the non-destructive verification of the thicknesses of selected members of steel load-carrying roof structure has been performed [6]. Within this control the thickness of 22 significant locations of load-carrying structure has been measured using ultrasound method.

A. Description of Ultrasound Method

The measurement of the thickness of the wall of selected steel members of the roof structure was realized using the ultrasound defectoscopy apparatus named “PosiTector UTG”, which is the instrument with the simple manipulation, high technical parameters and very high operating resistance. The measurement accuracy is ± 0.03 mm in the range from 1 mm to 125 mm. For the measurement the direct piezoelectric probe with the nominal frequency of 10 MHz; the impulse reflection method has been applied. The principle of the ultrasound method is based on the periodical mechanical oscillations, which are transmitted by the ultrasound probe to the tested material, where they are spreading by the constant speed. When the oscillations stumble upon the material non-homogeneity or upon the opposite side of tested subject, then they are reflected back with the lower energy; this process is recorded by ultrasound probe and after it is displayed on the screen of the evaluating apparatus. Time since sending ultrasound signal up to its returning back is proportional to the distance of non-homogeneity or of the opposite side. Ultrasound method is suitable for the measurement of thickness of steel structures and products.

The most accurate measurement is ensured by the probes with higher frequency, but for the usual probes with the nominal frequency of 5 MHz the reading error is about 0.3 mm. This error could be only eliminated by very high quality of material surface at the measured point, which is not usually real in practice. So it is important to measure the thickness in one point several times. Thus, the reading is more accurate, if the nominal frequency of the probe is higher. However, the usage of the probes with the higher frequency is limited by the material ability to conduct sound and by the quality of surface where the probe is touched. The thickness of the gap between the probe and material surface also very influences the accuracy of reading. On the other hand, the probes with the lower nominal frequency of $f = 4 \pm 5$ MHz are not so sensitive to the change of thickness of the gap between the probe and tested material, therefore they are mostly used for the thickness measuring. This is also in the case of our measuring, because the surface, to what the probe has been touched, was not perfectly planar. Each non-planarity of the surface under the probe is shown by four time higher error of reading. Thus, for the gap of 0.08 mm the error of reading is 0.32 mm, i.e. 0.4 mm after rounding to tenths. So that, in this case the read thickness is by 0.4 mm higher, and it can be only influenced by the better surface preparing, to obtain zero gap between the probe and material surface on the small area of the diameter of $\varnothing 10$ mm. The error of reading because of the surface non-planarity under the probe can be eliminated by the good preparation of material surface. For the calibration of ultrasound apparatus two basic gauges K1 and K2 (see Czech Standards ČSN EN ISO 2400 [16] and ČSN EN ISO 7963 [17]) have been applied. The gauge K1 is made of steel with following parameters: the speed of the propagation of longitudinal waves is $c_L = 5\,920 \pm 30$ ms⁻¹, the speed of propagation of transverse waves is $c_T = 3\,255 \pm 20$ ms⁻¹, the

attenuation is $\alpha = 0.05$ dBmm, the density is $\rho = 7.85 \cdot 10^3$ kgm⁻³. The gauge K2 is also made of steel with the same acoustic properties as the first one. This second type of the gauge is preferred in for the measuring in situ, for its smaller dimensions and weight.

B. Results of Thicknesses Measurement

The measurement of cross-sections thicknesses have been performed in the same locations as the verification of tensile strength. In total 22 measured locations have been verified; only two locations on the upper flanges of the arches have not been tested.

Before measuring the colour layers have been removed and the surface has been aligned to be the smoothest (see Figs. 8 or 9, for example). On each measuring base of the area of 30×30 mm, minimally 3 measurements of the wall thickness have been always performed and subsequently the mean values have been calculated. The results of the measurement of the thickness t of steel members are listed in Table 2.

Table 2 measured thicknesses t of verified members

Member type		Thickness mean value t [mm]
Roof girders	chords	7.57
	diagonals	3.56
Roof purlins	chords	3.48
	diagonals	2.79
Arches	flanges	10.46
	web	10.49

Using ultrasound device “SONIC 1200 HR”, the thicknesses of the walls of selected statically important structural members of the roof structure and arch main girders of the winter sport stadium in Znojmo city have been verified. Applying 10 MHz ultrasound probe and precise preparation of the verified members surface the measuring accuracy of ± 0.3 mm has been achieved. Based on the results of ultrasound measurement and available documentation of the roof structural system, it can be deduced, that the actual thicknesses of particular selected members, which have been measured, correspond with the thicknesses mentioned in drawing documentation.

V. CONCLUSION

Partial conclusions have been mentioned above – see paragraphs III. E. and IV. B. The paper shows the usage of indirect non-destructive methods for the verification of geometrical and mechanical properties, if destructive methods cannot be applied.

ACKNOWLEDGMENT

The paper has been elaborated within the framework of the solution of the following research projects supported by the Czech Ministry of Education, Youth and Sports: (i) the project

No. CZ.1.05/2.1.00/03.0097, within the activities of “AdMaS” Centre, and (ii) the project No. FAST-S-14-2544, within the specific university reserach.

REFERENCES

- [1] M. Karmazinová and J. Melcher J., “Material testing and evaluation of steel mechanical properties for classification of steel grade of existing civil engineering structure”, *Advanced Materials Research*, Trans Tech Publications: Zürich, Vol. 651 (2013), pp. 274-279, doi: 10.4028/www.scientific.net/AMR.651.274. ISSN 1022-6680.
- [2] M. Karmazinová and J. Melcher J., “On problems of mechanical properties of structural steel in load-carrying structure of historical building construction”, *Applied Mechanics and Materials*, Trans Tech Publications: Zürich, Vol. 249-250 (2012), pp. 1103-1108, doi: 10.4028/www.scientific.net/AMM.249-250.1103. ISSN 1660-9336.
- [3] M. Karmazinová and J. Melcher J., “Classification of structural steel of existing civil engineering structure based on testing and evaluation of yield and ultimate strengths”, *Applied Mechanics and Materials*, Trans Tech Publications: Zurich, Vol. 281 (2012), pp. 585-588, doi: 10.4028/www.scientific.net/AMM.281.585. ISSN 1660-9336.
- [4] M. Karmazinová, J. Melcher and L. Vitek, “Diagnostics of existing steel roof structures of sport stadiums”, In *New Developments in Structural Engineering & Constructino, Proceedings of the Seventh International Structural Engineering and Construction Conference “ISEC-7”* held in Honolulu., Research Publishing Services: www.rpsonline.com.sg, Singapore 2013, Vol. II, pp. 987-992, doi: 10.3850/978-981-07-5354-2_St-57-155. ISBN-13: 978-981-07-5354-2, ISBN-10: 981-07-5354-3.
- [5] M. Karmazinová, J. Melcher and J. Lánik, “Diagnostics of steel roof structures of sport stadiums”, In *Proceedings of the Thirteenth East Asia-Pacific Conference on Structural Engineering and Construction “EASEC-13”* held in Sapporo, http://hdl.handle.net/2115/54209, pp. A-3-5, 8 pp. Hokkaido University Library, 2013.
- [6] J. Melcher, M. Karmazinová, L. Vitek, P. Cikrle and J. Lánik, *Evaluation of Existing Load-Carrying Structure of Winter Sports Stadium in Znojmo city, Parts: Verification of tensile strength of selected structural members, Verification of cross-sections thicknesses of selected structural members* (original in Czech language), Final Report for ACIERCON Ltd., Brno University of Technology, Faculty of Civil Engineering, 17 pp. Brno, 2013.
- [7] M. Karmazinová, J. Melcher, M. Pilgr, M. Šmak and M. Štrba, *Olomouc City Hall – Steel Structures – Diagnostics of Structure – Part II* (original in Czech language), Final Report for OKF, Ltd., Brno University of Technology, Faculty of Civil Engineering, Brno, 2012.
- [8] J. Lánik, *Olomouc City Hall – Steel Structures – Diagnostics of Structure – Part I* (original in Czech language), Final Report for OKF, Ltd., Brno University of Technology, Faculty of Civil Engineering, Brno, 2012.
- [9] J. Melcher, M. Karmazinová, L. Vitek, P. Cikrle and M. Štrba, *Evaluation of existing load-carrying structure of Winter Stadium at Jihlava city*, Report for ACIERCON Ltd., Brno University of Technology, Faculty of Civil Engineering, Brno, 2012.
- [10] J. Melcher, “Full-Scale Testing of Steel and Timber Structures: Examples and Experience”, In *Structural Assessment – The Role of Large and Full Scale Testing*, E & FN SPON, London 1997, pp. 301-308.
- [11] ISO 13822 *Basis of Structural Design – Evaluation of Existing Structures*, CNI Praha, 2005.
- [12] ČSN EN 10027-1 (42 0011) *Designation systems for steels – Part 1: Steel names*, CEN: Brussels, 2006.
- [13] ČSN EN 10027-2 (42 0012) *Designation systems for steels – Part 2: Numerical system*, CEN: Brussels, 1995.
- [14] EN ISO 6892-1 *Metallic materials – Tensile testing – Part 1: Method of test at room temperature*, CEN Brussels, 2009.
- [15] EN 1990 *Basis of structural design*, CEN: Brussels, 2011.
- [16] ČSN EN ISO 2400 (35 6885) *Welds in steel. Reference block for the calibration of equipment for ultrasonic examination*, 1994.
- [17] ČSN EN ISO 7963 (01 5025) *Non-destructive testing – Ultrasonic testing – Specification for calibration block No. 2*, 2011.

Shafts renovation using coatings with nano elements

Dimitar N. Karastoyanov, Mara K. Kandeve and Kostadin G. Kostadinov

Abstract— The paper is concerned with the technological process of renovation of shafts used in industrial manufacturing for extruding of sheet material. We present an advanced nanotechnology based on nonelectric chemical laying of a nickel coating with included nanoparticles. The technology is environmentally harmless and the new coating features an increased hardness and wear resistance. Results from experimental tests of the nanostructured nickel coating are presented. A manipulator for inspection of coatings of renovating shafts is designed. The manipulator is a part of robotised systems for inspections of coatings with high mechanical wear-resistance and surface-smoothness

Keywords— Materials processing, nanoparticles, nickel coating, shafts renovation, micro robot.

I. INTRODUCTION

THE products of extruding (pressing by pushing) of sheet material from nonmetal materials (Plexiglas, PVC, packing folio, other plastics) are widely used in households. Gifts, flowers, sugar and chocolate packing is made from thin aluminum or Plexiglas sheets. Thin Plexiglas sheets are used to make pack boxes, and thick nylon sheets are used to make bags, raincoats, etc. The vast amount of production of smooth sheets of various sizes from these materials has brought to the development of technologies in which the material is pressed and pushed out (extruded) between shafts of various diameters (100–500 mm) and various lengths (1–3 m), [1]. The shafts are chromed, have very narrow tolerances of diameter size and very high degree of smoothness by polishing. Schematically, a technological line for sheet production is shown in fig. 1.

With the time and at high production rate, shafts age, their surface wears out, and sometimes scratches appear in incidents. All this makes the shaft surface not precisely circular and even. Because of the very high price of a new shaft, renovation of the defected shaft is performed by

This work was supported by the project AComIn - *Advanced Computing for Innovation*, Grant 316087, funded by the FP7 Capacity Program (Research Potential of Convergence Regions initials).

D. N. Karastoyanov is with the Institute of Information and Communication Technologies (IICT) - BAS, Sofia, Bulgaria (phone: +359-2-979-27-23; Sofia, Bulgaria, (e-mail: dkarast@inf.bas.bg).

M. K. Kandeve is with the Materials Processing Department, Technical University of Sofia, Sofia, Bulgaria, (e-mail: mkandeve@tu-sofia.bg).

K. G. Kostadinov is with the Institute of Mechanics – BAS, Sofia, Bulgaria; e-mail: kostadinov@imb.bas.bg.

applying a new coating and polishing it to mirror shine. However, renovation itself is a high precision operation which is also expensive, high energy and time consuming and in some cases it is a technological secret of the companies performing this operation.

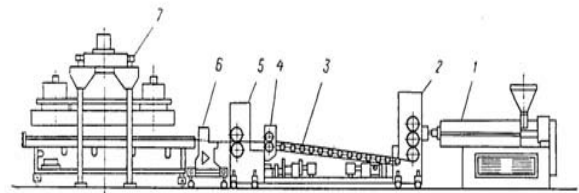


Fig. 1 Technological line for sheet production:
1- extruder; 2 – calender; 3 – rolling for the sheet cooling; 4 – unit for longitudinal cutting; 5 – stretching shafts; 6 – guillotine for crosswise cutting; 7 – packing unit

In view of the above, the problems of development of an industrially applicable technology and the design of the respective technological line are of great economical importance for the technical support of all kind of extruding and rolling mills producing sheets of various plastics and aluminum alloys. In this paper we describe an innovative nanotechnology for shafts renovation by laying a nickel coating with included nanoparticles. The results from laboratory tests of the new coating are presented and discussed.

II. AN ADVANCED TECHNOLOGY

A simple analysis of the existing technology for shafts renovation reveals the following general characteristics of this technology.

- All methods of finishing and polishing of shafts coating require special equipment, high processing precision and they consume large amounts of electrical energy.

- Chrome coatings, which are still in use, ensure the necessary hardness and wear resistance, but the technology is known to be harmful and it does not comply with the contemporary environmental and ecological requirements. In particular, the EU Directives characterize chrome coatings and waste products (cyanides) from chrome baths as highly harmful.

- As a rule the finishing and polishing of steel (from which shafts are made) is more developed, cheap and successful as

well as less harmful than processing with chrome, especially for big details and smooth finish.

Based on the above observations, an advanced technology for shafts renovation is developing by the authors and their co-workers under a project “New Methods and Means for Renovating of Shafts for Folio Extrusion” supported by the National Science Fund of Bulgaria.

Our technology is oriented to comparatively small shafts (400-800 kg) with cylindrical shape for extruding plastics. Fig. 2 shows a smooth (hollow) cylindrical shaft with the attachment journals.

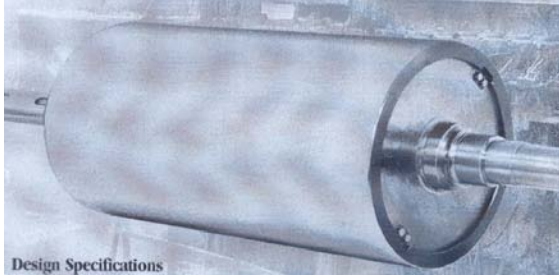


Fig. 2 Hollow smooth shaft for extruding of folio

The technology is based on nanostructured composite coatings obtained by electroless nickel plating method developed at the Technical University in Sofia [3]. It enables us to polish the steel base of the shaft by laying a thin (10-15 μm) nickel coating with nanoparticles in it, or by laying a thicker coating (25-50 μm) including other micro and nanodispersoids for increasing hardness and wear resistance. The usage of chemical nickel coating is characterized by several important advantages [3], [4]:

- High evenness in the layer thickness i.e. it is a sized coating requiring minimal finish processing;
- High hardness and wear resistance. The friction coefficient with many materials is relatively low;
- Low porosity/high corrosive resistance;
- Excellent polishing ability because of great hardness and microcrystal structure;
- Convenient disperse coatings matrix.

The application of disperse coatings with nickel-phosphor matrix is widely used. The disperse coatings can include microscale and nanoscale insertions. At present there is a large variety of the existing microscale dispersoids and nanoscale particles [5]. Microscale insertions are mainly on the basis of carbides of silicon, titanium, tungsten and cobalt, characterized by high hardness and good bonding with the nickel matrix. Nanoscale particles are mainly nanodiamonds obtained through various technologies.

The process of extruding of sheet material is characterized by several negative peculiarities and conditions as:

- High working temperature - 200° C;
- Abrasive effect of the extruded material;
- Significant normal forces on the contact surface of the shafts;

- Noninterruptive working process.

In view of the above properties, the new type of coating offers improved characteristics and exploitation advantages regarding:

- Wearing resistance and microhardness;
- Corrosion resistance;
- Reduced porosity;
- Rapid reduction of the friction coefficient;
- Increased cohesion and adhesion.

The listed improvements and physical-mechanical features, due to the nanostructured nickel coatings, can increase the exploitation time of the extruding shafts 2 to 10 times while at the same time reducing the thickness of the coatings 3 to 5 times. The reduced thickness compensates for the higher price of the operation. The increased working time is an additional advantage. Furthermore, the replacement of the chrome coating with nickel one satisfies the requirements of the EU Directives on environmental pollution.

We have developed a stand (Fig. 3) for testing of coating's wear-resistance at working temperature (200 °C).

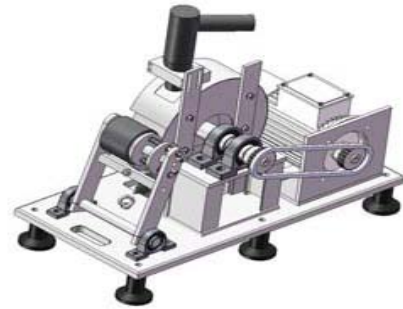


Fig. 3. Stand for testing of coating's wear-resistance

The stand consists of hollow shaft, driven by electric AC motor, and heater, blowing the shaft with hot air. A heat-resistant Teflon roller is pressed to the shaft, which serves as extruded material.

III. ABRASIVE WEAR

Experimental study of abrasive wear of Ni coatings is realized by means of the test rig TABER ABRASER according to the kinematical scheme „disk-on-disk” (Fig. 4).

The specimen 1 (the body) with deposited coating 2 is in the shape of disk and is fixed appropriately on carrying horizontal disk 3 driven by electrical motor 4 with a constant rotational speed $\omega = 1[\text{s}^{-1}] = \text{const}$. The counter-body 5 is an abrasive disk (roller) of special material CS 10 mounted on horizontal axis 6 in the device 8, by means of which is set the desired normal load P in the contact zone K . Thus, the body 1 and the counter-body 5 are located on two crossed axes. Because of the constant rotational speed of the body 1 and the constant nominal contact pressure p_a , the friction in the contact zone K supports constant speed of rotation of the counter-body 5.

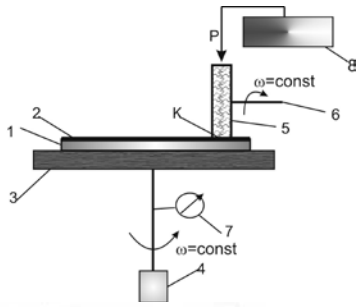


Fig. 4. TABER ABRASER – device for study of abrasive wear

The procedure of the experimental study on abrasive wear is realized in the following sequence of operations, [6]:

- clean-up, cleaning of lubricants and drying of the equal specimens. The specimens represent disks of diameter 100 mm and thickness 3 mm with the deposited coatings;
- measuring of roughness of the contact surfaces of the specimens before and after wear;
- measuring of specimens mass m_0 before and its mass m_1 after a given friction path L by electronic balance WPS 180/C/2 of accuracy 0,1 mg. At every measurement the specimens are cleaned with appropriate solution against static electricity;
- measuring of coating thickness h_1 before wear and h_2 after wear by means of *Pocket LEPTOSKOP 2021 Fe* device in 10 points of the surface; the average value is taken for thickness of the sample;
- the specimen 1 is fixed on the carrying horizontal disk 3; then the normal load P is set. The friction path L is determined by the number of cycles read by the revolution counter 8.

Abrasive wear for all coatings is obtained by fixed equal operating conditions – nominal contact pressure given with the normal load P , average sliding speed V and parameters of the abrasive surface.

The characteristics of the experiment are given in Table 1.

Table 1. Working parameters in the experiment:

Apparent contact area	$A_a = 0,26 \text{ cm}^2$
Nominal contact pressure	$p_a = 9,42 \text{ N/cm}^2$
Average sliding speed	$V = 22,3 \text{ cm/s}$
Abrasive material	CS 10

The experimental results are given in Fig. 5, Fig. 6 and Fig. 7.

The parameters of mass and linear wear are studied: speed, wear intensity, absolute and relative wearresistance and their change in time, respectively the friction path.

Wear intensity is determined as mass (or linear) wear for unit friction path, and absolute wearresistance - as the reciprocate value of wear intensity.

The relative wearresistance is the ratio between the absolute wearresistance of the tested coating and the absolute wearresistance of reference sample for equal friction path (number of cycles).

Two reference samples are used in the present work – Nickel coating without nanodiamond particles with heat treatment and without heat treatment.

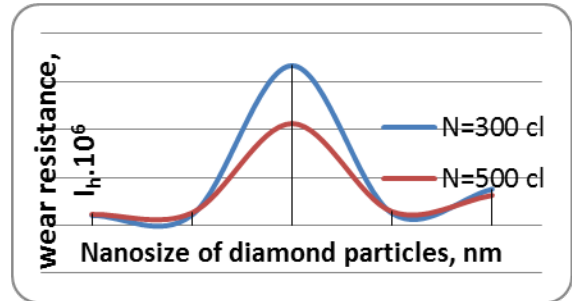


Figure 5. Dependence of wearresistance I_h on nanoparticles size for coatings without heat treatment

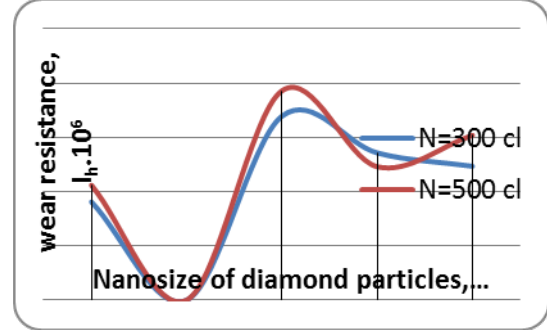


Figure 6. Dependence of wearresistance I_h on nanoparticles size for coatings with heat treatment

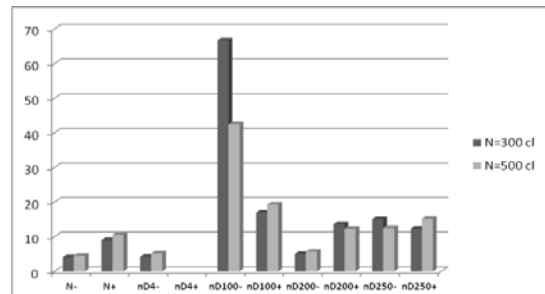


Figure 7. Wearresistance of Ni coatings without and with nanoparticles without and with heat treatment

The presence of nanodiamond particles affects the value and the character of the abrasive wear. This influence becomes more complicated along with the heat treatment of the coating.

For size of nanoparticles 4 nm and 100 nm coatings with heat treatment show higher wear, and for size 200 and 250 nm the opposite effect is observed – wear is lower than that of the case without heat treatment.

The dependence of wear on nanodiamond particles size is of nonlinear character, and the various coatings show different duration of the running-in process.

The boundary number of cycles N^* , where the whole coating is worn, is always bigger for coatings without heat treatment.

The highest wearresistance show Ni coatings with nanodiamond particles of the size $\delta = 100$ nm without heat treatment.

IV. THE MICRO ROBOT

The aim of it the case of testing is to design a manipulator - holder for micro-nano-positioning and orientation of the touchless sensors and gauges for measuring roughness, thickness of coat, deviation from cylindricity or micro-hardness of the shaft coating, [7]. The manipulator is positioned on the mobile platform of a specialized robot for measuring shaft coatings- fig. 8.

The co-operation of the macro and micro robots is necessary when the manipulated object has to be handled into a macro-space and carry out a precise finishing operation in a micro-zone. In mechanisms with incorporated macro – micro structures DoF, as well as the accessible area increase, the structures are compact and have fewer backlashes. Finally it will be investigated how the length variation of the piezo-ceramic links will influence the motion of the working tool.

Three and four-links mechanisms for manipulators with actuators links (fig.8.c) are synthesized. The manipulator is intended to position and orientate the noncontact sensors for inspection of shaft coating. It is positioned on a mobile platform of a specialized robot. In the kinematic scheme (fig.8a) piezo-ceramic links are illustrated as prismatic pairs. It is seen from the structural scheme (fig. 8b) that the basic loop is a five-link with two DoF (with two piezo-ceramic links), one of the links being the quarter link 3, which is also a part of a second closed four-link loop. In link DE of this loop the third piezo-ceramic element is built-in and link CH (number 8) is the output link (OL), [8], [9]. The small displacements realized by the piezo-ceramic links (actuators) require the use of elastic joints illustrated by arcs on the construction scheme of (fig.8c). OL of the manipulator can position point H and orientate link 8 in the plane of motion. According to equation (5) manipulator mechanism for micro positions has 3 DoF

$$h = 3n - 2p_5 = 3 \cdot 7 - 2 \cdot 9 = 3$$

where

h –Number of DoF, n – number of mobile links, p_5 –kinematical joints with 1 DoF.

Some problems of real time control and file system organization are discussed in [10], [11].

V. CONCLUSION

The main advantage of the proposed technology is the replacement of the chrome-coating in cyanide baths with nickel coating obtained by means of chemical nonelectric nickelling with included micro-scale dispersoids and nanoscale particles. The experimental results show a high wear resistance of the nanostructured coatings especially in the cases of heat processed composite nickel coatings. Manipulators have to micro-nano-positioning and orientation of the noncontact sensors and gauges for measuring roughness, thickness of coat, deviation from cylindricity or micro-hardness of the shaft coating. In most cases, when measuring roughness or hardness, as well as deviation from cylindricity of shafts and their micro-coating, it is required that sensors and gauges should be positioned exactly perpendicular to the shaft (along the shaft’s normal). This requires that the output link of the manipulator (sensor or gauge) should to be orientated or shifted along the normal to the measured surface. A further analysis and study of the microstructure and other physical and mechanical properties of the composite coatings is a subject of a future research.

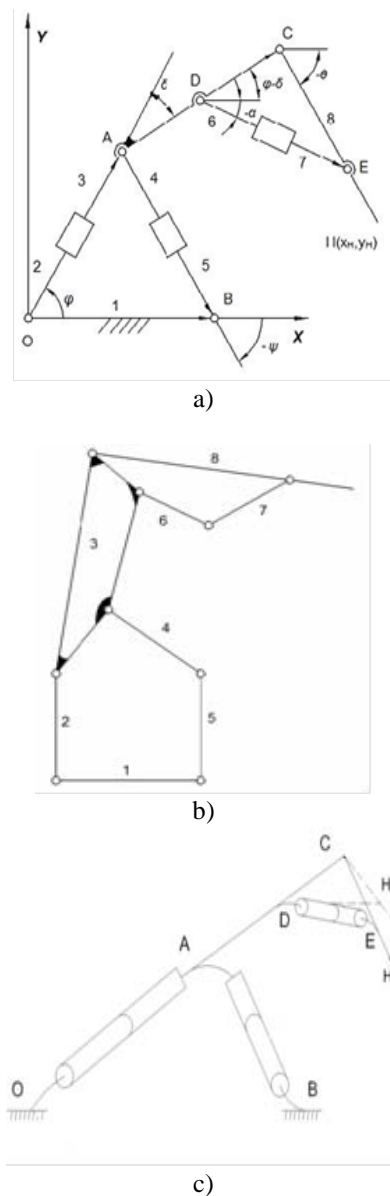


Fig.8. (a) Kinematic; (b) structural; (c) construction schemes of the manipulator mechanism.

REFERENCES

- [1] P.Velev, *Plastic manufacturing*, UCTM, Sofia, 2005.
- [2] V. Kovalenko, *Technology and equipment of electrophysical and electrochemical methods of material processing*, Kiev, Visha Schola, 1985 (in Russian).
- [3] G. Gavrilov, C. Nicolov, *Electroless Nickel and Composite Coatings*, Technika, Sofia, 1985.
- [4] G. Gavrilov and D. Karastoyanov, Disperse coatings on nickel basis including micro- and nano-dispersoids, in *Proc 19 International Conference "Robotics and Mechatronics'09"*, Varna, Bulgaria, 2009, pp.66-72.
- [5] D. Karastoyanov, T. Penchev, G.Gavrilov, Renovating of shafts for folio extrusion using new type coating with nano components, in *Proc. International Conference "Robotics, Automation and Mechatronics'11"*, Sofia Bulgaria, 2011, pp.m17-m20.
- [6] M. Kandeve, D. Karastoyanov, A. Andonova., Wear and tribothermal effects of nanostructured nickel chemical coatings., *Applied Mechanics and Materials* Vols. 157-158 (2012) pp 960-963
- [7] Kotev V., Kostadinov K., Genova P., Design of incorporated macro-micro robots for macro and micro operations., 8th International conference on informatics in control, automation and robotics (ICINCO 2011), 28-31 July 2011, Noordwijkerhout, The Netherlands. Proceedings ICINCO 2011, vol.2, pp: 273-276, 2011.
- [8] Genova P., Kostadinov K., Kotev V., Tyankov T., Bulgarian Patent № 110597, 2010, Micro-electro-mechanical device for manipulators.
- [9] Georgiev G., Kotev V., Tiankov T., Accuracy and calibration of micropositioning robotic systems., *Journal ACTA Technica corviniensis – Bulletin of engineering*, Fascicule 3, July – September, tome III, pp: 125-130, 2010.
- [10] Stanislav Simeonov, Neli Simeonova, Asen Iliev, Deterministic Model of CPU Scheduling in Real Time Operating System, UNITECH"13, GABROVO, II-p192-197;
- [11] Simeonov S., Germanov V., File System Performance Analysis, UNITECH 09, ISSN 1313-230X, p.424-428.

Dimitar N. Karastoyanov is a member of the Bulgarian Scientists Association. He was born in Stara Zagora, Bulgaria in 1952. He has a master degree in Electrical engineering. He graduated Technical University Sofia in 1977. The author received a doctoral degree in 1982, Robotics from the Institute of engineering cybernetics and robotics (BAS). Dr. Karastoyanov is a professor in Institute of Information and Communication Technologies (BAS). Prof. Dr. Karastoyanov is a key professor under AcomIn project at the ICT – BAS. He is conducting research on design, dynamics and intelligent control of robots and mechatronic systems. His professional interests refer to real time systems, adaptive control, industrial engineering and robotics.

Mara K. Kandeve is a member of the Bulgarian Scientists Association. He was born in Bourgas, Bulgaria in 1955. He has a master degree in Automotive engineering. He graduated Technical University Rousse in 1979. The author received a doctoral degree in 1986, Applied Mechanics from the Technical University Sofia. Dr. Kandeve is an assoc. professor in Technical University Sofia. Dr. Kandeve is a key assoc. professor at the TU-Sofia and Head of the Tribology Lab. He is conducting research on design, structure and tribology characteristics of materials. His professional interests refer to wear, erosion and thermal resistance of coatings including nano elements.

Kostadin G. Kostadinov is a member of the Bulgarian Scientists Association. He was born in Kazanlik, Bulgaria in 1957. He has a master degree in Electrical engineering. He graduated Technical University Sofia in 1983. The author received a doctoral degree in 1994, Applied Mechanics from the Institute of mechanics (BAS). Dr. Kostadinov is a professor in Institute of Mechanics and Head of GIS Transfer Centre. He is conducting research on design, dynamics and intelligent control of robots and mechatronic systems. His professional interests refer to mechanics and biomechanics, industrial engineering and robotics.

Analyzing Emission Sounds: A way for Early Detection of Bearing Faults in Rotating Machines

Mohamed FEZARI and Zahra TAIF

Abstract— Early detecting faults in main part of Rotating machines (RM) such as Bearing and gears will avoid non programmed stops of production of the machine. Different detection methods using vibration signature analysis, noise signature analysis and lubricant signature analysis were presented in literature reviews. In this paper emitted acoustic signal analysis and processing based on speech recognition features and classifiers were used to detect early faults in REB namely: faults in rolling ball, in inner race, outer race and protecting cage. Commonly used Speech recognition features were selected, also different classifiers were tested: Euclidian distance SVM and GMM then mixed to improve the rate of classifier and make comparison. We obtained as results using MFCC +LPC +SVM as classifier 90%, by including ACP to reduce features and then mixing SVM with GMM we reached the 92% as result. By combining other features kurtosis and Jitter and Shimmer we obtained the 94% in signature faults detection.

Keywords— Fault detection, Acoustic emission, KNN as classifier, ASR features.

I. INTRODUCTION

Bearing fault diagnosis has attracted significant attention from the research and engineering communities over the past decades. Generally, a bearing fault diagnosis process can be decomposed into three steps: data acquisition, feature extraction, and fault detection and classification. Vibration-based signal analysis in the time-frequency domain has been a major technique for bearing fault diagnosis. Several statistical parameters in the time domain and the frequency domain, such as the root mean square, kurtosis, and skewness, have been shown to be capable of fault detection [1,2]. In [1], nine features in the time domain and seven features in the frequency domain were used for bearing fault detection. The bearings are one of the targets of this maintenance among the elements composing the rotating system. Acoustic emission (AE) describes the phenomena that result in structure borne elastic waves being generated by rapid energy released from localized sources. AE signal is a high frequency signal, normally over 20 kHz but can be bounded to lower values depending on application. For the high sensitivity, AE becomes more and more popular in condition monitoring of

rotating machine. Mba [3] etc. used Acoustic Emission to detect and identify bearing and gearboxes defects. Choudhury and Tandon [4] used Acoustic Emission for detection of defects in ball bearing.

When defects appear on bearings, wide bandwidth periodic AE bursts can be observed. Then the task of bearing fault detection can be performed by finding out whether the AE bursts are periodic and whether it corresponds to one of the characteristic bearing defect frequencies for identifying the type of bearing defect.

Rotary machines are installed in large number of industrial firms. Due to this important number, for the operator, it is necessary to be informed on its mechanical status and early defect in order to take in advance better decision concerning the production and mechanical parts of the machine (when we can change one element at rest time before destruction of the rotary machine). RM (rotating machine) absorbs the energy and transforms it by rotation to another mechanical energy (rotation to translation). It is composed of rotary part called 'rotor' and fixed part called 'stator', to ease rotation it needs links and guidance provided by some mechanical elements namely: gears and bearings.

The bearing is the main element to provide link between two subjects in rotation mechanism, it provides relative rotation of elements under load with precision and minimal friction. Most of RM use roller bearing about 40% to 50% of faults are due the bearing defects (ball, outer race and inner race).

II. RELATED WORKS

The main drawback with the application of the AE technique is the attenuation of the signal and as such the AE sensor has to be close to its source. However, it is often practical to place the AE sensor on the non-rotating member of the machine, such as the bearing or gear casing. Therefore, the AE signal originating from the defective component will suffer severe attenuation before reaching the sensor. Typical frequencies associated with AE activity range from 20 kHz to 1 MHz. While vibration analysis on gear fault diagnosis is well established, the application of AE to this field is still in its infancy. In addition, there are limited publications on application of AE to gear fault diagnosis. Soares explored several AE analysis techniques in an attempt to correlate all possible failure modes of a gearbox during its useful life [5].

Based on Singh et al., 1996 work, early detection of gear pitting [6], Tan offered that AE RMS (Root Mean Square) levels from the pinion were linearly correlated to pitting rates;

Mohamed FEZARI Author is with Badji Mokhtar Annaba University Faculty of Engineering Dept. Electronics, BP:12, Annaba, 23000, ALGERIA (e-mail: mouradfezari@yahoo.fr).

Zahra TAIF Author is with is PhD student at Badji Mokhtar Annaba University Faculty of Engineering Dept. Electronics, BP:12, Annaba, 23000, ALGERIA (e-mail: Zahra.taif@yahoo.fr).

AE showed better sensitivity than vibration at higher torque level (220Nm) due to fatigue gear testing using spur gears. He made sure that the linear relationship between AE, gearbox running time and pit progression implied that the AE technique offers good potential in prognostic capabilities for monitoring the health of rotating machines [7].

On the other hand, AE signal as a signal processing method was studied using bearing and gearbox. The results of the research in papers [8][9] and [10], the envelope analysis was found to be useful to detect fault in rolling element bearing. The fault detection frequency of bearing can be presented in the power spectrum. Fault gear detection and classification using Wavelet transform was used by applying the signal processing method for the gearboxes [11], but wavelet transforms can give the different results with the envelope analysis. It can be shown the defect frequency, but the efficiency is lower than that of envelope analysis. Thus, the signal processing method for AE signal has not been completed until now, and it must be developed in the future. In this paper we proceed by using new features and classifier used in speech processing. LFCC and MFCC are very good discriminative features used in automatic speech recognition beside the SI features.

A. Acoustic emission in fault detection

Acoustic emission describes the phenomena that result in structure borne elastic waves being generated by rapid energy released from localized sources. AE signal is a high frequency signal, normally over 20 kHz but can be bounded to lower values depending on application. For the high sensitivity, AE becomes more and more popular in condition monitoring of rotating machine. Mba [12] etc. used Acoustic Emission to detect and identify bearing and gearboxes defects. Choudhury and Tandon [13] used Acoustic Emission for detection of defects in rolling element bearing.

When defects appear on bearings, wide bandwidth periodic AE bursts can be observed. Then the task of bearing fault detection can be performed by finding out whether the AE bursts are periodic and whether it corresponds to one of the characteristic bearing defect frequencies for identifying the type of bearing defect. The de-noising and enhancement of AE signals are of importance for it can reveal the occurrence of these bursts. The reduction of the number of signal coefficients can also greatly reduce the workload of post-analysis; particularly important since the sampling rate for AE signals is usually very high. The AE signals are highly non-stationary for their amplitude and frequency fluctuate. In this case, more adaptive schemes are needed.

B. Rolling Element Bearing in rotating machine

One of the most mechanical components used in rotating machines because of its performance over price, faults in bearing can be generated by a fatigue of material under normal or abnormal functioning conditions. In figure 1, The bearing

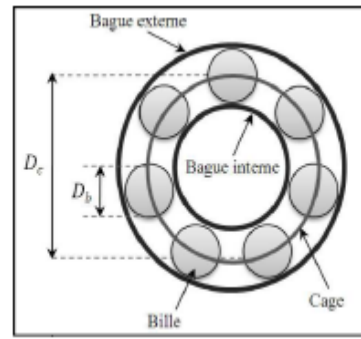


Fig. 1. Rolling element bearing

Bearing can be damaged by external effects:

- External particles contamination of bearing (sand granular, dust..)
- Corrosion engendered by water or acid penetration
- Bad alignment of rotor
- Inadequate lubrication may cause heat and cracks on bearing.
- Electric arc caused by current can affect bearing.
- Bad installation of the bearing

C.Default characteristic frequency

Each fault has its own signature and is characterized by a fundamental frequency which Can be computed from: the structure and dimension and rotation frequency. In vibration analysis, it is possible to observe certain frequencies bands and identify the fault type the characteristic frequencies are expressed as follow:

$$\text{Outer race fault: } F_{ex} = \frac{N_b}{2} F_r \left(1 - \frac{D_b}{D_c} \cos \alpha\right) \quad (1)$$

$$\text{Inner Race fault } F_{in} = \frac{N_b}{2} F_r \left(1 + \frac{D_b}{D_c} \cos \alpha\right) \quad (2)$$

$$\text{Rolling element Fault: } F_{bi} = \frac{D_c}{2D_b} F_r \left(1 - \left(\frac{D_b}{D_c} \cos \alpha\right)^2\right) \quad (3)$$

$$\text{Cage fault : } F_{ca} = \frac{1}{2} F_r \left(1 - \frac{D_b}{D_c} \cos \alpha\right) \quad (4)$$

With F_r is the rotor frequency rotation, D_b diameter of the rolling element and D_c is the diameter of bearing and N_b is the ball number as presented in figure 1. These expressions are well explained in [15].

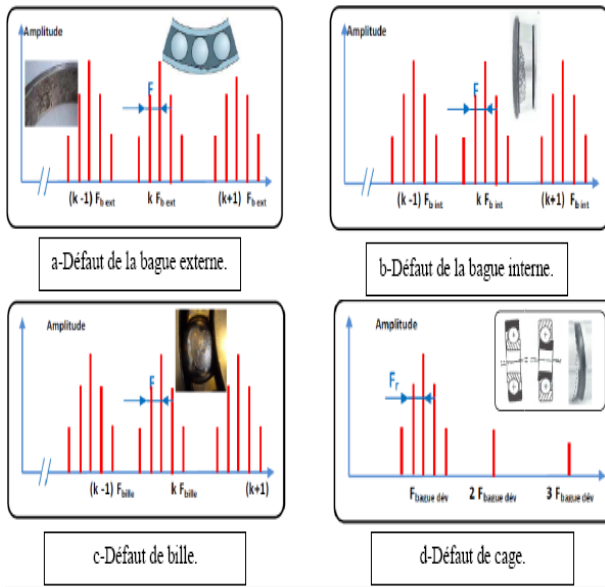


Fig. 2, illustration of some fault in ball bearing III. ACOUSTIC SIGNAL ANALYSIS

There are different techniques used in acoustic signal analysis in order to detect faults in rolling element bearing, in literature review, most of the work is based on frequency analysis of signal sensed by vibration sensors and processed by AE analysis. To detect faults, FFT to get signal frequencies, RMS (root mean square) to get mean energy, peak to peak to compute maximum amplitude between extreme values, and Kurtosis to compute impulsive corrector of signal it is used to detect chock type faults, these parameters are classified as scalar indicator (SI) features. In Temporal analysis, the samples are processed temporally using crossing zero, extremes and energy envelope. Frequency analysis such as FFT, LPC (linear predictive coefficients) has been used in AE analysis and early work on speech processing.

In our work, we explored classical features and classifiers used in ASR, they gave good results in ASR since they can distinguish between two words close in pronunciation combined with features used in vibration analysis i.e. SI features. We used Knn and ED as classifiers.

IV. IMPLEMENTATION:

A. Test bench description

The test bench used in experiment is illustrated in fig 3 , it is installed in the laboratory of industrial maintenance and pedagogy at university of 8 Mai Guelma and directed by D. Djabala Abderrazek , this test-bed allow user to create the existing principal faults in ball bearing and to acquire des relative measurements to these different emulated faults. The collected data is done with a microphone (type piezo-electric sensor) installed as near as possible to the noise source (REB), the sensor gets AE and data is stored in hard-disk. The tests need to install and remove respectively 4 type of REB containing the three type of REB fault in (external race, internal race and ball) and one clean REB. To facilitate the experimental set up, only REB belt side is disassembled. The set up experiment banc used is “SpectratQuest” Banc, it is essentially composed of:

- Rotating asynchronous machine with power 1.5 Kw, synchronism speed 50000 trs/mn, powered by a frequency variation from 0 to 50000 trs/mn that correspond to 0 to 50 Hz frequency variation.
- A Rolling element bearing linked to the motor via elastic coupling
- Microcomputer Type Toshiba, processor i3 (CPU) with 2.27 GHz , RAM: 2 Go, with Sound Card Conexant CX20371.
- Microphone type: FANCONG, FC-350, directivity: noise cancelling, low impedance, sensitivity reduction: within -3dB, and S/N Ratio: more than 36 bD.



Fig. 3 Set up the Test Bench “ Spectra Quest”

V. EXPERIMENTAL PROTOCOL

As illustrated in figure 4, We have to start by collecting data for the training of the developed classifier. We fix the simulation with a clean REB and speed equal to 30 Hz then 40 Hz. With voice toolbox in Matlab, we make 10 recordings of 5 seconds duration and frequency sampling $F_s = 10000$ Hz, we store files with extension “filexp_i.wav”.

We do the same work for the three types of faulty REB, the information collected will serve for creating models for four classes and also to test of the application.

Training: this phase is fundamental for supervised classifiers, it plays an important role in classification success, it depends on type of data and also in the quantity of collected data, it constitutes the knowledge to learn for better generalization and representation of different classes. It is composed of the following steps: data collection, data processing, features extraction, models construction.

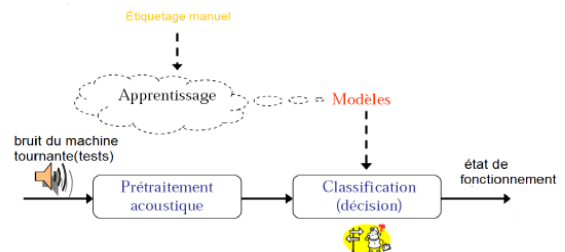


Fig. 4 fault monitoring flowchart.

The data collected from microphone is acoustically pre-processed using: hamming window where each segment of large 80ms with shifting in time of 30 ms, parameterization where the samples are processed and represented by a reduced quantity of information using three methods in our case (scalar indicator SI, linear predictive Coefficients LPC and Mel frequency Cepstral Coefficients MFCC), MFCC and LPC are computed using the bloc diagram in figure 5, more details on [14] .

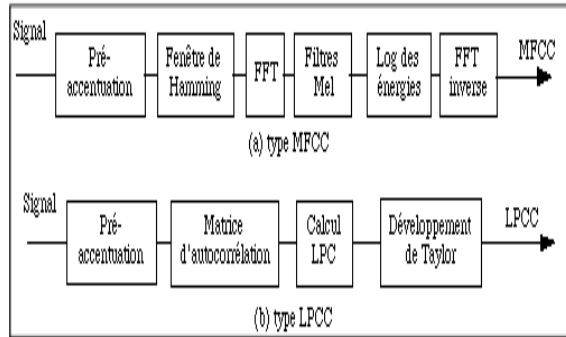


Fig. 5. Bloc diagram of MFCC and LPC computation.

In SI, we compute the following parameters: mean, Kurtosis which is used to detect shock type fault based on impulsive character of the signal, Energy, RMS where peak to peak and maximum amplitude between extreme values is computed, and variance.

For LPC we have taken the 10 first parameters and the 12 first parameters for the MFCC [14].

Model design and classification: we have used two techniques to classify data, and we tested for each type of feature the two classifiers, Euclidian distance and KNN (K nearest neighbor) despite it is a non parametric method.

Euclidian distance is a classic method to evaluate the proximity of two vectors of same dimension. Let $X_j=[x_{j1},x_{j2},x_{j3},\dots,x_{jn}]$ be the vector of a class j and $Y=[y_1,y_2,\dots,y_n]$ the vector corresponding to the test signal, the Euclidian distance between the two vector X and Y is defined by the equation:

$$D_j = \sqrt{\sum_{i=1}^n (x_{ji} - y_i)^2} \quad (5)$$

The minimum value of the distance D for $j=1\dots m$, where m is the number of classes, represents the class of the test signal.

Knn (K nearest neighbor): this technique uses as input a matrix X_{app} coordinates of points of characteristic vector for each signal, Y_{app} Class vector for each of training point, X_{test} matrix of points coordinates to classify, and K the number of near neighbor to take in consideration.

As output, we have Y_{pred} a class vector for the values to classify.

This function Knn allows classifying the K nearest neighbors, it computes the distance matrix between the test points (values) and training values, for each test point we get all distances with training points, and then we keep k nearest training points and affect the test point to this class. We do the same thing for all test points before returning the class vector for values to classify.

Techniques for dimension reduction: we used CPA (Corposant Principal Analysis) to reduce the number of features. The following program code presents the computation of PCA for

healthy, outer race fault, inner race fault and ball bearing fault using ACP1function.

```
function [wreduit]=acp1(W)
W1=W'; mx=mean(W1);
stdx=std(W1);ax=zeros(size(W1));
[r1,c1]=size(W1);
for i=1:r1
ax(i,:)=(W1(i,:)-mx)./stdx;
end
cov=ax'*ax/(r1-1);
[v,d]=eig(cov); d=diag(d);
[a,t1]=sort(d);
t1=t1(c1:-1:1);
d=d(t1); v=v(:,t1); t2=ax*v;
xe=ax*v(:,1:4)*v(:,1:4)';
s=t1(1:4,:);
wreduit=W1(:,t1(1:4,:))
end
```

```
[S] = acp1(Ws);    { for healthy motor }
[BX] = acp1(Wbx); { fault in outer race bearing }
[BI] = acp1(Wbi); { fault in inner race bearing }
[B] = acp1(Wb);   { fault in baal bearing }
```

The acoustic segment vector is represented by many features: 12 MFCC, 10 PLC, energy and SI features. The principal axes are determined by data covariance matrix, the directions to maximize the variability are determined due to proper values and associated proper values. At this stage, the new representation space has the same dimension as initial space, this new space ease the statistic de-correlation among axes. In order to reduce the acoustic segment vector dimension only the axes comporting maximum information (selected by large proper value) are conserved.

VI. TESTS AND RESULTS OF TWO SCENARIOS

First scenario, we used ED as classifier with different features , the results are presented in table 1.

Regarding obtained results in table 1, temporal features presented by SI lack of precision for bearing faults detection, however they give an acceptable result concerning gearbox fault detection (in our case the used gear has 3 broken teethes)

LPC and MFCC separately are compared and it is obvious that MFCC with 12 coefficients is better than LPC with 10 coefficients, but ball bearing degradation can be classified as inner race fault which explains the 50% and 75% in LPC and MFCC respectively.

Table 1. Fault detection results using ED classifier.

Test performance	Scal ar Indic	LP C	MFC C	SI+MF CC	SI+MFC C+ LPC	SI+MFCC+P CA
Healthy	75 %	90 %	92 %	95%	95%	98%
Outer race fault	50 %	92 %	96 %	96%	96%	97.5%
Inner race fault	25 %	90 %	95 %	97%	97%	98%

Ball fault	75 %	50 %	94 %	98%	98%	98.5%
gearbox	90 %	90 %	95 %	98%	98%	99%

By inserting temporal features SI, we did not see any improvement in result at columns 5 and 6, this is due to redundancy of features. Thus to improve the results we added features redactor algorithm PCA and results are in column 7. Second scenario, we used KNN as classifier, the obtained results are presented in table 2.

Table 2. Fault detection results using KNN classifier.

Test performance	Scalar Indicator	LPC	MFC	SI+MFCC	SI+MFC+C+LPC	SI+MFCC+PCA
Healthy	80 %	93 %	95 %	97%	97%	98.2%
Outer race fault	50 %	93 %	96 %	96.5%	97%	97.8%
Inner race fault	85 %	91 %	96 %	98%	98%	35%
Ball fault	25 %	25 %	97 %	75%	98%	98.75%
gearbox	50 %	94 %	96 %	98%	99%	99%

Based on results in table 2, we have got bad results concerning gearbox faults, ball and outer race faults using just Si features. KNN gave better results using LPC and MFCC compared to ED, except for ball bearing faults the result are less than 50% due to confusion in classification with inner and outer race faults class. Good results are reached by combining Si, MFCC and LPC as features as seen in column 6. This takes more time in classification due to more data to process, by inserting PCA algorithm in order to reduce the features we observed a decrease to 80% (due to 0% in ball bearing faults), this might be due to loss of some discriminate features with PCA.

We have observed that some values in tables 1 and 2 can be influenced by:

Number of features (including first and second derivative of MFCC), segment window dimension, number of training files for different faults, reducing number of classes (i.e : gearbox faults and bearing faults).

VII. CONCLUSION

In this work, a test bench for asynchronous motor has been used to validate the acoustic emission analysis, based on speech processing features, produced by ball bearing defaults. We have used LPC and MFCC including SI as features then we used two classifiers ED and KNN. Seven acoustic features (SI) are added to classical features to improve the rate of classification for common faults in asynchronous motor (bearing and gearbox faults). We have used five classes (three for bearing faults one for gearbox and one for healthy motor).

The selected classifiers have shown their aptitude to classify datasets for different type of indicators. Better results for ED are obtained using MFCC and SI features processed by PCA algorithm and the best results for KNN is reached using MFCC as feature without need to PCA. Computation time is reduced in the KNN case, PCA gave better results even if there is a computation time added in training phase. In future work, it would interesting to test the habitation GMM/HMM [16] as classifier and to process other type of faults within the RM [17].

ACKNOWLEDGMENT

We would like to thanks Professor Hassan NOURI from University of West England for his contribution to this work by allowing us to do training in his laboratory at UWE. Bristol, UK.

REFERENCES

- [1] Xu, Z.; Xuan, J., Shi, T.; Wu, B.; Hu, Y. A novel fault diagnosis method of bearing based on improved fuzzy ARTMAP and modified distance discriminant technique. *Expert Syst. Appl.* **2009**, *36*, 11801–11807. 2009
- [2] Li, B.; Zhang, P.L.; Wang, Z.J.; Mi, S.S.; Liu, D.S. A weighted multi-scale morphological gradient filter for rolling element bearing fault detection. *ISA Transactions* **2011**, *50*, 599–608.2011
- [3] D. Mba, "Prognostic opportunities offered by acoustic emission for monitoring bearings and gearboxes," 12th International Congress on Sound and Vibration, 2005.
- [4] A. Choudhury, N. Tandon., "Application of acoustic emission technique for the detection of defects in rolling element bearing," *Tribology International* **33**, 39-45.2000.
- [5] Soares, E. & Negro, A.A. "Condition monitoring of a gear box using acoustic emission Testing", *Material Evaluation*, Vol. 55, No. 2, (February 1997), pp.183-187, ISSN 00255327.1997.
- [6] Singh, A., Houser, D. R. & Vijayakar, S. (1996). "Early detection of gear pitting", *American Society of Mechanical Engineers*, Vol. 88, pp.673-678, ISSN 15214613.1996.
- [7] Yang, Y., Yu, D. & Cheng, J. « A fault diagnosis approach for roller bearing based on IMF envelope spectrum and SVM", *Measurement: Journal of the International Measurement Confederation*, Vol. 40, No. 9-10, (November 2007), pp.943-950, ISSN 0263-2231, 2007.
- [8] Sheen, Y.T. "An envelope detection method based on the first-vibration-mode of bearing vibration", *Measurement: Journal of the International Measurement Confederation*, Vol. 41, No. 7, (August 2008), pp.797-809, ISSN 0263-2231, 2008.
- [9] Sheen, Y.T. "An envelope analysis based on the resonance modes of the mechanical system for the bearing defect diagnosis", *Measurement: Journal of the International Measurement Confederation*, Vol. 43, No. 7, (August 2010), pp.912-934, ISSN 0263-2241, 2010.
- [10] Wu, J.D., Hsu, C.C. & Wu, G.Z. "Fault gear identification and classification using discrete wavelet transform and adaptive neuro-fuzzy inference", *Expert Systems with Applications*, Vol. 36, No. 3, (April 2009), pp.6244-6255, ISSN 0957-4174, 2009.
- [11] N. Tandon, A. Choudhury, "A review of vibration and acoustic measurement methods for the detection of defects in rolling element bearings," *Tribology International* **32**, 469-480, 1999.

- [12] D. Mba, "Prognostic opportunities offered by acoustic emission for monitoring bearings and gearboxes," 12th International Congress on Sound and Vibration, 2005.
- [13] A. Choudhury, N. Tandon, "Application of acoustic emission technique for the detection of defects in rolling element bearing," Tribology International 33, 39-45, 2000.
- [14] M. Fezari and M. Bedda, "Hybrid technique to enhance voice command system for a wheelchair", in proceedings of Arab Conference on Information Technology ACIT'05, Jordan, 2005.
- [15] Taif Zahra, Mebarki S., " Identification et Classification des defaults dans les machines tournante par etude fréquentielle des emissions sonores », Master thesis directed by M. FEZARI at dept. Electronics UBMA, 2011.
- [16] Mohamed FEZARI, Fethi AMARA, "Voice Disorder Detection based on Automatic Speaker Identification techniques" , ICIT 2013, Amman, Jordan, 2013.
- [17] Tan, C.K., Irving, P. & Mba, D. , "A comparative experimental study on the diagnostic and prognostic capabilities of acoustics emission, vibration and spectrometric oil analysis for spur gears", Mechanical Systems and Signal Processing, Vol. 21, No. 1, (January 2007), pp.208-233, ISSN 0888-3270, 2007.

M. FEZARI (MS'87–PhD2006 and HDR-2010) is Associate Professor At Badji Mokhtar Annaba University Faculty of Engineering dept. Electronics; He is recently member of TPC in many conferences, he has many published proceedings and publications in different journals. His research interests are: signal processing, speech processing, HMI and WSN.

PE and PP clay nanocomposite films – the comparison of the influence of a clay type and a compatibilizer concentration

D. Merinska, A. Tesarikova, M. Pospisil

Abstract— The influence of the clay type and a compatibilizer concentration on the PE and PP matrix was evaluated. Different types of clay nanofillers (Cloisite Na⁺, Cloisite 93 A and Cloisite 30B) were added into polyethylene (PE) and polypropylene (PP) matrix in various concentrations. The amount of clays was calculated as 5 wt% to the weight of PE/PP. The PE/PP and nanofillers were mixed on a one screw KO Kneader Buss with maleic-anhydride-modified matrices PEMA/PPMA as a compatibilizer. The content of compatibilizer in mixtures was 3, 5 and 7 wt % to the weight of matrix.

The level of MMT exfoliation in the nanocomposite systems was studied by XRD technique and TEM technique. The properties of samples were evaluated by the measurement of mechanical properties (yield stress and tensile strength). The permeability for O₂ and CO₂ was checked. The influence of different types of clays and compatibilizer concentrations on the properties of polyethylene/polypropylene nanocomposites is discussed.

Keywords— nanocomposite, polyethylene, polypropylene, montmorillonite, compatibilizer, barrier properties

I. INTRODUCTION

Polyolefin (PO), the group of PE, PP and the others polymer materials, is one of the most widely used group of polymers, especially in the package industry.

From this point of view PE or PP nanocomposites become a field of studies of the several research laboratories [1]- [5].

This work was supported in part by the project FR TI4/623 and in part by Operational Program Research and Development for Innovations co-funded by the European Regional Development Fund (ERDF) and national budget of Czech Republic, within the framework of project Centre of Polymer Systems (reg. number: CZ.1.05/2.1.00/03.0111). Some of here presented data were already published.

Dagmar Merinska is from Department of Polymer Engineering, Faculty of Technology, Tomas Bata University in Zlin, Nam. T. G. Masaryka 275, 762 72 Zlin, Czech Republic and ²Centre of Polymer Systems, University Institute, Tomas Bata University in Zlin, Nad Ovcirnou 3685, 760 01 Zlin , e-mail: merinska@ft.utb.cz.

Alice Tesarikova is from Department of Polymer Engineering, Faculty of Technology, Tomas Bata University in Zlin, Nam. T. G. Masaryka 275, 762 72 Zlin, Czech Republic (e-mail: atesarikova@ft.utb.cz).

Miroslav Pospisil is with Charles University Prague, Faculty of mathematic and physics, Prague, (e-mail: mpospisil@seznam.cz).

It is known that the nanocomposite preparation can involve two basic steps. The first one can be the modification of MMT by the organic compound, named organofilization. [6]- [7].

The reason of MMT modification with alkyl ammonium or alkylamine is to facilitate its affinity to a polymer, because the organic compound makes the hydrophilic MMT surface organophilic to form organophilic montmorillonite (OMT). At the same time, a wider interlayer allows the intercalation of the polymer into the silicate layers or even its exfoliation. The most suitable type of organic compound or the way of the organofilization can be also presumed by the using of the molecular modelling [8]. The value of calculated energies and d-spacing can help in the estimation of the treated MMT behaviour during the compounding of components.

In order to obtain a good interfacial adhesion of the hydrophilic clay to the hydrophobic polymer matrix it is necessary next to the MMT modification also to use for example maleic anhydride PP or PE as compatibilizer in a polymer matrix [9]- [10]. The problem lies in the change of the PE or PP structure, the arrangement of macromolecules goes down and this fact influences also the nanocomposite properties.

The process of the melt intercalation has been used for the preparation of thermoplastic nanocomposites based on polyolefin in several cases. Here it is the base thinks to choose the right way and compounding equipment [7].

In this work polyethylene and polypropylene have been used for the preparation of nanocomposites because of their considering like the packaging materials. As nanofillers commercial types and by own way prepared MMT were used in the 5 wt%. The influence of MMT treated by one or two different types of the organofilization on PE/PP nanocomposite properties was evaluated. Moreover, the influence of a compatibilizer concentration on the final properties of prepared films was observed.

II. EXPERIMENTAL

For the modification a Wyoming type of montmorillonite Cloisite Na⁺, 93A and 30B from Southern Clay Products, Inc. were used. For nanocomposite compounding experiments polyethylene Dowlex was used and the nanocomposite samples were prepared with maleic-anhydride-modified PE Amplify as a compatibilizer. In case of PP Mosten GB 003 produced by Chemopetrol Litvínov, Czech Republic was used as a polymer matrix, maleated polypropylene (PPMa)

EXXELOR PO 1015, contents of maleic groups 1 wt. % was used as a compatibilizer.

Nanocomposites with 5 % MMT and with 3,5 and 7 % of particular compatibilizer were compounded on *Buss KoKneader*, barrel diameter 30 mm, speed 50 rpm at the temperature of 180 °C. After pelletization the obtained strands pellets of mixtures were pressed into the plates for the measurement of mechanical properties. Mechanical properties were measured on the Alpha Technologies 2000 equipment.

Transmission electronic microscopy

For the purpose of TEM, ultra-thin cross-sections prepared on a special cutting device LEICA ULTRACUT UCT ultracyromicrotome at the temperature of -110°C were used. TEM was performed on a JEM 200CX (JEOL) device at 100 kV. The scans taken were digitised by means of a computer-controlled digital camera DXM1200 (Nikon).

Barrier properties

Molded blown films with the thickness about 50 µm were used for the measurement carried on the device for gas permeability with a pressure pickup LMP 150 (made in Tesla Rožnov, Czech republic), at the temperature 25°C and the hypertension 0,4 – 0,6 MPa. On this device oxygen and carbon dioxide permeability coefficient were carried out.

III. RESULTS AND DISCUSSION

TEM

Prepared samples with Cloisite Na⁺ and 30 B fulfilled our expectation that MMT without or with unsuitable modification is not able to show successful exfoliation of its particles in nonpolar PE or PP matrix. The picture a. shows the bad result where the MMT particles stayed in the bigger agglomerates not in the size of nanometers and the shape of particular leaves. This confirms the data of filler producer that these types are not for the polyolefin matrix. Presented pictures (Fig. 1. a-c) belong to the Cloisite 93A in PE matrix and show the good result going close to the MMT particles exfoliation in the line with the rising compatibilizer concentration. Particular leaves or platelets it is possible to see in the exfoliated form in the polymer matrix.

Mechanical properties

Tensile strength was one of the mechanical properties, which were measured. In the Figure 2 it is possible to see, that the improvement of this property was achieved again in the line with the PEMA or PPMa rising concentration, but the difference between 5 and 7 % is not so big, because the higher amount of the substance with the different structure disrupts the crystalline PE or PP arrangement and it causes the lowering of mechanical properties.

Barrier properties

Figures 3, 4 represent graphs showing permeability coefficient (OTR or generally GTR – gas transmission rate) for oxygen and carbon dioxide. Figure 3 belongs to the observation of oxygen permeability. Fig 4 is valid for CO₂. The values plotted here show the similar trend to the tensile strength observation. All measured samples for both evaluated films filled by Cloisite 93 A had lower OTR/GTR than nonfilled PE or PP matrix. But with the different PEMA or PPMa concentration it is possible to see that in the agreement with the disordering of the polymer crystalline structure the permeability for both gases more or less significantly goes up. It can be explicated by the shortening of the way and lowering the easiness which the gas is going through the polymer matrix

IV. CONCLUSION

The different types of MMT and their influence on PE/PP nanocomposite properties were evaluated. Moreover the effect of various compatibilizer concentrations was observed. Cloisite 93A reached the best result in case of MMT particles exfoliation. The differ in the compatibilizer concentration confirmed the support of higher concentration to the better exfoliation on the opposite hand the mechanical and barrier properties went down.

REFERENCES

- [1] Ren, Changyi; Jiang, Zhiyong; Du, Xiaohua; et al., Microstructure and Deformation Behavior of Polyethylene/Montmorillonite Nanocomposites with Strong Interfacial Interaction, J. of Physical Chemistry B, Vol.113, Issue: 43, pp: 14118-14127
- [2] Lomakin, S. M.; Dubnikova, I. L.; Shchegolikhin, A. N.; et al., Thermal degradation and combustion behavior of the polyethylene/clay nanocomposite prepared by melt intercalation, 31st International Conference on Vacuum Microbalance Techniques Location: Izmir Inst Technol, Izmir, Turkey, J. of Thermal Analysis and Calorimetry, Vol. 94, Issue: 3, pp. 719-726
- [3] Qin, HL; Zhao, CG; Zhang, SM; et al., Photo-oxidative degradation of polyethylene/montmorillonite nanocomposite, Polymer Degradation and Stability, Vol. 81, Issue: 3, pp. 497-500
- [4] Zehetmeyer, G.; Scheibel, J. M.; Soares, R. M. D.; et al., Morphological, optical, and barrier properties of PP/MMT nanocomposites, Polymer Bulletin, Vol. 70, Issue: 8, pp. 2181-2191
- [5] Furlan, L. G.; Ferreira, C. I.; Dal Castel, C.; et al., Effect of processing conditions on the mechanical and thermal

properties of high-impact polypropylene nanocomposites, *Mat. Sci. and Eng. A*, Vol. 528, Issue: 22-23, pp. 6715-6718

[6] Bala P., Samantaraya B.K., Srivastava S.K., Synthesis and characterization of Na-montmorillonite-alkylammonium intercalation compounds, *Mater Res. Bul.*, Vol. 35, Issue 10, pp.1717-24

[7] Merinska D., Malac Z, Pospíšil M , Chmielova M., Weiss Z.,Capkova P., Simonik J., Polymer/clay nanocomposites based on MMT/ODA intercalates, *Composite Interfaces*, Vol. 9, Issue 6, pp.529 – 540

[8] Pospíšil M., Merinska D., Malac Z, Capkova P., Simonik J., Structure analysis of montmorillonite intercalated with cetylpyridinium and cetyltrimethylammonium: Molecular simulations and XRD analysis, *J. Colloid and Interface Sci.*, Vol. 236, Issue 1, pp.127-131.

[9] Xu, Yuanyuan; Guo, Zhenghong; Fang, Zhengping; et al., Combination of Double-Modified Clay and Polypropylene-graft-Maleic Anhydride for the Simultaneously Improved Thermal and Mechanical Properties of Polypropylene, *J. of App. Pol. Sci.*, Vol. 128, Issue: 1, pp. 283-291

[10] Zhu, Shipeng; Chen, Jinyao; Li, Huilin; et al., Effect of polymer matrix/montmorillonite compatibility on morphology and melt rheology of polypropylene nanocomposites, *J. of App. Pol. Sci.*, Vol. 128, Issue: 6, pp. 3876-3884

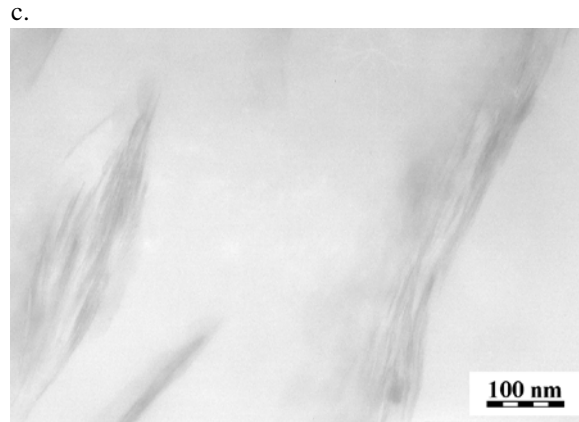
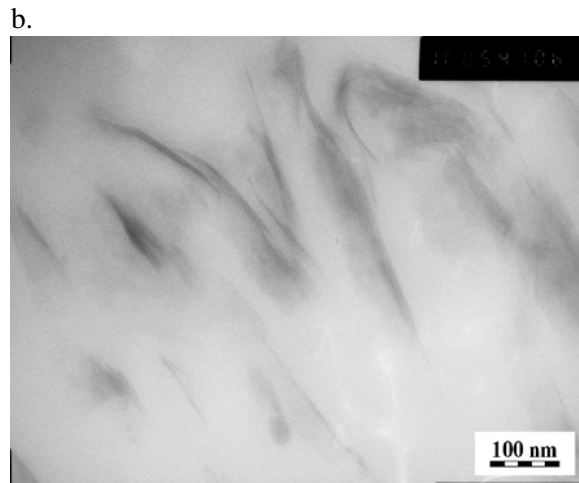
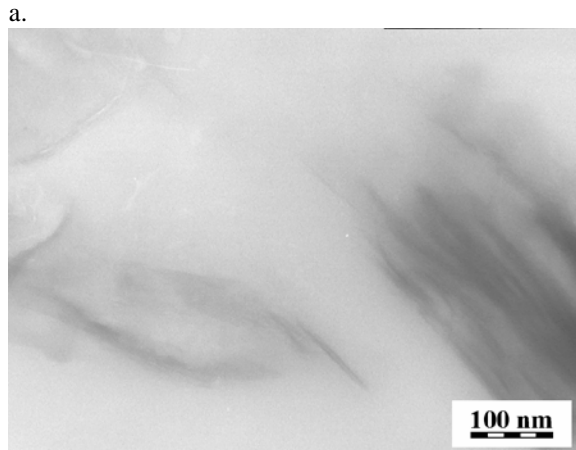


Fig 1 a-c TEM pictures of PE/Cloisite 93A nanofiller and with 3,5 and 7 % concentration of PEMA compatibilizer

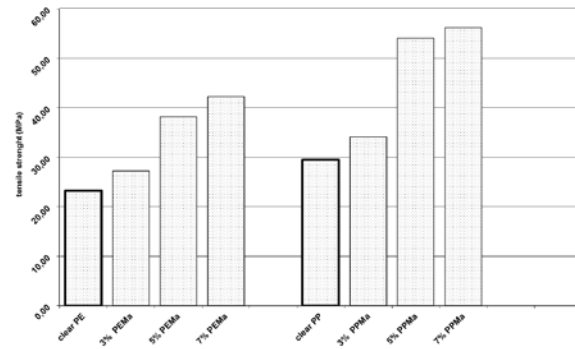


Fig 2 Tensile strength of prepared samples

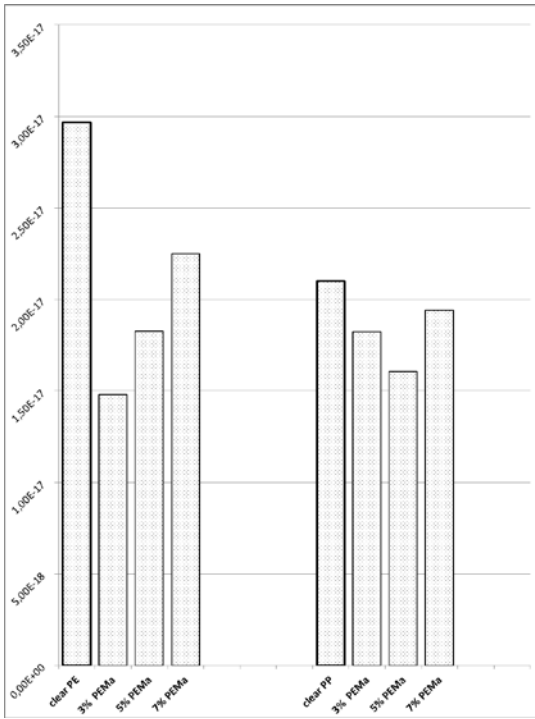


Fig 3 Permeability (OTR) for oxygen

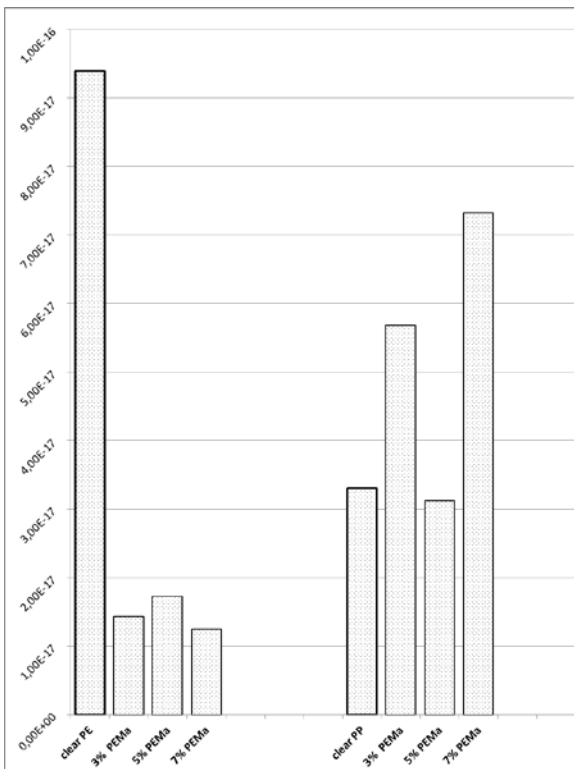


Fig 4 Permeability (GTR) for CO₂

Using the CONVAL® software for the petrochemical plant control valves checking.

Case study

C. Patrascioiu, G. Stamatescu, C. Lazar

Abstract — In the paper there are presented the researches into field of the CONVAL® software using to control valve checking. There are presented the main facilities of the CONVAL® software, including the description of the used functions. The CONVAL® software has been used to plant refinery control valves checking. The results have been validated 87 % of the investigated control valves.

Keywords — control, control valve, CONVAL software, refinery.

I. INTRODUCTION

The control valves are the most important control elements of the control systems. A detailed presentation is showed in specializes literature [1, 2]. A new component of the control valves is represented by the software for the control valve design.

The CONVAL® software, developed by the Ruhr University of Bochum, is used to simulate or design of the control valve [3]. The structure of this software contains the following elements [4]:

- a) A thermodynamic database;
- b) A mathematical model of the control valve;
- c) An industrial control valve database.

The CONVAL® software has been used to design the control valves in many industrial applications. For example, Siemers describes the priorities concerning of the control valves as follow: safety and reliability, control quality, environmental aspects, trouble-free life cycles and lowest cost [5]. The first element of the control valve design is the geometry of the plant s pipes. A good knowledge of a pipe pressure and drop pressure and in the same time the knowledge of the characteristics of the pumps is necessary.

C. Patrascioiu is with the Petroleum-Gas University of Ploiesti, Romania. He is now with the Automatics, Computers & Electronic Department. (e-mail: cpatrascioiu@upg-ploiesti.ro).

G.Stamatescu is with the Politehnica University of Bucharesti, Romania. He is now with the Automatics and Industrial Informatics Department. (e-mail: grigore.stamatescu@upb.ro).

C. Lazar was with FIWA Company, Sibiu, Romania. He is branch manager of the Romanian branch. (e-mail: office.ro@fiwagroup.com).

To obtaining the optimum control valve parameters, Siemers defines seven steps of the control valve design [6]. In this operation, the Conval® software is used to select the better control valve for the input conditions and with the graphical support to analyze the inherent and the work characteristics.

Another problem solved by the CONVAL® software is the estimation of the static controllability index, there is implemented in 8th version of the software.

The paper presents the author's researches in the field of the industrial control valves simulation. The control valves that have been investigated belong to the Romanian refinery plant. The investigation has been focused to verify the control valves in the new operating conditions.

II. THE CONVAL® SOFTWARE

In 1985, a team of experienced engineers from the fields of instrumentation and control, chemical processes and machine building, as well as various other branches of industry, joined forces with software development experts. At the end of a development phase lasting four years, they were able to present the first results - christened CONVAL® 1.0 - at INTERKAMA '89 [7].

The CONVAL® software is destined to design or checking the chemical plant elements, such as: pipes, heat exchangers, pumps, valves and control valves. Each component of the previous list may be activated using a specific command. To activate the control valves design / check, the user will activate the Control Valve command.

This program is based on:

- IEC 60534 2 1-3 standard to calculate liquid flow rate;
- VDMA 24422 standard to calculate the sound level;
- IEC 60534 8-3 and IEC 60534 8-4 standard to calculate the gas flow rate.

The main window of the Control Valve CONVAL® menu is presented in figure 1. The structure menu if the Control Valve window is follow:

- a) *Medium* – the menu used to data specification of the fluid that circulates into control valve;
- b) *Pipeline* – the menu associated to pipes data, upstream and downstream of the control valve;
- c) *Control valve* – the configuration menu of the design control valve parameters;

d) *Noise calculation* – the configuration menu of the fluid flow noise calculation.

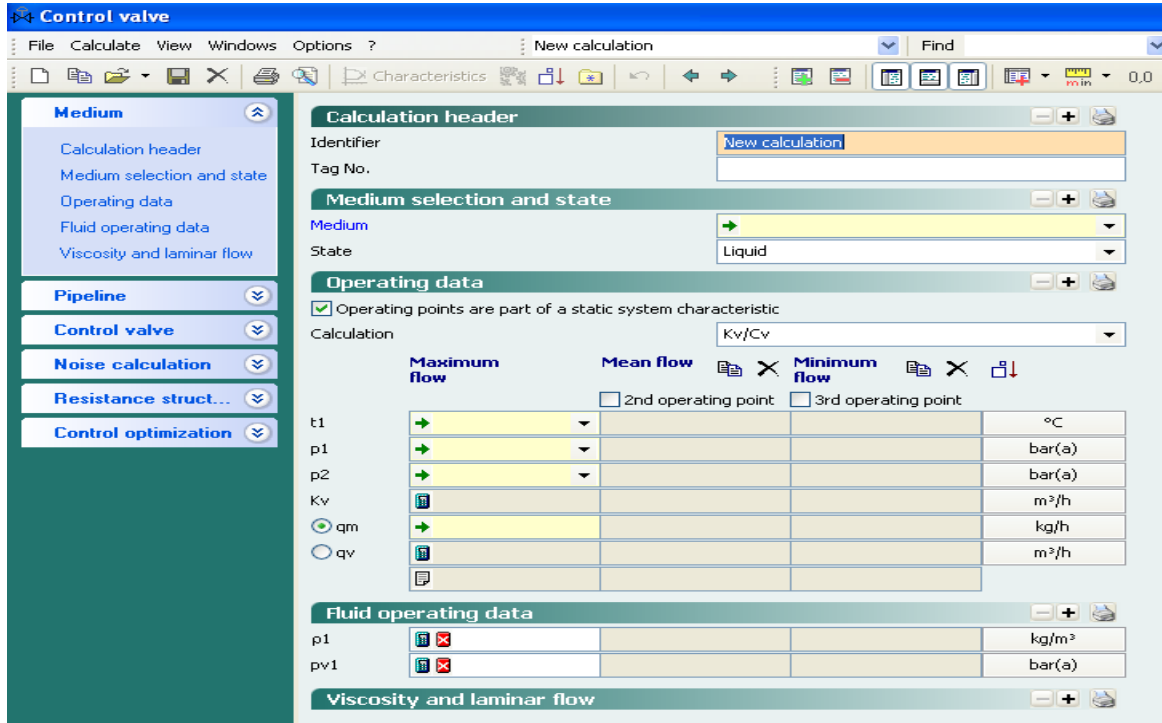


Fig 1 The *Control Valve CONVAL*® window.

All four Control Valve menus are the most used and for this reason there will be detailed in the next sections.

A. *The Medium menu*

In the Medium menu there are disposable five functions, as follow:

- 1) The *Calculation header* function has a obligatory character, there being destined to file specification (*Identifier*) and to name the control valve in the P&ID (*Tag No.*).
- 2) The *Medium Selection State* function specifies the fluid that circulates by the control valve. In this function exists the sub-function *Medium*, there is used to select the thermodynamic properties at thermodynamic data base. The *State* sub-function specifies the liquid or vapor fluid state.
- 3) In the *Operating data* function, the user must specify next information:
 - a) The calculated variable (*Calculation*), a variable selected from the list: demand flow module Kv/Cv ; mass flow rate q_m ; upstream pressure p_1 ; downstream pressure p_2 .
 - b) The operating point characteristics. These characteristics are dependent by the selected calculated variable. If the selected calculated is Kv/Cv , the operating point characteristics will be:
 - t_1 – the upstream temperature;
 - p_1 – the upstream pressure;
 - p_2 – the downstream pressure;
 - q_m or q_v – the mass or volume flow rate.

The user may define three operating points: first point is associated to minim flow rate, the second defines the nominal flow rate and the last point is represents the maximum flow rate.

- 4) *Fluid operating data* is the function used to calculate the fluid density (ρ_l) and the vapour pressure (p_{v1}), all properties being calculated in the upstream conditions. The calculus is made using the equilibrium equations and thermodynamic data of the CONVAL data base. If the user has better values, there may replace the calculated values.
- 5) The *Viscosity and laminar flow* function is used to determine the correction factor FR . This factor is calculated using the viscosity value and the Reynolds criterion. Viscosity is calculated with IEC 60534 standard. If the flow regime is turbulent, $Re > 100000$, the correction factor will be $FR = 1$.

B. *Pipeline menu*

The Pipeline menu contains the functions used to specify the pipes constructive characteristics. The functions are following:

- 1) The *Influence of fittings* function specifies the connection mode of the control valve to upstream and downstream pipe. The user may set the control valve nominal diameter with same pipe diameter. If this situation is not possible, the user must specify the following date:
 - a) *Flow coefficient of fittings*;

- b) *Piping geometric factor*, defined by the relation [6]

$$F_p = \left[1 + \frac{\sum K_i}{N_2} \left(\frac{C_v}{d^2} \right) \right]^{-0.5};$$

- c) *Valve modifier* for fittings.

- 2) The *Pipe downstream of valve* function is used to specify the pipe material and the pipe diameter. The CONVAL program has a data base which contains the pipe design information.

C. Control valve menu

The Control Valve menu is dedicated to select the calculated control valve from the produces data base. The Control valve menu has four functions, as follow:

- 1) The *Valve Selection* function is used to select:
 - a) *Valve manufacturer*;
 - b) *Series* of control valve;
 - c) *Valve selection*.
- 2) The *Valve data* function sets the user option of the next specifications:
 - a) *Size and pressure class*: Metric or ANSI.
 - b) *Valve type*, as follow: Globe valve, Rotary plug valve, Butterfly valve, Ball valve, Ball valve, Axial valve, Angle seat valve, Continuous globe valve, Diaphragm valve etc.
 - c) *Trim type*: Parabolic plug, V-port plug, Cage trim, Multihole plug and Seat-guided contoured plug.
 - d) *Flow direction* inside the control valve: FTO (fluid open), FTC (fluid close).
 - e) *Basic characteristic* of valve (intrinsic characteristic): Equal percentage, Linear, Modified and On/Off.

D. Noise Calculation menu

The Noise Calculation menu contains three functions for the control valve noise calculation. The functions implemented in this menu are:

- 1) *Noise prediction data* function is used to select:
 - a) *Calculation standard* – The standard used to calculate the noise generated by liquid flow: VDMA 24422(1979-05), IEC 60534-8-4(1994-05), IEC 60534-8-4(2005-08).
 - b) *Low noise design* is a special function used to select the control valve with the minimum sound level.
- 2) The *Minor noise prediction data* is a function which specifies the following data: Pressure ratio, Acoustical efficiency factor, Ring frequency, Peak

frequency, Sound velocity, Power loss, Mechanical stream power.

- 3) The *Spectrum* function is used to select the specifications of the spectral frequencies generated by the control valve.

III. PETROCHEMICAL CONTROL VALVES CHECKING

Technical sustainability check of a refinery plant consists in measurement systems checking, controller tuning and control valves checking. In this paper have been checked the control valves of a plant of catalytic reformer factory.

To check the control valves have been used the initial design data, an example being presented in table 1. These primary data contain:

- The name of the control valve system TAG;
- Information about the chemical composition of the stream;
- Specific gravity of the fluid;
- Temperature of the fluid;
- The input pressure of the valve;
- The output pressure of the valve;
- The flow rate of the stream;
- The type of the control valve.

There have been analyzed 38 control valves of the plant. In table 2 there is presented a partial list of the results obtained by using the CONVAL[®] software for the FV-001 control valve. The properties associated to the operating control valve are calculated for 25, 50, 75 and 100% of the stroke displacement. The relative stroke displacement s/s_{100} is identical with the test values. The flow module K_v has values between 11 and 237 m³/h, the higher value being higher than the maximal value of the input data (125 m³/h). In all situations (25, 50, 75 and 100% of stroke) the stream flow is non-critical. The fluid velocity increases up to 3.1 m/s, value that is acceptable for the higher flow rate that passes in the control valve. The noise of the control valve is 50 dB for the normal flow rate and the maximum noise value is 55 dB, value that is in admissible domain.

The CONVAL[®] software calculates the work characteristic of the control valve, figure 2. This characteristic is typical for the control valve characterized by *Equal percentage* inherent characteristic. The operating point of the control valve is a very good choice because the operating point is $s/s_{100}=0.76$, there represents that the operating point is into linear variation of the characteristic.

Table 1 Initial data about the control valves

Fluid	TAG	Stream		Specific gravity	T [°C]	P_1 [bar]	P_2 [bar]	Q ¹ [m ³ /h] ² [Nm ³ /h] ³ [kg/h]	Control valve type
Heptane	FV-001	Naphtha to V1	Normal	0.690	40	4.47	4.00	¹ 125	Fisher ET FTC
			Maxim	0.690	40	5.70	4.00	¹ 165	
Heptane	FV-002A	Naphtha to V1	Normal	0.690	40	9.80	4.00	¹ 20	Fisher ET FTC
			Maxim	0.690	40	9.80	4.00	¹ 45	
Octane	FV-005-1	Naphtha pass 1	Normal	0.690	38	69.01	4.00	¹ 20	Fisher ET FTC
			Maxim	0.690	38	69.01	4.00	¹ 40	
Octane	FV-005-2	Naphtha pass 2	Normal	0.690	38	69.01	4.00	¹ 20	Fisher ET FTC
			Maxim	0.690	38	69.01	4.00	¹ 40	
Octane	FV-005-3	Naphtha pass 3	Normal	0.690	38	69.01	4.00	¹ 20	Fisher ET FTC
			Maxim	0.690	38	69.01	4.00	¹ 40	
Octane	FV-005-4	Naphtha pass 4	Normal	0.690	38	69.01	4.00	¹ 20	Fisher ET FTC
			Maxim	0.690	38	69.01	4.00	¹ 40	
Methane	FV-006	Comb gas to H1	Normal	0.700	35	2.50	1.00	² 1540	Fisher EZ
			Maxim	0.700	35	3.00	1.00	² 2000	
Heptane	FV-006A	Naphtha from P1A	Normal	0.735	40	70.01	4.00	¹ 25	Fisher EZ
			Maxim	0.735	40	70.01	4.00	¹ 25	

Table 2 Selected results obtained with CONVAL[®] software

CONVAL[®] by F.I.R.S.T. Version 8.0 (Build 8.0.4)
Control valve: 001 1/29/2014 1:57:19 PM

Calculation header

Identifier

FV-001

Characteristics values table

Caption	Unit	25%	50%	75%	100%
s/s100	%	25.0	50.0	75.01	100.0
t1	°C	40.0	40.0	40.0	40.0
p1	bar(a)	4.47	4.47	4.47	4.47
p2	bar(a)	4.0	4.0	4.0	4.0
Kv	m ³ /h	11.02	39.06	119.4	237.0
qv	m ³ /h	9.247	32.78	100.2	198.9
qm	kg/h	6,1... 0	21,8... 0	66,8... 0	132,7... 0
Type of flow	-	Non-critical	Non-critical	Non-critical	Non-critical
va	-	1.0	1.0	1.0	1.0
pv1	bar(a)	0.1191	0.1191	0.1191	0.11...
ρ1	kg/m ³	667.4	667.4	667.4	667.4
LpAe	dB(A)	20.0	34.4	48.0	55.35
u1	m/s	0.1454	0.5152	1.574	3.126

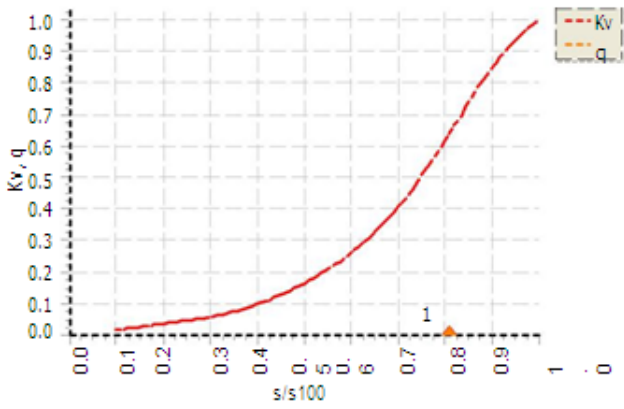


Fig 2 The flow characteristic of the FV-001 control valve.

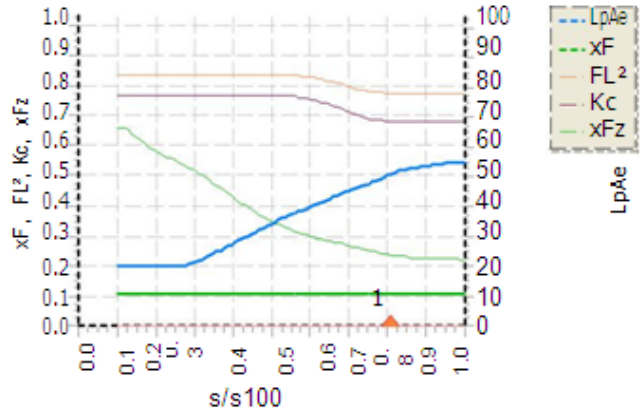


Fig 3 The characteristics of the associate parameters of the FV-001 control valve.

Figure 3 represents the following parameters:

- Sound pressure level $LpAe$;
- The recovery factor for valves installed without fittings attached, value can be found in the flow coefficient tables, xF [6];
- Rated liquid pressure recovery factor FL^2 , Kc , xFz .

Table 3 presents a comparison between the control valve specification and the simulation CONVAL results. The numerical results analysis has four components: the nominal flow Kvs , the valve open, the flow velocity and the sound pressure level.

Table 3 Example of the results obtained by using the CONVAL software

TAG	Specifications	The simulation CONVAL results				Observation
	Q ¹ [m ³ /h] ² [Nm ³ /h] ³ [kg/h]	Kvs Nominal flow [m ³ /h]	Valve Open [%]	Flow velocity [m/s]	Lp [dB(A)]	
FV-001	¹ 125	237.0	63.8	1.99	50.9	Acceptable
FV-002A	¹ 20	21.0	36.9	3.50	75.7	Acceptable
FV-005-1	¹ 20	21.0	24.9	2.81	54.7	Acceptable
FV-005-2	¹ 20	21.0	24.9	2.81	54.7	Acceptable
FV-005-3	¹ 20	21.0	60.3	2.81	54.7	Acceptable
FV-005-4	¹ 20	21.0	60.3	2.81	54.7	Acceptable
FV-006	² 1540	13.7	10.0	0.01	20.0	Acceptable
FV-006A	¹ 25	1.3	100.0	3.71	55.3	Non-acceptable

For example, at the input data presented in table 1 there have been validated 7 control valves. For these control valves, the nominal flow is greater than the input flow rate, the valve open is less than 60 %, the liquid flow velocity is less than 4 m/s and the sound pressure level is less than 75 dB(A).

The analyzed plant has are 38 control valve, each control valve being checked with CONVAL® software. For five of the analyzed control valves, the flow module value is less than the nominal flow rate value, there do not assure a gut function of the control valve.

IV. CONCLUSION

The paper presents the facilities of the CONVAL® software for the control valve checking. researches into field of the using to. The main facilities of the CONVAL® software are classified in Medium menu, Pipeline menu, Control valve menu and Noise calculation menu. The CONVAL® software has been used to check the plant refinery control valves. The results have been validated 87 % of the investigated control valves.

REFERENCES

- [1] Fliegen J., Grutesen L., *Industrial Process Control Valve*, Corporate Media GmbH, D-80992 Munich, Germany, 2007.
- [2] * * * *CONTROL VALVE HANDBOOK - Fourth Edition*, Fisher Controls International LLC 2005.
- [3] Siemers H., Control valve design aspects for critical applications in petrochemical plants – part I, *Valve World*, 2004.
- [4] Plant design and control valve selection under increasing cost and time pressure - Part I, *Valve World*, 2005.
- [5] Hinszen H., Controllability Index: the effective CONVAL 8.0 approaches to optimize your valve configuration, *Valve World*, 2009.
- [6] Siemers H., Control valve design aspects for critical applications in petrochemical plants – part II, *Valve World*, 2004.
- [7] http://www.firstgmbh.com/main.php?page=cv9_prod

Activation Energies for Initial and Intermediate Stage Sintering of Li_2TiO_3 Determined by a Two-Stage Master Sintering Curve Approach

Ahmad Reza Abbasian, Mohammad Reza Rahimipour, and Zohreh Hamnabard

Abstract— Lithium meta titanate (Li_2TiO_3) is considered as one of the most promising breeder materials for the fusion power. In this study, the activation energy and sintering kinetics of the Li_2TiO_3 is determined with the help of the master sintering curve (MSC). It was found that a better representation of the sintering behavior could be achieved by constructing MSC over two consecutive densification stages with the relative density of 66% set as the boundary. From the activation energy values of the two stages obtained, lattice diffusion enhanced with surface diffusion and solely lattice diffusion mechanisms were identified for the dominant sintering mechanism at initial and intermediate stages of the Li_2TiO_3 sintering, respectively.

Keywords— Fusion reactor, Li_2TiO_3 , Tritium breeding, Sintering, Activation energy.

I. INTRODUCTION

The breeding blanket is a key component of the fusion reactor because it directly involves tritium breeding and energy extraction, both of which are critical to the development of fusion power [1]. In the development of tritium breeding blankets, the lithium meta titanate (Li_2TiO_3) ceramic has interested multitude researchers' attention for its distinguished properties as one of the most promising solid breeder materials, such as reasonable lithium atom density, low activation characteristic, high chemical stability, good compatibility with structural materials, acceptable mechanical strength and considerably good tritium release characteristics at low temperatures [2]-[3]-[4]-[5]. Several methods are available for fabrication of a breeder ceramic material [6]. However, sintering is always the final and critical step for the fabrication of the ceramics, in which a preformed particulate body achieves its final shape and properties. In the conventional sintering procedure, the parameters such as time and temperature of the sintering are arbitrarily decided on the 'trial and error' basis. It could be beneficial for the nuclear

industry to predict the densification behavior from the sintering data that are readily available [7]. The ability to predict sintering behavior has been one of the long term objectives of sintering studies for many decades. Manifold attempts at simulation and modeling for the prediction of sintering have been reviewed in published literatures by previous authors [8]. One of the promising methods how to describe and predict sintering is the concept of a Master Sintering Curve (MSC) developed by Su and Johnson [9]. The MSC can be used to predict the densification behavior of a given powder and estimates its minimum sintering activation energy, as well as the understanding of sintering kinetics. The MSC has been successfully applied to several sintering systems such as ThO_2 [7], $\text{BaTi}_{0.975}\text{Sn}_{0.025}\text{O}_3/\text{BaTi}_{0.85}\text{Sn}_{0.15}\text{O}_3$ [10], ZnO [9]-[11], Gd-doped CeO_2 [12], TiO_2 [13], Al_2O_3 [9]-[14]-[15], BaTiO_3 [16], 3Y-TZP [17], $\text{Al}_2\text{O}_3 + 5\% \text{ZrO}_2$ [9], nickel and stainless steel powders [18]. However, the application of MSC to sintering of the Li_2TiO_3 has not been reported. The present work, therefore, aims to establish MSC for the Li_2TiO_3 based on non-isothermal sintering and systematically analysis of the sintering of the Li_2TiO_3 ceramic.

II. THEORY

Formulation of MSC was derived from the combined stage sintering model [9]-[19] including volume or grain boundary diffusion mechanism. For the construction of MSC the parameters of sintering are separated in those related to time and temperature dependence and the ones associated with the microstructure. In MSC theory, $\Phi(\rho)$, a function of density, can be given as the function of temperature and time:

$$\Phi(\rho) = \Theta(t, T(t)) \equiv \int_0^t \frac{1}{T} \exp\left(-\frac{Q}{RT}\right) dt \quad (1)$$

Where Q is the apparent activation energy for sintering, R is the gas constant, T is the absolute temperature, and t is the time. In this case, if the sintering process is dominated by only unique diffusion mechanism (either volume or grain boundary diffusion) and the microstructure is a function only of density, a unique MSC can be obtained. The relationship between density (ρ) and $\log[\Theta(t, T(t))]$, i.e. an S-shape curve, is the master sintering curve. For more details, the assumptions and limitations of the MSC have been well discussed in the original MSC papers by Su and Johnson [9]. For the

This work was supported by the NSTRI, and the Materials and Energy Research Center (no. 389052).

A. R. Abbasian is with Ceramic Department, Materials and Energy Research Center, Karaj, 31787-316, Iran (corresponding author to provide phone: 98-263 628 0040; e-mail: abbasian@merc.ac.ir).

M. R. Rahimipour is with Ceramic Department, Materials and Energy Research Center, Karaj, 31787-316, Iran (e-mail: m-rahimi@merc.ac.ir).

Z. Hamnabard is with the Lasers and Optics Research School, NSTRI, Tehran, 11365-8486, Iran (e-mail: zhamnabard@nrcam.org).

construction of MSC, the integral of Eq. (1) and the experimental density should be known. The dilatometry can be conveniently used to determine the density since the instantaneous density at all times can be obtained from the dilatometry data [20]. For the calculation of Θ , the activation energy for the sintering process must be known. If the activation energy is unknown, it can be estimated with good precision from Θ versus density (ρ) data [9].

III. EXPERIMENTAL

A. Fabrication of Green Pellet

A Li_2TiO_3 powder (~ 325 mesh, 40 0939, Sigma-Aldrich, Germany) was used in this investigation. Images of scanning electron microscopy (SEM) (Philips XL-30, Netherland) of the powder at two different magnifications are shown in Fig. 1. Fig. 1 (a) exhibits the particle shape is polygonal and Fig. 1 (b) indicates severe agglomeration with different sizes occurred between the particles. Fig. 2 shows the hard agglomerate size distribution of the powder was determined with a laser particle size analyzer (Fritch, Analysette 22, Germany). The mean hard agglomerate size of the powder was determined at approximately $23 \mu\text{m}$.

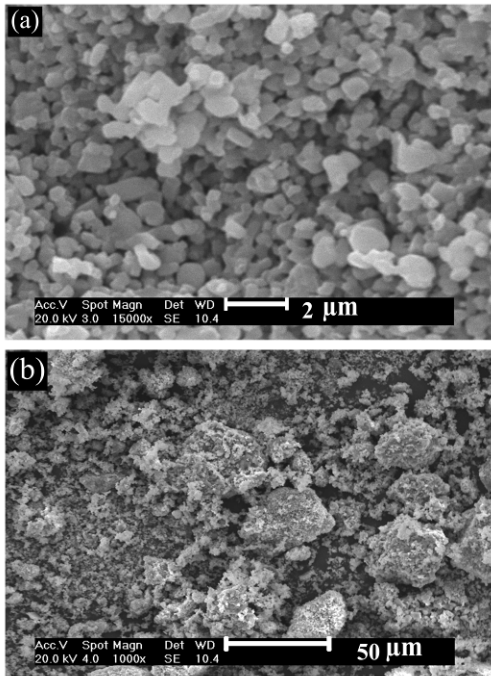


Fig. 1 (a and b) SEM analysis of Li_2TiO_3 powder at two different magnifications.

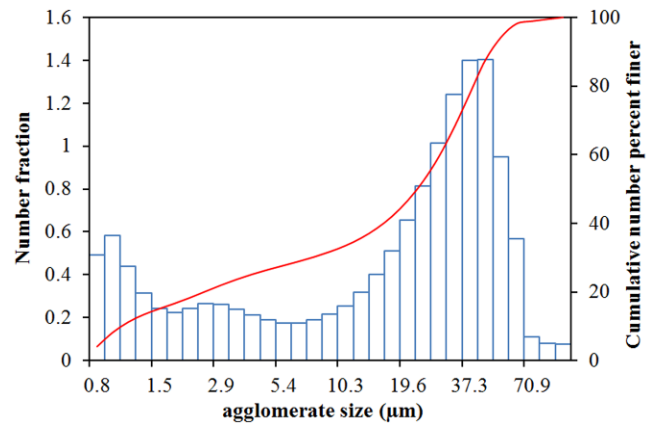


Fig. 2 The hard agglomerate size distribution of the Li_2TiO_3 powder.

B. Sample preparation

The as-received powder was pressed on a hydraulic press under pressure of about $300 \pm 3 \text{ MPa}$ at room temperature using stainless steel die to create bars of $\sim 5 \times 5 \times 50 \text{ mm}^3$. Before proceeding to sintering, to ensure the absence of any moisture, the compact powder was dried. The green density was measured by the geometric method. The green density of Li_2TiO_3 powder compacts was $2.15 \pm 0.03 \text{ g/cm}^3$. The value of 3.43 g/cm^3 was used as the theoretical density.

C. Shrinkage Measurements

An optical non-contact dilatometer (Misura ODLT, Expert System, ITALY) was used for monitoring the in situ dimensional changes of the powder compact during sintering in air at different heating rates. Two beams of light illuminate both the ends of a specimen 50 mm long placed horizontally into the furnace and two digital cameras capture the images of the last few hundreds microns of each tip. The specimen, completely free to expand or contract, is measured by the image that it projects on a Charge-Coupled Device (CCD). This instrument consists of a kiln equipped with an automatic temperature controller, which can reach a heating rate of 30 K per minute. The temperature increases from room temperature (RT) to 1200°C at the preset heating rate with no holding time. As a final result, the dimensional changes (expansion or shrinkage with respect to the initial size) of a material are plotted in percentage on a graph as a function of the temperature. Assuming isotropy in densification of all the specimens, the relative density of the sintered specimen (ρ_s) was calculated using the following equation [21]:

$$\rho_s = \left[\frac{1}{1 - dL/L_0 + \alpha(T - T_0)} \right]^3 \rho_g \quad (2)$$

Where dL/L is instantaneous linear shrinkage obtained by the dilatometer test, L_0 is the initial length of the specimen, T is the measured temperature, T_0 is the room temperature ρ_g is the green density, and α is the coefficient of thermal

expansion.

An average value α as a function of temperature, T , by the following estimation equations was determined from the cooling steps of the dilatometer runs performed with the different heating rate adopted during our investigations.

$$\alpha(K^{-1}) = 1.4635 \times 10^{-5} + 9.5499 \times 10^{-9} T - 4.3946 \times 10^{-12} T^2 \quad (25 < T < 1360) \quad (4)$$

$$\alpha(K^{-1}) = 1.9820 \times 10^{-5} \quad (T \geq 1360K) \quad (5)$$

The final densities after the dilatometer experiments as calculated in this way were in admissible agreement with those measured by the Archimedes technique.

IV. RESULTS AND DISCUSSION

A. Dilatometry

Based on a theoretical density 3.43 g/cm^3 for the Li_2TiO_3 , the average green density of the Li_2TiO_3 powder compacts was determined to be 62.78% theoretical density after pressing. The original shrinkage–temperature relation has been converted into the relative density dependence on temperature using Eq. (2). The final densities after the dilatometer experiments as calculated in this way were in admissible agreement with those measured by the Archimedes technique. Fig. 3 shows the dependence of density and densification rate on temperature of the Li_2TiO_3 at five different heating rates of 2, 3.5, 10, 20 and 30 K min^{-1} . It can be observed that the density–temperature curves displayed the classical sigmoidal shape and generally shifted to higher temperatures with increasing heating rate. It can be noted that the achieved sintered densities at any temperature showed a modest but systematic dependence on the heating rate. At some temperature, the density starts to increase slowly, then enters a second region where the density increases markedly, and after reaching value of 70-74% of the theoretical value, a third region is reached where the increase in density is slows and finally stops. The maximum density was found to depend upon the heating rate, the higher the heating rate the lower the sintered density. This behavior has also have reported for zirconia [22], alumina [15], cerium oxide [23], and magnesium aluminate spinel [24] systems. It is well documented that, at a lower heating rate, the compact is exposed to sintering for a longer time during heating period; hence, the amount of relative density is higher. This is ascribed to a prolonged time scale for mass transport and diffusion when a slower heating rate is used to reach the same temperature. It can be seen from Fig. 3 that with increase in heating rate, the height of the peaks increased and curves shifted to a higher temperature. Wang and Raj [25] demonstrated that a higher peak temperature and a greater height of the peak imply a larger activation energy. Therefore, position and height of the peak in densification rate ($\frac{d\rho}{dT}$) give an immediate indication of the activation energy.

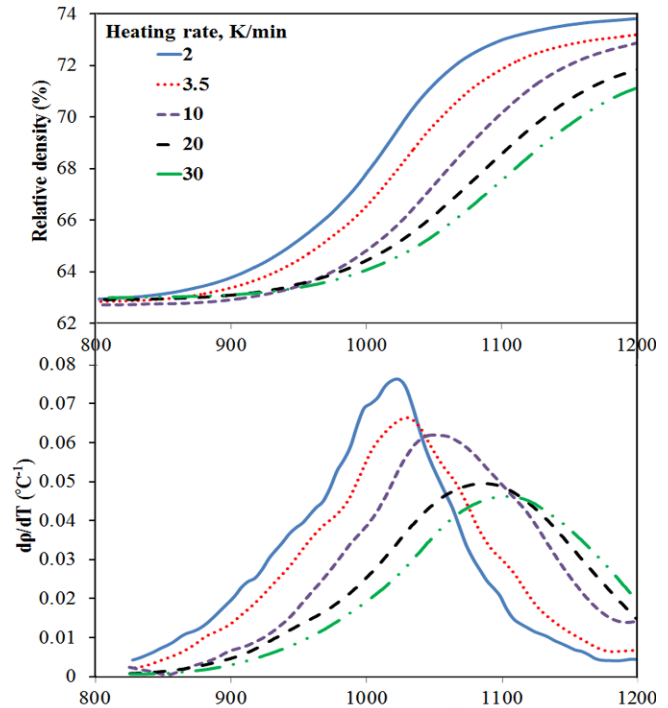


Fig. 3 Density evolution and densification rate as function of temperature at different heating rates.

B. Construction of MSC

As mentioned earlier, one of the essential data for obtaining the master sintering curve is the activation energy. The standard statistical approach to evaluating the scatter of experimental data is the minimization of mean residual squares (MRS). This criterion was used in many recent papers [9]-[14]-[17]-[26] to determine the sintering activation energy and construction of MSC and is described, for example, in [26] by the following formula:

$$MRS = \sqrt{\frac{1}{\rho_f - \rho_g} \int_{\rho_g}^{\rho_f} \frac{\sum_{i=1}^N ((\Theta_i / \Theta_{ave}) - 1)^2}{N} d\rho} \quad (5)$$

Where Θ_{avg} is the average of all Θ_i at a given density, N is the number of heating profiles used, and ρ_g or ρ_f are green or final densities of the sample.

Unfortunately, the calculation for minimization of MRS needs repeated numerical calculations which are user-unfriendly (complicated and time-consuming). Therefore, in this work we used simple software developed by Pouchly and Maca [27]. This newly developed software calculates the MSC and finds the optimal activation energy of a given material.

Following the above discussion, the MSC was calculated for the Li_2TiO_3 samples with using five different heating rates. A relative density range of 62%–70% was used to construct the MSC. This selected range of the relative density contributes to initial and intermediate stage of sintering. Fig. 4 shows the resulting master sintering curve for the Li_2TiO_3 powder compact. The inset shows the dependence of MRS on the activation energy. The minimum of the MRS, which is 0.3169, has been found for $Q=360 \text{ kJ/mol}$. However, it is difficult to establish a good fitting. The unsatisfactory construction of

MSC most likely revealed that different probable mechanisms dominate sintering over the entire relative density range studied.

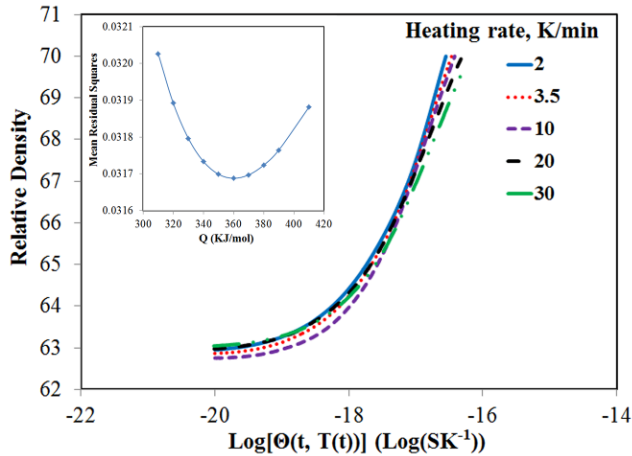


Fig. 4 The constructed MSC for sintering of Li_2TiO_3 powder using an activation energy of $Q = 360$ KJ/mol for the whole stage; inset figure shows the mean residual square as a function of an activation energy.

As suggested, a precise MSC can be constructed over several consecutive stages, based on either temperature [28] or density range [22]-[29]. Song and co-workers constructed MSC over two consecutive densification stage [30]. In the current study, we have divided sintering (in the range of 62%–70% relative density) into the initial and intermediate stages, with about 66% relative density as the boundary. Superior respective MSCs for the two stages are constructed separately and are shown in Figs. 5 and 6. For the initial stage, an activation energy value of $Q = 380$ kJ/mol was obtained via the best fitted ρ - $\log[\Theta(t, T(t))]$, curve. In the intermediate stage, the minimum was given at $Q = 320$ kJ/mol. The MRS yielded from the sigmoidal fitting are 0.3166 and 0.3171, respectively. Obviously, the constructed MSC based on two consecutive stages provide a better representation of the sintering behavior than using a single Q value alone for the whole sintering process chosen.

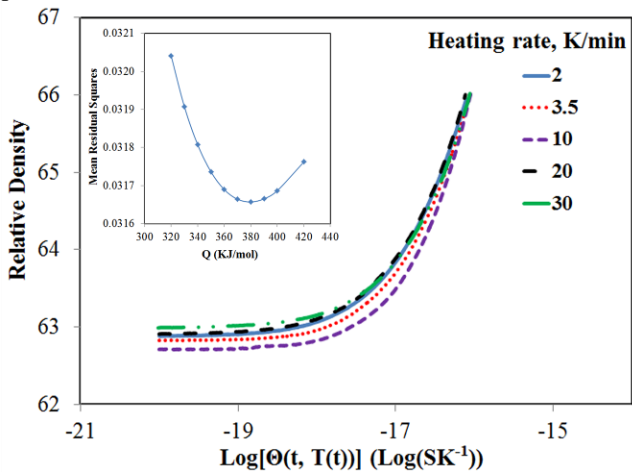


Fig. 5 The constructed MSC for sintering of Li_2TiO_3 powder during initial stage (62%–66% of the theoretical density); the minimum of mean residual square is given at energy of $Q = 380$ KJ/mol.

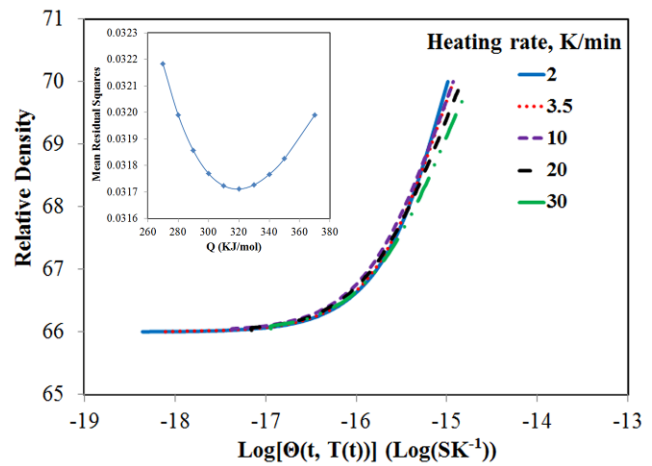


Fig. 6 The constructed MSC for sintering of Li_2TiO_3 powder during intermediate stage (66%–70% of the theoretical density); the minimum of mean residual square is given at energy of $Q = 320$ KJ/mol.

During the initial stage of sintering, the activation energy value of Li_2TiO_3 is determined to be 380 kJ/mol, which is in good agreement with value of $Q = 377 \pm 10$ kJ/mol that calculated by present authors at previous paper [31]. Wang and Raj [25]-[32] have derived the sintering-rate equation of Eq. (6) used for estimation of the activation energy at intermediate sintering stage by constant rates of heating techniques, noting that the sintering-rate equation in general can be separated into temperature-dependent, grain-size-dependent, and density-dependent quantities:

$$\ln\left(T \frac{dT}{dt} \frac{d\rho}{dT}\right) = -\frac{Q}{RT} + \ln[f(\rho)] + \ln A - n \ln dG \quad (6)$$

Here, Q is activation energy, T is the absolute temperature, t is the time, R is the gas constant, $f(\rho)$ is a function of density, G is the grain size (i.e., diameter), n is the grain size power-law exponent (i.e, $n = 4$ for grain boundary diffusion, $n = 3$ for lattice diffusion), and A is a material parameter (i.e., a constant) that is insensitive to G , T , and ρ . Using shrinkage data measured at different heating rates, the Q value can be determined from the slope of the Arrhenius-type plot of $\ln\left(T \frac{dT}{dt} \frac{d\rho}{dT}\right)$ versus $\frac{1}{T}$ at the same density, under a constant grain size. The Q value determined corresponds to an activation energy either for grain boundary diffusion or for lattice diffusion, because it is very difficult to determine the diffusion mechanism experimentally from Eq. (6). According above discussion, the activation energy for densification in the Li_2TiO_3 was determined from the slope an Arrhenius plot of the sintering data over a density range of 66%–70% relative density that related to intermediate sintering stage (Fig. 7).

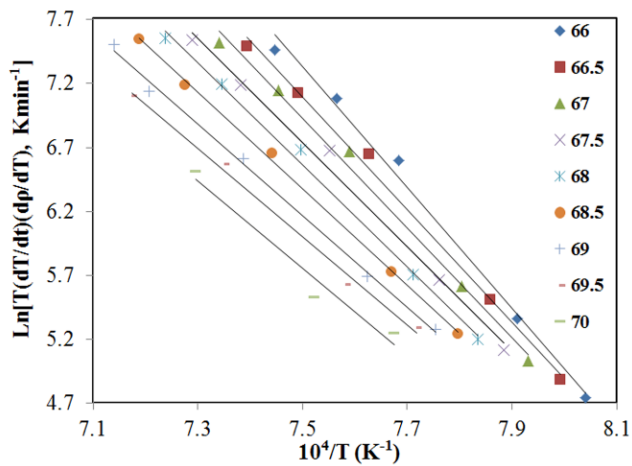


Fig. 7 Determination of the activation energy for densification via the constant rate of heating method.

The average activation energy for densification over the entire density range studied was then calculated from the activation energies determined at each density. An average activation energy for densification of $Q=330$ kJ/mol was determined, and the standard deviation in Q over the density range examined was 12 kJ/mol. The good linear fit to the data for each specific density in Fig. 10 establishes reasonably good confidence that a representative value of Q can be calculated for the Li_2TiO_3 from the Arrhenius plots. Additionally, the average activation energy of $Q=330\pm 12$ kJ/mol determined in this study is consistent with the activation energy of 320 kJ/mol determined using the two stage MSC theory for intermediate stage of sintering. The consistency of slope with density in Fig. 10, along with the relatively small standard deviation in Q with density, indicate that a single value of Q , and a correspondingly single dominant mechanism (i.e., grain boundary diffusion or lattice diffusion), controls densification in the Li_2TiO_3 from 66% to 70% theoretical density. Prevalently, sintering mechanisms of ceramic materials are a diffusion-controlled process and the diffusion of the slowest moving atoms/ions along the fastest diffusion path determines the rate of sintering. The activation energy for densification is a characteristic parameter reflecting the dependence of densification kinetics on temperature, and it is commonly used to identify the fundamental mass transport mechanism during the sintering process. In a practical case, several mechanisms (volume diffusion, grain-boundary diffusion, etc.) often operate simultaneously during solid-stage sintering. Therefore, the resultant activation energy may not be contributed from one specific sintering mechanism. It is most likely a weighted value contributed by multiple sintering mechanisms. In the present work, a single mechanism dominating the whole densification process was initially assumed by using constant activation energy to construct the MSC. However, a good fitting was not able to be achieved. It is probably that the MSC approach could not represent sufficiently the sintering behavior at the lower density range. One major complication arises from surface diffusion, which usually occurs in fine

powders at lower temperatures. As explained above, while the roles of the diffusion mechanism changes, the effectiveness of MSC based on constant activation energy will be impaired. Therefore, the densification process was divided into two consecutive stages according to the extent of densification, the MSCs of which were generated separately. The boundary between the first and second stage was assigned to be 66% of the theoretical density. Although somewhat arbitrary, it did reflect different temperature sensitivity for solid-state sintering during the low and intermediate density range. The two-stage MSC approach has been proved to provide a better representation of the sintering behavior (Figs. 5 and 6), and the activation energy is obtained via the best fitted MSC.

During the first stage of sintering, the activation energy of Li_2TiO_3 is determined to be 380 kJ/mol, which is in good agreement with that calculated by present authors [31]. On the other hand, present authors attributed the dominant sintering mechanism of the Li_2TiO_3 to lattice diffusion that may be enhanced with surface diffusion mechanism [31]. It has revealed that for the Li_2TiO_3 sample used, there is a little difference in the activation energy between the first and second stage of sintering. A little decrease (60 kJ/mol) of the activation energy indicates that no change in the dominant sintering mechanism has occurred. It has been pointed out that surface diffusion usually increases the apparent activation energy for densification, yet does not facilitate densification [18]. Surface diffusion may have contributed to the higher apparent activation energy. During the second stage, the value of activation energy obtained is comparable to value reported for volume diffusion [31]. Therefore, the dominant sintering mechanism is most appropriately assigned to lattice diffusion.

V. CONCLUSIONS

The activation energy of the Li_2TiO_3 was determined with the help of MSC. A better representation of the sintering behavior was obtained by applying the two-stage MSC approach.

REFERENCES

- [1] C.E. Johnson, "Ceramic breeder materials," *Ceramics International*, 17 (1991) 253-258.
- [2] J.P. Kopasz, J.M. Miller, C.E. Johnson, "Tritium release from lithium titanate, a low-activation tritium breeding material," *Journal of Nuclear Materials*, 212-215 (1994) 927-931.
- [3] J.M. Miller, H.B. Hamilton, J.D. Sullivan, "Testing of lithium titanate as an alternate blanket material," *Journal of Nuclear Materials*, 212-215 (1994) 877-880.
- [4] H. Kleykamp, "Chemical reactivity of SiC fibre-reinforced SiC with beryllium and lithium ceramic breeder materials," *Journal of Nuclear Materials*, 283-287 (2000) 1385-1389.
- [5] C. Alvani, S. Casadio, V. Contini, A. Di Bartolomeo, J.D. Lulewicz, N. Roux, " Li_2TiO_3 pebbles reprocessing, recovery of ^6Li as Li_2CO_3 ," *Journal of Nuclear Materials*, 307-311 (2002) 837-841.
- [6] X. Wu, Z. Wen, X. Xu, J. Han, B. Lin, "Fabrication and improvement of the density of Li_2TiO_3 pebbles by the optimization of a sol-gel method," *Journal of Nuclear Materials*, 393 (2009) 186-191.
- [7] T.R.G. Kutty, K.B. Khan, P.V. Hegde, J. Banerjee, A.K. Sengupta, S. Majumdar, H.S. Kamath, "Development of a master sintering curve for ThO_2 ," *Journal of Nuclear Materials*, 327 (2004) 211-219.

- [8] M.W. Reiterer, K.G. Ewsuk, "An Analysis of Four Different Approaches to Predict and Control Sintering," *Journal of the American Ceramic Society*, 92 (2009) 1419-1427.
- [9] H. Su, D.L. Johnson, "Master Sintering Curve: A Practical Approach to Sintering," *Journal of the American Ceramic Society*, 79 (1996) 3211-3217.
- [10] S. Marković, D. Uskoković, "The master sintering curves for $\text{BaTi}_{0.975}\text{Sn}_{0.025}\text{O}_3/\text{BaTi}_{0.85}\text{Sn}_{0.15}\text{O}_3$ functionally graded materials," *Journal of the European Ceramic Society*, 29 (2009) 2309-2316.
- [11] K.G. Ewsuk, D.T. Ellerby, C.B. DiAntonio, "Analysis of Nanocrystalline and Microcrystalline ZnO Sintering Using Master Sintering Curves," *Journal of the American Ceramic Society*, 89 (2006) 2003-2009.
- [12] D.Z. Florio, V. Esposito, E. Traversa, R. Muccillo, F.C. Fonseca, "Master sintering curve for Gd-doped CeO_2 solid electrolytes," *Journal of Thermal Analysis and Calorimetry*, 97 (2009) 143-147.
- [13] D. Li, S. Chen, W. Shao, X. Ge, Y. Zhang, S. Zhang, "Densification evolution of TiO_2 ceramics during sintering based on the master sintering curve theory," *Materials Letters*, 62 (2008) 849-851.
- [14] W.Q. Shao, S.O. Chen, D.Li, H.S.Cao, Y.C.Zhang, S.S. Zhang, "Prediction of Densification and Microstructure Evolution for $\alpha\text{-Al}_2\text{O}_3$ During Pressureless Sintering at Low Heating Rates Based on the Master Sintering Curve Theory," *Science of Sintering*, 40 (2008) 251-261.
- [15] [15] M. Aminzare, F. Golestani-fard, O. Guillon, M. Mazaheri, H.R. Rezaie, "Sintering behavior of an ultrafine alumina powder shaped by pressure filtration and dry pressing," *Materials Science and Engineering: A*, 527 (2010) 3807-3812.
- [16] [16] M.V. Nikolić, V.P. Pavlović, V.B. Pavlović, N. Labus, B. Stojanović, "Application of the Master Sintering Curve Theory to Non-Isothermal Sintering of BaTiO_3 Ceramics " *Materials Science Forum* 494 (2005) 417-422.
- [17] [17] M. Mazaheri, A. Simchi, M. Dourandish, F. Golestani-Fard, "Master sintering curves of a nanoscale 3Y-TZP powder compacts," *Ceramics International*, 35 (2009) 547-554.
- [18] [18] G. Sethi, S.J. Park, J.L. Johnson, R.M. German, "Linking homogenization and densification in W-Ni-Cu alloys through master sintering curve (MSC) concepts," *International Journal of Refractory Metals and Hard Materials*, 27 (2009) 688-695.
- [19] [19] J.D. Hansen, R.P. Rusin, M.-H. Teng, D.L. Johnson, "Combined-Stage Sintering Model," *Journal of the American Ceramic Society*, 75 (1992) 1129-1135.
- [20] [20] T.R.G. Kutty, P.V. Hegde, K.B. Khan, U. Basak, S.N. Pillai, A.K. Sengupta, G.C. Jain, S. Majumdar, H.S. Kamath, D.S.C. Purushotham, "Densification behaviour of UO_2 in six different atmospheres," *Journal of Nuclear Materials*, 305 (2002) 159-168.
- [21] [21] S. Ran, L. Winnubst, W. Wiratha, D.H.A. Blank, "Sintering Behavior of 0.8 mol%-CuO-Doped 3Y-TZP Ceramics," *Journal of the American Ceramic Society*, 89 (2006) 151-155.
- [22] [22] G. Bernard-Granger, C. Guizard, "Apparent Activation Energy for the Densification of a Commercially Available Granulated Zirconia Powder," *Journal of the American Ceramic Society*, 90 (2007) 1246-1250.
- [23] [23] Y. Kinemuchi, K. Watari, "Dilatometer analysis of sintering behavior of nano- CeO_2 particles," *Journal of the European Ceramic Society*, 28 (2008) 2019-2024.
- [24] [24] K. Rozenburg, I.E. Reimanis, H.-J. Kleebe, R.L. Cook, "Sintering Kinetics of a MgAl_2O_4 Spinel Doped with LiF," *Journal of the American Ceramic Society*, 91 (2008) 444-450.
- [25] J. Wang, R. Raj, "Estimate of the Activation Energies for Boundary Diffusion from Rate-Controlled Sintering of Pure Alumina, and Alumina Doped with Zirconia or Titania," *Journal of the American Ceramic Society*, 73 (1990) 1172-1175.
- [26] S.J. Park, R.M. German, "Master curves based on time integration of thermal work in particulate materials," *International Journal of Materials and Structural Integrity*, 1 (2007) 128-147.
- [27] V. Pouchly, K. Maca, "Master Sintering Curve – A Practical Approach to its Construction," *Science of Sintering*, 42 (2010) 25-32.
- [28] S. Kiani, J. Pan, J.A. Yeomans, "A New Scheme of Finding the Master Sintering Curve," *Journal of the American Ceramic Society*, 89 (2006) 3393-3396.
- [29] D.C. Blaine, S.-J. Park, R.M. German, "Linearization of Master Sintering Curve," *Journal of the American Ceramic Society*, 92 (2009) 1403-1409.
- [30] X. Song, J. Lu, T. Zhang, J. Ma, "Two-Stage Master Sintering Curve Approach to Sintering Kinetics of Undoped and Al_2O_3 -Doped 8 Mol% Yttria-Stabilized Cubic Zirconia," *Journal of the American Ceramic Society*, 94 (2011) 1053-1059.
- [31] A. R. Abbasian, M. R. Rahimipour, Z. Hamnabard, "Initial Sintering Kinetics of Lithium Meta Titanate at Constant Rates of Heating," *Iranian Journal of Materials Science & Engineering*, 10 (2013) 44-53.
- [32] J. Wang, R. Raj, "Activation Energy for the Sintering of Two-Phase Alumina/Zirconia Ceramics," *Journal of the American Ceramic Society*, 74 (1991) 1959-1963.

Numerical prediction of the fracture performance of wires for civil engineering applications with longitudinal crack-like laminations at varying locations

Kazeem K. Adewole, and Nikos E. Mastorakis

Abstract—The threat to the structural integrity of wires used for civil engineering applications by laminations and consequently the threat to the structural integrity of wire-reinforced structures cannot be overemphasized considering the fact that the presence of laminations in pre-stressing wires has been identified as the cause of the catastrophic failure of pre-stressed concrete pipes. In this paper, the effects of the locations of laminations on the fracture performance of wires for civil engineering applications are investigated using finite element (FE) analysis. FE analysis revealed that with the exception of the wires with mid-width lamination which is located at the middle of the wires' width, fracture initiation occurs in two locations at different displacements in wires with laminations located at any other distance below the wires' surface. FE analysis also revealed that the reduction in the displacement at fracture of the wires depends on the location of the laminations. The reduction in displacement at fracture of the wire is directly proportional to the distance of the lamination from the wires' surface, with the wire having laminations located 1mm and 6mm below the wires' top surface having the least and the largest displacements at first fracture initiation respectively. Laminations located between 1mm and 6mm (mid-width of the wire) below the wires' surface cause 10 to 33% reductions in the displacement at first fracture of the wires. Consequently, the closer to the surface of the wire the lamination is, the worse is its effects on the wires' displacement at fracture and consequently the worse is its effect on the ductility of the wires.

Keywords—Displacement at fracture, Finite element analysis, Laminations, Fracture performance, Laminations.

I. INTRODUCTION

CARBON steel wires are commonly used for the reinforcement of civil engineering structures. They are used in pre-stressed concrete structures and structural elements such as pre-stressed concrete pipes, beams, columns, slabs etc where they provide the required compressive stresses. Carbon steel wires are also used in the construction of suspended and

cable-stayed bridges, where they support the loads on the bridge decks and are also used in flexible pipes, where they serve as the longitudinal tensile and hoop (circumferential) tensile reinforcements. In civil engineering structures where carbon steel wires provide the required reinforcement, the wires are subjected to substantial tensile stresses. Consequently, the structural integrity of these wires is very important in order to prevent the catastrophic failure of wire-reinforced civil engineering structures.

The structural integrity of wires can be threatened by the presence of surface and/or internal defects such as cracks, laminations, scratches etc. The threat to the structural integrity of wires by laminations and consequently the threat to the structural integrity of wire-reinforced structures cannot be overemphasized considering the fact that the presence of pre-service laminations in the pre-stressing wires used to manufacture the pre-stressed concrete pipes used for the construction of Jordan Aqueduct has been identified as the cause of the catastrophic failure of the pipes/aqueduct by the [1]. The United States Bureau of Reclamation [1] observed that the long straight longitudinal cracks which are better described as crack-like laminations in the pre-stressing wires used to manufacture the Jordan Aqueduct pre-stressed concrete pipes were present at different locations around the circumference of the round pre-stressing wires. A lamination is an elongated line-type defect or a long crack which are usually invisible but which constitute a material separation or discontinuity [2]. Laminations result from the elongation of the cylindrical cavities, impurities (such as non-metallic inclusions), and defects (such as alloy segregation) by the rolling or drawing process used for wires production [3, 4].

As observed by [4], laminations can be present at different locations in wires. While the locations of laminations in round wires may not have any significant effect in round wires as the effects of laminations anywhere around the circumference of round wires may have the same effect on the wires, the effect(s) of the locations of laminations in rectangular wires needs to be investigated. In this paper, the effects of the location of laminations on the fracture performance of wires, which as stated by [5], remains a major concern in civil engineering construction and maintenance of civil engineering

K. K. Adewole is with the University of Ibadan in Nigeria (Tel: +234807083389335; e-mail: kkadewole@yahoo.com).

N. E. Mastorakis is with the Technical University of Sofia Department of Industrial Engineering, Sofia, 1000, BULGARIA (e-mail: mastor@tu-sofia.bg).

structures where wires provide the required structural reinforcements, are investigated using finite element (FE) analysis. The fracture performance of steel wires used for civil engineering applications remains a concern because their fracture performance cannot be estimated using the traditional classical fracture mechanics approach as the large specimen size requirement by the traditional classical fracture mechanics approach cannot be manufactured from the wire due to their small sizes. This explains why the research works conducted on the fracture performance and failure analysis of wires such as the works of [6] on bridge cable wires, and [7, 8] on pre-stressing wires were conducted with non-standardised fracture mechanics wire specimens. FE analysis was employed for the investigation of the fracture performance of the typical wires for civil engineering applications considered in this work not only because standard experimental fracture mechanics samples could not be obtained from the wires but also because, it is not experimentally possible to machine into the wires crack-like laminations such as those found in the pre-stressing wires of the ruptured Jordan Aqueduct by the [1].

II. EXPERIMENTAL

A. Laboratory tensile testing of lamination-free wires

The laboratory tensile testing was conducted with an Instron universal testing machine (IX 4505) with wedge grips and with a static capacity of ± 100 kN. Ten full-size 170 mm long, 50 mm gauge length specimens of 12mm x 5mm and 12mm x 7mm lamination-free wires recommended by [9] shown in Figure 1 were tested. The laboratory tensile testing of the lamination-free wire specimens were conducted at an ambient temperature of 20°C, a relative humidity of 38% and a cross head speed of 5 mm/min. The displacement was measured with an Instron 2630-112 clip-on strain gauge extensometer with the same 50 mm gauge length as the specimen which ensured that only the elongation within the 50 mm gauge length was measured.

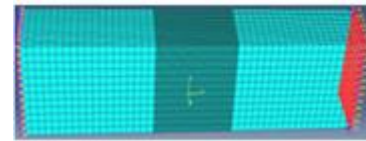


Figure 1: Experimental wire specimen.

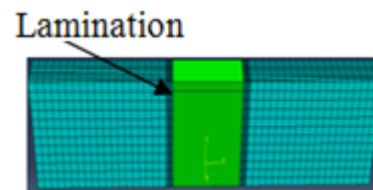
B. FE element tensile testing simulation and Equation

The FE simulations of the tensile testing were conducted with the isotropic elastic-plastic model combined with the micromechanical-based phenomenological shear failure fracture model which have been established by [10] to be a suitable model combination for the accurate prediction of tensile and fracture behaviours of the wires considered in this work. Details of the modelling parameters for the two models can be found in the work of [10]. Taking the advantage of the symmetry of the wire specimens to reduce computation time and FE results' file size, models with half of the wire's thickness were used for the simulations. The FE tensile testing simulations were conducted on lamination-free wire specimens

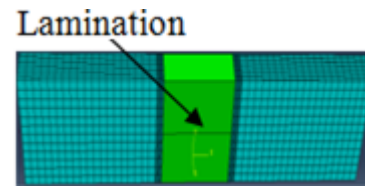
shown in Figure 2(a) and on wire specimens with 1mm to 10mm long across-the-thickness laminations located at 1mm, 2mm, 3mm, 4mm, 5mm and 6mm below the wire specimens' top surface. The crack-like laminations are not visible in meshed images as they were modeled as seams which are partition lines used in Abaqus to model cracks. Consequently, the model of the wire with unmeshed middle showing the crack-like laminations located 1mm and 6mm (hereinafter referred to as mid- width lamination) below the top surface of the wire are shown in Figures 2(b) and (c).



(a) Lamination-free wire



(b) Lamination 1mm below surface



(c) Mid- width lamination

Fig. 2: FE models of wires with and without laminations

Fig. 2: FE models of wires with and without laminations

The outer regions of the models of both the lamination-free wire specimen and the wire specimen with laminations were meshed with 1mmx1mmx1mm elements, while the middle region was meshed with refined mesh consisting of 0.1mm x 0.1mm x 1mm C3D8R elements as shown in Figure 2. This element size combination was established through mesh convergence study as the optimum mesh size for an accurate prediction of the tensile and fracture behaviours of the wires with and without laminations. The tensile testing simulation was conducted with the left hand end of the model completely fixed and the right hand end of the model which is free only the longitudinal tensile loading direction subjected to a longitudinal displacement as shown by the arrows in Figures 2(a).

C. Results

The FE predicted deformed shapes and force-displacement responses for the two wire sizes are similar, consequently, only

the result of the 12mmx7mm wire is presented. With the exemption of the lamination-free wire and the wires with the mid-width lamination, the FE predicted fracture process and fracture shapes for all the wires with laminations are the same. Consequently, only the FE predicted deformed shapes of: the lamination-free wire, the wire with the mid-width lamination and the wires with the lamination located 3mm below the wire's top surface (which typically represents the wires with lamination at varying locations) showing the fracture initiation points and the completely fractured wires are presented in Figures 3 and 4 respectively. The normalised force-displacement curves (normalized for confidentiality purposes) for the wires with and without laminations are shown in Figure 5. The first and second fracture initiation points (FIPs) which are associated with the first and second fracture initiations exhibited by the wires with laminations located at 1mm, 2mm, 3mm, 4mm and 5mm designated as 1st FIP¹, 1st FIP², 1st FIP³, 1st FIP⁴, 1st FIP⁵ and 1st FIP⁶; and 2nd FIP¹, 2nd FIP², 2nd FIP³, 2nd FIP⁴ and 2nd FIP⁵ respectively are shown in Figures 6 and 7. The force-displacement curves for the wire specimens with laminations located at 1mm, 4mm and 6mm, and for the wire specimens with laminations located at 2mm, 3mm and 5mm below the wires' top surface showing the 1st FIP and 2nd FIP are shown in Figures 6 and 7 respectively. The experimental and FE predicted fracture initiation points designated as "Lam-free wire FIP" are also shown in Figures 6 and 7. The variations of the displacements at fracture with varying lamination locations are shown in Figures 8.

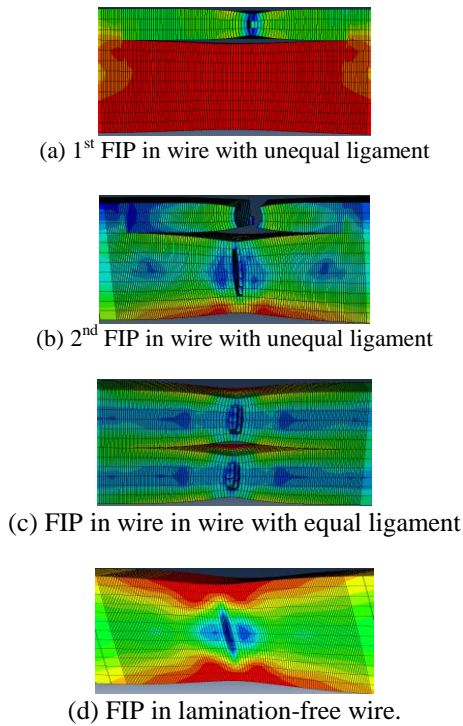


Fig 3: Fracture initiation points in wires with and without laminations.

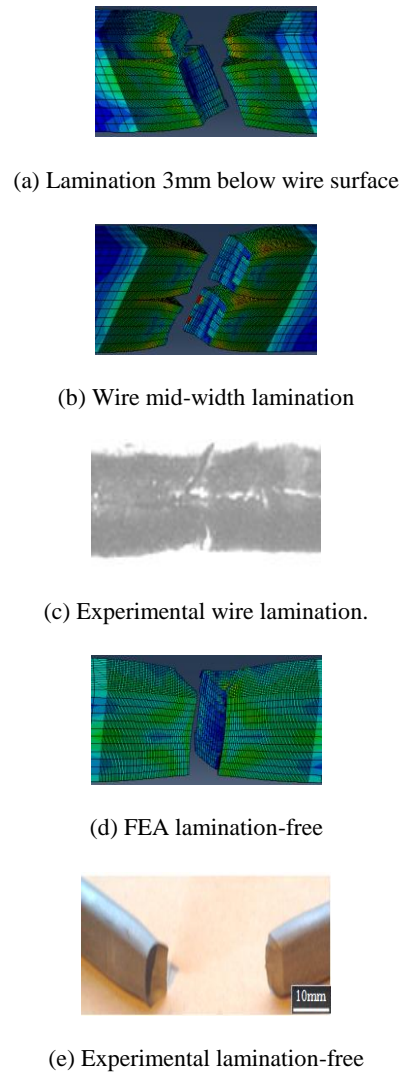


Fig 4: Fractured wire specimens

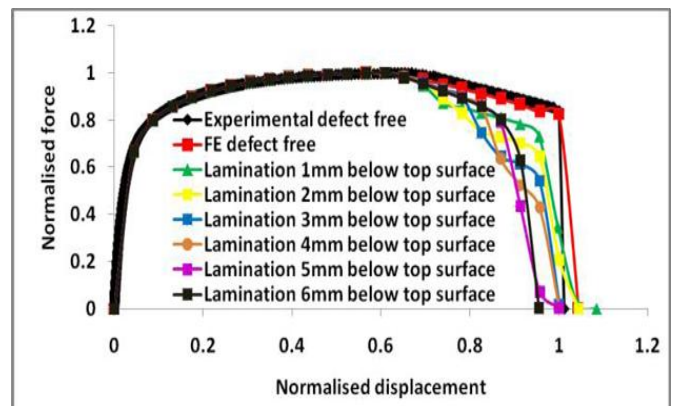


Figure 5: Force-displacement curves for all wire specimens.

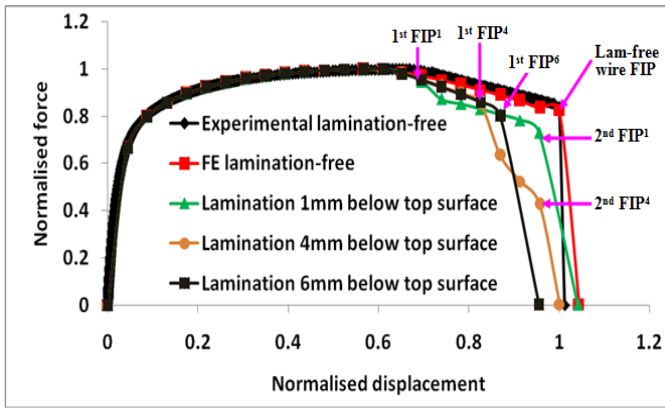


Figure 6: Fracture initiation points for wires with 1mm, 4mm and 6mm laminations below wires' top surface.

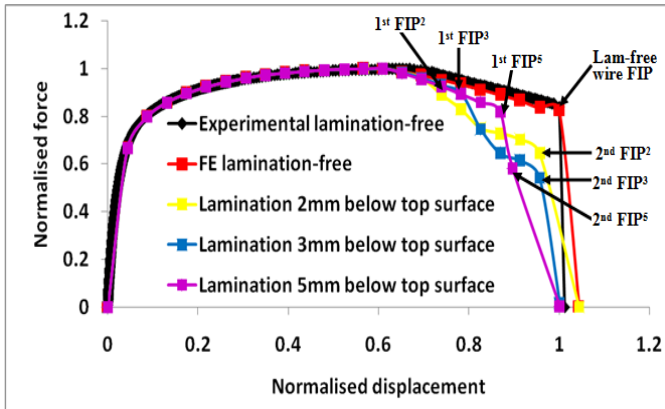


Figure 7: Fracture initiation points for wires with 2mm, 3mm and 5mm laminations below wires' top surface.

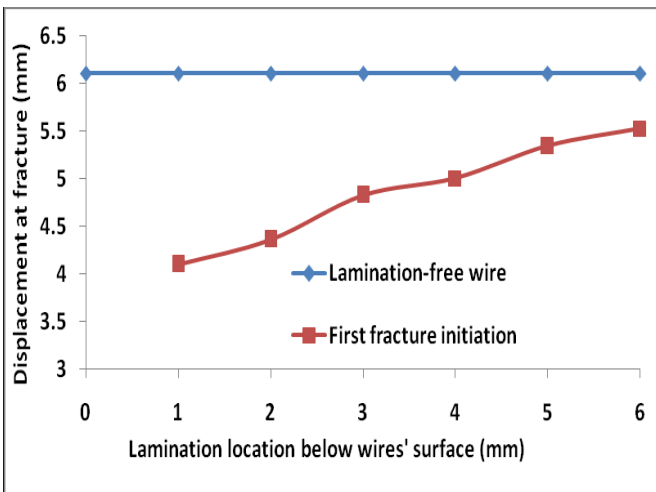


Figure 8: Variation of displacement at fracture with lamination location

III. DISCUSSION

The ability of the FE simulation to predict: the force-displacement curves that agrees with the experimental force-displacement curves (Figures 5 to 7) and the cup and cone

fracture shape that agrees with the experimental cup and cone fracture shape exhibited by the lamination-free wires (Figure 4(d) and (e)) demonstrates the accuracy of the simulation techniques employed in this work. An experimental verification of the accuracy of the finite element simulations of the tensile testing of the wire specimens with laminations was not conducted due to the fact that the longitudinal line-type/crack-like laminations that are parallel to the length of the wire specimens and which cuts through the thickness of the wire specimens could not be machined into the wire specimens. However, the ability of the FE simulation to predict a cup and cone fracture with an opening, resulting from the laminations (Figures 4(a) and (b)), that agrees with the fracture shape exhibited by the fractured wire with pre-service lamination reported by the US Bureau of Reclamation, (1994) shown in Figures 4(c), further establishes the accuracy of the simulation techniques employed for the prediction of the tensile responses of the wires with laminations.

The presence of laminations separates/divides the wire specimens with laminations into two ligaments along the wire's width. With the exception of the wire specimen with the mid-width lamination located 6mm below the wire's top surface which divides the wire into two equal ligaments, the presence of laminations located at 1mm, 2mm, 3mm, 4mm, and 5mm below the wire's top surface divides the wire into a thin top ligament and a thick bottom ligament as shown in Figure 2(b) and (c). As shown in Figure 3(a) to (c), fracture initiation occurred separately at two locations, one in each of the ligaments of the wires with laminations. The first and the second fracture initiations occurred in the thin ligament and in the thick ligament of the wires with unequal ligaments as shown in Figure 3(a) and 3(b) respectively. Fracture initiation occurred simultaneously in each of the two equal ligaments of the wire with the mid-width lamination as shown in Figure 3(c), while fracture initiation occurred in one location at the center of the lamination-free wire as shown in Figure 3(d). Fracture initiation occurred first in the thin ligament of the wires with unequal ligaments because the strain and stress in the thin ligament is higher than the strain and stress in the thick ligament due to its smaller size.

The point at which fracture initiation occurred is marked by a sudden drop in load and a sudden increase in displacement on the force-displacement curves. Except for the lamination-free wire and the wire specimen with mid-width lamination where fracture initiation in the two equal ligaments occurred simultaneously at the same load and displacement, the first and second fracture initiations occurred at different loads and displacement values in the wire specimens with laminations located 1mm to 5mm below the wires' top surface. This explains why with the exception of the force-displacement curves for the lamination-free wires and the wire with the mid-width lamination, all the force-displacement curves for the wire specimens with the laminations located at 1mm to 5mm below the top surface of the wire have two fracture initiation points as shown in Figures 5 to 7. The values of the displacement at which the first

fracture initiation occurs can be said to be the true displacement at fracture of the wires with laminations as the values of the displacement at which the second fracture initiation occurs contains the values of the sudden increase in displacement associated with the first fracture initiation. Thus, the values of the displacement at which the second fracture initiation occurs are unrealistically high and cannot be relied on as the displacement at fracture of the wires. Consequently, the effects of the location of laminations on the fracture performance/ displacement at fracture of the wires is based the displacement at 1st fracture initiation occurred which is associated with the fracturing of the thin ligaments of the wires with laminations located at 1mm to 5mm below the wires' top surface and the equal ligaments of the wire with mid-width lamination.

From Figures 5 to 7, the main differences between the force-displacement responses/curves of the lamination-free wire and the wire with laminations; and amongst the wires with laminations at varying locations are the differences in the displacements at which fracture initiations occurred and the differences in the fracture trajectories (the portion of the force-displacement curves beyond the fracture initiation point). The displacements at the 1st FIP in all the wires with laminations are lower than the displacement at fracture of lamination-free wires because fracture initiations occurred in the separate ligaments of the wires with laminations at a lower displacement value than that at which fracture initiation occurred in the lamination-free wire. This is due to the fact that the stresses in the separate ligaments with cross-sectional dimensions ranging from 1mm x 7mm to 6mm x 7mm for the wires with laminations located 1mm to 6mm below the wire's top surface) are more than the stress in the lamination-free wire with a cross sectional dimension of 12mm x7mm.

As shown in Figure 8, the displacement at which the first fracture initiation occurs is directly proportional to the distance of the lamination from the wires surface, with the wire having the laminations located 1mm and 6mm below the wires' top surface having the least and the largest displacements at first fracture initiation respectively. This is due to the fact that the closer to the surface of the wire the lamination is, the thinner the thin ligament and the smaller the displacement to which it can be stretched/tensioned before fracturing. This explains why the wires having the lamination located 1mm and 6mm below the wires' top surface have the least and the largest displacements at first fracture initiation respectively. The lamination located 1mm below wires surface causes a 10% reduction in the displacement at fracture of the wire while the lamination located 6mm below wires surface causes a 33% reduction in the displacement at fracture of the wire. The laminations located between 1mm and 6mm cause between 10 to 33 % reductions in the displacement at fracture of the wire. Consequently, the closer to the surface of the wire the lamination is, the worse is its effects on the wires' displacement at fracture and consequently, the worse is its effects on the fracture strain and the ductility of the wires.

IV. CONCLUSIONS

This study presents the investigation of the effects of the location of longitudinal laminations on the fracture performance in terms of the displacement at fracture of rectangular carbon steel wires used for civil engineering applications using finite element analysis. The investigation revealed that the lamination located at the middle of the width of the wire which is referred to as a mid-width lamination divides the wire into to equal ligaments while laminations located at any other distance along the wires' width divides the wire two unequal ligaments referred to as thin and thick ligaments. Fracture initiations occurred at two points and at two locations, one in each ligament of the wires with laminations. The first and second fracture initiations occurred in the thin and thick ligaments of the wires with unequal ligaments respectively at different load and displacement values, while fracture initiation occurred simultaneously in the two equal ligaments of the wire with the mid-width lamination at the same load and displacement values. Thus, the force-displacement curve of wire with mid-lamination exhibits only one fracture initiation point while the force-displacement curves of wire with laminations located at any other distance along the wires' width exhibit two fracture initiation points. The displacement at first fracture initiation represents the true displacement at fracture of the wires with laminations as the values of the displacement at second fracture initiation contains the values of the sudden increase in displacement associated with the first fracture initiation and thus is unrealistically high.

The investigation also revealed that, the location of laminations has an effect on the wires' displacement at first fracture. Laminations located between 1mm and 6mm (mid-width of the wire) below the wires' surface cause 10 to 33% reductions in the displacement at first fracture of the wires. The reduction in displacement at first fracture is directly proportional to the distance of the lamination from the wires' surface, with the wire having laminations located 1mm and 6mm below the wires' top surface having the least and the largest displacements at first fracture respectively. Consequently, it can be concluded that the closer to the surface of the wire the lamination is, the worse is its effects on the wires' displacement at fracture and consequently the worse is its effects on the ductility of the wires.

REFERENCES

- [1] Bureau of Reclamation. "Pre-stressed Concrete Pipe Failure Jordan Aqueduct, Reach 3"1994. All U.S. Government Documents (Utah Regional Depository), Paper284. <http://digitalcommons.usu.edu/govdocs/284>, assessed on 20/04/2014.
- [2] W. K. Chen, *Linear Networks and Systems* (Book style). Belmont, CA: Wadsworth, 1993, pp. 123–135.
- [3] S. Peet and A. Wilde, "Laminations-origin, detection and assessment", Congreso Internacional de Ductos, Merida Yucatan, 14-16 November, 2001.
- [4] K. A. Escoe, "Piping and pipeline assessment guide". Gulf Professional Publishing, 2006, pp.45, ISBN 13: 978-0-7506-7880-3.

- [5] J. Toribio and F. J. Ayaso, "Anisotropic fracture behaviour of cold drawn steel: a materials science approach", *Materials Science and Engineering*, 2003,A343, pp. 265-272.
- [6] K. M, Mahmoud, "Fracture strength for a high strength steel bridge cable wire with a surface crack", *Theoretical and Applied Fracture Mechanics*, 2007, vol 48(2), pp.152-160.
- [7] J, Toribio and A, Valiente, "Approximate evaluation of directional toughness in heavily drawn pearlitic steels", *Materials Letters*, 2004, vol. 58(27-28), pp. 3514-3517,
- [8] J, Toribio and A, Valiente, "Failure analysis of cold drawn eutectoid steel wires for pre-stressed concrete", *Engineering Failure Analysis*, 2006, vol. 13(3), pp. 301-311.
- [9] Standard Test Method for Tension Testing of Metallic Materials. American Society for Testing of Materials, ASTM E8M-2009.
- [10] K. K. Adewole, "Appropriate Micromechanical Fracture Model for Predicting Fracture Performance of Steel Wires for Civil Engineering Applications", *Global Journal of Researches in Engineering, Civil and Structural Engineering*, 2013, vol. 13(3), pp. 25-34.

A novel Meta heuristic inspired of the biologic nephron performance

Reza Behmanesh, Fatemeh Rokni

Abstract—as we know complexity of some problems increases with their size, therefore the solution space of these problems also increases exponentially, and there is need to optimization search techniques to solve these Np-hard problems. Despite of designing the several approaches with balanced exploration and exploitation in searching to solve such as these problems, there are some drawbacks to make suitable adjustment between exploring and exploiting in performance of the Meta heuristic algorithms. In this paper, the algorithm was designed inspired of the biologic nephron performance so that it can adjust between intensification and diversification strategies intrinsically, to make efficient optimization technique.

Keywords—Meta heuristic, nephron, intensification, diversification

I. INTRODUCTION

IN mathematical optimization and computer science, a meta-heuristic is defined a higher-level procedure or heuristic (partial search algorithm) that may provide a sufficiently good solution for an optimization problem, however, with incomplete information or limited computation capacity.[1] Meta-heuristics may be usable for a variety of problems. Besides, these algorithms, compared to optimization algorithms and iterative approaches do not guarantee that a global solution can be found on some class of problems [2]. Therefore, they are useful approaches for optimization problems.[1] Several books and survey papers have been published on the subject [1-4]. In nature-inspired meta-heuristic algorithms, there are two key components including local intensification and global diversification. Their interaction can significantly affect the efficiency of a meta-heuristic algorithm [5]. In this paper we intend to introduce new algorithm inspired of nature to find optimal balance between mentioned key components.

A. Nephronology

A nephron (derived from Greek νεφρός (nephros) meaning "kidney") is defined as the fundamental structural and functional unit of the kidney. Its principal function is to regulate water and soluble substances by filtering the blood,

R. Behmanesh. Author is with the Dept. of Industrial Eng., Science and Research Branch, Islamic Azad University, Tehran, Iran (corresponding author to provide phone: 913-186-0461; e-mail: rezaehs@yahoo.com).

F. Rokni. Co-Author is with the Dept. of Industrial Eng., Science and Research Branch, Islamic Azad University, Tehran, Iran (e-mail: rokni.f@gmail.com).

reabsorbing what is needed and excreting the rest as urine. Nephrons eliminate wastes from the body, regulate blood volume and pressure [6]. Each nephron is composed of an initial filtering component (the "renal corpuscle") and a tubule for reabsorption and secretion (the "renal tubule"). The renal corpuscle filters out large solutes from the blood, delivering water and small solutes to the renal tubule for modification. About 20% of the blood plasma is forced out of glomerulus (specialized capillaries) and across the membrane Bowman's capsule. It acts to filter some of the substances that are located in blood plasma from others. The renal tubule is the portion of the nephron containing the tubular fluid filtered through the glomerulus [7]. The components of the renal tubule are (Figure1):

- Proximal convoluted tubule (PCT lies in cortex and lined by simple cuboidal epithelium with brushed borders which help to increase the area of absorption greatly)
- Loop of Henle (hair-pin like i.e. U-shaped and lies in medulla)
- The ascending limb of loop of Henle is divided into 2 segments: Lower end of ascending limb is very thin and is lined by simple squamous epithelium. The distal portion of ascending limb is thick and is lined by simple cuboidal epithelium.
- Thin ascending limb of loop of Henle
- Thick ascending limb of loop of Henle (enters cortex and becomes DCT-distal convoluted tubule.) Distal convoluted tubule (DCT)

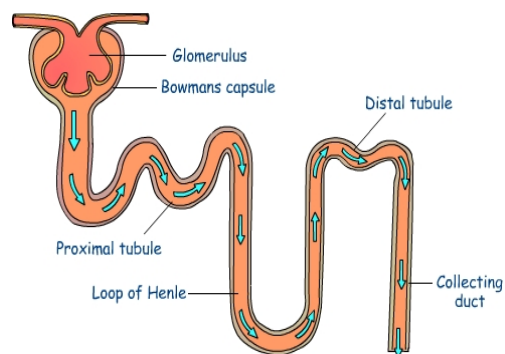


Fig. 1 Nephron anatomy

B. Darcy's law

Darcy's Law is a generalized relationship, which was indicated by Henry Darcy according to the results of

experiments in 1956 [8]. It shows the discharge rate is a function of the flow area, elevation, fluid pressure and proportionality constant. Below figure indicates visual Darcy's law.

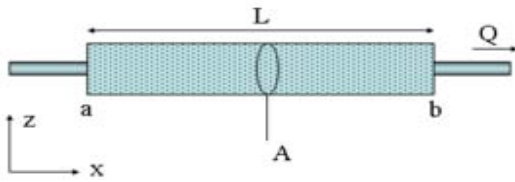


Fig. 2 Diagram for Darcy's law

As it is seen in equation (1) there is a simple proportional relationship between the instantaneous volumetric flow rate through a porous medium, the viscosity of the fluid and the pressure drop over a given distance [3].

$$Q = \frac{-kA}{\mu} \frac{(P_a - P_b)}{L} \quad (1)$$

where Q is total discharge (units of volume per time, e.g., m³/s), k is the the intrinsic permeability of the medium (m²), A is the cross-sectional area to flow (units of area, e.g., m²), expression of (P_b - P_a) is the total pressure drop (Pascals), μ is the viscosity of aqua (Pa·s) and L is the length over which the pressure drop is taking place (m). The negative sign is needed because fluid flows from high pressure to low pressure. Assuming that the inlet and outlet are at different elevations, the elevation head must be considered. If the change in pressure is negative (where P_a > P_b), then the flow will be in the positive 'x' direction. Dividing both sides of the equation by the area and using more general notation leads equation (2) as below:

$$q = \frac{-k}{\mu} \nabla P \quad (2)$$

Where q is the flux (discharge per unit area, with units of length per time, m/s) and ∇P is the pressure gradient vector (Pa/m) [8-10].

It is noted that discharge between nephron and vein in reabsorption phase or secretion will be computed based of second relationship of Darcy's law.

II. NOVEL META HEURISTIC ALGORITHM

A. Procedure Description

In this paper, one algorithm is proposed in order to solve the Np-hard problems with its intrinsic adjusting functions. Aforementioned algorithm was inspired based on natural biologic nephron performance so that data are clustered and analyzed step by step to optimize solution by strong search techniques. Role of nephron's functions in separating and

screening of data is important; this methodology can aid us to separate bad data from good data among whole dataset, according to principals of nephron performance. The rules of nephron are able to balance between intensification and diversification strategies throughout stages so as to obtain optimal solution. This algorithm guarantees a local solution near to global solution. Conceptual framework of nephron algorithm is shown in figure 3.

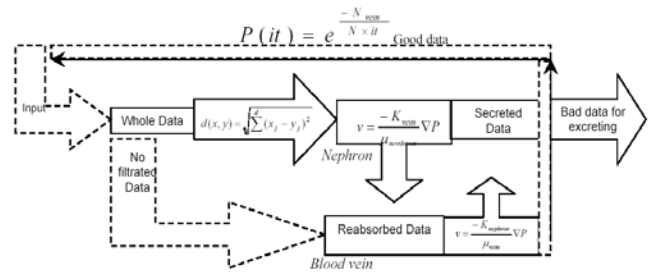


Fig. 3 Theoretical (conceptual) framework

In order to implement the algorithm, steps are as below:

1. *Initialization* : define the parameters and generate random data
 - a. Maximum iteration of algorithm (MaxIt)
 - b. The number of generated solution in each iteration (N)
 - c. The percentage of filtrated data to Bowman's capsule (α %)
 - d. The viscosity of nephron and vein data (μ_n, μ_v)
 - e. The intrinsic permeability of nephron and vein data (K_n, K_v)
 - f. The maximum iteration in each reabsorption or secretion in the case of local trap (M)
 - g. The threshold (ε) in order to terminate reabsorption or secretion.
2. *Filtration*: in the first place, whole data must be evaluated and the best solution should be saved according to fitness/cost function, then according to the rule of the filtration in nephron, α percent of data must be input of it, so for this purpose, percentage of whole data which are similar to best solution were considered as filtered. Filtrating criteria of this part is based on similarity equation of Euclidean distance [11-12]. (equation (3))

$$d(x, y) = \sqrt{\sum_{j=1}^d (x_j - y_j)^2} \quad (3)$$

X ₁	X ₂	...	X _j	...	X _d
----------------	----------------	-----	----------------	-----	----------------

Fig. 4 Solution

Y ₁	Y ₂	...	Y _j	...	Y _d
----------------	----------------	-----	----------------	-----	----------------

Fig. 5 The best solution:

It is indicated that α % of solutions with the least $d(x,y)$ are more similar solutions to best solution. It would be indicated according aforementioned equation that α % of whole data must entered to nephron part as bad data and rest of them would be transported to blood part. This strategy is to eliminate maximum number of data whose attributes are similar to the best solution in order to prevent high intensification in preliminary iterations.

$$N_{nephron} = (\alpha\%) \times N \tag{4}$$

$$N_{vein} = (1 - \alpha\%) \times N \tag{5}$$

Where N is the number of the whole solutions, $N_{nephron}$ is the number of the filtrated solutions, and N_{vein} is the number of the rest. In the last phase of filtration, filtrated data (solutions set) must be mutated (equation (6)) in order to diverse solutions that are more similar to the best solution.

$$\{newnep_i\} = \{Mutate(nep_i)\} \tag{6}$$

Where, nep_i and $newnep_i$ are solution set and new solution set after mutation inside the nephron respectively.

3. *Reabsorption*: this operation is done in PCT part of nephron, some existing data in nephron must be entered to vein based on this rule. So, data will be transferred to vein so as to intensify local optimized solutions.

Operation in this part is to generate more optimize solution in vein as well as nephron.

Firstly, pressure drop over a unit distance is calculated based on mean of solution in each part such as nephron and vein (equation (7))

$$\nabla P = \frac{\sum_i nep_i[t]}{N_{nephron}} - \frac{\sum_i vein_i[t]}{N_{vein}} \tag{7}$$

Then, with contributing two parameters K_v , μ_n in relationship velocity of solution discharge is computed to generate new solution as below:

$$q = \frac{-K_{vein}}{\mu_{nephron}} \nabla P \tag{8}$$

q is a vector such as solutions, so it can update old solutions to new solutions in each reabsorption phase. Adding the best solution data of the nephron to the existing solutions of the vein can be continued while $P_{nephron} > P_{vein}$.

As we know, the nature of P is vector and comparison between vectors or matrix is based on norms computation. To compare between $P_{nephron}$ and

P_{vein} , we take into account similarity rules among several clusters [6-7]. According to rule, the data point orients to cluster, which have nearest distance to it. Therefore, we evaluate distance (Euclidean or City) between the best solution of the nephron and average solutions of the vein (P_{vein}) as evaluation of $P_{vein} (D_{b-v})$, and distance between the worst solution of the vein and average solutions of the nephron ($P_{nephron}$) as evaluation of $P_{nephron} (D_{w-n})$. As a result, if $D_{b-v} < D_{w-n}$ then $P_{vein} < P_{nephron}$.

Also, after each discharging process, K_v is decreased and μ_n is increased according to logic of this law.

In the reabsorption operation, there are two equations as below:

$$newnep_i[t] = nep_i[t] - \frac{N_{nephron}}{N_{vein}} \times bnep[t] - q[t] \tag{9}$$

$$newvein_i[t] = vein_i[t] + \frac{N_{nephron}}{N_{vein}} \times bnep[t] + q[t] \tag{10}$$

Where $newnep[t]$, $nep[t]$, $newvein[t]$ and $vein[t]$ are new solutions and old solutions of two parts in moment of $[t]$. And $bnep[t]$ is the best solution of the nephron in same moment. It must be mentioned that after each operation, both dataset of vein and nephron must be evaluated in order to update the best solution.

4. *Secretion*: this operation is carried out in DCT part of nephron, some existing data in vein must be entered to nephron based on this rule. So, data will be transferred to nephron so as to intensify local optimized solutions and updating the best solution.

Operation in this part is to generate more optimize solution both in vein and nephron.

Firstly, pressure drop over a unit distance is calculated based on mean of solution in each part such as nephron and vein (equation (11))

$$\nabla P = \frac{\sum_i vein_i[t]}{N_{vein}} - \frac{\sum_i nep_i[t]}{N_{nephron}} \tag{11}$$

Then, with contributing two parameters K_n , μ_v in relationship velocity of solution discharge is computed to generate new solution as below:

$$q = \frac{-K_{nephron}}{\mu_{vein}} \nabla P \tag{12}$$

In this part v is also a vector such as solutions, so it can update old solutions to new solutions in each secretion phase. Adding the worst solution data of the vein to the existing solutions of the nephron can be continued while $P_{vein} > P_{nephron}$.

Contrary to the reabsorption phase, comparing vectors in secretion stage would be as bellow:

If $D_{b-v} > D_{w-n}$ then $P_{vein} > P_{nephron}$

In the secretion operation, there are two equations as below:

$$newnep_i[t] = nep_i[t] + \frac{N_{vein}}{N_{nephron}} \times wvein[t] + q[t] \quad (13)$$

$$newvein_i[t] = vein_i[t] - \frac{N_{vein}}{N_{nephron}} \times wvein[t] - q[t] \quad (14)$$

Where $wvein[t]$ is the worst solution of the vein in moment of $[t]$, after each operation in this stage, dataset of vein as well as nephron should be assessed so as to update the best solution.

It is cited for termination in secretion or reabsorption stages, there are two cases:

- a. If the value of the objective function is not optimized in (M) sequences of same operation
- b. If $|P_{vein} - P_{nephron}| \leq \varepsilon$, where ε is defined threshold.

5. *Excreting and repeating*: according to this step, existing data of nephron must be excreted as bad data (non suitable solutions for optimization) and the rest data of the vein must be repeated by previous steps, but before the first step, below rules are executed for generating new solutions.

Boltzmann relationship can aid us to make a suitable balance between intensification and diversification in data for any iteration.

If the local electrostatic potentials at two nearby locations are Φ_1 and Φ_2 , the Boltzmann relation for the electrons takes the form [13-15]:

$$n_e(\phi_2) = n_e(\phi_1) e^{-(\phi_2 - \phi_1) / k_B T_e} \quad (15)$$

Where n_e is the electron number density, T_e the temperature of the plasma, and k_B is Boltzmann constant.

In this section we can inspire from Boltzmann equation and replace its parameters with our algorithm's parameters. For example instead of expression $(\Phi_1 - \Phi_2)$, value of N_{vein} in last step of iteration is replaced because it indicates reductions or increases from the first of iteration to last of it. Also, the number of data in iteration can be replaced with k_B , since it is constant through algorithm computations. Iteration parameter can be used instead of temperature variable so that it can be effective as a variable parameter from first iteration to last iteration. So, we can utilize the Boltzmann equation in this algorithm as below:

$$P(it) = e^{\frac{-N_{vein}}{N \times it}} \quad (16)$$

Where (it) refer to iteration no. , P is probability of iteration.

$$N_{selected} = P(it) \times N_{vein} \quad (17)$$

Where $(N_{selected})$ refer to number of vein solutions that are selected for computing new generation.

The logic of this relationship is to contribute some better solutions of any iteration in generation of new solutions for next iteration, so that from first generation to last generation, diversification is decreased and intensification is increased. As we know, this is the strategy of all Meta heuristic algorithms to converge solutions.

Also, in any iteration there is suitable balance between diversification and intensification end of excretion phase, therefore with using Boltzmann equation, algorithm can generate intensified or diversified data in an adjusted decision.

After selecting the best solution and $N_{selected}$ of the vein solutions, the new generation is associated with them as below scheme:

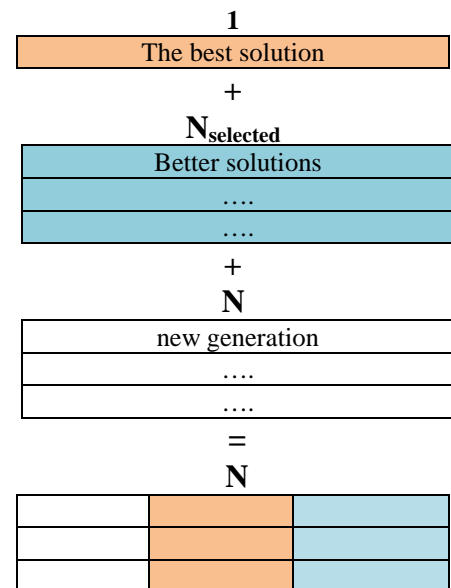


Fig. 6 Appending Selected solutions to new generation

6. *Termination condition*: if the stopping criteria are met, then stop; else go to the first step.

- 6.1. Provided that the iteration is received to maximum iteration.
- 6.2. If the value of the objective function is not optimized in a long time scale or some iterations.

B. Value of parameters in nature

This section represents value of some parameters in nature and we can assign suitable value to important parameters in algorithm.

For example, viscosity of liquid water at different temperatures up to the normal boiling point is increasing, and value of viscosity depends on type of material. However, we can define all parameters of Darcy's equation basis on type of

material i.e. μ that pertains to a material. Range of viscosity of water can be changed from 0.28 to 1.3, and this value in temperature 37 degrees is in interval of 0.6531 to 0.7978. Also, viscosity of blood is in interval of [0.003 0.004] for temperature 37 degrees. In our research, best proposition for this parameter is 0.72 for water and 0.0035 for blood. As we know, blood is fluid of vein and water is fluid of nephron. So, $\mu_n = 0.72$ and $\mu_v = 0.0035$.

In future researches we will determine suitable value for K (permeability coefficient) but our suggestion is 0.1 for K_n and K_v .

Percentage of filtration is important parameter because it can affect on many parameters in algorithm, but according the rule of nephron membrane it is suggested 0.2 approximately.

C. Metaphor

In this section, we present a table for metaphor of biologic nephron. In this metaphor, the comparison between natural nephron and nephron algorithm optimization is described.

NAO	Biologic Nephron
feasible solution	Plasma within nephron and vein
Objective function	Diagnose for screening useful & harmful material
Local search	Material flow between vein and nephron
Global search	Excreting harmful and absorbing useful particles, then iterating mechanism of entrance
Operations	Darcy's law operating in secretion and reabsorption
Optimizing	Iteration of separating excretion and nutrition
Control parameter K , and μ	Permeability coefficient & viscosity of materials
Control parameter α %	The percentage of filtrated data to Bowman's capsule

The components of algorithm are as below:

- 1- Representation scheme
- 2- Evaluation of solutions by objective function
- 3- Nephron operations in order to optimize
- 4- Excrete and repeat in order to regenerate
- 5- Termination condition

Consequently, we can have pseudo code as below:

[Initialization]:

Parameter Setting (M, N, MaxIt, ϵ , α , K, μ)
 Generate solution set or Plasma (randomly)

[Evaluation]:

Evaluate fitness or cost of each solution set and save the Best Solution

For $i=1$ to MaxIt do

[Filtration]:

Differentiate solution set to two parts ($\alpha\%$ of N within Nephron and rest of them within Vein)
 Data points inside the Nephron must be more similar to the Best Solution
 Mutating solutions inside the Nephron

While ($|P_{vein} - P_{nephron}| \leq \epsilon$ or M is met) do

[Reabsorption / Secretion]:

If ($P_{vein} < P_{nephron}$)

Reabsorbing operation & Updating the Best Solution

Else

Secreting operation & Updating the Best Solution

End If

End While

[Excretion]:

Eliminating solution set inside the Nephron

Selecting the number of better solution inside the Vein with probability $p(i) = e^{-N_{vein}/N} \times i$

[Repeat]:

Generate solution set (randomly)

Appending new generation to the Best Solution, and Better Solutions

End For

[Termination]:

Returning the Best Solution after meeting the stop criteria

Flowchart (Figure 7) indicates process of NAO from start to end completely.

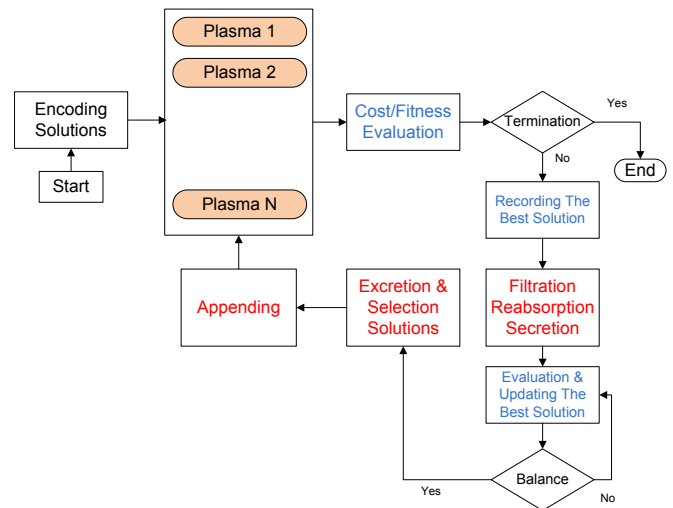


Fig. 7 Flowchart of the Nephron algorithm optimization

III. CONCLUSION

In this paper we presented a new metaheuristic algorithm for NP-Hard problem inspired of biologic nephron performance. This algorithm like nephron has three steps including Filtration, Reabsorption, and Secretion. Data points of the nephron must be excreted as bad data and the rest of them inside the vein must be repeated by previous step. For balancing between intensification and diversification we proposed different formula based on Darcy's Law and Boltzmann relation. Intensification is possible in Reabsorption and Secretion stage. Furthermore, diversification is done in Filtration and Excreting and repeating stage.

REFERENCES

- [1] Bianchi, Leonora; Marco Dorigo, Luca Maria Gambardella, and Walter J. Gutjahr. "A survey on metaheuristics for stochastic combinatorial optimization". *Natural Computing: an international journal* 8 (2): 2009, pp. 239–287.
- [2] Blum, C.; Roli, A., *Metaheuristics in combinatorial optimization: Overview and conceptual comparison* 35 (3). *ACM Computing Surveys*. 2003, pp. 268–308.
- [3] Goldberg, D.E., *Genetic Algorithms in Search, Optimization and Machine Learning*. Kluwer Academic Publishers, 1989.
- [4] Glover, F.; Kochenberger, G.A., *Handbook of metaheuristics* 57. Springer, International Series in Operations Research & Management Science, 2003.
- [5] Xin-She Yang, Suash Deb, and Simon Fong., *Metaheuristic Algorithms: Optimal Balance of Intensi_cation and Diversi_cation*, *Information Journal*, 2013.
- [6] Maton, Anthea; Jean Hopkins, Charles William McLaughlin, Susan Johnson, Maryanna Quon Warner, David LaHart, Jill D. Wright., *Human Biology and Health*. Englewood Cliffs, New Jersey, USA: Prentice Hall., 1993.
- [7] University of Colorado, 2007, Retrieved august 7, 2012, from <http://en.wikipedia.org/wiki/Nephron>.
- [8] H. Darcy, *Les Fontaines Publiques de la Ville de Dijon*, Dalmont, Paris 1856.
- [9] Brinkman, H. C. "A calculation of the viscous force exerted by a flowing fluid on a dense swarm of particles". *Applied Scientific Research* 1, 1949, pp. 27–34. doi:10.1007/BF02120313.
- [10] A. Bejan, *Convection Heat Transfer*, John Wiley & Sons, 1984.
- [11] Momeni, M., Faal Ghayoomi, M., *Statistical analysis using SPSS*. Momeni, 2010, p. 174.
- [12] Momeni, M. . *Data clustering*. Momeni, 2011, pp.174-178.
- [13] Arkeryd, Leif . "On the Boltzmann equation part II: The full initial value problem". *Arch. Rational Mech. Anal.* 45, 1972, pp. 17–34. Bibcode:1972ArRMA..45...17A. doi:10.1007/BF00253393.
- [14] Arkeryd, Leif . "On the Boltzmann equation part I: Existence". *Arch. Rational Mech. Anal.* 45:1972, pp. 1–16. Bibcode:1972ArRMA..45....1A. doi:10.1007/BF00253392.
- [15] DiPerna, R. J.; Lions, P.-L. "On the Cauchy problem for Boltzmann equations: global existence and weak stability". *Ann. Of Math. (2)* 130: 1989, pp. 321–366. doi:10.2307/1971423.

F. Rokni from Iran, with birth date of 12/10/1983. B.A. degree of textile engineering from Poly Techniques University of technology, Tehran, Iran graduated in 30/8/2006. M.A. degree of Industrial engineering from Yazd University, Yazd, Iran graduated in 30/01/2011. She is currently PHD student of industrial engineering in University of Science and Research branch, Tehran, Iran. The Co-author's major field of study is supply chain management (SCM), and data mining techniques include Decision tree (DT), DNA, and relative efficiency technique such as Data Envelopment Analysis (DEA). She has 6 months job experience in civil co. as a planner. Her first publication pertains to reliability of the Nephron algorithm, which has been published in IJSEL. Her current research interest is to predict supplier's performance using meta-heuristic algorithms.

R. Behmanesh from Iran, with birth date of 3/2/1979. B.A. degree of mining engineering from Isfahan University of technology, Isfahan, Iran graduated in 30/8/2001. M.A. degree of Industrial engineering from Yazd University, Yazd, Iran graduated in 30/8/2010. He is currently PHD student of industrial engineering in University of Science and Research branch, Tehran, Iran. The author's major field of study is supply chain management (SCM), Quality control (QC), and data mining techniques include Neural Networks (NNs), Decision tree (DT), DNA, and technique of Data Envelopment Analysis (DEA).

He has 3 years job experience in EORC as a planner in maintenance workshop, he has accompanied with 6sigma team in the course of 6 month in order to decline response time of maintenance process. His first publications pertain to prioritizing the improvable HRM process in EORC, which has been published in IEEE. His next is about same issue extensively, but it was published in the journal of operation and product management. His current research interest is to predict supplier's performance using new data mining methods.

Estimation of failure probability of B737 pneumatics system by fault tree analysis

H.MAHFOUD, A.ELBARKANY, A.ELBIYAALI

Abstract— in airline industry where reliability and safety are paramount and in such difficult economic environment today, it's essential to adopt a strategy of mastery and rationalization of maintenance costs to perform the optimum level of capability. Fault tree analysis (FTA) is one of the most important logic and probabilistic techniques used in probabilistic risk assessment (PRA) and reliability analysis. It's an effective decision support tool that helps to find operational weaknesses in complex systems and then uncover and prioritize safety improvements and maintainability cost optimization. The objective of this research is to develop an analytical method based on FTA to improve the reliability and maintainability of a large complex system of Boeing 737 next generation responsible for several key operations during flight, namely the pneumatic system; in order to optimize its preventive maintenance and availability of aircraft, intolerable thing in such us area where the lost of time means simply a waste of money.

Keywords—B737 aircraft, Fault tree analysis, Maintenance costs, PRA, reliability.

I. INTRODUCTION

FAULT TREE ANALYSIS has become the most important tool to evaluate safety and reliability of complex and large systems. It's a logical and probabilistic approach for evaluating the possibility of an accident resulting from sequences and combinations of failure events. It's simply a technique by which many events that interact to produce other events can be related using simple logical relationships. This method is a graphic model of the various parallel and sequential combinations of faults that will result in the occurrence of the predefined undesired event. The faults can be events that are associated with component hardware failures, human errors, or any other pertinent events which can lead to the undesired event. A fault tree thus depicts the logical interrelationships of basic events that lead to the undesired event-which is the top event of the fault tree [1].

II. ROLE OF FAULT TREES IN A PRA

Probabilistic risk assessment, or PRA, models sequences of

Hassana MAHFOUD(Mah.hassana@gmail.com),
Abdellah.ELBARKANY(a_elbarkany2002@yahoo.fr),
Ahmed El BIYAALI (biyaali@yahoo.fr) are all with Faculty of Sciences and
Techniques,Mechanical Engineering Laboratory, Sidi Mohammed Ben
Abdellah University, B.P. 2202 – Route d'Imouzzer – Fes, Morocco.

events which are usually called an accident sequence that need to occur in order for undesired end states to occur. A model of a simple event sequence in PRA is shown below.

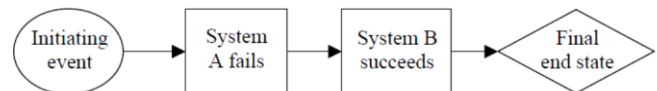


Fig. 1 simple PRA events sequence

If an event is independent of the others in the sequence and failure data exist, the probability can be directly estimated from the data. But form more complex events, the fault tree is developed to a level that encompasses the dependencies between systems or to a level where failure data exist for that basic events, whichever is lower [2].

III. GENERAL PROCEDURE FOR FTA CONSTRUCTION

To elaborate a comprehensive FTA, we follow these steps:

- 1) Define the system of interest
- 2) Define the top event for the analysis
- 3) Define the treetop structure
- 4) Explore each branch in successive levels of detail
- 5) Solve the fault tree for the combinations of events contributing to the top event
- 6) Identify important dependent failure potentials and adjust the model appropriately
- 7) Perform quantitative analysis
- 8) Use the results in the decision making [3]

IV. QUANTITATIVE FAULT TREE ANALYSIS

A. Boolean modeling

FTA is a mathematically Boolean tool for modeling a system's unreliability. The conventional analysis, proposed by Vesely, determines the probability of failure (POF) of a system from a set of components that make up that system. Boolean AND and OR gates are used to connect components with one another [4].

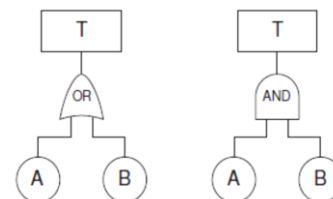


Fig. 2 AND/OR gates

For an AND gate, the probability of system failure, P_T can be calculated from:

$$P_T = P_A \times P_B \quad (1)$$

Where, P_A and P_B are the corresponding failure rates of each component, respectively.

In general, the top event probability for a set of N components through AND gates, is shown in Equation 2:

$$P_T = \prod_{i=1}^N P(C_i) \quad (2)$$

Likewise, top event failure for a simple OR gate is predicted by:

$$P_T = P_A + P_B - (P_A \times P_B) \quad (3)$$

In general, the top event probability for a set of N components through OR gates, is shown in Equation 4:

$$P_T = \sum_{i=1}^N P(C_i) - \sum_{i=1}^{N-1} \sum_{j=i+1}^N P(C_i \times C_j) + \sum_{i=1}^{N-2} \sum_{j=i+1}^{N-1} \sum_{k=j+1}^N P(C_i C_j C_k) \times \dots + (-1)^{N+1} P(C_1 C_2 C_3 \dots C_N) \quad (4)$$

The rare-event approximation is often used to simplify this equation.

$$P_T = \sum_{i=1}^N P(C_i) \quad (5)$$

B. Importance factors

The importance factors are used to quantify the contribution of each components failure to the top event occurrence probability [5].

1) Fussell-Vesely's Factor

It's a measure of a referred element contribution to the system failure. The mathematical definition of the importance of VF is as follows [6]:

$$FV = \frac{P(T) - P(T/E=0)}{P(T)} \quad (6)$$

Where $P(T)$: top event probability
 $P(T/E=0)$: conditional probability of the top event occurrence given that the occurrence of $E=0$.

2) Birnbaum's Factor

It's a measure of the difference between the value of a top event probability when E occur ($P(E)=1$) and when it doesn't occur.

$$BI = P(T/E = 1) - P(T/E = 0) \quad (7)$$

3) Risk achievement worth's Factor

It's a measure of the growth of a top event probability when the E is unavailable:

$$RAW = \frac{P(T/E=1)}{P(T)} \quad (8)$$

V. CASE STUDY: PNEUMATIC SYSTEM FAULT TREE ANALYSIS

A. System description

The pneumatic system supplies compressed air to the airplane user systems:

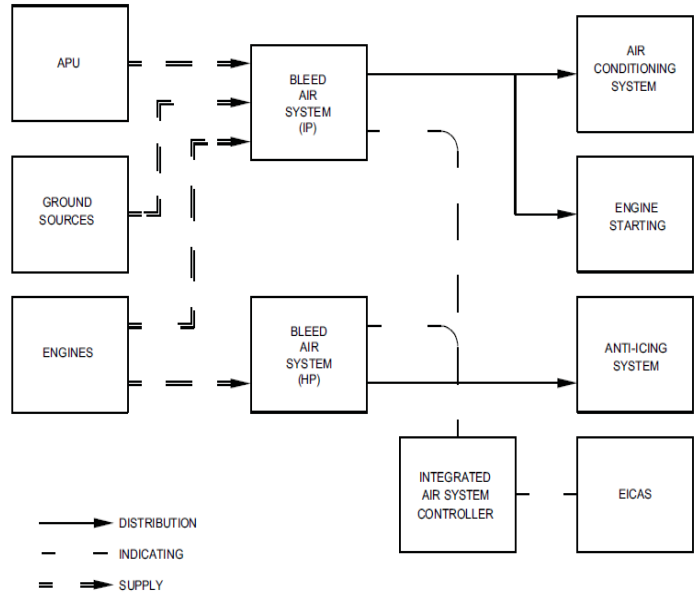


Fig. 3 Pneumatic general description

- These are the sources of pneumatic power [7]:
- Engines bleed air system
- Auxiliary power unit (APU) bleeds air system
- Pneumatic ground air connection.

The pneumatic manifold collects the compressed air from the sources and supplies it to the user systems:

- Engine start systems
- Air conditioning and pressurization systems
- Engine inlet cowl anti-ice systems
- Wing thermal anti-ice systems

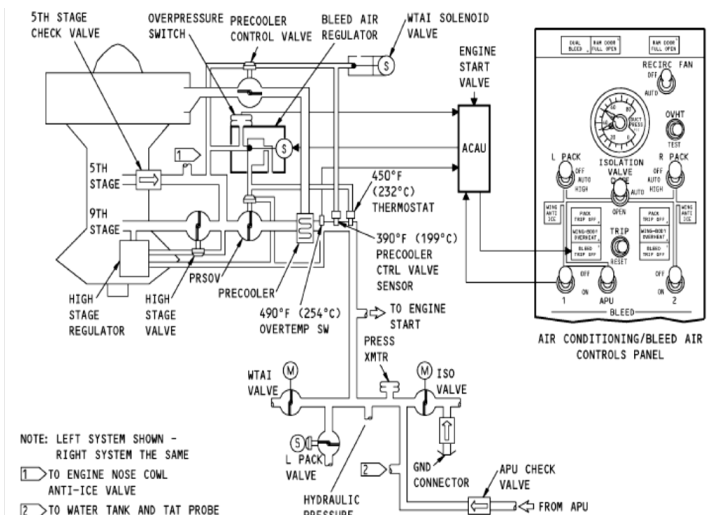


Fig. 4 Pneumatic functional description

B. Structural analysis

Functional block diagram allows interconnecting different system functions.

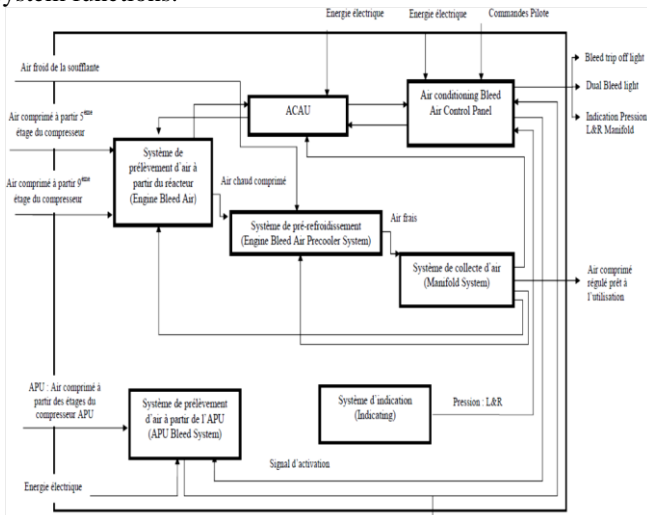


Fig. 5 Pneumatic functional bloc diagram

C. The potential accident Top event

After mapping the system by establishing functional description, it was time to define the most penalizing equipment in terms of reliability. At this level, we based on the maintenance rappsorts to better target the system potential failure that will be a little further subject of our study to overcome the problems of unavailability of 737/NG Boeing fleet RAM caused by an abnormality related to ATA 36.

Figure below show the distribution of unexpected failures related to our system that have led to interventions of maintenance just before the plane takes off, these abnormalities cause delays compared to pre flight schedules.

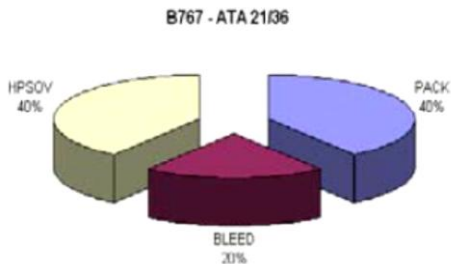


Fig. 6 Pneumatic failures distribution

Combining criteria of failure frequency, number of equipment removals, and consequences on availability and safety, we will consider in our study “Bleed Trip off” as a top event.

D. Treetop structure

At this stage we determine the events and conditions that most directly lead to the top event until the fault tree model is complete. We use *PTC windchill quality solutions* software.

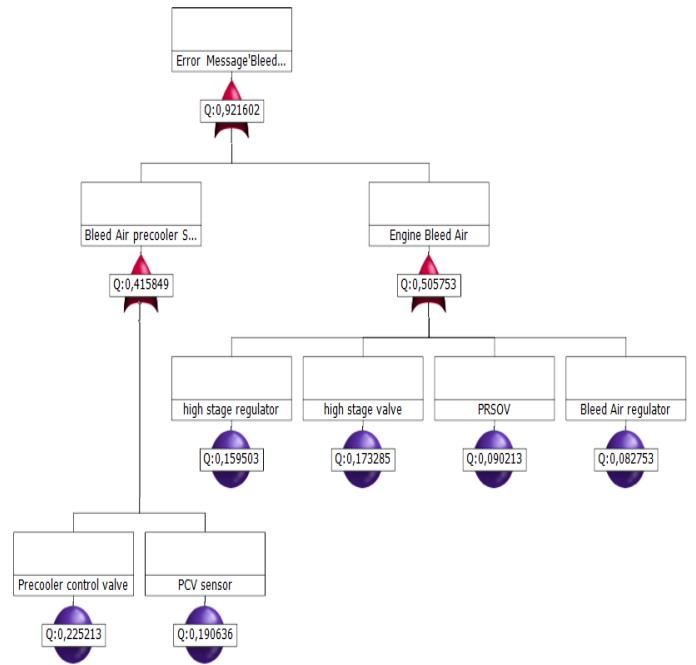


Fig. 7 Pneumatic fault tree

E. Input data (MTBF)

Once the history is prepared and, Time Between failure is spotted, we determine by the weibull law the Mean Time Between Failure, which constitute the probability input data.

Nom	Type de porte/évén	Type d'entrée	TD/MTBF	Valeur	Unités d'entrée
Bleed Air precooler System	Porte OU				
Bleed Air regulator	Événement basique	TD/MTBF	MTBF	11577,00 0000	Heures
Engine Bleed Air	Porte OU				
Error Message'Bleed Fault'	Porte OU				
high stage regulator	Événement basique	TD/MTBF	MTBF	5755,000 000	Heures
high stage valve	Événement basique	TD/MTBF	MTBF	5255,000 000	Heures
PCV sensor	Événement basique	TD/MTBF	MTBF	4728,000 000	Heures
Precooler control valve	Événement basique	TD/MTBF	MTBF	3919,000 000	Heures
PRSOV	Événement basique	TD/MTBF	MTBF	10577,00 0000	Heures

Fig. 8 Events MTBF

F. Quantitative assessment

For more precision, the software explicit for each event contributor to the potential accident it's unreliability, unavailability and frequency in the first 1000 hours.

Nom du fich pneumatics.rfp
 Porte supé Error Message'Bleed Fault'

Heure de Début du calcul (h): 0
 Heure de fin du calcul (h): 1000
 Méthode de calcul: Somme de coupes

Nom	Temps	Non-fiabilité	Indisponibilité	Nombre de défaillances	Fréquence
Bleed Air precooler System	0	0,000000	0,000000		466,673057
	100	0,046122	0,046122		455,817899
	200	0,091172	0,091172		445,217344
	300	0,135174	0,135174		434,865373
	400	0,178153	0,178153		424,756110
	500	0,220133	0,220133		414,883819
	600	0,261138	0,261138		405,242900
	700	0,301189	0,301189		395,827887
	800	0,340311	0,340311		386,633445
	900	0,378523	0,378523		377,654364
	1000	0,415849	0,415849	0,4158	368,885559

Fig. 9 Bleed air precooler system factors

In the table below, “Precooler control valve” is the element which contribute first to the top failure analyzed with a fussell-Vesely factor=0.244 and high criticality that exceed 0.2.

PTC Windchill
 Quality Solutions

Mesures d'importance AAD

Nom du fich pneumatics.rfp
 Porte supé Error Message'Bleed Fault'

Événement	Birnbaum	Criticité	Fussell-Vesely
Bleed Air regulator	1,000000	0,089792	0,089792
PRSOV	1,000000	0,097887	0,097887
high stage regulator	1,000000	0,173072	0,173072
PCV sensor	1,000000	0,206852	0,206852
Precooler control valve	1,000000	0,244371	0,244371
high stage valve	1,000000	0,188026	0,188026

Fig. 10 Importance Factor measures

VI. MAINTENANCE COSTS OPTIMIZATION

According to the system tree analysis results, Precooler control valve is the defaulting element among the other events contributing to the general system failure. Thus the preventive maintenance is imperative to optimize its reliability.

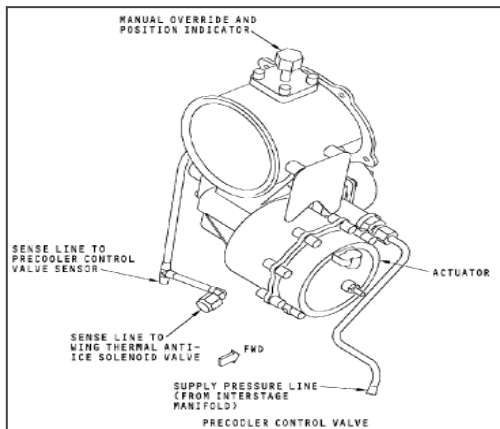


Fig. 11 Precooler control valve

A. Necessary expenses to control the Precooler control valve operation.

This maintenance action must be done every 1234 (FH), which will take 6hours of work and need the acquisition of some consumables and materials.

The cost of this operation is evaluated at **3924 DH**.

B. Damage caused in case of an unexpected failure

An unexpected failure of the precooler control valve leads to its replacement by a new one and its expedition to a foreign subcontractor to be repaired.

- Reparation costs: 61550DH
- Freight charges: 2500DH
- Labor costs: 866DH
- Immobilization: 2h

The cost of this failure is about **64 916 DH**

Consequently, the inspection and control of precooler control valve provides gain of **94%** over expenses of an unexpected failure.

VII. CONCLUSION

This study deals with the pneumatic system reliability, by using the Fault tree Analysis. This method enables the estimation of the system breakdown probability, result of failure sequences that contribute to the top event. Thus the main result is the knowledge of the system characteristics to master maintenance costs.

REFERENCES

- [1] W. Vesely et al., Fault Tree Handbook, NUREG-0492, Nuclear Regulatory Commission,1981.
- [2] W. Vesely et al., Fault Tree Handbook, NASA Office of Safety and Mission Assurance NASA Headquarters, Washington, DC 20546,2002.
- [3] United States Coast Guard. 2004. Risk-based Decision-making (RBDM) Guidelines (3rd Ed.), Vol. 3 – Risk Assessment Tools Reference, Chapter 9 –Fault Tree Analysis.
- [4] Justin F. Murtha, Virginia Polytechnic Institute and State University “Evidence Theory and fault tree analysis to cost-effectively improve reliability in small uav design”
- [5] Marvin Rausand, Department of Production and Quality Engineering System Reliability Theory (2nd ed.), Wiley, 2003
- [6] Michel demers, « developpement d’une methodologie d’optimisation de la maintenance par la fiabilité pour les systems complexes application à un groupe electrogène diesel de secours », 1998
- [7] Department of Transportation, Federal Aviation Administration, Aviation Maintenance Technician Handbook Airframe, Volume 2, 2012

H. MAHFOUD is a PhD candidate at the Department of Mechanical Engineering, the University of Sidi Mohammed Ben Abdellah in Morocco. She received her Engineering degree from the National School of Applied Sciences in July2011.

A. EI BARKANY is an Associate Professor at the Mechanical Engineering Department in Faculty of Sciences and Techniques. He obtained his PhD in Mechanical Engineering from University Hassan II of Casablanca (2008). He received his Engineering degree from the same university in 1997.

Ahmed EI BIYAALI is Professor of Mechanical Engineering and Head of Mechanical Engineering Department, Sidi Mohammed Ben Abdellah University. He holds BS and PhD degrees in Mechanical Engineering.

Factors affecting Productivity of Infrastructure Development Project

attributable to Insecurity due to Terrorism

Muhammad Sohail Anwar Malik^{1*}; Dr. Shazia Nauman²

Abstract— Pakistan's construction industry has suffered an all-time low productivity after 9/11 as a result of insecurity caused by terrorism. The construction projects suffered mainly because of reduced availability of the required resources and unwillingness of the stakeholders to work in an insecure environment. Besides this, the projects faced huge financial losses as a result of terrorist acts thus ending up the projects in the midway. In the present study, we sought to identify risks affecting productivity of development projects owing to insecurity due to terrorism. We identified the risks affecting project objectives of time, cost, scope and quality of the development projects from literature review and structured interviews of project management professionals having working experience in terrorism affected areas. The identified risks were validated through national level questionnaire survey of the client, consultant and contractor organizations working in terrorism affected areas or having experience of work in such areas. The results of this study might help in increasing the productivity of development projects in terrorism affected areas by addressing those identified factors.

Keywords— Overrun cost, overrun time, low quality, terrorism, development projects.

I. INTRODUCTION

CONSTRUCTION projects are exposed to more risks compared to other business projects (e.g developing a new product or service or developing a new or modified information system) due to their complexity. A construction project normally involves many people with various skills and interests besides coordination of numerous interrelated activities. All of this is compounded by much external uncertainties. It is common to find construction projects to overrun costs, delayed time and poor quality¹. Various researchers^{2,3} have identified risks causing project delays that were classified as physical risks, design risks, construction risks, legal risks, financial risks and political risks. Abdallah and Hussein⁴ investigated the project delaying causes categorized into eight groups: client related, contractor related, consultant related, materials related, labor and equipment factors, contract factors, contractual relationship factors and external factors (weather conditions, changes in regulations, problems with neighbors and site conditions). Delay in project because of 'insecurity due to terrorism' has traditionally been looked as *force majeure*, an act of God over which no one has got any control^{5,6}. Pakistan is a highly security affected country. Frequent terrorist acts and counter terrorism activities, besides costing thousands of lives, have created a feeling of insecurity amongst the common masses. This growing feeling of insecurity has adversely affected the productivity of construction industry. The development

projects suffer badly due to reduced availability of the required resources and because of unwillingness of stakeholders to work in an insecure environment. However, limited literature is available on effects of insecurity due to terrorism on productivity of development projects.

A. Research Motivation

Federally Administered Tribal Areas (FATA) and Swat are two areas located in western region of Pakistan, part of Khyber Pakhtunkhwa Province (see Figure 1 for the location map of FATA and Swat). FATA comprises of seven agencies: Bajaur Agency, Mohmand Agency, Khyber Agency, Orakzai Agency, Kurram Agency, North Waziristan Agency and South Waziristan Agency. Most part of these areas is a mountainous terrain. FATA, until the late 1990's, used to be a no-go area due to numerous terrorism attacks⁷.



Figure 1. Map showing location and agencies of FATA and Swat

In 2001, the FATA was required to be opened up to establish the writ of government. It had to be done with a view to integrate the people of the FATA into the Pakistani political system without having to a fight with them. To achieve this objective, it was decided to take up developmental projects for the uplift of the area to win the hearts and minds of the people of the areas.

Until now, scores of construction projects with an approximate total value of US\$ 65 m have been executed in FATA⁸. Commenced in December 2001, numerous development projects including roads, tracks, schools, hospitals, water supply schemes and dug wells were initiated in all the agencies. Few of the developmental works executed in FATA are as shown in Table 1 below:

¹Asstant Professor at Military College of Civil Engineering, National University of Science and Technology, Rislapur Campus, Pakistan.

² Assistant Professor at Department of Management Sciences, Air University Islamabad, Pakistan.

Table-1. Developmental Works Executed by Army Engineers in FATA

Nature of work	Quantity		Total
	In Progress	Completed	
Roads	460.38 km	252.62 km	713 km
Shingle tracks	44.12 km	1099.38 km	1143.5 km
Schools/ Colleges	35	35	70
Hospitals	3	3	6
Water Supply Schemes	27	23	50
Hand Pumps	1201	1128	2329
Tube Wells	64	55	119
Dug Wells	171	139	310
Children Parks	49	32	81
Karaizes (underground water channels)	5	5	10
Funeral Places	4	4	8

The developmental projects initiated in that area suffered badly due to insecurity due to terrorism to the extent that most projects have come to a halt. The problem and its visualizable effects on the projects can be comprehended from the fact that from 2003 to 2011, a total of 3482 bomb blasts and 281 suicide attacks have occurred in FATA and other parts of the country killing 11695 people and 27985 injured⁹. Pakistan’s security forces have also faced a heavy death toll in the fight against terrorism in last decade in which 3,733 security forces personnel and 21,067 terrorists have been killed¹⁰.

These security incidences led to insecurity amongst the stakeholders bringing many projects consequently to a halt in the midway. Those few projects that are still in progress today under local security arrangements were suffering badly due to frequent terrorism incidences.

The project management techniques in this complex security situation become unique as the security concern became the main focus of project management practice. The effects observed to be caused by insecurity due to terrorism over development projects in remote areas under adverse security climate yielding all time low productivity are as shown in Figure 2.

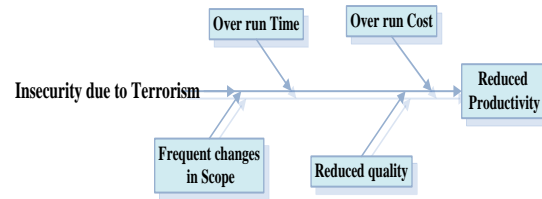


Figure 2: Effects of insecurity due to terrorism on developmental projects

B. Research objective. To identify the factors of productivity related to time, cost, scope and quality of development projects attributable to insecurity due to terrorism.

C. Significance of the study

The overarching purpose of the present study is to investigate the affected factors of productivity in construction projects attributable to insecurity as a result of terrorism. Since limited literature is available in this area, we addressed this gap in the present study by identifying the affected factors of productivity which can later be resolved through adoption of mitigation measures.

II. RESEARCH DESIGN

The study design was retrospective-prospective and semi experimental in nature. Primary data was utilized for study, in that self-administered questionnaire and structured interviews were used as instruments for conducting survey. The examples of using empirical study based on the methodology of questionnaire survey, structured interviews and semi structured interviews exist, in which Akintoye and MacLeod¹¹, Lyons and Skitmore¹², Shen ¹³ and Tang *et al.*¹⁴ have used this methodology.

The research objectives were met through four tasks as graphically represented in Figure 3.

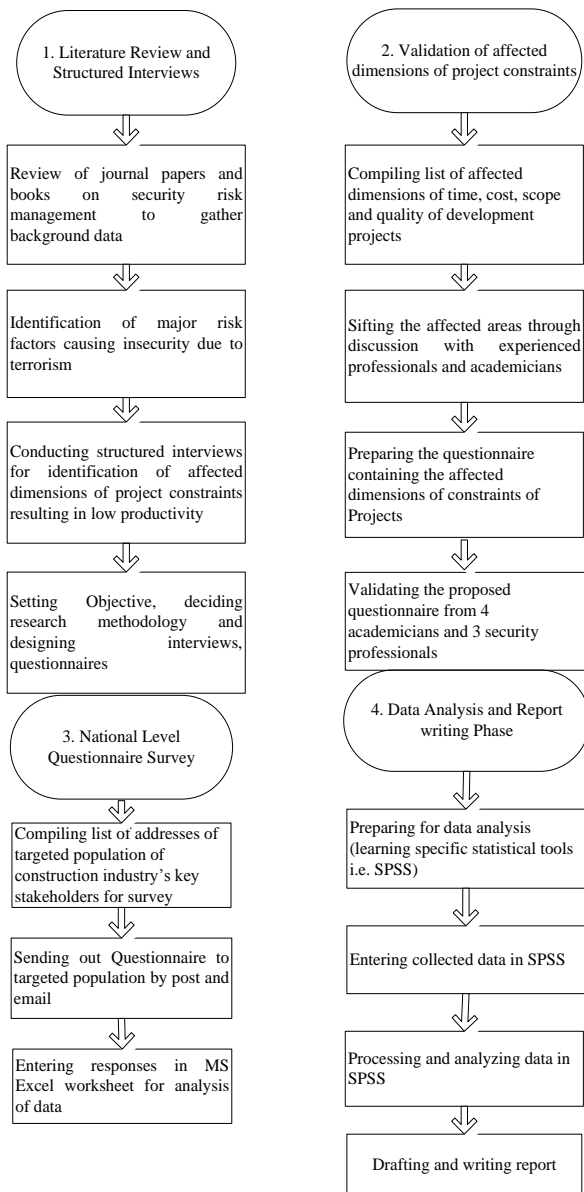


Figure 3. Research tasks leading to research objectives

A. Research design

We used two pronged approach. First, the research commenced with the intense literature review to identify the affected dimensions of project management objectives due to insecurity due to terrorism. Second, twenty structured interviews were conducted with project managers working in terrorism affected areas to identify the effects of insecurity due to terrorism over project constraints of developmental projects. Further, the identified affected dimensions of project constraints (time, cost, scope and quality) due to insecurity attributable to terrorism resulting in low productivity were modeled as shown in Figure 4.

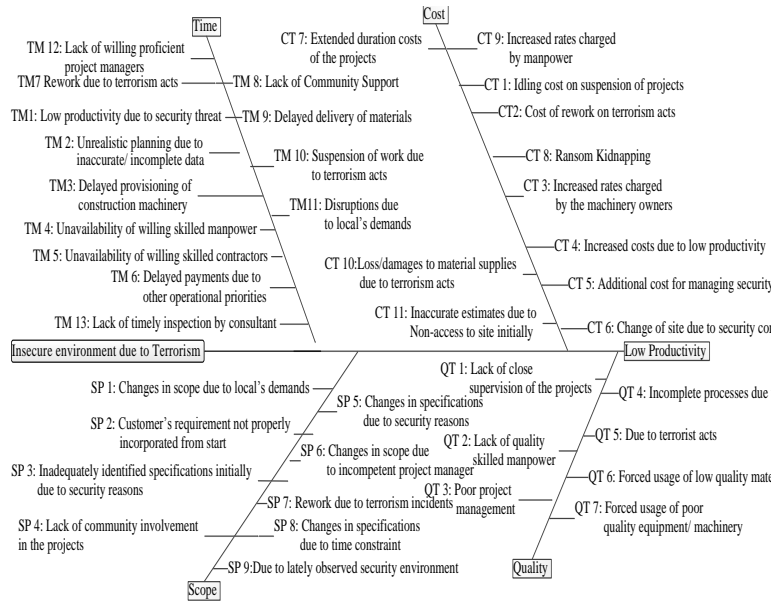


Figure 4. Affected dimensions of project constraints attributable to insecurity due to terrorism affecting productivity

Based on the model in Figure 4, we developed a questionnaire to establish the related affected dimensions of time, cost, scope and quality with a view to ascertain the impact of risk factors generating terrorism over development projects. To measure the criticality of affected dimensions of projects constraints, we used five-point likert scales (shown in Table 2).

Table-2.

Rating system to measure criticality of affected dimensions of projects constraints

Rating	Risk criticality
1	Strongly disagreed
2	Disagreed
3	Neutral
4	Agreed
5	Strongly agreed

We got the measurement instrument evaluated by four academics and three field expert project managers for establishing the face/content validity. The construct validity of the instrument was checked with IBM SPSS-18 software package. Inter-item validity of the questionnaires was established through factor analysis. The instrument was slightly modified as a result..

Sample Selection

We used the non-random sampling design with judgmental sampling, i.e. selection of sample on the basis of researcher judgment. Pakistan is a security affected country. Almost every geographic region of the country has been directly or indirectly affected by terrorism. Therefore we planned the sample to be constituted from entire Pakistan based on the severity of terrorism in each part. The province wise data of suicide attacks and bomb blasts is as shown in Table 3 below ¹⁵:

Table-3. Year wise state of Suicide Attacks/ Bomb Blasts in Pakistan from year 2001-2011

Year	KPK	Baluchi -stan	Sindh	Punjab	FATA
2001	4/7	1/9	1/13	2/2	9/24
2002	2/14	2/3	1/22	1/2	15/22
2003	6/15	1/13	2/5	1/6	13/28
2004	4/43	3/57	2/11	4/13	1/33
2005	1/98	1/154	1/2	1/14	2/48
2006	4/10	1/214	2/1	3/12	1/36
2007	27/124	3/243	1/3	10/18	13/141
2008	32/221	1/242	1/1	12/17	13/92
2009	47/195	2/134	1/2	19/29	6/112
2010	26/137	4/101	1/9	6/20	12/190
2011	23/198	4/194	3/31	3/13	8/185
Total	176/1062	23/1364	16/100	62/146	93/911

Based on the number of incidences of terrorism acts i.e. bomb blasts and suicide attacks, Malik *et. al.*, (2104) categorized Pakistan in high security zone, medium security zone and low security zone. Correspondingly we planned to collect the data proportionately from each zone as follows:

- High Security Zone- KPK (30%), Baluchistan (30%) and FATA (20%)
- Medium Security Zone- Punjab (10%)
- Low Security Zone- Sindh (10%)

The selected sample population constituted key stakeholders of developmental project i.e. sponsors, consultants and contractors registered with Pakistan Engineering Council. Based on above consideration, following matrix (Table 4) is developed for the sample:

Table-4. Locations and constituents of sample

Location	Clients (30%)	Consultants (30%)	Contractors (40%)
KPK (30%)	√	√	√
Baluchistan (30%)	√	√	√
FATA (20%)	√	√	√
Sindh (10%)	√	√	√
Punjab (10%)	√	√	√

The project managers of all the three organizations were contacted for responding. The questionnaires were handed over in person or sent through post and email.

Sample Size

Keeping the level of confidence at 95%, a sample size of 70 for this study was given by Power and Precision software. A sample size of 30 was selected from the above mentioned population for a pilot study. The instrument was slightly modified based on the results of pilot study.

The survey was carried out from April to July 2013 targeting the above mentioned population. A total of 110 questionnaires were sent out, of which 81 valid replies were received.

Data Analysis Techniques

We analyzed the collected data using SPSS- 18. Statistical tests/ techniques used for data analysis were:

- Reliability analysis
- Sample Population mean
- Relative Importance Index (RII)

III. RESULT AND ANALYSIS

The data was collected from the locations as discussed above in the proportions as shown in Figure 5 below.

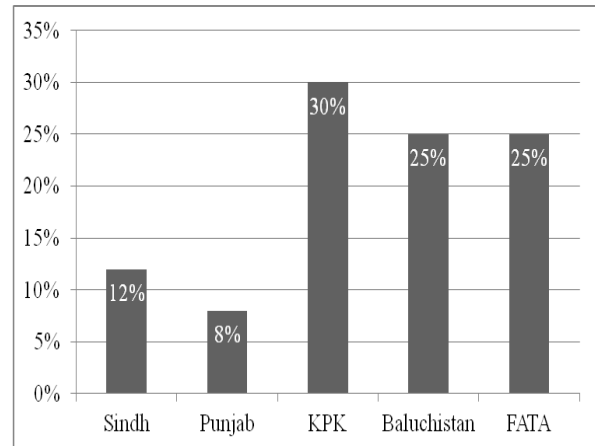


Figure 5. Proportions of data collected from different provinces

A. Cronbach's alpha

Cronbach alpha internal reliabilities were assessed for each scale. Reliabilities were: Overrun time, $\alpha = 0.860$; overrun cost, $\alpha = 0.866$ change in scope, $\alpha = 0.878$ and low quality, $\alpha = 0.464$ thereby indicating high internal construct consistency and reliability.

B. Overall ranking of the identified risks

The risks were ranked based upon the mean score and their relative importance index. The same is shown in Table 7.

Table 7: Mean Score and overall ranking of the identified risks (n=81)

Code	Affected Dimension	Mean	Std Dvn	RII	Rank
TM 8	Lack of local community support	4.67	0.50	0.93	1
QT 7	Forced usage of poor quality	4.62	0.72	0.92	2

Code	Affected Dimension	Mean	Std Dvn	RII	Rank
	equipment/ machinery				
TM 12	Lack of willing proficient Project Manager	4.57	0.55	0.91	3
TM 5	Unavailability of willing skilled contractors	4.56	0.92	0.91	4
TM 10	Suspension due to terrorist acts	4.51	0.73	0.90	5
TM 11	Disruptions due to local's demands	4.51	0.74	0.90	6
QT 1	Lack of close supervision of projects by consultants	4.68	0.54	0.90	7
SP 4	Lack of community involvement	4.49	0.78	0.90	8
TM 7	Rework due to terrorism incidents	4.47	0.79	0.89	9
CT 5	Additional costs for managing of security	4.40	0.80	0.88	10
CT 1	Idling cost on suspension of projects	4.37	0.80	0.87	11
QT 4	Incomplete processes due to time constraint	4.28	0.91	0.86	12
TM 4	Unavailability of local skilled manpower	4.27	1.06	0.85	13
TM 1	Low productivity due to insecure environment	4.27	1.06	0.85	14
CT 10	Loss/ damages to material supplies due to terrorism acts	4.27	1.06	0.85	15

Code	Affected Dimension	Mean	Std Dvn	RII	Rank
SP 6	Due to incompetent project manger	4.27	0.99	0.85	16
TM 13	Lack of timely inspections by consultant	4.23	0.94	0.85	17
QT 5	Due to damages by terrorist acts	4.19	0.84	0.84	18
CT 11	Inaccurate cost estimates due to inaccess to site because of security reasons	4.17	1.01	0.83	19
CT 7	Additional costs attributable to extended duration of the projects	4.09	1.15	0.82	20
QT 3	Poor project management	4.09	1.12	0.82	21
TM 2	Unrealistic planning	4.07	0.91	0.81	22
SP 1	Due to local's demand	4.05	1.18	0.81	23
TM 6	Delayed payments due to other operation priorities	4.04	1.16	0.81	24
CT 9	Increased rates charged by manpower	4.01	0.84	0.80	25
QT 2	Lack of quality skilled manpower	4.01	1.15	0.80	26
CT 3	Increased rates of machinery due to involved security risk	3.98	0.87	0.80	27
CT 8	Ransom kidnapping	3.98	1.00	0.80	28
TM 9	Delayed delivery of materials	3.96	1.08	0.79	29
CT 2	Cost of rework on account of terrorism acts	3.81	0.96	0.76	30

Code	Affected Dimension	Mean	Std Dvn	RII	Rank
CT 4	Increased costs due to low productivity	3.77	0.88	0.75	31
CT 6	Change of site due to security reasons	3.73	0.92	0.75	32
TM 3	Delayed provisioning of construction machinery	3.64	0.91	0.73	33
SP 7	Rework due to terrorism acts	3.54	0.95	0.71	34
QT 6	Forced usage of low quality materials	3.52	1.09	0.70	35
SP 9	Due to lately observed security environment	3.48	1.05	0.70	36
SP 8	Due to time constraint	3.41	1.14	0.68	37
SP 2	Customer's requirements not being incorporated properly	3.37	0.98	0.67	38
SP 5	Due to security reasons	3.37	0.90	0.67	39
SP 3	Unrealistic preliminary planning due to insecure environment	3.16	1.18	0.63	40

IV. DISCUSSION

The top five factors are discussed here.

A. Delay in Time due to Lack of Community Support

Lack of community support can have a devastating impact on a project especially if you lack it in terrorism affected areas. Owing to the unique culture of those areas, community support is considered a must factor for swift execution of a project. The biggest negative fallout of a non-supportive community could be frequent stoppages of work which can delay a project for a considerable time frame. The stoppages may be a result of not giving access to certain area by a community, non-cooperation in terms of material, manpower or emotional

support, restriction to collect material from a nearby quarry site.

B. Poor Quality due to Forced Usage of Inferior Equipment/ Plant/ Machinery

Keeping aside other factors, good quality can be achieved by using best quality equipment, plant and other machinery which most of the time is non-existent in terrorism affected areas. Hence a project manager has to make best use of the available resources and may have to compromise on quality to some extent if his prime focus is on low cost and saving time.

C. Delay in Project due to Lack of Willing Proficient Project Manager

Owing to the precarious security situation, lack of basic living facilities, low pay-packages and uncertainties in achieving success of projects in terrorism affected areas, proficient project managers are reluctant to undertake projects of such areas. Proficient project managers can always seek employment opportunities elsewhere and are really difficult to be found in insecure environment. Projects are delayed not only due to wastage of time in finding a proficient project manager but also non-conformance of best project management practices by the available project manager.

D. TM 5- Unavailability of Willing Skilled Contractor

Tribal areas have an acute shortage of skilled contractors particularly specialty contractors. Therefore, project face considerable delay especially when a contractor either leaves the project suddenly or when there is an immediate requirement to hire a new contractor due to poor performance of an old one. Poorly skilled contractors are unable to foresee, plan and execute a project efficiently. Therefore, these contractors may cause frequent stoppages due to failure in timely procurement of equipment and material, delay in forwarding check requests and other approval documents, frequent reworks due to bad quality and poor application of project management best practices. All of this would finally result in the delay of a project.

E. TM 10- Suspension due to Terrorist Acts

FATA is badly affected by acts of terrorism especially in the post 9/11 era. While affecting other areas of society, the changed socio-political environment has a devastating effect on the development projects as well. Notwithstanding these acts, projects are being undertaken but facing time delays owing to frequent stoppages, damage to men and material and non-availability of ample resources in a timely manner. Till the time a stable security situation prevails, timely completion of projects would be a tough asking.

V. LIMITATIONS

The study has been carried out in an environment of intense insecurity due to terrorism and the results are based upon the opinions of project managers having firsthand experience of development projects in insecure environment due to terrorism. Although the sample was collected from different parts of the country representing different cultures, however the results may be inflated due to common source bias.

VI. CONCLUSION

Development projects by virtue of their dynamic environment are subject to changes in time, cost, scope and quality plans. Various researchers identified and studied numerous factors contributing to those changes in the project plans. However, the impact of insecurity due to terrorism on development projects has traditionally been looked as force majeure and not been studied much. This study was conducted with the aim to identify the factors affecting productivity of development projects attributable to insecurity due to terrorism. Affected dimensions of productivity identified from the literature and structured interviews of project management professional were assessed for criticality through a national level survey of the project management professional working in or experienced of working in terrorism affected areas. Top ten factors out of thirty nine were found to be delay in time due to lack of community, poor quality due to forced usage of inferior equipment/ plant/ machinery, delay in project due to lack of willing proficient project manager, unavailability of skilled contractors, suspension due to terrorism acts, disruptions due to local's demands, poor quality due to lack of supervision by the consultants, changes in scope due to lack of community involvement, delay in time because of rework due to terrorism incidents, and cost overrun due to uncertain costs for managing security. The findings of this study might be helpful in increasing the productivity of infrastructure development projects initiated in terrorism affected areas by addressing these issues.

- [16] Malik, M. S. A., Sandholzer, M., Khan, M. Z., and Akbar, S. (2014). Identification of Risk Factors Generating Terrorism in Pakistan. *Terrorism and Political Violence*, 0:1–20

REFERENCES

- [1] Shen, L.Y., 1997. Project risk management in Hong Kong. *International Journal of Project Management*, 15, 101-105.
- [2] Flanagan, R., and Norman, G. (1993). *Risk management and construction*: Blackwell Scientific Oxford.
- [3] Perry, J.G. and Hayes, R.W. (1986) Risk and its management in construction projects. *Proceedings of Institution of Civil Engineers*, Part 1, 78, 499–521.
- [4] Abdalla M. Odeh and Hussien T. Battaineh (2002), Causes of construction delay: traditional contract, *International Journal of Project Management*. 20: 67-73.
- [5] FIDIC, 17.3, 1999. Red Book, Fédération Internationale des Ingénieurs-Conseils, Geneva, Switzerland
- [6] FIDIC, 19.1, 1999. Red Book, Fédération Internationale des Ingénieurs-Conseils, Geneva, Switzerland
- [7] FATA, 2005. In 'The history of FATA' last accessed on 25 Feb 2011. Retrieved from www.fata.gov.pk
- [8] Interviews, 2011. Interviews with Project Managers experienced in project management in terrorism affected areas.
- [9] Gill, K.P.S, 2011. Terrorists incidences in Pakistan. Retrieved June 8, 2011 from <http://www.satp.org>.
- [10] Ibid
- [11] Akintoye, A.S. and MacLeod, M.J., (1997). Risk analysis and management in construction. *International Journal of Project Management*, 15(1), 31-38.
- [12] Lyons, T. and Skitmore, M., (2004). Project risk management in the Queensland engineering construction industry: a survey. *International Journal of Project Management*, 22(1), 51-61.
- [13] See note 1 above.
- [14] Tang, W., Qiang, M., Duffield, C., Young, D., and Lu, Y., (2007). Risk Management in the Chinese Construction Industry. *Journal of Construction Engineering and Management*, 133(12), 944-956.
- [15] See note 9 above.

Auhtors Index

Abbasian, A. R.	291	Fezari, M.	275	Kostelecký, J.	85
Abbatantuono, G.	89, 197	Filip, F.-C.	203	Kotev, V. K.	174
Adewole, K. K.	297	Finaev, V.	17, 28, 211	Koutsomichalis, A.	61
Alonso-Montes, C.	34	Florut, S. C.	155	Kozak, V.	125
Arapatsakos, Ch.	178	Fofiu, M.	93, 247	Kudaibergenov, S.	80
Auzins, J.	66	Foti, D.	105	La Scala, M.	89, 197
Babankov, V. A.	137	Garcia, I.	34	Lagomarsino, S.	147
Barg, M. A.	137	Gherfi, K.	165	Láník, J.	264
Bartolozzi, F.	77	Giannoccaro, N. I.	105	Lazar, C.	285
Behmanesh, R.	303	Gomes, G.	117	Mahfoud, H.	309
Beloglazov, D.	17, 28, 211	Hamnabard, Z.	291	Major, S.	143
Bendjama, H.	165	Hasif, M.	241	Malik, M. S. A.	313
Bezděk, A.	85	Hobst, L.	125	Mărăscu-Klein, V.	203
Bindean, I. A.	93, 247	Horváth, G.	185	Mastorakis, N. E.	297
Blagikh, E.	80	Houassine, H.	221	Melcher, J.	264
Boukroune, S.	165	Hubálovský, S.	143	Melnikovs, A.	66
Boviatsis, J.	23	Ibrayeva, Z.	80	Merinska, D.	101, 281
Bruno, S.	89, 197	Idiou, D.	165	Moulahoum, S.	221
Burde, G. I.	191	Ivorra, S.	105	Moussaoui, D.	221
Burdinsky, I. N.	252	Jakl, V.	143	Nagornov, O. V.	98
Caldas, R. B.	169	Janushevskis, A.	66	Nagy-Gyorgy, T.	155
Cetin, S.	41	Janushevskis, J.	66	Nasibullayev, I. Sh.	191
Cikrle, P.	264	Kalendova, A.	101	Nauman, S.	313
Contreras, I. S. D.	226	Kandeva, M. K.	270	Neto, A. A. S. C.	169
Costa, A. A. R.	169	Karastoyanov, D. N.	174, 270	Neto, P. D. A.	169
Dan, D.	110	Karmazínová, M.	264	Neves, J.	117
Darlis, N.	258	Kechagias, J.	61	Ntintakis, I.	61
De Santis, D.	89, 197	Khudzari, A. Z. M.	258	Osman, K.	258
Diaconu, D.	155	Klokočník, J.	85	Otcheskiy, S. A.	252
Diaferio, M.	105	Kobersy, I.	28, 211	Pantokratoras, I.	178
Dillon, J.	258	Kornaev, A.	72	Partene, E.	93, 247
Dursun, M.	217	Kornaeva, E.	72	Paspalakis, E.	23
Elbarkany, A.	309	Kosenko, E.	17, 28	Pataki, A.	185
Elbiyaali, A.	309	Kosionis, S. G.	23	Patrascioiu, C.	285
Fekete-Nagy, L.	247	Kostadinov, K. G.	270	Penchev, T. N.	174

Piscitelli, C.	129	Sbrizzai, R.	197	Syafalny, S.	241
Polandov, I. H.	137	Selicato, F.	129	Szczepanik, R.	160
Poór, P.	233	Selicato, S.	129	Taif, Z.	275
Pospisil, M.	281	Shafii, N. S.	258	Terzis, A. F.	23
Pshikhopov, V.	48	Shapovalov, I.	17, 28, 211	Tesarikova, A.	101, 281
Puganeshwary, P.	241	Silva, C. J. M.	226	Todut, C.	110
Rahimipour, M. R.	291	Šimon, M.	233	Vala, J.	125
Ramezani, A.	34	Soloviev, V.	17, 28, 211	Vaxevanidis, N.	61
Remaki, L.	34	Stamatescu, G.	285	Vicente, H.	117
Rodrigues, F. C.	169	Starostin, N. V.	98	Vítek, L.	264
Rokni, F.	303	Stavropoulos, P.	61	Zargaryan, J.	17, 211
Rotondo, F.	129	Stoian, V.	93, 110, 155	Zhalij, A.	191
Rozainy, M. A. Z. M. R.	241	Stoian, V.	247		
Savin, L.	72	Supriyanto, E.	258		